NASA/CR–20205005698

Subsonic Ultra Green Aircraft Research: Phase III – Mach 0.75 Transonic Truss-Braced Wing Design

Christopher K. Droney, Anthony J. Sclafani, Neal A. Harrison,
Adam D. Grasch, and Michael D. Beyar
Boeing Research and Technology, Huntington Beach, California

September 2020

NASA STI Program . . . in Profile

Since its founding, NASA has been dedicated to the advancement of aeronautics and space science. The NASA scientific and technical information (STI) program plays a key part in helping NASA maintain this important role.

The NASA STI program operates under the auspices of the Agency Chief Information Officer. It collects, organizes, provides for archiving, and disseminates NASA's STI. The NASA STI program provides access to the NTRS Registered and its public interface, the NASA Technical Reports Server, thus providing one of the largest collections of aeronautical and space science STI in the world. Results are published in both non-NASA channels and by NASA in the NASA STI Report Series, which includes the following report types:

- TECHNICAL PUBLICATION. Reports of completed research or a major significant phase of research that present the results of NASA Programs and include extensive data or theoretical analysis. Includes compilations of significant scientific and technical data and information deemed to be of continuing reference value. NASA counter-part of peer-reviewed formal professional papers but has less stringent limitations on manuscript length and extent of graphic presentations.

- TECHNICAL MEMORANDUM. Scientific and technical findings that are preliminary or of specialized interest, e.g., quick release reports, working papers, and bibliographies that contain minimal annotation. Does not contain extensive analysis.

- CONTRACTOR REPORT. Scientific and technical findings by NASA-sponsored contractors and grantees.

- CONFERENCE PUBLICATION. Collected papers from scientific and technical conferences, symposia, seminars, or other meetings sponsored or co-sponsored by NASA.

- SPECIAL PUBLICATION. Scientific, technical, or historical information from NASA programs, projects, and missions, often concerned with subjects having substantial public interest.

- TECHNICAL TRANSLATION. English-language translations of foreign scientific and technical material pertinent to NASA's mission.

Specialized services also include organizing and publishing research results, distributing specialized research announcements and feeds, providing information desk and personal search support, and enabling data exchange services.

For more information about the NASA STI program, see the following:

- Access the NASA STI program home page at http://www.sti.nasa.gov

- E-mail your question to help@sti.nasa.gov

- Phone the NASA STI Information Desk at 757-864-9658

- Write to:
  NASA STI Information Desk
  Mail Stop 148
  NASA Langley Research Center
  Hampton, VA 23681-2199

NASA/CR–20205005698

Subsonic Ultra Green Aircraft Research: Phase III – Mach 0.75 Transonic Truss-Braced Wing Design

Christopher K. Droney, Anthony J. Sclafani, Neal A. Harrison,
Adam D. Grasch, and Michael D. Beyar
Boeing Research and Technology, Huntington Beach, California

National Aeronautics and
Space Administration

Langley Research Center
Hampton, Virginia 23681-2199

Prepared for Langley Research Center under
Contract NNL10AA05B /NNL14AB51T

September 2020

Abstract

This design report summarizes the Transonic Truss-Braced Wing (TTBW) work accomplished by the Boeing Subsonic Ultra-Green Aircraft Research (SUGAR) team during the time period of July 2014 through October 2016 under SUGAR Phase III.

In Phase II, aerodynamic estimates were derived from conceptual methods that predict drag based on a database of designed shapes. An empirical database for TTBW strut-wing intersections is not known to exist and this study is oriented toward gaining the prerequisite data for lower-order design space exploration by exercising higher-order tools and ultimately wind tunnel test. The detailed design exercise conducted during Phase III utilized modern Navier-Stokes-based computational fluid dynamics tools and determined vehicle cruise drag to be within 1% of the Phase II conceptual estimate, however, some disagreements exist on a component-by-component basis. Through the use of these high-fidelity methods, uncertainty in the predicted fuel consumption of the truss-braced wing configuration has been greatly reduced.

The main strut was found to account for approximately 10% of the total airplane drag, with interference effects between the wing and strut making up about 1% of the airplane drag. Aerodynamic operability requirements were met at the cruise Mach number, but some uncertainty remains regarding buffet margin at the maximum operating Mach number. A key source of this uncertainty is a lack of confidence in the applicability of buffet prediction methods that were empirically-derived using data from cantilever wings. In addition, exploration of active technology that can be used to mitigate buffet at Mach numbers higher than cruise without impacting dispatch reliability have not been studied. Further investigation into this issue should be considered.

The current TTBW configuration, in conjunction with technology insertion outlined in previous phases of study, has the potential to reduce fuel consumption by 57% as compared to a consistently sized cantilever configuration with technology levels representative of the 2008 single-aisle fleet. A final truss-braced wing geometry, which is appropriate for a high-speed wind tunnel test, has been generated. A 4.5% scale wind tunnel model has been constructed and tested in the NASA Ames Research Center’s Unitary Plan Wind Tunnel (UPWT) 11-Foot Transonic Wind Tunnel (11-Foot TWT).

Test data shows that drag rise data collected compares well with CFD prediction indicating that interference effects are minimal and that the truss system is not changing the overall cruise speed of the configuration. The stability and control data indicates the configuration compares well with pretest predictions in all areas except spoiler effectiveness at dive Mach number. Here spoilers indicate reversal at low deflections, a phenomenon the test team has experienced in prior configurations that should clear at higher deflections. Test data could not be generated to

verify this due to model load limitations. The drag buildup data shows mixed results with some increments matching and some that do not. The root cause for this has been determined to be an unacceptably high level of surface roughness that is unable to be closed via post-test analysis. This also caused the overall drag levels of the wind tunnel test data to be offset from the test predictions by 30 counts at the design lift coefficient and Mach number. It is recommended the model be stripped of paint, polished, and a second tunnel entry be made.

The test team employed several methods of data collection including PSP, IR, and MDM data. These techniques were important for test due to the limited surface pressure data available from the physical pressure taps. In the future, surface roughness caused by using these techniques should be carefully considered during the test planning phase. Recommendations for testing using these techniques have been developed.

Acknowledgements

This project and report reflect the combined efforts of the Boeing SUGAR team. Funding for this effort is provided by the NASA Advanced Air Vehicles Program, through the Advanced Air Transport Technology Project. The contract number is NNL10AA05B task order NNL14AB51T.

The team would like to thank Sally Viken and Greg Gatlin of the NASA Langley Research Center for their guidance as the NASA Contracting Officer Technical Representatives and Boeing advisors Marty Bradley, Chet Nelson, Dino Roman and Dave Pitera. In particular, credit for this work is due to the Boeing team members noted below.

Additional Boeing Team Members:

Andreas Grothues
Antonio Gonzales
Christopher Hill
Daniel Chen
David Bruns
David Lazzara
Edward Lawson
Eric Dickey
Jeffrey Jonokuchi
John Winkler
Kareem El-Gohary
Kevin Fisk
Lie-Mine Gea
Norman Princen
Peter Camacho
Robert Creason
Ryan Polito
Timothy Allen

Table of Contents

Abstract i
Acknowledgements iii
Table of Contents iv
List of Tables, Figures and Acronyms vii
  Tables vii
  Figures vii
  Acronyms xv
1.0 Introduction 1
2.0 Truss-Braced Wing Configuration Design 3
  2.1 SUGAR High Configuration Evolution 3
  2.2 SUGAR High Configuration Description 4
    2.2.1 Integration 5
    2.2.2 Wing 7
    2.2.3 Main Strut and Jury Strut 11
    2.2.4 Alternate Strut 15
    2.2.5 Vertical Fin 16
    2.2.6 Horizontal Stabilizer 17
    2.2.7 Fuselage 17
    2.2.8 Landing Gear 20
    2.2.9 Propulsion 21
3.0 Aeroelastic Analysis 23
  3.1 Wing FEM Description 23
  3.2 Strut/Jury FEM Description 25
  3.3 Center Body/Sponson FEM Description 28
  3.4 Finite Element Model Integration 30
  3.5 Mass Case Descriptions 32
  3.6 Aerodynamic Model and Corrections 32
  3.7 Load Conditions 34
  3.8 Structural Sizing and Optimization 35
  3.9 Stress/Buckling Sizing Results 36
  3.10 Stress/Buckling Sizing Conclusions 53
  3.11 Structural Optimization with Flutter Constraints 53
  3.12 Aeroelastic Conclusions 61
4.0 Aerodynamic Design 63
  4.1 Methodology 64
    4.1.1 Strut Airfoil Design and Optimization 65
    4.1.2 3D Design and Analysis Toolset 68

- 4.1.3 CFD Grid Generation and Post Processing ... 69
- 4.2 Design Overview ... 70
  - 4.2.1 Summary of 765-095-RF (Rev-F) Design Cycle ... 71
  - 4.2.2 Summary of 765-095-RG (Rev-G) Design Cycle ... 81
  - 4.2.3 Summary of 765-095-RH (Rev-H) Design Cycle ... 90
  - 4.2.4 Summary of 765-095-RJ (Rev-J) Design Cycle ... 96
- 4.3 Final Configuration Aerodynamic Performance ... 105
  - 4.3.1 Flight Reynolds Number Results ... 109
  - 4.3.2 Reynolds Number Effects ... 113
  - 4.3.3 Alternate Strut ... 117
- 5.0 Stability & Control Design and Analysis ... 125
  - 5.1 Longitudinal S&C ... 125
  - 5.2 Directional S&C ... 128
  - 5.3 Lateral S&C ... 129
- 6.0 Configuration Analysis and Final Performance ... 131
  - 6.1 Aerodynamics ... 131
    - 6.1.1 High Speed ... 131
    - 6.1.2 Low Speed ... 134
  - 6.2 Mass Properties ... 139
  - 6.3 Performance and Sizing ... 140
    - 6.3.1 Sizing Requirements ... 141
    - 6.3.2 Sizing Results ... 142
- 7.0 Wind Tunnel Test and Design Validation ... 148
  - 7.1 Test Introduction ... 148
  - 7.2 Test Facility and Envelope ... 149
  - 7.3 Model Description ... 151
  - 7.4 Wind Tunnel Data Reduction ... 153
    - 7.4.1 Pressure Sensitive Paint (PSP) ... 154
    - 7.4.2 Infrared (IR) Imaging ... 155
    - 7.4.3 Tunnel Corrections ... 155
    - 7.4.4 Model Roughness Effects ... 158
    - 7.4.5 Model Deformation Measurement (MDM) System Results ... 169
    - 7.4.6 Boundary Layer Trip Effects ... 171
  - 7.5 Post-Test CFD Investigations ... 173
    - 7.5.1 Model Twist Correction ... 173
    - 7.5.2 Sting Effects ... 181
  - 7.6 Performance Predictions ... 196
    - 7.6.1 Reynolds Number Effects ... 196
    - 7.6.2 Baseline and Alternate Strut Performance ... 197

7.6.3 Additional Component Increments ... 198
7.6.4 Drag Divergence and Long Range Cruise ... 200
7.6.5 Final CFD Predictions vs. Test Data ... 201
7.7 Stability and Control ... 202
7.7.1 Aileron Effectiveness ... 202
7.7.2 Spoiler Effectiveness ... 204
7.7.3 Horizontal Tail Effectiveness ... 205
7.7.4 Lateral Directional ... 206
7.8 Test Conclusions ... 207
7.9 Recommendations for future testing ... 208
7.9.1 Model Deformation Measurement System ... 209
7.9.2 Infrared Imagery ... 209
7.9.3 Pressure Sensitive Paint ... 209
7.9.4 Model Design Changes ... 210
7.9.5 Computational modeling ... 210
8.0 Future Technical Milestones ... 211
8.1 High Speed Design ... 211
8.2 Low Speed Design ... 211
8.3 Additional Risk Mitigation Tasks ... 212
9.0 Summary ... 213
9.1 Technical Results ... 214
9.2 Conclusions ... 215
9.3 Recommendations ... 216
References ... 217
Appendix A – Wind Tunnel Data ... 1

List of Tables, Figures and Acronyms

Tables

Table 2.1 – 765-095 (Mach 0.7) revision history 4
Table 2.2 – Body Axis Component Origins (units are inches) 5
Table 2.3 – Principal characteristics 7
Table 2.4 – Wing reference geometry 9
Table 2.5 – Main strut spar locations 11
Table 2.6 – Jury strut spar locations 11
Table 2.7 – SUGAR High (765-095 Rev-J) vertical tail planform parameters 17
Table 2.8 – SUGAR High (765-095 RJ) horizontal planform parameters 17
Table 2.9 – gFan+ key characteristics 22
Table 3.1 – Wing Stiffness Properties 25
Table 3.2 – Payload and Fuel Combinations 32
Table 3.3 – Overflow Correction Conditions 34
Table 3.4 – Sized Structure Weight Summary (weights in pounds) 53
Table 3.5 – Flutter Sized Structural Weight Summary (weights in pounds) 61
Table 5.1 – Engine-Out Minimum Control Speed Results 129
Table 6.1 – 765-095 Rev-J High Speed Buildup 132
Table 6.2 – 765-095 Rev-H Group Weight Statement 139
Table 6.3 – 765-095 Rev-D and Rev-J Mission Performance 144
Table 6.4 – 765-095 Rev-D and Rev-J Mission Performance Comparison 145
Table 7.1 – Test Operating Conditions 151
Table 7.2 – Configuration Codes used in wind tunnel testing 153

Figures

Figure 2.1 – Phase II configuration evolution 3
Figure 2.2 – Phase III configuration evolution 4
Figure 2.3 – SUGAR High (765-095 Rev-J) geometry development 5
Figure 2.4 – SUGAR High Mach 0.745 (765-095 Rev-J) general arrangement 6
Figure 2.5 – SUGAR High (765-095 Rev-D) planform (projected, units are inches) 8
Figure 2.6 – Wing corner point drawing (wing reference plane, units are inches) 10
Figure 2.7 – SUGAR main strut structural concept 12
Figure 2.8 – SUGAR High (765-095 Rev-J) strut corner points (units are inches) 12
Figure 2.9 – Jury strut corner point drawing (jury strut reference plane, units are inches) 13
Figure 2.10 – Main strut outboard attachment concept 13
Figure 2.11 – Main strut outboard attachment structural arrangement overview 14
Figure 2.12 – Jury strut to main strut attachment concept 15

Figure 2.13 – Alternate strut structural concept 16
Figure 2.14 – SUGAR High (765-095 Rev-J) vertical tail planform (units are inches) 16
Figure 2.15 – SUGAR High (765-095 Rev-J) horizontal planform (units are inches) 17
Figure 2.16 – 765-095 fuselage cross section (units are inches) 18
Figure 2.17 – SUGAR High (765-095) layout of passenger accommodations 19
Figure 2.18 – SUGAR High (765-095 Rev-J) landing gear layout 20
Figure 2.19 – SUGAR High (765-095 Rev-J) landing gear arrangement 21
Figure 2.20 – gFan+ concept layout 22
Figure 3.1 – Wing FEM Geometry 24
Figure 3.2 – Wing Rib and Spar Caps Modeled as Beam Elements 24
Figure 3.3 – Wing Rib/Spar Webs and Strut and Jury Attach 25
Figure 3.4 – Strut Skins 26
Figure 3.5 – Strut Webs 26
Figure 3.6 – Titanium Splitter Plate 27
Figure 3.7 – Strut Rib and Spar Caps 27
Figure 3.8 – Jury Skins, Webs, and Caps 28
Figure 3.9 – Sponson FEM 29
Figure 3.10 – Center Body FEM 29
Figure 3.11 – Primary vertical connection between wing and body 30
Figure 3.12 – Primary forward/aft connection between wing and body 31
Figure 3.13 – Primary lateral connection between wing and body 31
Figure 3.14 – Integrated FEM 31
Figure 3.15 – Doublet Lattice Aerodynamic Model 33
Figure 3.16 – Section Lift Curve Slope and AC Comparison M=.745 33
Figure 3.17 – Sectional Lift and Moment Comparison M =.745, C_L = .73 34
Figure 3.18 – Limit Loads 2.5g and -1g Balance Maneuvers 35
Figure 3.19 – Wing Sized Upper (Top) and Lower (Bottom) Skin Thickness 37
Figure 3.20 – Sized Strut Upper (Top) and Lower (Bottom) Skin Thickness 38
Figure 3.21 – Wing Upper (Top) and Lower (Bottom) Skin Failure Mode 39
Figure 3.22 – Strut Upper (Top) and Lower (Bottom) Skin Failure Mode 40
Figure 3.23 – Wing Upper (Top) and Lower (Bottom) Skin Stringer Web Height 41
Figure 3.24 – Strut Upper (Top) and Lower (Bottom) Skin Stringer Web Height 42
Figure 3.25 – Wing Upper (Top) and Lower (Bottom) Skin Stringer Web Thickness 43
Figure 3.26 – Strut Upper (Top) and Lower (Bottom) Stringer Skin Web Thickness 44
Figure 3.27 – Wing Upper (Top) and Lower (Bottom) Skin Stringer Cap Width 45
Figure 3.28 – Strut Upper (Top) and Lower (Bottom) Skin Stringer Cap Width 46
Figure 3.29 – Wing Upper (Top) and Lower (Bottom) Skin Stringer Cap Thickness 47
Figure 3.30 – Strut Upper (Top) and Lower (Bottom) Skin Stringer Cap Thickness 48
Figure 3.31 – Wing Upper (Top) and Lower (Bottom) Skin Stringer Foot Width 49

Figure 3.32 – Strut Upper (Top) and Lower (Bottom) Skin Stringer Foot Width 50
Figure 3.33 – Wing Upper (Top) and Lower (Bottom) Skin Stringer Foot Thickness 51
Figure 3.34 – Strut Upper (Top) and Lower (Bottom) Skin Stringer Foot Thickness 52
Figure 3.35 – Baseline Model Updates 55
Figure 3.36 – Upper Wing Skin Membrane Stiffness Comparisons G11 and G12 55
Figure 3.37 – Wing Skin Membrane Stiffness Comparisons Upper G22 and Lower G11 55
Figure 3.38 – Wing Lower Skin Membrane Stiffness Comparisons G12 and Lower G22 56
Figure 3.39 – Flutter Sized Wing Spar and Rib Web Thicknesses 56
Figure 3.40 – Flutter Sized Strut Skin Thicknesses 56
Figure 3.41 – Flutter Sized Strut Spar and Rib Web Thicknesses 57
Figure 3.42 – Flutter Sized Strut Tip Steel Structure Thicknesses 58
Figure 3.43 –Full Fuel Flutter Damping and Frequency Results 58
Figure 3.44 – Reserve Fuel Flutter Damping and Frequency Results 59
Figure 3.45 – Critical Complex Flutter Mode – 3.42 Hz at Dive Speed 59
Figure 3.46 – Primary Bending Mode – 1.64 Hz 60
Figure 3.47 – Primary Torsion Mode – 3.13 Hz 60
Figure 3.48 – Nonlinear Flutter Damping Results 61
Figure 4.1 – SUGAR TTBW Configuration 765-095-RD used as a starting point for the high-fidelity transonic design. 63
Figure 4.2 – Wing and strut defining stations used for strut airfoil design optimization, with critical regions indicated. 66
Figure 4.3 – Required strut box out-of-plane bending stiffness as a function of span. Determined from Phase II FEM analysis. 66
Figure 4.4 – a) Initial guess geometry. Section cl = 0.6874, cd = 0.0208, weight factor = 1.0; b) Optimizer result. Section cl = 0.6874, cd = 0.0173, weight factor = 2.43 67
Figure 4.5 – SUGAR Phase III revision block diagram with primary aerodynamic design focus defined. 70
Figure 4.6 – Configuration nomenclature defined for the high-speed design effort. 71
Figure 4.7 – OVERFLOW solutions comparing initial modification to the WB fairing. Contours on the left of the symmetry plane are Cp, contours on the right are Cf. 72
Figure 4.8 – Wing planform showing defining stations. 72
Figure 4.9 – FLO-22 wing sectional lift distribution at the wing-body design C_L of 0.73. 73
Figure 4.10 – Estimation of Long Range Cruise (LRC) Mach number for a WB configuration. 74
Figure 4.11 – OVERFLOW wing-body LRC Mach number trends. 75
Figure 4.12 – Athena Vortex Lattice (AVL) model created for preliminary wing/strut loading study. 75

Figure 4.13 – Preliminary AVL inviscid results indicated that the same value of the optimum spanwise efficiency factor could be reached with a lifting or Non-lifting strut. 76
Figure 4.14 – Rev-F strut layout showing location of airfoil defining stations. 77
Figure 4.15 – Rev-F wing and strut twist distributions. 77
Figure 4.16 – WBS spanload comparison showing effect of wing twist. 78
Figure 4.17 – Orientation of the off-body flow field interrogation plane. 79
Figure 4.18 – WBS off-body Mach contours showing effect of a local nose-up wing twist change. 79
Figure 4.19 – Baseline Nacelle Geometry 80
Figure 4.20 – History of WBS drag levels showing a continuous reduction over the Rev-G design cycle. 81
Figure 4.21 – Main strut weight-drag Pareto front at 87% strut span 82
Figure 4.22 – Free-Form Deformation (FFD) boxes used for Cart3D adjoint optimization of the wing-strut juncture region. 84
Figure 4.23 – OVERFLOW drag improvement obtained using Cart3D to clean up wing-strut juncture region. 85
Figure 4.24 – Cart3D optimization (Opt001) cleaned up the supersonic flow and the resulting shock system in the juncture region at the mid-cruise design CL of 0.73. Seed Geometry: RG-des04, Final Geometry: RG-des07. 86
Figure 4.25 – The Cart3D optimization Opt001 deformed the lower surface of the wing and the upper surface of the strut in an attempt to minimize drag by removing the juncture shock system. Seed geometry: RG-des04. Final geometry RG-des07. 86
Figure 4.26 – Application of CDISC to inboard strut region smoothed pressure distributions. 87
Figure 4.27 – WB fairing refinement: initial (left) and final (right). 88
Figure 4.28 – Wing-Strut Fairing 88
Figure 4.29 – SUGAR Rev-G jury strut sweep study. 89
Figure 4.30 – An in-depth comparison of the jury strut installation on 765-095-RF (Rev-F) configuration and the RG-des04 configuration highlighted the effect of the strut flowfield on the jury-strut aerodynamics. 90
Figure 4.31 – Rev-H Configuration Development. 91
Figure 4.32 – Example of BUFFET code output for evaluating the susceptibility of the strut to buffet. 92
Figure 4.33 – The strut realignment that occurred at the end of the Rev-H design cycle (765-095-RH) produced a shock in the wing/strut juncture region, which was addressed during the Rev-J design cycle. 93

Figure 4.34 – Simplified alternate strut pylon used for alternate strut offset distance sensitivity study. 94
Figure 4.35 – Process used to create alternate strut geometry for the alternate strut offset distance sensitivity study. 94
Figure 4.36 – Normal Mach comparison on strut upper surface from BUFFET at M_{MO}=0.795 and C_L=0.64. Line color differences are insignificant. 96
Figure 4.37 – Areas of design focus during the Rev-J design cycle. 97
Figure 4.38 – Y-station 570 shows sonic flow in wing/strut juncture for the RJ-des06 configuration and the dashed re-contouring after using CDISC. 98
Figure 4.39 – Inboard upper surface strut pressures were cleaned up through a combination of twist and a redesign of the sponson to strut fairing. M=0.745, CL=0.73. 98
Figure 4.40 – Wing pressure comparison of the initial and near-final wing designs from the Rev-J design cycle. 99
Figure 4.41 – Pressure cuts at various stations across the final jury strut design validated that the jury strut was properly aligned with the local flow. RJ-des31, WBSJNVH configuration. 100
Figure 4.42 – Unequal pressure distributions between each side of the jury showed the influence that the presence of the nacelle-pylon and tail had upon the RJ-des31 jury design. 101
Figure 4.43 – Shock system in the juncture of the wing-pylon-alternate-strut at Mach 0.795 and C_L = 0.64. 102
Figure 4.44 – Initial alternate strut pylon. 103
Figure 4.45 – Alternate strut pylon revision. 104
Figure 4.46 – The Typhoon Fairing (v3 shown) effectively eliminates the flow separation behind the alternate strut pylon. 105
Figure 4.47 – Comparison of wing thickness distribution between the initial wing and the final wing designed for an efficient strut installation. 106
Figure 4.48 – Comparison of 1g wing twist distribution between the initial wing and the final wing designed for an efficient strut installation. 107
Figure 4.49 – Wing and strut spanloads for the final Rev-J WBSJN configuration at the design condition. 108
Figure 4.50 – Final Rev-J wing pressure comparison at the design condition. 109
Figure 4.51 – Tail-off drag polars at flight conditions for the final Rev-J configuration. 110
Figure 4.52 – Trimmed drag polar at flight conditions for the final Rev-J configuration. 111
Figure 4.53 – Tail-off long range cruise (LRC) Mach number for the final Rev-J configuration. 112
Figure 4.54 – Tail-off drag rise curves for the final Rev-J configuration. 112

Figure 4.55 – Effect of C_L on the Long Range Cruise (LRC) Mach number for the final Rev-J configuration. 113
Figure 4.56 – Effect of Reynolds number at Mach = 0.745 on the tail-off idealized drag polars for the final Rev-J configuration. 114
Figure 4.57 – Effect of Reynolds number at C_L = 0.73 on the tail-off drag rise curves for the final Rev-J configuration. 115
Figure 4.58 – Surface pressure and streamlines on the pylon, strut and jury at flight Reynolds number. 116
Figure 4.59 – Surface pressure and streamlines on the pylon, strut and jury at wind tunnel Reynolds number. 116
Figure 4.60 – Effect of lift coefficient on wing-strut juncture flow at the cruise Mach number. 118
Figure 4.61 – Front view of the baseline and alternate strut configurations. 119
Figure 4.62 – Drag polar comparison between alternate strut and strut 765-095-RJ (Rev-J) final configurations. 120
Figure 4.63 – Drag rise comparison of baseline vs. alternate strut. 121
Figure 4.64 – Surface pressure and streamlines of WBA at Mach 0.745 and C_L = 0.73 for flight and wind tunnel Reynolds number. 122
Figure 4.65 – Off-body Mach contour comparison of WBS and WBA configurations at Mach 0.795 and C_L = 0.64. 123
Figure 4.66 – Buffet onset evaluation for the baseline and alternate strut upper surface at Mach 0.795. 124
Figure 4.67 – Final all-up TTBW configuration with off-body flow field parameters indicating a successful design. 124
Figure 5.1 – Horizontal Tail Sizing “Scissor” Plot 126
Figure 5.2 – S&C CG Limits on Airplane Loading Diagram 127
Figure 5.3 – Engine-Out Controllability Plot 128
Figure 5.4 – Roll Control Performance 130
Figure 6.1 – CASES Standard Buildup: CD = $C_{Dp} + C_{Di} + C_{Dc} + C_{Dtrim}$ 131
Figure 6.2 – 765-095 Rev-J – Wing NLF Drag Improvement 133
Figure 6.3 – 765-095 Rev-J – M * L/D Total 133
Figure 6.4 – Leading edge Krueger in the deployed position. 134
Figure 6.5 – Trailing edge flap with flaperon at the max landing deflection. 135
Figure 6.6 – Sample $C_{L,max}$ analysis case using ΔCp-peak criteria. 136
Figure 6.7 – Low speed lift curves with the leading edge Krueger deployed, free-air. 137
Figure 6.8 – Low speed drag polars with the leading edge Krueger deployed, free air. 138
Figure 6.9 – Low speed lift-to-drag ratio with the leading edge Krueger deployed, free-air. 138

Figure 6.10 – Airplane Sizing Using CASES / ModelCenter 140
Figure 6.11 – Payload-Range Requirements 141
Figure 6.12 – 2035 Mission Profile with NextGen Air Traffic Management................................ 142
Figure 6.13 – 765-095 Sized Payload-Range Curve 145
Figure 6.14 – Block Fuel Reduction Compared to NASA Goal 146
Figure 6.15 – Fuel Consumption per Segment 146
Figure 6.16 – Fuel Consumption vs. Range 147
Figure 7.1 – NASA Ames Unitary Plan Wind Tunnel (UPWT) Aerial View 149
Figure 7.2 – NASA Ames 11' Transonic UPWT Test Section 149
Figure 7.3 – Operating Characteristics of the 11' UPWT Transonic Wind Tunnel 150
Figure 7.4 – LB-649A Transonic Truss Braced Wing (TTBW) Model 151
Figure 7.5 – Model Components 152
Figure 7.6 – Model Moment Transfer Diagram.. 152
Figure 7.7 – The left-hand side of the model was coated with pressure-sensitive paint. (on top of the base layer of primer) 154
Figure 7.8 – Comparison of Pressure Sensitive Paint (PSP) with CFD Results 154
Figure 7.9 – The right-hand side of the model was coated with black paint to provide additional contrast for IR imaging. (on top of the base layer of primer) 155
Figure 7.10 – Sample IR image showing aft trip 155
Figure 7.11 – Drag Coefficient Data Corrections for test data (Config 24, Run 381, M=0.745, Re=8.0M/ft)... 156
Figure 7.12 – Lift Coefficient Data corrections for test Data (Config 24, Run 381, M=0.745, Re=8.0M/ft)... 157
Figure 7.13 – Pitching Moment Data Corrections for test data (Config 24, Run 381, M=0.745, Re=8.0M/ft)... 158
Figure 7.14 – Cavity Correction Magnitude (As-built geometry, including aft fuselage fairing. Config. 24, Run 381, M=0.745, Re=8.0M/ft) 158
Figure 7.15 – Admissible roughness for aircraft wings (14) 160
Figure 7.16 – Force and Moment Coefficients comparing the effects of model roughness (Re=4.0M/ft).. 162
Figure 7.17 – Force and Moment Coefficients comparing the effects of model roughness (Re=6.3M/ft).. 164
Figure 7.18 – Force and Moment Coefficients comparing the effects of model roughness (Re=8.0M/ft).. 166
Figure 7.19 – Effects of Roughness on model drag for constant Reynolds Number (approximation)... 168
Figure 7.20 – Comparison of pressure data on the wing (x-axis is chord, y axis is pressure coefficient) 169
Figure 7.21 – Model Deformation Measurement (MDM) System 170

Figure 7.22 – Data acquired by NASA Model Deformation Measurement (MDM) System 171
Figure 7.23 – Infrared (IR) Images of Boundary Layer Trip Effects 172
Figure 7.24 – Effects of Boundary Layer Trip Location 172
Figure 7.25 – Model Deformation Process 173
Figure 7.26 – Non-Linear FEM was used to determine the 1G-to-jig Twist Conversion 174
Figure 7.27 – Post-shim wing and strut twist measurements from TriModels as compared to desired loft show good agreement 175
Figure 7.28 – Wing Twist Distribution from MDM measurements in tunnel within 0.3deg of target 1G distribution 176
Figure 7.29 – Strut twist distribution from MDM measurements has a 0.5deg offset mid-strut 177
Figure 7.30 – Twist correction applied to the 1G (design) wing CFD Grid 178
Figure 7.31 – Twist correction applied to the 1G (design) strut CFD Grid 178
Figure 7.32 – Wing Cp Distribution showing the effect of the MDM twist measurements 179
Figure 7.33 – Strut Cp Distribution showing the effect of MDM twist measurements 179
Figure 7.34 – Wing-Only Configuration twist distribution as compared to 1G target 180
Figure 7.35 – Delta twist distribution (1G vs. measured in tunnel) for wing-only configuration (Run 213, CL=0.7221) 181
Figure 7.36 – Results from CFD Analysis of Re-twisted 'wing-only' case shows very little effect 181
Figure 7.37 – Model experienced a bi-modal instability in yaw 182
Figure 7.38 – Model Installation on Sting (Pretest configuration) 183
Figure 7.39 – Pretest Modeling of sting did not include gap and cavity between fuselage and sting 183
Figure 7.40 – Pretest CFD predictions show forward movement of shock, decrease in drag of 25.5 cts 184
Figure 7.41 – Sting increases incidence on the tail 185
Figure 7.42 – Sting effects on aircraft force and moment coefficients (Pretest CFD) 186
Figure 7.43 – Pretest CFD model did not accurately represent sting-fuselage interface 187
Figure 7.44 – CFD grid modified to model as-built sting-fuselage geometry including cavity (view looking fwd from aft of fuselage) 188
Figure 7.45 – The aft body flow is significantly altered when incorporating the as-built geometry 188
Figure 7.46 – CFD Predictions for Installed Model (all curves for Re=8M/ft) 189
Figure 7.47 – Force and Moment Effects for the As-Built Geometry 190
Figure 7.48 – Incorporation of the 'as-built' sting-fuselage interface (no aft fairing installed) had virtually no effect on tail effectiveness relative to the pretest CFD estimate 190

Figure 7.49 – Drag and Sideforce Coefficient for RANS and URANS Analysis of As-built Configuration (pre-fuselage modification) 191
Figure 7.50 – Snapshots in time from URANS analysis of the as-built geometry shows significant unsteadiness 191
Figure 7.51 – Unmodified Aft Fuselage Geometry 192
Figure 7.52 – Flow from unaltered aft fuselage has a strong flow across the sting 192
Figure 7.53 – Aft fuselage with fairing (red) installed 193
Figure 7.54 – The Aft Fuselage fairing reduces model sting interaction by directing the flow parallel to the sting 193
Figure 7.55 – Effect of the aft fairing on vehicle drag coefficient (Re=8M/ft) 194
Figure 7.56 – Force and Moment Corrections for As-Built Model Geometry (including aft fuselage fairing) 195
Figure 7.57 – Reynolds number effects 196
Figure 7.58 – Strut Increments of Drag Coefficient (Nacelle increment removed from Re=8.0M/ft) 197
Figure 7.59 – Test data comparing baseline and alternate strut performance shows that at the design Mach the alternate strut outperforms the baseline strut at low lift coefficients 198
Figure 7.60 – Alternate Strut Performance -- Effect of Mach number 198
Figure 7.61 – Nacelle and Pylon Drag Coefficient Increments 199
Figure 7.62 – Empennage Increment of Drag Coefficient 200
Figure 7.63 – Component Drag Coefficient Increments from Wind Tunnel Test at Mach=0.745 200
Figure 7.64 – Drag Rise Curves for CFD and Wind Tunnel Test 201
Figure 7.65 – Performance Comparison of Full Configuration – 'Final' CFD Model (including as-built fuselage, aft fuselage fairing, and CL=0.73 aeroelastic twist) vs. Test Data (Run 472) 202
Figure 7.66 – Inboard Aileron Deflections Mach = 0.77, Reynolds Number = 4.0 M/ft 203
Figure 7.67 – Outboard Aileron Deflections, Mach = 0.77, Reynolds Number = 4.0 M/ft 203
Figure 7.68 – Spoiler Deflections Mach = 0.77, Reynolds Number = 4.0 M/ft 204
Figure 7.69 – Spoiler Deflections Mach = 0.87, Reynolds Number = 4.0 M/ft 205
Figure 7.70 – Horizontal Tail Effectiveness, Mach = 0.2, Reynolds Number = 2.8 M/ft 206
Figure 7.71 – Lateral Directional Data 207

Acronyms

ALPHA – Angle of Attack
ALPWICS – Corrected Angle of Attack
AVL – Athena Vortex Lattice
BET – Boeing Equivalent Thrust

BMAP – Boeing Mission Analysis Program
CAD – Computer Aided Design
CASES – Computer Aided Sizing and Evaluation System
C_D – Drag Coefficient
C_{DC} – Compressibility Drag Coefficient
CDFSC – Stability Axis Coefficient of Drag Force Corrected
CDFSU – Stability Axis Coefficient of Drag Force Uncorrected
CDFSUBOY – Stability Axis Coefficient of Drag Force (CDFSUCAV) Corrected for Buoyancy
CDFSUCAV – Stability Axis Coefficient of Drag Force (CDFSU) Corrected for Cavity
CDFSUWIC – Stability Axis Coefficient of Drag Force (CDFSUBOY) Corrected for Wall Interference
C_{Di} – Induced Drag Coefficient
CDISC – Constrained Direct Iterative Surface Curvature
C_{Dp} – Pressure Drag Coefficient
C_f – Skin Friction Coefficient
CFD – Computational Fluid Dynamics
CG – Center of Gravity
CGT – Chimera Grid Toolset
C_L – Lift Coefficient
CLFSC – Stability Axis Coefficient of Lift Force Corrected
CLFSU – Stability Axis Coefficient of Lift Force Uncorrected
CLFSUBOY – Stability Axis Coefficient of Lift Force Corrected for Buoyancy
CLFSUCAV – Stability Axis Coefficient of Lift Force Corrected for Cavity
CLFSUWIC – Stability Axis Coefficient of Lift Force Corrected for Wall Interference
C_M – Pitching Moment Coefficient
CMC – Ceramic Matrix Composite
C_P – Pressure Coefficient
CPMSC – Stability Axis Coefficient of Pitching Moment Corrected
CPMSU – Stability Axis Coefficient of Pitching Moment Uncorrected
CPMSUBOY – Stability Axis Coefficient of Pitching Moment Corrected for Buoyancy
CPMSUCAV – Stability Axis Coefficient of Pitching Moment Corrected for Cavity
CPMSUWIC – Stability Axis Coefficient of Pitching Moment Corrected for Wall Interference
CQUAD4 – Nastran Quadrilateral Plate Element
CRMSC – Stability Axis Coefficient of Rolling Moment Corrected
CYMSC – Stability Axis Coefficient of Yawing Moment Corrected
DF – Ducted Fan
DTE – Divergent Trailing Edge
e – Oswald Efficiency Factor
E – Modulus of Elasticity
EC – Economy Class
EI – Bending Stiffness
eTAPS – Efficient Twin-Annular Premixing Swirler
FA2J – Nastran Lift at Zero Alpha Matrix
FAA – Federal Aviation Administration

FAR – Federal Aviation Regulations
FC – First Class
FEM – Finite Element Model
FFD – Free-Form Deformation
Fn – Engine Thrust
FS – Fuselage Station
FTG – Fitting
FWD – Forward
G11 – Shear Modulus (For Wing, Parallel to Front Spar)
G12 – Shear Modulus (For Wing, In Wing Skin Plane)
G22 – Shear Modulus (For Wing, Perpendicular to Front Spar)
GE – General Electric
gFan+ – A General Electric Gas Turbine Defined in Phase II
HLFC – Hybrid Laminar Flow Control
HPT – High Pressure Turbine
ICAC – Initial Climb Altitude Capability
INBD – Inboard
IR – Infra-Red
ISA – International Standard Atmosphere
KEAS – Knots Equivalent Air Speed
L/D – Lift-to-Drag Ratio
LE – Leading Edge
LEMAC – Leading Edge of the Mean Aerodynamic Chord
LH – Horizontal Tail Arm
LH – Left Hand
LOPA – Layout of Passenger Accommodations
LP – Low Pressure
LPT – Lower Pressure Turbine
LRC – Long Range Cruise
LV – Vertical Tail Arm
LWR – Lower
M – Mach Number
MAC – Mean Aerodynamic Chord
M_{DD} – Drag Divergence Mach Number
MDM – Model Deformation Measurement System
MDO – Multidisciplinary Optimization
MEW – Manufacturers Empty Weight
MFR – Mass Flow Ratio
MLG – Main Landing Gear
MLW – Maximum Landing Weight
M_{MO} – Mach Max Operating
MP – Mass Properties
MRC – Maximum Range Cruise
MTOGW – Maximum Takeoff Gross Weight (same as MTOW)

MTOW – Maximum Takeoff Weight (same as MTOGW)
MZFW – Maximum Zero Fuel Weight
N&P – Nacelle and Pylon
NASA – National Aeronautics and Space Administration
NLF – Natural Laminar Flow
NLG – Nose Landing Gear
OD – Outside Diameter
OEI – One Engine Inoperative
OEW – Operating Empty Weight (same as OWE)
OML – Outer Mold Line
OWE – Operating Weight Empty (same as OEW)
PAX – Passengers
PR – Pressure Ratio
PSI – Pounds Per Square Inch
PSP – Pressure Sensitive Paint
Q – Dynamic Pressure
QCR – Quadratic Constitutive Relation
RANS – Reynolds Averaged Navier-Stokes
RBE3 – Nastran Interpolation Constraint Element
Re – Reynolds Number
RH – Right Hand
RN – Reynolds Number
RNWICS – Reynolds Number Corrected
ROC – Rate of Climb
S&C – Stability and Control
SFC – Specific Fuel Consumption
SOB – Side-of-Body
SOW – Statement of Work
STA – Fuselage Station
SUGAR – Subsonic Ultra-Green Aircraft Research
t/c – Thickness to Chord Ratio
TE – Trailing Edge
TMI – TriModels Inc.
TOFL – Takeoff Field Length
TOGW – Takeoff Gross Weight
TTBW – Transonic Truss-Braced Wing
UDF – Unducted Fan
UPWT – Unitary Plan Wind Tunnel
URANS – Unsteady Reynolds Averaged Navier-Stokes
V_{MC} – Velocity of Minimum Control in Air
V_{MCG} – Velocity of Minimum Control on Ground
V_{MCL} – Velocity of Minimum Control in Air in Landing Configuration
V_{MO} – Maximum Operating Speed
W2GJ – Nastran Downwash Matrix

WB – Wing Body
WB_LG-Off – Wing Body Landing Gear Off
WBA – Wing Body Alternate Strut
WBS – Wing Body Strut
WBSJ – Wing Body Strut Jury
WBSJN – Wing Body Strut Jury Nacelle
WBSJNV – Wing Body Strut Jury Nacelle Vertical
WBSJNVH – Wing Body Strut Jury Nacelle Vertical Horizontal
WICS – Wall Interference Correction System
WL – Waterline
WT – Wind Tunnel
x/c – Chord Ratio
ν – Poisson’s Ratio

1.0 Introduction

In 2009-2010, Boeing conducted the Subsonic Ultra-Green Aircraft Research (SUGAR) study for NASA. In this study, Boeing identified and analyzed advanced concepts and technologies for aircraft that would fly in the 2030-2035 timeframe. Large possible improvements in fuel consumption, emissions, and noise were identified and roadmaps developed for key technologies. Recommendations for future work were made in the SUGAR Phase I Final Report (1), including a more detailed consideration of hybrid-electric gas turbine propulsion and a comprehensive, multidisciplinary study of the high aspect-ratio transonic truss-braced wing (TTBW) configuration. These research objectives were pursued during subsequent, focused Phase II efforts addressing TTBW design space exploration (2), hybrid-electric propulsion evaluation (3) and a TTBW aeroelastic analysis and wind tunnel test (4).

After multidisciplinary optimization using a design environment developed by Phase II partner Virginia Tech, a TTBW configuration was selected promising significant reduction in fuel consumption relative to the reference industry standard that is documented in the Phase I report. It was also determined that airport compatibility could be achieved even for very high-span designs through the use of a folding wing. While hybrid-electric propulsion enabled yet further improvement in fuel consumption, it was determined that this would not likely be accomplished without a net increase in energy use. This effect is primarily driven by the fact that battery energy densities remain lower than those of petroleum fuel for the foreseeable future. Additional strategies and mechanisms for achieving hybrid electric propulsion remain unexplored. Detailed aeroelastic analysis and test in the NASA Transonic Dynamics Tunnel (TDT) determined that aeroelastic impacts to TTBW designs are both manageable and analytically predictable, and that the corresponding wing weight is not sufficient to significantly erode the aerodynamic benefit of increased span.

Specific avenues of further investigation were identified in the Phase II reports, including:

1. A detailed, high-fidelity aerodynamic design effort to determine achievable levels of interference between the primary components, and to reduce uncertainty in configuration performance estimates
2. Consideration of both Mach 0.7 and 0.8 designs
3. Low and high-speed wind tunnel tests to validate predicted aerodynamic performance
4. Initial planning for possible TTBW demonstrator aircraft

Considering the recommendations of Boeing and the other contractor teams, as well as program objectives, NASA developed these Research Objectives for Phase III:

1. Using high fidelity aerodynamic analyses, refine the design of a transonic TTBW aircraft at Mach 0.7.
2. Verify the performance of the TTBW aircraft by building a wind tunnel model and conducting a high-speed wind tunnel test.
3. Identify remaining technical challenges associated with the application of a TTBW to a modern transport aircraft and provide recommendations.
4. Update the TTBW aircraft design to a higher cruise Mach number, approaching Mach 0.8.
5. Validate the Virginia Tech Truss-Braced Wing (VT-TTBW) multidisciplinary optimization design environment relative to the Mach 0.7 SUGAR configuration work performed, including aeroelastic effects.

Boeing structured the SUGAR Phase III program to address the research objectives provided by NASA as well as the recommendations from the Phase II reports. This report will describe work done in support of the first research objective in particular, in preparation for an upcoming high-speed wind tunnel test. A separate document will address Task 4, and a subsequent report, submitted after performance of the test, will address the remaining objectives.

Particular areas of focus for the work presented here are:

1. Refinement of the Phase II TTBW configuration using 3D Navier-Stokes aerodynamic analysis, with particular focus on interference effects between the wing and strut
2. Development of a closed configuration respecting structural, aeroelastic, control and propulsive constraints
3. Production of a final design appropriate for transonic wind tunnel test

The approach and results are discussed in the sections that follow.

2.0 Truss-Braced Wing Configuration Design

The "SUGAR High" configuration documented in this report was initially generated in response to NASA Subsonic Fixed Wing N+3 design requirements that were initiated under a Phase I contract and were further refined under a Phase II contract. The following sections document the Phase III development and final design of the SUGAR High Mach 0.745 aircraft.

2.1 SUGAR High Configuration Evolution

The final Phase III SUGAR High Mach 0.745 configuration represents a refinement of the configuration developed during Phase II. The final released configuration for Phase II is 765-095-RD (Revision D). The final released configuration for this phase is 765-095-RJ (Revision J). The evolution of the Phase II and Phase III configurations are depicted in Figure 2.1 and Figure 2.2, respectively. It should be noted that Revision E was reserved and used internally for analysis revision control and is omitted from this flowchart due to a lack of configuration change.

This configuration revision history is outlined in Table 2.1. Revision D was the final released Phase II configuration and was the starting point for Phase III development.

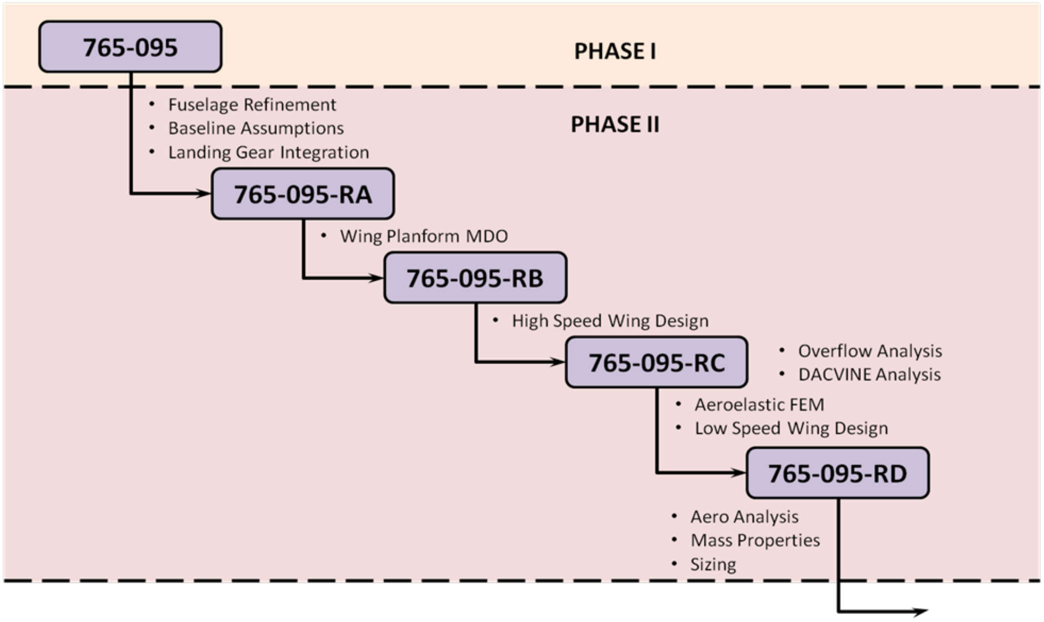

Figure 2.1 – Phase II configuration evolution.

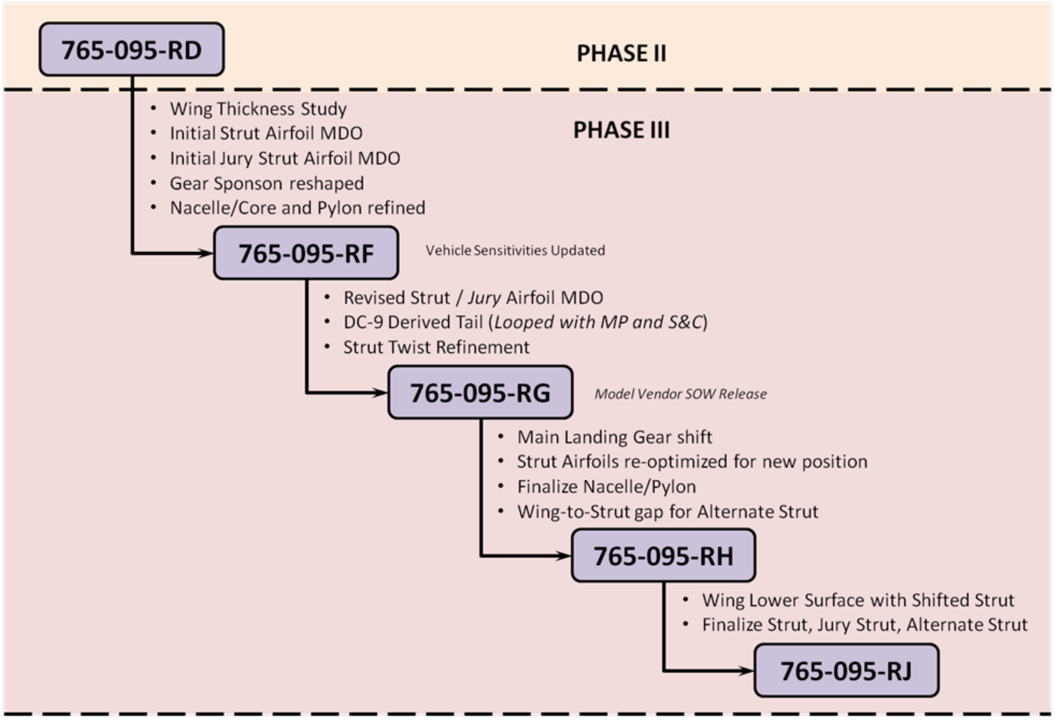

Figure 2.2 – Phase III configuration evolution.

Table 2.1 – 765-095 (Mach 0.7) revision history.

Rev.	Description of Major Changes	Date
New	SUGAR Phase I Exit	6/4/2009
	Beginning of Phase II	
A	Fuselage Refinement, Landing Gear Integration	5/2/2011
B	Wing Planform MDO	11/7/2011
C	High Speed Wing Design	1/5/2012
D	Strut Planform, Low Speed Wing Design, Engine Pylon Integration	10/8/2012
E	No Configuration Change	
	Beginning of Phase III	
F	Turbulent Wing Airfoils, Wing Twist Variation, Loft of Fairing and Nacelle/Pylon	10/28/2014
G	Wing Lower Surface Design, Main Strut Twist Variation, Jury Strut Design	1/13/2015
H	MLG shift, Re-optimized Strut Airfoils, Final Nacelle/Pylon, Wing-to-Strut Gap for Alternate Strut	3/3/2015
J	Re-optimized Wing Lower Surface Design, Final Main Strut, Final Jury Strut, Final Alternate Strut	5/6/2015

2.2 SUGAR High Configuration Description

The “SUGAR High” configuration (Model 765-095) represents a single member of a 737-class airplane family. It is a tube and wing configuration with a high mounted truss-braced wing, twin wing mounted engines, a T-tail empennage, and pylon mounted main landing gear. The 154 passenger dual class fuselage is a 6-abreast seating arrangement, the lower lobe is bulk loaded.

2.2.1 Integration

The aircraft configuration walk-around and general arrangement drawing are shown in Figure 2.3 and Figure 2.4, respectively. Table 2.2 and Table 2.3 show the component axis system origins relative to the body axis and the principal characteristics.

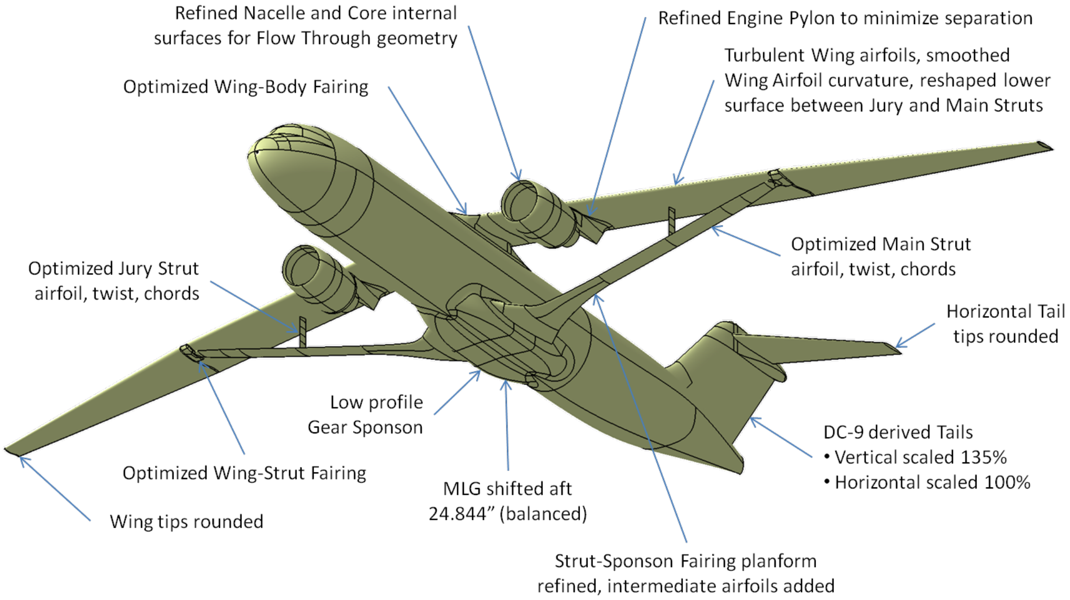

Figure 2.3 – SUGAR High (765-095 Rev-J) geometry development.

Table 2.2 – Body Axis Component Origins (units are inches).

Component	X	Y	Z
Fuselage	0.00	0.00	0.00
Wing	696.40	0.00	299.12
Vertical Fin	1356.02	0.00	281.49
Horizontal Stabilizer	1575.97	0.00	468.05
NLG*	235.00	0.00	92.34
MLG*	872.20	110.00	87.00

* To Centroid of the Bogie Contact Patch

PROJECTED CHARACTERISTICS			
	WING TOTAL	V-TAIL TRAP	H-TAIL TRAP
AREA (SQ FT)	1477.11	292.99	276.94
ASPECT RATIO	19.55	0.82	4.93
SPAN (IN)	2039.3	186.56	443.32
TAPER RATIO	0.35	0.80	0.35
MAC (IN)	110.29	227.07	96.83
DIHEDRAL (DEG)	-1.5	-	-3.00
¼ CHORD SWEEP (DEG)	12.52	43.50	31.60
ROOT CHORD (IN)	130.31	251.16	133.04
TIP CHORD (IN)	45.13	201.14	46.88
TAIL VOLUME COEFFICIENT	-	0.0662	1.434
Y_{MAC} ; Z_{MAC} ; Y_{MAC} (IN)	444.57	355.05	93.14
L_H ; L_V (IN)	-	681.08	843.73

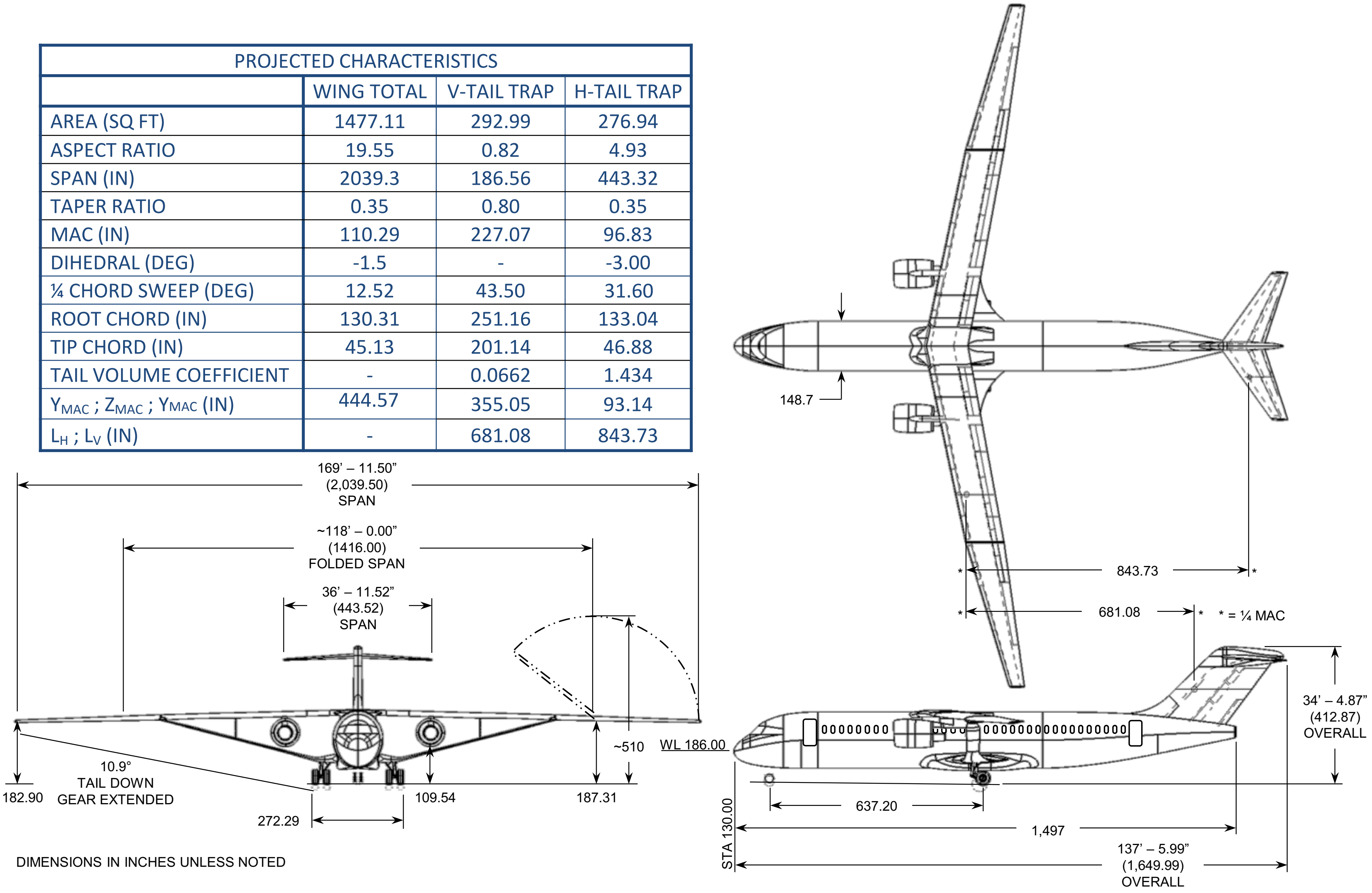

Figure 2.4 – SUGAR High Mach 0.745 (765-095 Rev-J) general arrangement.

Table 2.3 – Principal characteristics.

Model 765-095 Rev. J (As Drawn)	
Maximum Takeoff Weight (MTOW)	150,000 lbm
Maximum Landing Weight (MLW)	137,700 lbm
Maximum Zero Fuel Weight (MZFW)	129,700 lbm
Operating Empty Weight (OEW)	83,700 lbm
Engine Type	gFan+
Boeing Equivalent Thrust	23,000 lbf
Fan Diameter	71 in
Overall Dimensions	
Length	137.5 ft
Height	34.4 ft
Fuselage Length	124.8 ft
Fuselage Cross Section (Height x Width)	166.5 x 148.7 in
Passenger Cabin Length	1127 in
Wing	
Reference Area	1477.11 ft^2
Span	169.9 ft
Projected Sweep	12.52 deg
Passenger, Baggage, Fuel Capacities	
Passenger Count (Dual Class)	154
Class Distribution (FC / EC)	12 / 142
Cargo Capacity	Bulk
Fuel Capacity	5,416 USG
Landing Gear	
Wheel Base	637.20 in
Main Track	272.29 in
Main Tire Size	45x17R21
Nose Tire Size	30x10.5R15

2.2.2 Wing

The wing is high aspect ratio, truss-braced, low sweep and designed for a 0.745 long range cruise Mach number. Although the Phase II wing design was designed for natural laminar flow, the Phase III wing (all configuration revisions) incorporates turbulent airfoils, a decision that was made to simplify the design without impacting the focus of the study (strut-wing interference). Laminar flow technology is carried at the conceptual level and the airplane performance includes this increment. The wing layout incorporates a fold at 118 feet of span to accommodate existing code C gate and taxiway infrastructure.

The Phase III wing characteristics, spar locations, and control surface definitions shown in the Revision J General Arrangement (Figure 2.5) are unchanged from the final released Phase II design (Revision D).

The leading edge is populated with full span Krueger flaps broken by the engine pylon, planform break, and the wing fold. The extent and number of Krueger breaks bears further study. The front spar accommodates a leading edge device chord ratio ranging from ten percent at the root to fifteen percent at the tip. The trailing edge of the wing is fitted with single slotted flaps extending from the side of body to the wing fold. A small flap segment acts as an aileron at high speed (flaperon). Outboard of the wing fold there is a low speed aileron. Spoilers are assumed to cover the entire flapped span with the exception of the portion reserved for the high speed aileron. These spoilers are assumed to be drooped for takeoff. The control surface and high lift system layout is the result of trade-offs between low speed aerodynamics and stability and control. The Revision D planform is illustrated in Figure 2.5, and the projected reference quantities are shown in Table 2.4. It should be noted that the reference quantities are displayed for a planform with no leading or trailing edge breaks at the side-of-body. A detailed wing corner point drawing is presented in Figure 2.6.

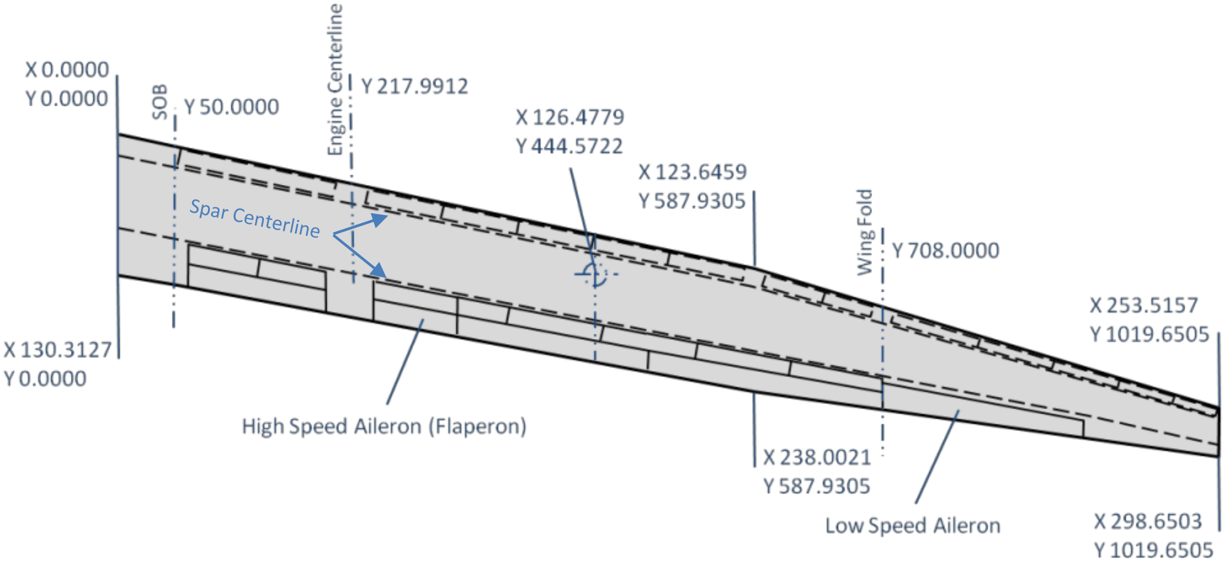

Figure 2.5 – SUGAR High (765-095 Rev-D) planform (projected, units are inches).

Table 2.4 – Wing reference geometry.

Parameter	Units	Total (Projected)	Parameter	Units	Total (Projected)
Area	ft^2	1477.11	**MAC**	In	110.286
Aspect Ratio		19.552	**Y_{bar}**	In	444.5722
Span	in	2039.301	**$X_{LE, MAC}$**	In	98.9065
Taper Ratio		0.346	**$X_c/4$**	In	126.478
Root Chord	in	130.3127			
Tip Chord	in	45.1346			**(Reference)**
SOB Chord	in	128.9557	**Krueger Area**	ft^2	138.89
Sweep LE	deg	13.47	**High Speed Aileron (Flaperon) Area**	ft^2	41.73
Sweep 25%	deg	12.52	**Single Slot Flap Area**	ft^2	264.21
Sweep TE	deg	9.61	**Low Speed Aileron Area**	ft^2	52.98
Dihedral	deg	-1.50	**Spoiler Area**	ft^2	118.81

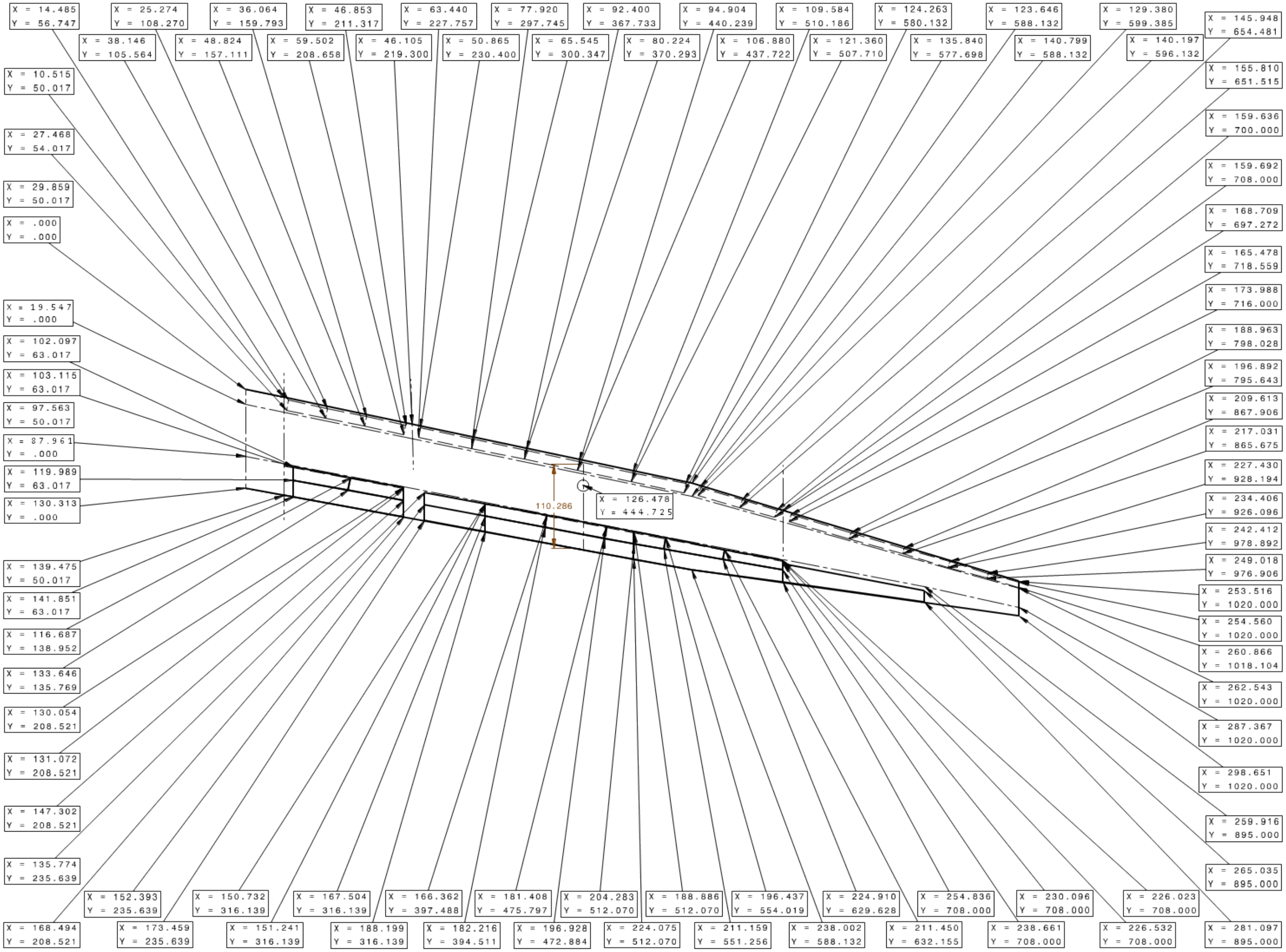

Figure 2.6 – Wing corner point drawing (wing reference plane, units are inches).

2.2.3 Main Strut and Jury Strut

A 24.844" aft shift of the main landing gear (MLG) was dictated by stability and control and loadability requirements, and the main strut axis was modified relative to Revision D to accommodate both the shift and to improve the load path. The Phase II main strut axis was aligned with the MLG front bulkhead. The Phase III main strut axis is such that the strut front spar aligns with the MLG front bulkhead. The strut rear spar kicks aft in the strut-sponson fairing region to align with the MLG rear bulkhead. The attachments of the main strut at the sponson and wing are pinned joints (axis normal to the bending plane). The sponson-strut-wing structural concept is shown in Figure 2.7.

The main strut dihedral is 14.36 degrees, and its sweep is -0.35 degrees (forward sweep). The front spar and rear spar locations are defined in Table 2.5 and the strut corner points are shown in Figure 2.8.

The jury strut location relative to wing span is approximately the same as the Phase II configuration. The dihedral was changed to 90 degrees to eliminate the outboard cant. The elastic axis is vertical and is located 2.5" forward of the main strut rear spar to allow integration of attachment structure. The upper end of the elastic axis is ~9.6" forward of the wing rear spar. The attachments at the wing and main strut are pinned joints (axis aligned streamwise). The jury strut spar locations are defined in Table 2.6 and the corner points are shown in Figure 2.9.

Both the main strut and jury strut have a linear chord distribution between defining airfoils. The defining airfoils for the main strut are at Y locations 116.367, 251.230, 365.020, 405.058, and 452.470 inches in the main strut reference plane (see Figure 2.8). The defining airfoils for the jury strut are at Y locations 0.000, 13.763, 27.527, 41.290, and 55.053 inches in the jury strut reference plane (see Figure 2.9). Future aircraft refinements will likely include smoothing of the struts between linear lofted segments.

Table 2.5 – Main strut spar locations.

Y (in.)	Front Spar x/c	Rear Spar x/c
233.724	0.1581	0.7157
364.364	0.1680	0.6110
474.592	0.0946	0.6896
513.376	0.0878	0.7031
559.304	0.1467	0.6689

Table 2.6 – Jury strut spar locations.

Z (in.)	Front Spar x/c	Rear Spar x/c
225.000	0.1000	0.8000
238.750	0.0800	0.7634
252.500	0.0800	0.7634
266.250	0.0800	0.7634
280.000	0.1000	0.8000

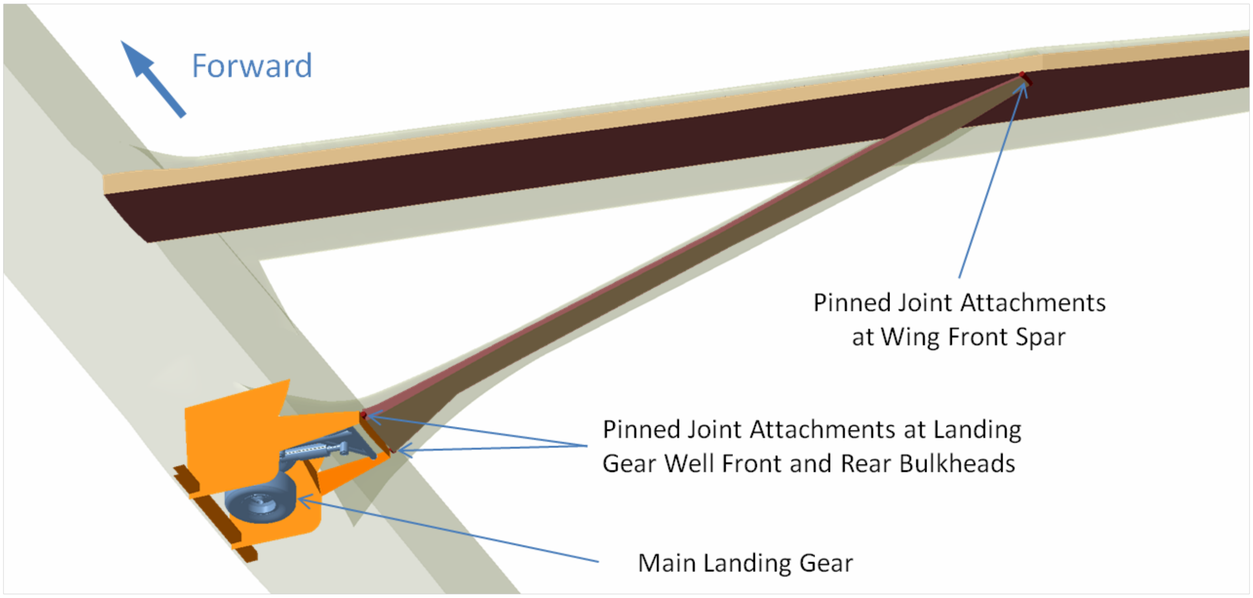

Figure 2.7 – SUGAR main strut structural concept.

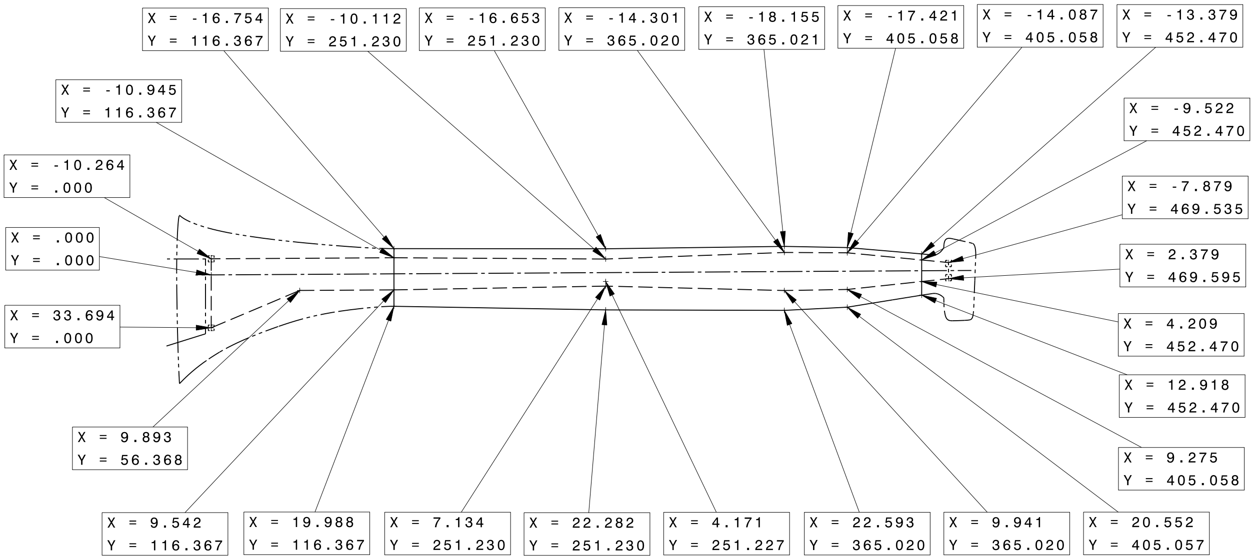

Figure 2.8 – SUGAR High (765-095 Rev-J) strut corner points (units are inches).

Structure for the main strut attachment to the wing was sized based on preliminary FEM loads and structural arrangement. Fail safety for single point component failure and bird-strike damage was achieved by providing two attachments that were sized to carry limit loads, assuming the loss of the other load path. The basic strut structure contains a leading edge titanium splitter that protects the strut integrity from bird-strike damage. Bird-strike fail safety of the outboard strut attachment to the wing, where providing a splitter feature is challenging, is achieved through separation of the two attachment load paths. A structural arrangement concept of the main strut to wing joint is shown in Figure 2.10 and Figure 2.11.

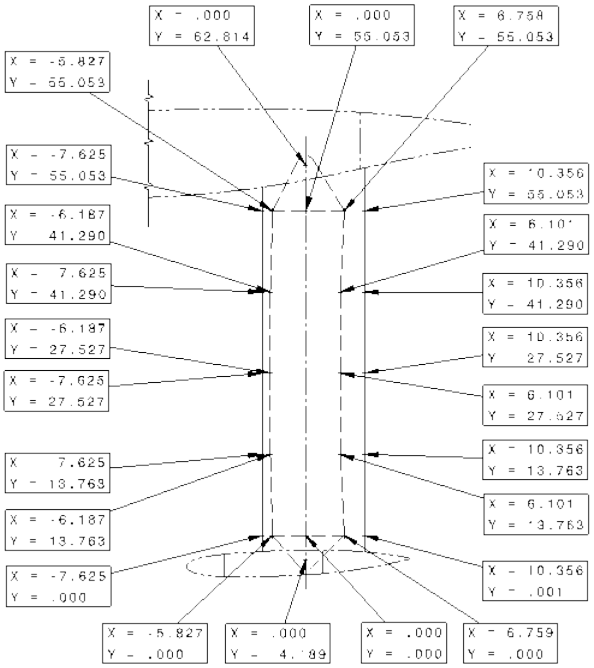

Figure 2.9 – Jury strut corner point drawing (jury strut reference plane, units are inches).

The jury strut attachment to the main strut is a pinned joint (axis normal to the wing bending plane). Fail safety is achieved through the use of multiple components in the joint design in combination with a main strut leading edge splitter to provide protection from bird-strike. A structural arrangement concept of the jury strut to main strut is shown in Figure 2.12.

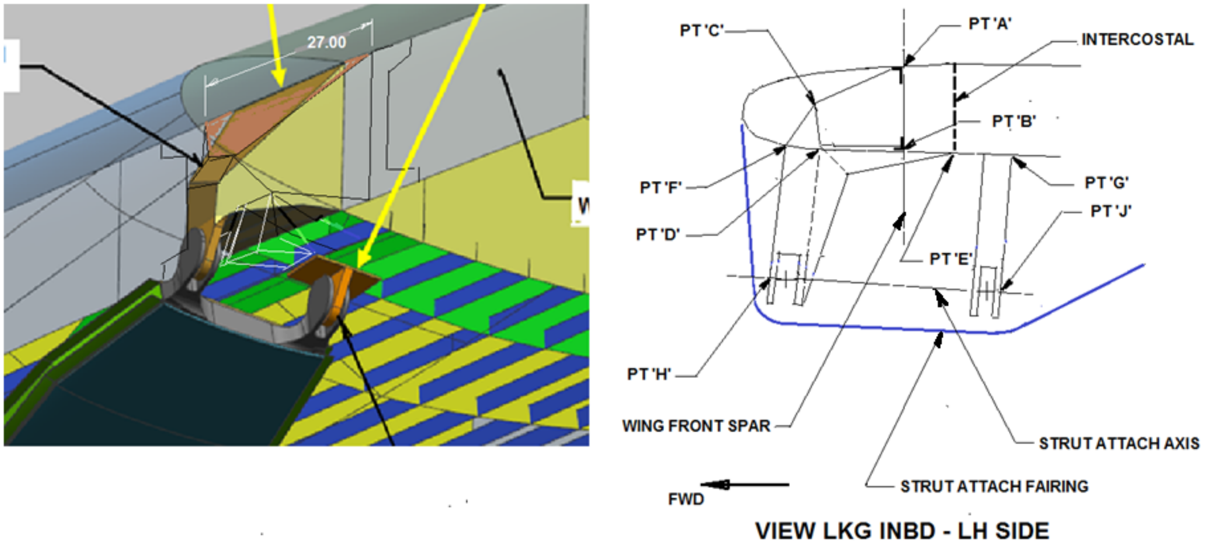

POINT LTR	A	B	C	D	E	F	G	H / J
WIDTH 'W'	27.00	27.00	9.00	9.00	9.00	9.00	9.00	4.25 (LUG WIDTH)

Figure 2.10 – Main strut outboard attachment concept.

The jury strut attachment to the wing is 9.6” forward of the wing rear spar and the attachment concept mirrors the jury strut lower pinned joint with the exception that the structure to which the joint longitudinal members attach in the wing are lateral back to back intercostals at the forward end of the joint, and the aft end of the longitudinal members attach to the wing rear spar and a separate rear spar web doubler. This arrangement provides the requisite fail safety features.

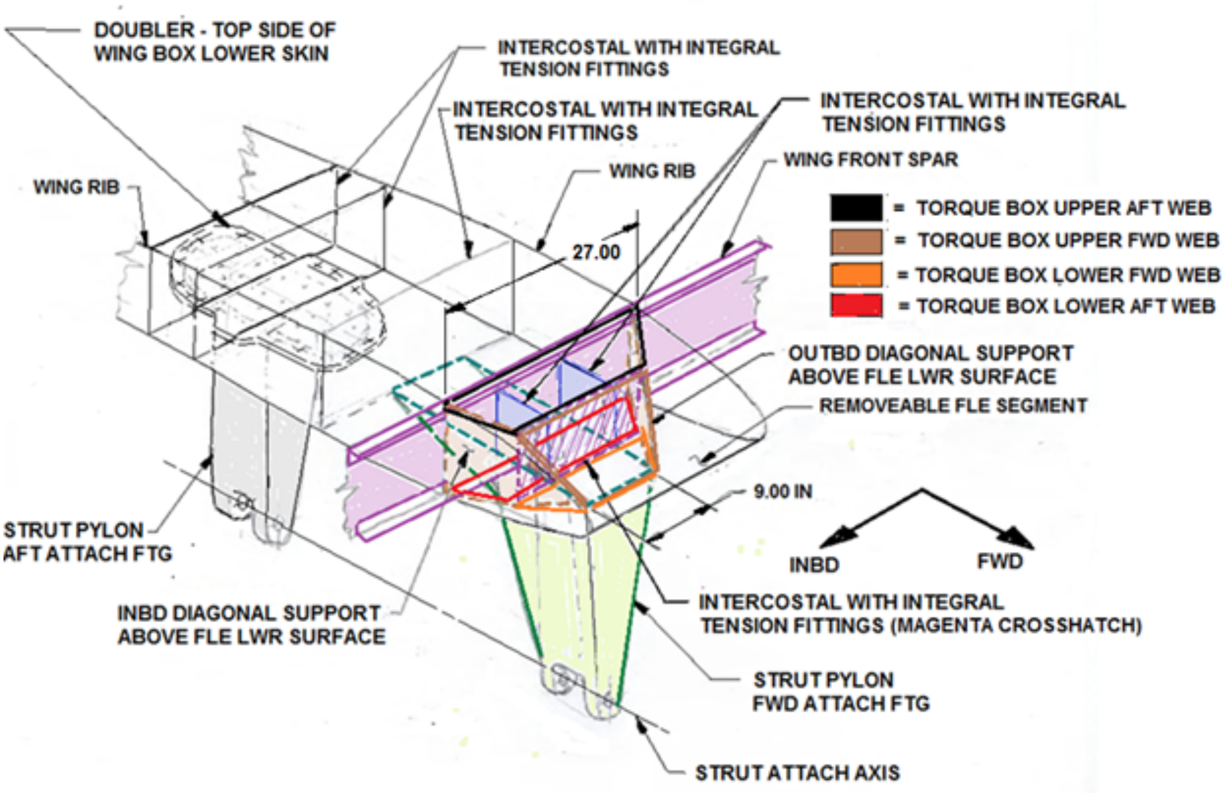

Figure 2.11 – Main strut outboard attachment structural arrangement overview.

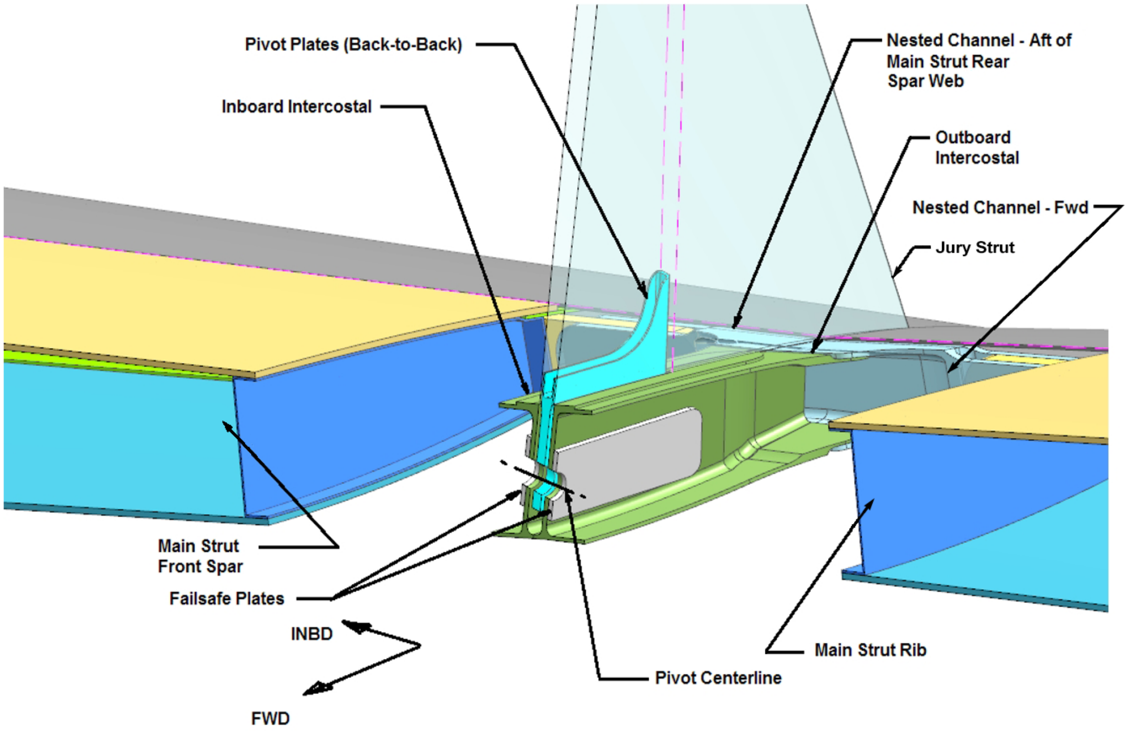

Figure 2.12 – Jury strut to main strut attachment concept.

2.2.4 Alternate Strut

An alternate pylon-mounted main strut concept was also developed as a method to improve the aerodynamic characteristics at the wing-strut junction by effectively moving the strut away from the wing.

The alternate strut offset at the pylon is 22 in. The offset is measured from the wing lower skin to the centerline of the strut attachment clevis. For the purpose of defining the pylon outer mold line, the pylon structure was assumed to have a trapezoidal envelope with a base at the wing of 10 in. (spanwise direction) by 13 in. (streamwise direction). The strut attachment clevis envelope is 2.1 in. radius. There is a lug/clevis joint at both the front and rear spar of the strut. The alternate strut structural concept is shown in Figure 2.13.

The dihedral of the alternate strut is 12.13 degrees. The sweep is unchanged from the baseline strut.

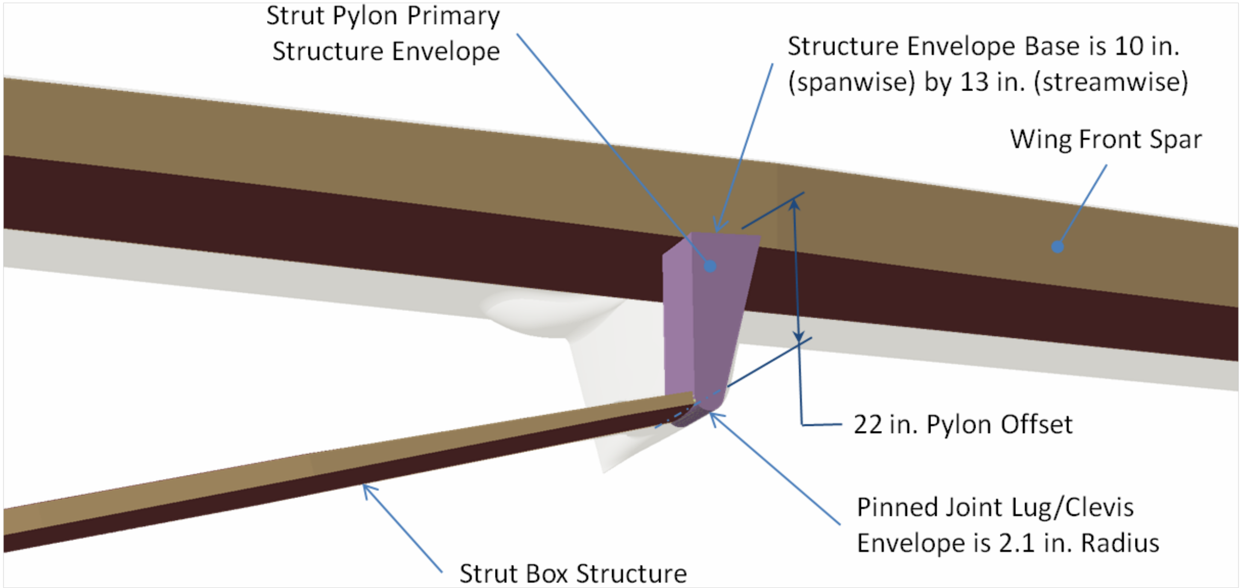

Figure 2.13 – Alternate strut structural concept.

2.2.5 Vertical Fin

The vertical tail planform is a 134.67% scale version of a DC-9 twin-jet tail and is sized to provide a tail volume coefficient of 0.066. It is a two spar layout with a two surface simple hinged rudder. The front spar breaks and converges on the rear spar at the vertical tip where the horizontal stabilizer pivot is mounted. The horizontal jack screw mechanism is above the front spar. The vertical planform is illustrated in Figure 2.14, and the reference planform parameters are shown in Table 2.7.

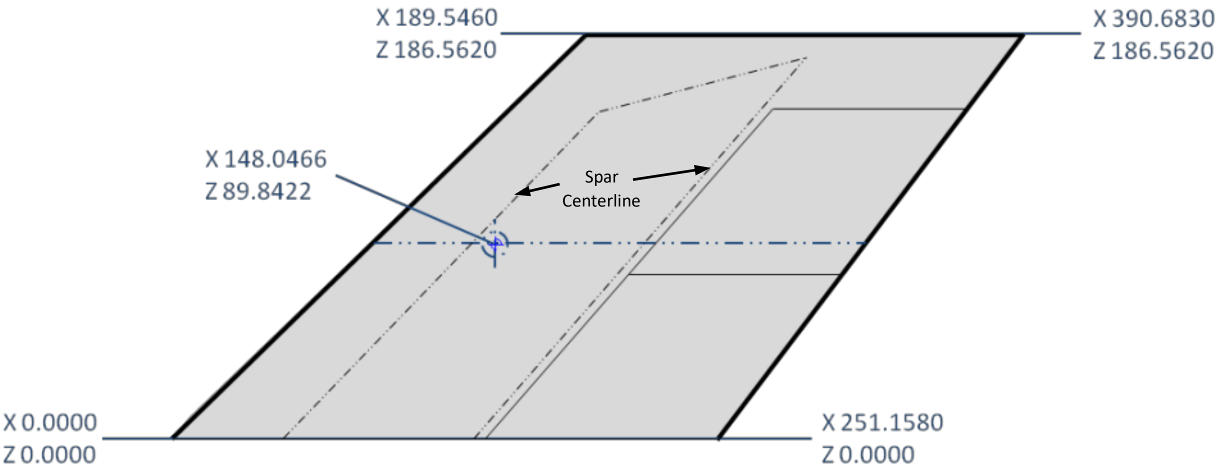

Figure 2.14 – SUGAR High (765-095 Rev-J) vertical tail planform (units are inches).

Table 2.7 – SUGAR High (765-095 Rev-J) vertical tail planform parameters.

Parameter	Units	Total (Projected)
Area	ft^2	292.99
Aspect Ratio		0.825
Span	in	186.56
Taper Ratio		0.80
Root Chord	in	251.16
Tip Chord	in	201.14
Sweep 25%	deg	43.50
MAC	in	227.07
Y_{bar}	in	89.84
$X_c/4$	in	148.05

2.2.6 Horizontal Stabilizer

The horizontal stabilizer planform is a 100.25% scale version of a DC-9 twin-jet tail and is sized to provide a tail volume coefficient of 1.43. The stabilizer is trimmable with a pivot behind and below the rear spar and a jack screw acting in front of the front spar. The elevator is split into two separate spanwise segments. The horizontal planform is depicted in Figure 2.15, and the projected planform parameters are shown in Table 2.8.

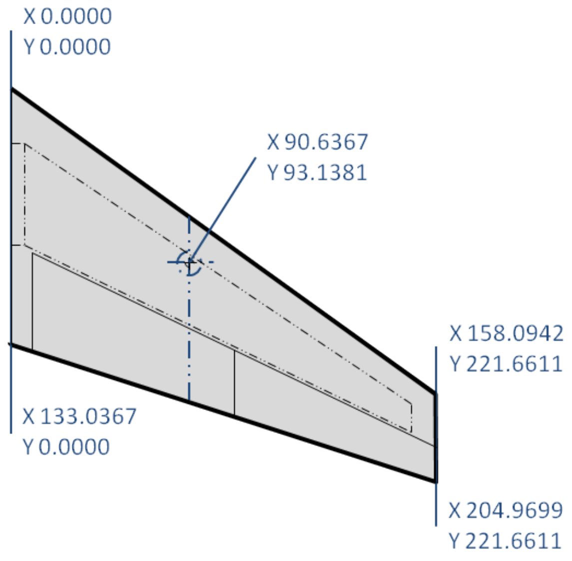

Figure 2.15 – SUGAR High (765-095 Rev-J) horizontal planform (units are inches).

Table 2.8 – SUGAR High (765-095 RJ) horizontal planform parameters.

Parameter	Units	Total (Projected)
Area	ft^2	276.94
Aspect Ratio		4.93
Span	in	443.32
Taper Ratio		0.35
Root Chord	in	133.04
Tip Chord	in	46.88
Sweep 25%	deg	31.60
Dihedral	deg	-3.00
MAC	in	96.83
Y_{bar}	in	93.14
$X_c/4$	in	90.64

2.2.7 Fuselage

The SUGAR High fuselage is a single-aisle layout with three-by-three seating. The cargo compartment is bulk loaded and is not designed for containerized cargo. The cross-section is illustrated in Figure 2.16 and a Layout of Passenger Accommodations (LOPA) is shown in Figure 2.17. The LOPA and cross-section were defined in Phase I and have not changed.

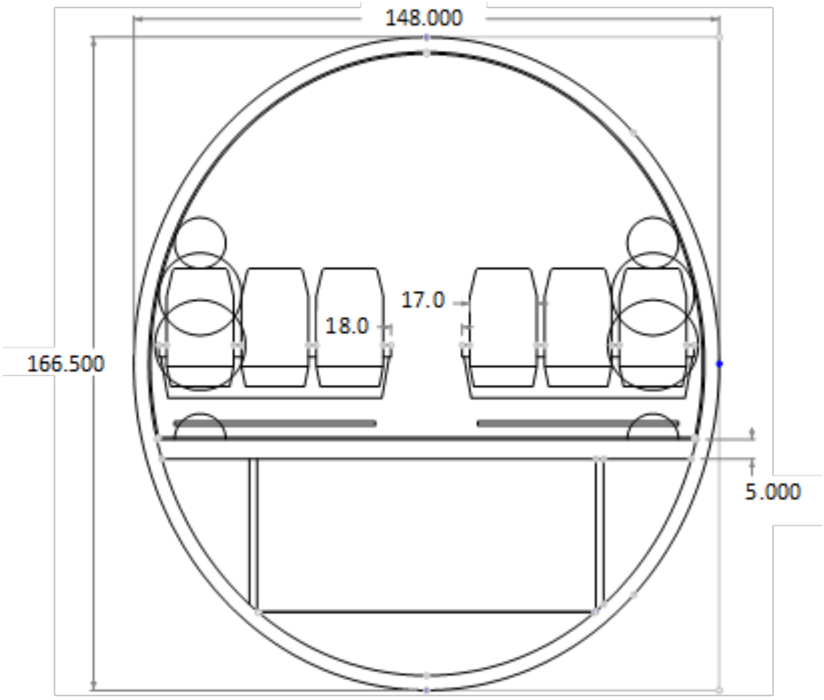

Figure 2.16 – 765-095 fuselage cross section (units are inches).

Interior Arrangement

SUGAR

IAC Short / Medium Range – Dual Class

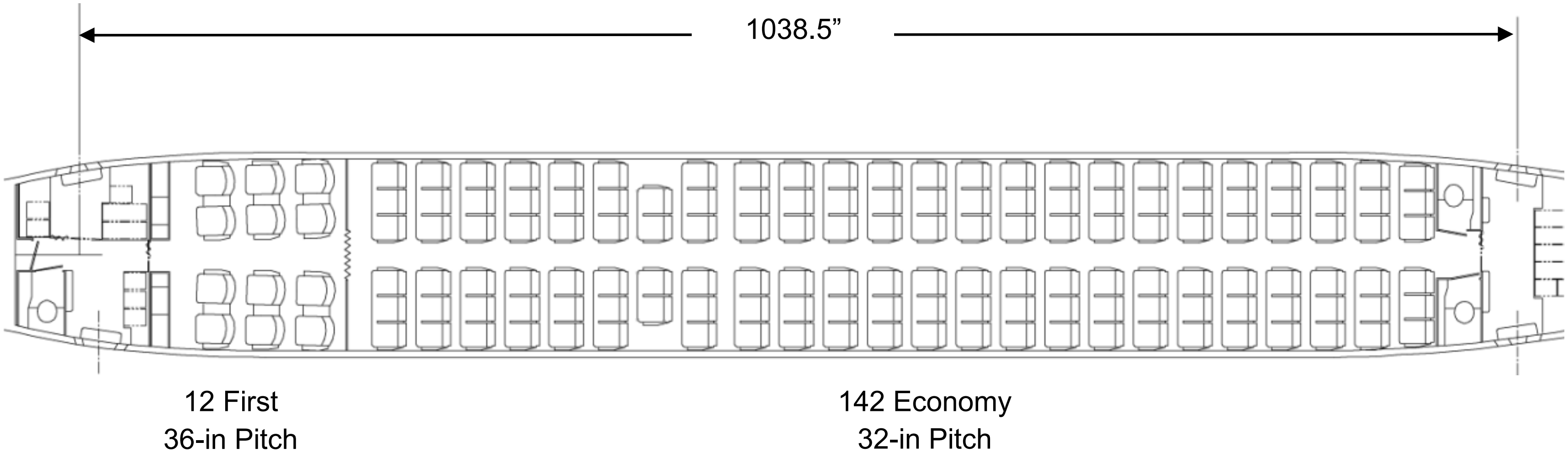

	Class (%)	Carts (qty)	Cart Ratio (Carts/Pax)	Lavatory Ratio (Pax/Lav)	Closet Ratio (Rod-in/Pax)
First	7.79	3.0	0.250	12	4.00
Economy	92.20	7.0	0.049	71	0.00
Total	100.00	10.0	0.649	–	–

Figure 2.17 – SUGAR High (765-095) layout of passenger accommodations.

2.2.8 Landing Gear

The high aspect ratio, high lift-curve slope SUGAR High configuration allows for a low static ground line. The configuration uses a levered landing gear arrangement to enable this low stance. The landing gear attaches to the gear sponson, a stub wing-like structure that carries landing gear and strut loads. The sponson OML was updated to a lower profile, lower drag design that more closely encloses the main gear system and primary structure.

The Phase III landing gear design is unchanged from the Phase II design. However, the main gear was moved aft by 24.844” to optimally balance the configuration. An overview of the kinematic arrangement is illustrated in Figure 2.18, and the ground footprint is shown in Figure 2.19 (not to scale).

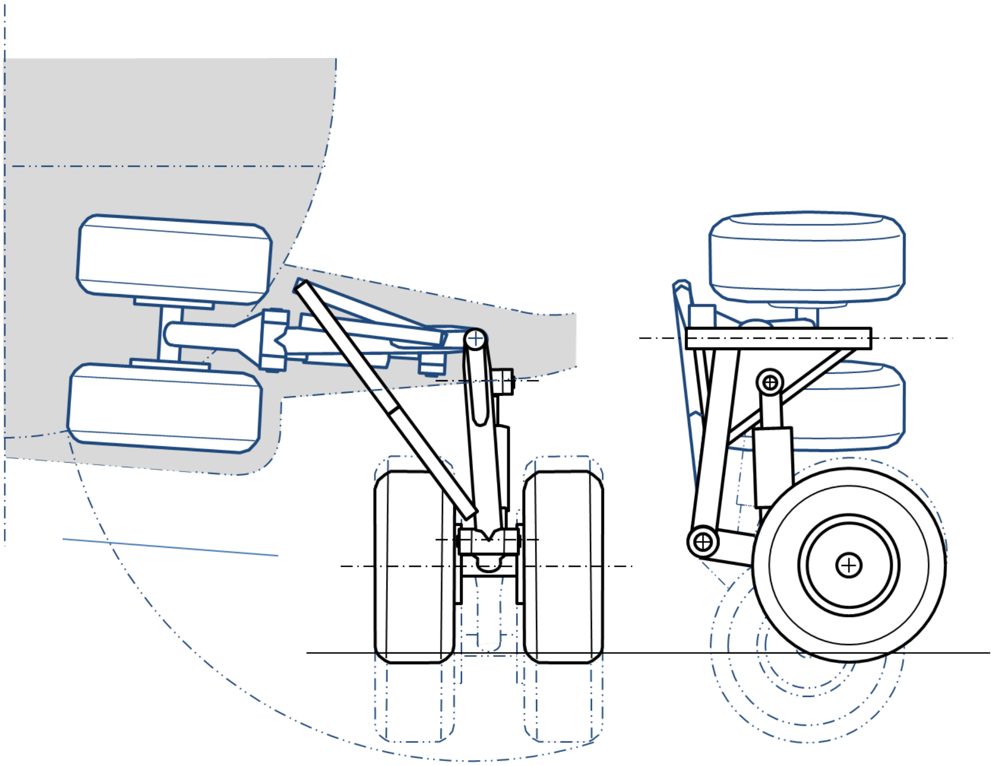

Figure 2.18 – SUGAR High (765-095 Rev-J) landing gear layout.

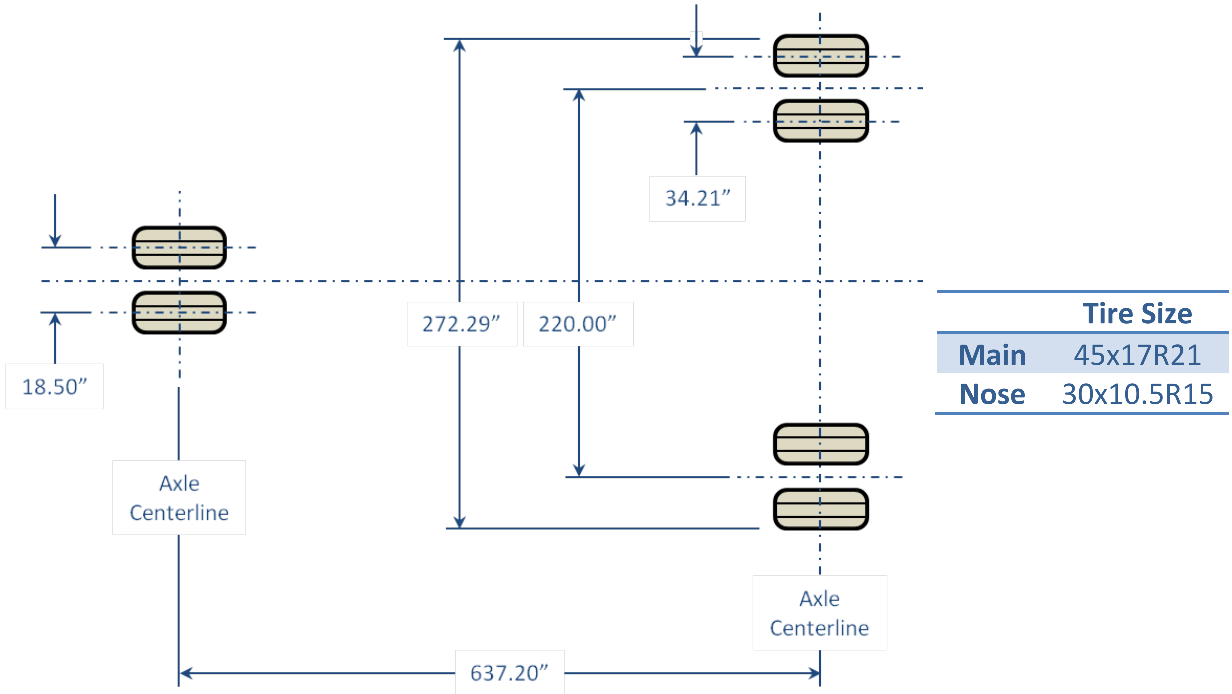

	Tire Size
Main	45x17R21
Nose	30x10.5R15

Figure 2.19 – SUGAR High (765-095 Rev-J) landing gear arrangement.

2.2.9 Propulsion

The SUGAR High propulsion system design was not modified significantly during the Phase III effort. The Phase II gFan+ engine features a pressure ratio of 1.46, which was selected from a GE parametric study accounting for vehicle-level sensitivities. The selected pressure ratio sacrifices SFC but achieves a lighter weight, lower drag design relative to a higher bypass ratio engine. A conceptual layout of the Phase II gFan+ is shown in Figure 2.20, and a summary of the propulsion system key characteristics is provided in Table 2.9. The maximum range cruise Mach number of the Phase III configuration is higher than the Phase II by approximately 0.02 Mach. An SFC factor was applied to the engine dataset within the performance routine to adjust the design point of the engine accordingly.

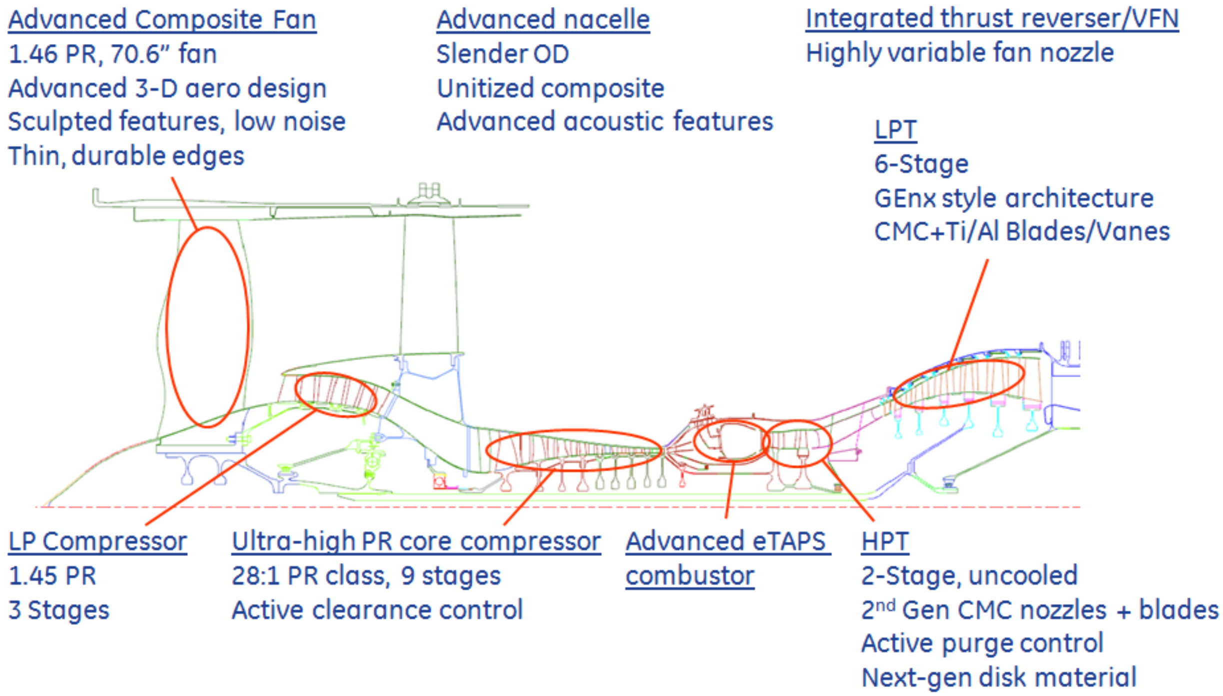

Figure 2.20 – gFan+ concept layout.

Table 2.9 – gFan+ key characteristics.

JP+2035GT+DF	
Fan Diameter	70.6 in
Length	129 in
Propulsion System Weight	6,335 lbm

Performance	Thrust (lbf)	SFC (lbm/lbf/hr)
Sea Level Static	21,943	0.220
Takeoff	16,592	0.295
Top of Climb	3,931	0.467
Cruise	3,145	0.455

3.0 Aeroelastic Analysis

The aeroelastic analysis performed in Phase II was updated with new geometry to verify that the aerodynamic analysis and refinement did not significantly impact the vehicle flutter speed. A more detailed definition of the strut, which did not exist in Phase II, also allowed for a higher fidelity analysis.

This activity produced a detailed finite element model (FEM) of the SUGAR aircraft, including all relevant load paths, sized to meet strength, buckling and flutter constraints. The aeroelastic analysis was generated using the Revision H geometry and should be considered up-to-date as the Revision J geometry was comprised of changes that are structurally imperceptible.

3.1 Wing FEM Description

The wing FEM (Figure 3.1) was generated to match the Rev-H outer mold line (OML) using Boeing's proprietary *RapidFem* process that generated skins, spar webs, rib webs, spar caps, rib caps, and control surfaces. A two spar arrangement was used with streamwise ribs spaced 24 inches apart. The spars and ribs have caps modeled as beam elements as illustrated in Figure 3.2. Additional ribs and an auxiliary spar were added to reinforce the wing where the strut attaches. The strut attaches to the wing at two locations matching the front and rear spar of the strut. The strut front spar attaches at a wing rib between the wing front spar and auxiliary spar and the strut rear spar attaches at a wing rib just aft of the auxiliary spar. This attachment is shown in Figure 3.3. The forward and aft wing/strut attach fixture is assumed to be free in the global 4 rotational direction, which is streamwise vertical bending. The fixture is rigid in the 3 translational directions and has an assumed stiffness in the pitching and yawing rotational directions. The jury attaches to the wing on a few grids on a rib. This attachment is shown in Figure 3.3. The wing/jury attach fixture is assumed free in the global pitching rotational direction and rigid in all other directions.

Engine/nacelle/pylon weight and air-load application grids attach to the wing using Nastran interpolation constraint elements (RBE3s). The RBE3 element attaches to the wing at the skin and rib intersection grids between the front spar and rear spar. The RBE3 element reacts all rigid body deflections at the independent grid but adds no stiffness to the model at the dependent rib intersection grids.

Control surfaces are modeled using Nastran quadrilateral plate elements (CQUAD4s). Control surfaces are supported at inboard and outboard hinges, which result in none of the wing bending being reacted by the control surfaces. Control surface hinge moments are reacted at the inboard hinge.

All wing elements are of composite material. Wing skins are made of 0, +/-45, 90 degree tape composite layers with bonded I-shaped composite stringers. The skin thickness, percent of plies laid up in each direction, and stringer geometry were determined using the Hypersizer optimization code. This code takes the local panel loads from a Nastran run and optimizes the skin and stringer design to meet strength and buckling constraints. The stringer geometry is I-shaped and the spar and rib webs are modeled using T-shaped smeared stringers. The foot or base of the stringer was assumed to be 0.5 inch wide and 0.05 inch thick. The web of the stringer was assumed to be 0.1 inch with a height of 1 inch. Spar and rib web stringer spacings were assumed to be 5 inches.

The 2D element lamina stiffness for all wing skins, webs, and stringers, and the 1D element laminate stiffness used for wing caps are shown in Table 3.1.

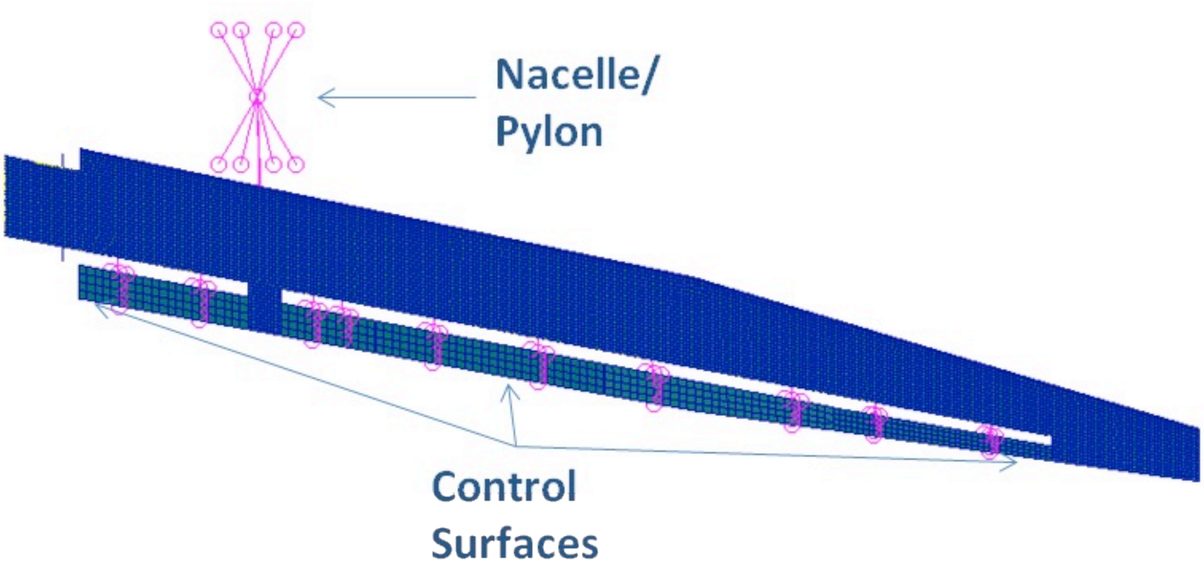

Figure 3.1 – Wing FEM Geometry.

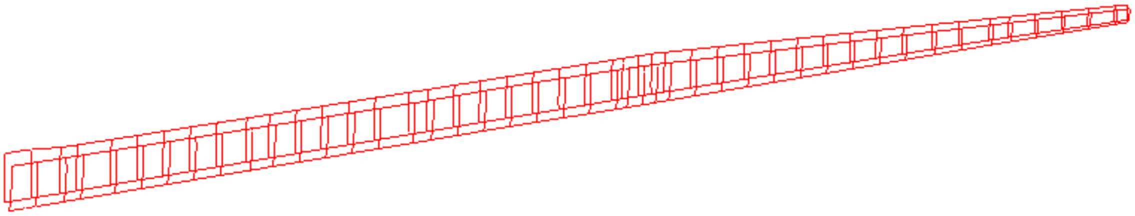

Figure 3.2 – Wing Rib and Spar Caps Modeled as Beam Elements.

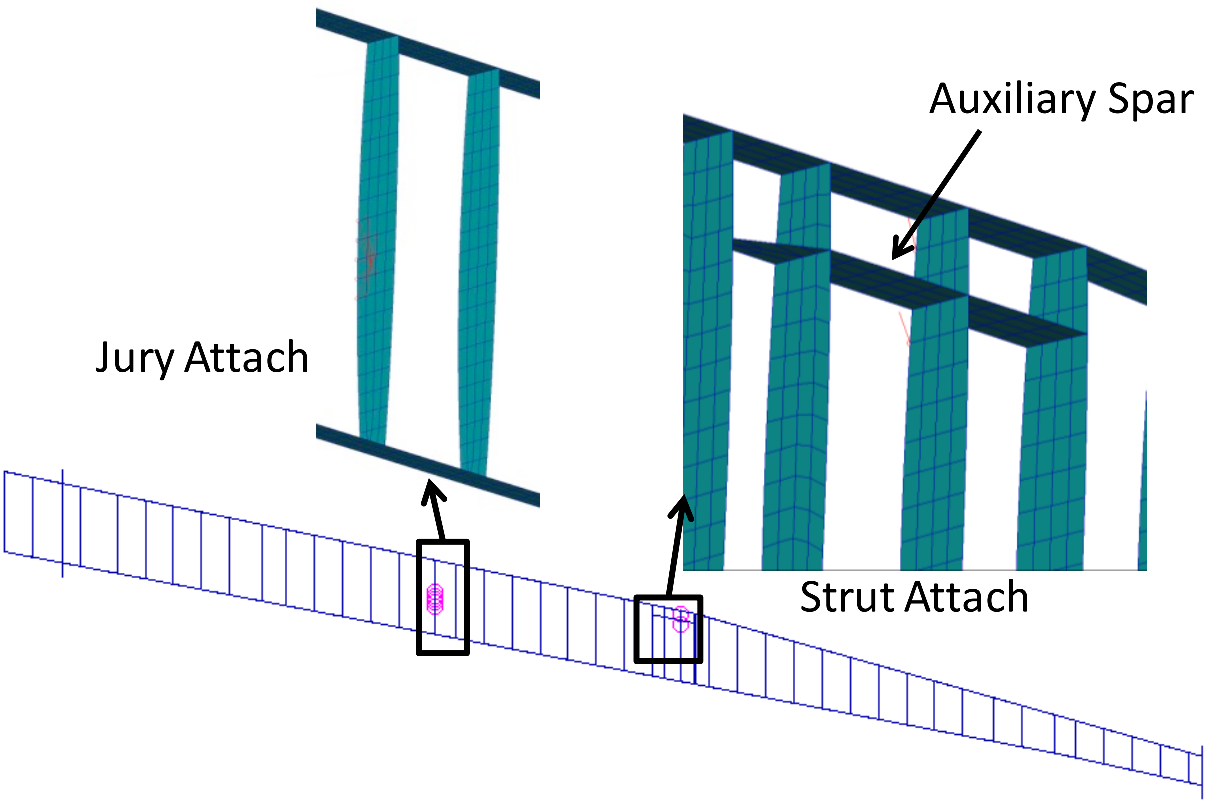

Figure 3.3 – Wing Rib/Spar Webs and Strut and Jury Attach.

Table 3.1 – Wing Stiffness Properties.

2D Element Lamina Stiffness		
E1	2.35×10^7	lb/in^2
E2	1.06×10^6	lb/in^2
ν	0.34	
G12	8.00×10^5	lb/in^2

1D Cap Laminate Stiffness		
E	1.05×10^7	lb/in^2
ν	0.30	
G12	4.04×10^6	lb/in^2

3.2 Strut/Jury FEM Description

The strut and jury FEM was generated to match the Rev-H OML including skins, spar webs, rib webs, spar caps, and rib caps (Figure 3.4 through Figure 3.8). A two spar arrangement was used with streamwise ribs spaced between 30 and 40 inches. The wing attaches to the outboard end of the strut at the front and rear spar. The forward and aft wing/strut attach fixtures are constrained as discussed in Section 3.1. The root of the strut spars attach to the forward and aft spars of the sponson. This joint is free in the global rolling moment direction and rigid in the other direction. The top of the jury spars attaches to the wing and the bottom attaches to a strut rib between the spars. These joints are free in the global pitching rotational direction. A strut titanium splitter plate (Figure 3.6) is formed by extending from the top and bottom of the front spar to a line offset 1 inch aft of the leading edge of the strut. It is assumed that the jury strut, a nearly solid composite element, will withstand bird strike without a splitter due to its very small leading edge.

All strut and jury elements are of composite material except for the titanium splitter plate. Like the wing, strut skins are made of 0, +/-45, 90 degree tape composite layers with bonded I-shaped composite stringers and the skin thickness, percent 0, 45, and 90 layers and stringer geometry was determined using the Hypersizer panel optimization code. Figure 3.4 through Figure 3.7 show the strut skins, rib webs, spar webs, titanium splitter plate, rib caps, and spar caps. Jury skins, spar and rib webs are modeled using T-shaped smeared stringers with the same geometric and material assumptions discussed in Section 3.1. The strut chordwise spar locations are the result of a joint aero-structural optimization process described in Section 4.1.1, and vary with span.

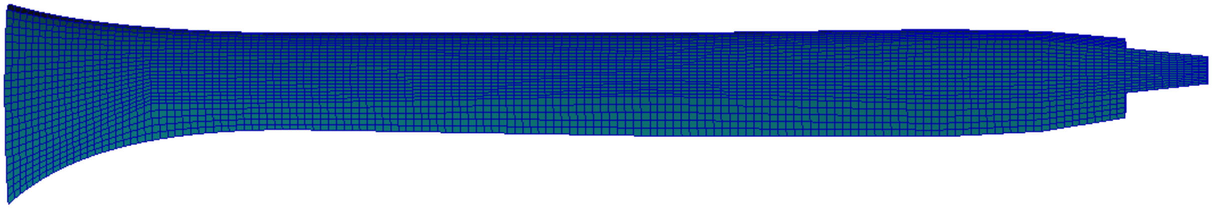

Figure 3.4 – Strut Skins.

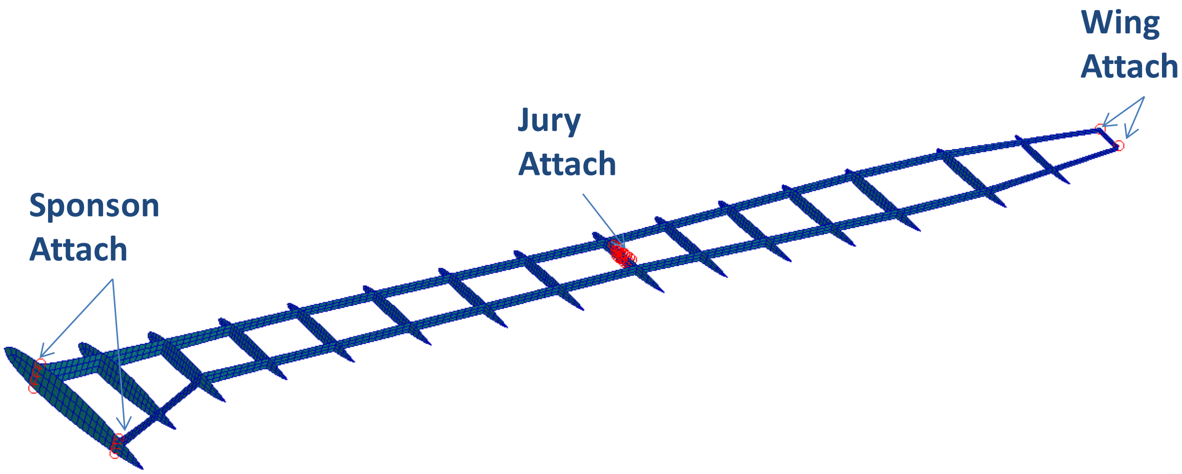

Figure 3.5 – Strut Webs.

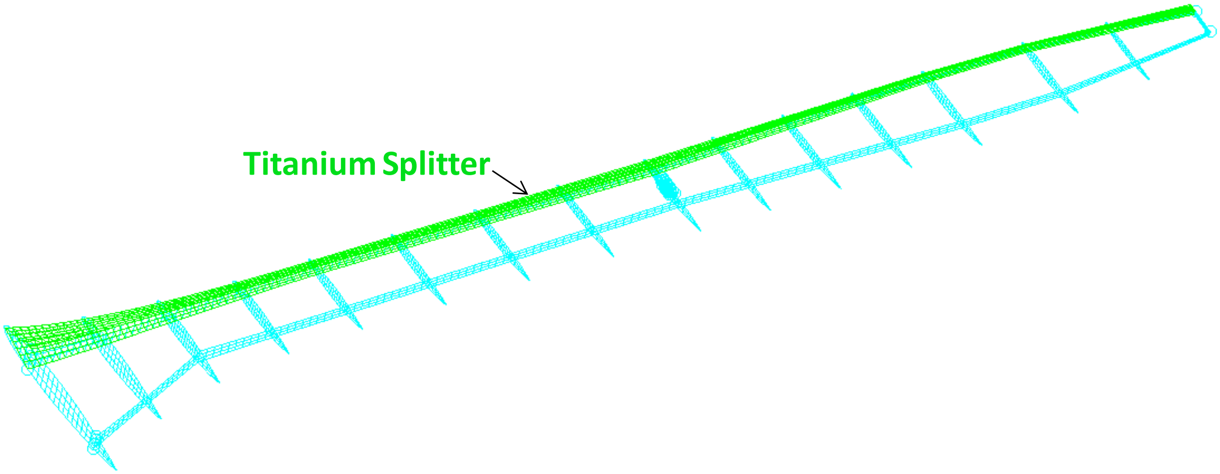

Figure 3.6 – Titanium Splitter Plate.

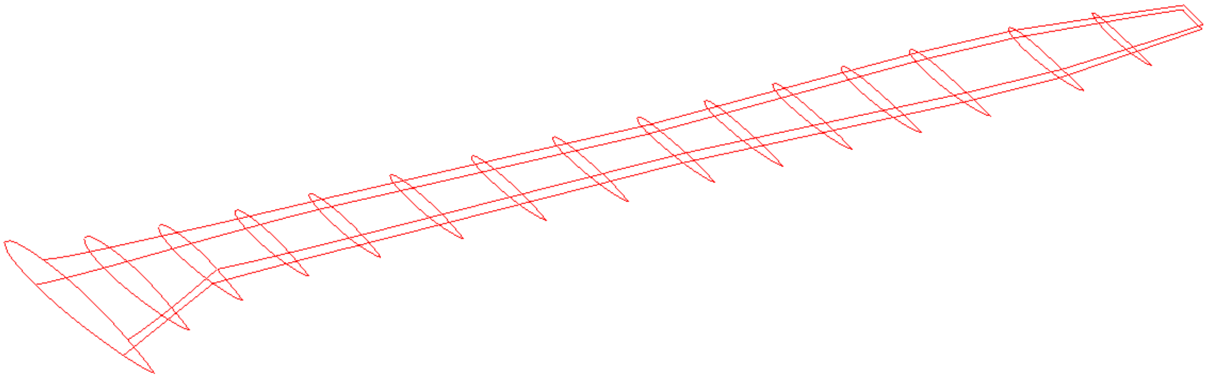

Figure 3.7 – Strut Rib and Spar Caps.

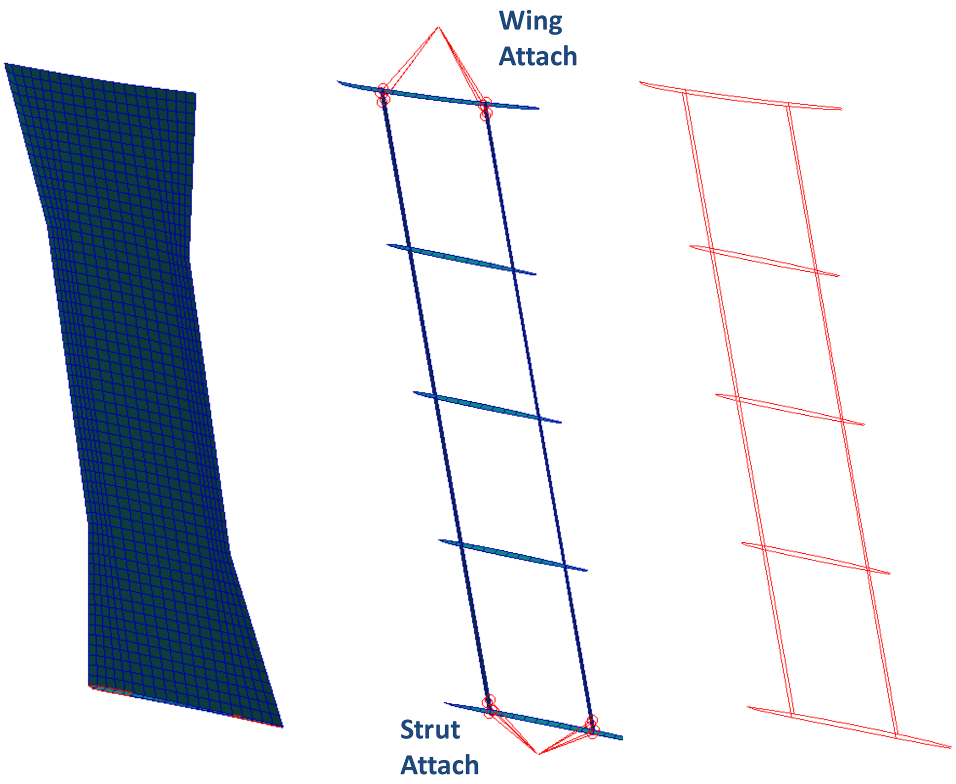

Figure 3.8 – Jury Skins, Webs, and Caps.

3.3 Center Body/Sponson FEM Description

The sponson (Figure 3.9) connects the root of the strut to the fuselage. It includes upper skin, two spars, ribs, and a fuselage bulkhead. Although no gear loads were included in the current study, the sponson also reacts to gear loads, and a gear beam model was attached to the sponson. Gear conditions are not critical for the structure sized in the current study and would not be expected to impact results. All sponson elements are of the same composite as the rest of the model. Sponson 2D elements are modeled using T-shaped smeared stringers with the same dimensional and material assumptions as used for the wing and struts.

The center body (Figure 3.10) includes skin with wing and sponson cutouts, frames, and an upper and lower floor. Aluminum properties were used for the center body. The center body was included to produce the correct detailed boundary conditions for the wing.

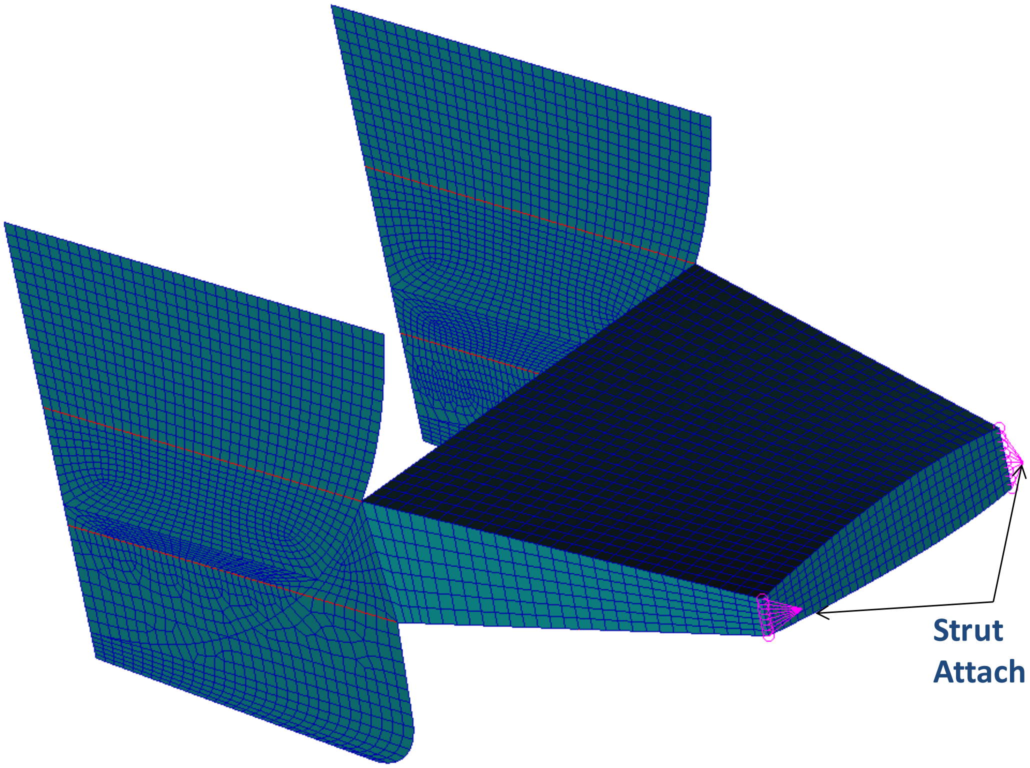

Figure 3.9 – Sponson FEM.

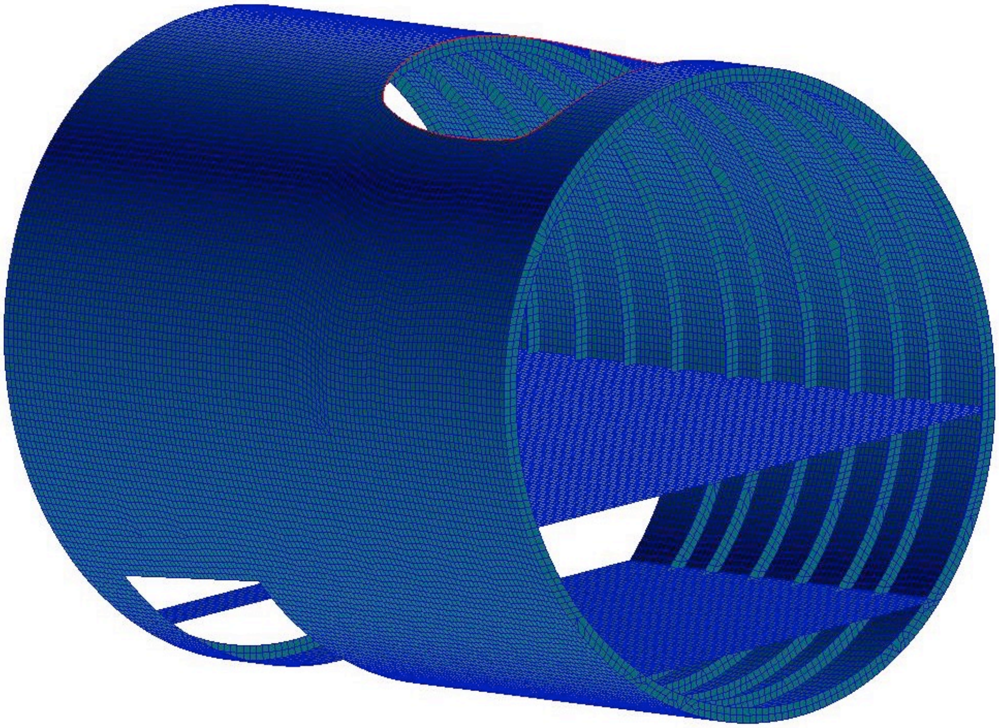

Figure 3.10 – Center Body FEM.

3.4 Finite Element Model Integration

Integration of the FEM involved adding nearly rigid fuselage and tail beam elements and joining the centerbody FEM to the wing FEM. Using nearly rigid beam elements for the forward fuselage, aft fuselage, and tail instead of building a 3D FEM simplified the model generation and analysis. The goal of the finite element analysis was to size the wing, and hence the assumption was made that the dynamics of the forward and aft fuselage and tail would not significantly impact the wing dynamics. Body and tail aerodynamics were applied to the model through the beam elements. The forward fuselage and aft fuselage/tail attach to the 3D centerbody FEM using an RBE3 element, which adds no stiffness to the centerbody.

The wing is attached to the centerbody using three fitting types. The first is the primary vertical connection between the wing and fuselage, and occurs at the wing front and rear spars. Here, a frame-mounted post extends up from the fuselage and attaches to a trap panel. The trap panel extends from the post to the front and rear spars of the wing at the side-of-body rib. This arrangement is shown in Figure 3.11.

The second is the primary fore and aft connection between the wing and fuselage. Here, the grids along the fuselage wing cutout are connected, in the x-direction only, to the closest grids on the wing's lower skin. This is shown in Figure 3.12.

The third is the primary lateral connection between the wing and fuselage, where the end grids of three fuselage frames are connected, in the y-direction only, to grids on the wing lower skin. This is shown in Figure 3.13.

The integrated FEM with 751,170 degrees of freedom is shown in Figure 3.14.

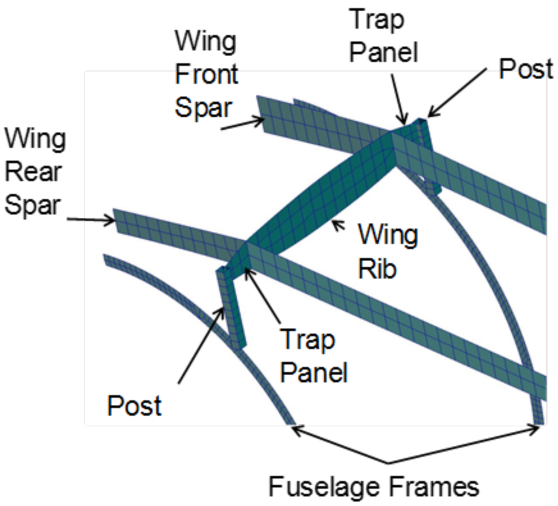

Figure 3.11 – Primary vertical connection between wing and body.

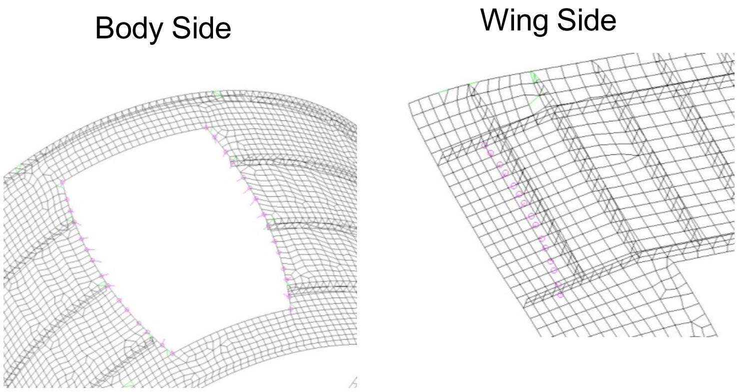

Figure 3.12 – Primary forward/aft connection between wing and body.

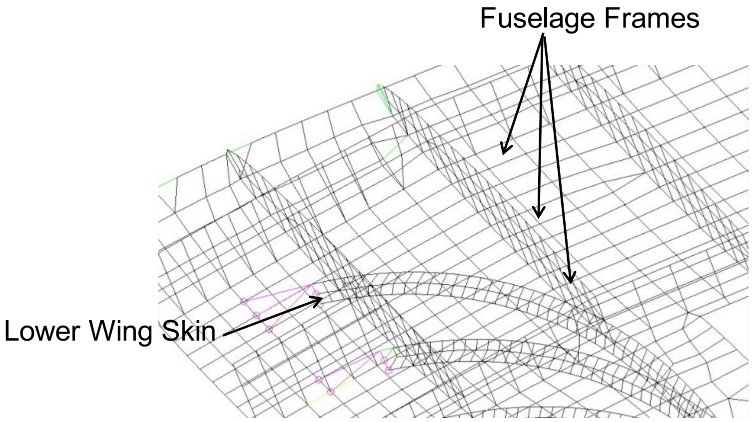

Figure 3.13 – Primary lateral connection between wing and body.

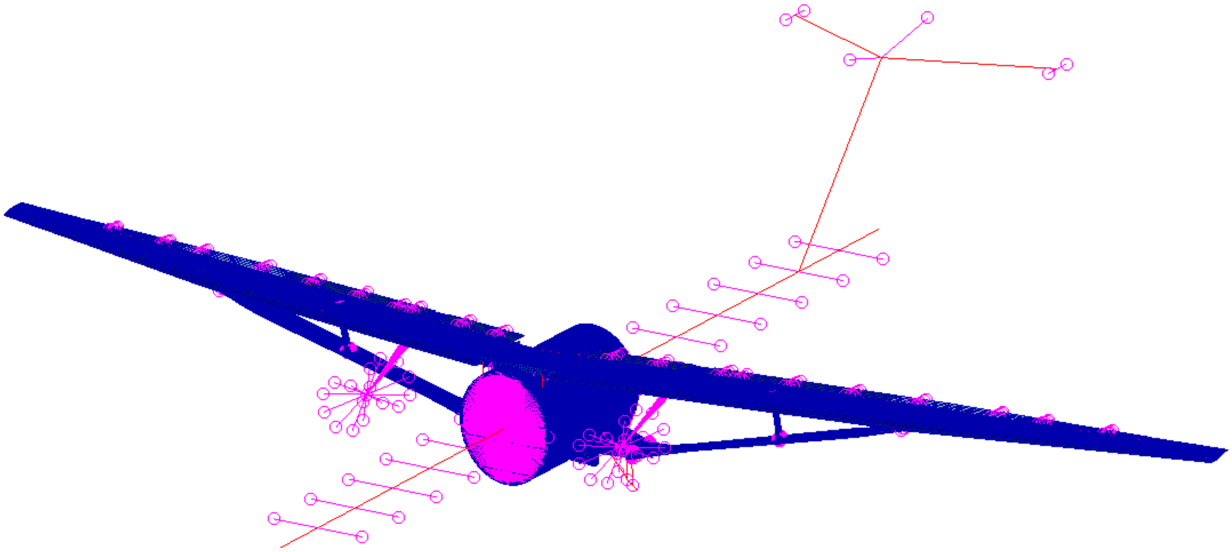

Figure 3.14 – Integrated FEM.

3.5 Mass Case Descriptions

The FEM includes weight computed from density and volume for all sized structural items, which includes the wingbox, strut, and jury. The density of the composite material was increased to represent cutouts, fasteners, and other unmodeled features. All remaining weight is provided to match the vehicle group weight statement, and is spread on the model as concentrated mass items. Spread weight representing Operating Weight includes the fuselage and tails, engine/nacelle/pylon, wing control surfaces, and wing systems. Spread weights representing estimated joint weights at the interfaces of the wing/strut, strut/jury, strut/landing gear pylon, strut/wing, and of the wing fold joint were included in the model.

Table 3.2 lists the fuel and payload combinations that were analyzed. Concentrated mass items were spread to represent the five distinct cases.

Table 3.2 – Payload and Fuel Combinations.

Fuel	Payload
Fuel to reach MTOW from MZFW	Max to Reach MZFW
Full	Max to reach MTOW with Full Fuel
Full	None
Reserve	Max to Reach MZFW
Reserve	None

3.6 Aerodynamic Model and Corrections

The doublet lattice aerodynamic model of the SUGAR TTBW configuration is shown in Figure 3.15, with panels representing the wing, body, tails, nacelles, and struts.

Correction factors were calculated to match sectional Overflow results calculated at flight Reynolds number for a Rev-H wing, body, and strut model. This was done for both the wing and strut. The process starts by calculating the Overflow sectional lift curve slope and aerodynamic center between two angles of attack. The Mach number and angles of attack used are listed in Table 3.3. Lift curve slope correction matrices are calculated so the corrected doublet lattice rigid aerodynamics match the Overflow lift curve and aerodynamic center. Figure 3.16 shows the corrected doublet lattice sectional lift curve slope and aerodynamic center matching the Overflow results at Mach 0.745. Next, a lift at zero alpha (FA2J) matrix is found so the corrected 1g elastic doublet lattice results match the Overflow results at Mach 0.745 and C_L=0.73. Figure 3.17 shows the corrected 1g elastic doublet lattice sectional lift and moment matching the Overflow results at C_L=0.73. A downwash matrix (W2GJ) is found so the corrected rigid results with the FA2J matrix match the Overflow results at Mach 0.745 and C_L=0.73. This w2gj matrix represents the downwash between the jig shape and the 1g shape. The W2GJ matrix is then used to find the FA2J for all the other Mach numbers. These steady correction factors were used in the loads survey described in the next section.

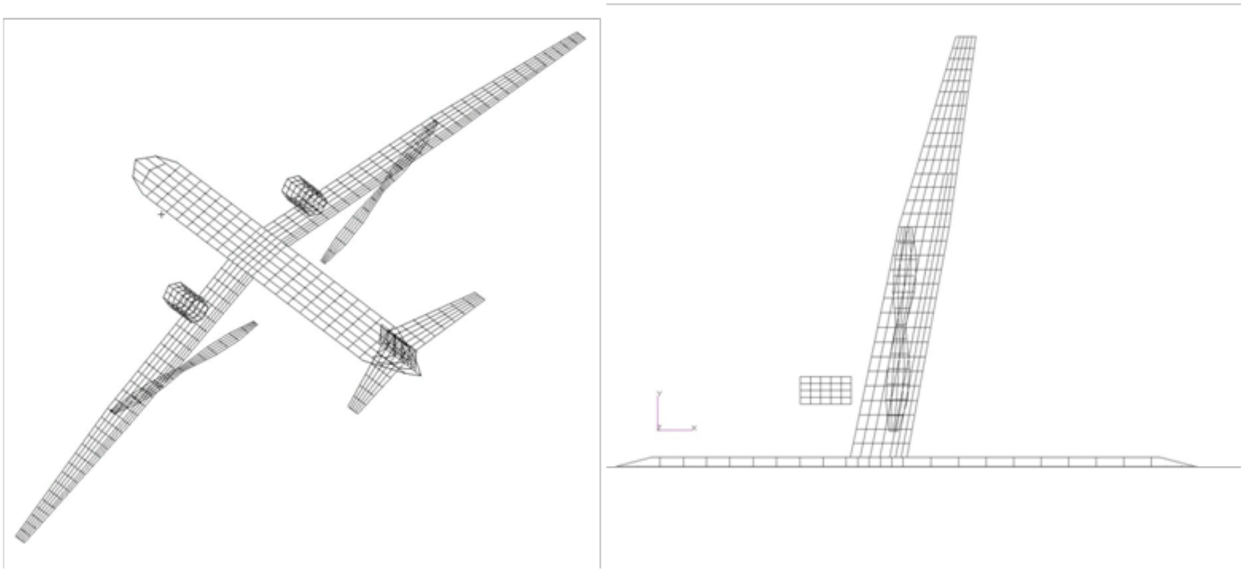

Figure 3.15 – Doublet Lattice Aerodynamic Model.

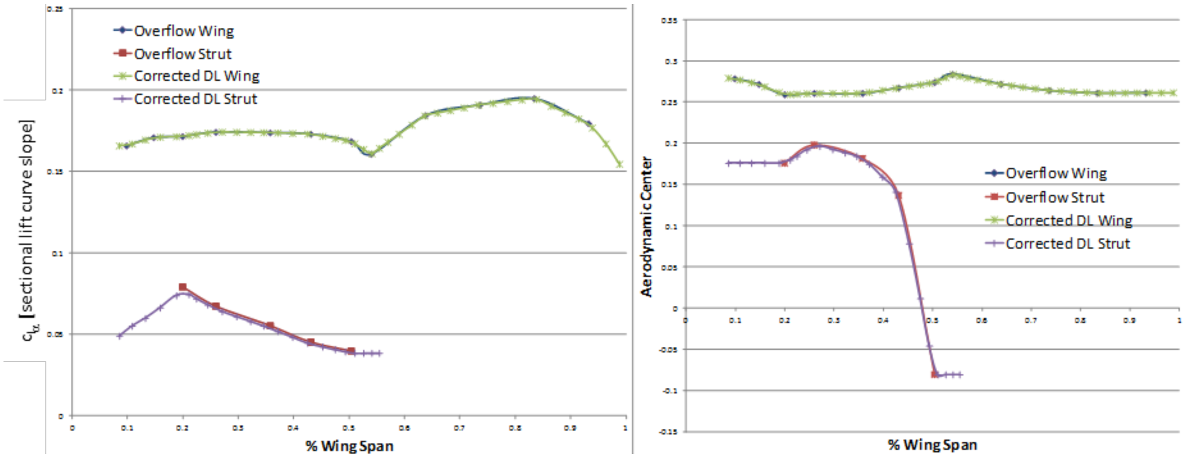

Figure 3.16 – Section Lift Curve Slope and AC Comparison M=.745.

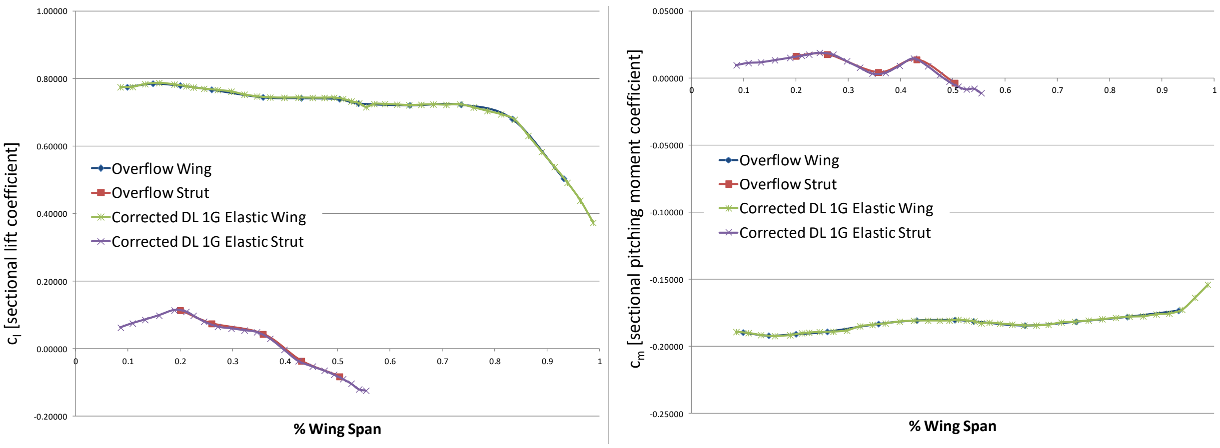

Figure 3.17 – Sectional Lift and Moment Comparison M =.745, C_L = .73.

Table 3.3 – Overflow Correction Conditions.

Mach	Alpha 1 [deg]	C_L 1	Alpha 2 [deg]	C_L 2
0.50	1.52	0.550	2.86	0.730
0.71	0.84	0.550	1.90	0.730
0.745	0.66	0.550	1.61	0.730
0.76	0.58	0.550	1.56	0.730
0.78	0.72	2.06	4.00	0.730

3.7 Load Conditions

Load conditions investigated include 2.5g and -1g balance maneuvers. Balance maneuvers are FAA required symmetric pitch conditions with a specified load factor and tail loads calculated to produce zero pitch acceleration. Flight loads were calculated in Nastran Sol 144 with the horizontal tail being used to trim the vehicle. Doublet lattice aerodynamics were corrected to match Overflow CFD results as described in the previous section.

A survey of 2.5g and -1g balance maneuvers was done to determine critical load conditions. Critical load conditions were chosen using the external and internal loads results. Critical 2.5g and -1g conditions are at Mach 0.76 with maximum payload and fuel to reach maximum takeoff weight. Four conditions were used for sizing which were 2.5g and -1g at maximum and minimum dynamic pressure. The internal and external loads for the four design conditions are shown in Figure 3.18. The internal loads plots show the large decrease in loads inboard of where the strut removes load from the wing. The bending moment drops significantly inboard of the strut attachment, nearly reaching zero at the jury, then growing slightly to the fuselage side-of-body. Torsion increases at the strut but does not increase much going inboard, resulting in a significant benefit at the side-of-body.

Gust loads were not investigated since they were not found to be critical in a survey performed in Phase II.

The loads used for the sizing runs were calculated using the initial unsized structural model and not updated for the sized model. These loads are conservative because the wing for the sized model washes out more and provides more aeroelastic relief to the wing loads.

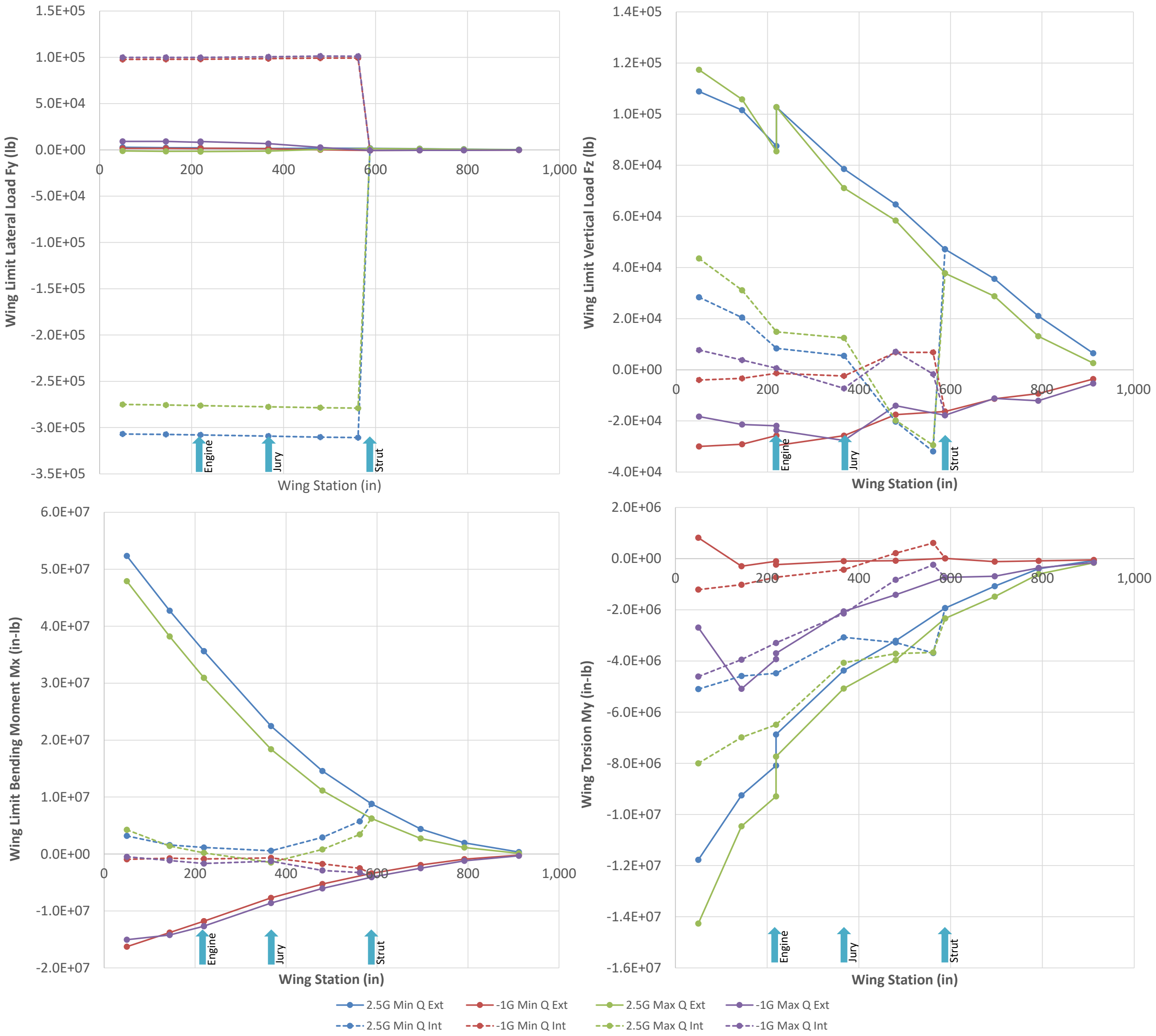

Figure 3.18 – Limit Loads 2.5g and -1g Balance Maneuvers.

3.8 Structural Sizing and Optimization

The wing, strut, and jury structure was optimized using Nastran Sol 200 and Hypersizer local panel code to meet strength and buckling constraints. Hypersizer provides a more comprehensive higher fidelity buckling analysis than the Sol 200 analysis. It enables rapid optimization of both skin panels and stringer geometry to lower weight. It also allows for a rapid assessment of stringer spacing. Hypersizer reads in the internal loads and panel geometry from Nastran. The model is first optimized in Sol 200 and the loads from the optimized model are read in to Hypersizer. Hypersizer is run and generates an updated Nastran deck. The updated Nastran deck is run and the updated loads are read into Hypersizer. This process is repeated to convergence. The wing and strut skins were optimized in Hypersizer. All other components were optimized in Sol 200.

The strength constraint for 2D elements was lamina principal strain less than 0.0045 at ultimate load. The strength constraint for cap elements was laminate stress less than 90,000 PSI at ultimate load. No buckling was allowed at ultimate load. Minimum gauge was 0.1 inch for the skins.

3.9 Stress/Buckling Sizing Results

A converged solution was found that met all strength and buckling constraints. An assessment of skin stringer spacing showed significant weight benefit from reducing the 5-inch stringer spacing to 4 inches. There was not much reduction when a 3-inch spacing was optimized so 4-inch stringer spacing was used for all skins. Figure 3.19 and Figure 3.20 show the sized results for the wing and strut upper and lower skins. The strut upper skin at the wing attach sized up to 1.4 inches. This can be minimized with a more detailed analysis with local pad up around the attach joint. Comparing the skin thickness to the Phase II results shows fewer design regions with minimum gauge. This is due to Hypersizer increasing above minimum gauge to prevent buckling of the skin between stringers. This buckling mode was not addressed in the Phase II analysis because the strut was modeled as a simple beam box element. Figure 3.21 and Figure 3.22 show failure modes for the wing and strut upper and lower skins. This plot shows which regions were critical for strength constraints and which regions were critical for buckling constraints. The plot also shows which of the multiple buckling modes were critical. The results show most of the skin is critical for buckling. Figure 3.23 through Figure 3.34 show the stringer geometry for the sized upper and lower wing and strut skins. The sized stringer weight to total weight came in less than the 33% factor that was assumed in the Phase II analysis. Overall weight comparison with the Phase II results is shown in Table 3.4. The current results are in line with previous results. The splitter plate and strut LE/TE fairing forward of the front spar and aft of the rear spar were not included in the Phase II analysis.

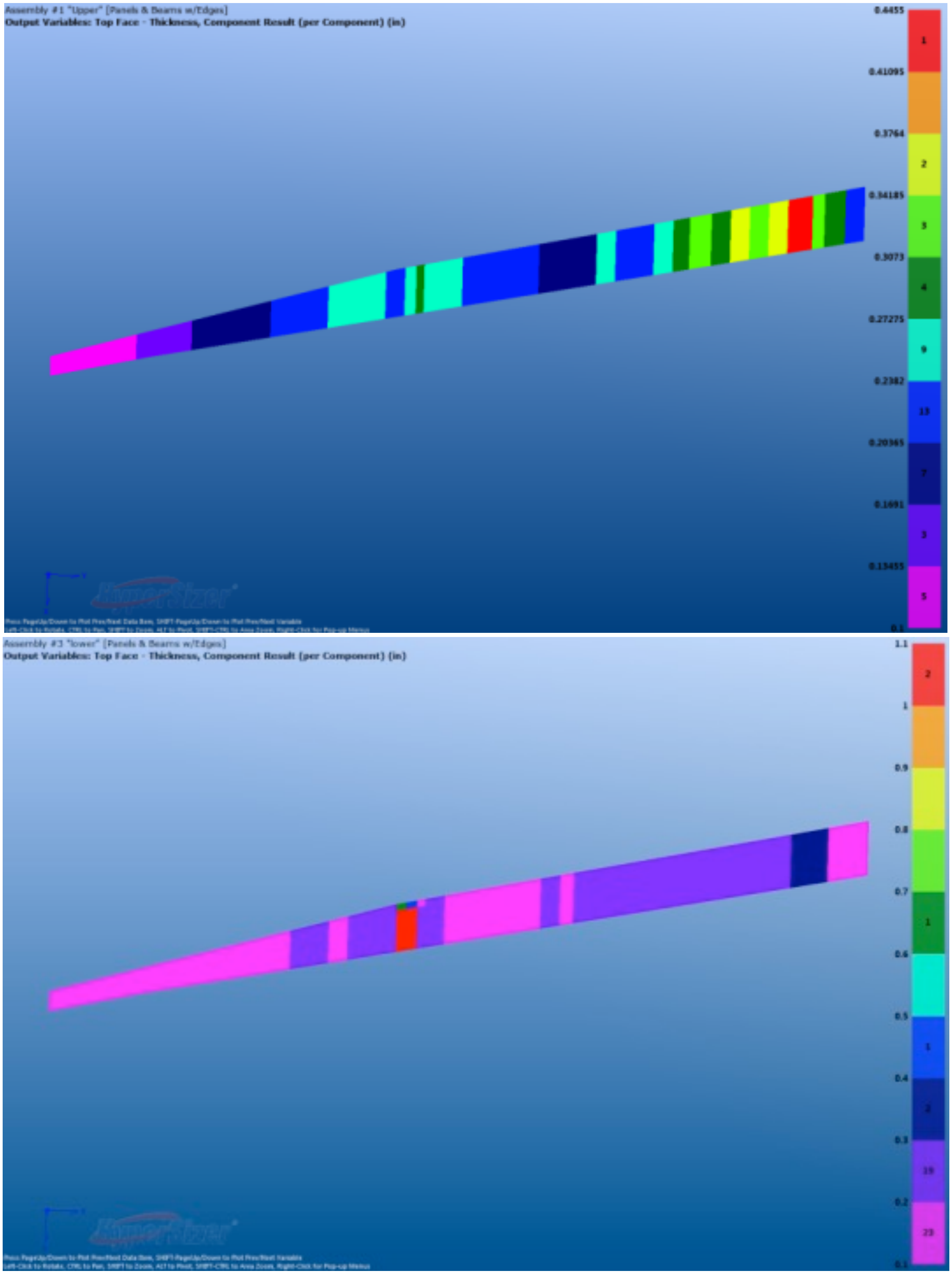

Figure 3.19 – Wing Sized Upper (Top) and Lower (Bottom) Skin Thickness.

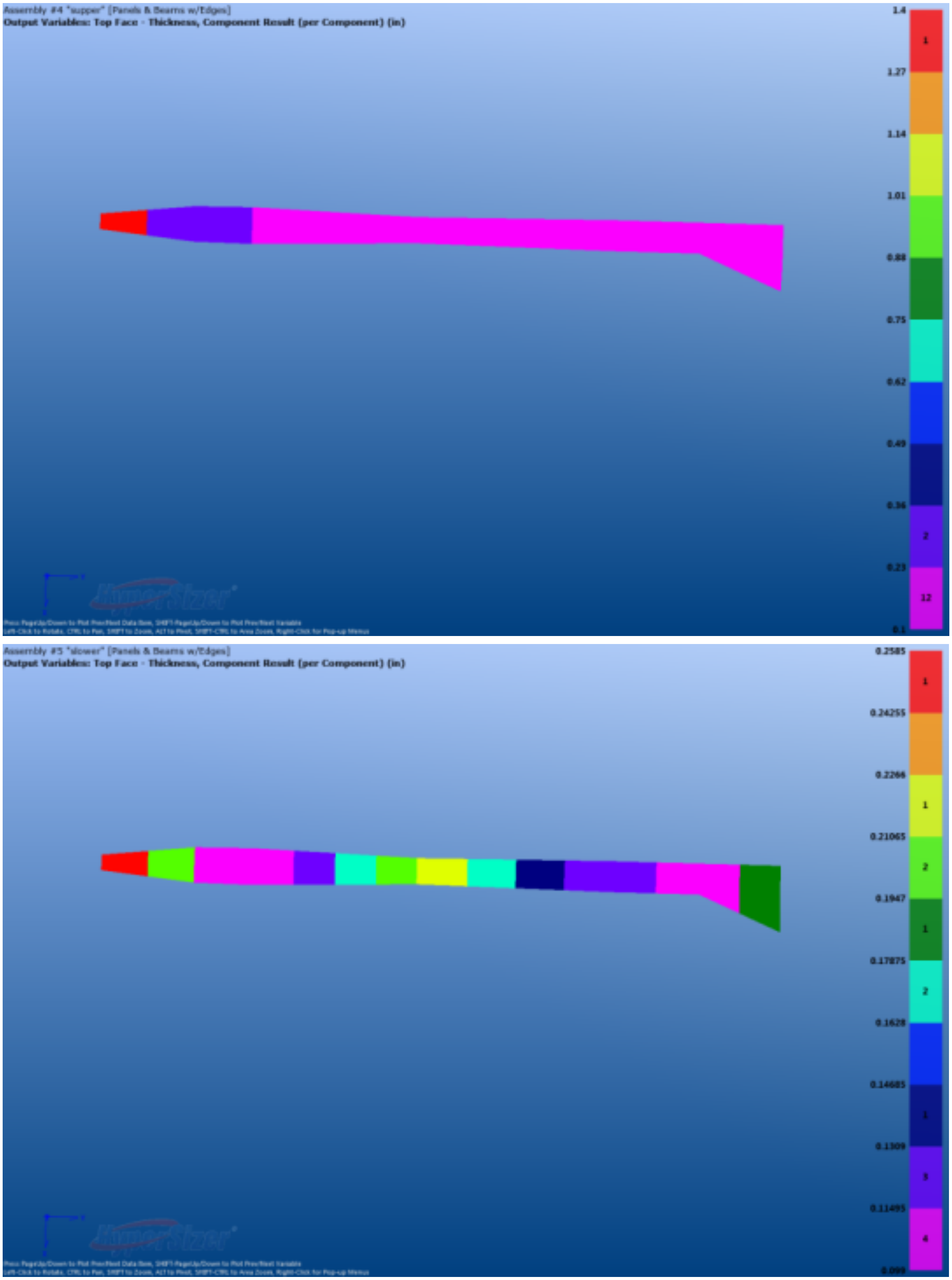

Figure 3.20 – Sized Strut Upper (Top) and Lower (Bottom) Skin Thickness.

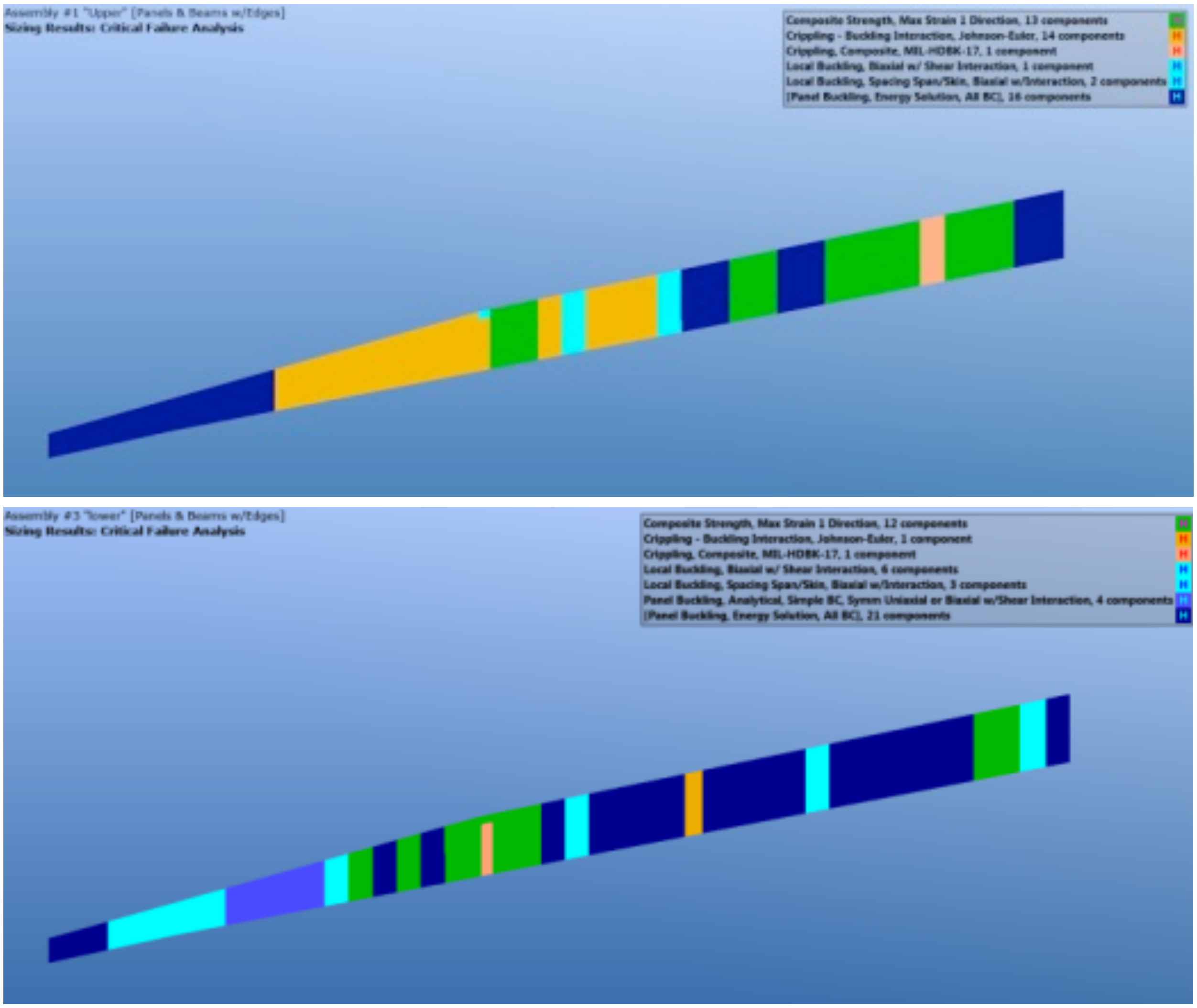

Figure 3.21 – Wing Upper (Top) and Lower (Bottom) Skin Failure Mode.

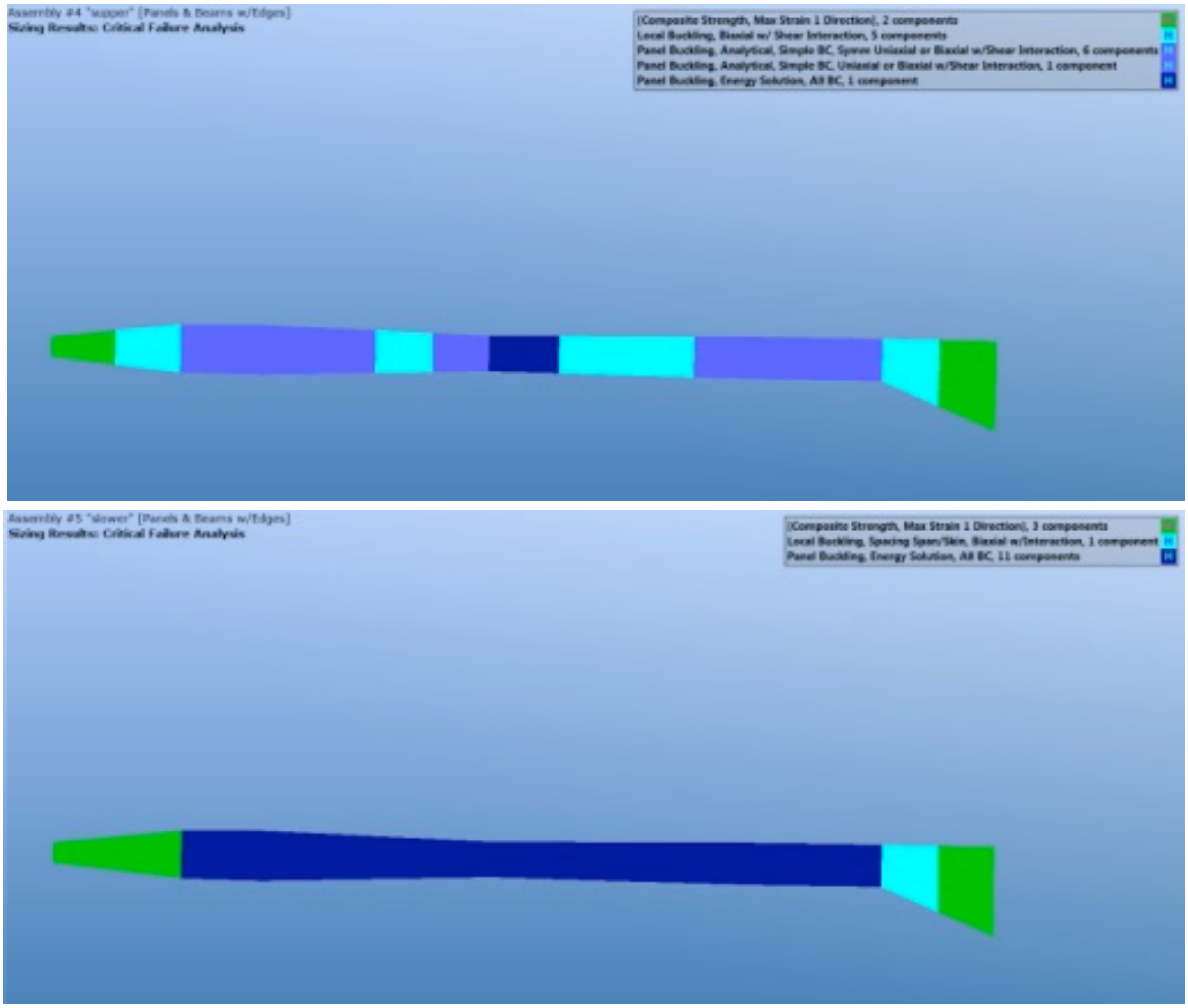

Figure 3.22 – Strut Upper (Top) and Lower (Bottom) Skin Failure Mode.

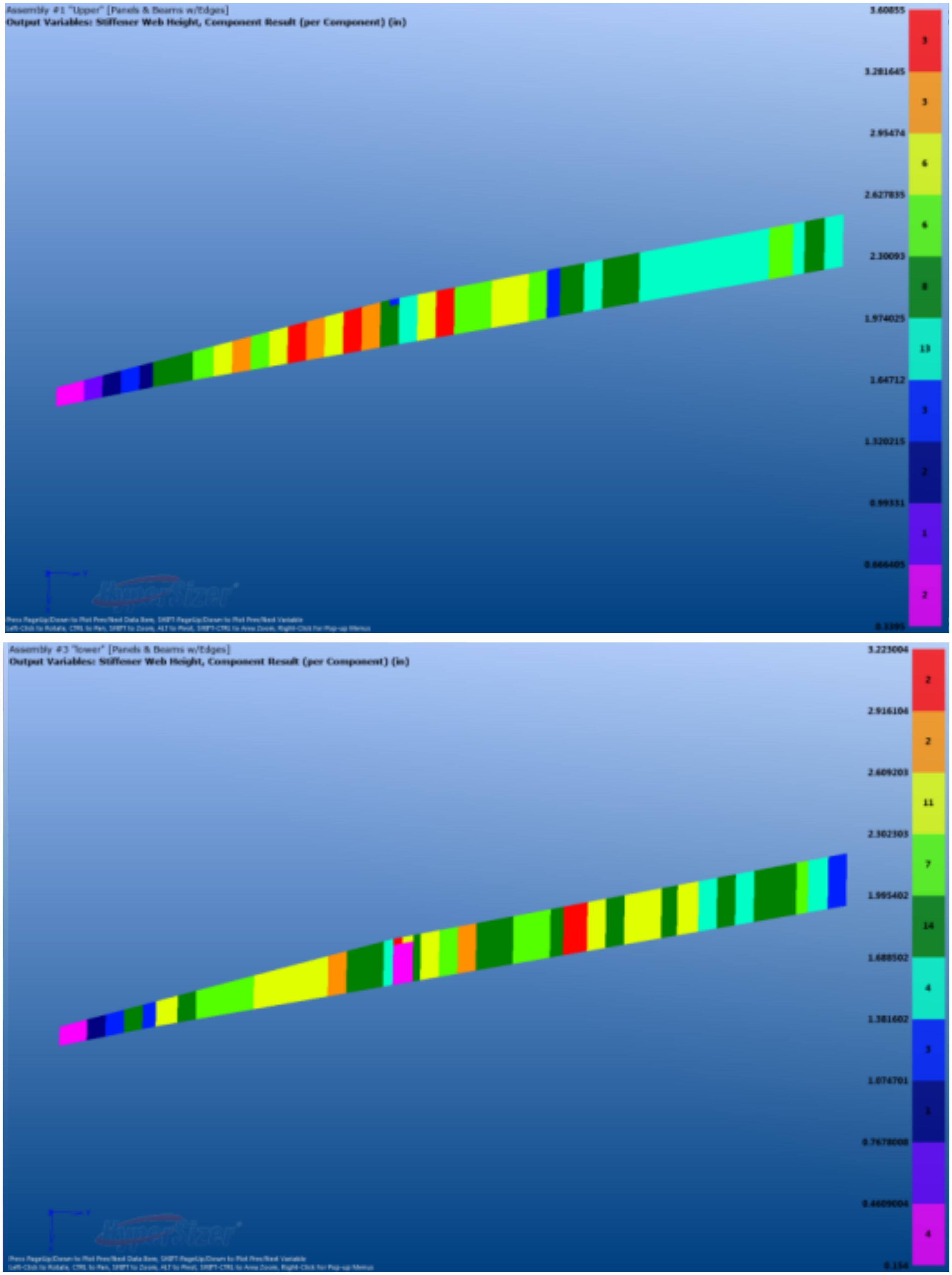

Figure 3.23 – Wing Upper (Top) and Lower (Bottom) Skin Stringer Web Height.

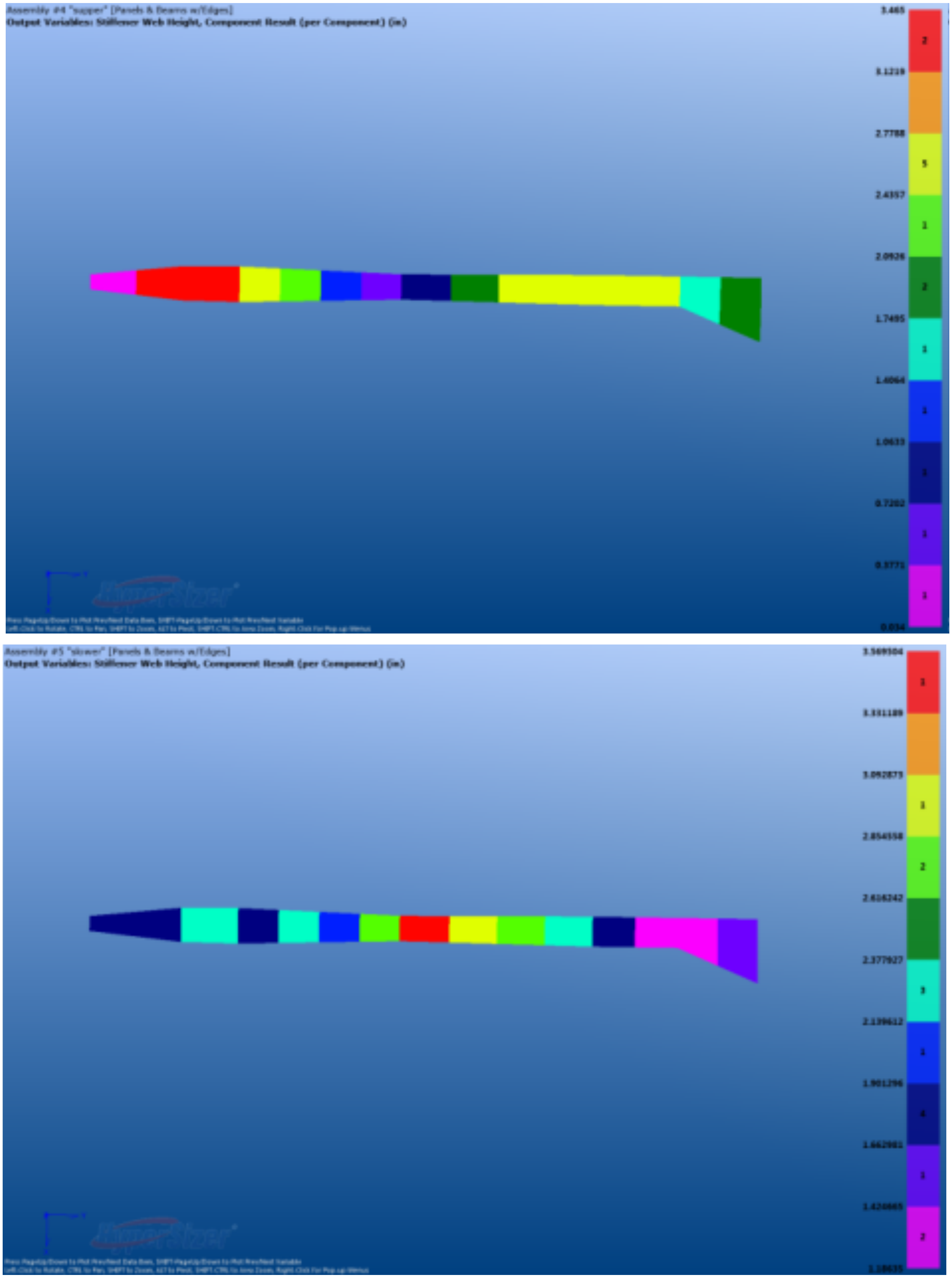

Figure 3.24 – Strut Upper (Top) and Lower (Bottom) Skin Stringer Web Height.

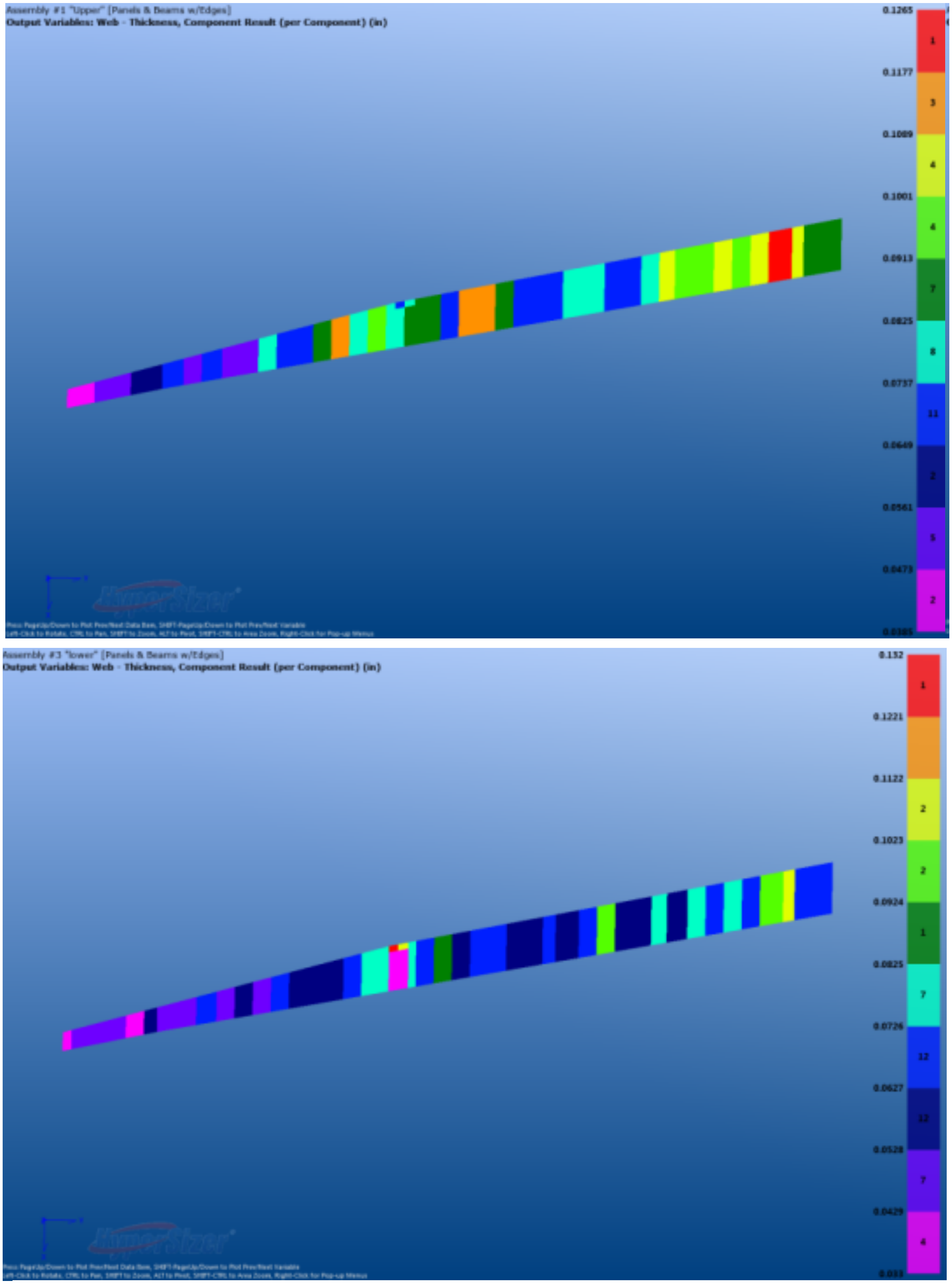

Figure 3.25 – Wing Upper (Top) and Lower (Bottom) Skin Stringer Web Thickness.

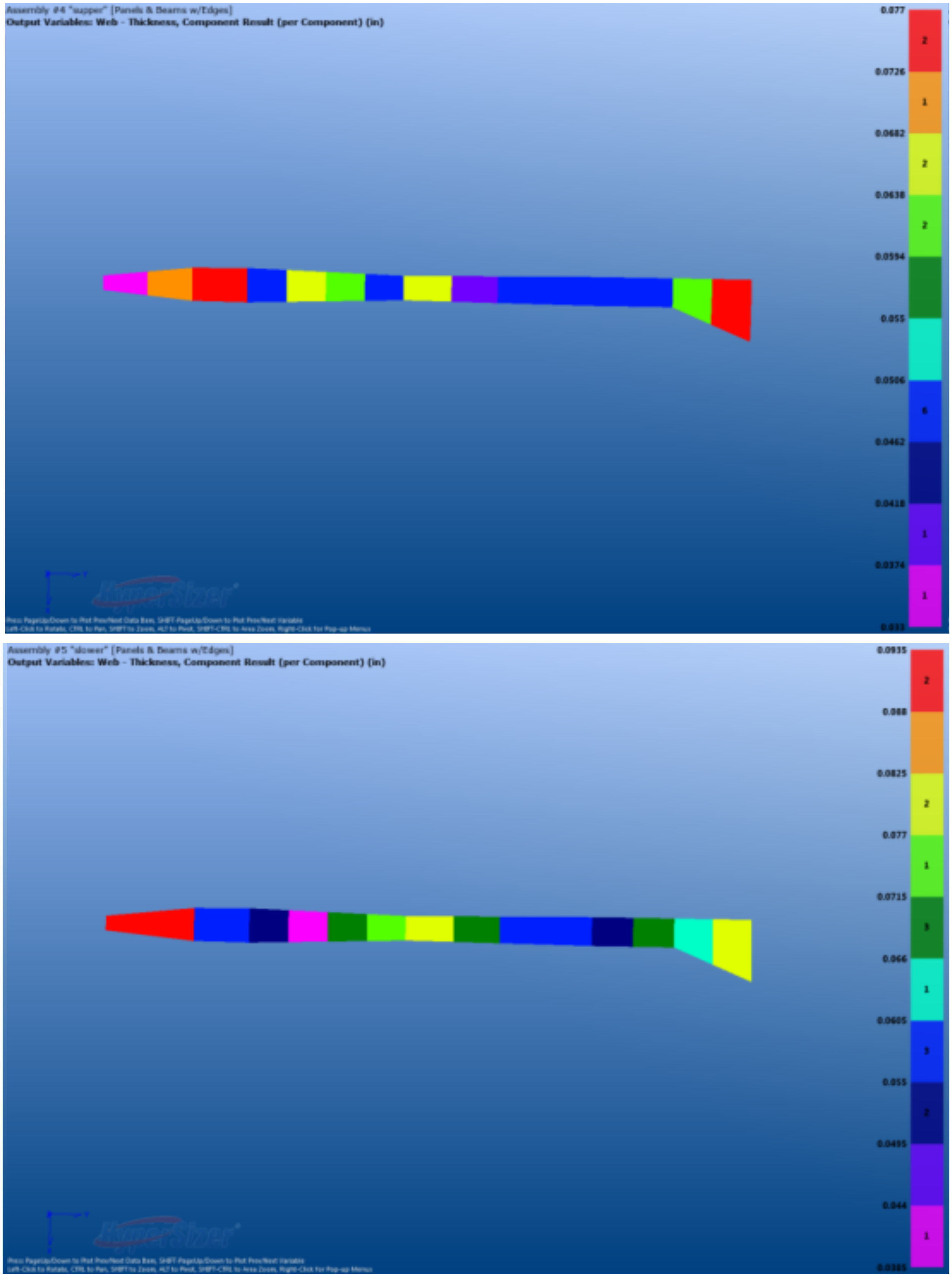

Figure 3.26 – Strut Upper (Top) and Lower (Bottom) Stringer Skin Web Thickness.

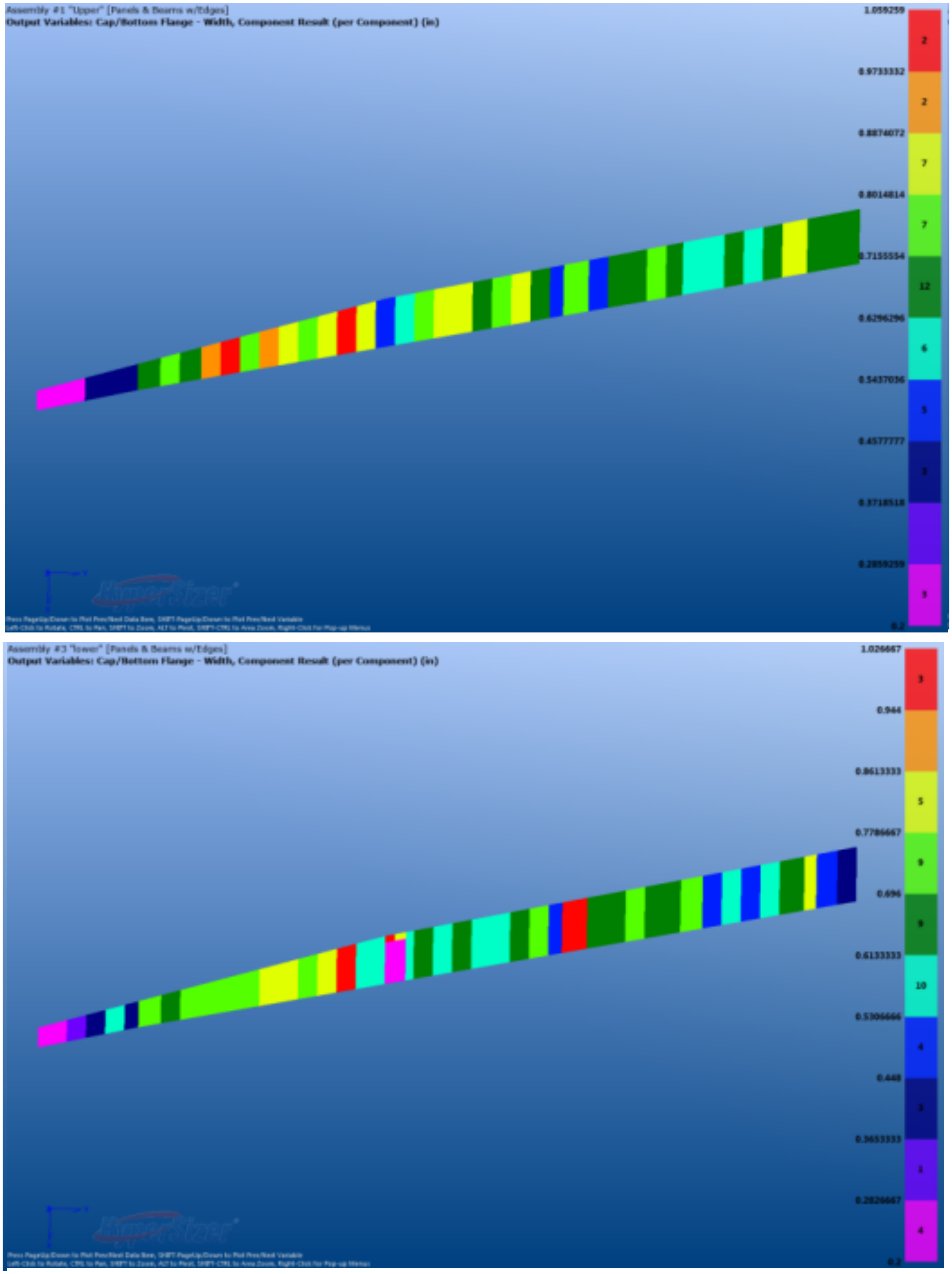

Figure 3.27 – Wing Upper (Top) and Lower (Bottom) Skin Stringer Cap Width.

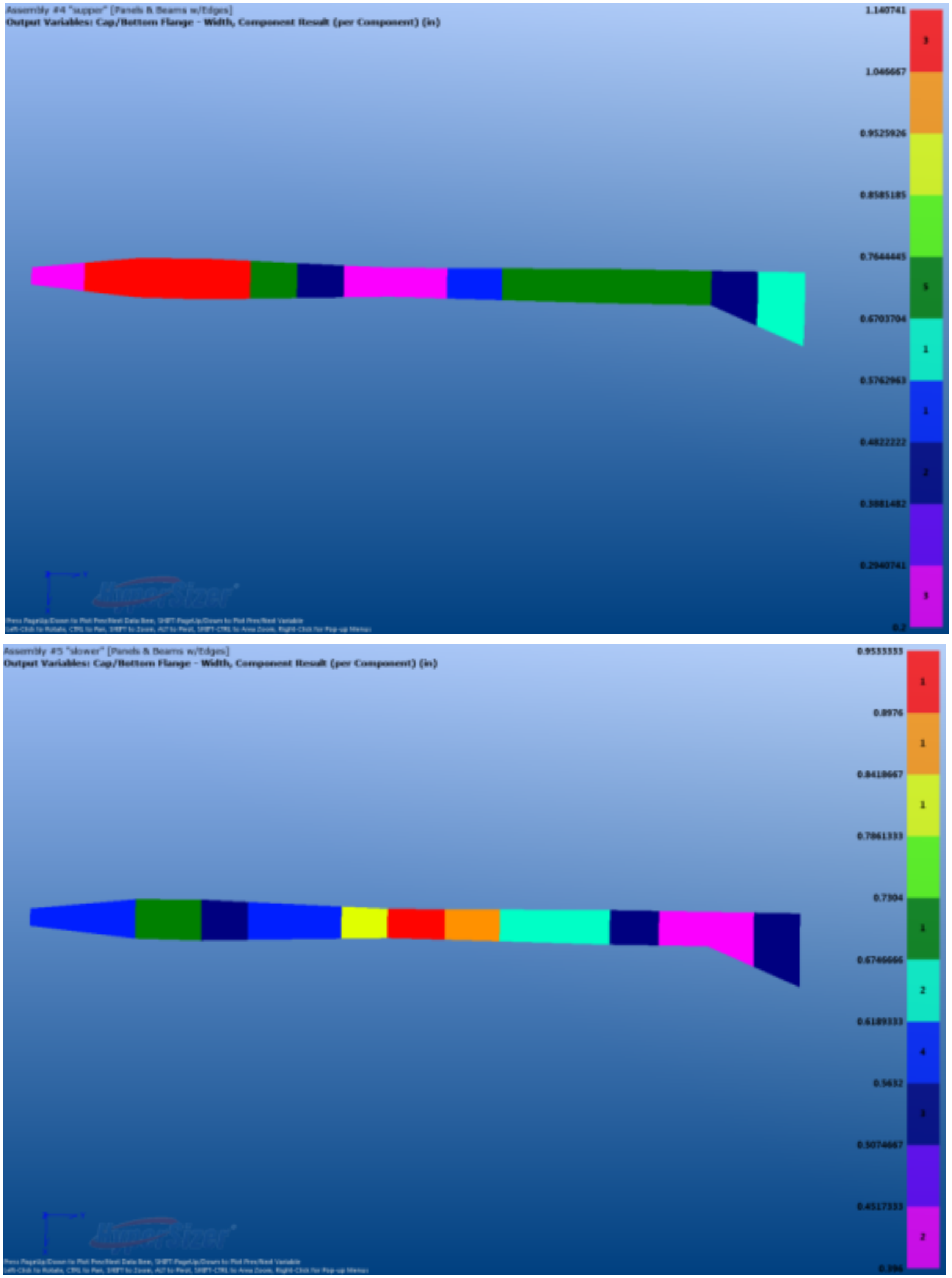

Figure 3.28 – Strut Upper (Top) and Lower (Bottom) Skin Stringer Cap Width.

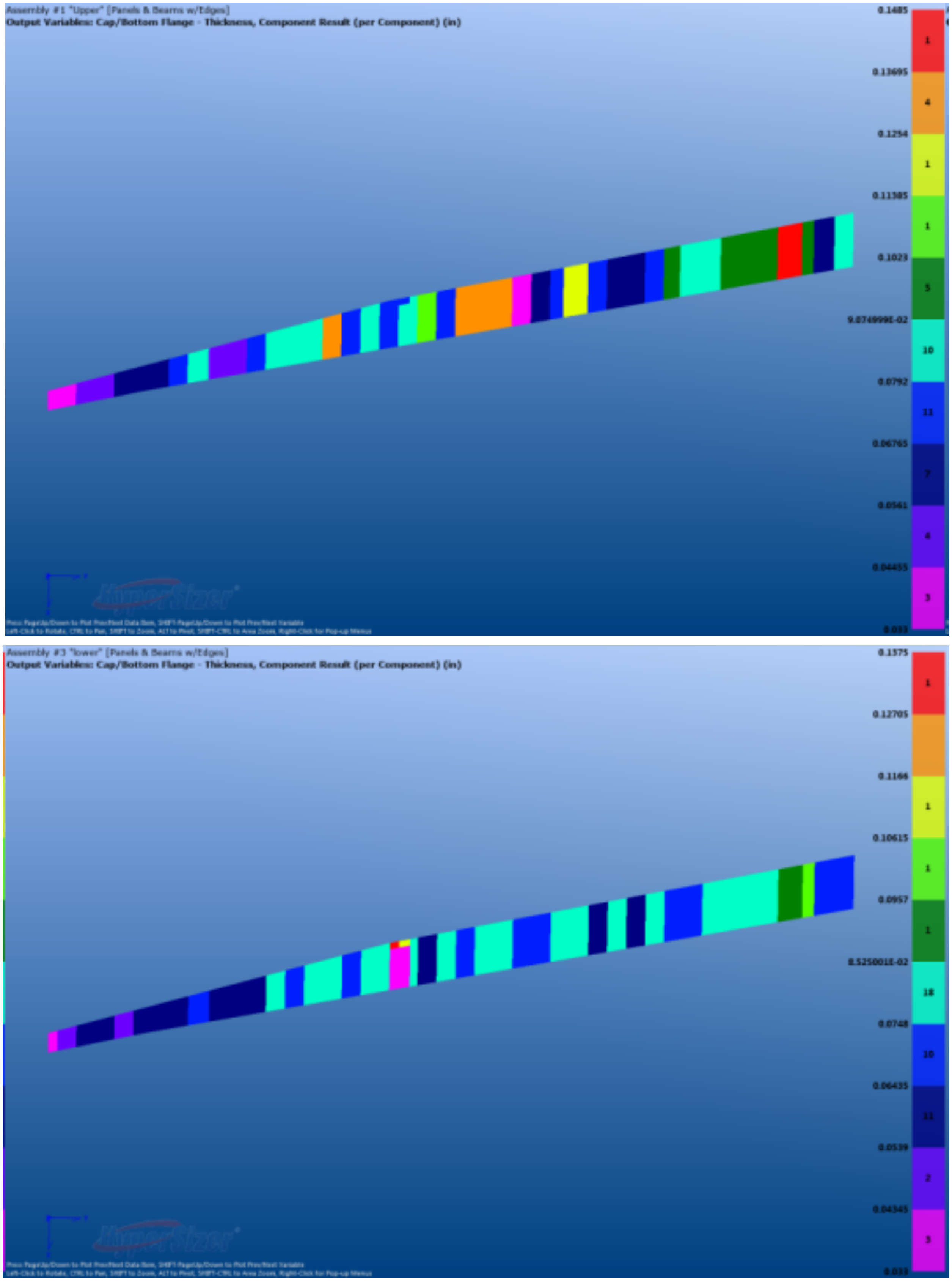

Figure 3.29 – Wing Upper (Top) and Lower (Bottom) Skin Stringer Cap Thickness.

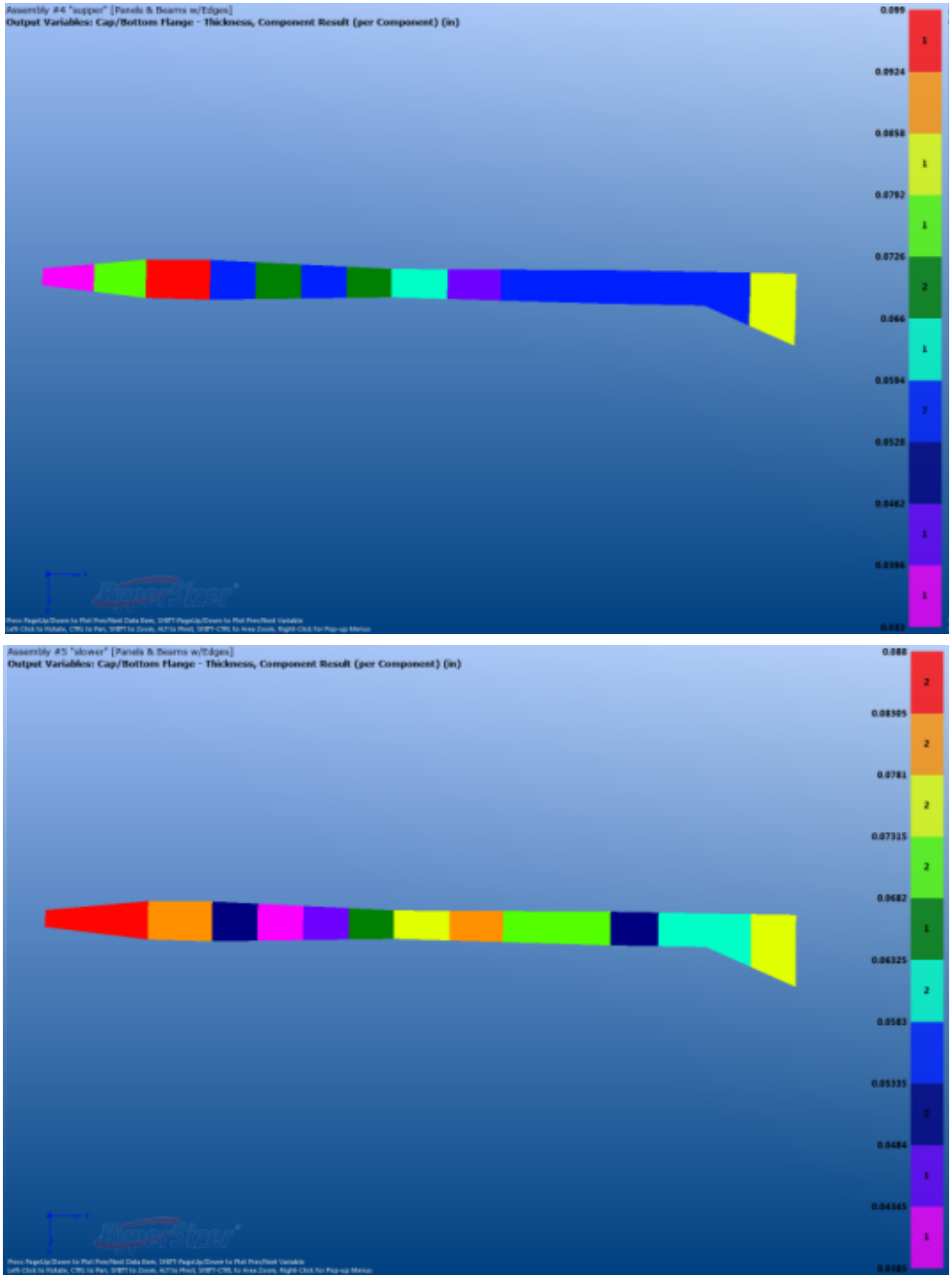

Assembly #4 "supper" [Panels & Beams w/Edges]
Output Variables: Cap/Bottom Flange - Thickness, Component Result (per Component) (in)

Assembly #5 "slower" [Panels & Beams w/Edges]
Output Variables: Cap/Bottom Flange - Thickness, Component Result (per Component) (in)

Figure 3.30 – Strut Upper (Top) and Lower (Bottom) Skin Stringer Cap Thickness.

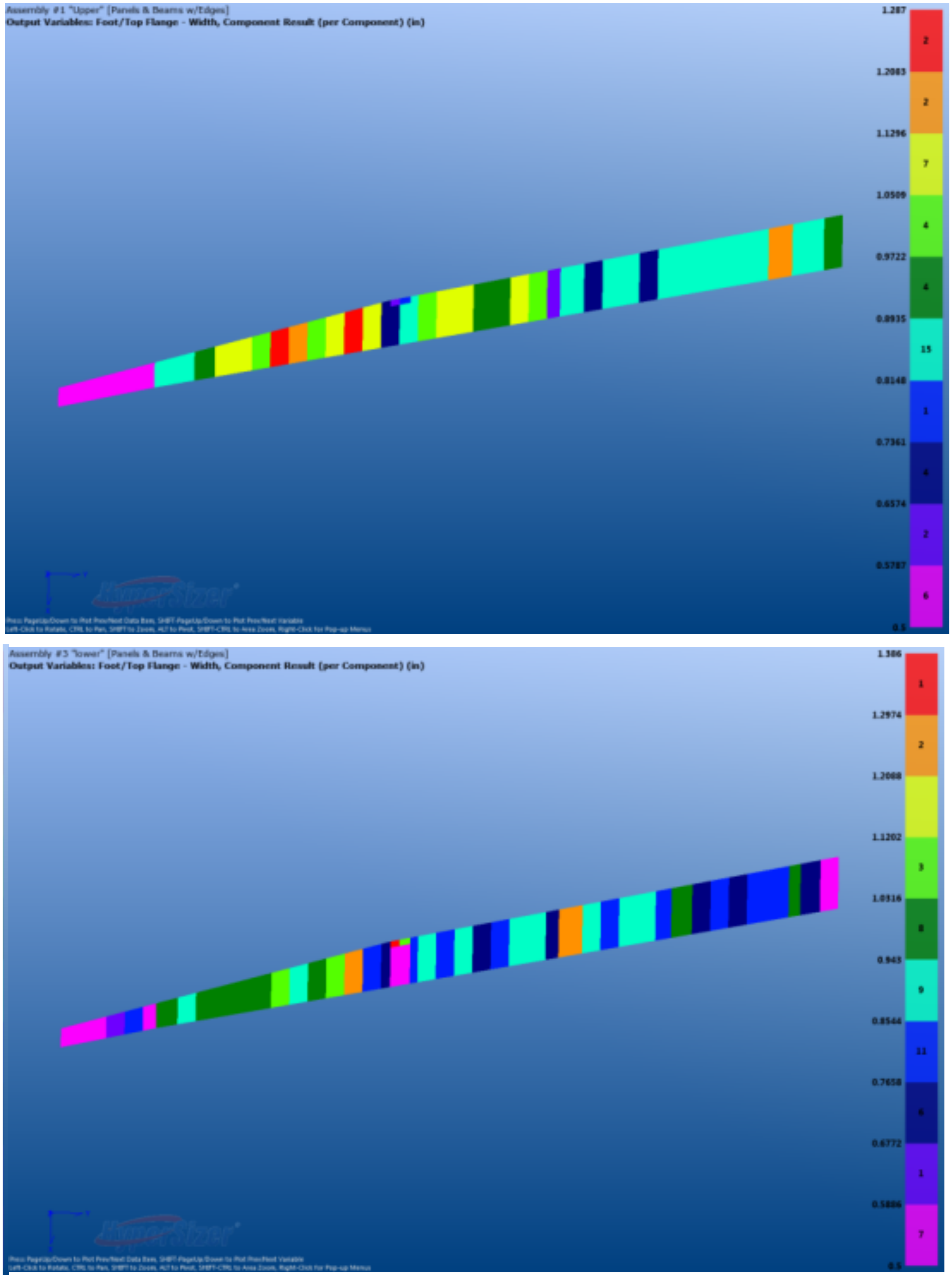

Figure 3.31 – Wing Upper (Top) and Lower (Bottom) Skin Stringer Foot Width.

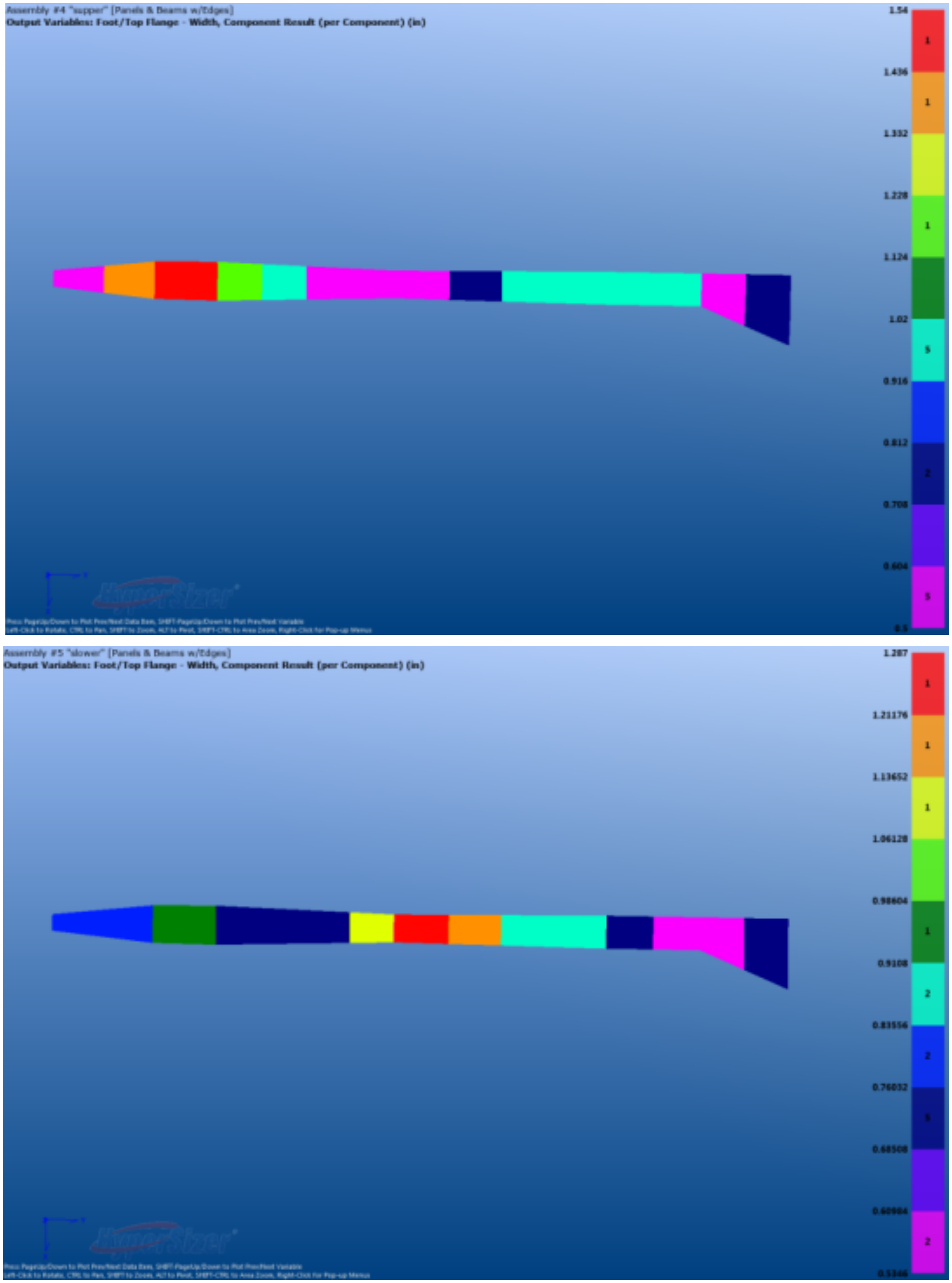

Figure 3.32 – Strut Upper (Top) and Lower (Bottom) Skin Stringer Foot Width.

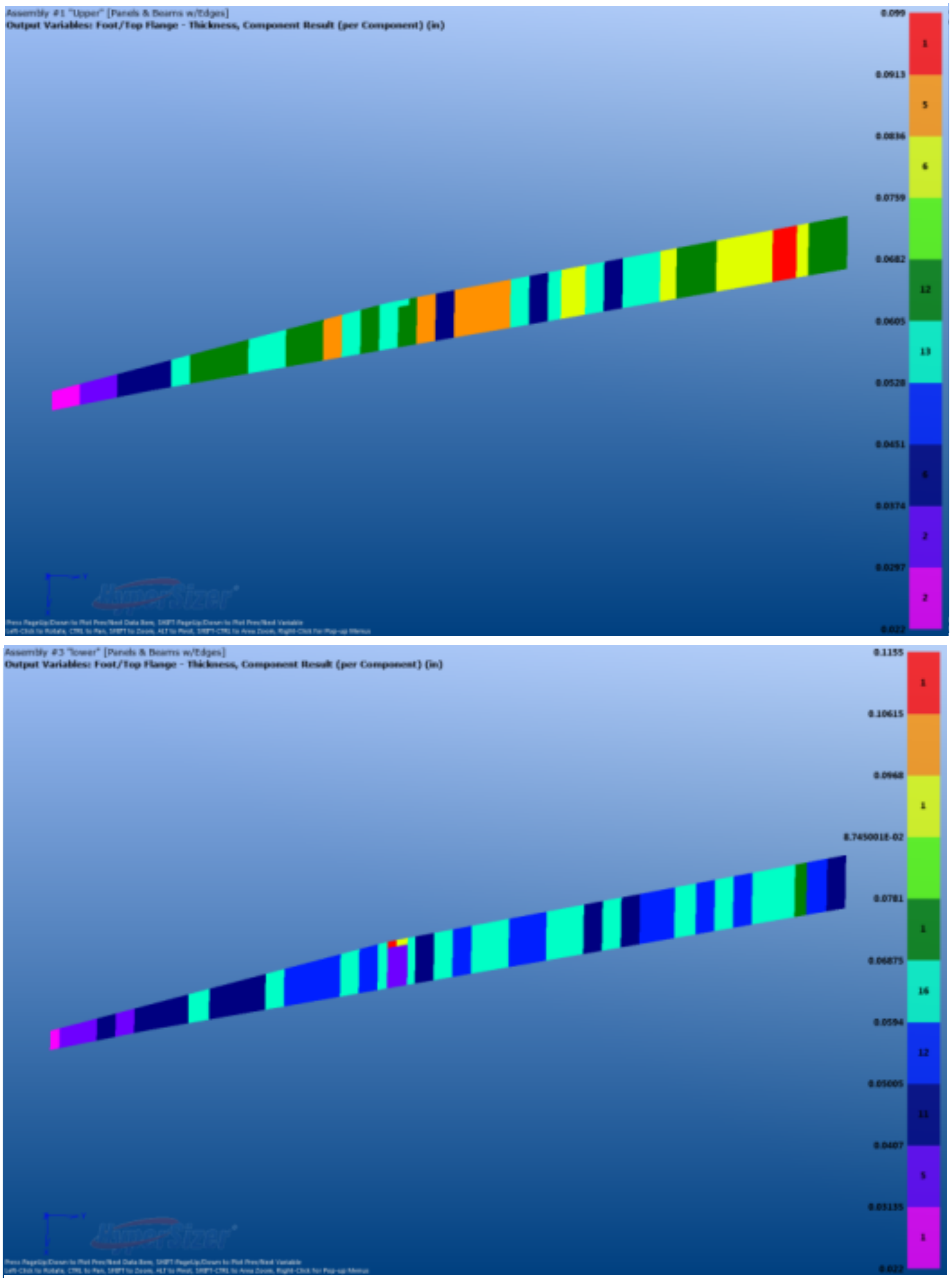

Figure 3.33 – Wing Upper (Top) and Lower (Bottom) Skin Stringer Foot Thickness.

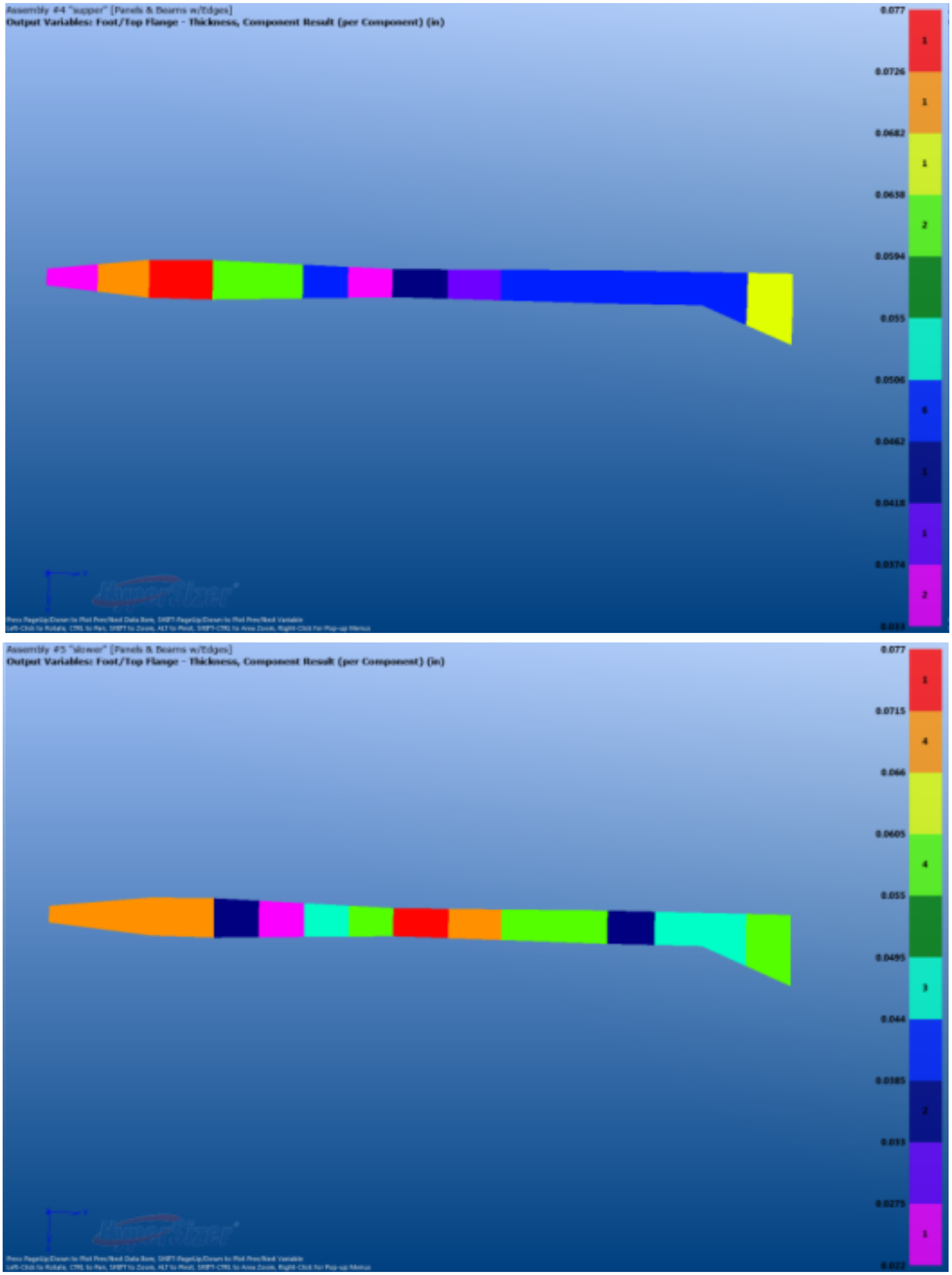

Figure 3.34 – Strut Upper (Top) and Lower (Bottom) Skin Stringer Foot Thickness.

Table 3.4 – Sized Structure Weight Summary (weights in pounds).

	Phase II	Current	
	No Flutter	No Flutter	Delta
Skin	5557.8	5439.0	-118.8
Spar	765.8	879.7	113.9
Ribs	705.4	515.2	-190.2
Spar Caps	229.6	214.9	-14.7
Rib Cap	160.9	99.5	-61.4
Strut	787.1	913.5	126.4
Jury	21.4	43.9	22.5
Splitter		250.5	
Strut LE/TE		289.7	

3.10 Stress/Buckling Sizing Conclusions

The results of the detailed FEM sizing analysis for this very high aspect ratio wing show a significant truss-braced configuration benefit in structural weight relative to a cantilevered wing of similar aspect ratio. The loads and sized structure inboard of the strut both show the benefit of the truss bracing.

3.11 Structural Optimization with Flutter Constraints

The sized strength and buckling constrained model was the baseline for optimization including flutter constraints. The high fidelity strength and buckling sizing results in smeared skin properties, which cannot be used directly in the Nastran optimization. The strength and buckling optimized smeared membrane stiffnesses are set as a minimum for the flutter constrained model. The flutter constrained optimization can then only add stiffness above the strength and buckling optimized model. As was done in Phase II, flutter constraints were run for both full fuel and reserve fuel mass cases.

Preliminary runs of the baseline model sized up the strut at the wing attachments to gauges larger than can be practically produced with composite materials. Therefore, the strut most outboard rib and the skin and spars between the most outboard rib and the next inboard rib were changed to steel. An extra strut spar was added halfway between the front and rear spar in the outboard bay. This extra spar was attached to the wing bringing the strut wing attachment locations to three. In addition, the auxiliary spar in the wing at the strut attachment location was changed to steel. These changes are shown in Figure 3.35. Using the updated model Nastran Solution 200 found a reasonable solution to meet the linear flutter constraints. Figure 3.36 through Figure 3.38 show the flutter constrained sized wing skin membrane stiffnesses compared to the strength and buckling results. The two results are identical for the first 15 stations since the strength and buckling smeared properties were used in this region. The optimizer has added stiffness around the strut attachment on both the upper and lower skin to meet the flutter constraints. It has also added stiffness at the tip of the wing. All of the flutter stiffnesses are greater than strength and buckling stiffnesses except outboard for the G22 stiffness. Increasing this stiffness will have little effect on the flutter results but means the weight estimate is slightly optimistic.

Figure 3.39 shows the sized wing spar and rib web thicknesses. The spars have sized up at the root around the fuselage attachment and the front spar at the strut attachment. All ribs are minimum gauge except the wing tip rib, which has sized up. Figure 3.40 shows the strut upper and lower skin thickness. The most outboard bay is not included in this figure because it has been changed to steel material and is plotted separately. The results show the inboard strut skins at minimum gauge with the skins by the steel structure sizing up. Figure 3.41 shows the strut spar and rib webs, again with the steel structure removed. The spar and rib webs are near minimum gauge everywhere except the outboard rib at the steel structure interface, which sized up to a large value. The strut tip steel structure sizing results are shown in Figure 3.42. The tip rib and rear spar have sized up to nearly 3 inches. This is clearly the critical area for meeting the flutter constraints. The linear flutter damping and frequency results for the sized model are shown in Figure 3.43 and Figure 3.44. Data below the red line satisfy the flutter damping requirement. The full fuel critical antisymmetric mode just meets the zero damping requirement at dive speed. This mode has a small pad on the .02 G damping requirement at 1.15 dive speed. The reserve fuel mass condition flutter mode crosses zero damping above 500 KEAS. As in Phase II, the flutter mode is a coalescence of wing bending and torsion modes. The 3.42 Hz critical complex flutter mode at dive speed is shown in Figure 4.45. Although other modes make significant contributions to the damping, the primary bending and torsion mode are shown in Figure 3.46 and Figure 3.47. As before, the torsion mode shows significant deflection at the engine attachment.

The linear flutter sized model was run using nonlinear structural preload and large displacement effects. The same methods used in Phase II were used for this study. Nonlinear Nastran Sol106 runs were completed at 290 KEAS and cruise speed at -1g, and at 290 KEAS, cruise, and dive speeds at 0g. The resulting stiffness and mass matrices were used in the Sol145 flutter solution. The matrices calculated at dive speed and 0g were used for all flutter points above dive speed. The nonlinear flutter results (Figure 3.48) show no unstable modes. This means for this model nonlinear structural effects improve damping on the critical flutter modes. The flutter weight increment could be reduced by taking advantage of the nonlinear effects. To stay conservative, the documented weight results (Table 3.5) are for the linear flutter sized model. The results show 500 lbs were added to meet flutter constraints above the strength and buckling sized model. It should be noted that the changes made to the structure, an addition of an auxiliary spar and material changes to steel are not necessarily the most efficient or recommended methods to solve the strut to wing interface stiffness requirements highlighted by the aeroelastic analysis. This area deserves greater study.

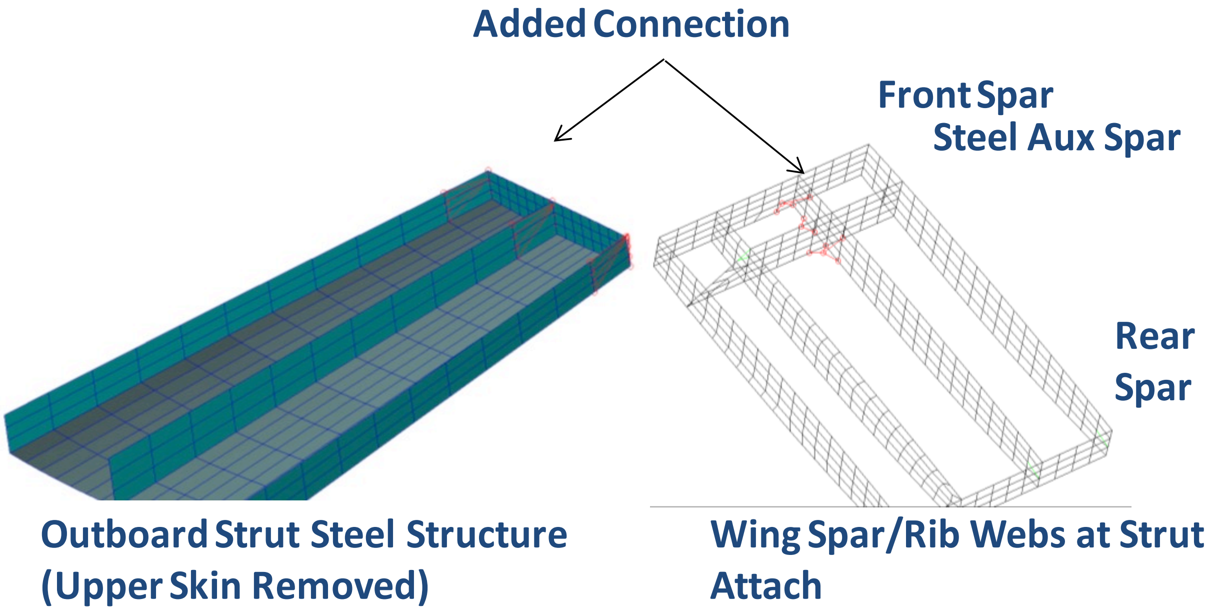

Figure 3.35 – Baseline Model Updates.

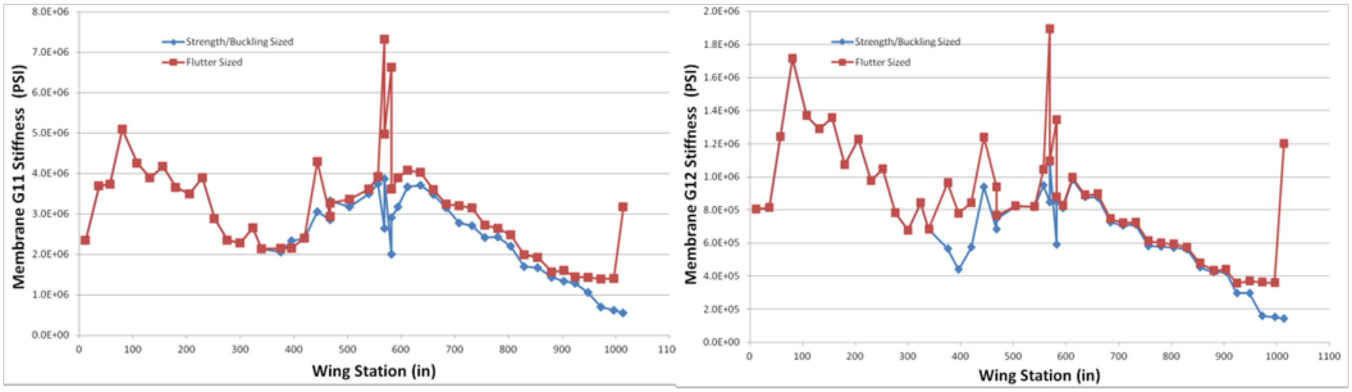

Figure 3.36 – Upper Wing Skin Membrane Stiffness Comparisons G11 and G12.

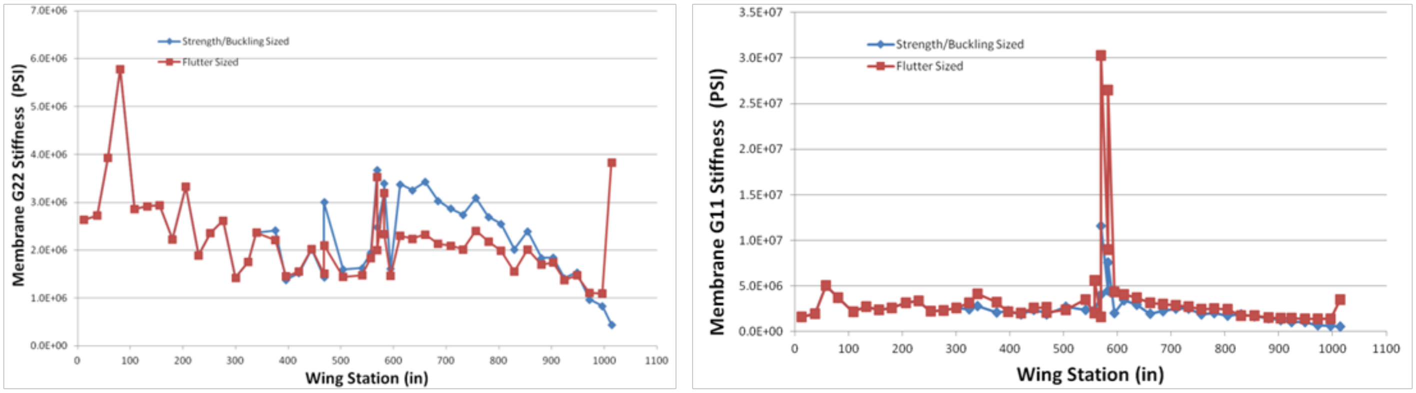

Figure 3.37 – Wing Skin Membrane Stiffness Comparisons Upper G22 and Lower G11.

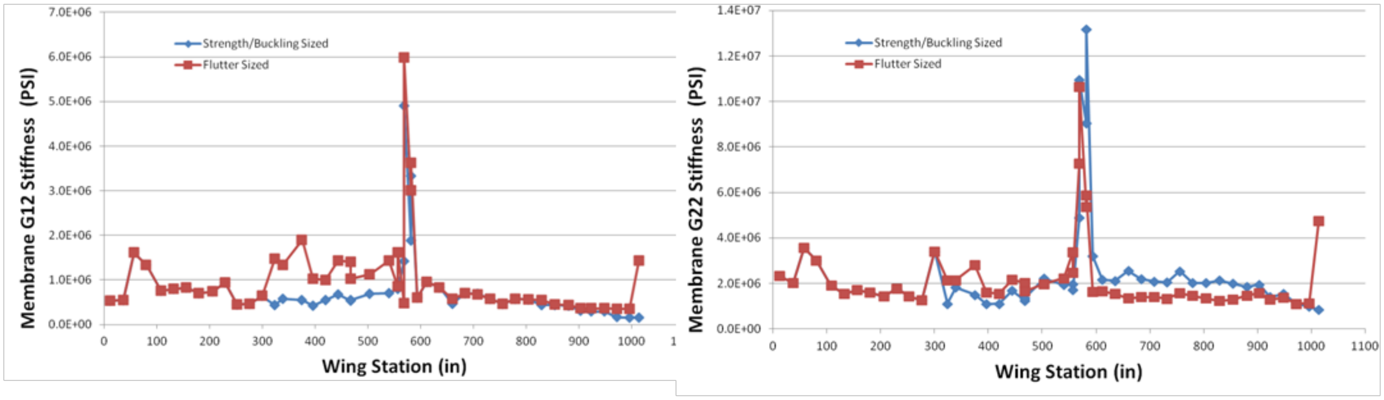

Figure 3.38 – Wing Lower Skin Membrane Stiffness Comparisons G12 and Lower G22.

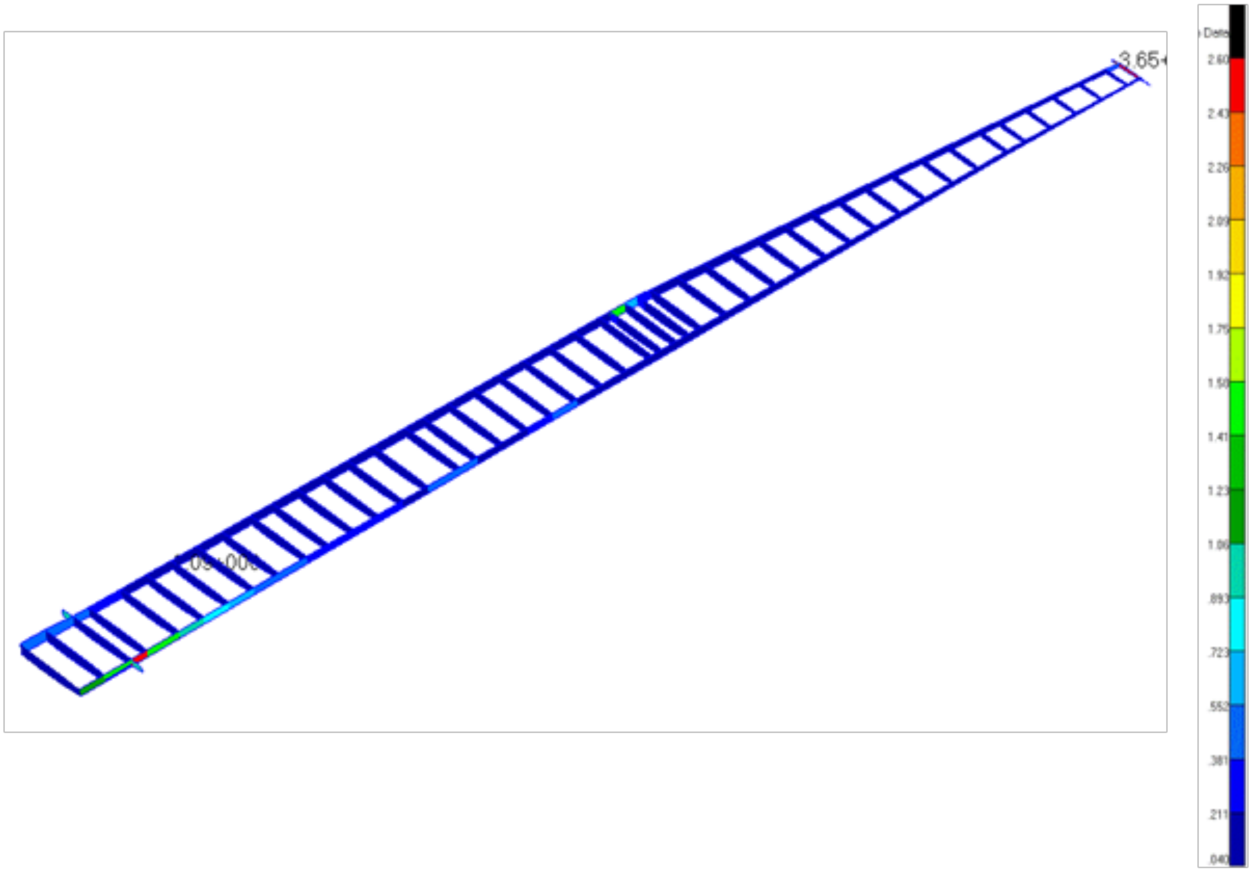

Figure 3.39 – Flutter Sized Wing Spar and Rib Web Thicknesses.

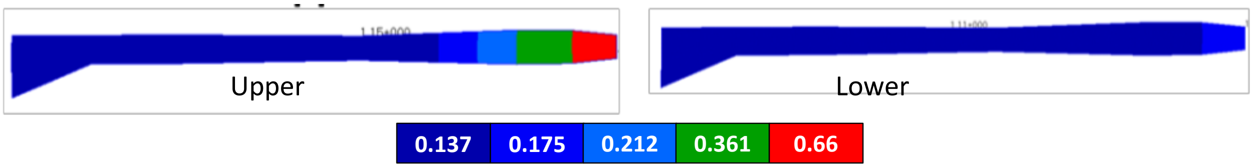

Figure 3.40 – Flutter Sized Strut Skin Thicknesses.

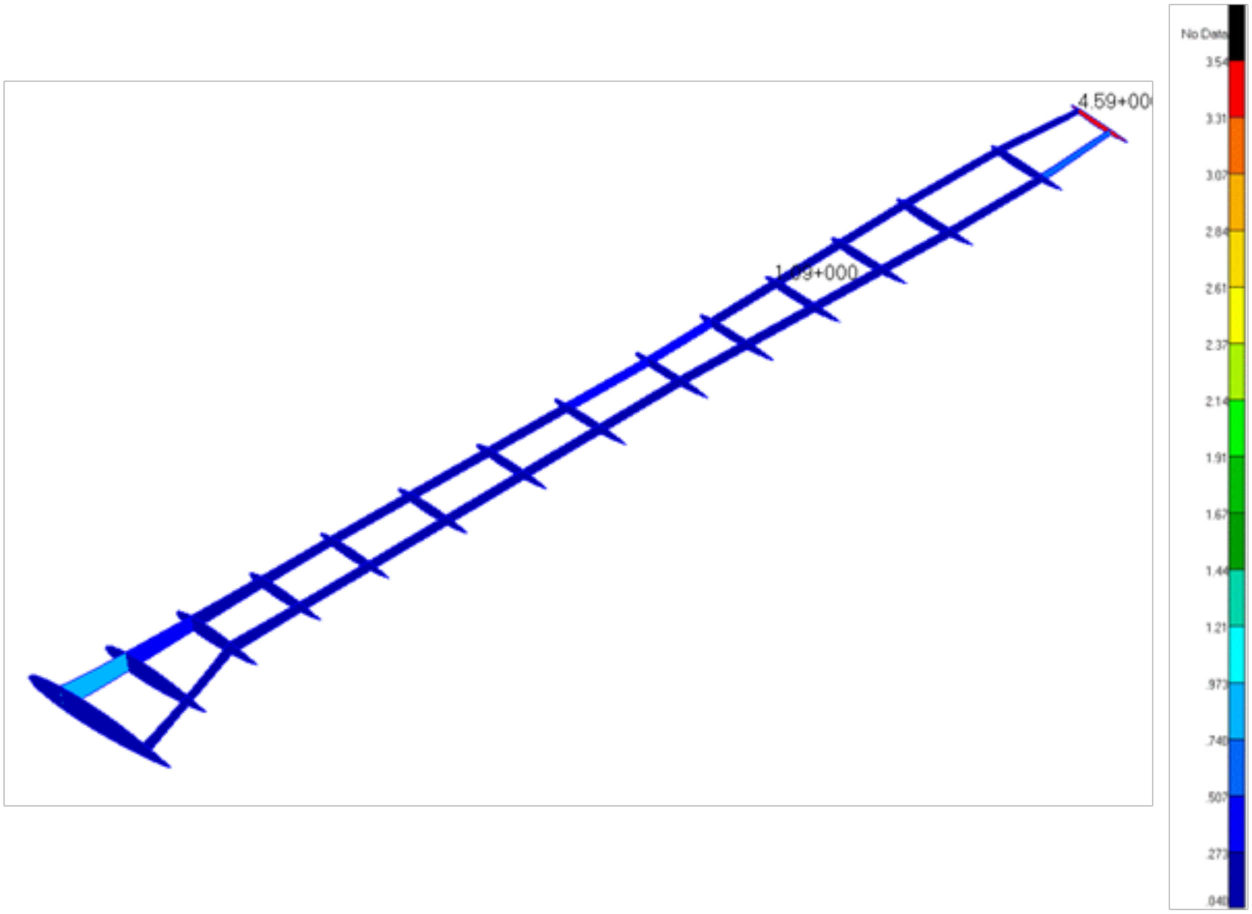

Figure 3.41 – Flutter Sized Strut Spar and Rib Web Thicknesses.

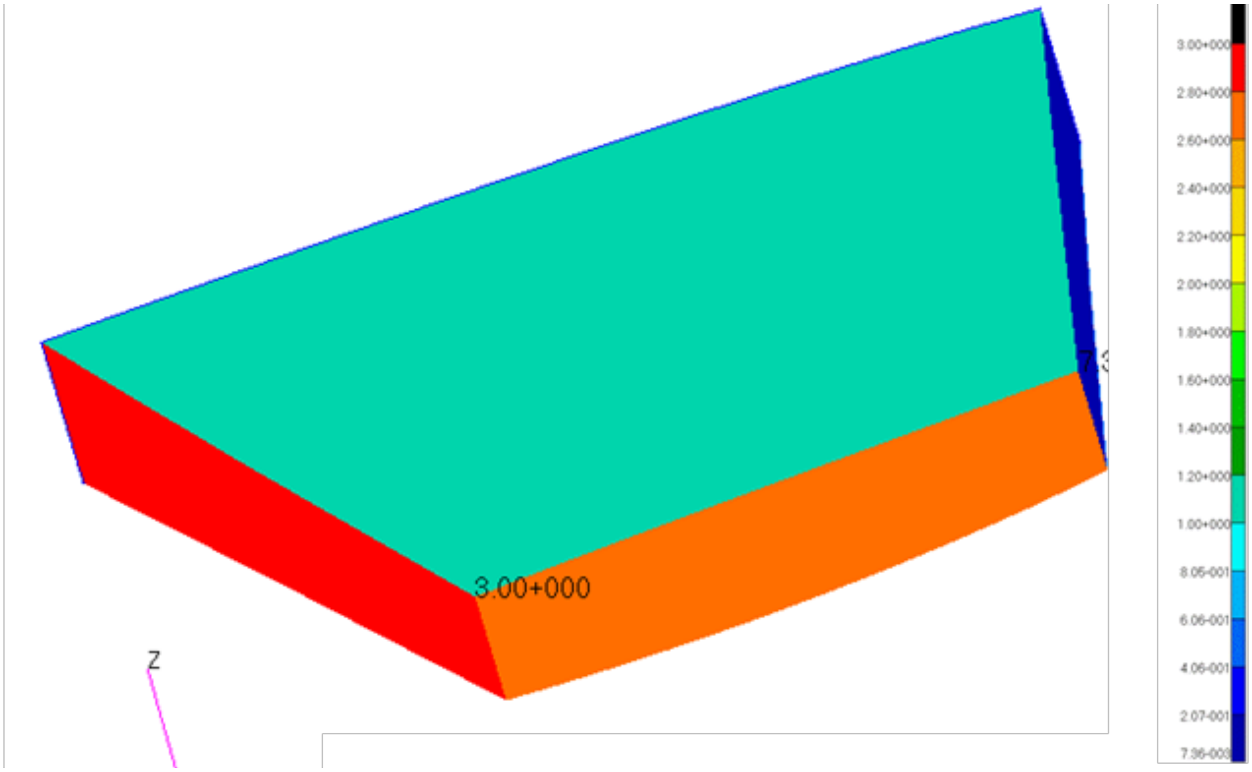

Figure 3.42 – Flutter Sized Strut Tip Steel Structure Thicknesses.

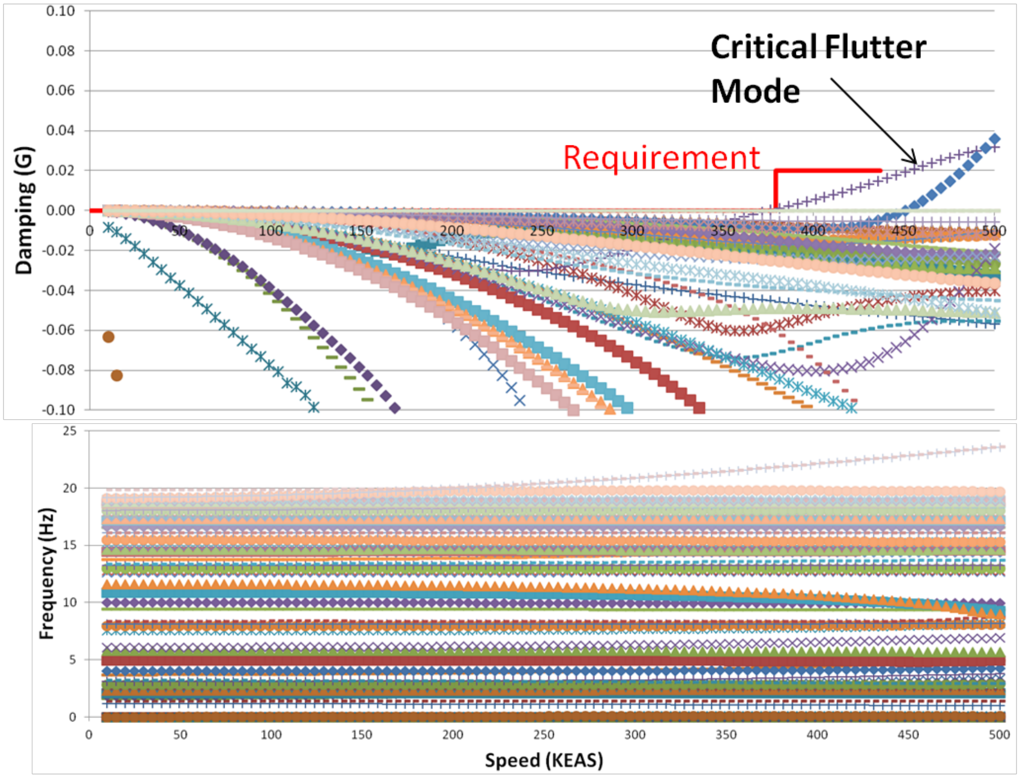

Figure 3.43 –Full Fuel Flutter Damping and Frequency Results.

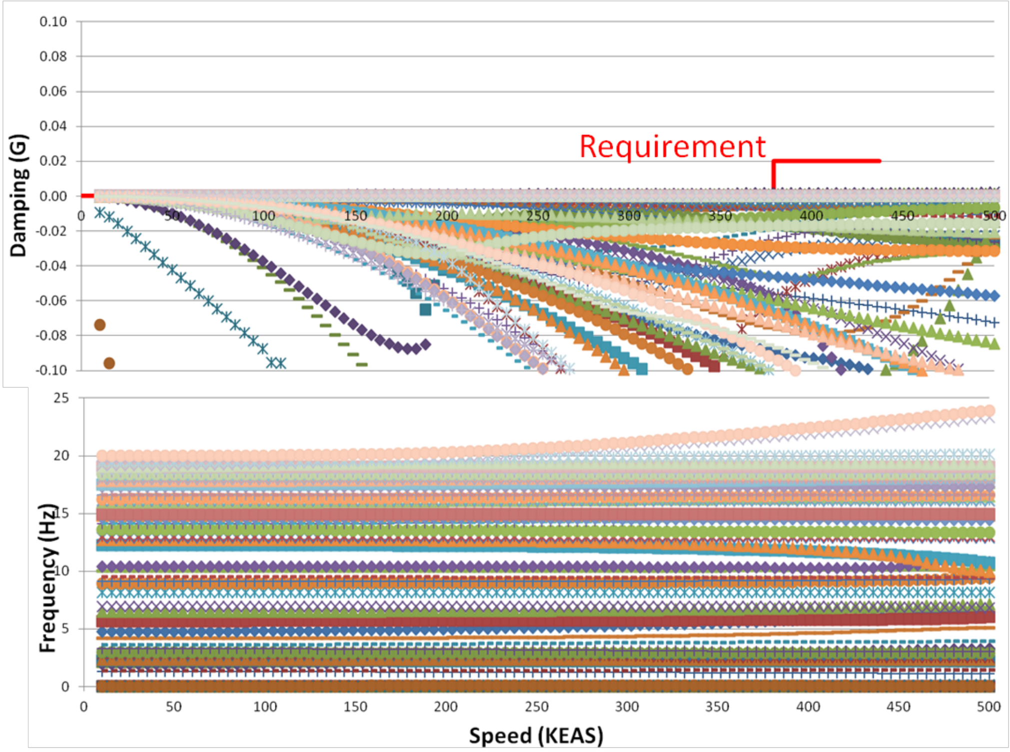

Figure 3.44 – Reserve Fuel Flutter Damping and Frequency Results.

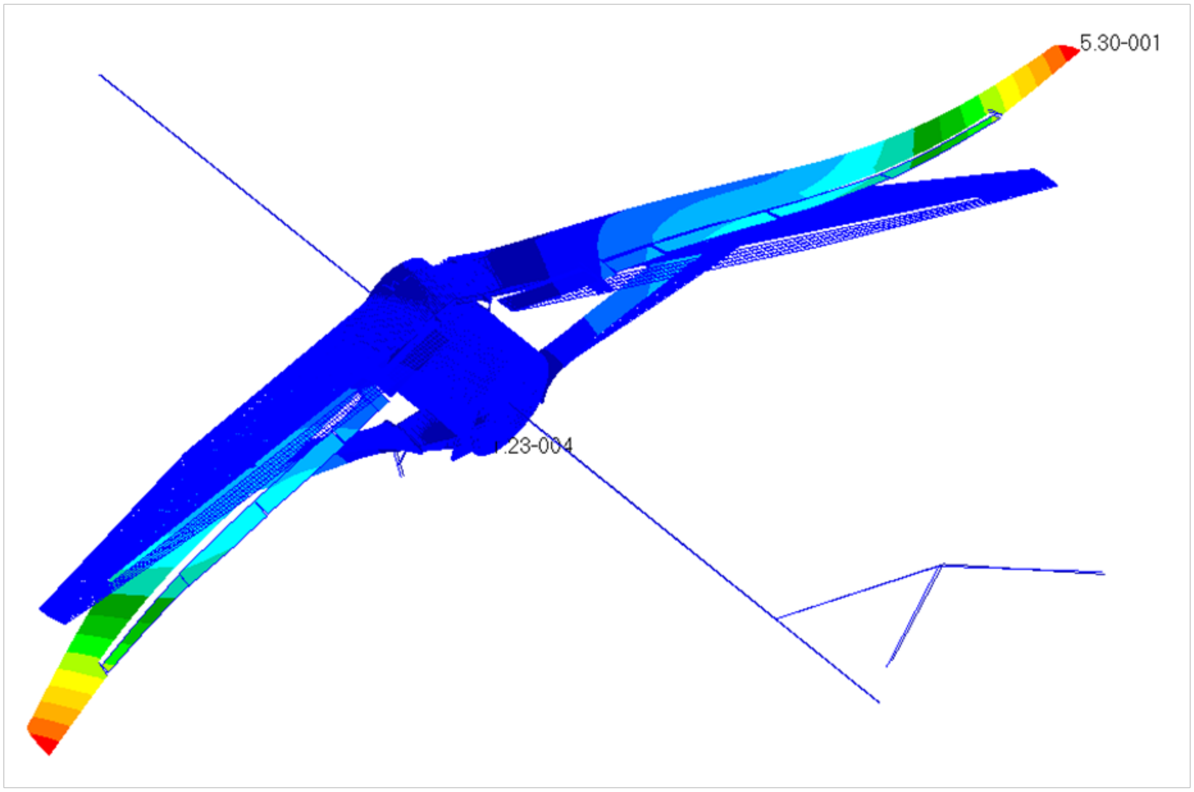

Figure 3.45 – Critical Complex Flutter Mode – 3.42 Hz at Dive Speed.

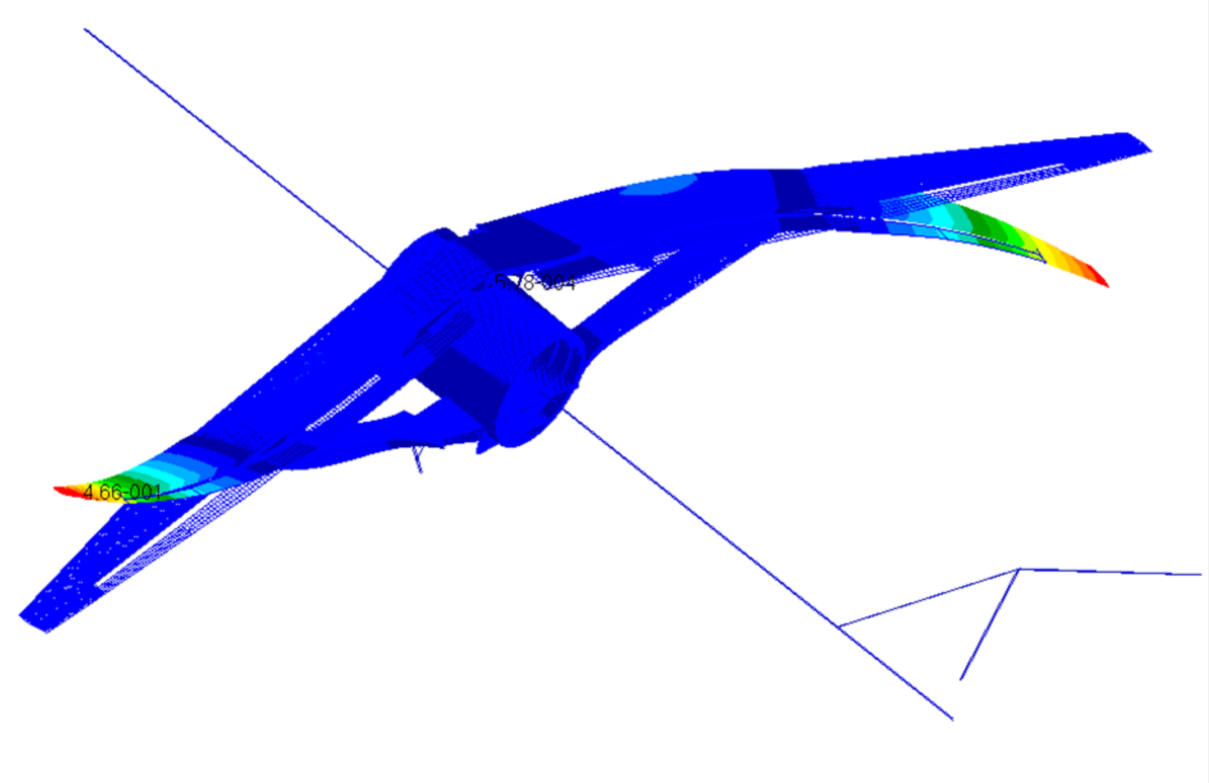

Figure 3.46 – Primary Bending Mode – 1.64 Hz.

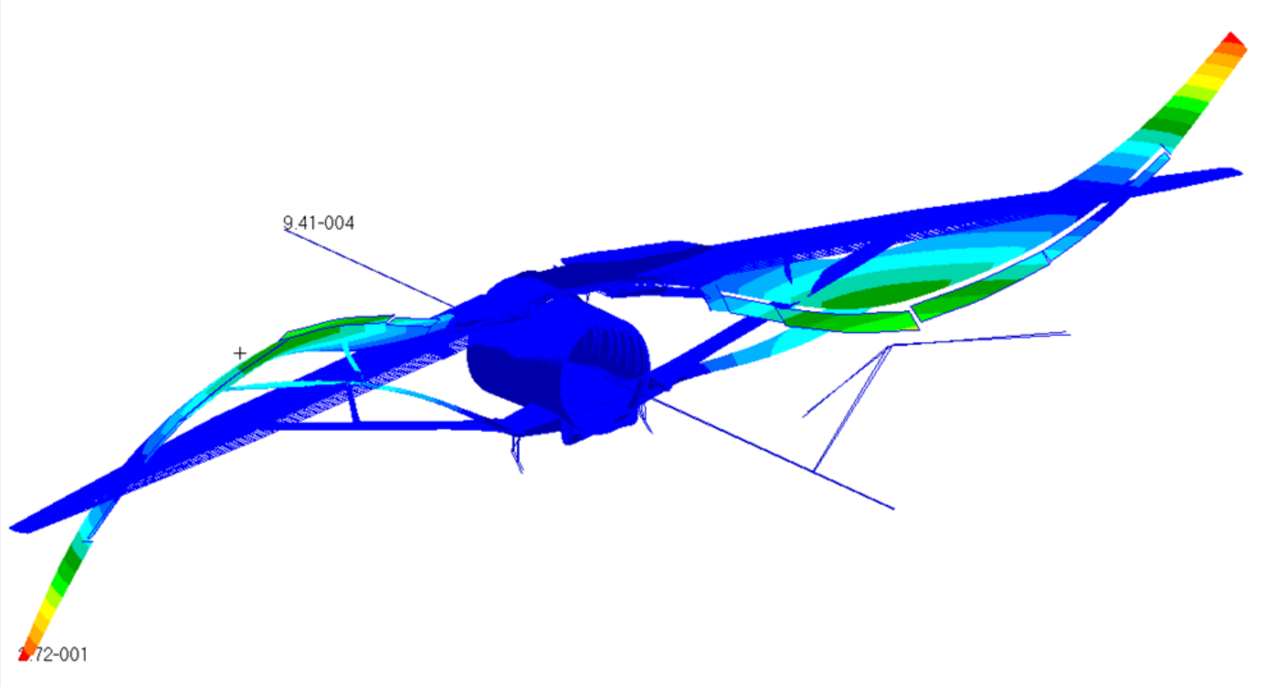

Figure 3.47 – Primary Torsion Mode – 3.13 Hz.

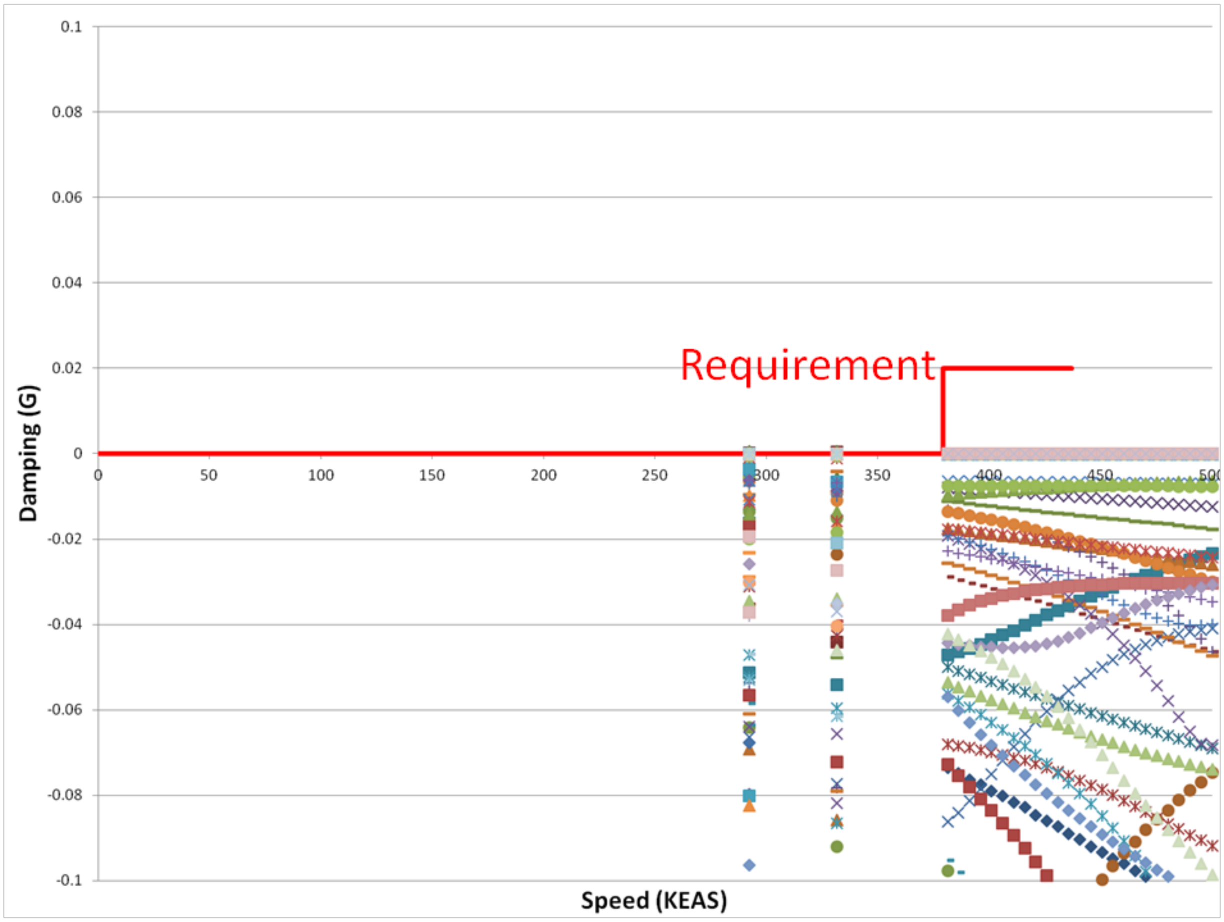

Figure 3.48 – Nonlinear Flutter Damping Results.

Table 3.5 – Flutter Sized Structural Weight Summary (weights in pounds).

	No Flutter	With Flutter Constraints	Delta
Skin	5,439.0	5,660.0	221.0
Spar	879.7	734.4	-145.3
Ribs	515.2	573.3	58.1
Spar Caps	214.9	126.9	-88.0
Rib Cap	99.5	80.9	-18.6
Strut	913.5	1,390.1	476.6
Jury	43.9	41.7	-2.2
Total	8,105.7	8,607.3	501.7

3.12 Aeroelastic Conclusions

The flutter weight increment is in line with Phase II results and shows only a small amount of weight is required for the truss-braced wing to meet flutter constraints. The results show the additional weight above static and maneuver loads required to clear flutter is sensitive to the strut stiffness at the wing attachment. The added degrees of freedom of the 3D modeled strut over the beam strut are significant and required to produce an accurate flutter weight increment. Most of the flutter weight increment was due to the steel structure added to the outboard tip of the strut, which was added to obtain a high stiffness interface between the wing and the strut. This steel structure and the FEM sizing require further investigation which could ultimately lead to a more efficient design. The benefit of the nonlinear structural effects on damping was not consistent with Phase II results. This is presumably due to some combination of the wing skin changes to meet the high fidelity buckling, the increased strut stiffness at the wing attachment, and the increased degrees of freedom of the 3D strut versus the beam strut used in Phase II. More investigation of this positive trend is warranted so it can be utilized in future designs.

4.0 Aerodynamic Design

A high fidelity aerodynamic design was conducted on the SUGAR Transonic Truss-Braced Wing (TTBW) configuration. The primary objective of this design effort was to refine the TTBW's outer mold line (OML) to minimize interference effects associated with the wing-truss system at transonic conditions and determine if the zero interference drag Phase II goal between the wing and strut are feasible. Geometry modifications required to accomplish this objective include updates on airfoil parameters (e.g., thickness, camber and leading-edge radius), wing and strut twist distributions, and the use of carefully designed fairings to improve flow field characteristics in juncture regions. Making changes to the basic airplane layout in order to achieve a more optimized TTBW configuration is outside the scope of the current design effort so parameters such as wing span, sweep and truss span were locked-down from the start. After completion of this aerodynamic study, validated interference drag assumptions can be applied for a design space exploration on the TTBW with some confidence that design goals can be achieved. The starting configuration used for the detailed high-speed design (765-095-RD) was carried-over from the second phase of the SUGAR program and is shown in Figure 4.1 below.

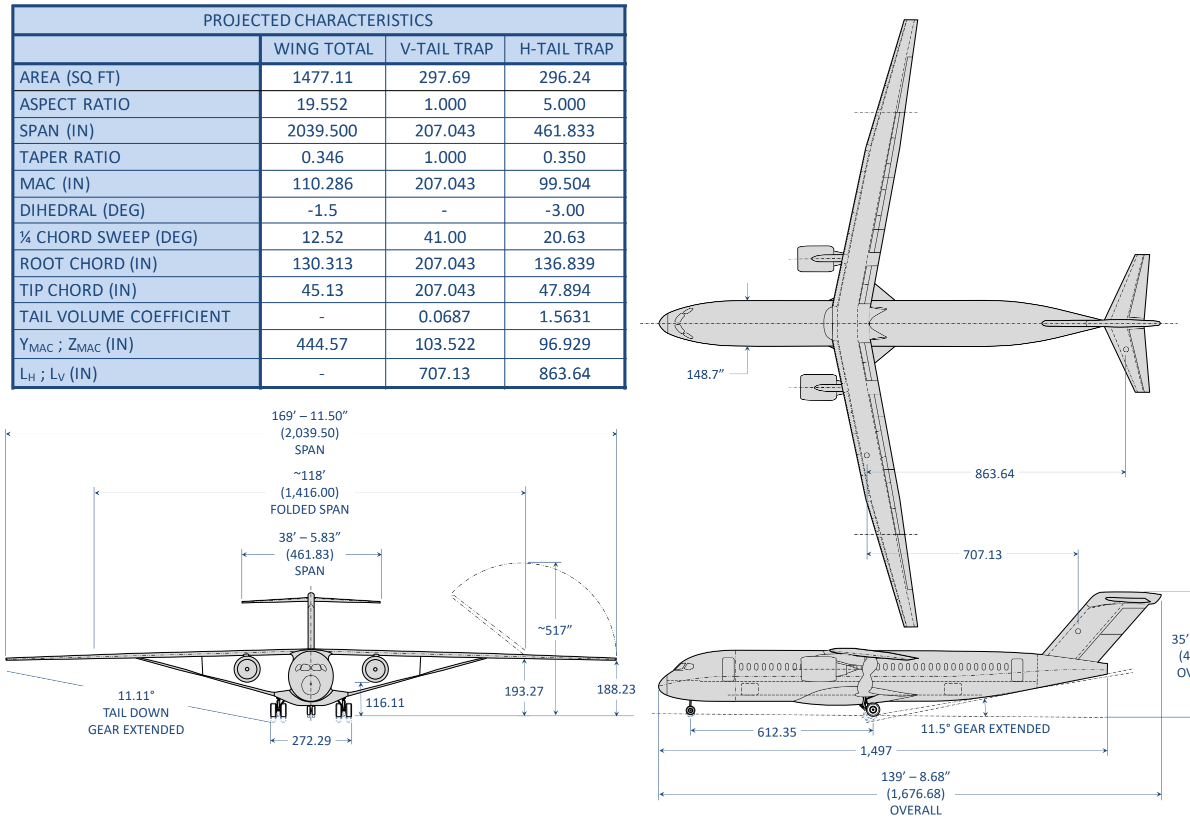

PROJECTED CHARACTERISTICS

	WING TOTAL	V-TAIL TRAP	H-TAIL TRAP
AREA (SQ FT)	1477.11	297.69	296.24
ASPECT RATIO	19.552	1.000	5.000
SPAN (IN)	2039.500	207.043	461.833
TAPER RATIO	0.346	1.000	0.350
MAC (IN)	110.286	207.043	99.504
DIHEDRAL (DEG)	-1.5	-	-3.00
¼ CHORD SWEEP (DEG)	12.52	41.00	20.63
ROOT CHORD (IN)	130.313	207.043	136.839
TIP CHORD (IN)	45.13	207.043	47.894
TAIL VOLUME COEFFICIENT	-	0.0687	1.5631
Y_{MAC} ; Z_{MAC} (IN)	444.57	103.522	96.929
L_H ; L_V (IN)	-	707.13	863.64

Figure 4.1 – SUGAR TTBW Configuration 765-095-RD used as a starting point for the high-fidelity transonic design.

The following list is a more comprehensive summary of key requirements and ground rules established for the TTBW high-speed aerodynamic design.

- Minimize aerodynamic interference associated with the installation of the nacelle and truss system at flight and wind tunnel conditions.
- Adhere to 765-095-RD configuration layout (see Figure 4.1).
- Design for cruise Mach number of 0.7.
- Design the wing for turbulent flow (as opposed to a natural laminar flow design) in an effort to simplify the design effort.
- Include a flow-through nacelle and core but do not attempt to simulate engine power effects.
- Do not account for changes in wing/strut twist due to flight condition.

To ensure the final design meets these aerodynamic requirements while satisfying those from other disciplines such as structures, a strict configuration control process was established and followed throughout the study. As a given design cycle was being worked, OML changes were tracked in a spreadsheet that provided configuration numbers and descriptions as well as links to geometry files. At the conclusion of a major design cycle, geometry was released to the entire team via IGES and STEP files. A total of four cycles were completed as the aerodynamic design progressed: Rev-D (initial), Rev-F, Rev-G, Rev-H, and Rev-J (final). More information will be provided for each of these cycles in the “Design Overview” section of the High-Speed Aerodynamics report.

This portion of the SUGAR Phase III Final Design Report is organized in three major sections: Methodology, Design Overview and Final Configuration. The Methodology section provides some background on the aerodynamic and geometric design and analysis tools employed for this study. A comprehensive summary of the design process is given in the Design Overview section, which is organized by configuration revision block release. Finally, the Final Configuration section includes comparisons of the computed flow field and integrated body forces using a build-up approach. This last section also includes a discussion on the alternate strut geometry.

4.1 Methodology

The methods used for the high-speed TTBW OML development were carefully selected to give the assembled team the greatest chance of meeting all program goals within cost and extremely aggressive time constraints. A compressed schedule had to be weighed against the required aerodynamic fidelity and code set-up time. The team chose a suite of tools capable of delivering an appropriate level of accuracy for each element of the problem while minimizing the net turn-around time. The use of multiple tools also provided the opportunity to work parts of the design in parallel by more than one person. User experience and confidence in code applicability were heavily weighted when evaluating the various options. The design tools chosen are described below.

4.1.1 Strut Airfoil Design and Optimization

One of the key challenges facing a truss-braced wing configuration is the issue of aerodynamic coupling between the wing and strut, particularly in the outboard region near the wing-strut join. At transonic Mach numbers, there is a tendency for a normal shock to develop in the juncture region that, if not adequately addressed during aerodynamic design, may contribute significant drag and potentially drive separation on the wing lower and strut upper surfaces. The degree of coupling is such that it is impractical to attempt design of the strut airfoils in isolation; they must be considered in the presence of the wing.

Additionally, it is not obvious a priori what pressure architectures are desirable for strut airfoils in such close proximity to the wing, or what the distribution of lift between the two elements should be. In order to assist the design in this region, a 2D gradient-based optimization tool was developed by coupling Matlab and MSES (5). MSES is a 2D, multielement aerodynamic analysis code, which interacts an integral boundary layer method with a hybrid full-potential/Euler solution in the external flow. It is compressible and capable of capturing both transition and separation. Matlab optimization routines and logic are used to script the aerodynamic solution, perturb the geometry, converge the optimization and post-process results for a number of 2D slices along the span of the wing and strut per Figure 4.2.

As also indicated by Figure 4.2, a key constraint on the optimization is presented by the strut structural requirements. The sizing condition for the strut structural box is a 1g push-over maneuver, in which the wing is flexed downward and the strut is in compression. This tends to induce buckling in the relatively long, slender strut, and it is specifically to address this issue that the jury strut exists. The jury strut stabilizes the main strut near its midspan, but the unsupported regions between the side-of-body and jury and between the jury and the wing-strut join remain buckling critical. These define the required out-of-plane box bending stiffness, *EI*, which varies with span as shown in Figure 4.3 and give its characteristic double-peak shape.

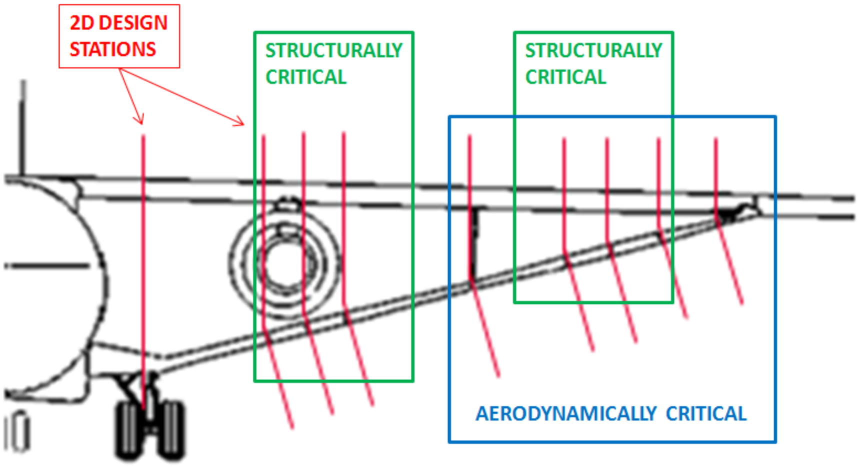

Figure 4.2 – Wing and strut defining stations used for strut airfoil design optimization, with critical regions indicated.

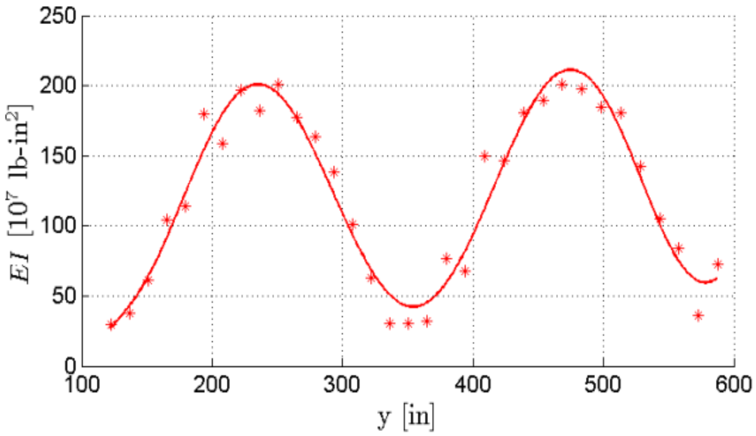

Figure 4.3 – Required strut box out-of-plane bending stiffness as a function of span. Determined from Phase II FEM analysis.

The strut box *EI* is a function of the box height, width, skin and spar thickness and material properties. Commonly such considerations are handled in aerodynamic design by means of a surrogate constraint such as a specified minimum thickness or 'keep-out' box. It is possible, however, to compute the strut box *EI* directly for each airfoil considered during the optimization using as structural suboptimization loop, which sizes skin and spar thicknesses, spar locations and scale factor for a given airfoil to find the minimum scale airfoil meeting the *EI* requirement with a specified box material area. This makes the *EI* constraint implicit, and the specified material area reflects the weight per unit span of the strut box. This allows the optimizer to iterate on airfoils of the same weight and structural stiffness to minimize drag. The dominant trade is between box depth and width, with higher t/c airfoils driving an increase in wave drag while longer chord, lower t/c airfoils incur an increase in skin friction.

It is also worth noting that the above method allows exact computation of the strut box centroid, which allows the optimizer to position every airfoil along the design elastic axis. It is important that this elastic axis remain straight from the gear sponson to the wing-strut join to avoid exacerbating strut buckling concerns. The ability for the suboptimization to move chordwise spar position means that the optimizer has some freedom to translate strut airfoils longitudinally, so long as the centroid remains on the elastic axis.

A last advantage offered by this approach is the ability to easily trade weight and drag. Phase II fuel consumption sensitivities to weight and drag on the design mission have been computed by a separate performance analysis, and these can be used as influence coefficients scaling the weight/unit span computed from the strut box material area against the drag/unit span computed by MSES. If the specified box material area is pulled into the outer optimization as a top-level variable, this allows for multiobjective optimizations minimizing weight and drag to maximize performance on the design mission.

The optimization tool was run in this mode at a subset of the spanwise stations shown in Figure 4.2. The results for one such optimization at a station approximately 87% of the way along the strut span are shown in Figure 4.4. This station was found to be among the most critical because it is far enough outboard that the vertical spacing between airfoils is small, and yet far enough inboard that the required strut box *EI* is still high. Further outboard stations actually become somewhat easier to address, as the falling *EI* constraint allows a reduction in strut thickness.

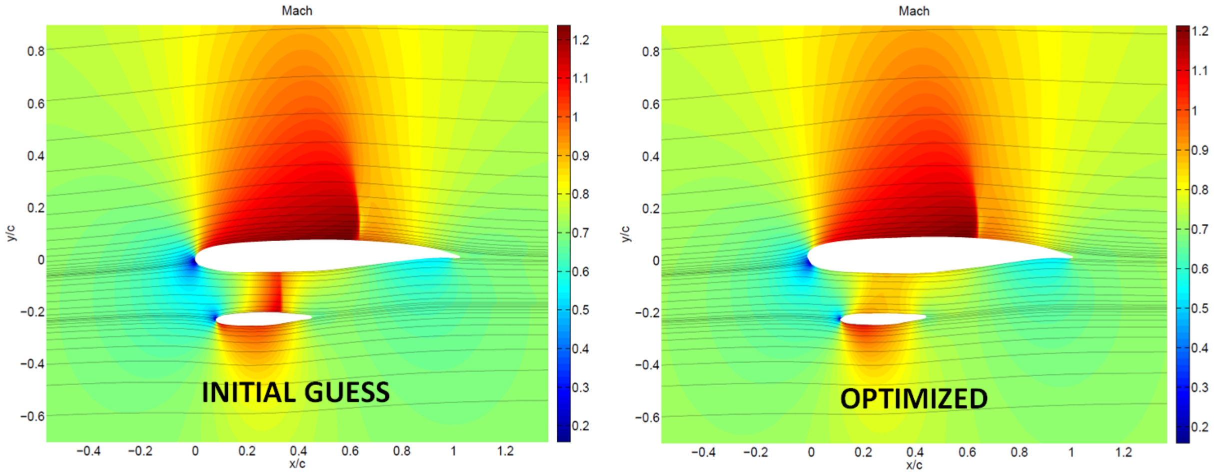

Figure 4.4 – a) Initial guess geometry. Section c_l = 0.6874, c_d = 0.0208, weight factor = 1.0; b) Optimizer result. Section c_l = 0.6874, c_d = 0.0173, weight factor = 2.43.

It can be seen from the above Mach contour comparison that, by altering the strut airfoil, the optimizer eliminated the strong normal shock between the wing and strut, and also cleaned up a small area of separation on the strut upper surface near the trailing edge. The total 2D sectional drag was reduced by 17% for the same combined wing plus strut net sectional lift. The weight per unit span of the strut box was increased by a factor of 2.43 from the nominal, however, as weight was allowed to increase to reduce drag. This is a local effect, and the magnitude of the weight increase reflects the extent to which this is an aerodynamically critical station. Further inboard, where the coupling between the wing and strut is less pronounced, the optimizer found results that are structurally lighter with the correct balance of increased drag.

It is of interest that the optimizer seeks negative lift on the strut over the outboard portions of the span. This allows a significant Mach number reduction in the region between the two airfoils, and is compensated for by a corresponding increase in wing lift. Separate analyses of spanload using both OVERFLOW and a vortex lattice method have shown that as long as the combined loading remains roughly elliptical in the Trefftz plane, the slight increase in induced drag resulting from this negative outboard strut loading is more than outweighed by the reduction in compressibility drag. A key driver of this effect is the fact that the inboard wing and strut form a closed lifting system not unlike a box wing configuration. This allows significant freedom in shifting loading inside the closed loops. The vortex lattice analysis encompassed trim effects.

This 2D optimization tool was used to define strut airfoils at multiple locations along the span, which were then lofted into 3D and analyzed in OVERFLOW. This process was repeated multiple times as the OML matured.

4.1.2 3D Design and Analysis Toolset

Various software tools were used in the design, development, and analysis of the SUGAR TTBW concept. Key tools included but were not limited to AVL, FLO-22, CART3D, CDISC, OVERFLOW and BUFFET. Each tool is briefly described below with an explanation as to how it was used for the detailed SUGAR design:

- AVL: AVL is an aerodynamic analysis program that utilizes an extended vortex lattice model for lifting surfaces and a slender-body model for nacelles and fuselages (6). This method provided a quick first-order assessment of spanload and the corresponding twist distribution necessary to obtain the ideal elliptical load distribution.

- FLO-22: FLO-22 (7) (8) is a full potential, 3D transonic flow code for the aerodynamic analysis of wings modeled out of a wall. It was used for wing-spanload evaluation and preliminary dragrise estimation of the SUGAR TTBW concept.

- Cart3D: Cart3D is a NASA-developed inviscid aerodynamic analysis software package capable of automated CFD analysis of complex 3D geometries (9). The adjoint capability implemented within Cart3D can be used to efficiently and effectively optimize desired aerodynamic quantities. Both the Cart3D flow solver and adjoint solver were used in a gradient optimization framework driven by SNOPT to reduce the interference drag in the wing-strut juncture region of the SUGAR TTBW design.

- CDISC: CDISC, which stands for Constrained Direct Iterative Surface Curvature, is an inverse design tool developed at NASA Langley for 2D or 3D configurations (10). This tool adjusts the geometry such that the resulting pressure distribution matches the distribution specified by the designer. CDISC was used to reduce shock strength by smoothing pressure distributions throughout the SUGAR TTBW design.

- OVERFLOW: OVERFLOW (11) is a node-based RANS code specifically designed for structured, overset grids systems. It is capable of computing steady or unsteady flow about an arbitrary body across a wide range of Mach numbers using a number of different approaches. Depending on the type of simulation, the solver can be run in 2D or 3D, thin-layer or full Navier-Stokes, central or upwind differencing, static or moving body. OVERFLOW 2.2g was used to solve for the full 3D viscous solution over the entire SUGAR TTBW configuration and was the primary tool used to estimate the aerodynamic performance characteristics. A consistent solver setup was maintained throughout the project with the Spalart-Allmaras one-equation turbulence model, the Quadratic Constitutive Relation (QCR) and 3rd-order HLLE++/SSOR differencing schemes employed.

- BUFFET: BUFFET is a Boeing-proprietary code that estimates a configuration's sensitivity to buffet by computing shock strength and position and comparing it against a database of 2D high Reynolds number data from conventional and supercritical airfoil tests. The method provides an indication of when shock-induced separation leads to buffet onset. The BUFFET program has been historically shown to be quite accurate for predicting buffet onset for T-tailed twinjet transport designs and was used to assess buffet characteristics for the TTBW wing and strut.

4.1.3 CFD Grid Generation and Post Processing

CAD geometry was provided for grid generation using both NX and CATIA. MADCAP, a Boeing proprietary grid generation code, and the Ansys ICEM CFD meshing software package were used to import the CAD surface definition and generate the necessary surface grids. Additional surface grid generation, volume grid generation and OVERFLOW input file creation was accomplished using scripts contained within NASA's Chimera Grid Toolset (CGT) (12). The CGT script BuildVol was used in conjunction with required input files to build all of the volume grids using one of two hyperbolic grid generators: HYPGEN (13) or LEGRID. All grids were built within a common model directory, which was broken up into subdirectories that were tied to the major components of the configuration. This use of the CGT script system facilitated configuration control throughout the SUGAR design process and provided a clear history of how each grid was built.

After the volume grids were built for each configuration, the BuildPeg5i CGT script was used to build a configuration-specific input deck for Pegasus5. Pegasus5 was used to cut holes in grids that penetrate solid walls as well as to establish communication between the individual volume grids. This is a step in the process known as domain or grid connectivity. Next, a force and moment integration surface was created using an internal Boeing code called POLYMIXSUR. This program eliminates grid overlap on the surface and connects neighboring zones with zipper grids comprised of triangles. POLYMIXSUR produces a closed integration surface used to compute forces and moments. Finally, the BuildOveri CGT script was used to create a configuration-specific input deck for OVERFLOW.

Both Tecplot and Fieldview were used for the generation of flow visualization images from the OVERFLOW results. A Boeing internal tcl script system facilitated the efficient generation of a common set of images across the entire polar. Common images were collected inside PowerPoint presentations and were viewed in flipbook mode in order to understand how the flow field changes as a function of angle-of-attack. These images helped to qualitatively explain the behavior of quantitative results and showed the designer where modifications were required to improve the design.

4.2 Design Overview

A detailed overview of the design progression is provided in this section with various aspects of each of the four geometry releases discussed. Multiple geometry releases were performed throughout the TTBW development to keep the team synchronized on the most recent design available. These design cycles are represented by revision blocks labeled 765-095-RF (Rev-F), 765-095-RG (Rev-G), 765-095-RH (Rev-H) and 765-095-RJ (Rev-J) in Figure 4.5 below.

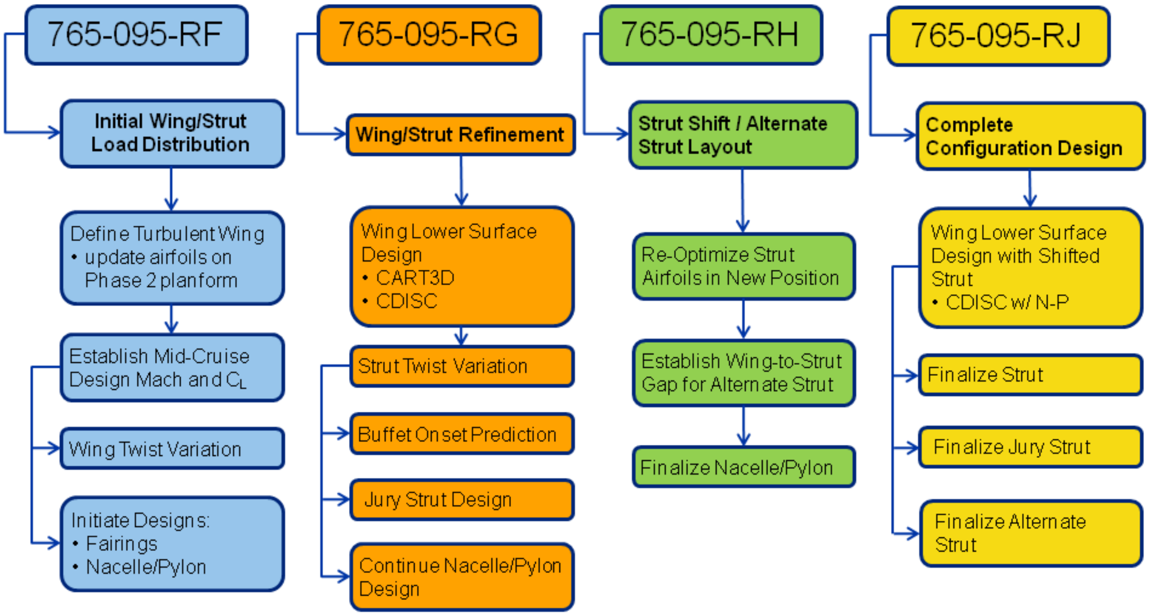

Figure 4.5 – SUGAR Phase III revision block diagram with primary aerodynamic design focus defined.

As the diagram in Figure 4.5 suggests, multiple activities were typically worked in parallel to keep the project on schedule. Before details of each of the four design cycles are discussed, the configuration nomenclature used to track components and datasets is defined. The series of images shown in Figure 4.6 represent the variation in geometric fidelity explored as the TTBW was refined. The abbreviations given in parentheses are commonly used to describe configurations under study and the associated data.

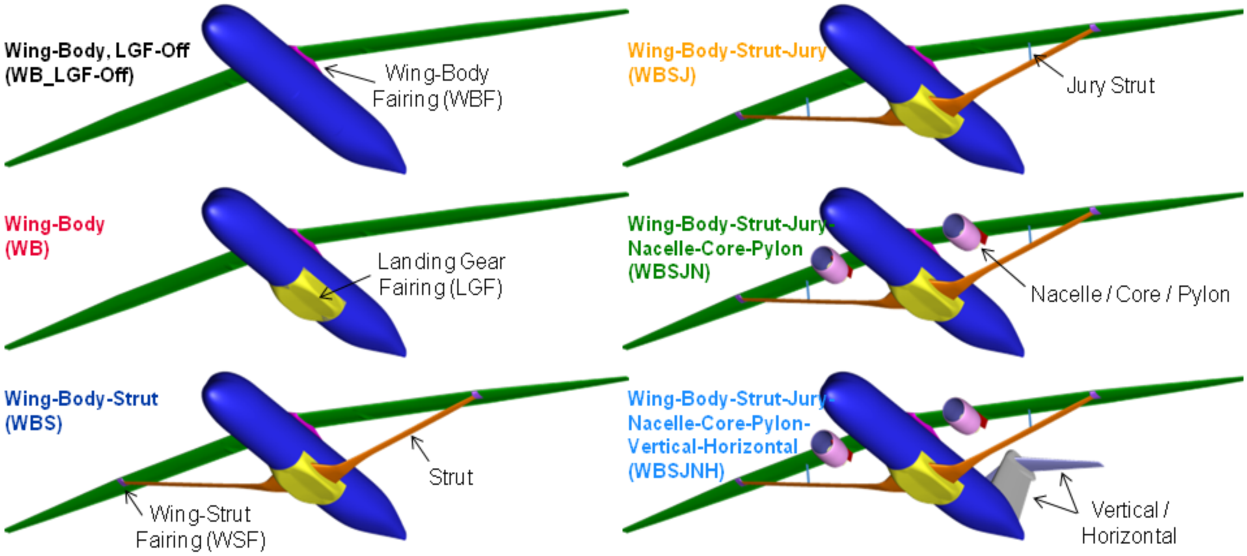

Figure 4.6 – Configuration nomenclature defined for the high-speed design effort.

4.2.1 Summary of 765-095-RF (Rev-F) Design Cycle

Multiple objectives were set for this initial design cycle, but top priority was placed on the need to better understand how the wing and strut spanload distributions can be made to interact in an aerodynamically favorable manner. Before this was done, there were a number of fundamental changes made to the wing-body (WB) configuration that helped to jump-start the design process. These changes included moving the wing vertically closer to the fuselage by 5 inches ($\Delta Z = -5''$), growing the size of the main landing gear fairing and improving the shape of the WB fairing. The WB fairing was known to have issues from CFD performed during Phase II of the SUGAR program, so this was an obvious region of the WB geometry that would benefit from some basic improvements in fairing opening/closing angles. These geometric improvements were verified with OVERFLOW as shown in Figure 4.7.

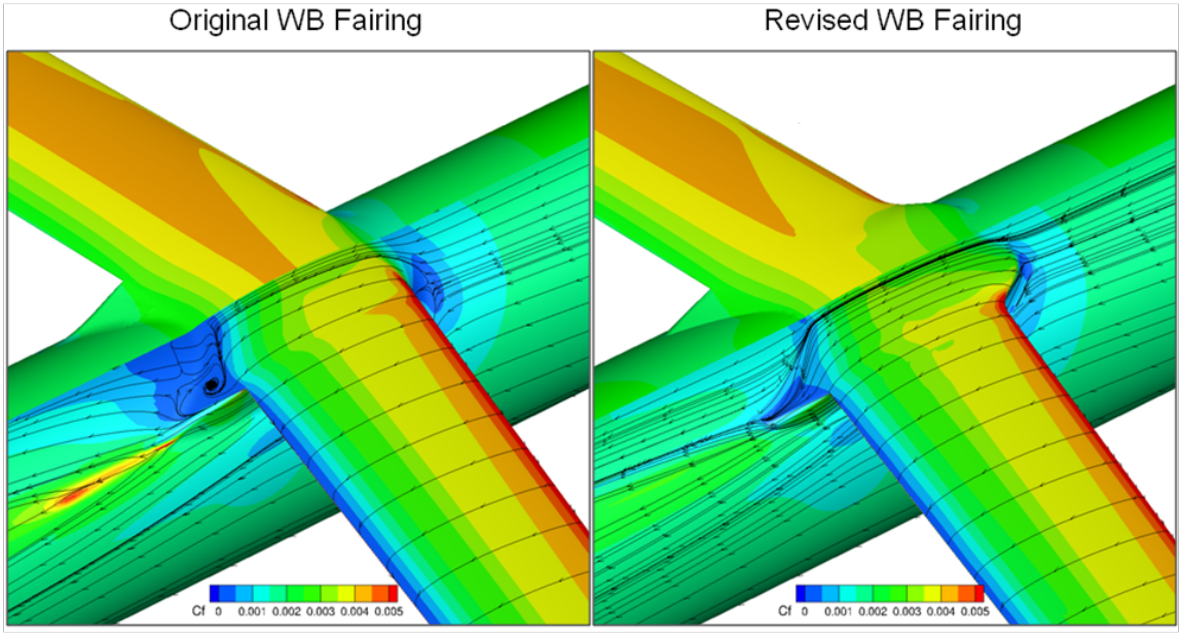

Figure 4.7 – OVERFLOW solutions comparing initial modification to the WB fairing. Contours on the left of the symmetry plane are C_p, contours on the right are C_f.

With these up-front changes made to the WB configuration, the geometry was released to the aero team and five areas were studied: 1) Preliminary Wing Design, 2) Preliminary Wing/Strut Loading Study, 3) Strut Airfoil Design Optimization, 4) Wing-Body-Strut Design, and 5) Preliminary Nacelle-Core-Pylon Definition.

4.2.1.1 Preliminary Wing Design

The starting wing geometry was designed for natural laminar flow during the second phase of the SUGAR program, so the first step in the preliminary wing design process was to replace the airfoils with ones that would operate more efficiently with a turbulent boundary layer. The laminar airfoils were replaced at each of the ten wing defining stations shown in Figure 4.8.

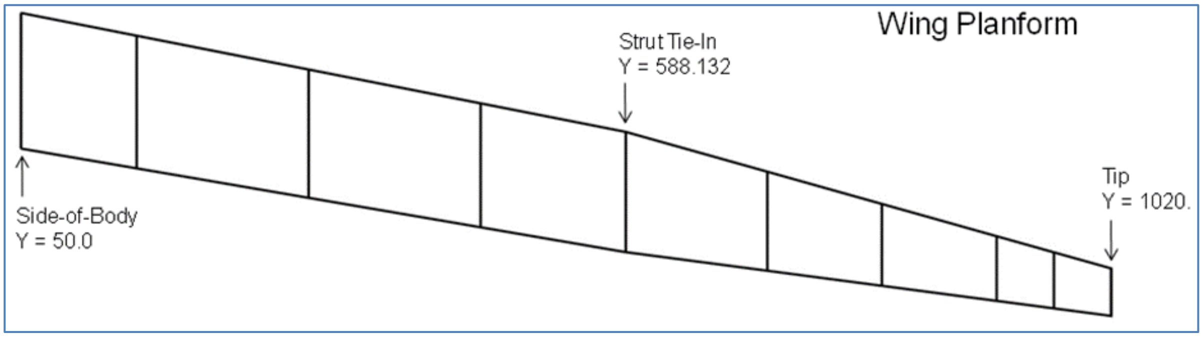

Figure 4.8 – Wing planform showing defining stations.

The new wing loft with updated airfoils was initially analyzed using FLO-22 to evaluate sectional wing loading across a range of lift coefficients. Knowing that the airfoils were originally designed to operate at Mach 0.74 and a sectional lift coefficient of 0.8, a wing-body (WB) C_L of 0.73 was selected as the design condition by simply interrogating the FLO-22 results at the Mean Aerodynamic Chord (MAC). The MAC station was assumed to fall somewhere between 30% and 40% semispan, which according to the sectional lift distribution shown in Figure 4.9, will produce close to the intended design loading. Note that sweep effects were considered to be small for this preliminary design effort and ignored.

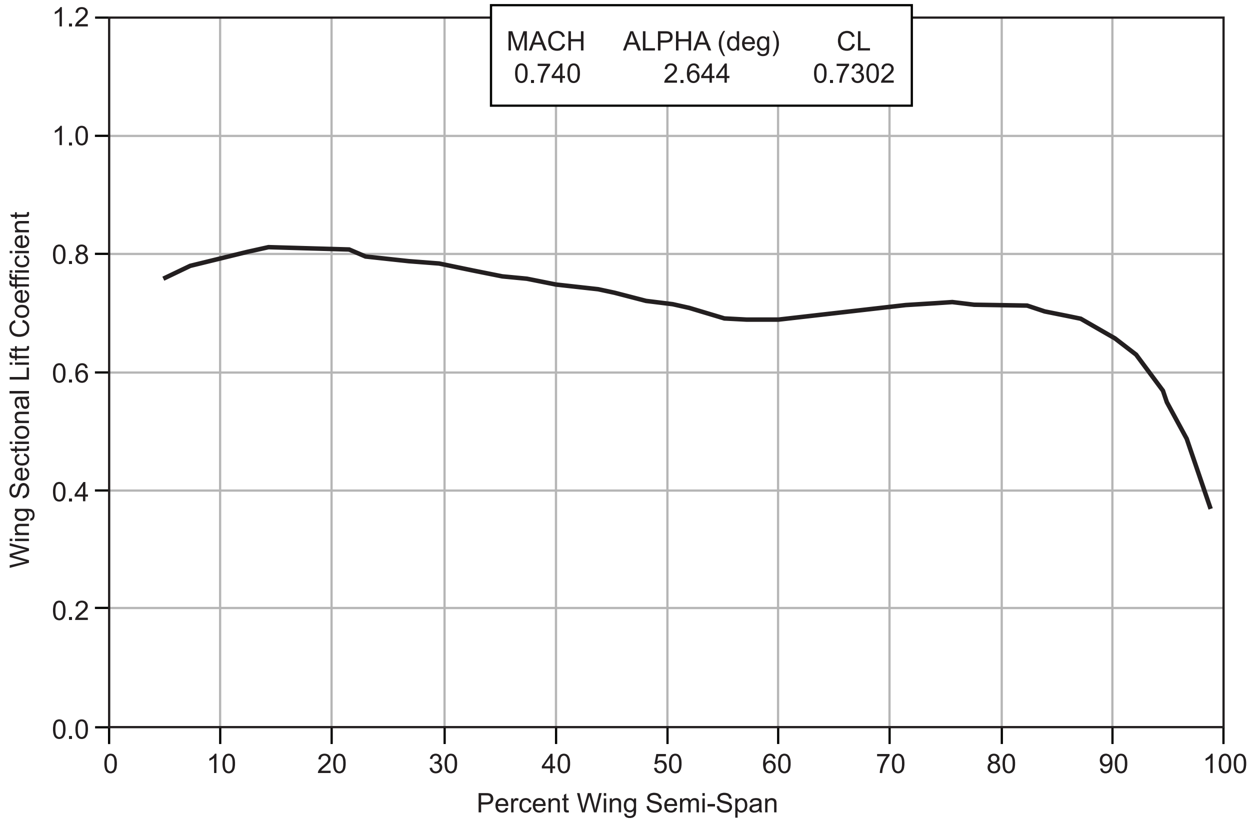

Figure 4.9 – FLO-22 wing sectional lift distribution at the wing-body design c_l of 0.73: Re_{mac} = 12.3 million.

With the WB design C_L defined, OVERFLOW was used to compute drag rises for estimating a mid-cruise Mach number. Instead of applying an assumed drag rise slope to the data as was done for the Phase II Preliminary Wing Design, the OVERFLOW data were post-processed to plot a pseudo range factor (the square root of the Mach number multiplied with L/D) as a function of Mach number, which approximates the L/D contribution to range. This plot is shown in Figure 4.10. The solid circles in the figure correspond to Maximum Range Cruise (MRC) while the open circles represent Long Range Cruise (LRC) as defined by a 1% reduction in range factor.

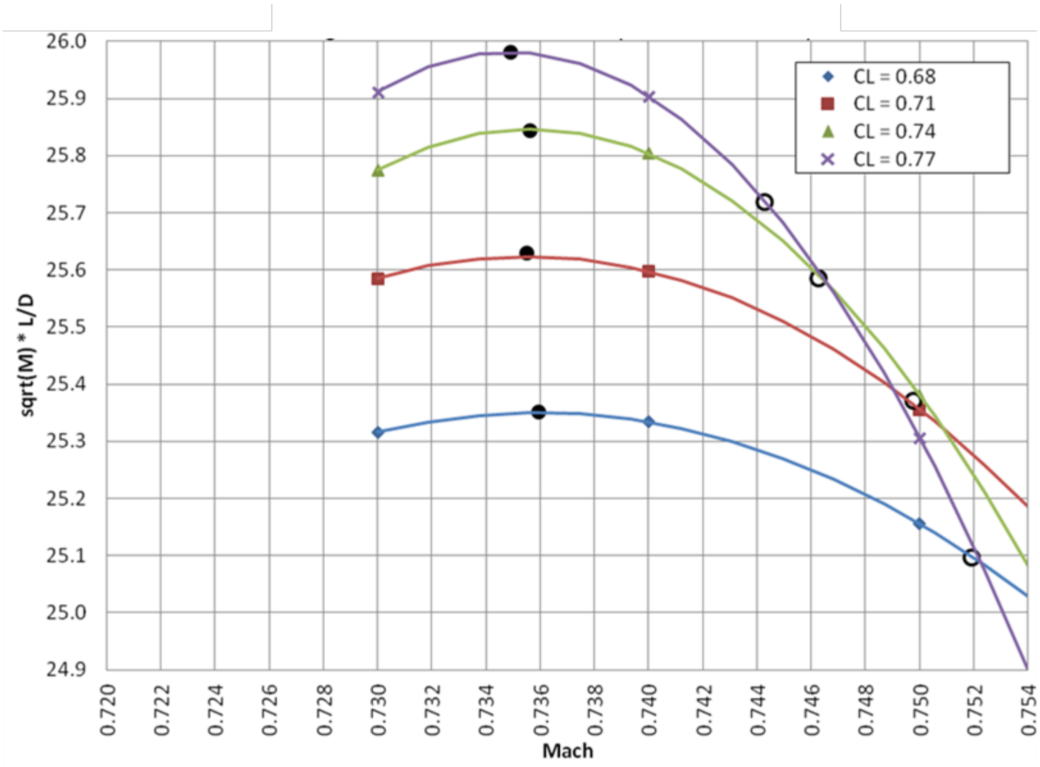

Figure 4.10 – Estimation of Long Range Cruise (LRC) Mach number for a WB configuration: Re_{mac} = 12.3 million.

This analysis was done for wings with a maximum t/c of 12.5% (data shown in Figure 4.10) as well as 13% to quantify the effect of wing thickness on LRC Mach number. The corresponding LRC Mach trend lines are shown in Figure 4.11. The 0.5% increase in maximum wing thickness lowered LRC Mach at C_L = 0.73 by roughly 0.005. Any further increase in wing thickness was considered high risk in that the aerodynamics of the wing/strut flow field had yet to be explored. The outcome of this preliminary WB performance evaluation was a reasonable design Mach number (0.745) and lift coefficient (0.73) to use for the development of the WBS configuration.

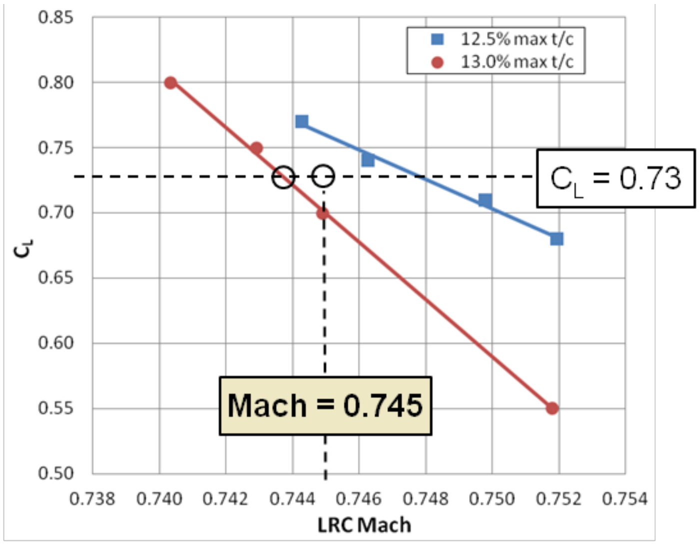

Figure 4.11 – OVERFLOW wing-body LRC Mach number trends.

4.2.1.2 Preliminary Wing/Strut Loading Study

In order to make a preliminary assessment as to what strut loading would produce an optimum total spanload for the configuration, a basic model of the wing-body-strut configuration was defined in AVL as shown in Figure 4.12. This study attempted to gain insight as to whether the strut should be loaded up or have no loading in order to maximize the inviscid spanwise efficiency, *e*. In other words, it attempted to answer the question "can planform efficiency be increased by carrying a portion of the lift on the strut?" Such knowledge could then be applied in the initial aerodynamic design of the strut and wing combination using OVERFLOW. AVL results in Figure 4.13 indicated that the optimum inviscid spanwise efficiency of 0.946 for a lifting strut was only marginally better than the 0.942 value for the case of a nonlifting strut. While these inviscid results indicated that the level of strut loading has limited effect on performance, optimum strut loading was revisited later with higher-order CFD.

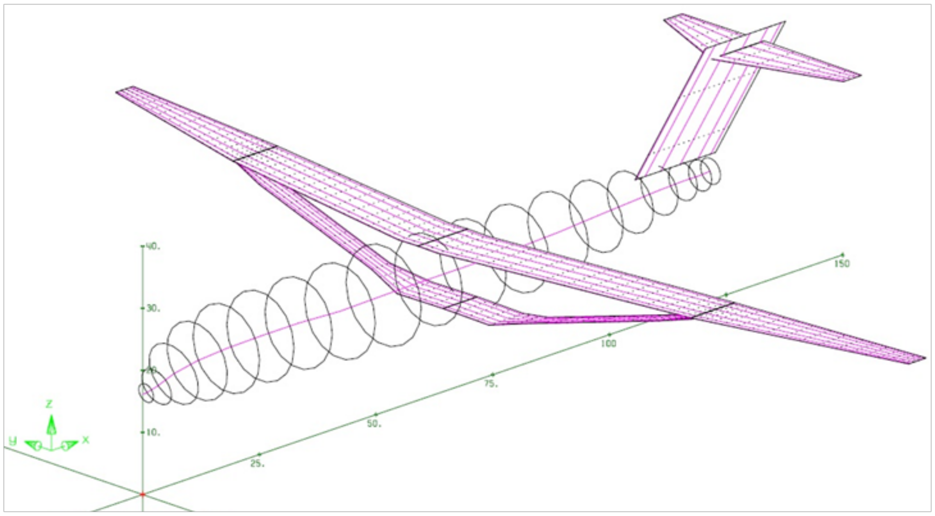

Figure 4.12 – Athena Vortex Lattice (AVL) model created for preliminary wing/strut loading study.

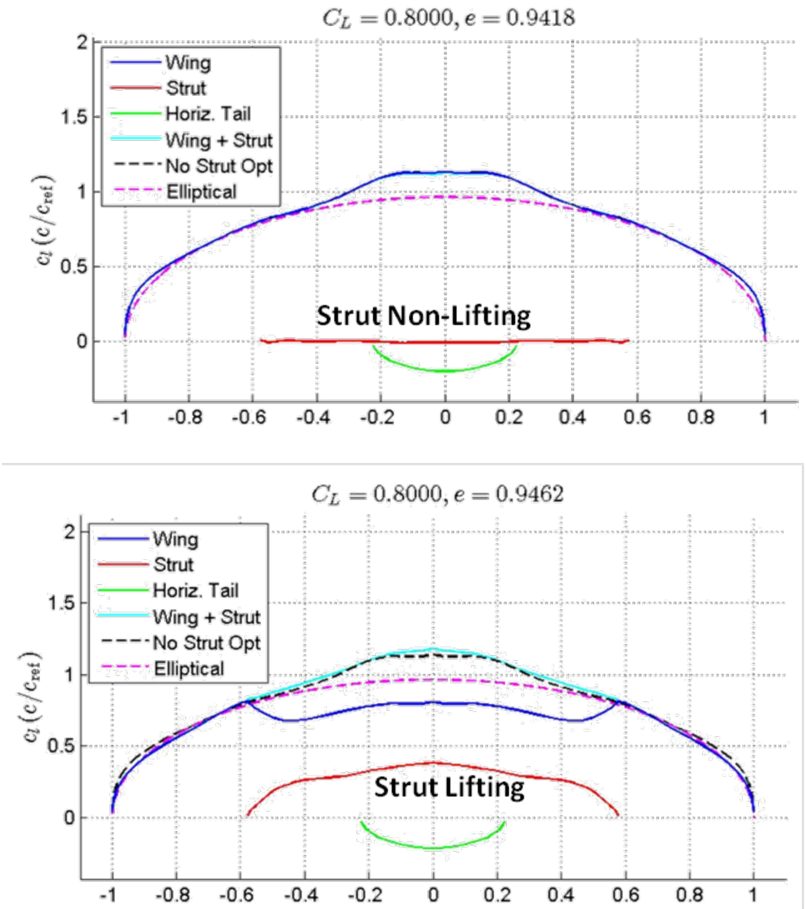

Figure 4.13 – Preliminary AVL inviscid results indicated that the same value of the optimum spanwise efficiency factor could be reached with a lifting or nonlifting strut.

4.2.1.3 2D Strut Airfoil Design Optimization

The design philosophy for the strut airfoils created during Rev-F had the optimizer (discussed in Section 4.1.1) iterating on airfoils of the same weight and structural stiffness to minimize drag. The dominant trade was between box depth and width, with higher t/c airfoils driving an increase in wave drag while longer chord, lower t/c airfoils incur an increase in skin friction. Trading increased weight for reduced drag was not attempted for Rev-F because the fuel consumption sensitivities to weight and drag on the design mission had not been computed by a separate performance analysis. These performance derivatives became available during the Rev-G design cycle, so their application to strut design will be discussed in Section 4.2.2.

4.2.1.4 Wing-Body-Strut Analysis

The wing-body-strut (WBS) system was analyzed using OVERFLOW during the Rev-F design cycle. Strut design was limited to the 2D process discussed in Sections 4.1.1 and 4.2.1.3, and the resulting airfoil stack was linearly lofted as suggested by the faceted strut surface shown in Figure 4.14 where design stations 1-5 are denoted. The number of stations increased to 8 as the strut design evolved through Rev-G and included regions marked “not designed” on the Rev-F strut in Figure 4.14.

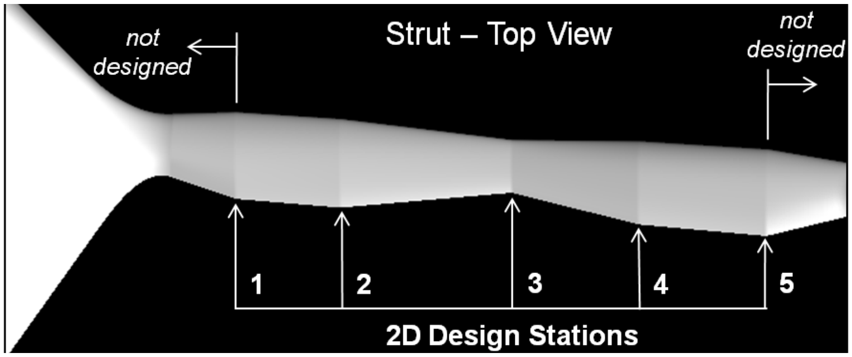

Figure 4.14 – Rev-F strut layout showing location of airfoil defining stations.

The 2D strut airfoil optimization effort completed during Rev-F offered insight on how the wing and strut want to be loaded relative to each other. With the wing incidence held fixed (solid, black line in Figure 4.15), the strut incidence or local twist angle (dashed, black line in Figure 4.15) tends to decrease as the gap between the wing and strut approaches zero. The reason for this is directly related to the amount of air moving through the wing-strut channel. Increasing strut download with a nose-down incidence diverts air down and below the strut instead of through the channel, which lowers velocity and reduces compressibility effects. The focus of the 3D CFD effort during Rev-F was on altering wing twist in the presence of the strut so the wing-strut system, when integrated together, gave a reasonable balance between induced and wave drag. This balance was struck by adjusting wing twist from black, red, and then to purple lines in Figure 4.15. Note how the local wing incidence trends in a nose-up (positive) direction as the wing-strut join is approached to offset the strut’s download.

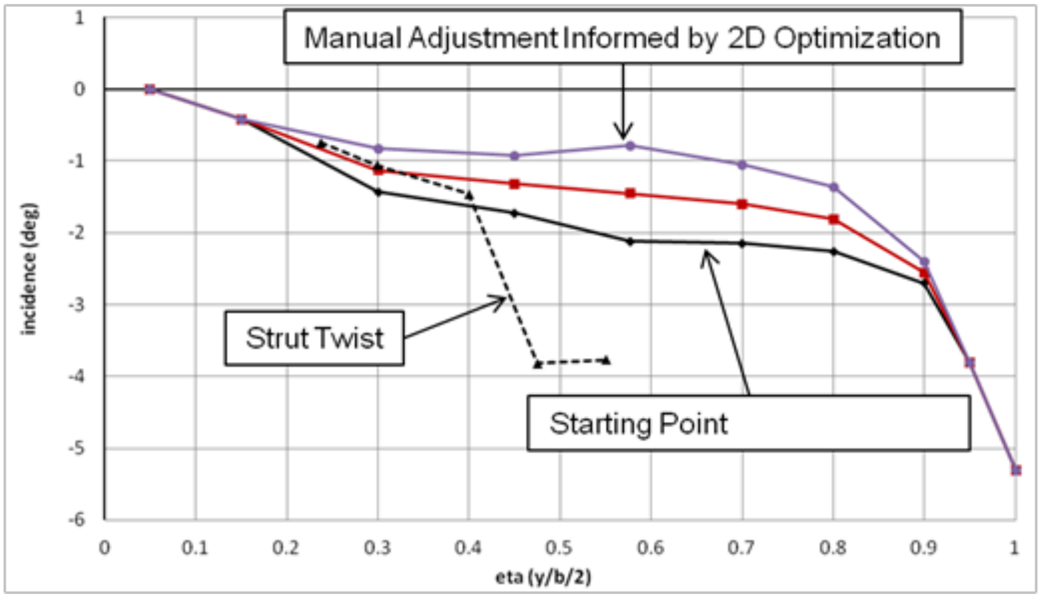

Figure 4.15 – Rev-F wing and strut twist distributions.

The resulting wing and strut spanload distributions at the design condition are compared in Figure 4.16 where the RF-des04 design corresponds to the black line in Figure 4.15 and RF-des08 corresponds to the purple line. The total (wing + strut) load distribution is shown as the black solid and black dash-dot lines in the spanload comparison. The combined loading for RF-des08 is considerably closer to the ideal elliptic distribution suggesting an induced drag benefit is realized by increasing wing incidence in a manner that offsets the strut download.

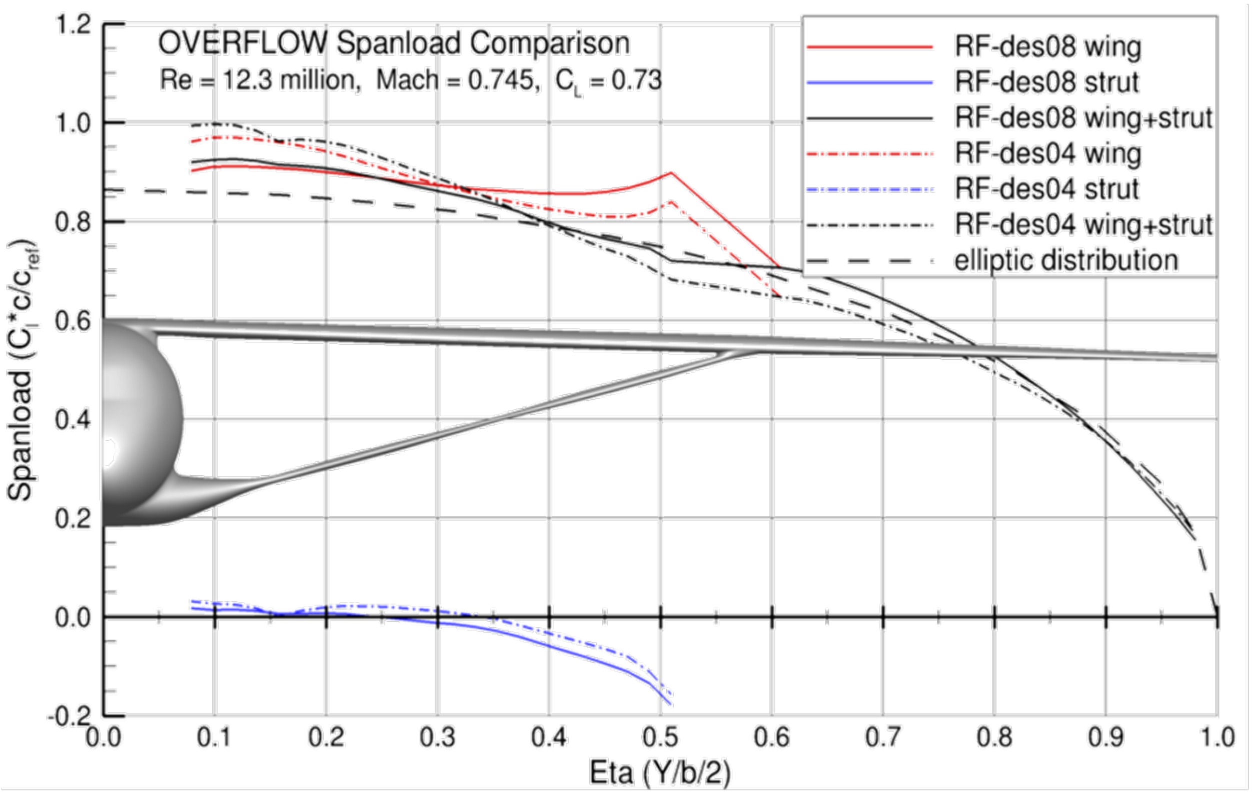

Figure 4.16 – OVERFLOW WBS spanload comparison showing effect of wing twist: Re_{mac} = 12.3 million, Mach = 0.745, and C_L = 0.73.

A qualitative assessment of the wing-strut juncture flow is offered by cutting the OVERFLOW solution using a plane that is aligned with the shock system on the strut's upper surface (see Figure 4.17). By coloring the interrogation plane with a scalar quantity such as Mach number, the effect of changing wing twist per Figure 4.15 is captured with a diminishing region of red seen between the wing and strut. Note that the "RF-des04" solution at the top of Figure 4.18 corresponds to the black wing twist curve in Figure 4.15 while the "RF-des08" solution corresponds to the purple curve.

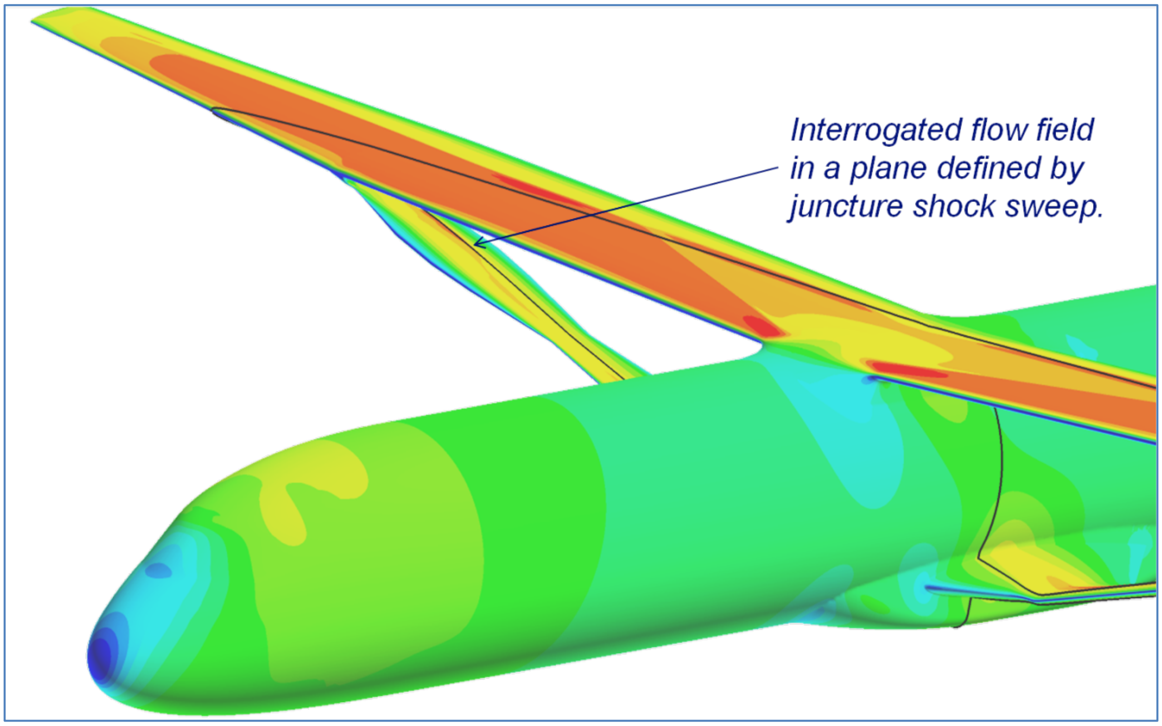

Figure 4.17 – Orientation of the off-body flow field interrogation plane.

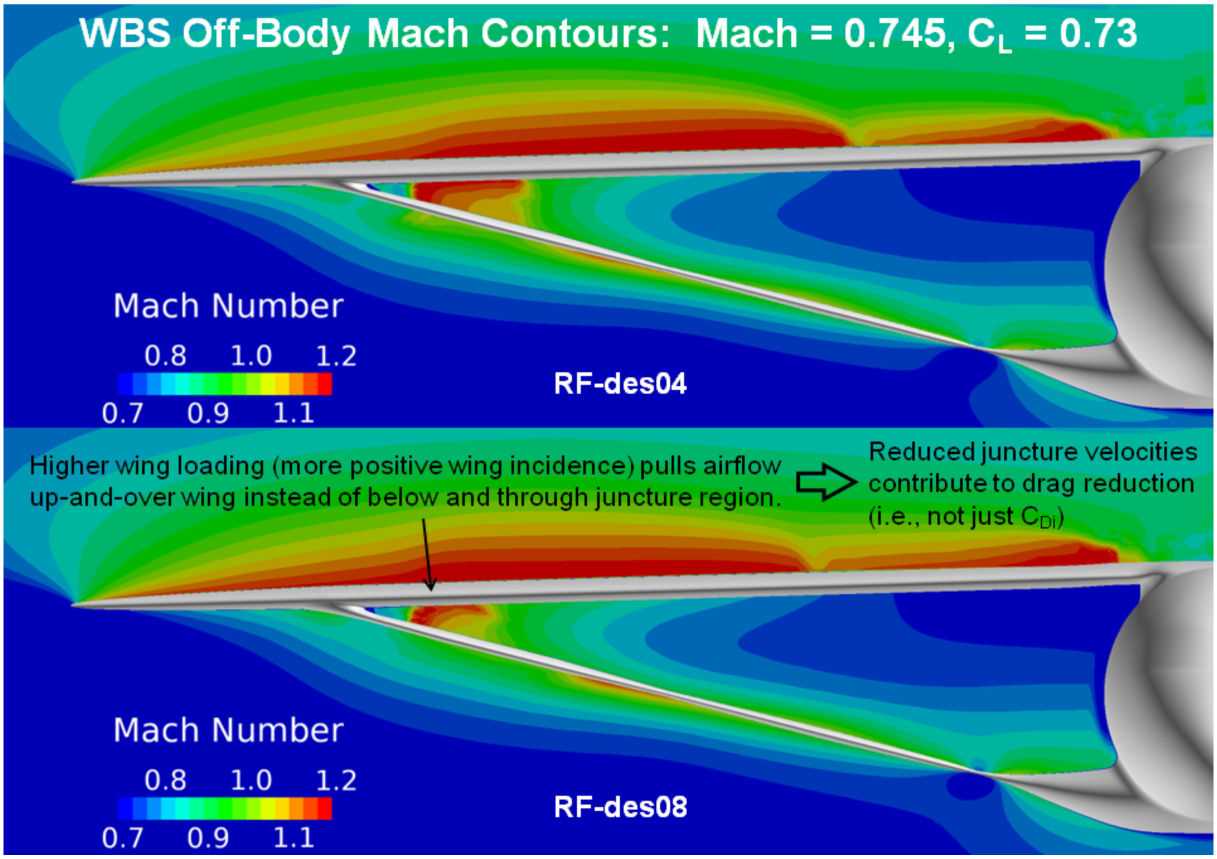

Figure 4.18 – WBS off-body Mach contours showing effect of a local nose-up wing twist change: Mach = 0.745 and C_L = 0.73.

Before the WBS wing twist distribution was locked-down, the BUFFET program (see description in Section 4.1.2) was employed to ensure adequate high-C_L buffet onset margin for the wing upper surface at the design Mach number of 0.745. This method was revisited during the Rev-G design cycle as well. Each time this check was made, an adequate buffet onset margin was predicted. Buffet onset for a Rev-G design was predicted to occur at 1.37 times the WB design C_L of 0.73. In other words, initial buffet C_L is 1.00 at flight conditions.

4.2.1.5 Preliminary Nacelle-Pylon Design

The preliminary engine nacelle geometry was modeled for the GE gFan+ to have the proper critical areas (highlight area, throat area, bypass exit area, core exit area) as dictated by the engine operating conditions. The engine location and orientation (including toe and tilt angles) was set during the preliminary layout and design. In order to simplify the CFD evaluation and create commonality between the computational predictions and wind tunnel test design validation, the internal loft of the nacelle was modified to create a flow-through wind tunnel geometry. A preliminary nacelle (with a separate fan and core flow) was established. This nacelle was then analyzed and modified in CFD to ensure that the engine mass flow ratio (MFR) met the design criterion. Maintaining the engine MFR is critical for matching the aerodynamic characteristics of the powered engine since it determines the correct balance of ingested vs. spilled air.

The preliminary pylon geometry was a constant-width design over the majority of the pylon that tapered from a constant wing x/c to near zero-thickness at the wing trailing edge. The pylon trailing edge (at the wing intersection) did not extend past the trailing edge of the wing.

OVERFLOW results of the preliminary nacelle-pylon geometry shown in Figure 4.19 revealed that the flow over the nacelle was relatively benign, with a mild acceleration on the inside of the nacelle inlet. There was no detected flow separation on the nacelle at the design point.

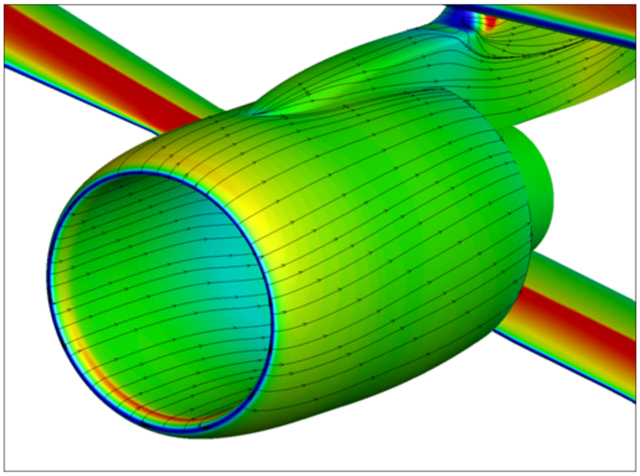

Figure 4.19 – Baseline Nacelle Geometry.

Based on the preliminary CFD analysis, the nacelle geometry appeared to be acceptable in its initial form. Although optimization of the location and orientation of the engine could potentially result in improved aerodynamic performance, it will not be a determining factor in the evaluation of the relative merits of truss-braced-wing technologies.

4.2.2 Summary of 765-095-RG (Rev-G) Design Cycle

With a basic understanding of optimal wing/strut loading and a reasonable wing twist distribution defined from the Rev-F design cycle, strut optimization efforts dominated Rev-G. This section summarizes work completed during the Rev-G cycle with an emphasis on improvements made to the WBS configuration using multiple design tools. Some discussion is given for other components worked in parallel, including the jury strut design.

4.2.2.1 Wing-Body-Strut Design

Computed WBS drag from OVERFLOW is compared in the bar chart of Figure 4.20 for the design condition. This comparison illustrates how the design effort yielded a steady reduction in cruise drag relative to Rev-F. The inset bar chart in the upper right portion of Figure 4.20 compares the (WBS – WB) drag increment which is another indicator of the significant performance gains realized during this phase of the TTBW design. The blue colored bars in the main chart represent data from the wing with no lower surface modification and the red colored bars correspond to a wing where the lower surface outer mold line was redesigned using Cart3D as discussed subsequently.

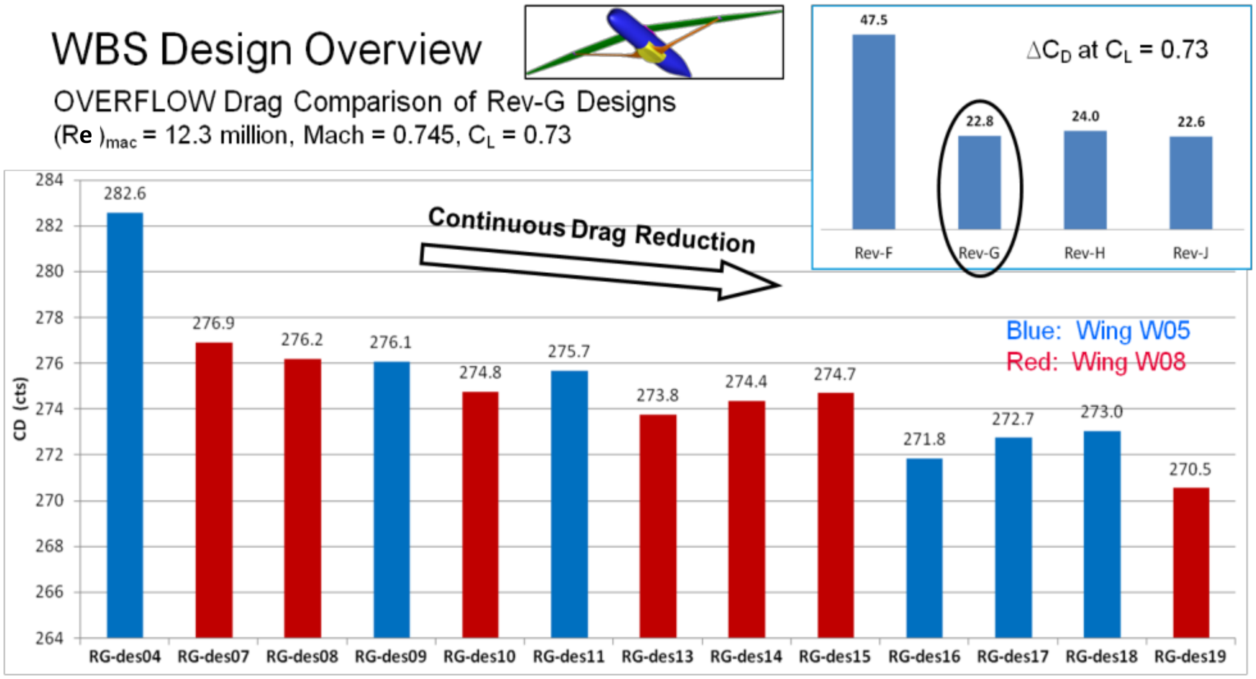

Figure 4.20 – History of OVERFLOW WBS drag levels showing a continuous reduction over the Rev-G design cycle: Re_{mac} = 12.3 million, Mach = 0.745, and C_L = 0.73.

2D Strut Airfoil Design Optimization

A key realization during the Rev-G design cycle was the importance of the weight-drag trade in strut airfoil design. During Rev-F, the strut structural box material area was held constant relative to the Phase II FEM data at each spanwise station. The airfoils were hence optimized to minimize drag at a fixed weight. When fuel consumption sensitivities were evaluated on the economic design mission, however, it was determined that 1,000 lbs of structural weight generated roughly the same fuel consumption increment as about 3 counts of drag and hence it became obvious that strut aerodynamic performance was being unfairly compromised to save on weight.

The 2D optimization method described in Section 4.1.1 was then modified to enable a weight-drag trade at each spanwise design station. Weight computed from the strut structural box material area and density was combined with drag computed via MSES in the objective function, with weighting factors determined from the performance sensitivities. In the aerodynamically critical outboard portions of the strut, the optimizer elected for a higher weight, lower drag solution than found during Rev-F. The evolution of the design along the weight-drag Pareto front is shown in Figure 4.21 for a representative station at 87% of the strut span. It is worth noting that further inboard, where aerodynamic coupling between the wing and strut is less pronounced the drag increment associated with strut thickness is reduced. This causes inboard stations to favor thicker sections for the same weight/drag vs. fuel consumption objective.

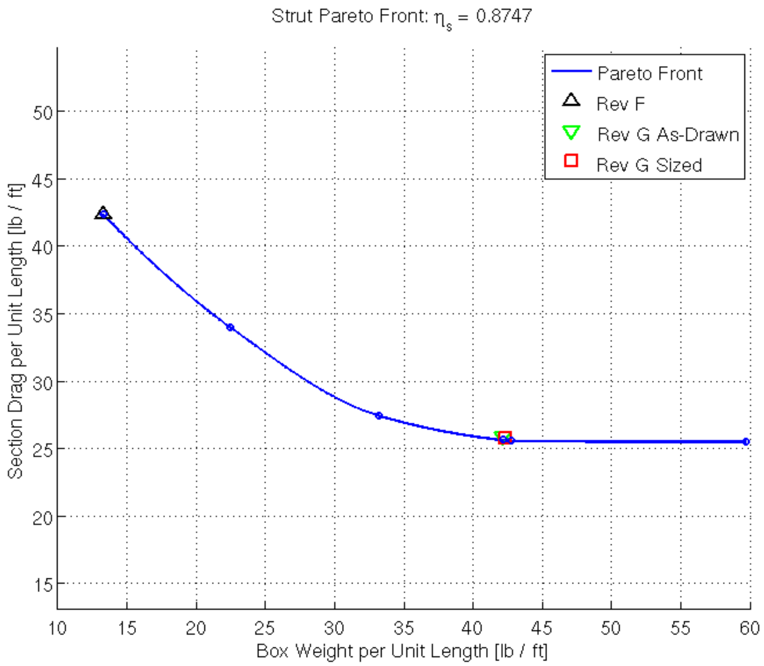

Figure 4.21 – Main strut weight-drag Pareto front at 87% strut span.

Cart3D Optimization of Wing-Strut Juncture Region

Cart3D (see description in Section 4.1.2) was used for its gradient-based optimization capability in an attempt to remove the shock system present in the wing-strut juncture region. The process involved splitting the geometry into wing, body, and strut components as separate water-tight geometries. The inboard wing component was extended inward into the body component so that the Cart3D surface grid generator would be able to intersect the wing and the body grids. Likewise, the strut was extended on each end so that it intersected the body and wing components. MADCAP was then used to create an unstructured water-tight surface mesh on each component geometry before importing, and these surface grids were then imported into Cart3D. For the initial run, the Cart3D surface grid tools generator automatically determined the grid intersections of these three components and created a single water-tight grid for the entire intersected geometry that could be processed with its flow solver. The Cart3D Cartesian volume grid generator then created the associated volume grid with cut-cells around the embedded surface grid before passing the full domain definition to its flow solver.

Free-Form-Deformation (FFD) boxes were set up around the wing and the strut surface grids in the vicinity of the juncture region, as shown in Figure 4.22, to enable shape optimization of the wing and strut. Various deformation modes were attempted to explore the effect of changing design space on the best solutions found during optimization. This initial optimization ignored structural constraints.

An unconstrained 2-point optimization was set up to minimize an objective functional at the design C_L of 0.73 and a low C_L of 0.60. The objective functional for each design point was defined as follows:

$$J1 = 1000 * C_{D1_{strut}} + 1000 * C_{D1_{wing}} + 1000 * \left(C_{L1} - C_{L1_{desired}}\right)^2$$

$$J2 = 1000 * C_{D2_{strut}} + 1000 * C_{D2_{wing}} + 1000 * \left(C_{L2} - C_{L2_{desired}}\right)^2$$

The multipoint optimization aimed to minimize the sum of the two design point functionals J1 and J2. Weighting constants were also selected to better scale the optimization design space. The initial optimization, denoted Opt001, did not use the “C_L-steering” capability in Cart3D to solve for C_L as previous studies identified issues with its robustness. Instead, this optimization used angle of attack as a design variable to help minimize the penalty incurred in the functional J when C_L deviated from a desired value.

A typical optimization run would consist of multiple design cycles. The run started with a flow solve on the baseline grid, followed by an adjoint solve, construction of gradients and determination of design variable changes. Each grid component would then be perturbed with FFD boxes based on the new design variable values computed by the optimizer. The Cart3D surface grid tools would then reintersect the new grid components, creating a new surface grid, before regenerating a new volume grid. Using this approach, the various components could be deformed in isolation without inadvertently deforming neighboring components.

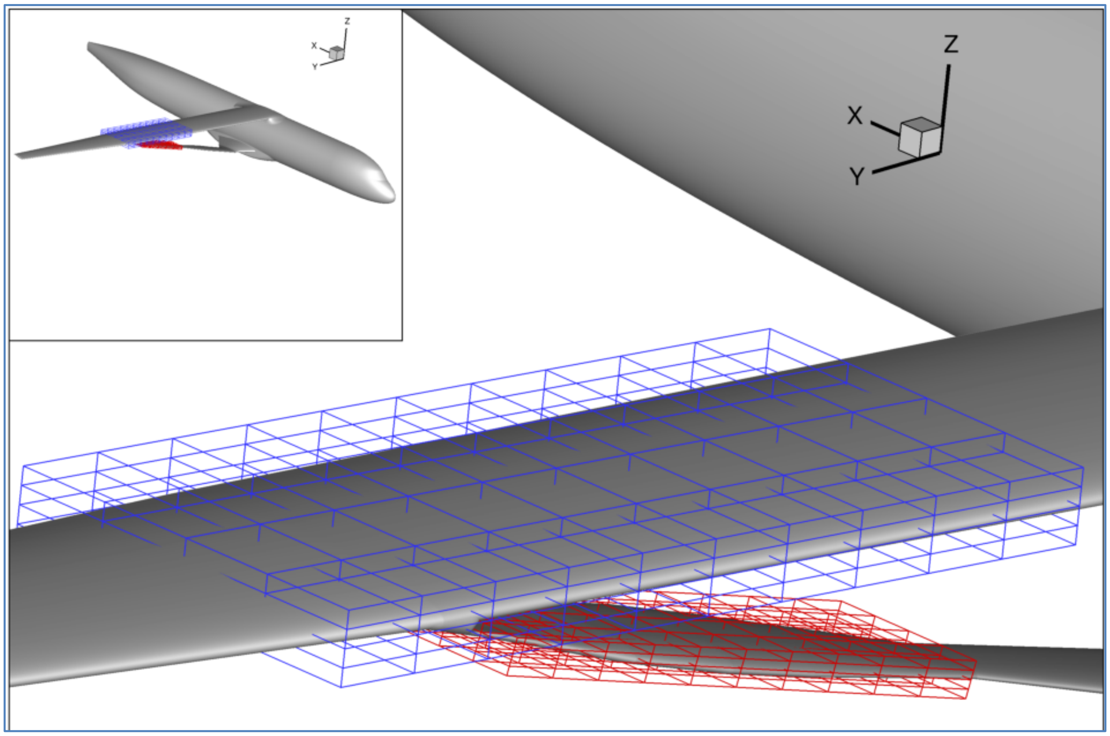

Figure 4.22 – Free-Form Deformation (FFD) boxes used for Cart3D adjoint optimization of the wing-strut juncture region.

As shown in Figure 4.23, OVERFLOW results for the Wing-Body-Strut (WBS) configuration of RG-des04 indicated a decrease in drag relative to the 765-095-RF Wing-Body (WB) configuration with a change in the character of the curve, as the drag stopped decreasing around a C_L of 0.49 and started increasing as C_L was dropped further. A quick survey of the flow field in the wing-strut juncture region revealed a significant portion of supersonic flow that resulted in an undesirable shock system in the juncture. Cart3D optimization was conducted on the RG-des04 geometry as described above, and the perturbed geometry from the optimization was manually gridded and run in OVERFLOW as RG-des07. The drag decreased by 5.6 cts at the midcruise design C_L of 0.73 and by 8.7 cts at a C_L of 0.55 relative to the baseline RG-des04 configuration. In addition, the shape of the RG-des07 drag polar noticeably improved relative to the RG-des04 drag polar in the lower C_L range (see Figure 4.23). The drag reduction obtained from the Cart3D optimization was a direct result of the removal of the supersonic flow and the resulting shock system in the juncture region (see Figure 4.24 and Figure 4.25).

The fact that the initial Cart3D inviscid optimization (Opt001) reduced the drag by such a significant amount was likely due to the juncture flow field being dominated by compressibility effects as opposed to viscous effects. An additional 23 Cart3D optimizations were performed to pursue further drag reduction by varying the size of the deformation boxes and adding strut chord, strut twist, strut camber, and wing twist design variables. Other options such as fixed alpha runs, single design point runs, and usage of the "C_L-steering" option were also investigated. Running with the "C_L-steering" option (akin to fixing C_L) proved to be robust for this configuration and yielded a similar drag reduction to Opt001. Unfortunately, no further drag reductions beyond the initial reduction were obtained with the additional Cart3D runs.

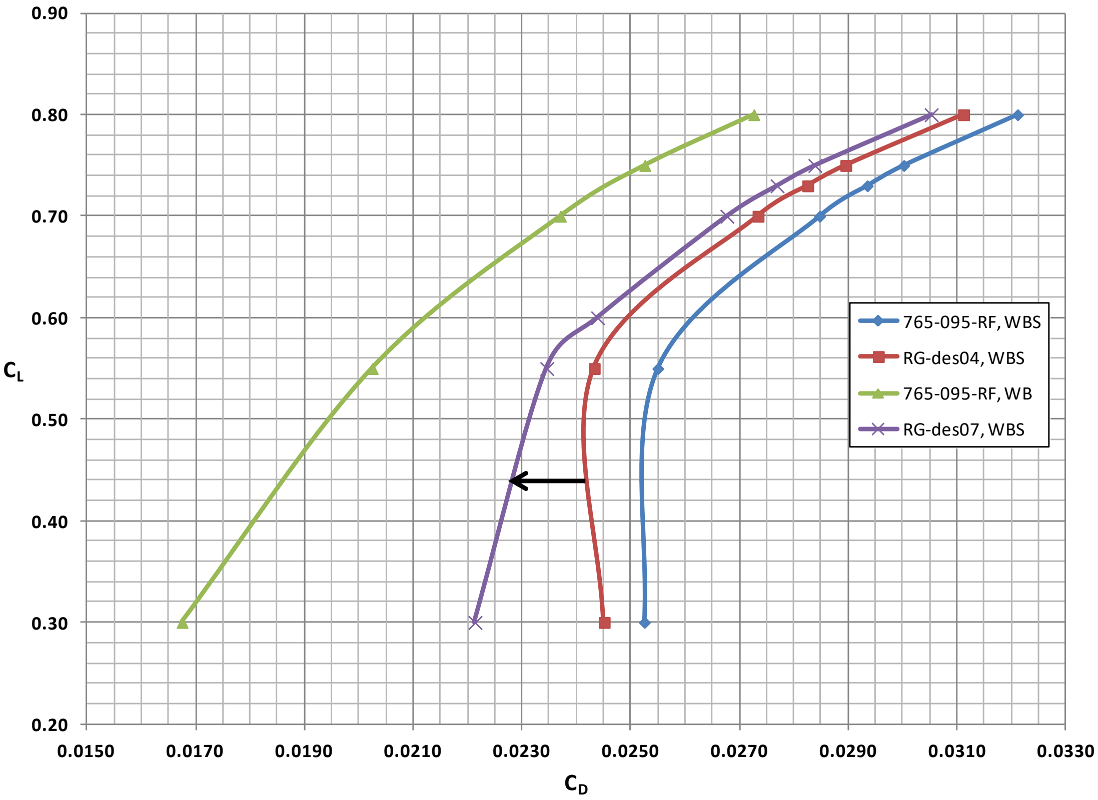

Figure 4.23 – OVERFLOW drag improvement obtained using Cart3D to clean up wing-strut juncture region.

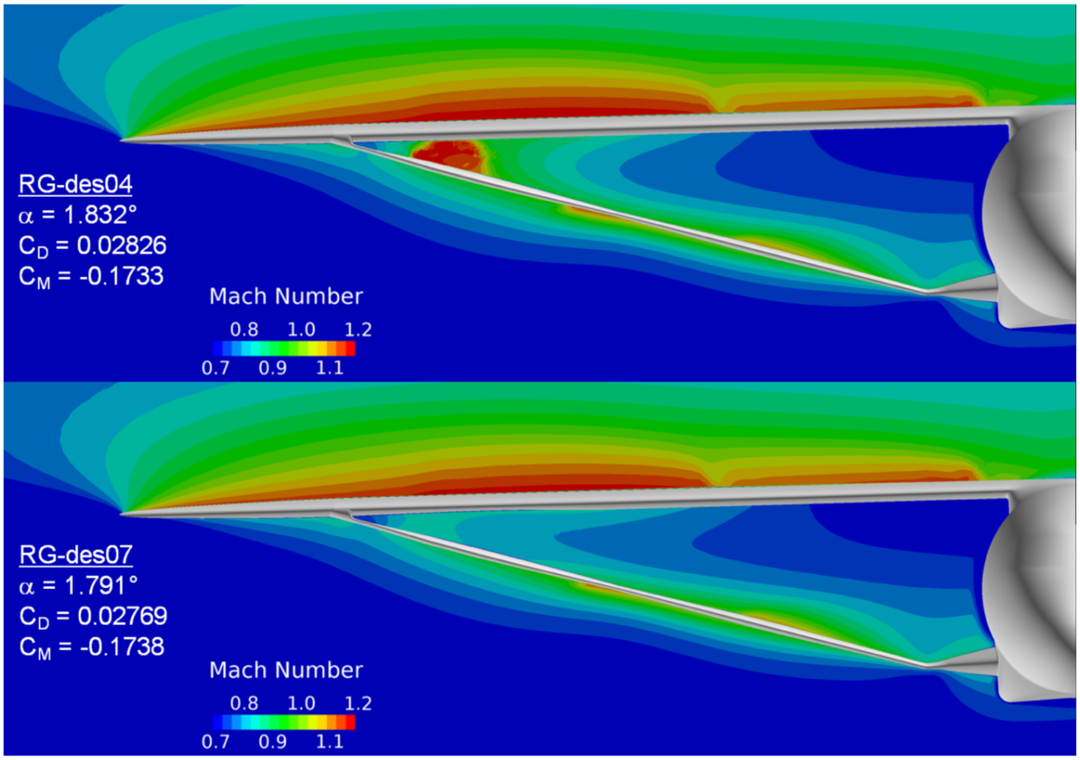

Figure 4.24 – Cart3D optimization (Opt001) cleaned up the supersonic flow and the resulting shock system in the juncture region at the midcruise design C_L of 0.73. Seed Geometry: RG-des04, Final Geometry: RG-des07.

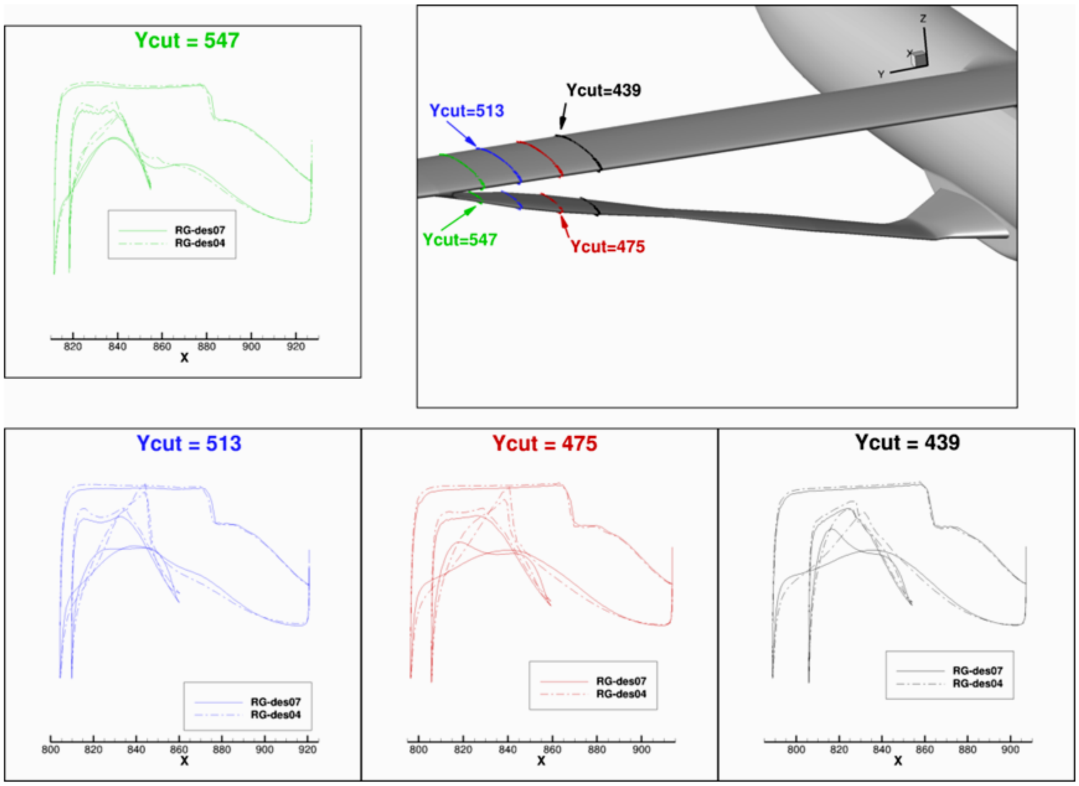

Figure 4.25 – The Cart3D optimization Opt001 deformed the lower surface of the wing and the upper surface of the strut in an attempt to minimize drag by removing the juncture shock system. Seed geometry: RG-des04. Final geometry RG-des07.

Inboard Strut Design Using CDISC

While Cart3D was used to optimize the complex flow field in the wing-strut juncture region, CDISC was applied in the inner strut region to improve pressure distributions computed by OVERFLOW. As seen in Figure 4.26, a surface pressure constraint (called “cpsmo”) within CDISC effectively smoothed the pressure distribution where shock strength was high. The strut airfoils were perturbed in a way that drove the original pressure distribution (solid, black line in Figure 4.26) toward the target pressure distribution (dotted, black line in Figure 4.26). After 10 iterations, the improved pressure distribution is shown as the red line in the figure. The horizontal dashed line represents the critical C_p level. The CDISC inverse design tool was utilized in this manner throughout the Rev-G, Rev-H and Rev-J design cycles on both the wing and strut.

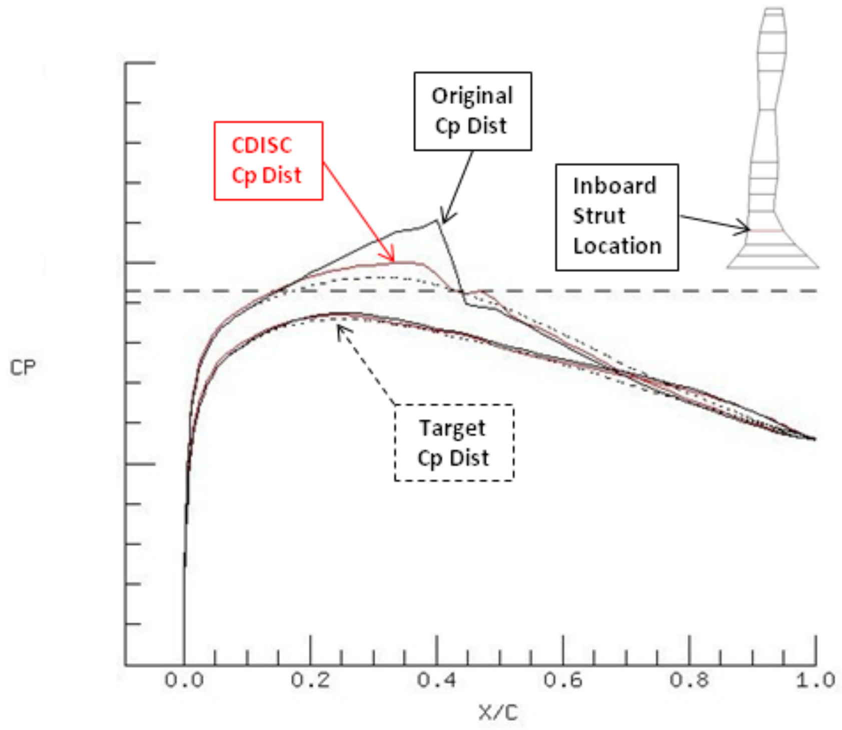

Figure 4.26 – Application of CDISC to inboard strut region smoothed pressure distributions.

Wing-Body and Wing-Strut Fairing Design

The wing-body (WB) fairing for the SUGAR aircraft was modeled with a similar design as used on the C-17 high-wing aircraft. The shape of this fairing was designed to eliminate the “horseshoe” vortex and reduce the strength of the wing lambda-shock, reducing drag at cruise. These design goals are shown to be met in a qualitative sense by comparing the right/left surface pressure contour images of Figure 4.27 where the solution on the left side of this figure is an early design and the solution on the right is the final design. Note the reduced concentration of dark orange in the C_p distribution on the right of Figure 4.27 where the redesigned fairing weakened the second (i.e., aft shock) at the wing/body intersection. This can be seen in the right side of the figure as a weak double-shock C_p structure as opposed to a single, stronger shock seen in the contours on the left side of the figure. Also note how the surface streamlines transition from the fairing to the fuselage at the wing trailing edge in a more uniform manner.

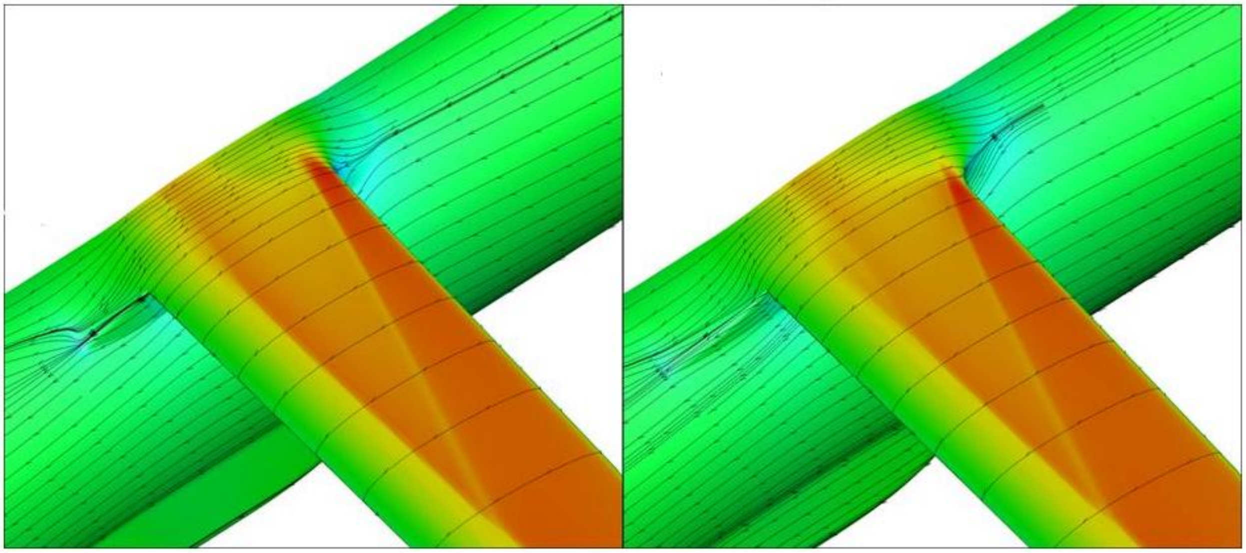

Figure 4.27 – WB fairing refinement: initial (left) and final (right): Re_{mac} = 12.3 million, Mach = 0.745, and C_L = 0.73.

The wing-strut fairing shown in Figure 4.28 was designed to mitigate the interference of the wing-strut interaction by controlling both the Mach number entering the channel flow, as well as limiting the flow acceleration through the channel. The fairing works in conjunction with local wing shaping to control the channel cross-sectional area distribution to prevent a strong normal shock from forming. Since the fairing limits the channel Mach by spilling flow over the wing upper surface and strut lower surface (in a sense), the fairing shape is also designed to ensure that the spilled flow does not culminate in a strong shock.

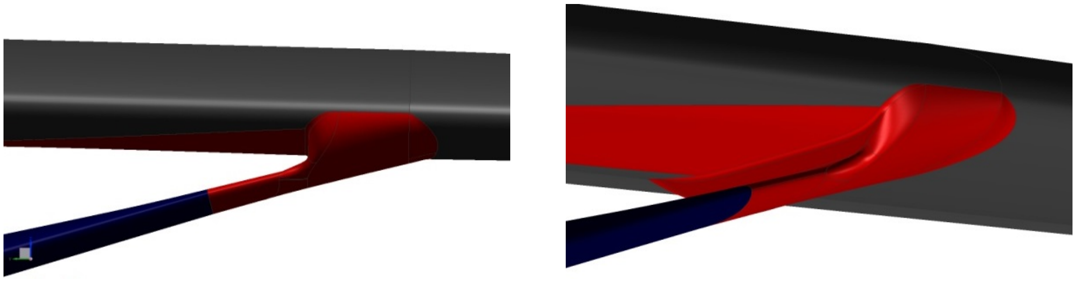

Figure 4.28 – Wing-Strut Fairing.

The wing-strut fairing was updated and improved multiple times throughout the TTBW design to account for the evolving configuration changes such as strut twist and main landing gear movement. The NX CAD package was used to define the OML for both the wing-body and wing-strut fairings.

4.2.2.2 Jury Strut Design

A jury strut design study, initiated early-on during the Rev-G configuration development, led to some important discoveries which affected the point at which the jury strut was fully integrated into the aerodynamic design process. The jury strut sweep angle was varied forward and aft as shown in Figure 4.29 in order to see how sweep affected the overall drag. Both the forward sweep of RG-des05 and the rearward sweep of RG-des06 improved the drag level relative to RG-des04 which had no sweep. Additional studies involving fillets at either end of the jury strut and retwisting the jury strut to align it with the onset flow were initially planned in order to optimize the design. A comparison of the flow field around the Rev-F jury strut and the RG-des04 jury strut, however, highlighted the strong effect of the local flow field on the aerodynamics of the jury strut (See Figure 4.30). Because both the onset Mach number and incident flow angle in the vicinity of the jury strut are highly dependent on the flow field between the strut and the wing, a decision was made to postpone the aerodynamic optimization of the jury strut until after the strut design was finalized.

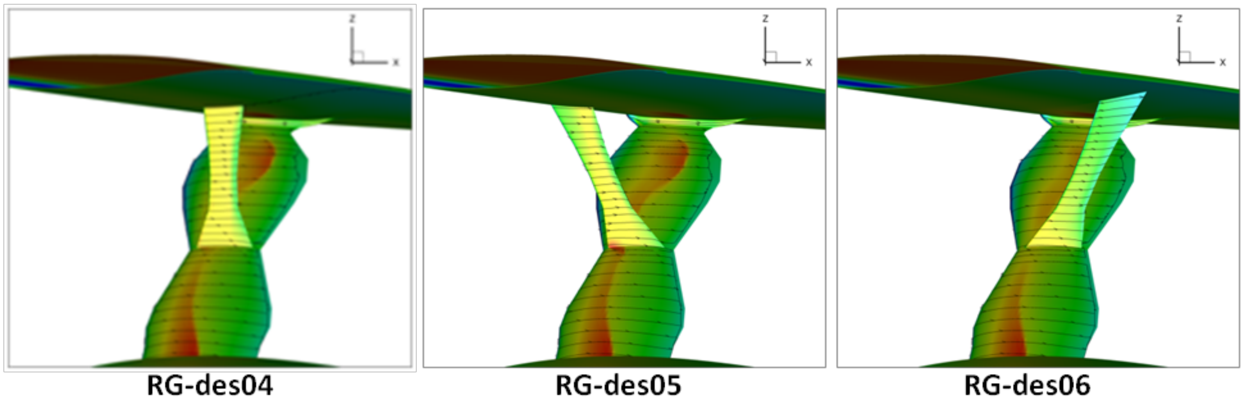

Figure 4.29 – SUGAR Rev-G jury strut sweep study: Re_{mac} = 12.3 million, Mach = 0.745, and C_L = 0.73.

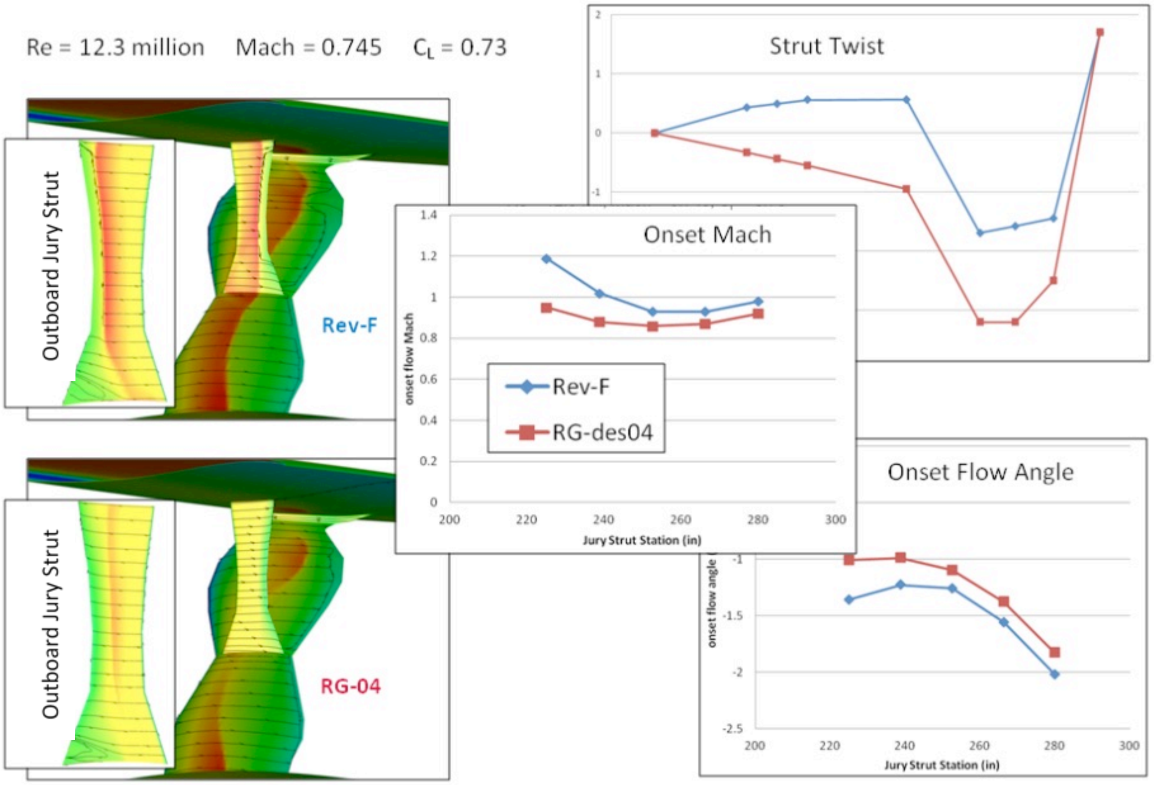

Figure 4.30 – An in-depth comparison of the jury strut installation on 765-095-RF (Rev-F) configuration and the RG-des04 configuration highlighted the effect of the strut flowfield on the jury-strut aerodynamics: Re_{mac} = 12.3 million, Mach = 0.745, and C_L = 0.73.

4.2.3 Summary of 765-095-RH (Rev-H) Design Cycle

During the Rev-H design cycle, the strut from the Rev-G configuration was updated using new airfoils from the 2D optimization process, and a buffet prediction capability was developed by modifying existing tools to be compatible with a TTBW design. The modified buffet method was then used to perform a sensitivity study to determine the ideal distance of the strut from the wing for the alternate strut design. Finally, the landing gear was shifted rearward by 24.8”, thereby moving the inboard strut attachment point and reducing the strut sweep from 4° to 0°. These key configuration development items from the Rev-H design cycle are summarized in Figure 4.31.

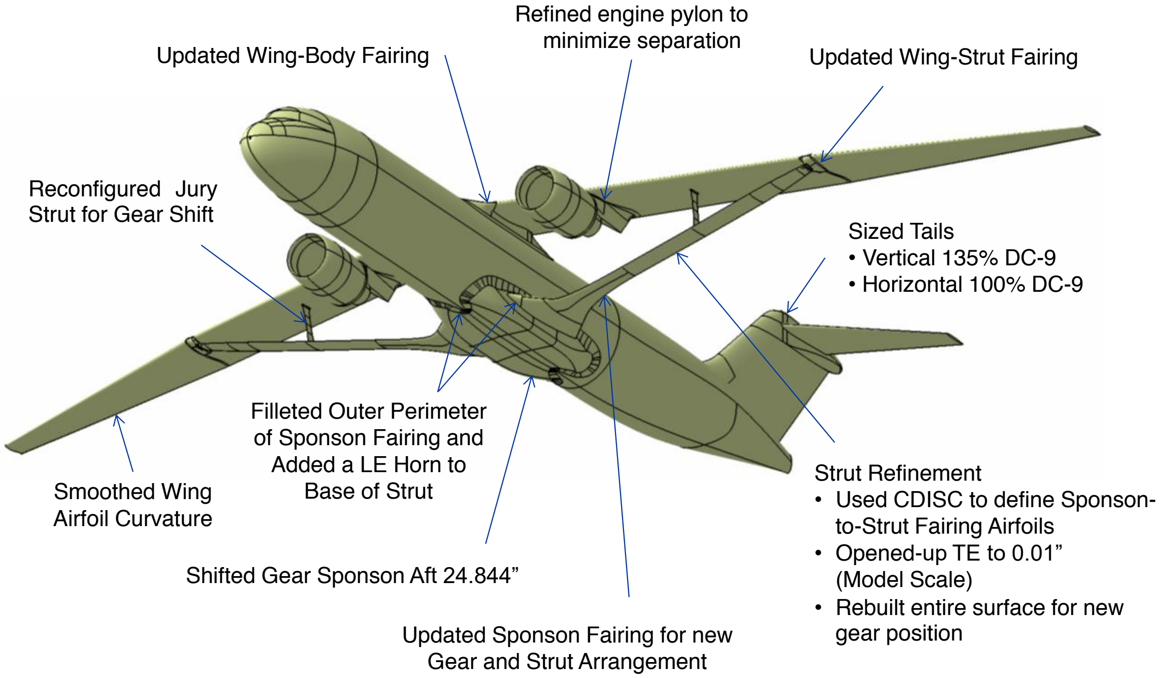

Figure 4.31 – Rev-H Configuration Development.

4.2.3.1 Wing-Body-Strut Design

The WBS design effort focused on two things: 1) The development of a buffet boundary prediction method that could be used on the strut as well as the wing, and 2) Adjusting the strut design in response to the main landing gear shift.

Estimation of Buffet Onset

Up until this point, the focus on the aerodynamic design centered around maximizing the cruise performance. The final design, however, would also need to possess reasonable buffet characteristics for reasons discussed in Section 4.3.3.1. A proprietary code called BUFFET was used to evaluate the aircraft's buffet performance based on input CFD solutions. The BUFFET program was developed for use with FLO-22 solutions. It was not developed for use on complex configurations such as the SUGAR trust-braced-wing concept nor has its accuracy been validated when used with OVERFLOW. The code was therefore modified to allow analysis of the strut flow field, and an approach was developed to apply the modified BUFFET code to the upper and lower surfaces of both the wing and the strut, with an emphasis on the wing/strut juncture region. An effort to validate this buffet method constitutes further research.

Figure 4.32 provides an example of how the results from the modified BUFFET code were used to determine the buffet sensitivity of the TTBW designs. The dotted red line represents the critical normal Mach number boundary determined by the code using the empirical database, while the solid red line represents the OVERFLOW-computed normal Mach number on the upper surface of the RH-des01 strut. The difference between the dotted and solid curves provides a measure of how close a given design is to being buffet critical. If the solid and dotted lines cross at a given station, then the solution was predicted to have an unacceptable amount of shock-induced separation at that station. This example shows that the RH-des01 strut was buffet critical on the most outboard region of the strut. This type of analysis was used in later stages of the design in order to evaluate a configuration's susceptibility to buffet onset.

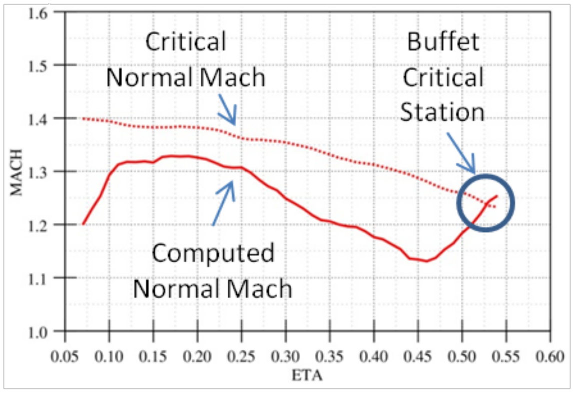

Figure 4.32 – Example of BUFFET code output for evaluating the susceptibility of the strut to buffet.

Effect of Main Landing Gear Shift on Strut Design

At the end of the Rev-H design cycle, a 24.8 inch rearward shift in the main landing gear position forced the inboard attachment point of the strut to move. As the strut was redesigned to account for the new gear location, the outboard attachment point where the strut meets the wing moved forward toward the leading edge of the wing to keep the strut spars straight. This latter movement aggravated the juncture flow between the strut and wing as seen in the left and middle images in Figure 4.33, and the shock that resulted had to be addressed at the beginning of the Rev-J design cycle.

The change in the strut position altered the onset flow conditions and decreased the downward loading in the region of the wing/strut juncture. This elevated the Mach number in the juncture and caused a shock to form. The strut was retwisted for the RJ-des06 configuration in order to increase the downward loading of the strut in the vicinity of the wing, and the wing-strut fairing was relofted in order to maintain a more constant juncture area distribution similar to what was present prior to the landing gear shift. The improvement in the juncture flow field of RJ-des06 as seen in Figure 4.33 was a direct result of those changes.

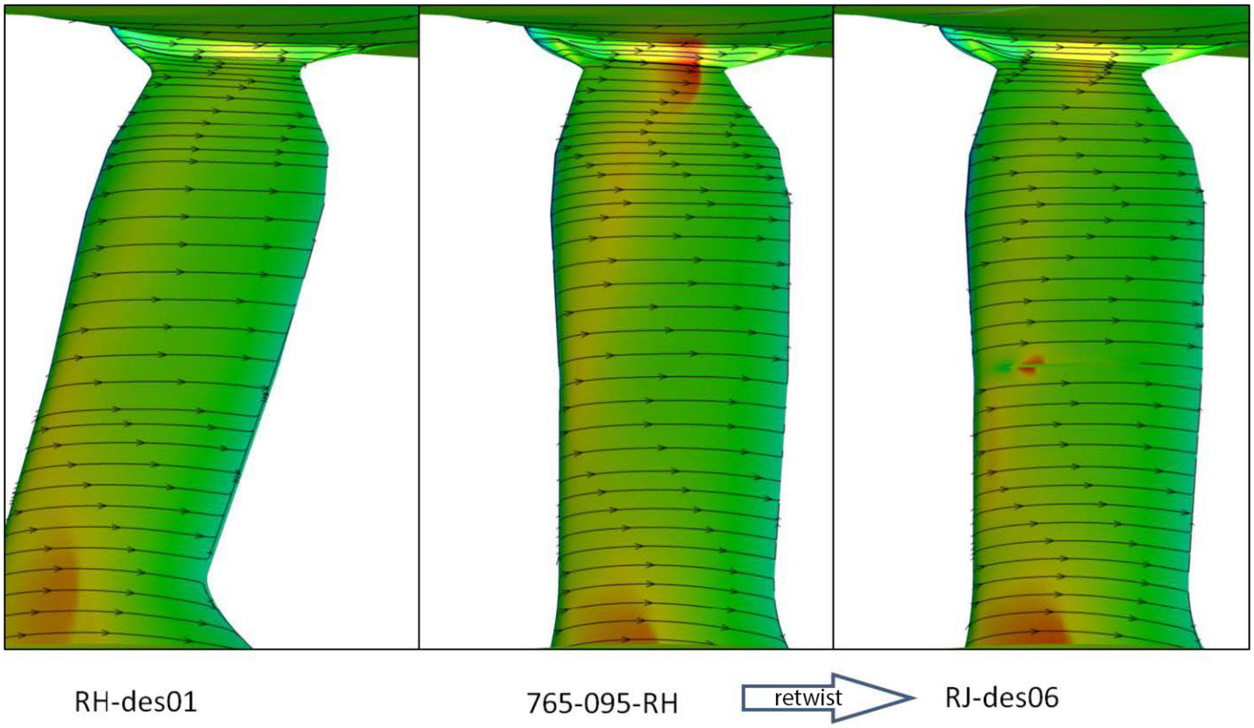

Figure 4.33 – The strut realignment that occurred at the end of the Rev-H design cycle (765-095-RH) produced a shock in the wing/strut juncture region, which was addressed during the Rev-J design cycle: Re_{mac} = 13.1 million, Mach = 0.745, and C_L = 0.73.

4.2.3.2 Alternate Strut – Preliminary Design

Buffet boundary concerns as discussed in Section 4.3.3.1 indicate the possible need for an alternate strut arrangement.

Prior to initiating a detailed design for the alternate strut, a preliminary sensitivity study was performed to determine the effect of strut-wing offset distance on the aerodynamic performance of the configuration. A simplified alternate strut pylon that ignored structural constraints was placed at the same spanwise location on the wing where the baseline strut design attached. For the sensitivity study, the simplified pylon was made using a symmetric airfoil stack designed for a local Mach number of 0.92 and twisted to align with the local onset flow (see Figure 4.34).

The goal of this sensitivity study was to determine a nominal strut offset distance so a more complete design cycle could be initiated that included design of a proper pylon that met all structural constraints. Figure 4.35 describes the process used to efficiently generate alternate strut geometries for the sensitivity study.

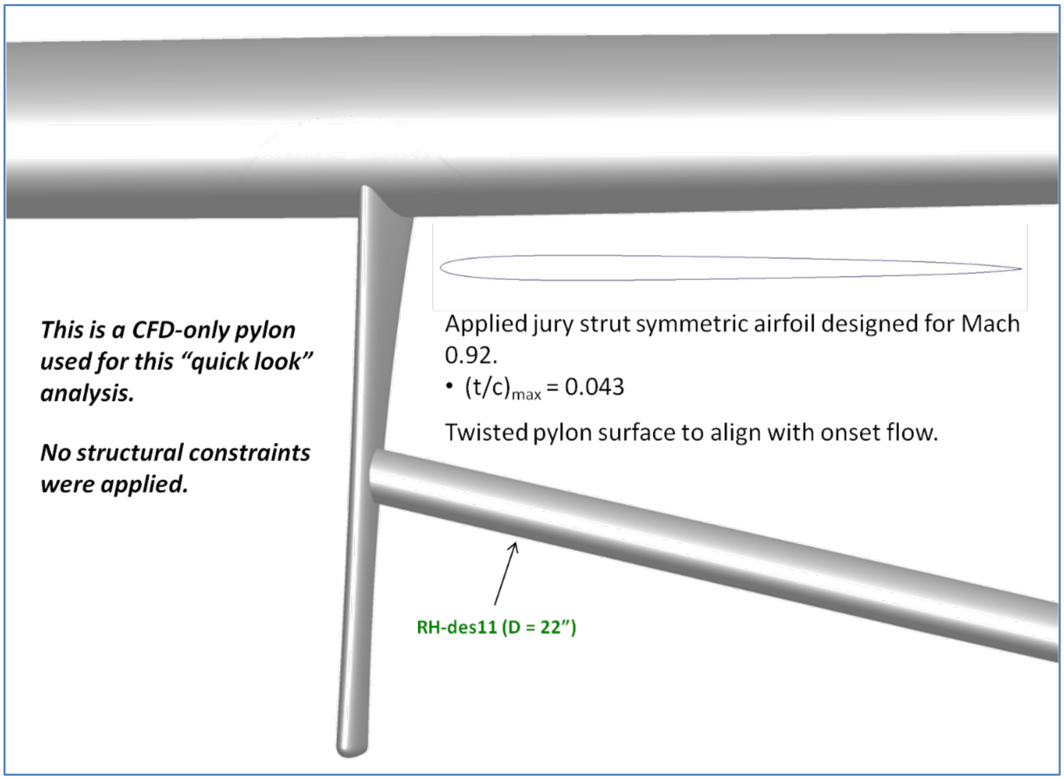

This is a CFD-only pylon used for this "quick look" analysis.

No structural constraints were applied.

Applied jury strut symmetric airfoil designed for Mach 0.92.

- $(t/c)_{max} = 0.043$

Twisted pylon surface to align with onset flow.

Figure 4.34 – Simplified alternate strut pylon used for alternate strut offset distance sensitivity study.

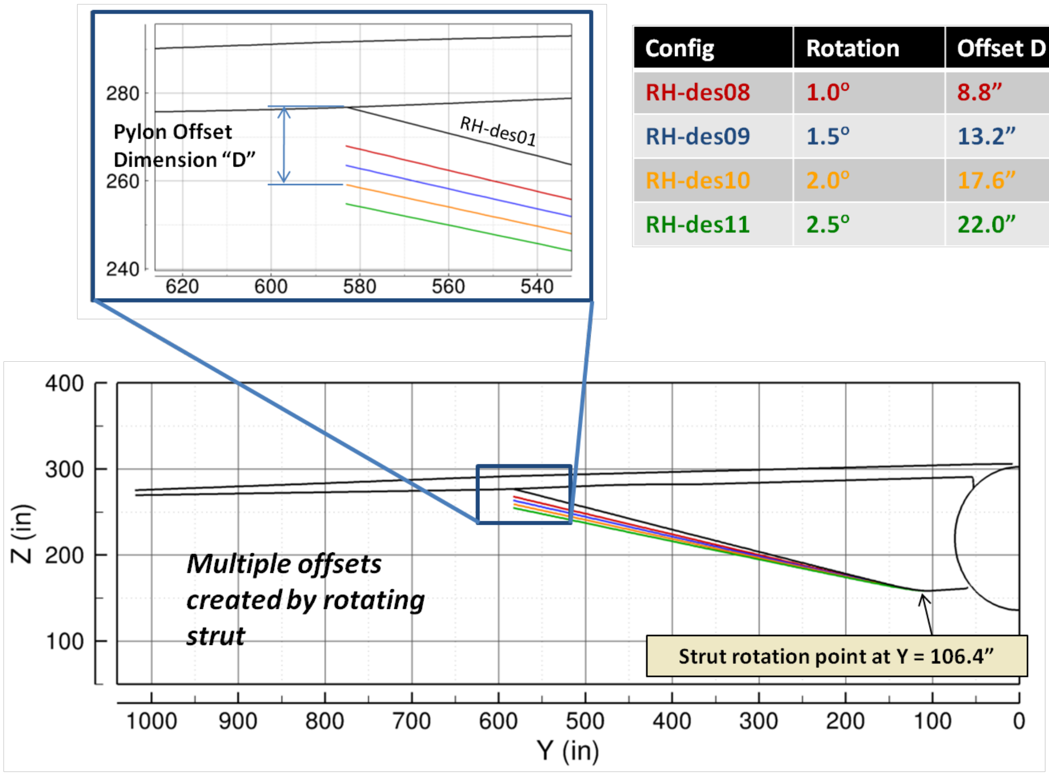

Config	Rotation	Offset D
RH-des08	1.0°	8.8"
RH-des09	1.5°	13.2"
RH-des10	2.0°	17.6"
RH-des11	2.5°	22.0"

Multiple offsets created by rotating strut

Strut rotation point at Y = 106.4"

Figure 4.35 – Process used to create alternate strut geometry for the alternate strut offset distance sensitivity study.

For each new alternate strut design, the baseline strut design (labeled RH-des01 in the inset image in Figure 4.35) was rotated downward about a common point in order to achieve the desired offset distance D. Because the optimum airfoil section contour created at each spanwise station was a function of the distance to the wing, simply rotating the strut would produce a design that would not have an optimal airfoil distribution. To correct for this issue, the rotated strut was stretched along the span such that the various airfoil stations on the new strut would be located closer to their intended design offset distance from the wing.

A set of four different alternate strut designs (RH-des08 through RH-des11) with offset distances “D” of 8.8, 13.2, 17.6, and 22.0” were analyzed at two different maximum operating speed flight conditions—one at cruise and one at descent. The cruise condition was analyzed at Mach 0.795 and C_L = 0.64, while the descent case was selected by using conditions at the flight envelope corner: Mach=0.795 and C_L = 0.27. Each alternate strut design was evaluated on its buffet susceptibility using the modified BUFFET code as described in Sections 4.1.2 and 4.2.3.1. As shown in Figure 4.36, only the alternate strut design RH-des11 with the 22” offset distance passed the buffet-free criteria in the channel between the strut and the wing for M_{MO} = 0.795 at the cruise condition, while none of the designs produced acceptable buffet onset characteristics on the strut for the M_{MO} = 0.795 descent condition. In addition, the strut lower surface shock remained strong for all offsets analyzed. The results of this study produced an offset distance and suggested that the airfoil sections should be redesigned for this new offset and the higher M=0.795 operating speed. This information was carried through to the Rev-J design cycle where a more realistic pylon that faired over the required structure was instituted as well.

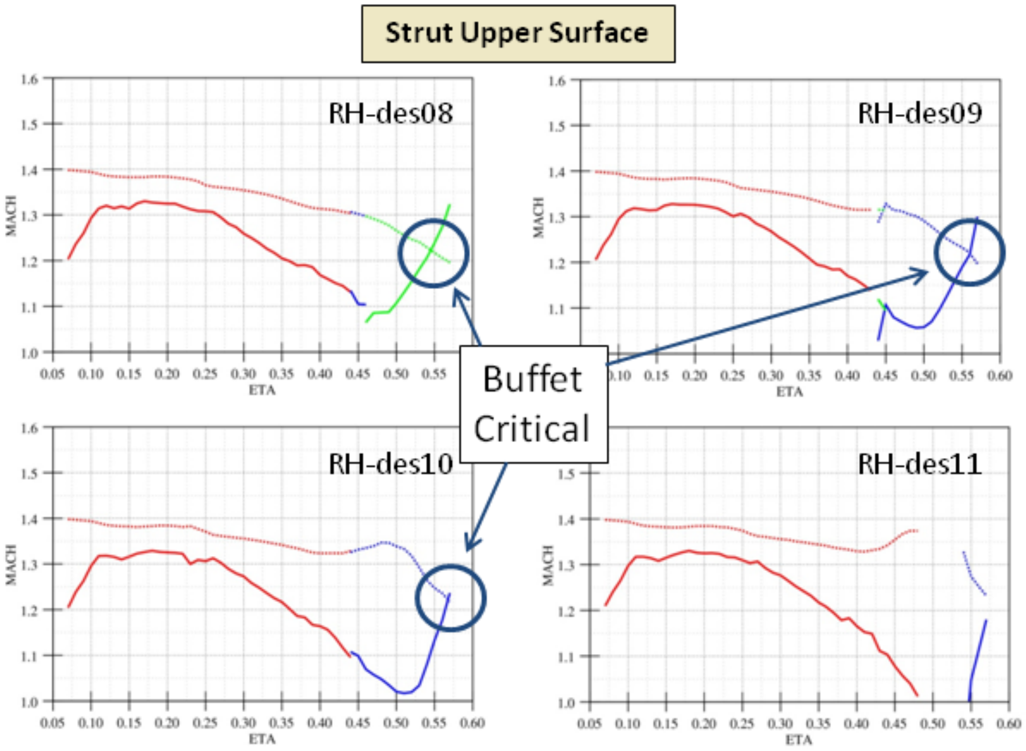

Figure 4.36 – Normal Mach comparison on strut upper surface from BUFFET at M_{MO} = 0.795 and C_L = 0.64. Line color differences are insignificant.

4.2.4 Summary of 765-095-RJ (Rev-J) Design Cycle

Including the final configuration, the Rev-J design cycle consisted of a total of 49 different design configurations. The primary goal was to finalize the outer mold line (OML) for both the standard strut and alternate strut designs. Figure 4.37 highlights the key improvements made during the Rev-J design cycle.

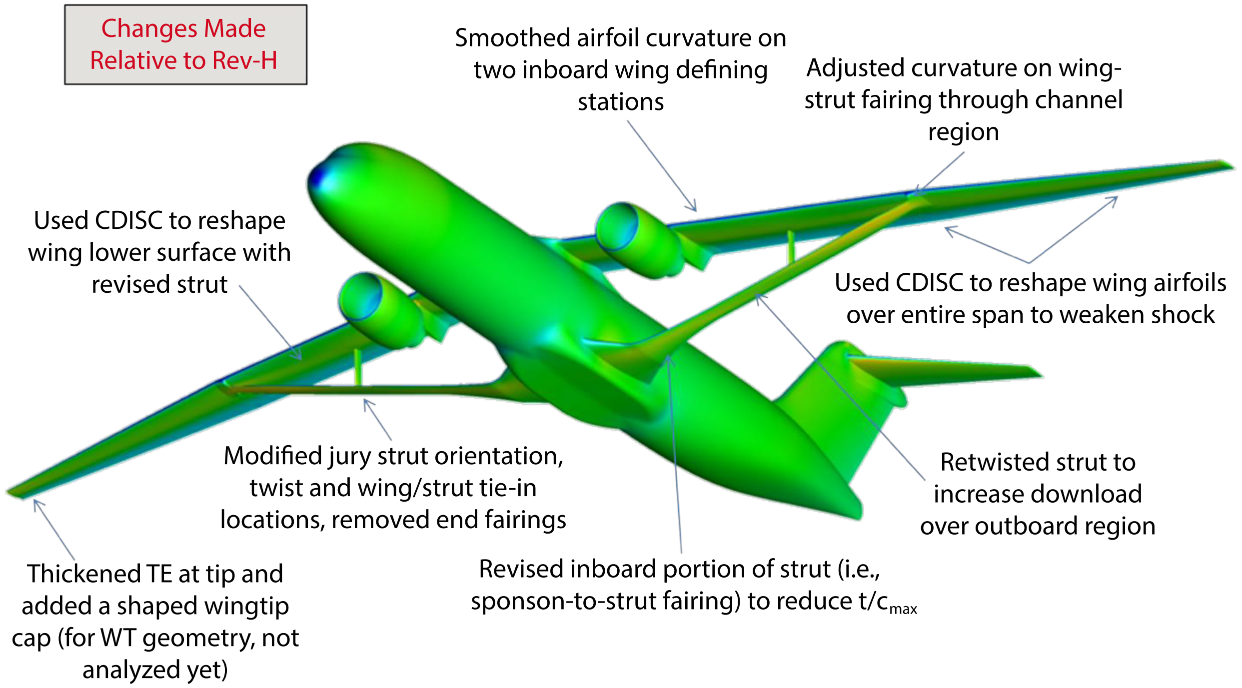

Figure 4.37 – Areas of design focus during the Rev-J design cycle.

4.2.4.1 Final wing and strut design on complete configuration

The strut design evolved considerably during the Rev-J design cycle. This was driven primarily by the main landing gear shift that occurred at the end of the Rev-H design cycle. As previously mentioned in Section 4.2.3.1, the landing gear shift caused the strut inboard and outboard attachment points to move, and this resulted in shock formation in the wing-strut juncture. This was addressed by retwisting the strut and relofting the strut-wing fairing in order to maintain a more constant juncture area distribution, resulting in the RJ-des06 design. Although RJ-des06 was a noticeable improvement over the final Rev-H design, the Mach number in the juncture region still approached sonic conditions as seen in Figure 4.38.

CDISC was used to recontour the lower surface of the wing from the jury strut spanwise location out to the wing-strut attachment point, resulting in the configuration analyzed in RJ-des14. This minor reshaping of the lower wing surface helped to smooth out pressures and lowered the Mach number in the juncture between the strut and the wing as seen by the dashed strut in Figure 4.38.

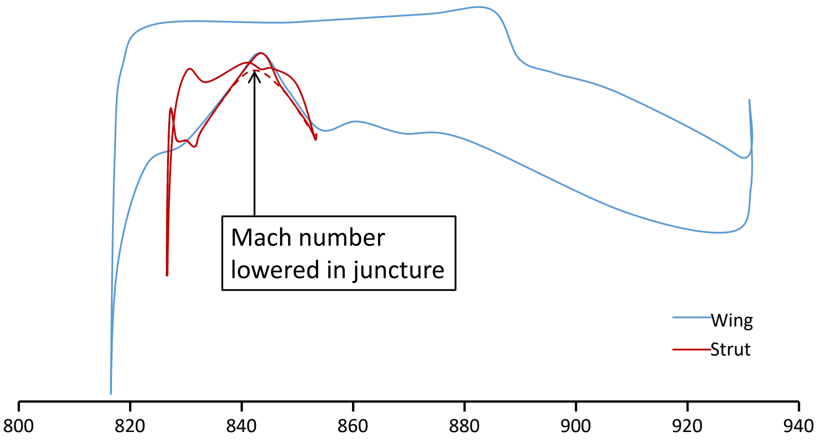

Figure 4.38 – Y-station 570 shows sonic flow in wing/strut juncture for the RJ-des06 configuration and the dashed recontouring after using CDISC: Re_{mac} = 13.1 million, Mach = 0.745, and C_L = 0.73.

After addressing the flow field in the juncture region, attention was focused on fixing the pressures on the upper surface of the inboard strut. The upper surface of the inboard strut for RJ-des14 was plagued by a region of low pressure near the leading edge denoted by the red area in the left-hand side of Figure 4.39. A small portion of this was cleaned up by adjusting the incidence by 2 degrees nose-down at Y=234 inches, but the majority of the issue was fixed through a redesign of the sponson to strut fairing. This redesign was accomplished by increasing the chord of the sponson to strut fairing and effectively lowering the t/c. As a result, the pressure contours of the upper surface inboard strut in the right-hand side of Figure 4.39 showed a noticeable improvement for RJ-des19 over RJ-des14.

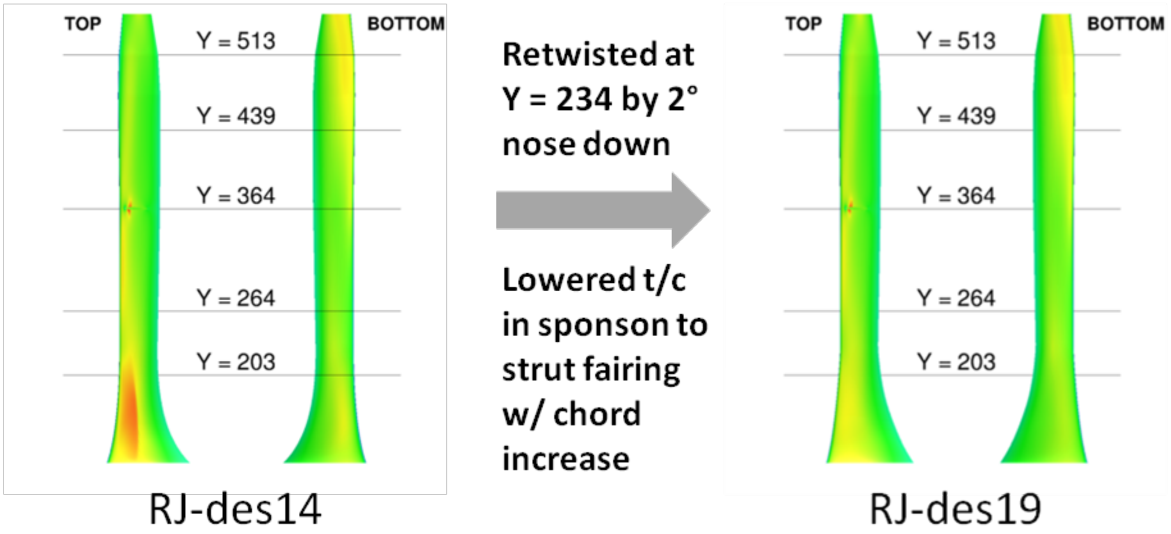

Figure 4.39 – Inboard upper surface strut pressures were cleaned up through a combination of twist and a redesign of the sponson to strut fairing: Mach = 0.745 and C_L = 0.73.

While using CDISC to recontour the lower surface of the wing helped lower the Mach number in the juncture region (see Figure 4.38), it had the unintended effect of mildly strengthening the shock on the upper surface of the wing. CDISC essentially increased the downward loading on the strut (which helped the juncture flow), but the wing loading had to increase in order to compensate and maintain the same C_L (by flying at a slightly higher angle of attack). In order to address this issue, CDISC was reapplied over the entire wing to weaken the shock on the upper surface. Finally, the section airfoil curvature at spanwise stations Y = 153” and 306” (in the wing reference plane) was smoothed to fix issues discovered during the CDISC process, a tip cap was added to the geometry, and a final CAD lofting of the wing was performed using the NX CAD package. Figure 4.40 contains a comparison of the pressure distributions from the initial (W08b) and near-final (W08d) wing designs from the Rev-J design cycle along with a table of drag and pitching moment coefficients. The W08d design does not include the effect of surface curvature smoothing which had a minimal impact on pressures. Note the weakened shock waves going from W08b to W08d on the lower surface at station 513.3 and upper surface across most of the span which is a direct result of the pressure smoothing inverse design process employed via CDISC.

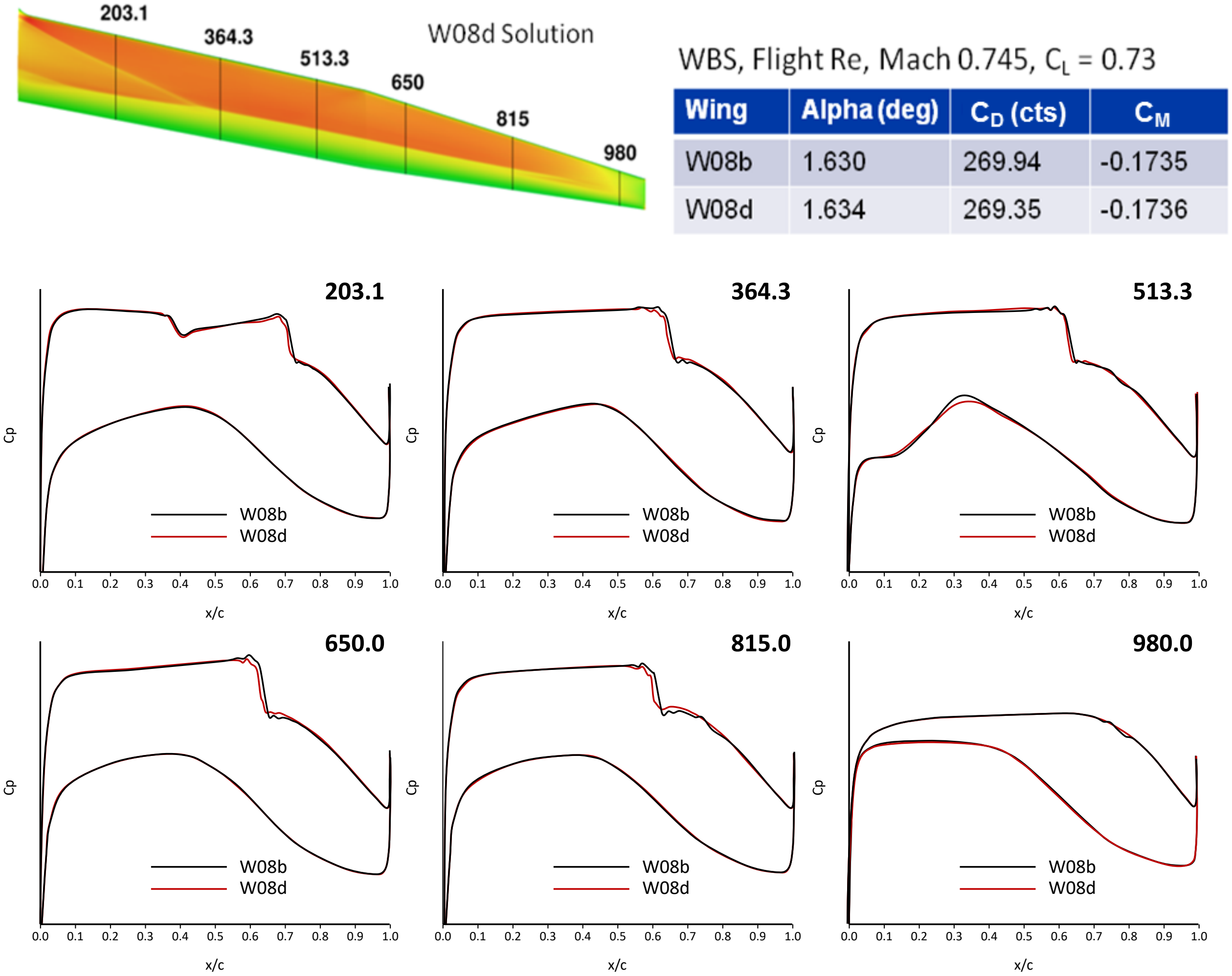

WBS, Flight Re, Mach 0.745, C_L = 0.73

Wing	Alpha (deg)	C_D (cts)	C_M
W08b	1.630	269.94	-0.1735
W08d	1.634	269.35	-0.1736

Figure 4.40 – Wing pressure comparison of the initial and near-final wing designs from the Rev-J design cycle: Re_{mac} = 13.1 million, Mach = 0.745, and C_L = 0.73.

4.2.4.2 Final jury strut design

The initial attempt at jury strut optimization during the Rev-G design phase (see 4.2.2.2) highlighted the importance of delaying the jury strut design until after the wing and strut outer mold lines were finalized. This was largely due to the sensitivity of onset flow conditions to the optimum wing and strut load distributions. This concept was further reinforced when it was discovered that the presence of the nacelle-pylon had a noticeable effect on the orientation of the local flow field as well. Figure 4.41 shows the pressure distributions at several spanwise Z locations along the height of the jury strut for the complete (WBSJNVH) configuration of RJ-des31. The shock-free, zero load pressure distribution at each station was determined by adjusting the local incidence of that station until the pressure distribution for the upper and lower surfaces of the symmetric airfoil matched, as this indicated the airfoil section at that station was aligned with the local flow. Figure 4.42 shows the pressure distributions over the same jury strut design for RJ-des31 in the wing-body-strut-jury (WBSJ) configuration. The asymmetry between each side of the jury (especially at Z=225") indicated that the lack of the presence of the nacelle pylon and/or tails had enough of an effect on the flow field that it was no longer properly aligned with the jury strut. It also highlighted the fact that the final jury strut design was noticeably sensitive to the local flow field angle, and this might present issues during sideslip testing in the wind tunnel.

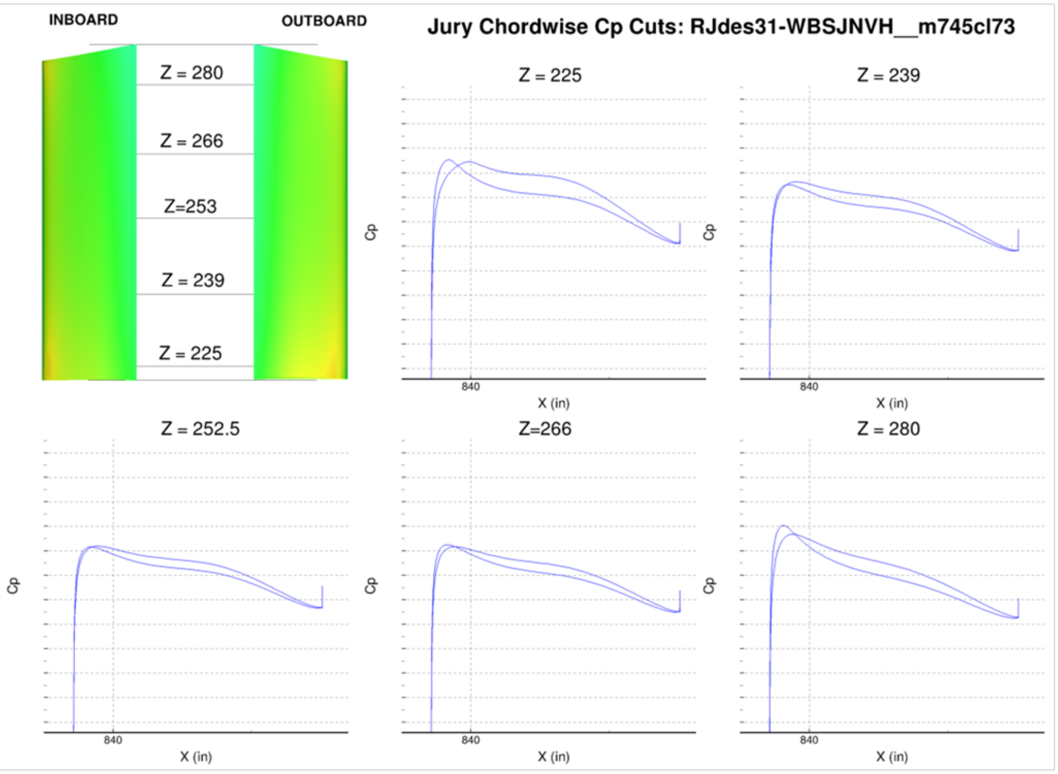

Figure 4.41 – Pressure cuts at various stations across the final jury strut design validated that the jury strut was properly aligned with the local flow. RJ-des31, WBSJNVH configuration: Re_{mac} = 13.1 million, Mach = 0.745, and C_L = 0.73.

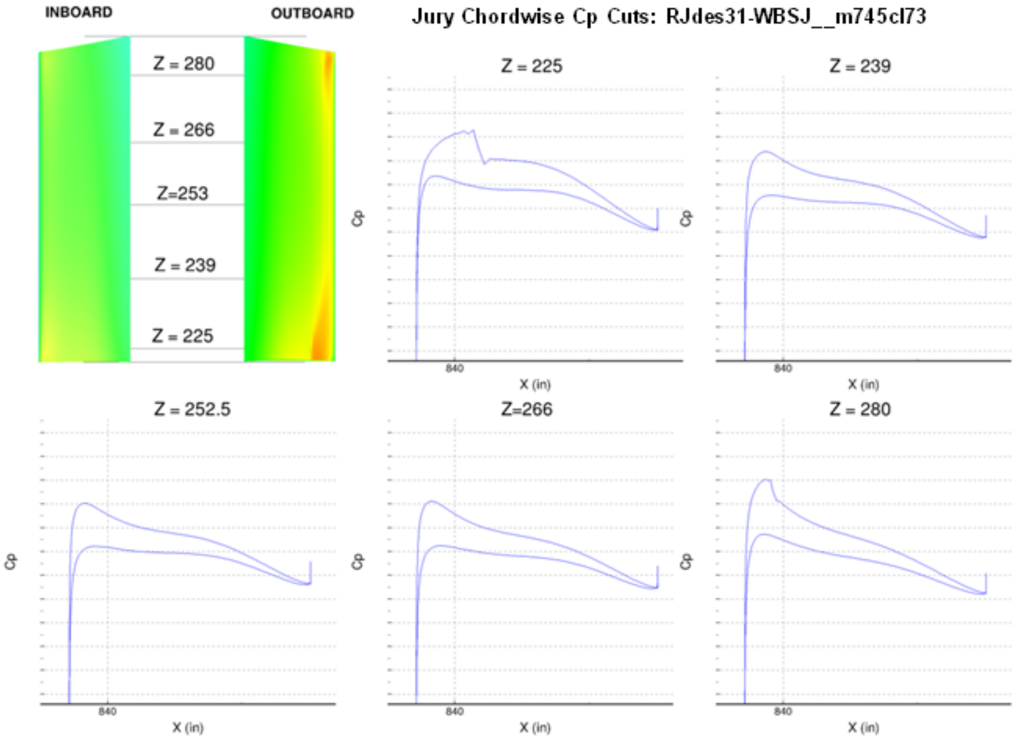

Figure 4.42 – Unequal pressure distributions between each side of the jury showed the influence that the presence of the nacelle-pylon and tail had upon the RJ-des31 jury design: Re_{mac} = 13.1 million, Mach = 0.745, and C_L = 0.73.

4.2.4.3 Alternate Strut – Detailed Design

Applying the information gathered during the preliminary design of the alternate strut where a sensitivity study was performed to better understand the effect of offset distance between the wing and strut on shock strength (see Section 4.2.3.2), attempts were made to improve the airfoils to make them better suited for Mach 0.8 operation. This airfoil redesign effort was done using the down-selected offset distance of 22” and a more realistic pylon described later in this section. Two design approaches were evaluated: 1) Use the alternate strut defined for the sensitivity study and retwist to improve loading and minimize pressure peaks, and 2) Use the 2D strut airfoil optimization method to create an all new design. Both approaches had strengths and weaknesses and the resulting designs from both were heavily influenced by the wing-pylon-strut juncture flow field which is characterized by a strong shock system as shown in Figure 4.43. In the end, the alternate strut from design approach #1 was selected because it was predicted to have a slightly weaker shock and it was a direct descendant of the baseline strut. This exercise highlighted the need for a more in-depth design effort for the challenging Mach 0.8 flight condition where the aerodynamics of the wing-pylon-strut flow field must be actively traded against structural requirements. In other words, there is much room for improvement for the alternate strut at Mach 0.8 if aerodynamic and structural requirements are equally weighted and meaningfully traded to achieve a more acceptable solution.

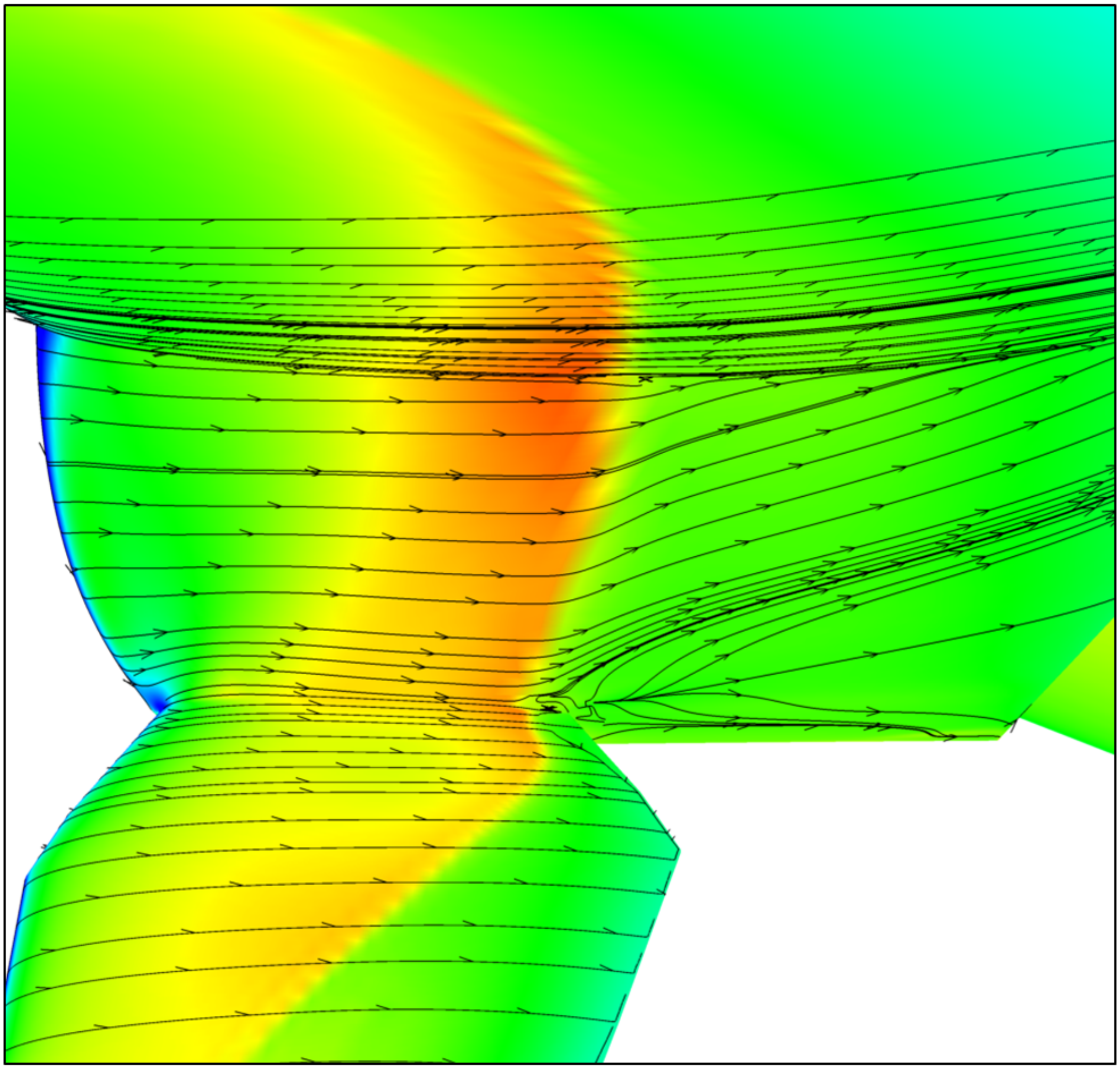

Figure 4.43 – Shock system in the juncture of the wing-pylon-alternate-strut at Mach 0.795 and C_L = 0.64.

The alternate strut’s pylon was designed to enclose the required structural members that attach the strut to the wing. The offset strut structural arrangement is comprised of a trapezoidal member extending perpendicular from the wing front spar downward to the strut attachment. This structure has a width of 10” in the span direction at the pylon-wing attachment, and has a 4.2” diameter pin at the pylon-strut attachment. The initial pylon shown in Figure 4.44 was sized to enclose this structure.

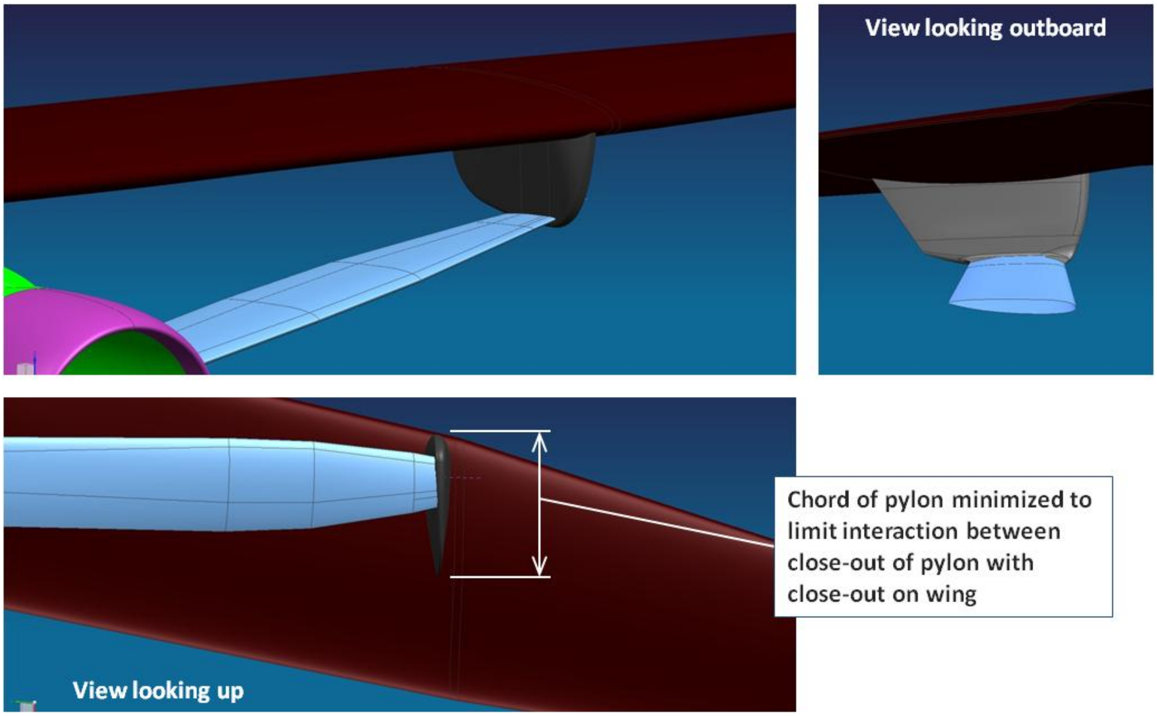

Chord of pylon minimized to limit interaction between close-out of pylon with close-out on wing

Figure 4.44 – Initial alternate strut pylon.

The first iteration of the pylon design attempted to close the pylon aggressively to avoid expected issues associated with closing a surface in the adverse wing pressure gradient. This resulted in a pylon with a t/c_{max} in excess of 14%. The flow interaction of the pylon with the wing and strut resulted in considerable local flow acceleration in the channel, and considerable drag. To decrease this acceleration the pylon max thickness was held and the pylon was stretched in the streamwise direction to reduce t/c_{max} to ~9%, as shown in Figure 4.45. This change pushed the trailing edge of the pylon into the adverse pressure gradient region on the lower surface of the wing, which resulted in significant flow separation on the top of the pylon and downstream on the wing (i.e., in the wing-pylon juncture).

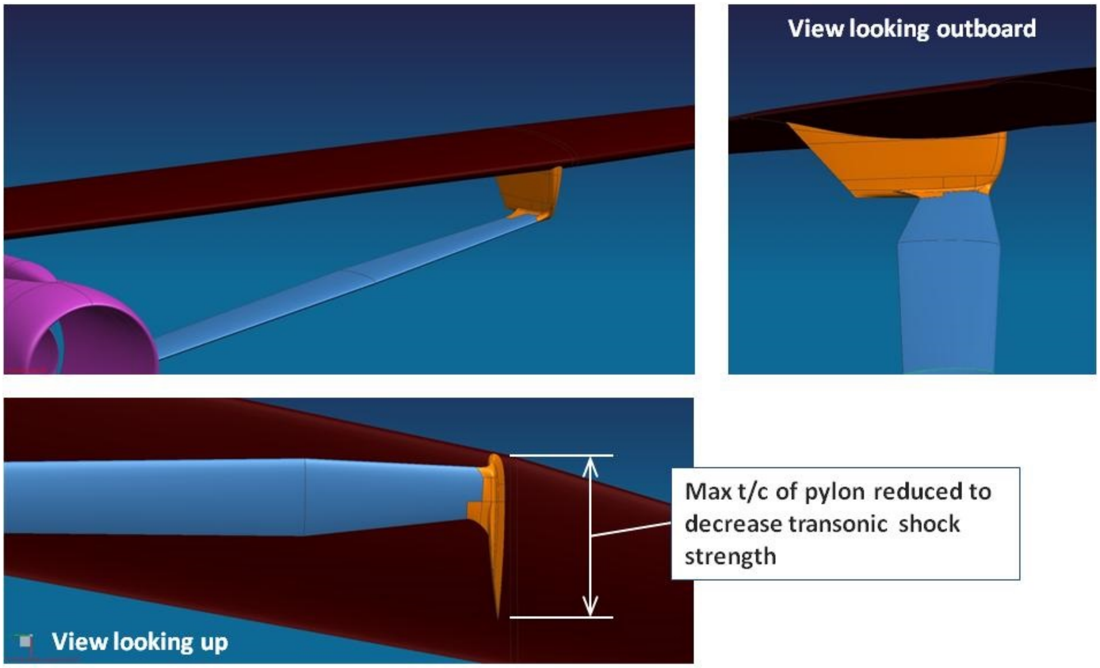

Figure 4.45 – Alternate strut pylon revision.

Since extending the chord even further to the trailing edge would result in a considerable increase in pylon wetted area, an aggressive fillet was designed to counteract the effects of the local pressure gradient (See Figure 4.46). The goal of the fillet is to provide local relief to the adverse pressure gradients by aggressively filling in the volume behind the pylon. This fairing design provides a ‘fix’ for the local flow separation behind the alternate strut pylon, but is not considered to be a ‘preferred’ configuration. Rather, a decrease in the required pylon thickness would support a reduction in pylon chord while maintaining the maximum t/c ratio. If a sufficient reduction in thickness is possible, this would move the trailing edge of the pylon forward out of the region of severe adverse pressure gradients, thereby eliminating the necessity of a fairing. The alternate strut pylon thickness was not reduced because of program schedule and budget constraints. In other words, iterating on the pylon design between Aerodynamics and Structures to the level required for such refinement was outside the scope of the study.

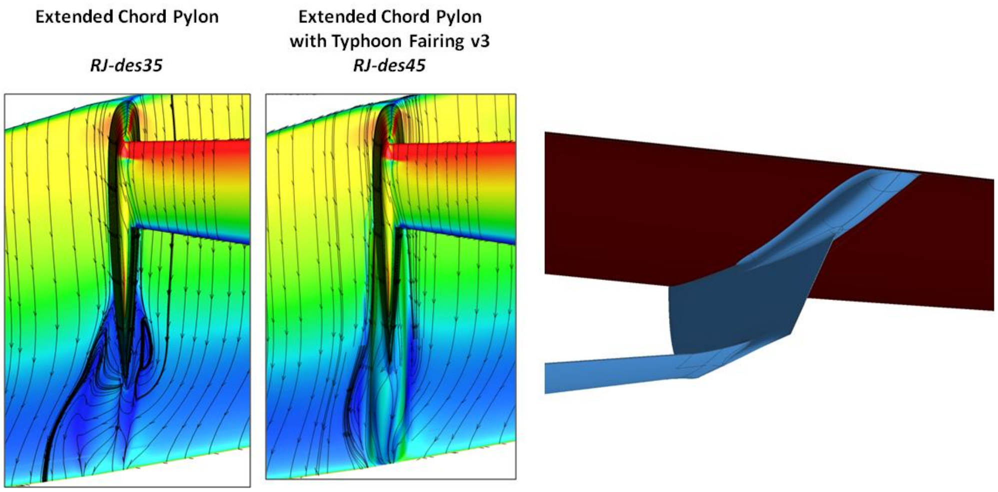

Extended Chord Pylon
RJ-des35

Extended Chord Pylon with Typhoon Fairing v3
RJ-des45

Figure 4.46 – The Typhoon Fairing (v3 shown) effectively eliminates the flow separation behind the alternate strut pylon.

4.3 Final Configuration Aerodynamic Performance

A thorough OVERFLOW analysis was performed on the final geometry at both flight and wind tunnel Reynolds numbers. Since aeroelastic data were not available at the time of this analysis, the wind tunnel simulation was done using a wing and strut with the theoretical 1g twist and bending distributions based on flight conditions. In other words, the same geometry was analyzed at both low and high Reynolds numbers. A build-up approach, much like that planned for the wind tunnel test, was followed for this final evaluation where a wing-body (WB) was first analyzed followed by a wing-body-strut (WBS) all the way through to the configuration with the highest geometric fidelity. Refer to Figure 4.6 for an illustration of the geometry analyzed and the associated nomenclature.

In addition to tracking incremental effects of the various airplane components, the influence that two major wing modifications had on the WB aerodynamics was also quantified. As discussed throughout Section 4.2 of this report, the wing was modified to operate more efficiently with the strut installed. The two primary changes made to the wing for WBS design purposes are thickness and twist. The change to wing thickness distribution, as shown in Figure 4.47, is a direct result of the Cart3D optimization discussed in Section 4.2.2.1 where the design space was limited to the juncture region between the jury strut and the wing-strut intersection. At the thinnest portion of this region, the thickness was decreased by 1.3%.

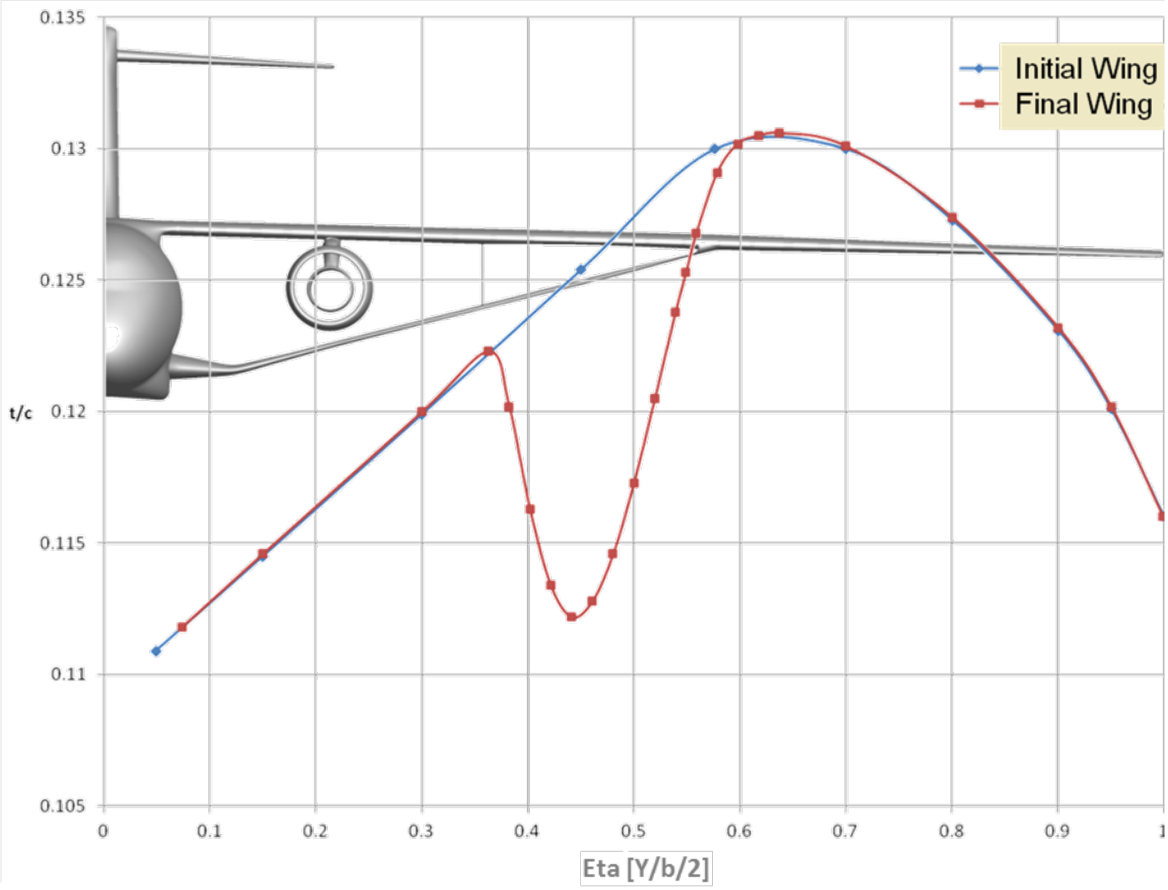

Figure 4.47 – Comparison of wing thickness distribution between the initial wing and the final wing designed for an efficient strut installation.

A back-to-back OVERFLOW analysis was performed to assess the aerodynamic impact of the local thinning shown in Figure 4.47 and the results show a drag reduction of 1.3 counts at the design condition of Mach 0.745 and $C_L = 0.73$. There is a potential structural impact to thinner airfoils as well due to the fact that the wing's front spar depth is reduced. While a dedicated structural assessment was not performed, a general weight/drag trade factor was applied to approximate the equivalent weight for a 1.3 count drag reduction. Using a performance-derived trade of 1,000 lbs for every 3 counts yields 433 lbs of equivalent weight, which is thought to be considerably greater than the expected wing structural weight increase caused by the local wing thinning. The mass properties buildup and aeroelastic FEM were performed on Revision H which includes local wing thinning.

The second important wing characteristic that was adjusted to improve the wing-strut flow field is twist. This topic was discussed in some detail in Section 4.2.1.4 where results from a preliminary wing twist study are presented in Figure 4.15. The final change made to the wing's 1g twist distribution is shown in Figure 4.48. Note the basic incremental trends between wing twist as well as the strut twist is similar to that shown in Figure 4.15.

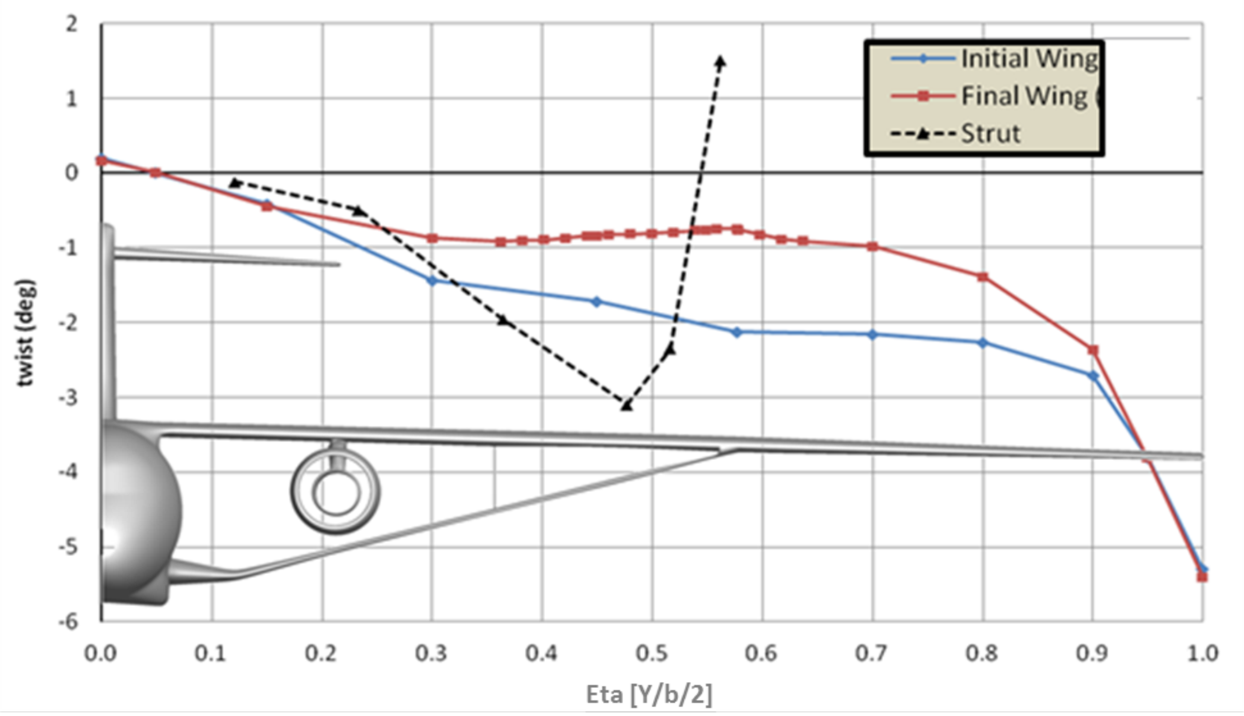

Figure 4.48 – Comparison of 1g wing twist distribution between the initial wing and the final wing designed for an efficient strut installation.

The wing and strut spanloads are shown in Figure 4.49 for the Rev-J WBSJN configuration with the final wing twist. The intended strut download between the jury and the wing-strut join is offset by the wing's nose-up incidence so that the combined loading is near elliptical. The inboard wing twist could be driven more nose-down to bring the combined loading closer to elliptic between the side-of-body and nacelle but preliminary wing twist studies indicated that the lift loss associated with reduced inboard wing loading offset the induced drag improvement because the angle of attack had to be increased to maintain total configuration lift.

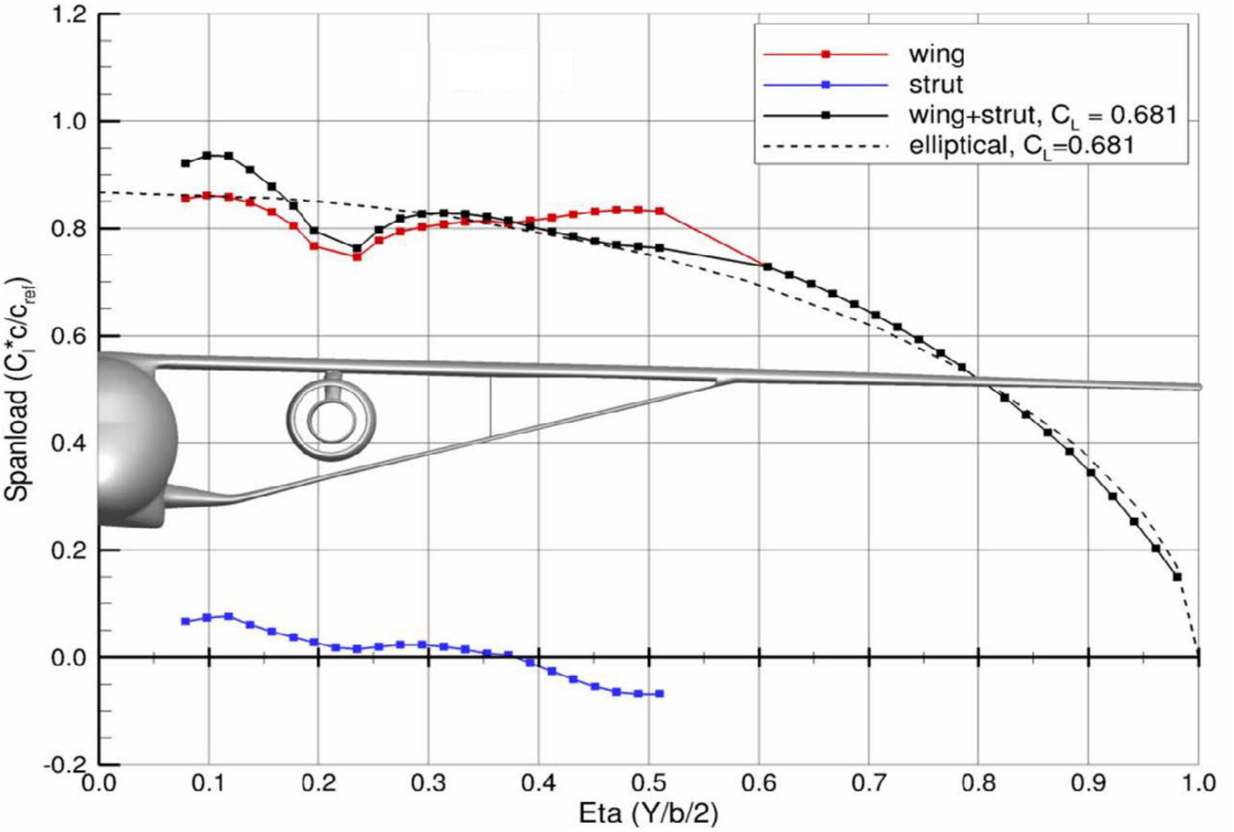

Figure 4.49 – Wing and strut spanloads for the final Rev-J WBSJN configuration at the design condition: Re_{mac} = 13.1 million, Mach = 0.745, C_L = 0.73, and α = 1.872°.

Figure 4.50 is a comparison of wing pressures for the initial and final wings at Mach 0.745 and C_L = 0.73. The nose-up twist change is seen in this comparison via the values for angle of attack in the legend where the final WB requires more than 0.5 degrees less alpha to maintain lift. The thickness change is seen indirectly as an airfoil shape change for the Y = 565" span station C_p comparison.

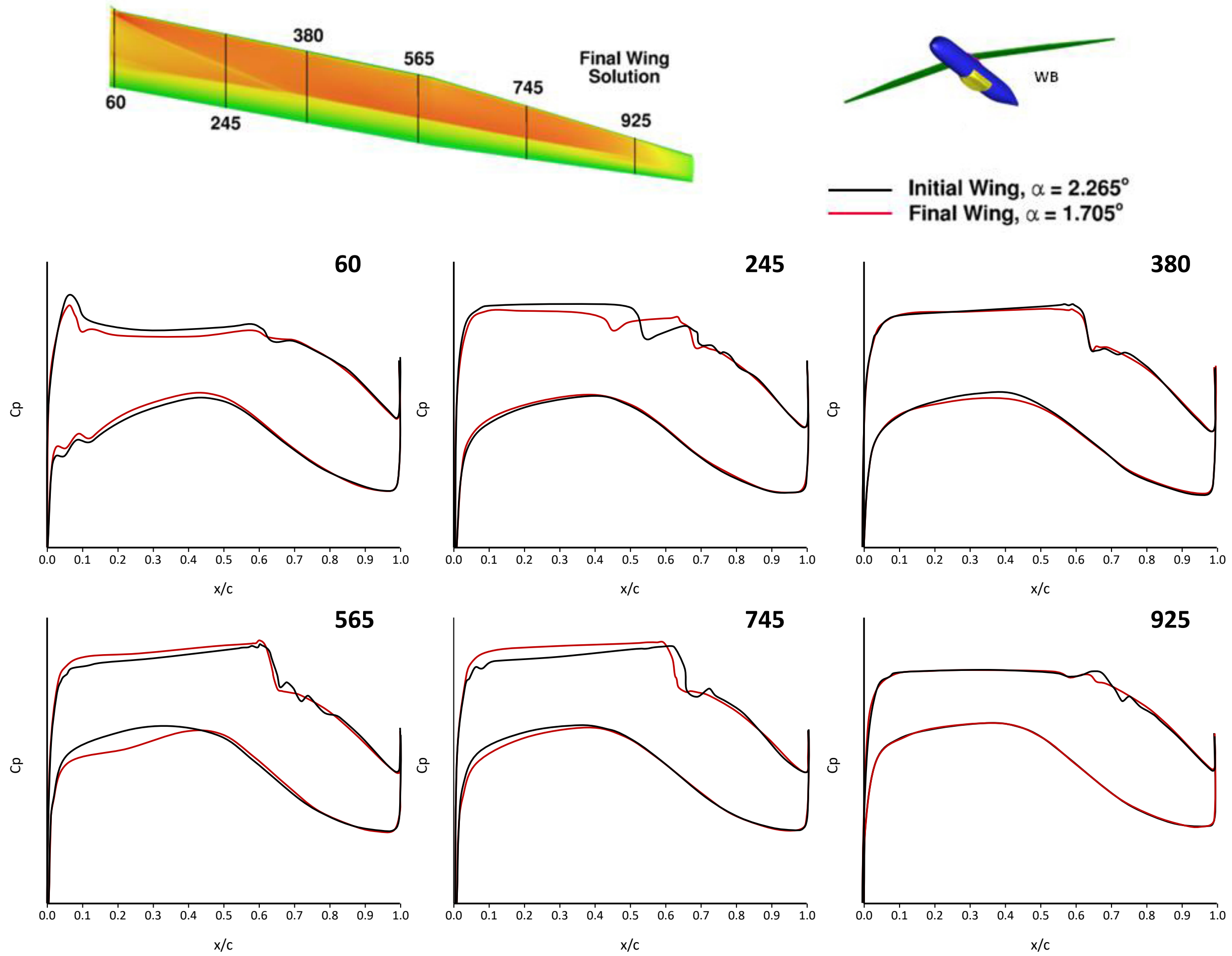

Figure 4.50 – Final Rev-J WB wing pressure comparison at the design condition: Re_{mac} = 13.1 million, Mach = 0.745, and C_L = 0.73.

The combined effect of wing thickness and twist is captured in the following comparison of flight Reynolds number data where two sets of WB results are plotted; one set is labeled "WB (Initial Wing)" and the other "WB." Wind tunnel Reynolds number results are also summarized followed by a discussion on the alternate strut.

4.3.1 Flight Reynolds Number Results

The final geometry released as 765-095-RJ was analyzed at flight Reynolds number across a range of Mach and C_L. The purpose of this analysis was to show that the design offers reasonable incremental data as the configuration is built-up with no predicted regions of separated flow at the design Mach of 0.745. The fully turbulent OVERFLOW data produced by this analysis was also used in the final performance calculations.

A tail-off drag polar comparison is shown in Figure 4.51, which includes tabulated data for the various cases analyzed at C_L = 0.73. The thickness and twist changes made to the wing reduce drag at the design condition by 1.5 counts. Since the final wing (red curve labeled "WB" in Figure

4.51) is predicted to have less drag for the full range of lift analyzed, it can be considered a more appropriate baseline to assess incremental drag simply because the deltas are larger than for the initial wing. Regardless of which wing is used as a baseline, the drag polar story is consistent. OVERFLOW predicts a fairly consistent shift across a wide range of C_L's as the strut, jury and nacelle are added suggesting a robust design was achieved at Mach 0.745. The computed drag increments tabulated in Figure 4.51 are considered to be reasonable for the purposes of this study.

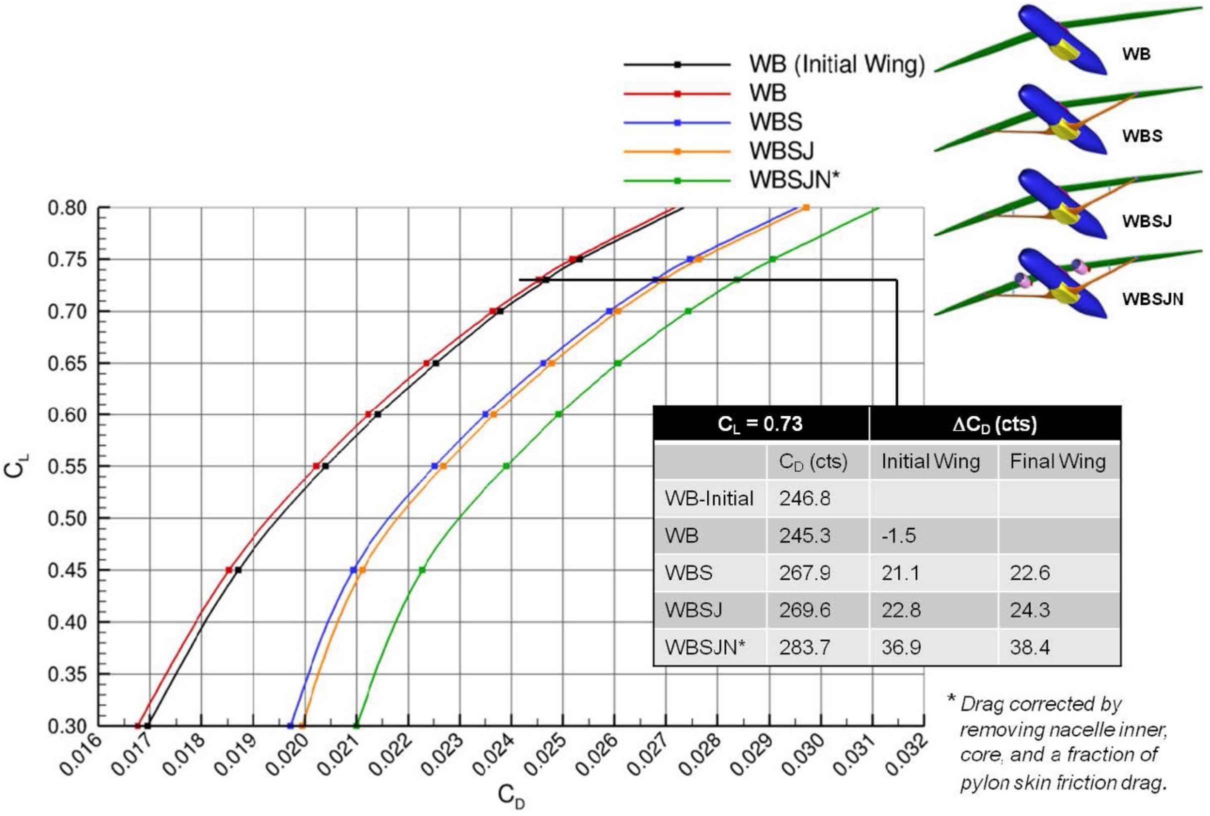

C_L = 0.73		ΔC_D (cts)	
	C_D (cts)	Initial Wing	Final Wing
WB-Initial	246.8		
WB	245.3	-1.5	
WBS	267.9	21.1	22.6
WBSJ	269.6	22.8	24.3
WBSJN*	283.7	36.9	38.4

** Drag corrected by removing nacelle inner, core, and a fraction of pylon skin friction drag.*

Figure 4.51 – Tail-off drag polars at flight conditions for the final Rev-J configuration: Altitude = 40,000 ft, Re_{mac} = 13.1 million, Mach = 0.745, and C_L = 0.73.

The WBSJN data shown in Figure 4.51 (green line) is plotted again in Figure 4.52 together with a trimmed polar over a smaller C_L range. As indicated in the figure, the drag increase from adding the tail and trimming is 31 counts at the design condition. Roughly 80% of this increment (around 25 counts) is from tail drag alone. Note that skin friction drag from the inner nacelle surface, core and a portion of the pylon (from engine thrust scrubbing) was removed from the OVERFLOW data as stated in the notes for Figure 4.51 and Figure 4.52. The inset plot shown in Figure 4.52 shows maximum L/D for the all-up configuration occurs at C_L = 0.765 or 0.035 higher than the WB design C_L.

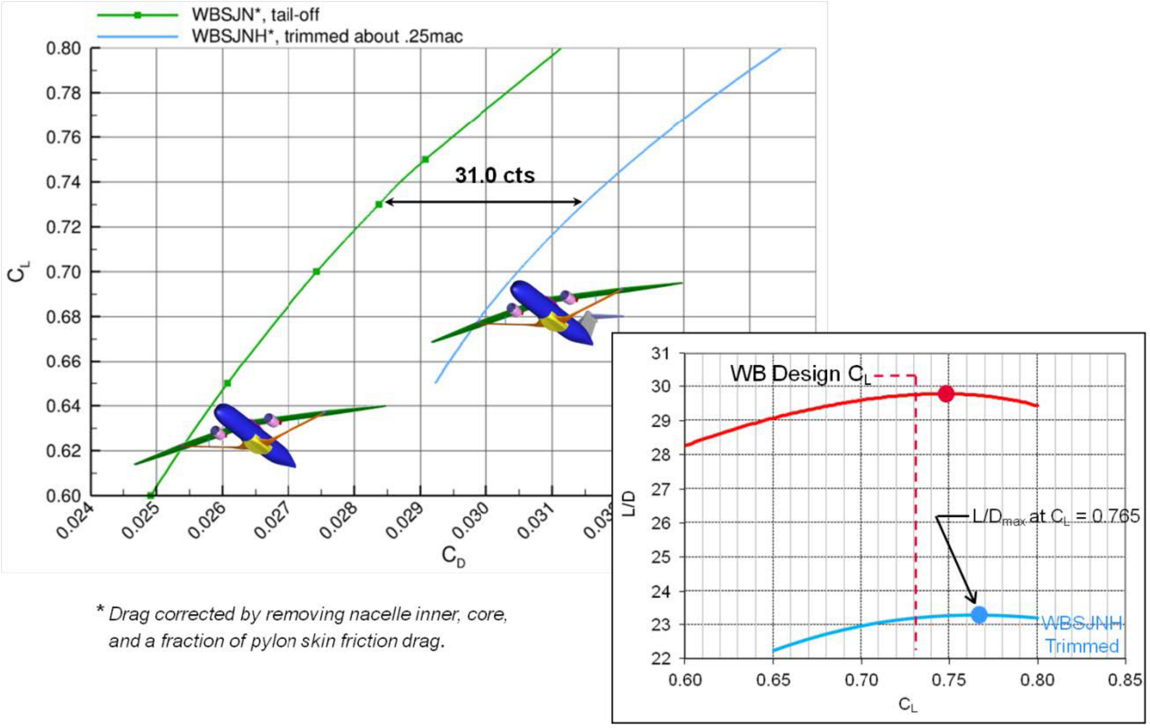

* *Drag corrected by removing nacelle inner, core, and a fraction of pylon skin friction drag.*

Figure 4.52 – Trimmed drag polar at flight conditions for the final Rev-J configuration: Altitude = 40,000 ft, Re_{mac} = 13.1 million, Mach = 0.745, and c.g. = 25%.

The same method for estimating Long Range Cruise (LRC) Mach number during the Preliminary Design Phase (see Section 4.2.1.1) was applied to the final configuration. This method assumes that the square root of the Mach number multiplied with L/D is a good surrogate for LRC, which is a reasonable assumption as it can be shown that the variation of specific fuel consumption with Mach can be approximated with a power of 0.5 for the high bypass engine technology under study. Figure 4.53 compares how this “range factor” varies with Mach number as the configuration is built-up from WB to WBSJN for C_L = 0.73. LRC Mach number, which is the value 1% down from the peak of the curve, is predicted to be nearly the same for all cases. This is another indication that the final geometry represents a well-designed airplane exhibiting minimal interference effects due to the nacelle and strut installations.

Drag rise curves for the same set of data shown in Figure 4.53 are compared in Figure 4.54 with LRC Mach numbers indicated by open circles. The set of curves in both figures have similar shapes for each level of the configuration build-up. The difference in compressibility drag numbers given in Figure 4.54 is an indication that there is some variation in the way each configuration climbs up the drag rise where the WBS carries 2.3 counts more compressibility drag compared to the corresponding WB case.

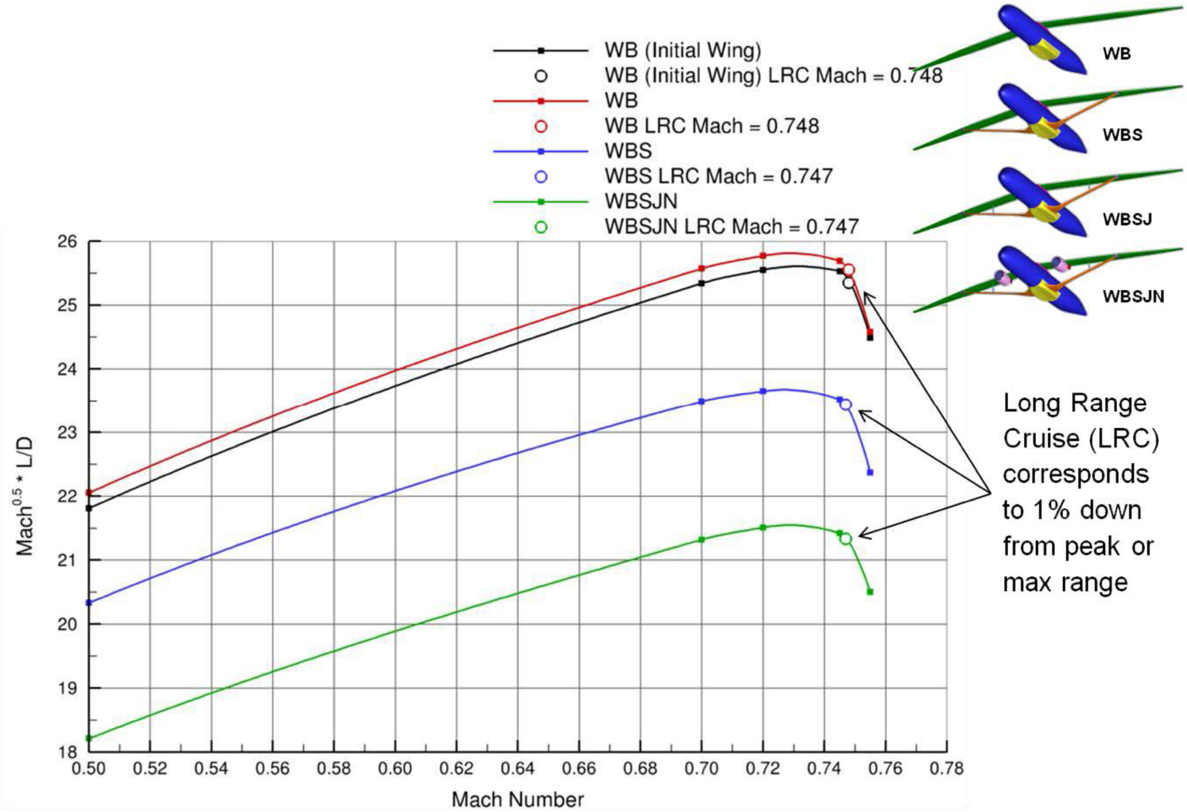

Figure 4.53 – Tail-off long range cruise (LRC) Mach number for the final Rev-J configuration: Altitude = 40,000 ft, Re_{mac} = 13.1 million, and C_L = 0.73.

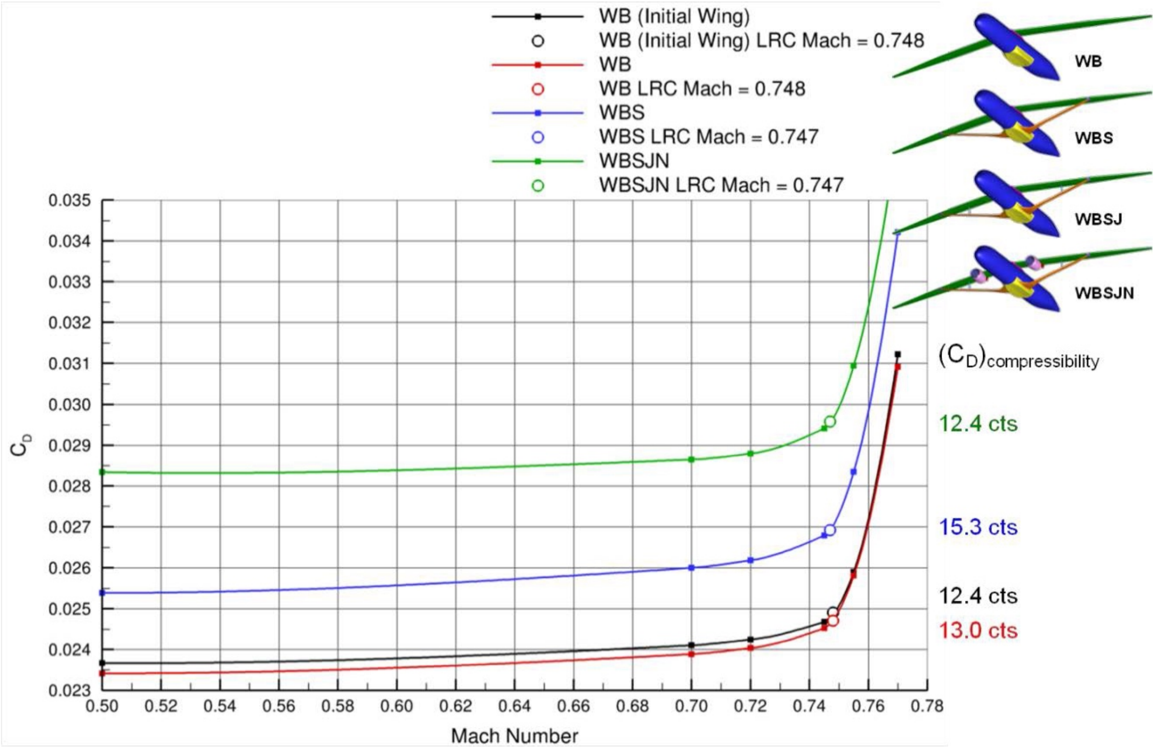

Figure 4.54 – Tail-off drag rise curves for the final Rev-J configuration: Altitude = 40,000 ft, Re_{mac} = 13.1 million, and C_L = 0.73.

Since the complete trimmed airplane configuration is predicted to have a maximum L/D at a C_L of 0.765 (Figure 4.52), LRC Mach number was recomputed and compared against the C_L = 0.73 results. This comparison is provided in Figure 4.55 for the tail-off configuration with strut, jury and nacelle installed. In this figure, both Maximum Range Cruise (MRC) and Long Range Cruise (LRC) are marked by open circles as well as tabulated for a C_L of 0.73 and 0.78. The 0.78 solution was the closest available to 0.765. The higher C_L dataset has a reduced LRC Mach number due to stronger compressibility effects related to a strengthened wing shock system. The tail-off LRC Mach is predicted to be 0.74 at C_L = 0.78.

WBSJN	MRC	LRC
C_L = 0.73	0.728	0.747
C_L = 0.78	0.724	0.740

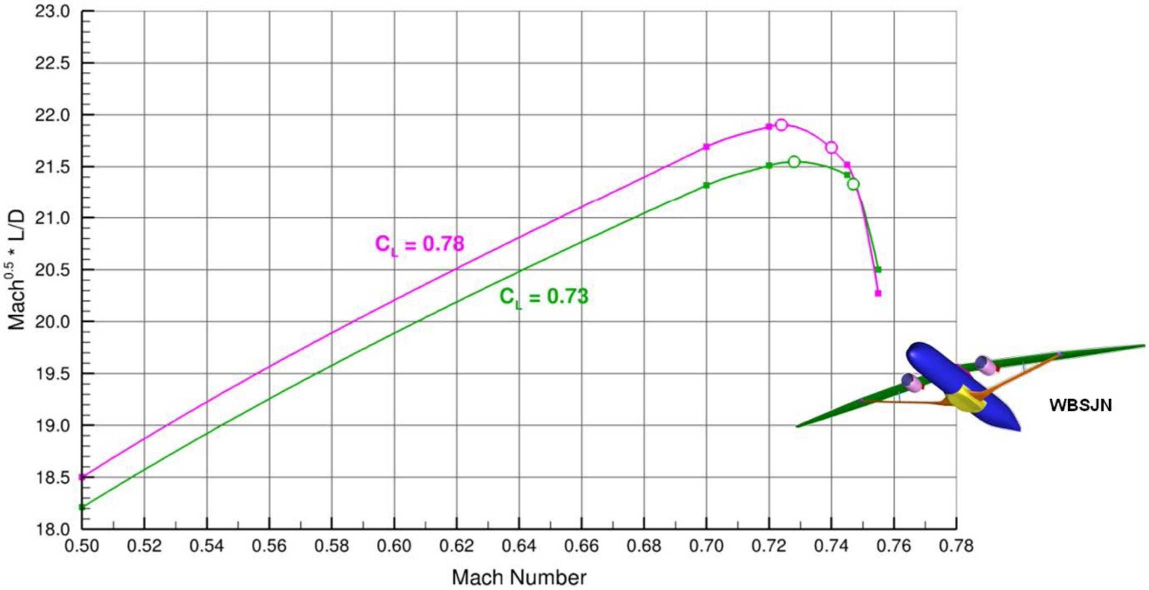

Figure 4.55 – Effect of C_L on the Long Range Cruise (LRC) Mach number for the final Rev-J configuration: Altitude = 40,000 ft and Re_{mac} = 13.1 million.

4.3.2 Reynolds Number Effects

Another OVERFLOW analysis for the final TTBW configuration build-up was done at the expected wind tunnel conditions for the NASA Ames Research Center 11 ft by 11 ft transonic facility. A reference chord Reynolds number of 3.31 million (based on 8.0 million/ft) was selected, and the Rev-J geometry was analyzed with a fully turbulent boundary layer. In reality, the boundary layer on the wind tunnel model will have a laminar run before transitioning to fully turbulent but that effect was ignored for this series of check-out runs. Wind tunnel model wing/strut aeroelastics and installation effects were also ignored. While the results of a fully turbulent, theoretical 1g free-air analysis cannot be compared to wind tunnel data, some insight was gained on the general performance characteristics relative to the flight Reynolds number results.

An “idealized” drag polar comparison is presented in Figure 4.56 for three configurations at flight and wind tunnel Reynolds number. Drag is made “ideal” by removing induced drag assuming an ideal Oswald efficiency number of 1.0. The resulting polar shape is near vertical over the C_L range of interest which allows for tighter drag scales to be used in the plot and clearer comparisons fall-out. The drag comparison in Figure 4.56 shows a nearly identical polar shape going from high to low Reynolds number with an expected drag increase due primarily to effects of a thickening boundary layer.

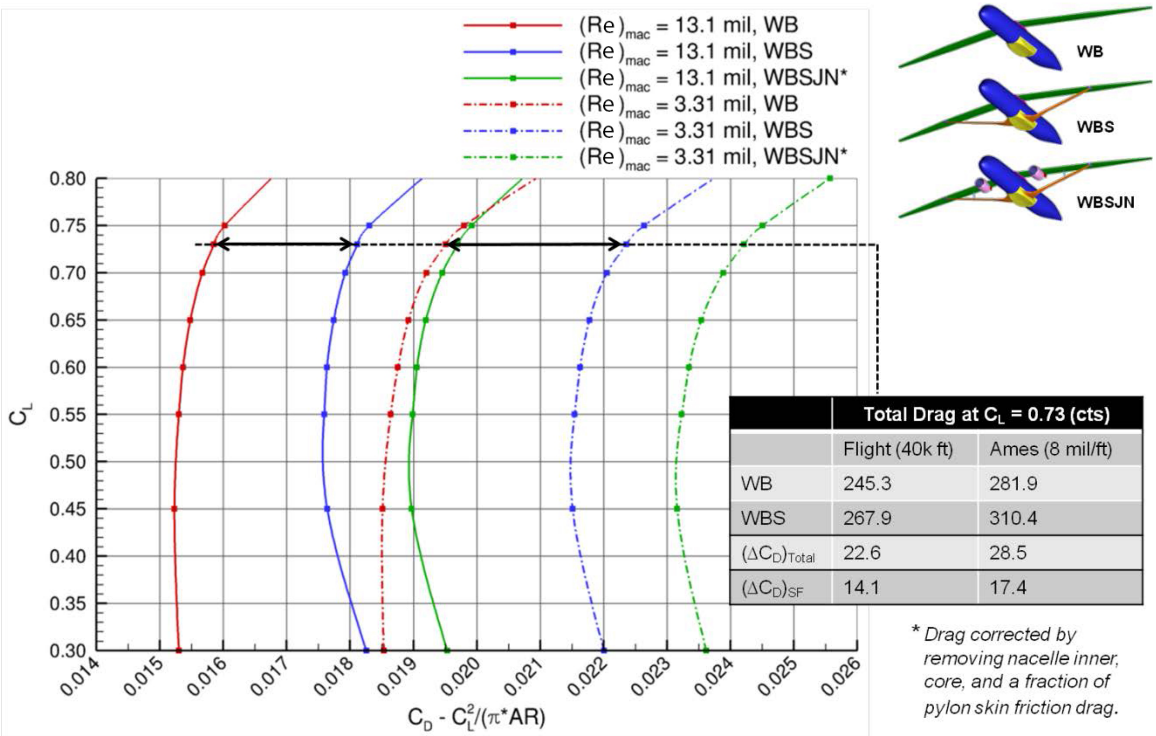

	Total Drag at C_L = 0.73 (cts)	
	Flight (40k ft)	Ames (8 mil/ft)
WB	245.3	281.9
WBS	267.9	310.4
$(\Delta C_D)_{Total}$	22.6	28.5
$(\Delta C_D)_{SF}$	14.1	17.4

** Drag corrected by removing nacelle inner, core, and a fraction of pylon skin friction drag.*

Figure 4.56 – Effect of Reynolds number at Mach = 0.745 on the tail-off idealized drag polars for the final Rev-J configuration.

Drag rise curves and compressibility drag are compared in Figure 4.57 at the design C_L. As with the drag polars, reducing Reynolds number does not significantly alter the shape of the curves suggesting the final design will not experience adverse flow field characteristics at wind tunnel conditions over the lift and Mach range of interest. The increase in compressibility drag for the wind tunnel simulations is consistent across the three configurations analyzed and is of reasonable magnitude. Since the final wing design was completed in the presence of the nacelle and pylon, when these components are removed the drag rise shows an increase in compressibility drag (relative to the installed nacelle-pylon case) arising from the nonoptimal pressure distributions. The jury strut has a negligible contribution to the vehicle drag, whether the nacelle and pylon are installed or not.

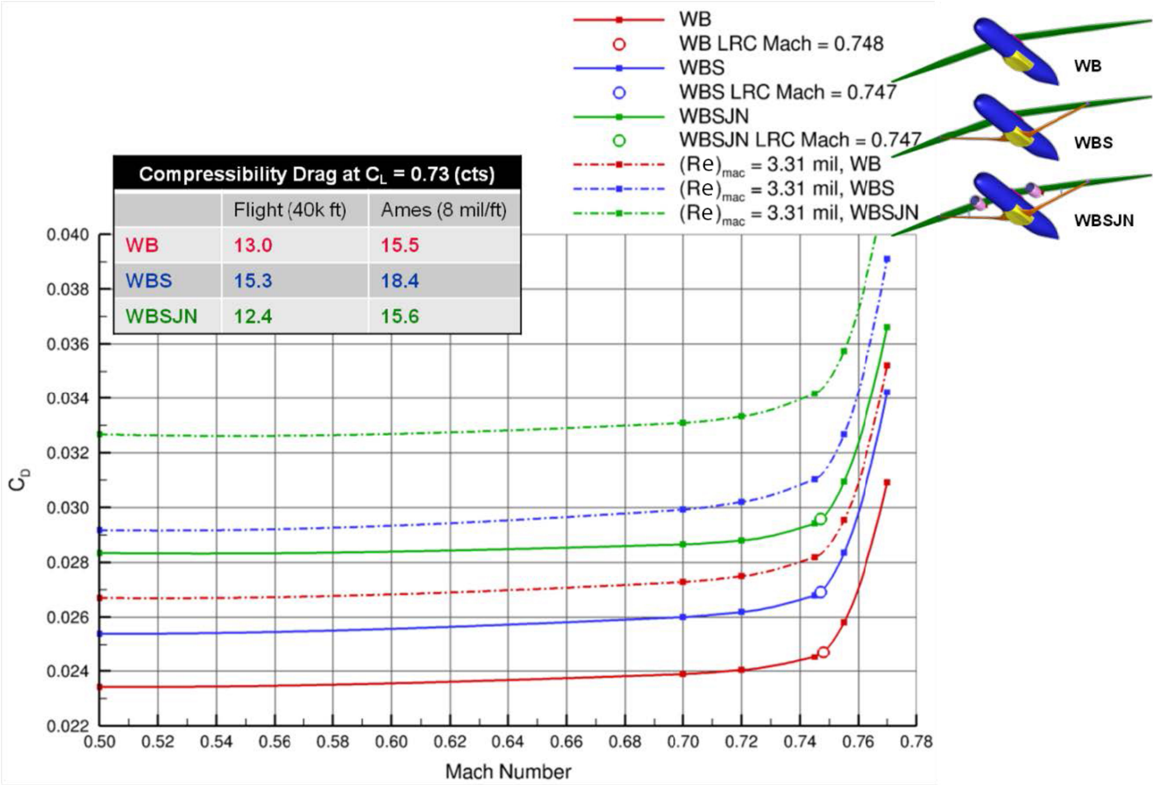

Compressibility Drag at C_L = 0.73 (cts)

	Flight (40k ft)	Ames (8 mil/ft)
WB	13.0	15.5
WBS	15.3	18.4
WBSJN	12.4	15.6

Figure 4.57 – Effect of Reynolds number at C_L = 0.73 on the tail-off drag rise curves for the final Rev-J configuration.

A qualitative surface pressure and streamline comparison is made in Figure 4.58 (flight Reynolds number) and Figure 4.59 (wind tunnel Reynolds number) for the all-up configuration at the design condition. The viewing angle for these flow visualization images shows the inboard side of the pylon and jury strut as well as most of the strut's upper surface. At flight Reynolds number, the boundary layer is fully attached all the way to the trailing edge for all surfaces with the exception of a small region on the strut directly behind the jury strut. This separation region does grow in size as Reynolds number is lowered from 13.1 million to 3.3 million, but the extent is considered small and will have a minimal impact on the jury strut drag increment. Also note that the strut streamlines in Figure 4.59 indicate some amount of trailing-edge separation inboard of the jury strut. This behavior is also present in the wing's upper surface boundary layer (not shown in the flow visualization images).

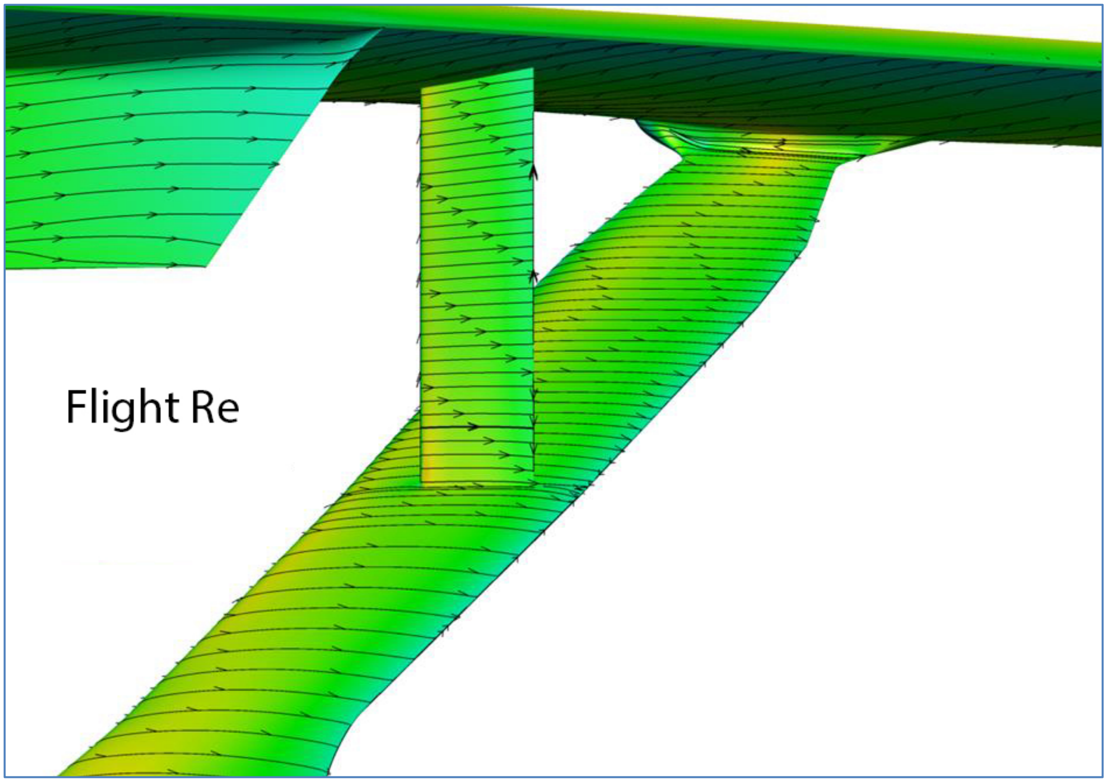

Figure 4.58 – Surface pressure and streamlines on the Rev-J WBSJNVH pylon, strut and jury at flight Reynolds number: Re_{mac} = 13.1 million, Mach = 0.745, C_L = 0.73, and α = 1.872°.

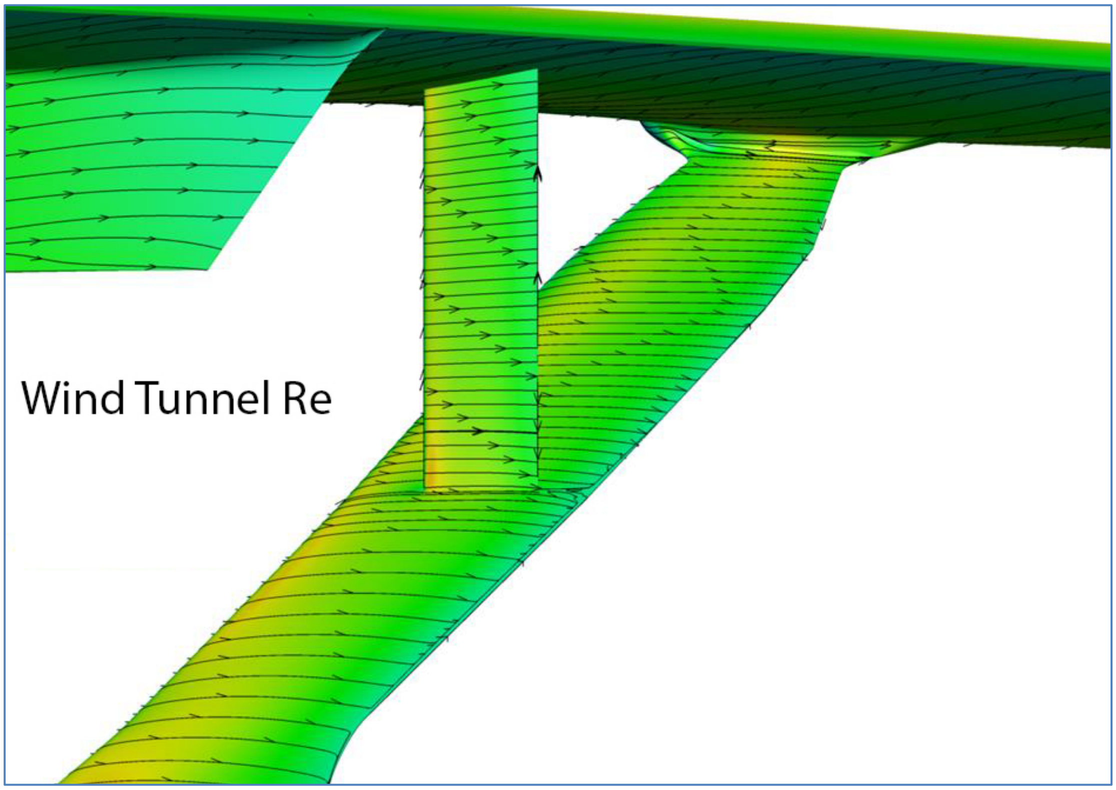

Figure 4.59 – Surface pressure and streamlines on the Rev-J WBSJNVH pylon, strut and jury at wind tunnel Reynolds number: Re_{mac} = 3.3 million, Mach = 0.745, C_L = 0.73, and α = 2.193°.

4.3.3 Alternate Strut

In this section of the High-Speed Aerodynamics report, the design intent behind the alternate strut configuration is summarized. This discussion is followed by on overview of OVERFLOW results at flight and wind tunnel Reynolds number as well as a buffet onset assessment for the strut's upper surface.

4.3.3.1 Design Intent

High-speed buffet onset is a critical feature of a transonic transport aircraft that has the potential of limiting an aircraft's performance envelope via parameters such as maximum cruising altitude. It is typically created by shock-induced separation at off-design conditions. This separation or buffeting acts as a forcing function that could result in unacceptable vibration levels in the airframe's structure. There are well established FAR/JAR regulatory requirements that must be met for aircraft certification that include the following.

- airplane must be demonstrated in flight to be free from any vibration and buffeting that may interfere with control, cause excessive fatigue to crew, or structural damage
- must provide a sufficient range of speeds and load factors for normal operations
- no perceptible buffeting condition in the cruise configuration in straight flight at any speed up to V_{MO}/M_{MO}

For a TTBW configuration, all forcing functions that have the potential to drive high-speed buffet must be identified and understood. The high-C_L buffet onset for the wing upper surface (see Section 4.2.3.1) is one obvious source, and the BUFFET program, discussed in Section 4.1.2, is well suited to estimate initial buffet for this condition. However, there are other potential buffet-critical regions for a TTBW that require further study. One such region is the wing-strut juncture as highlighted in Figure 4.60. The drag polar and off-body Mach contour images in this figure show how CFD predicts a growing region of supersonic flow in the juncture with reduced angle of attack. This drives higher interference (i.e., wave) drag at the low end of the polar due to a strengthening shock system and creates the possibility of having a low-C_L buffet boundary.

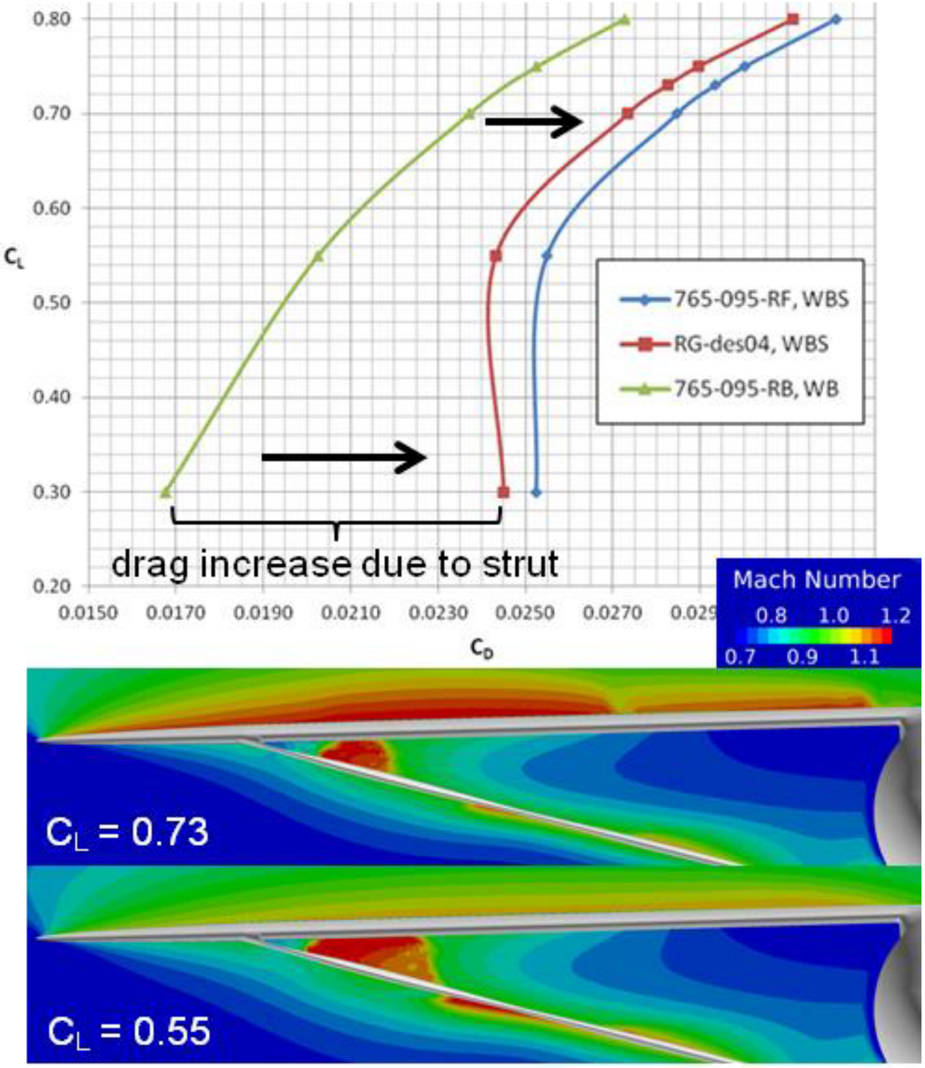

Figure 4.60 – Effect of lift coefficient on wing-strut juncture flow at the cruise Mach number: Re_{mac} = 12.3 million and Mach = 0.745.

Since additional aerodynamic and structural analysis/testing for buffet onset prediction was outside the scope of the SUGAR Phase III design effort, an alternate strut concept was conceived instead. The primary goal of the alternate strut design was to improve the aerodynamic characteristics of the wing-strut flow field at off-design conditions by simply moving the strut further away from the wing.

As shown in the previous sections that summarize results for the final Rev-J configuration, the Mach 0.745 drag increment due to adding the baseline strut is relatively constant across a wide range of C_L compared to the increment shown in Figure 4.60. This characteristic is by-design as the baseline wing-strut system is meant to operate with minimal interference effects over a C_L range covering ±1.3g's. Based on the design C_L of 0.73, the negative g limit is C_L = 0.51 and the positive g limit is C_L = 0.95. Therefore, an assumed maximum operating Mach number of 0.795

was used to design the alternate strut because the baseline strut is predicted to be critical at this higher speed using the BUFFET method. The details of this analysis will be covered at the end of Section 4.3.3.2.

It is worth noting once again that the buffet methods used here were constructed for cantilever configurations, and their applicability to this configuration requires further investigation. The buffet issues discussed here could be either more or less severe than they presently appear. It is also worth noting that while additional technologies such as flow control, smart materials or simple hinged flaps may mitigate these higher Mach concerns, they were not investigated as part of this study.

4.3.3.2 Results

The drag polars shown in the previous section summarizing final Rev-J CFD data is presented again with the addition of wing-body-alternate-strut (WBA) results. The genesis of the final WBA configuration is covered in Sections 4.2.3.2 and 4.2.4.3. A front view comparing the baseline and alternate struts is provided in Figure 4.61 for reference.

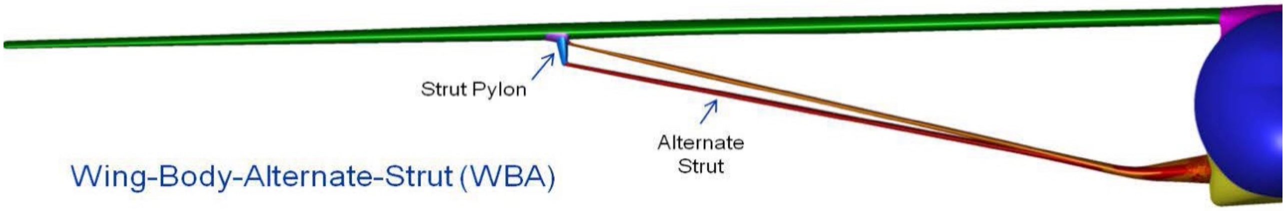

Figure 4.61 – Front view of the baseline and alternate strut configurations.

The WBA and WBAJNH configurations were analyzed using OVERFLOW at the design Mach of 0.745 and flight Reynolds number. The drag polars are compared in Figure 4.62 where the alternate strut data are plotted using dashed lines. Relative to the baseline strut, the computed drag is the same at the lowest C_Ls and increases to roughly 2 counts greater at the highest C_Ls analyzed. While not ideal, it was considered acceptable that the alternate strut configuration had a higher cruise drag level since the purpose of its design was to minimize interference effects at a maximum operating Mach number of 0.795. Cruise performance was considered a fall-out of the design.

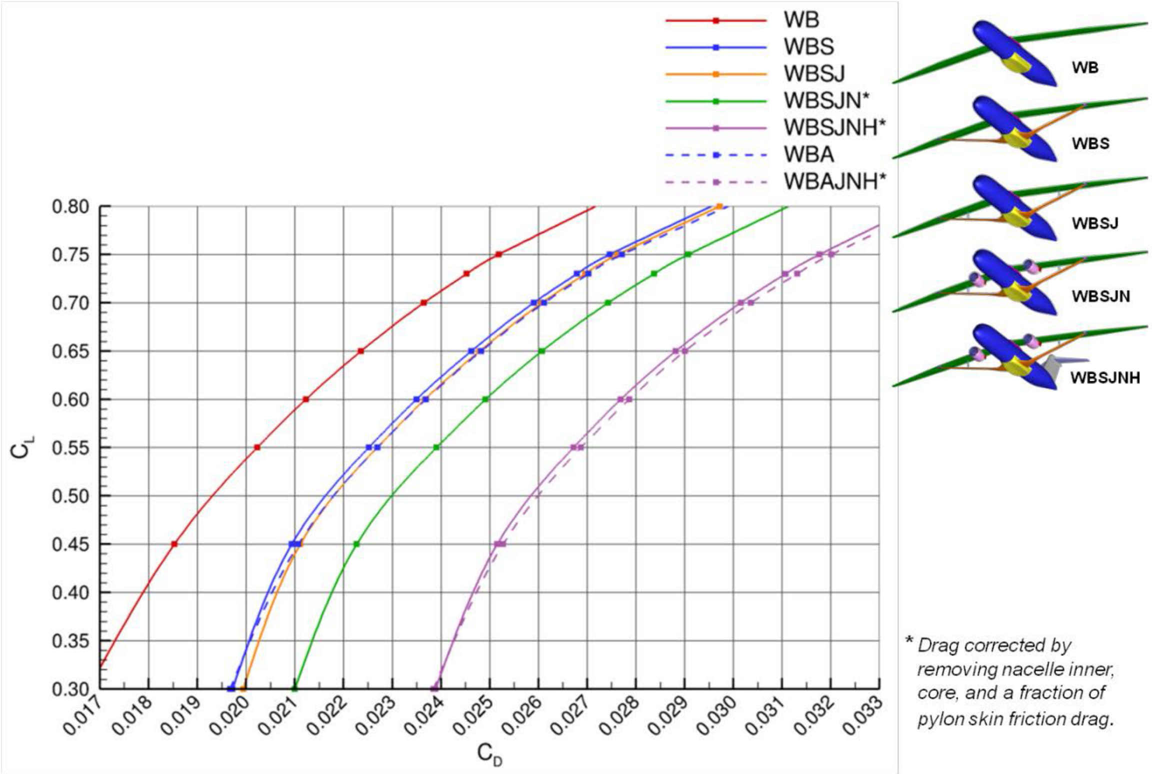

* *Drag corrected by removing nacelle inner, core, and a fraction of pylon skin friction drag.*

Figure 4.62 – Drag polar comparison between alternate strut and strut 765-095-RJ (Rev-J) final configurations at flight conditions: Altitude = 40,000 ft, Re_{mac} = 13.1 million, and Mach = 0.745.

A drag rise was also computed for the WBA configuration at the design C_L of 0.73 and flight Reynolds number. The results, shown in Figure 4.63, indicate the drag rise curve has nearly the same shape with essentially a constant increase in drag from Mach 0.5 to 0.77. This suggests both struts have similar levels of compressibility drag.

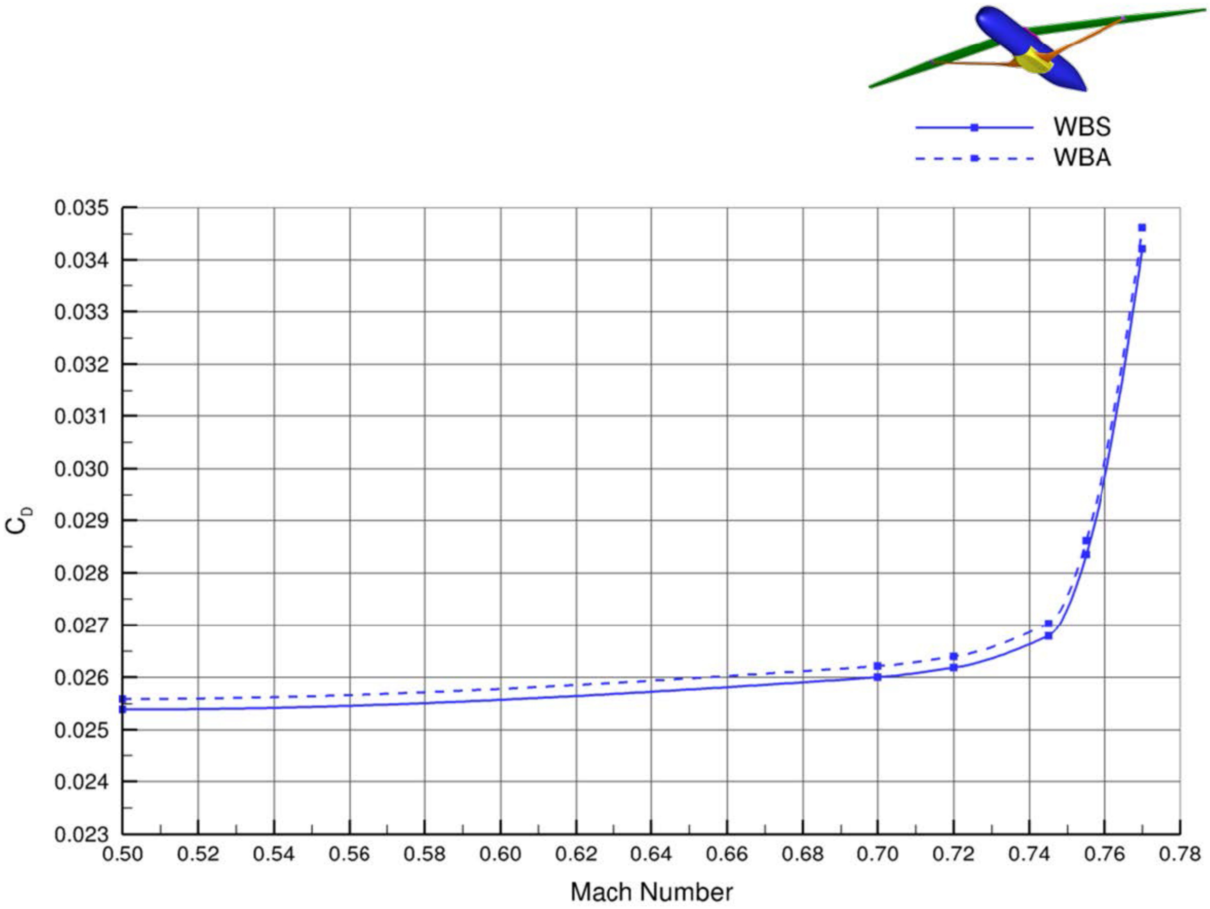

Figure 4.63 – Drag rise comparison of baseline vs. alternate strut at flight conditions: Altitude = 40,000 ft, Re_{mac} = 13.1 million, and C_L = 0.73.

Reynolds number effects are qualitatively assessed using the surface pressure and streamlines comparison of Figure 4.64 where WBA results at flight conditions are shown across the top and wind tunnel results across the bottom. The most noticeable difference is seen in the streamlines on the outboard side of the pylon fairing (right side of figure) just forward of the wing trailing-edge. The lower Reynolds number solution exhibits a larger area of separated flow on the wing's lower surface.

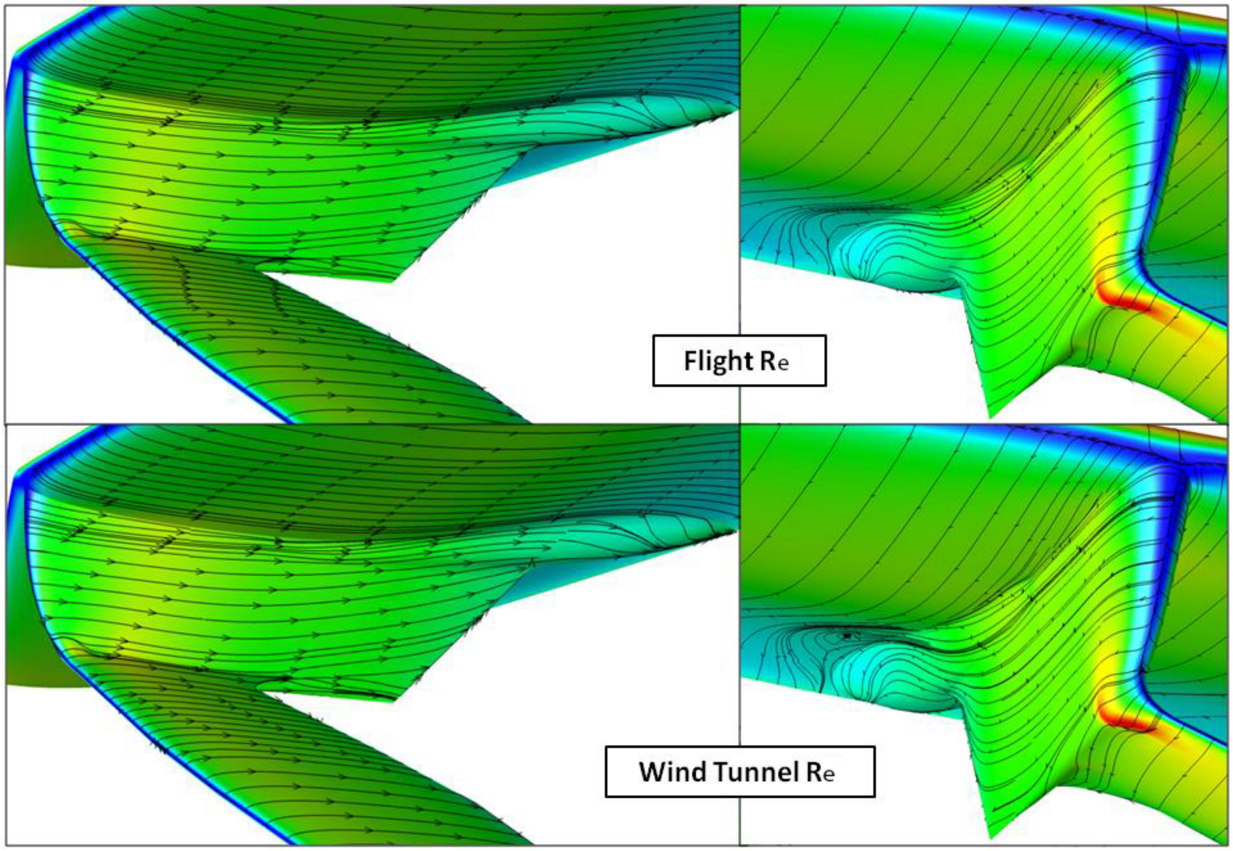

Figure 4.64 – Surface pressure and streamlines of WBA at Mach 0.745 and C_L = 0.73 for flight and wind tunnel Reynolds number.

The alternate strut was analyzed using the WBA configuration shown in Figure 4.61 at an assumed maximum operating Mach number (M_{MO}) of 0.795. The selection of lift coefficient was based on a scenario where the pilot advances the throttles while holding altitude and weight. This drops C_L from 0.73 to 0.64 for an altitude of 40,000 ft. A comparison of off-body Mach contours in a plane aligned with the strut shock is shown in Figure 4.65. These images illustrate that the airflow moving between the wing and strut is decelerated with the larger strut offset distance given the reduced area of red in this region. Total configuration drag is also reduced by about 10 counts while pitching moment is essentially unchanged which are additional indicators of a weakened wing-strut juncture shock system.

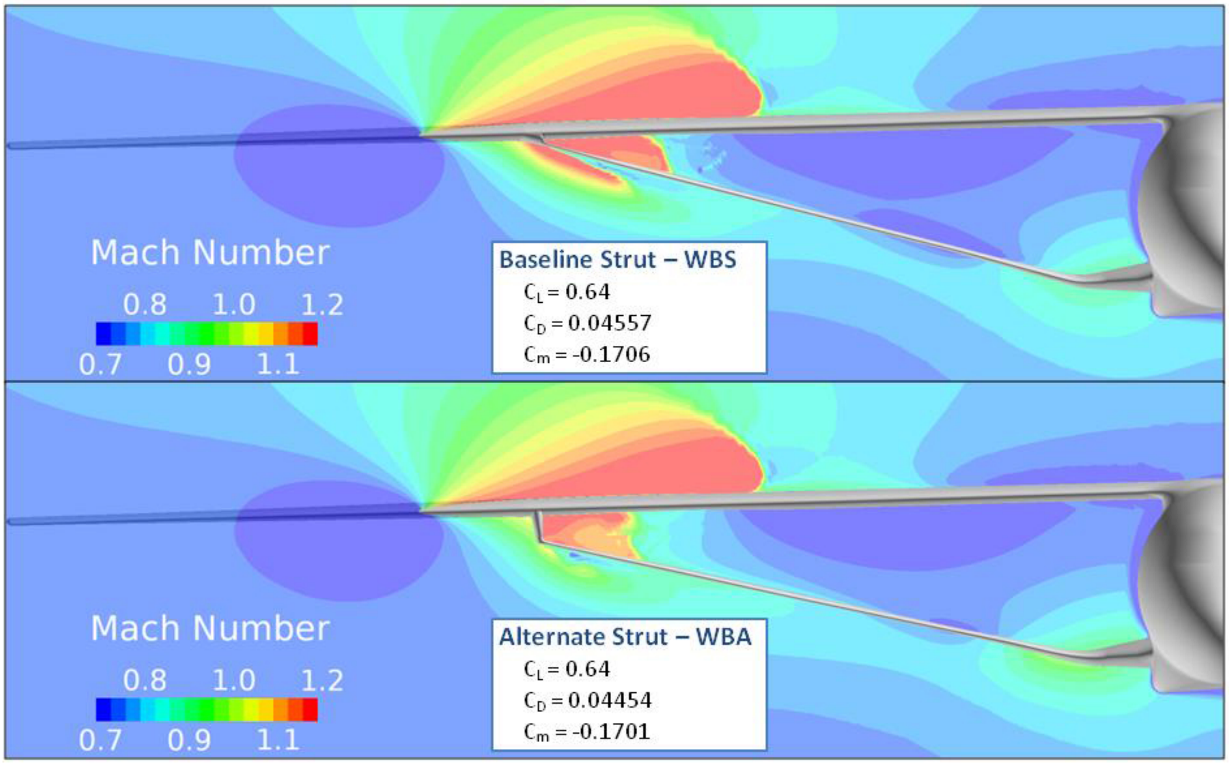

Figure 4.65 – Off-body Mach contour comparison of WBS and WBA configurations at Mach 0.795 and C_L = 0.64.

The BUFFET program was used to guide the design of the alternate strut by quantifying shock strength on the strut's upper surface and comparing it against an estimated critical level. Figure 4.66 contains plots of Mach number as a function of strut span station normalized by the wing's semispan. At the M_{MO} condition, the baseline strut is predicted to be buffet critical over the most outboard portion closest to the wing while the alternate strut has some margin over the entire span. Recall from the discussion in Section 4.3.3.1 that regulations for "buffet free" flight are based on the perception of buffet created by a structural response to separation somewhere on the airplane. It is unclear if the BUFFET results for the baseline strut summarized in Figure 4.66 are a true indicator of (local) buffet on the strut. It is also unknown if such local buffeting would even be felt by the pilot and deemed unacceptable. Further study and dedicated testing is needed to answer these questions.

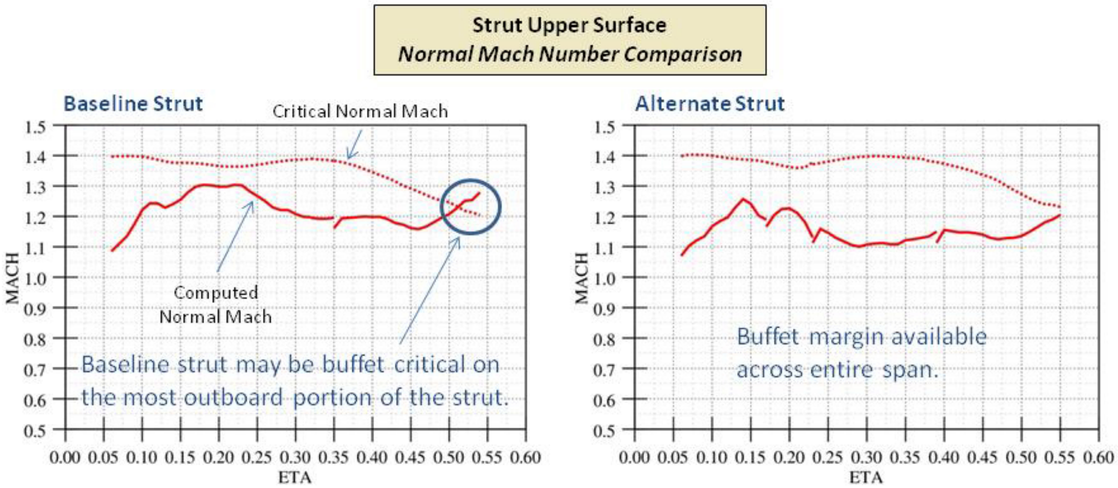

Figure 4.66 – Buffet onset evaluation for the baseline and alternate strut upper surface at flight conditions: Altitude = 40,000 ft, Mach 0.795, and C_L = 0.64.

The final all-up TTBW configuration designed by the High-Speed Aerodynamics Team at Boeing is shown in Figure 4.67 with OVERFLOW-computed Mach = 1 surfaces and total pressure contours as well as the strut wake defined by streamline traces. This CFD solution is for the design Mach number of 0.745 and a C_L of 0.75, which is close to the final cruise design C_L. This image highlights a successful design by illustrating a well behaved flow field dominated by attached flow, which shocks in regions of the configuration where they are intended.

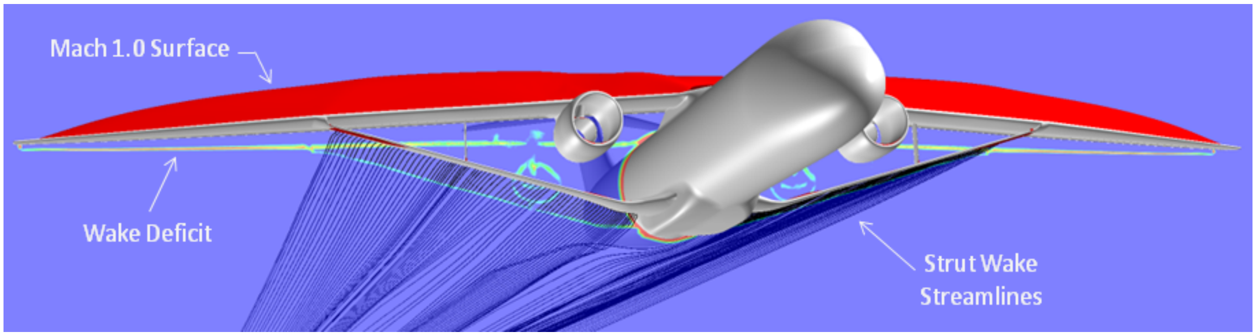

Figure 4.67 – Final all-up TTBW configuration with off-body flow field parameters indicating a successful design.

5.0 Stability & Control Design and Analysis

This section describes work performed to define control surfaces and evaluate the TTBW configuration against the Stability and Control (S&C) design requirements.

5.1 Longitudinal S&C

Longitudinal S&C analysis in the configuration design phase is mainly focused on defining a center of gravity (CG) envelope that can be compared to the airplane load-ability requirements defined by the Weights group. If the CG envelopes from S&C and Weights do not match, then options for correcting the discrepancy include shifting the location of the wing on the fuselage, moving the longitudinal position of the main landing gear, changing the size of the horizontal tail, and/or changing the design of the elevators. The S&C CG envelope is defined by various requirements that provide the stability and control authority necessary to successfully certify the airplane with the FAA. None of these requirements are explicitly defined in 14 CFR Part 25, but years of application by Boeing have shown these requirements to enable meeting the explicit requirements in Part 25. A summary of each design requirement is presented below. Also defined is the nomenclature used on the following CG limit plot.

The forward CG limit is determined by the most critical (most aft) of the following individual requirements. At takeoff rotation speed, with the most critical weight, thrust, and high lift settings, the airplane must rotate from the ground attitude to the takeoff attitude with a pitch acceleration that has been shown to provide the pilot with adequate pitch authority to accomplish the rotation. This requirement is labeled “NWLO 2” (nose wheel lift off 2) on the presented CG limit plot. While trimmed on a -3 degree flight path on landing approach, with the most critical weight and high lift settings, the airplane must rotate from the approach attitude to the go-around climb attitude with a pitch acceleration that has been shown to provide the pilot with adequate pitch authority and minimal loss of altitude (not presented on the plot as it is off the axis scale). After main gear touchdown on landing, with the most critical weight and high lift settings, the pilot must be able to hold the nose wheel off the ground down to the stall speed of the airplane. This requirement is labeled “NWLO” on the presented CG limit plot.

The aft CG limit is determined by the most critical (most forward) of the following individual requirements. 14 CFR 25.145(a) specifies that the pilot must be able to make a “prompt” nose down recovery at any point during a stall maneuver. Boeing has translated this requirement into a specific nose down pitch acceleration that must be achievable at the stall point with the most critical weight and high lift settings. This requirement is labeled “Stall Rec 1” on the presented CG limit plot. When the airplane sits statically on the ground, Boeing requires a certain percentage of the airplane weight be on the nose landing gear for adequate steering capability. This requirement is labeled “NW Steering” on the presented CG limit plot. Studies conducted by Boeing have shown that a minimum static margin is required so that the pilot can adequately control the airplane for safe flight and landing after failure of pitch stability augmentation systems. This requirement is labeled "Static Margin" on the presented CG limit plot.

In order to evaluate these requirements, an aerodynamic database must be created for the airplane. Aerodynamic data from the MD-90 airplane was used as a basis for estimate and adjusted using results from the Athena Vortex Lattice (AVL) code (6). AVL was run for both the MD-90 and the 765-095-RF airplanes. The AVL increments and ratios were used to adjust the MD-90 nonlinear aero data to produce the aero database for the 765-095-RF. This was then loaded into a Boeing CG limit evaluation tool along with pertinent airplane geometry, thrust data, and mass properties estimates. The tool was then run to produce forward and aft CG limits for different horizontal tail areas. This results in the "scissor" plot shown in Figure 5.1. The labels for the limit lines are defined in the paragraphs above.

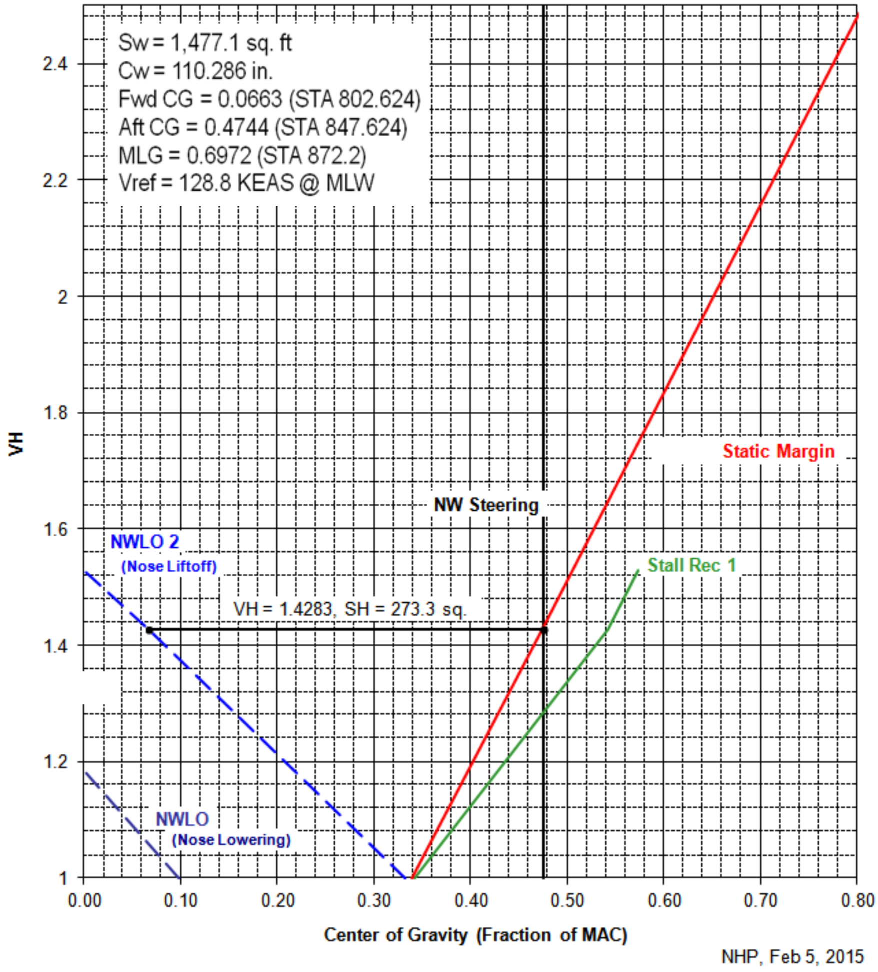

Figure 5.1 – Horizontal Tail Sizing "Scissor" Plot.

The Weights group identified that a 45 inch CG range (about 41% MAC) was desirable for load-ability of the airplane. The resulting load-ability bar is placed in the "V" of the scissor plot to determine the horizontal tail area. The main landing gear position was shifted aft from Station

847.7” to 872.2” so that the nose wheel steering requirement was simultaneously critical with the static margin requirement. This produces the minimum tail area that satisfies all of the S&C requirements. The final sized horizontal tail volume coefficient (V_H) is 1.4283 and the final horizontal tail area (S_H) is 273.3 ft^2, which is approximately the horizontal tail area of a DC-9. This produces a forward CG limit of 6.63% MAC and an aft limit of 47.44% MAC with the required 45 inch loading range.

Figure 5.2 shows how the S&C CG limits compare to various missions on the loading diagram produced by Weights. The baseline mission, Maximum Zero Fuel Weight (MZFW) mission, and the ferry mission all fit easily within the CG limits. The forward biased loading also fits within the CG limits as long as fuel is loaded and burned along the rear of the fuel loading bubble. The aft biased loading case does not fit within the CG limits, but this is not a major problem. Airlines are accustomed to moving passengers and baggage to load the airplane within its limits and will make adjustments to the loading when necessary. It is much more common to have a forward loading than an aft loading because people tend to sit in the front of the airplane. Because the S&C CG limits and Weights loading diagram match up well, a wing shift on the fuselage is not necessary.

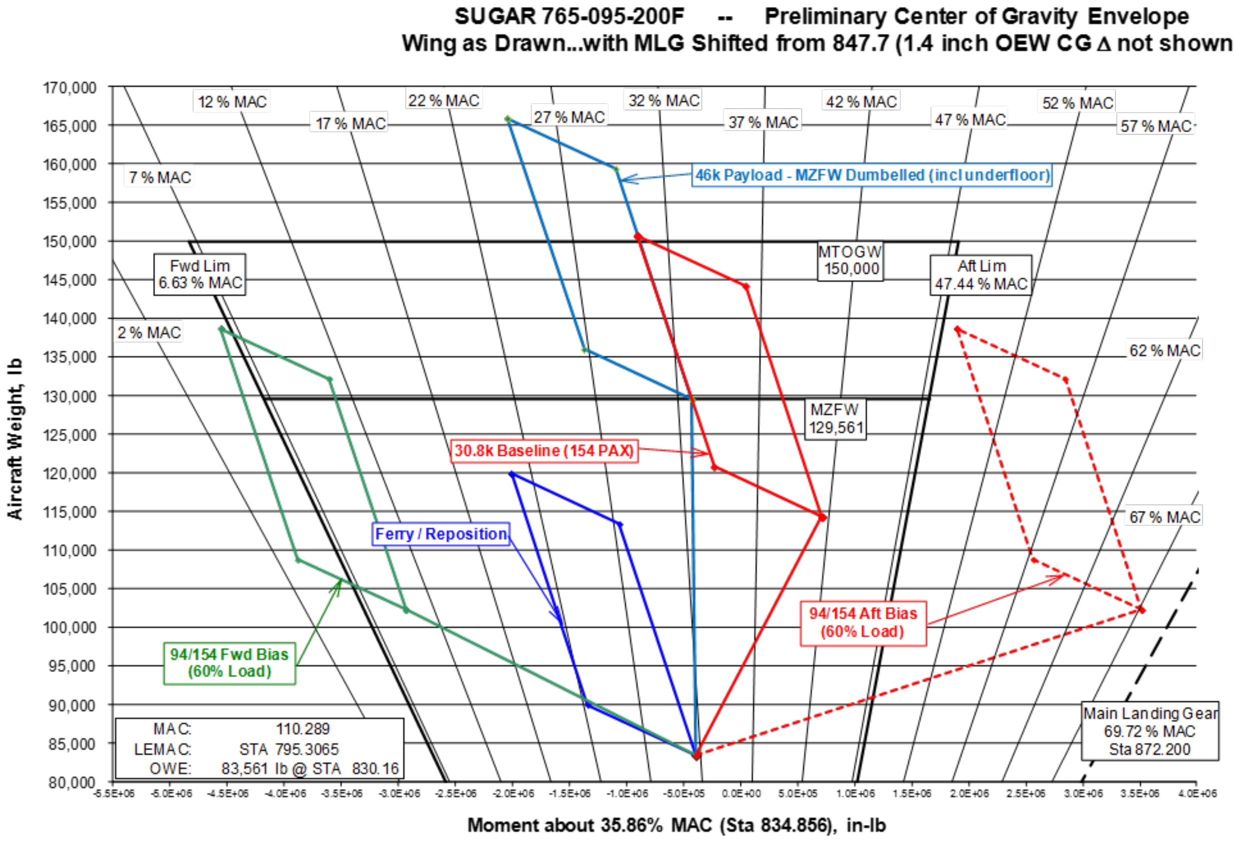

Figure 5.2 – S&C CG Limits on Airplane Loading Diagram.

5.2 Directional S&C

Directional control analysis was performed for the 765-095-RF airplane, including engine out minimum control speed on the ground (V_{MCG}), engine out minimum control speed in air (V_{MC}), and crosswind landing trim. Engine data used were from the GE gFan+ ducted fan engine provided on January 9, 2012. Aerodynamic data from the MD-90 airplane were used as a basis for estimate and adjusted using results from the AVL code. AVL was run for both the MD-90 and the 765-095-RF airplanes. The AVL increments and ratios were used to adjust the MD-90 nonlinear aero data to produce the aero database for the 765-095-RF. Conditions analyzed were for the 20 deg takeoff flap setting. Figure 5.3 shows the engine out controllability plot for determination of both V_{MC} and V_{MCG} for a vertical tail area of 1.7 times the baseline DC-9 vertical tail area. Engine out moment is plotted versus airspeed, along with rudder moment about the CG for V_{MC} and rudder moment about the main landing gear (MLG) for V_{MCG}. Nose wheel steering is not allowed for calculation of V_{MCG}. The points where the rudder moment curves cross the engine out moment curve define the engine out control speeds. The final engine out control speed values are also provided in the text box on the plot.

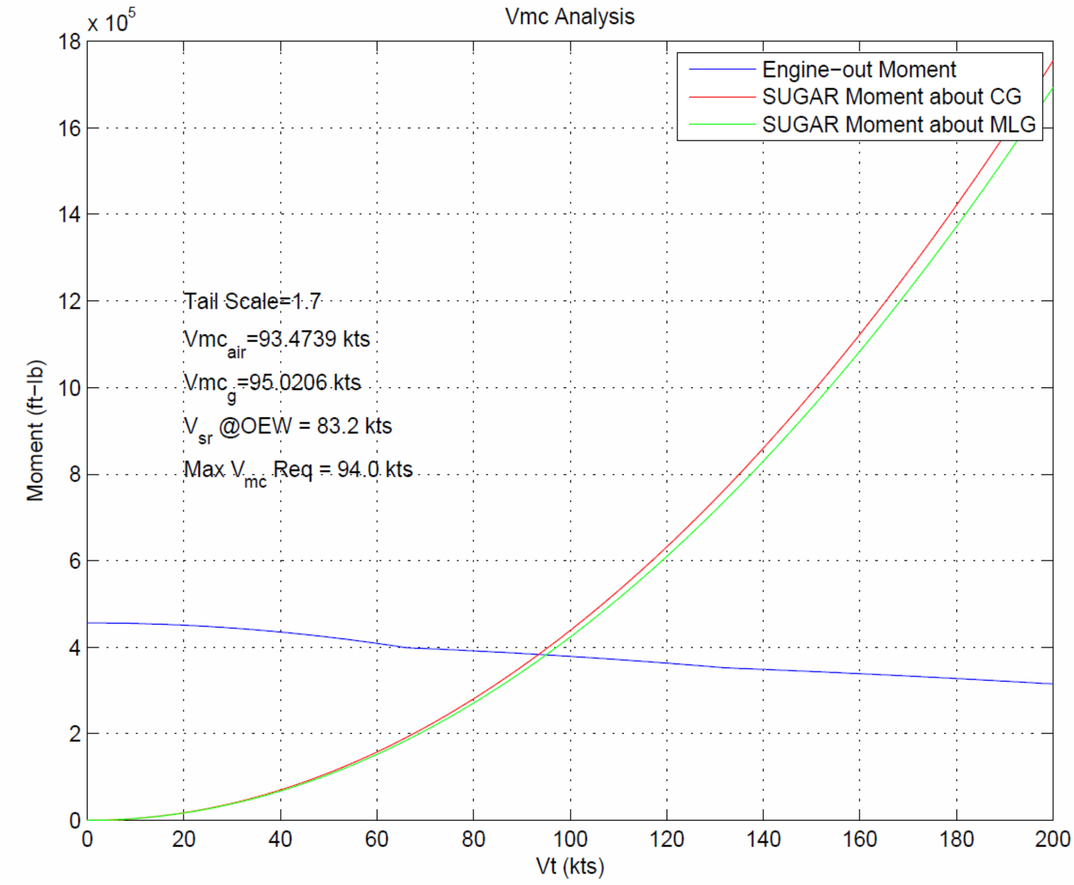

Figure 5.3 – Engine-Out Controllability Plot.

The final engine out control speeds must be checked against FAA requirements. Table 5.1 summarizes the engine out control speeds compared to 14 CFR Part 25 airspeed requirements. The CFR parts that define the various engine out control speeds are in white. Other CFR parts that use the engine out control speeds as constraints in defining performance speeds are shown in colored cells. In the speed column, the relationships of the engine out control speeds to the performance speeds are defined. It should be noted that V_{MCL} was assumed to be the same as V_{MC} because it is expected that the landing flap setting may be the same as takeoff flap setting. The color coding of green indicates that all performance speeds are consistent with the engine out control speeds for a vertical tail area of 1.7 times the baseline DC-9 vertical tail. The most critical requirement is CFR Part 25.149(c), which is satisfied for the vertical tail area chosen.

Table 5.1 – Engine-Out Minimum Control Speed Results.

14 CFR Part	Requirement	Speed (KEAS)
25.149(b)	Defines Minimum Control Speed (V_{MC})	$V_{MC} = 93.5$
25.149(c)	V_{MC} may not exceed 1.13 V_{SR} (Reference Stall Speed)	$V_{MC} < 1.13*83.2 = 94.0$
25.149(e)	Defines Minimum Control Speed on the Ground (V_{MCG})	$V_{MCG} = 95.0$
25.149(f)	Defines Minimum Control Speed Landing (V_{MCL})	$V_{MCL} = 93.5$
25.107(a)(1)	Engine Failure Speed (V_{EF}) may not be less than V_{MCG}	$V_{MCG} < 105.7$
25.107(b)(3)	Engine Out Climb Speed (V_2) may not be less than 1.10 times V_{MC}	$V_{MC} < 111.1/1.10 = 101.0$
25.107(e)(1)(ii)	Rotation Speed (V_R) may not be less than 105 percent of V_{MC}	$V_{MC} < 108.2/1.05 = 103.0$
25.125(b)(2)(i)(B)	V_{REF} (Reference Landing Speed) may not be less than V_{MCL}	$V_{MCL} < 102.3$

Landing trim with a 35 knot crosswind at the slowest approach speeds was also evaluated. This condition was not found to be critical in sizing the vertical tail, so the final vertical tail area is set by the engine out control requirements. A vertical tail area of 1.7 times the baseline DC-9 vertical tail area meets all directional control requirements, resulting in a final vertical tail area of 273.7 ft^2.

5.3 Lateral S&C

TTBW lateral control analysis focused on maximum steady state roll rate and time-to-bank 30 degrees. The goal of the analysis during the design phase is to minimize the span extent of the wing trailing edge that is dedicated to roll surfaces, instead of flaps. Ideally, only spoilers would be used for roll control as they do not take trailing-edge space away from the flaps, but unfortunately, the drag and nonlinearity of spoilers prevents their use in meeting all roll requirements (e.g., roll trim).

A baseline roll control surface layout was created during Phase II and analyzed at that time (2). In the current Phase, the topic of roll control was revisited to determine if Inboard Aileron, Outboard Aileron, or Spoiler areas needed to change to meet roll requirements. The large aspect ratio of the TTBW results in more than adequate high lift performance, even though considerable trailing-edge space is devoted to ailerons. As a result, it was decided not to modify the roll control surface layout from the one chosen and analyzed in Phase II.

A summary plot of the roll control performance results from Phase II is provided in Figure 5.4. It can be seen that the inboard aileron and spoilers combine to provide performance in excess of the roll rate and time-to-bank requirements over the majority of the dynamic pressure range investigated. Only at low dynamic pressures is the outboard aileron necessary to augment the inboard aileron and spoilers in meeting the time-to-bank requirement. This will also be necessary in the high lift configurations for takeoff and landing, which will result in even lower dynamic pressures. The figure indicates the need for the outboard aileron at low dynamic pressures and illustrates the increase in authority at Mach 0.7. In summary, the lateral control layout defined in Phase II is adequate for meeting the lateral control requirements and should not be reduced in size.

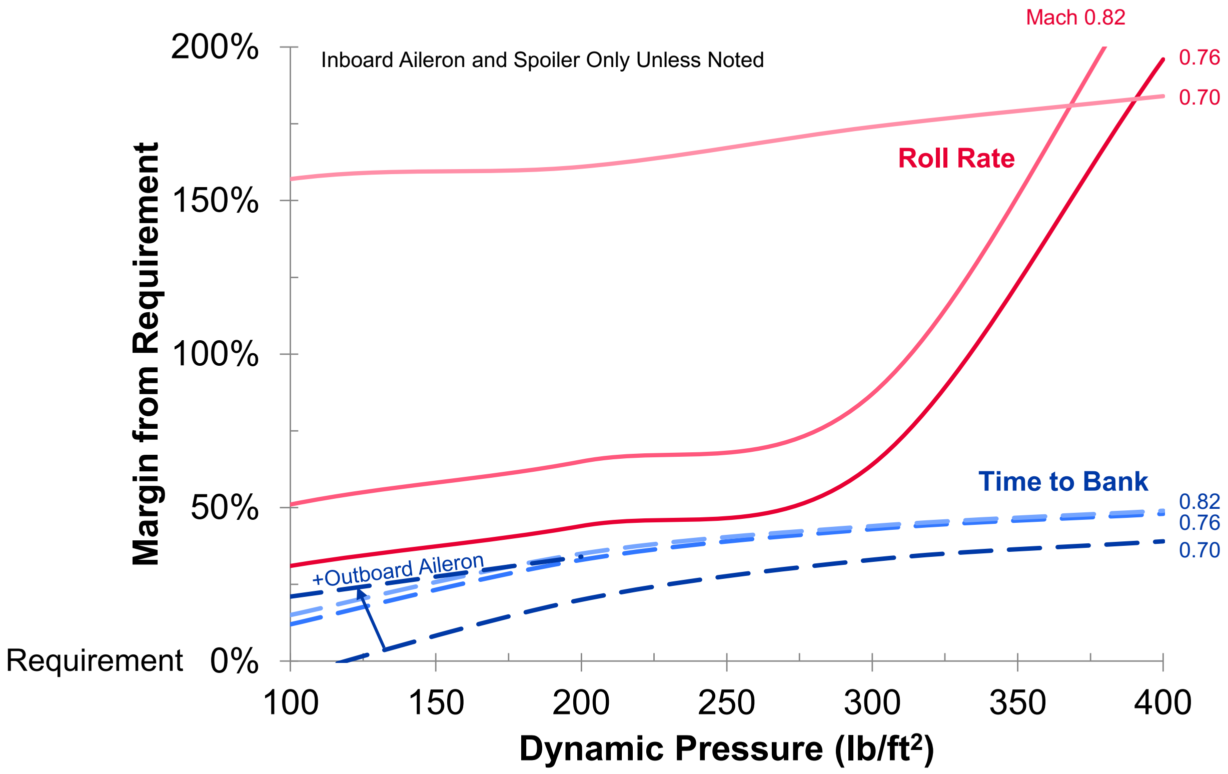

Figure 5.4 – Roll Control Performance

6.0 Configuration Analysis and Final Performance

This section includes the discipline analyses of the configuration documented in Section 2.2. This analysis data is representative of Revision J. The results of the FEM analysis performed on Revision H is not included in this analysis, however, the aeroelastic weight increase for this Phase of study is not unlike that of Phase II, which is included in the mass properties prediction.

6.1 Aerodynamics

The aerodynamics analyses are divided into high-speed and low-speed sections.

6.1.1 High Speed

Computer Aided Sizing and Evaluation System (CASES) cruise drag bookkeeping is shown in Figure 6.1. Parasite drag represents the incompressible zero-lift drag. Induced drag accounts for the drag due to lift based on airplane efficiency factor at Mach 0.50. Compressibility drag is a function of both Mach and lift coefficient while trim drag accounts for pitching moment on the configuration.

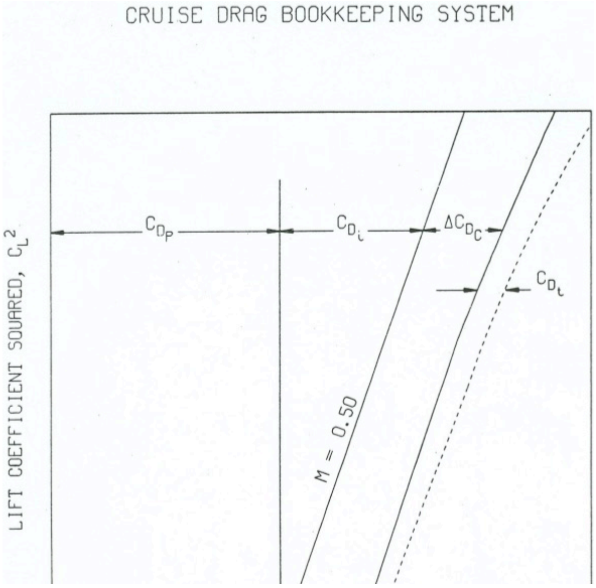

Figure 6.1 – CASES Standard Buildup: CD = C_{Dp} + C_{Di} + C_{Dc} + C_{Dtrim}.

Using CASES accounting and incorporating the wing-body-(landing gear fairing) CFD solutions, the high-speed aerodynamic buildup for 765-095 Rev-J is compared to Phase II 765-095 Rev-D as shown in Table 6.1. For Revision J, an overflow drag build-up was available as a base for the aerodynamic database. Due to the availability of this database, the bookkeeping relative to Revision D has changed thus explaining why some rows show zero drag levels for Revision J.

It should be noted that the aerodynamic technologies benefit (NLF/HLFC/Riblets) does not include the wing natural laminar flow (NLF) benefit. Wing upper surface NLF was book-kept under airplane compressibility drag during the Phase II study, and that convention is maintained here. Negative compressibility drag in the bookkeeping is due to the effect of laminar flow above Mach 0.50 as illustrated by Figure 6.2.

Table 6.1 – 765-095 Rev-J High Speed Buildup.

CONFIGURATION	765-095 Rev-D	765-095 Rev-J
WING AREA	1477	1477
SWEEP (DEG)	12.58	12.58
T/C-AVE	0.154	0.120
AIRFOIL TYPE	SUPERCRIT. DTE	SUPERCRIT. DTE
F BUILD-UP (FT^2)		
FUSELAGE	8.6959	8.4463
WING	10.1543	10.1499
STRUT / JURY	2.8963	3.1527
FLAP SUPPORT	0.2519	0.2604
HORIZONTAL	1.8904	1.6693
VERTICAL	1.7194	1.9116
N&P	1.9020	1.8450
CANOPY	0.0405	0.0000
GEAR PODS	3.0872	1.3043
NLF / HLFC	-2.4115	-2.6182
RIBLETS	-1.1814	-0.9787
EXCRESCENCE	2.6450	2.393
STRUTS C_{DC}	0.5900	0.0000
UPSWEEP	0.3414	0.0000
WING TWIST	0.1640	0.630
TURBULENT C_{DC} INCREMENT	-1.5656	0.0000
FUSELAGE BUMP	0.3675	0.0000
F-TOTAL (FT^2)	29.5873	28.1653
E-VISC	**0.931**	**0.9068**
CRUISE CD BUILD-UP		
M-CRUISE	0.710	0.745
C_L-CRUISE	0.750	0.775
CRUISE ALTITUDE	42000	40000
C_{D0}	0.02003	0.01907
C_{DI}	0.00981	0.01069
C_{DC}	-0.00063	-0.00074
C_{DTRIM}	0.0006	0.0006
C_{DTOT}	0.02981	0.02961
L/D	25.159	26.174
M L/D	17.863	19.500

Configuration 765-095 Rev-J aerodynamic characteristics reflect the design Mach number of 0.745. The resulting high-speed data are shown in Figure 6.3. The figure illustrates the maximum aerodynamic efficiency (M*L/D) occurring at the design cruise Mach (0.745) and C_L (0.775). In the performance results, this is representative of the long range cruise (LRC) speed while minimum fuel consumption occurs at lower Mach number.

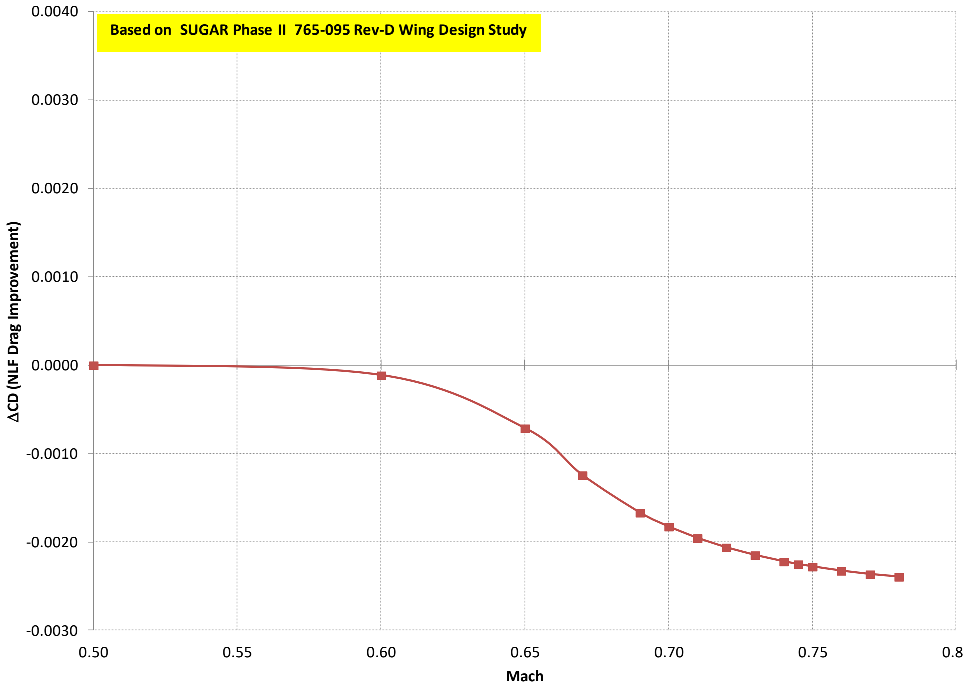

Figure 6.2 – 765-095 Rev-J – Wing NLF Drag Improvement.

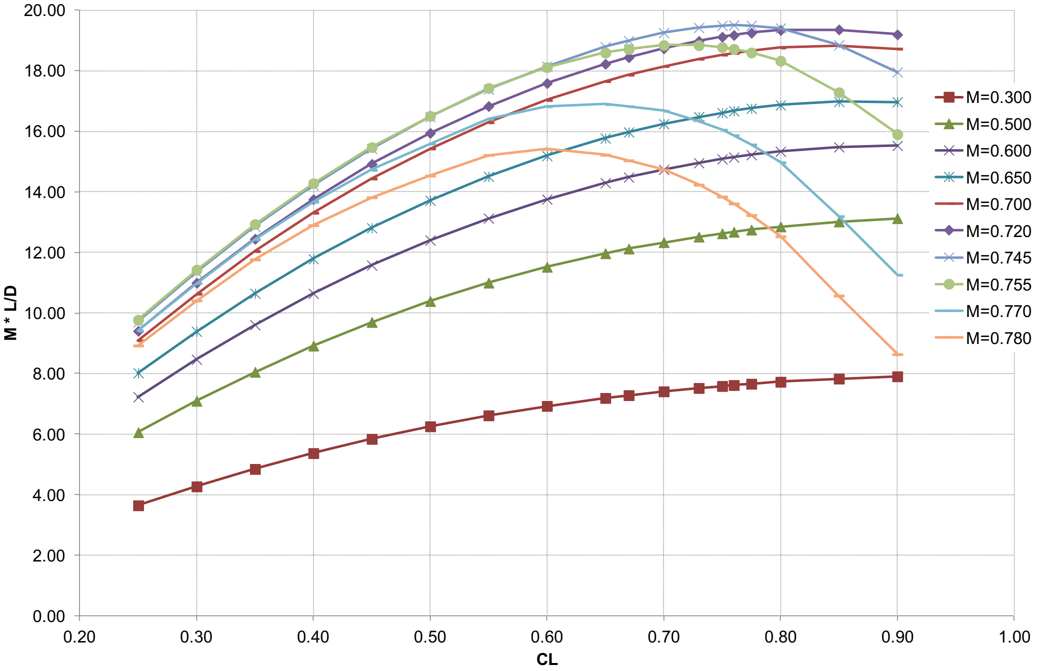

Figure 6.3 – 765-095 Rev-J – M * L/D Total.

6.1.2 Low Speed

The design of the high-lift system for the Truss-Braced Wing configuration Rev-H design cycle was based on prior work done for the Rev-C version. The loft surfaces for the leading- and trailing-edge high-lift devices were generated from the cruise wing lofted surface definition of the Rev-H configuration using UG NX. The changes made to the configuration for the Rev-J design cycle were not expected to have an appreciable effect on the low-speed aerodynamic characteristics and therefore, it was deemed unnecessary to reevaluate the high lift system design for the Rev-J configuration.

The high-lift leading-edge device consists of a full-span folding bull-nose type Krueger with spanwise cutouts for the engine pylon, wing strut attachment point, and the wing fold location. The parametric shape of the Krueger and the rigging optimization were carried over from the earlier work done for the Rev-C configuration. The Krueger rigging position was selected based on previous RANS- based optimization results with consideration given to the Krueger deflection, gap, and overhang positions, which would be necessary for the Krueger to function as an insect shield during the takeoff and landing phases of the flight in order to maintain laminar flow control during the cruise portion of the flight.

The trailing-edge device consists of a 28% chord single-segment Fowler motion flap. The flap span extends from the side-of-body to the wing fold location with a cutout for the engine pylon. During the design of the high-lift system the configuration was evaluated with an inboard high-speed aileron as well as a combined aileron-flap (i.e., flaperon) which would deploy like a flap for takeoff and landing. Flap deflections of 10°, 20°, and 30° were analyzed during the design process and low-speed lift and drag predictions were developed for configurations with and without the inboard flaperons. The resulting predictions for the low-speed performance indicated that the use of an inboard flaperon would be necessary in order to meet the landing $C_{L,max}$ target.

The leading-edge Krueger for the Rev-H configuration is shown in Figure 6.4 and the trailing-edge flap with inboard flaperon is shown in Figure 6.5.

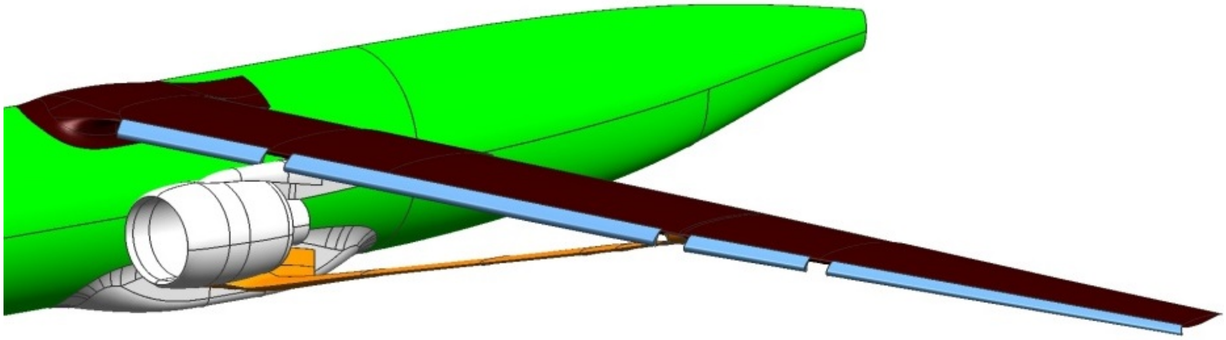

Figure 6.4 – Leading edge Krueger in the deployed position.

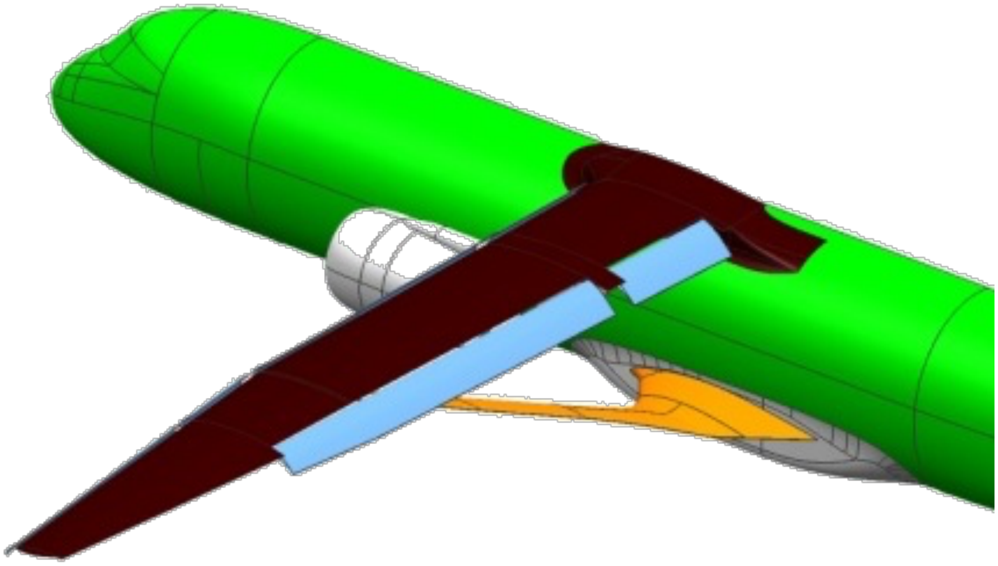

Figure 6.5 – Trailing-edge flap with flaperon at the max landing deflection.

The low-speed aerodynamic characteristics were predicted using the heritage panel method DACVINE which has proven to yield robust low-speed flow solutions for the complex configurations typical of high-lift systems. The solutions from the panel method were coupled with a ΔC_p-peak $C_{L,max}$ analysis in order to provide accurate predictions for the takeoff and landing configurations. A sample case showing the application of the ΔC_p-peak $C_{L,max}$ analysis is shown in Figure 6.6 for the landing configuration with the leading-edge Krueger deployed and 30° flap deflection.

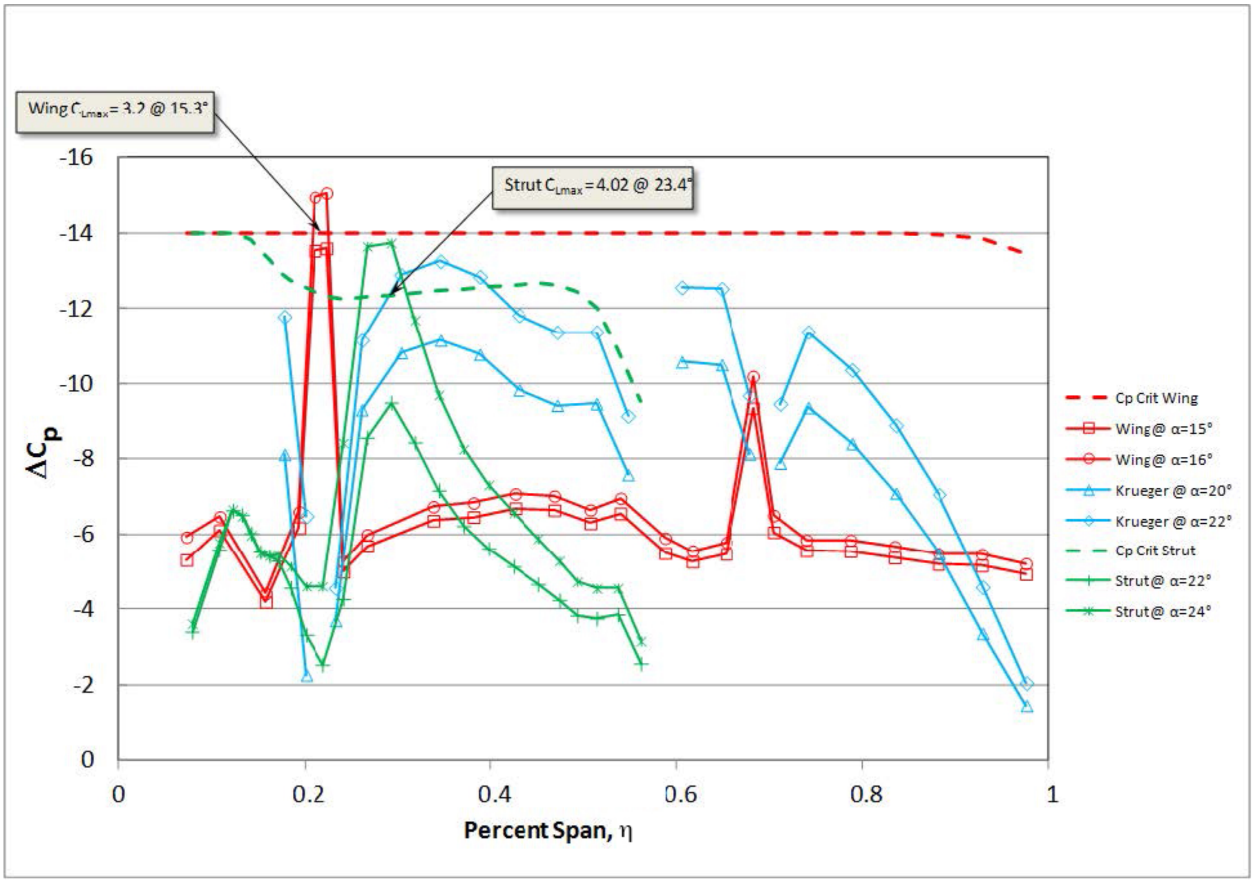

Figure 6.6 – Sample predicted $C_{L,max}$ analysis case on the SUGAR 765-095 Rev H using leading-edge ΔC_p-peak criteria: δ_{KR} = 50° / δ_{FLAP} = 30°_30°.

The low-speed lift curves and drag polars for the Rev-H configuration were determined using the following buildup procedure:

Lift curves

- $C_{L_{\alpha=0}}$, C_{L_α} – DACVINE predictions
- $C_{L_{max}}$ – DACVINE predictions with $\Delta C_{p_{peak}}$ criteria
- $\Delta C_{L_{trim}}$ = 3% (conceptual estimate)

Drag polars

- $C_{D_{total}} = C_{D_o} + C_{D_i} + C_{D_p} + \Delta C_{D_{trim}} + \Delta C_{D_{gear}}$
- C_{D_o} – parasite drag from high-speed buildup using CASES, no correction for Reynolds number was applied.
- C_{D_i} – induced drag from the DACVINE prediction
- C_{D_p} – profile drag due to leading and trailing edge high-lift devices derived from Boeing proprietary experimental database.

- $\Delta C_{D_{trim}}$ – trim drag increment estimated as 3%C_{Dtotal}
- $\Delta C_{D_{gear}}$ – gear drag from CASES conceptual estimate

The final low-speed aerodynamic characteristics for the Truss-Braced Wing are shown in Figure 6.7 through Figure 6.9.

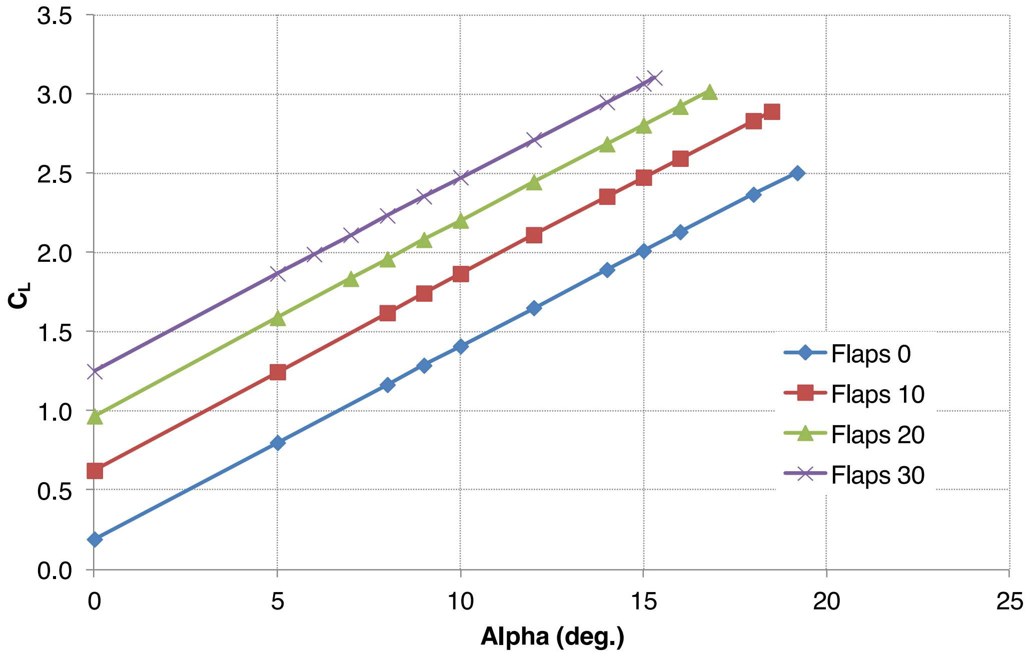

Figure 6.7 – 765-095 Rev-J Low speed lift curves with the leading-edge Krueger deployed, free-air: Mach = 0.20.

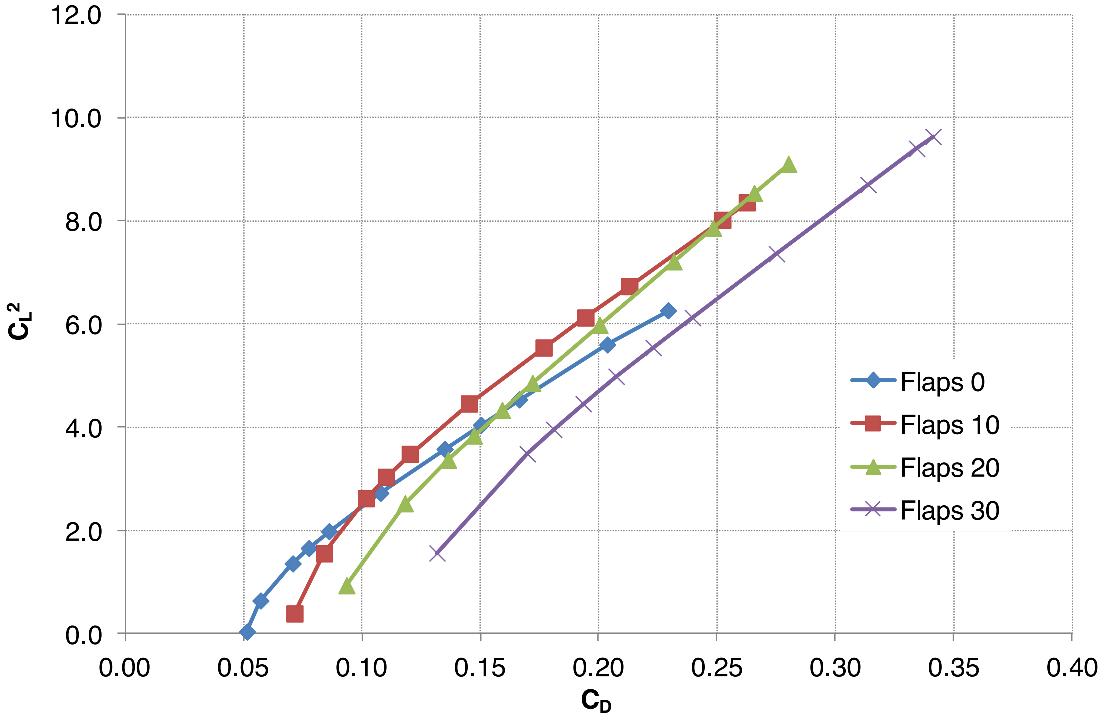

Figure 6.8 – 765-095 Rev-J Low speed drag-due-to-lift (C_L^2) vs drag with the leading-edge Krueger deployed, free-air: Mach = 0.20.

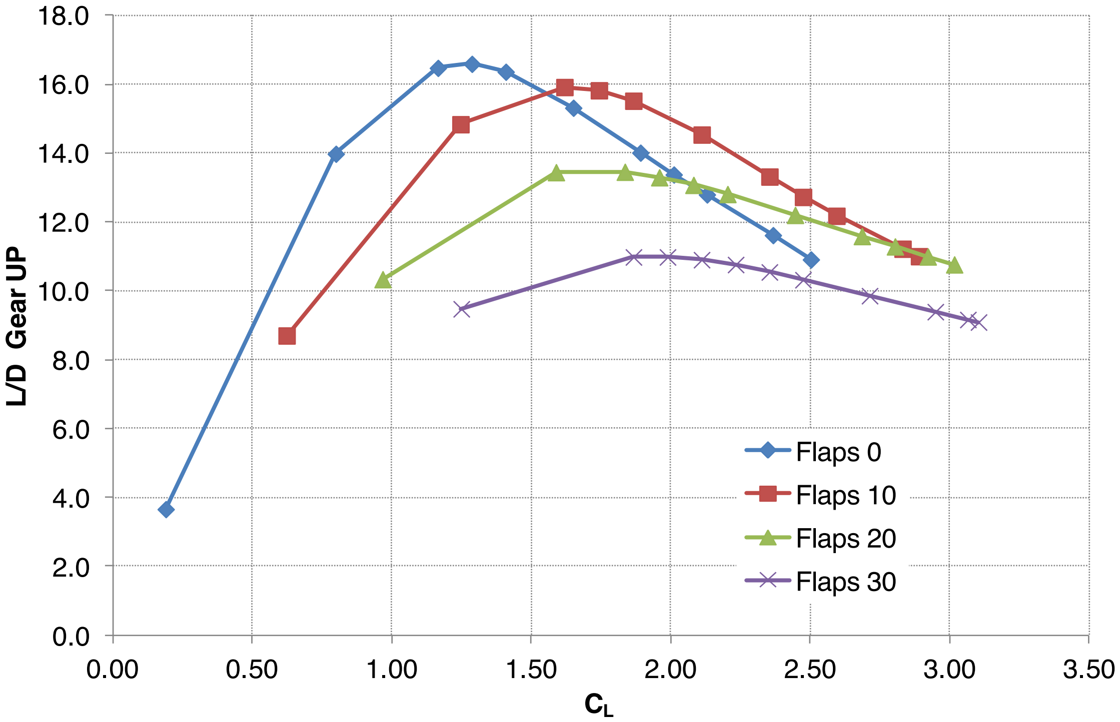

Figure 6.9 – 765-095 Rev-J Low speed Lift-to-Drag ratio with the leading-edge Krueger deployed and gear up, free-air: Mach = 0.20.

6.2 Mass Properties

The group weight statement for 765-095-Rev-H is shown in Table 6.2. These weights include data generated with the aeroelastic FEM discussed in Phase II. The FEM data were essential for such a high aspect ratio strut-braced wing configuration. The group weight data was generated using a takeoff gross weight of 150,000 pounds, a first-cut estimate used to start the sizing process. The masses represented here were used for the Revision H FEM analysis and no looping has been performed.

Table 6.2 – 765-095 Rev-H Group Weight Statement.

GROUP	WEIGHT (LB)	
WING	**14,736**	
BENDING MATERIAL		6,120
SPAR WEBS		828
RIBS AND BULKHEADS		893
AERODYNAMIC SURFACES		2,936
SECONDARY STRUCTURE		3,959
TAIL	**2,759**	
FUSELAGE	**15,345**	
LANDING GEAR	**5,077**	
NACELLE & PYLON	**4,902**	
WING STRUT & JURY & INSTALLATION	**3,836**	
PROPULSION	**10,173**	
ENGINES		8,436
FUEL SYSTEM		1,737
FLIGHT CONTROLS	**2,659**	
COCKPIT CONTROLS		252
SYSTEM CONTROLS		2,407
POWER SYSTEMS	**4,071**	
AUXILIARY POWER PLANT		1,014
HYDRAULICS		760
PNEUMATICS		0
ELECTRICAL		2,297
INSTRUMENTS	**774**	
AVIONICS & AUTOPILOT	**1,504**	
FURNISHINGS & EQUIPMENT	**9,114**	
AIR CONDITIONING	**1,441**	
ANTI-ICING	**121**	
MANUFACTURER'S EMPTY WEIGHT (MEW)	**76,511**	
OPERATIONAL ITEMS	7,207	
OPERATIONAL EMPTY WEIGHT (OEW)	**83,718**	
USABLE FUEL	35,482	
DESIGN PAYLOAD	30,800	
TAKEOFF GROSS WEIGHT (TOGW)	**150,000**	

6.3 Performance and Sizing

Boeing’s Computer Aided Sizing and Evaluation System (CASES) is the principal tool used by Boeing Research & Technology to calculate mission performance such as payload, range, or fuel consumption. The CASES tool consists of separate programs for analyzing mission, takeoff, and landing performance respectively, all of which have been validated over time to actual airplane performance. These analyses can be calculated for various atmospheric conditions. The low-speed, field length analyses consist of all-engine and one engine inoperative (OEI) calculations.

Performance and sizing for SUGAR was performed within a ModelCenter environment, which serves as a wrapper for the various CASES performance analysis components. In this environment, the aero, propulsion, and performance data are specified. The basic empty weight and sizing weight derivatives from the weight statement are also specified. ModelCenter provides a platform for running the parametric trade studies and optimizations necessary for performance and sizing and also provides some data visualization tools. Engine thrust and wing area were varied to minimize block fuel per seat while enforcing Takeoff Field Length (TOFL), Initial Cruise Altitude Capability (ICAC), and fuel margin constraints to size the SUGAR 765-095 configuration. The sizing process is illustrated in Figure 6.10.

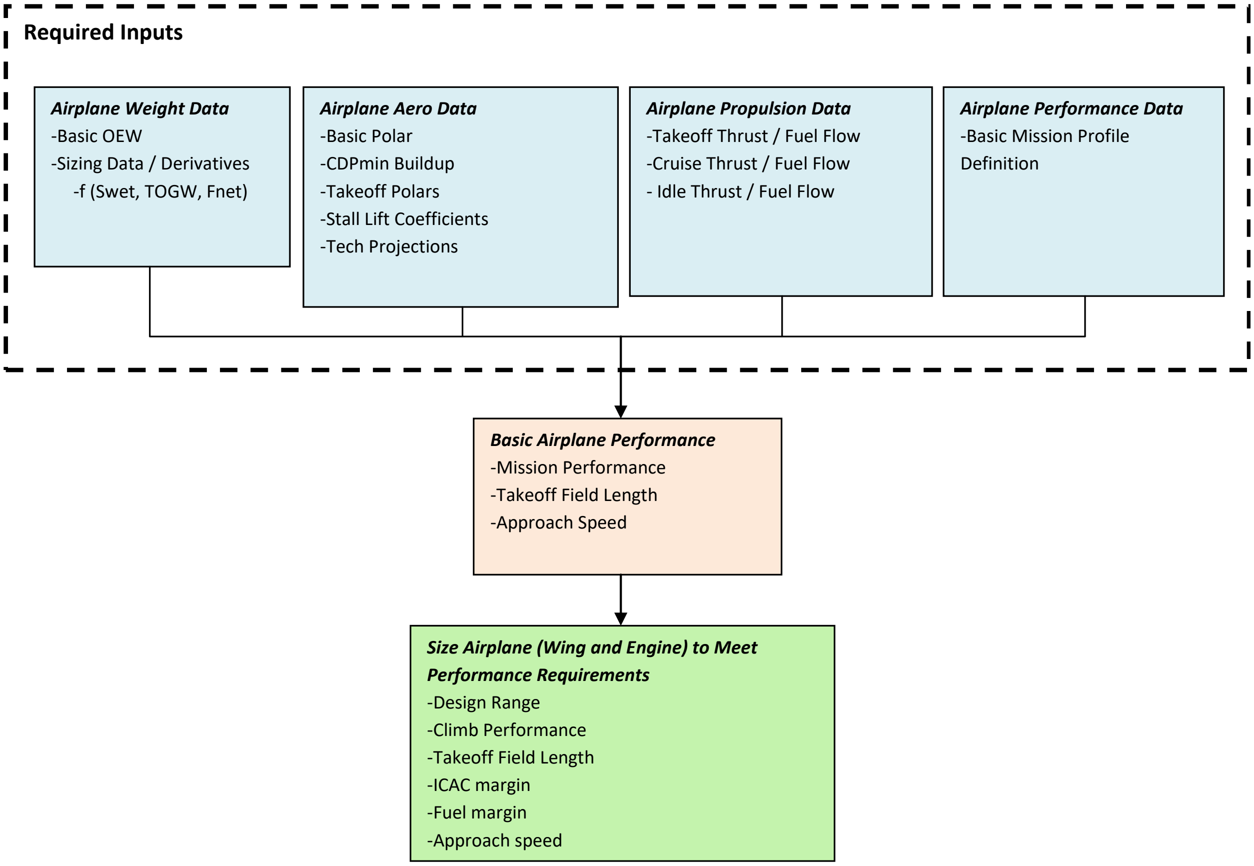

Figure 6.10 – Airplane Sizing Using CASES / ModelCenter.

6.3.1 Sizing Requirements

A set of top level requirements for the SUGAR vehicles was generated from the future scenario previously reported in SUGAR Phase I (1). These top-level requirements were turned into specific payload-range requirements, which are illustrated in Figure 6.11. The figure has several points of interest called out and described below.

1. The airplane is required to fly the average range (900 nm) at the maximum payload condition (which is the same as the maximum zero fuel weight condition). The maximum payload is required to be 15,200 pounds heavier than the payload corresponding to Point 2.
2. The airplane is required to fly the maximum range (3,500 nm) at the full passenger payload using an average weight allowance of 200 pounds per passenger (including bags) and no additional revenue payload. This point must be achieved using less than 90% of the useable fuel.
3. Point 3 is used to calculate vehicle fuel consumption and takeoff field length (TOFL) performance for the SUGAR program. This is the point that represents the most common operating condition for this vehicle class, and corresponds to a range of 900nm.

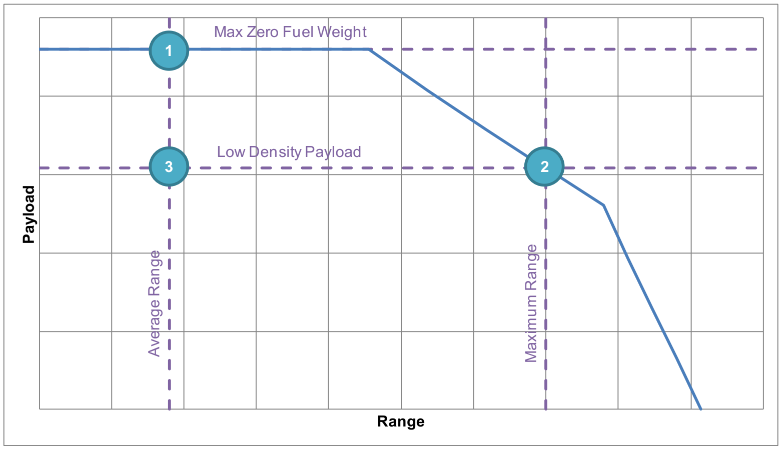

Figure 6.11 – Payload-Range Requirements.

Both Points 1 and 2 are required for sizing because airplane characteristics may alter which of these two is critical. The mission profile for SUGAR 2035 concepts is shown in Figure 6.12. SUGAR High is evaluated using the illustrated mission while SUGAR Free is flown with a nonadvanced air traffic management system. These missions are further documented in Phase I (1).

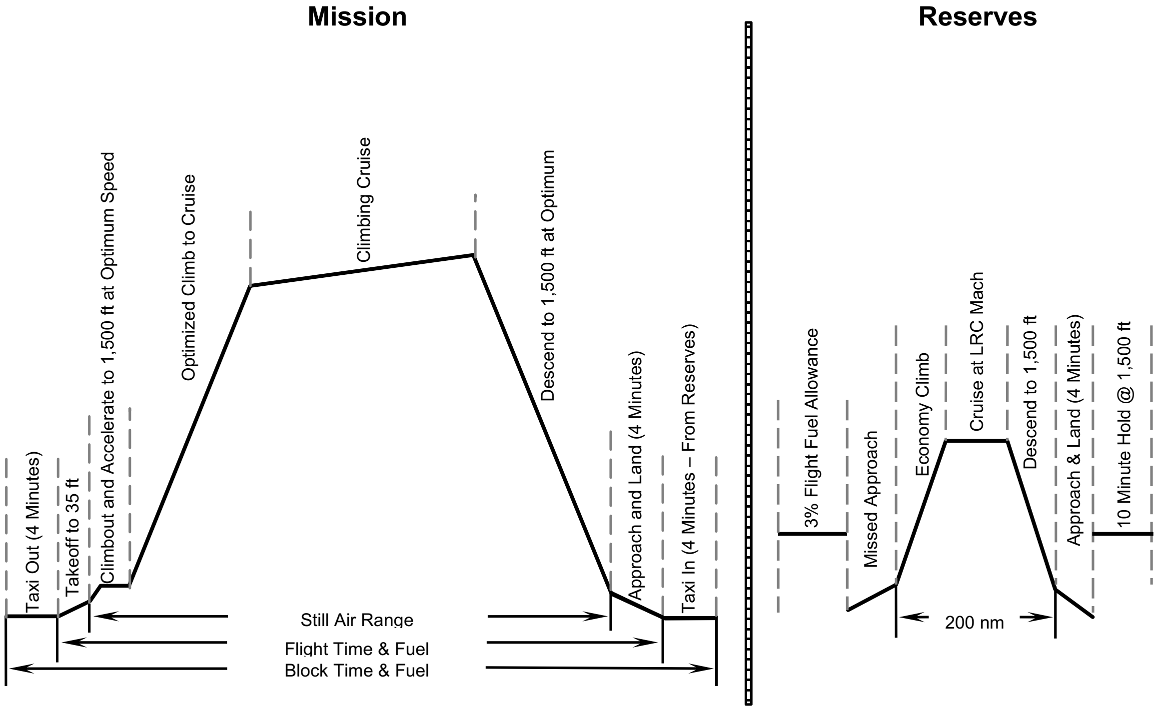

Figure 6.12 – 2035 Mission Profile with NextGen Air Traffic Management.

6.3.2 Sizing Results

The performance of the latest SUGAR High configuration (765-095-RJ) is shown in Table 6.3. Because the primary performance tool was switched from the Boeing Mission Analysis Program (BMAP) to CASES between Phase II and III, the 765-095-RD, which was presented in Phase II, was analyzed again using CASES. The performance for this configuration is also shown in Table 6.3.

There are several different sizing cases shown; from left to right, the first two columns are referred to as 'As-Drawn' meaning the performance was run at the reference wing area, thrust, and MTOW used to generate the baseline vehicle data. In this case, the thrust, wing area, and MTOW are higher than the mission requires. The next set of columns is sized data for minimum fuel consumption constrained by initial cruise altitude capability (ICAC) and fuel margins. The ICAC constraint requires the aircraft be able to climb to the altitude yielding best specific range (its optimum altitude). It should be noted that the takeoff field length, climb performance, and approach speed constraints were inactive. These configurations were sized at max range cruise (MRC) Mach, which seeks to maximize range. The remaining two columns illustrate the corresponding fallout performance data for the MRC-sized configurations run at long-range cruise (LRC) Mach, which seeks to fly at 99% of the max specific range. Operation at LRC allows an increase in aircraft productivity with only a modest impact to fuel consumption.

The performance of the airplane is shown relative to the SUGAR Free baseline (configuration 765-093 with mission performance run in BMAP) in Table 6.4. This shows a 54.1 and 57.0 percent reduction in fuel consumption for the 765-095-RD and 765-095-RJ, respectively.

Performance was exercised at various combinations of fuel and payload weight to generate a payload-range curve shown in Figure 6.13. This curve shows that 765-095-RJ variant does not meet the stated range requirements at the maximum payload condition with only 762 nautical miles of range. The airplane was not sized to accommodate this maximum payload condition in an effort to maintain consistency with the 765-095-RD UDF and clearly illustrate the improvements made during the Phase III study. The flat upper portion of the curve (at 46,000 lb. payload) represents the maximum zero fuel weight constraint of the airplane. The shallow sloped portion of the curve is set by Maximum Takeoff Weight (MTOW). The final region of the chart is set by the airplanes fuel volume limit.

Table 6.3 – 765-095 Rev-D and Rev-J Mission Performance.

Model Sizing Level		765-095-RD As-Drawn	765-095-RJ As-Drawn	765-095-RD Sized, MRC Min Fuel	765-095-RJ Sized, MRC Min Fuel	765-095-RD LRC fallout	765-095-RJ LRC fallout
PASSENGERS / CLASS		154 / DUAL	154 / DUAL	154 / DUAL	154 / DUAL	154 / DUAL	154 / DUAL
MAX TAKEOFF WEIGHT	LB	150,000	150,000	134,913	132,246	134,913	132,246
MAX LANDING WEIGHT	LB	137,206	138,987	132,411	131,824	132,411	131,824
MAX ZERO FUEL WEIGHT	LB	129,206	130,987	124,411	123,824	124,411	123,824
OPERATING EMPTY WEIGHT	LB	83,206	84,987	78,411	77,824	78,411	77,824
FUEL CAPACITY REQ / AVIL	USG	5,979 / 5,417	5,684 / 5,417	4,273 / 4,273	3,928 / 3,928	4,273 / 4,273	3,928 / 3,928
ENGINE MODEL		gFan+	gFan+	gFan+	gFan+	gFan+	gFan+
FAN DIAMETER	IN	71	71	66	66	66	66
BOEING EQUIVALENT THRUST (BET)	LB	23,000	23,000	19,981	19,866	19,981	19,866
WING AREA / SPAN	FT^2 / FT	1,478 / 170	1,478 / 170	1,210 / 154	1,124 / 148	1,210 / 154	1,124 / 148
ASPECT RATIO (EFFECTIVE)		19.56	19.56	19.56	19.56	19.56	19.56
INITIAL CRUISE OPTIMUM C_L		0.7325	0.7463	0.7431	0.8174	0.7105	0.7515
INITIAL CRUISE L/D @ OPT C_L		24.814	26.202	23.303	24.958	22.864	24.310
MID-CRUISE CL – L/D		0.733 – 24.554	0.742 – 25.964	0.738 – 23.086	0.813 – 24.775	0.705 – 22.658	0.745 – 24.045
DESIGN MISSION RANGE	NMI	4,915	4,944	3,500	3,500	3,469	3,467
PERFORMANCE CRUISE MACH*		0.705 (MRC)	0.720 (MRC)	0.704 (MRC)	0.718 (MRC)	0.716	0.745
LONG RANGE CRUISE MACH (LRC)		0.716	0.747	0.716	0.745	0.716	0.745
INITIAL CRUISE THROTTLE SETTING	%	0.948	0.951	0.965	0.957	0.970	0.964
CLIMB CL (INITIAL – END)		0.4784 - 0.7325	0.4699 - 0.7463	0.5158 - 0.7431	0.5092 - 0.8174	0.5158 - 0.7109	0.5092 - 0.7515
ROC (INITIAL - END)	FT / MIN	3,604 - 315	3,645 - 299	3424 - 299	3,589 - 301	3,424 - 300	3,589 - 304
THRUST ICAC (MTOW, ISA)	FT	40,246	41,363	38,386	40,011	38,151	39,754
TIME / DIST (MTOW, 35k FT, ISA + 15C)	MIN / NMI	21 / 122	21 / 121	23 / 138	21 / 126	23 / 141	21 / 131
OPTIMUM ALTITUDE (MTOW, ISA)	FT	40,078	42,626	38,386	40,011	38,267	39,926
BUFFET ICAC (MTOW, ISA)	FT	40,489	43,546	38,504	40,417	39,010	40,984
TOFL (MTOW, SEA LEVEL, 86 DEG F)	FT	3,540	3,846	4,525	5,282	4,527	5,286
APPROACH SPEED (MLW)	KT	117.4	116.5	127.5	130.1	127.5	130.1
BLOCK FUEL / SEAT (900 NMI)	LB	43.75	42.5	41.99	39.38	42.23	39.61

* Cruise Mach is set as MRC or LRC which is then calculated and reported by the performance routine

Table 6.4 – 765-095 Rev-D and Rev-J Mission Performance Comparison.

Model Sizing Level		765-093 SUGAR Free	765-095-RD Sized, MRC Min Fuel	765-095-RJ Sized, MRC Min Fuel
PASSENGERS / CLASS		154 / DUAL	154 / DUAL	154 / DUAL
MAX TAKEOFF WEIGHT	LB	182,600	134,913	132,246
MAX LANDING WEIGHT	LB	149,400	132,411	131,824
MAX ZERO FUEL WEIGHT	LB	140,400	124,411	123,824
OPERATING EMPTY WEIGHT	LB	94,400	78,411	77,824
FUEL CAPACITY REQ / AVIL	USG	9,633 / 9,633	4,273 / 4,273	3,928 / 3,928
ENGINE MODEL		CFM56-7B27	gFan+	gFan+
FAN DIAMETER	IN	62	66	66
BOEING EQUIVALENT THRUST (BET)	LB	27,900	19,981	19,866
WING AREA / SPAN	FT^2 / FT	1,406 / 121	1,210 / 154	1,124 / 148
ASPECT RATIO (EFFECTIVE)		10.41	19.56	19.56
OPTIMUM C_L		0.584	0.7431	0.8174
CRUISE L/D @ OPT C_L		17.997	23.303	24.958
DESIGN MISSION RANGE	NMI	3,680	3,500	3,500
PERFORMANCE CRUISE MACH		0.79 (LRC)	0.704 (MRC)	0.718 (MRC)
LONG RANGE CRUISE MACH (LRC)		0.79 (LRC)	0.716	0.745
THRUST ICAC (MTOW, ISA)	FT	36,200	38,386	40,011
TIME / DIST (MTOW, 35k FT, ISA + 15C)	MIN / NMI	23 / 148	23 / 138	21 / 126
OPTIMUM ALTITUDE (MTOW, ISA)	FT	34,900	38,386	40,011
BUFFET ICAC (MTOW, ISA)	FT	36,200	38,504	40,417
TOFL (MTOW, SEA LEVEL, 86 DEG F)	FT	8,190	4,525	5,282
APPROACH SPEED (MLW)	KT	126	128	130
BLOCK FUEL / SEAT (900 NMI)	LB	91.51 (Base)	41.99 (-54.1%)	39.38 (-57.0%)

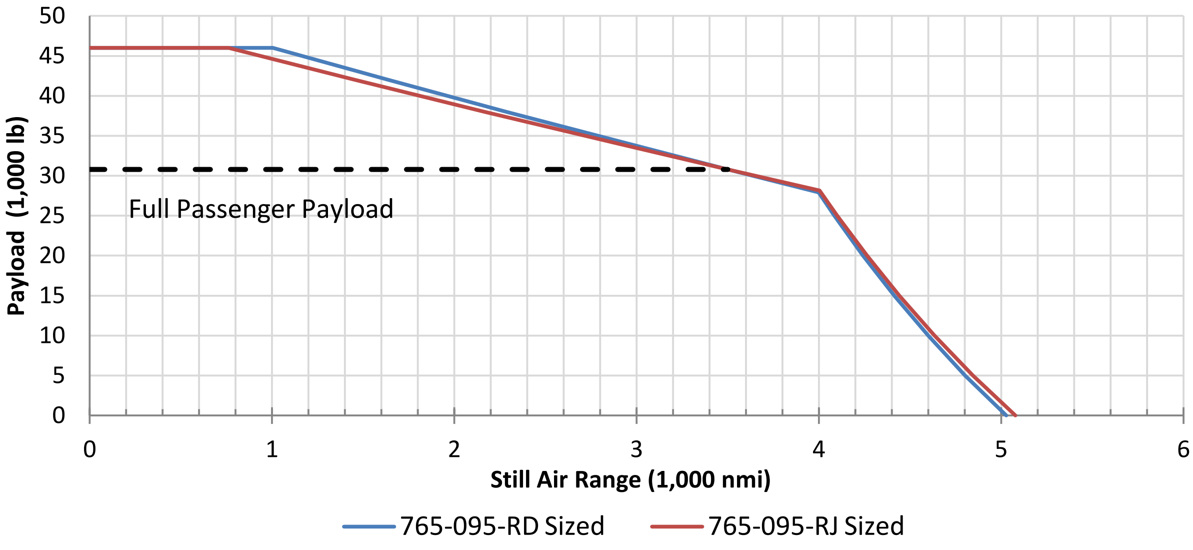

Figure 6.13 – 765-095 Sized Payload-Range Curve.

Block Fuel for each configuration is compared to the SUGAR Free. NASA goals aim for a 60% reduction. Figure 6.14 shows Rev-D and Rev-J configurations relative to these goals. Fuel consumption per segment in comparison to SUGAR Free is shown in Figure 6.15 for the 900 nautical mile economic mission. It is worth noting that because the SUGAR Free configuration has a lower L/D than the truss-braced wing aircraft, it has a steeper glide slope and therefore spends less time in descent. Fuel consumption as a function of range is illustrated by Figure 6.16.

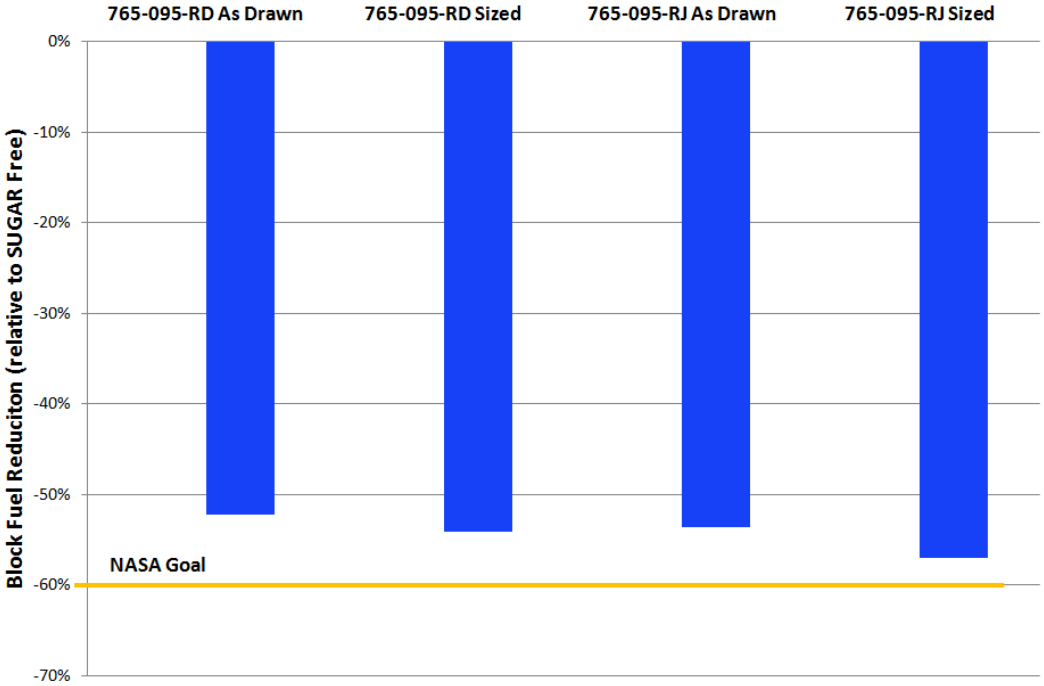

Figure 6.14 – Block Fuel Reduction Compared to NASA Goal.

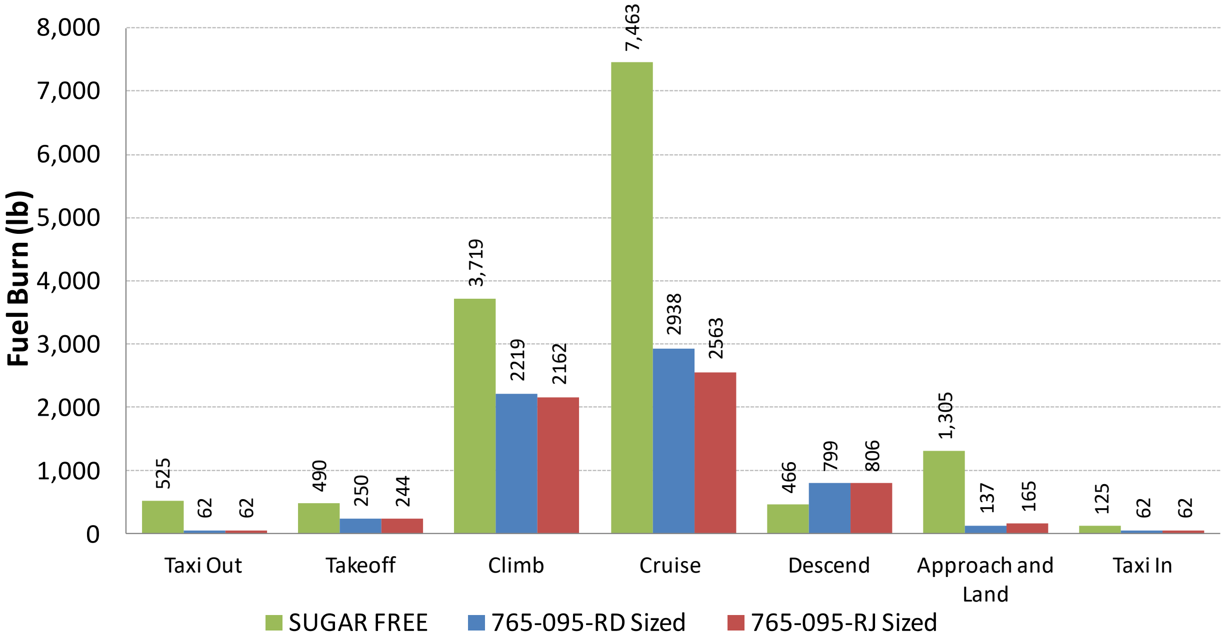

Figure 6.15 – Fuel Consumption per Segment.

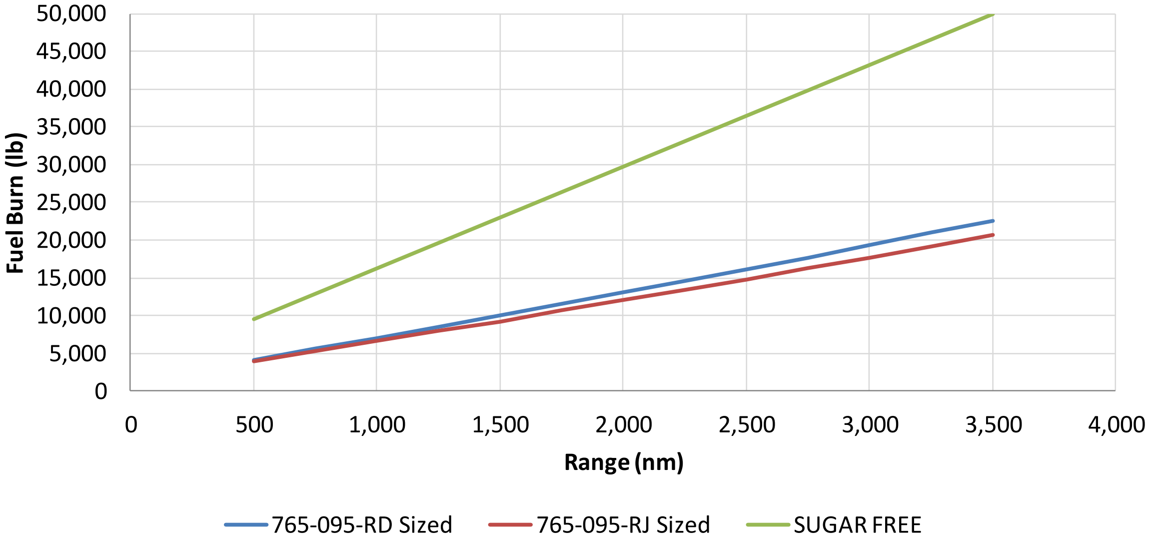

Figure 6.16 – Fuel Consumption vs. Range.

7.0 Wind Tunnel Test and Design Validation

This section summarizes the results and post-test analysis of the Transonic Truss-Braced Wing (TTBW) wind tunnel test conducted at the NASA Ames 11-Foot TWT facility located at Moffett Field, CA from January 11 to February 3, 2016. The model was 4.5% scale and had a wingspan of 7.7 feet. The test focused on determining the model drag buildup at Mach 0.5, determining drag polars from cruise Mach number to max operating Mach number, verifying the CFD based truss system drag increment, and verifying the drag rise of the overall configuration. In addition, stability and control data was collected to dive Mach number.

7.1 Test Introduction

This report focuses on the results and post-test analysis of the Transonic Truss-Braced Wing (TTBW) wind tunnel test conducted at the NASA Ames 11-Foot TWT facility located at Moffat Field, CA. The testing occurred from January 11 to February 3, 2016 for a total of 260 occupancy hours. The Boeing test designation for this entry is LB-649A.

The model is a 4.5% scale representation of the current TTBW configuration (765-095-RJ), with a design cruise Mach number of 0.745. The general arrangement of this configuration is shown in Figure 2.4.

The primary purpose of the test was to evaluate the high-speed aerodynamic performance of the vehicle, and make preliminary assessments of stability and control characteristics. The specific test objectives were as follows:

- Validate lift and drag performance (including drag divergence)
- Assess longitudinal and lateral-directional stability characteristics
- Assessment of preliminary flight controls effectiveness
- Evaluate the truss system impact on high-speed performance

Additional objectives:

- Acquire supplemental surface pressure measurements using Pressure Sensitive Paint (PSP) techniques
- Acquire infrared images to identify boundary layer transition location
- Collect measurements of model aeroelastic deflection in the tunnel using the NASA Model Deflection Measurement (MDM) System
- Flow Visualization using oils as needed

7.2 Test Facility and Envelope

The test was conducted at the NASA Ames Unitary Plan Wind Tunnel (UPWT) 11-Foot Transonic Wind Tunnel (11-Ft TWT) facility located at Moffett Field, CA. A depiction of the UPWT facility is shown in Figure 7.1.

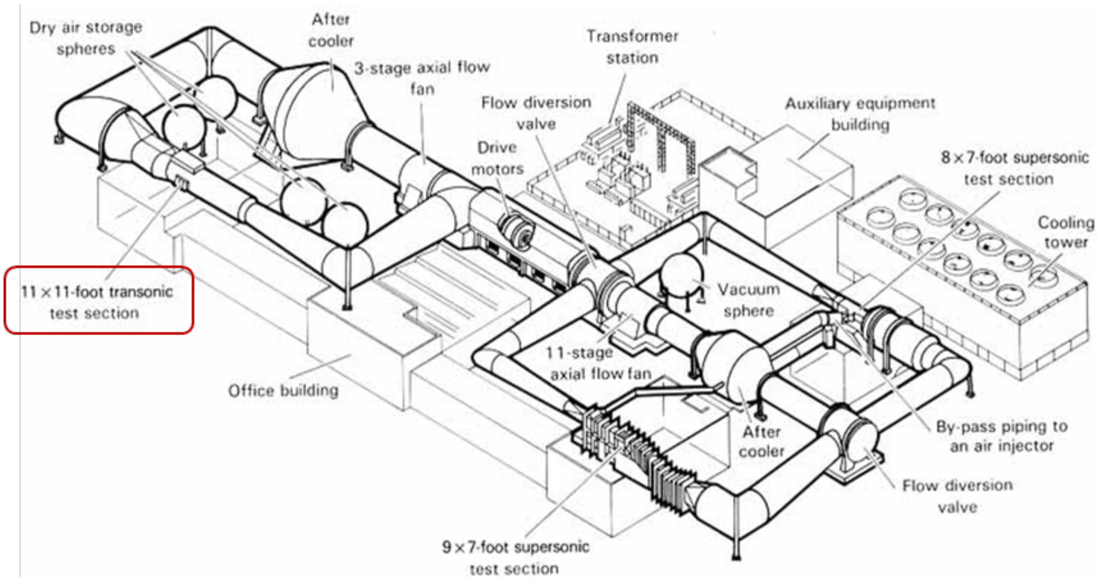

Figure 7.1 – NASA Ames Research Center Unitary Plan Wind Tunnel (UPWT) Aerial View.

The Mach capability in the 11-Foot test section ranges from 0.2 to 1.45 with a Reynolds number variation from 0.3-9.8M per foot. Tunnel operating pressure can be varied from 432-4,608 psfa. The transonic test section (Figure 7.2) is 11' high, 11' wide, and is 22' in length.

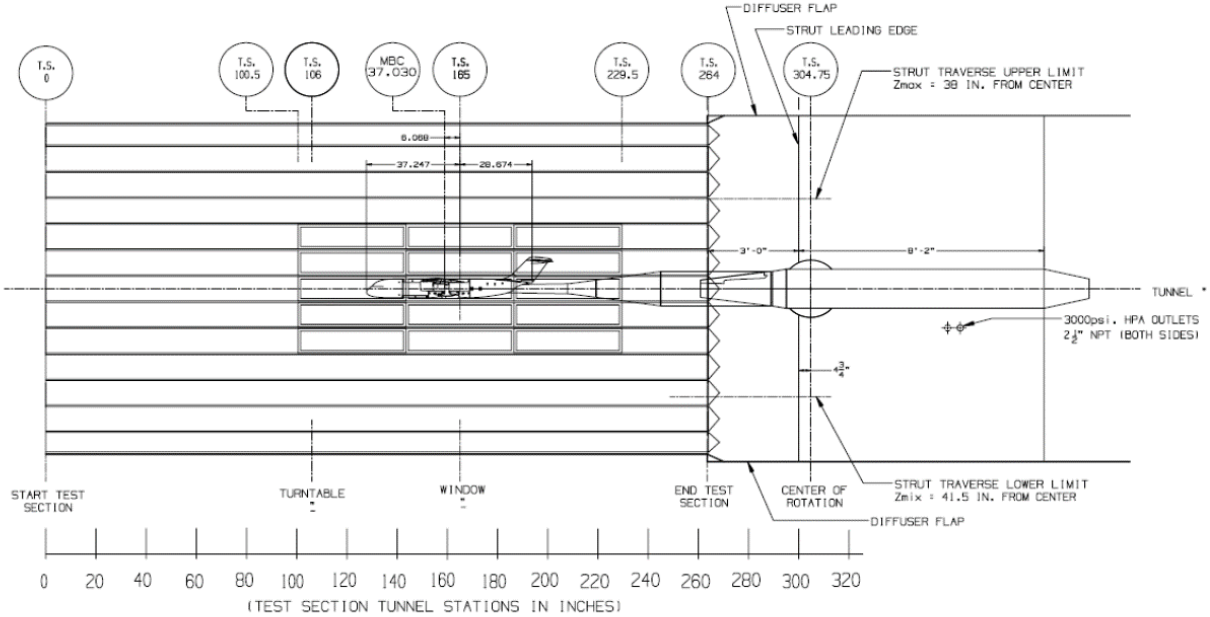

Figure 7.2 – NASA Ames 11-Ft Transonic Wind Tunnel (TWT) Test Section.

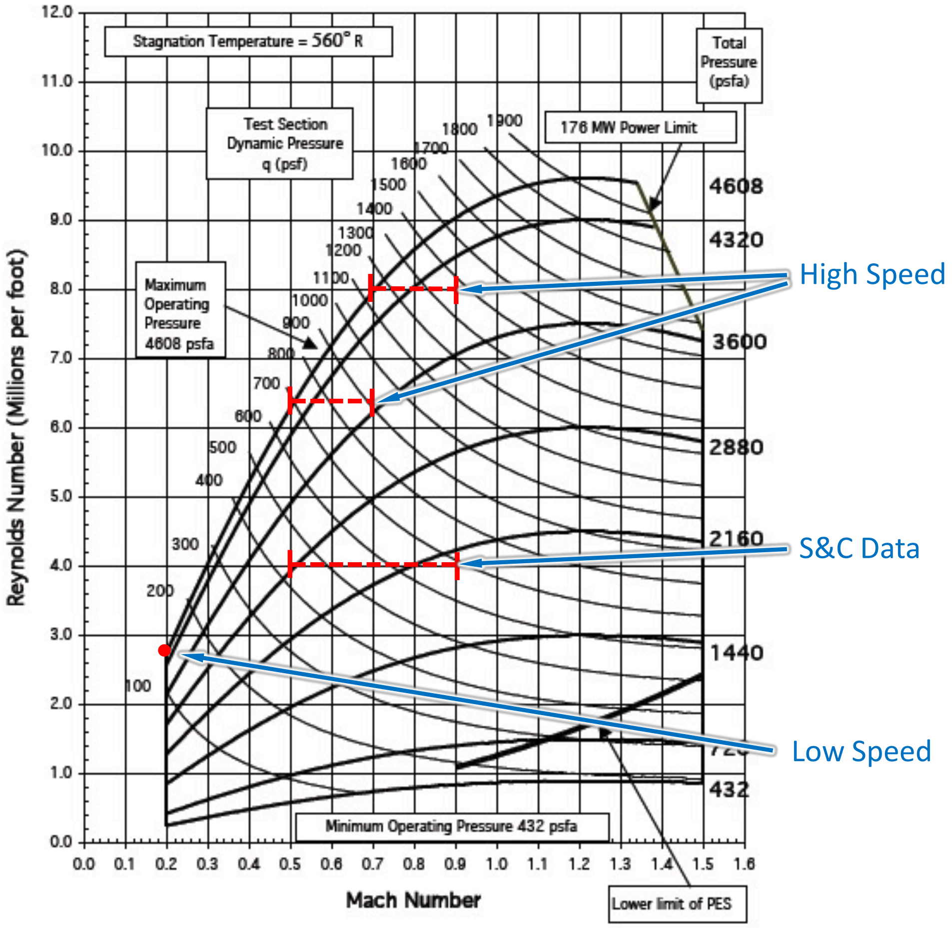

Figure 7.3 – Operating Characteristics of the 11-Foot TWT.

The TTBW test was carried out over a range of conditions as permitted by allowable model loads. These loads were measured by a series of strain gauges on the model wing, and were continuously monitored in order to ensure safety while testing. The nominal conditions established for the test are shown in Figure 7.3. High-speed testing was completed at different dynamic pressures based on the configuration tested. For a complete configuration including the wing and strut, testing was conducted at a unit Re=8M/ft. When the strut was removed, test Reynolds number was decreased to 6.3M/ft to maintain acceptable safety margins. Depending on the configuration being tested, occasional reductions in the angle of attack sweeps resulted from reaching maximum limit loads (including safety margin) on the model. Component build-up of the model was carried out at lower Mach number where compressibility effects are significantly reduced. Stability and control data were acquired across a larger range of Mach numbers to include additional controls-critical conditions, including MMO. The summary of Reynolds number and Mach ranges tested are presented below in Table 7.1.

Table 7.1 – Test Operating Conditions

Re (M/ft)	Mach	Configuration
4.0	0.30 – 0.87	S&C data, high Mach, Wing Only cases
6.3	0.50 – 0.79	High-Speed Data
8.0	0.70 – 0.79	Full configuration only, high-speed data

7.3 Model Description

The LB-649A wind tunnel model (Figure 7.4) is a full-span, 4.5% scale representation of the M=0.745 TTBW (765-095-RJ) aircraft configuration developed in earlier stages of this contract. The model has a high aspect ratio wing (AR~19.5) supported at 56% span by a strut that attaches to the landing gear sponson.

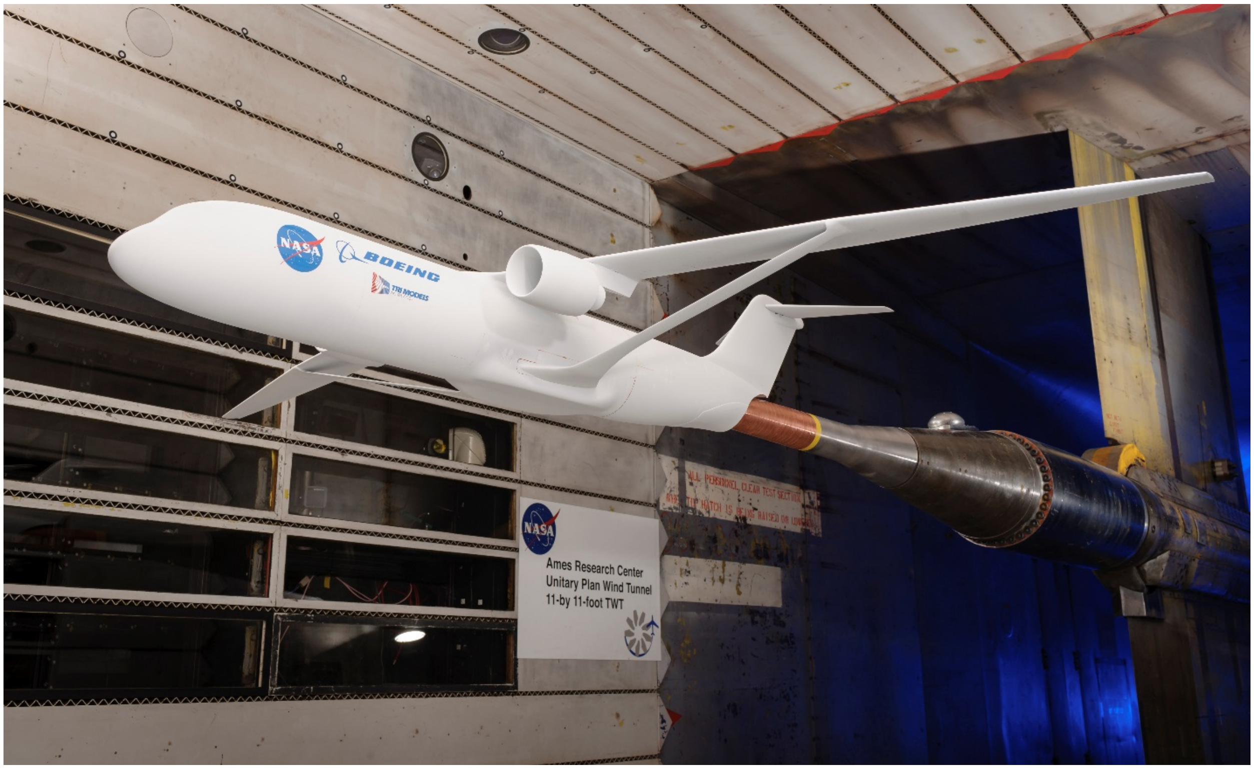

Figure 7.4 – LB-649A Transonic Truss Braced Wing (TTBW) Model.

The model is modular so that the individual components of the wing truss system could be tested separately to determine the net effect of each component. In this way the test results could be used to validate the conceptual build-up methodology used to layout and size TTBW aircraft. Removable components (shown in Figure 7.5) include the: strut, wing, engine and pylon, pylon-wing fillet, landing gear sponson, wing-body fairing, horizontal tail, and vertical tail. (Only the strut could not be tested individually since it could not be mounted to the model except when the wing was installed.) The model also included an alternate strut design that increased the separation between the wing and strut at the wing attachment point to reduce interference. The final model configuration also included an aft fuselage fairing to alter the shape of the fuselage-sting interface, a modification developed during testing. The model is mounted to the tunnel support sting via an aft-sting that penetrates the fuselage with clearance to prevent fouling during testing.

The model moment transfer used in the data reduction is shown in Figure 7.6.

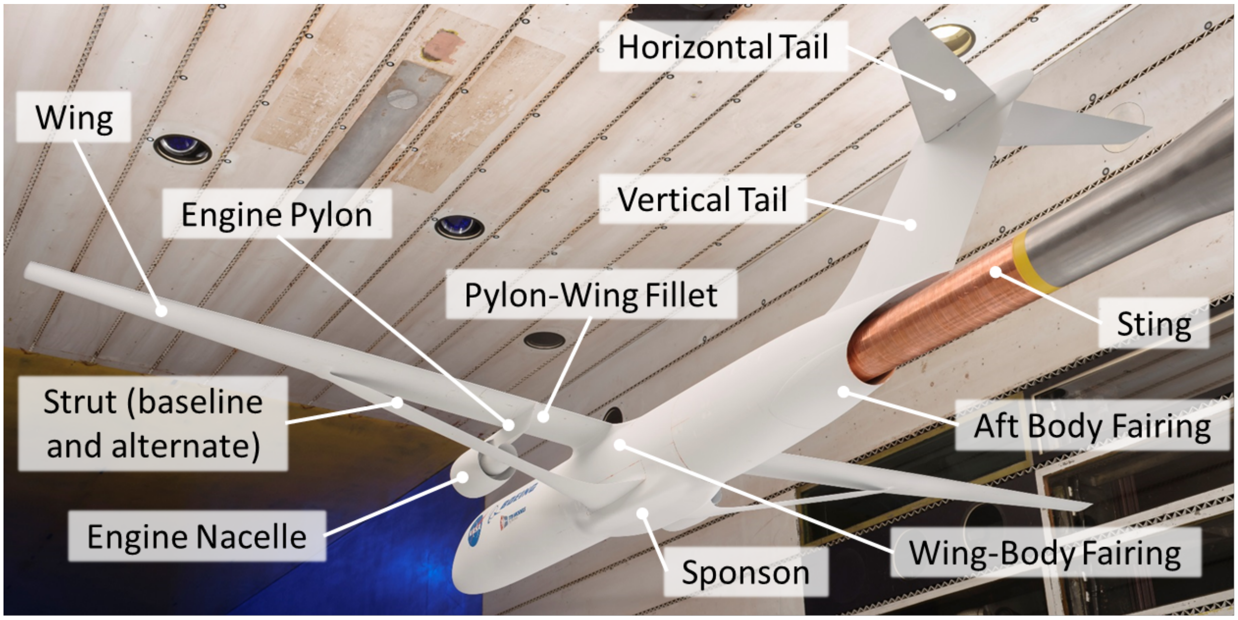

Figure 7.5 – Model Components.

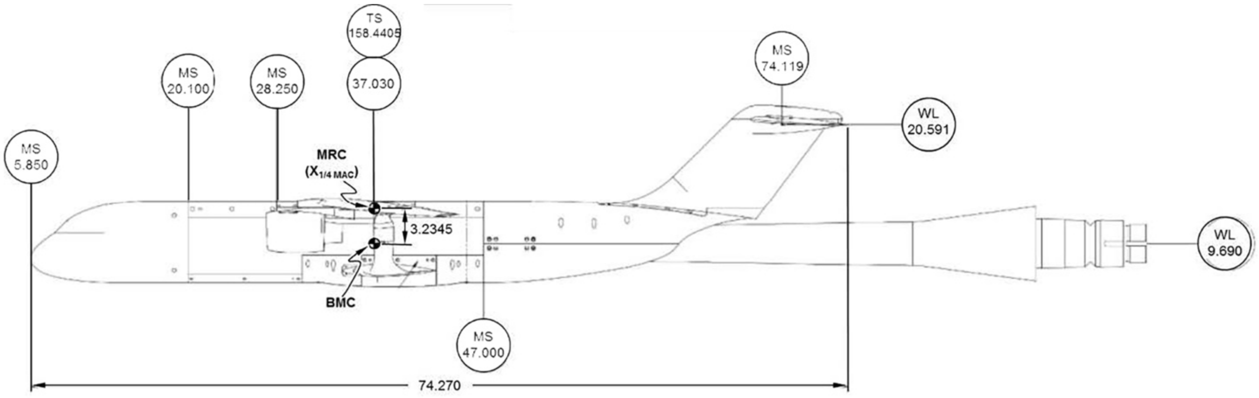

Figure 7.6 – Model Moment Transfer Diagram.

The various configurations analyzed in the test were represented by a series of configuration numbers in the run matrix. These configurations are described in Table 7.2.

Table 7.2 – Configuration Codes used in wind tunnel testing.

Config Name	Fuselage	Wing Bump	LG Fairing	Wing	Strut	Jury Strut	Nacelle, Core, Pylon	Vertical	Horizontal	Aft Body Fairing	Pylon Fairing	Alternate Strut
C1	X											
C2	X							X				
C3	X	X						X				
C4	X	X	X					X				
C5	X		X	X				X				
C6	X		X	X			X	X				
C7	X		X	X	X			X				
C8	X		X	X	X		X	X				
C9	X		X	X	X		X					
C10	X		X	X	X	X	X	X				
C11	X		X	X	X		X	X	X			
C12	X		X	X	X	X	X	X	X			
C13	X		X	X				X				X
C14	X		X	X			X	X				X
C15	X		X	X		X	X	X				X
C16	X		X	X			X	X	X			X
C17	X		X	X		X	X	X	X			X
C18	X		X	X								
C19	X		X	X						X		
C20	X		X	X				X		X		
C21	X		X	X	X			X		X		
C22	X		X	X	X		X	X		X		
C23	X		X	X	X		X	X		X	X	
C24	X		X	X	X		X	X	X	X	X	
C25	X		X	X	X		X			X	X	
C26	X		X	X	X		X	X			X	
C27	X		X	X			X	X		X	X	X
C28	X		X	X			X	X	X	X	X	X
C29	X		X	X			X	X	X		X	

* Shaded rows not tested

7.4 Wind Tunnel Data Reduction

Several different sources of data were acquired during the test in addition to standard force and moment balance data. The model was instrumented with a limited set of static pressure orifices, employed pressure-sensitive paint (PSP), and utilized infrared (IR) imaging. Model aeroelastic deflections were measured while the tunnel was operating using the NASA Model Deformation Measurement (MDM) system. Additionally, a selection of runs at the end of the test were dedicated to the investigations using surface oil flow visualization techniques, in which regions of potential flow separation were investigated in detail.

7.4.1 Pressure Sensitive Paint (PSP)

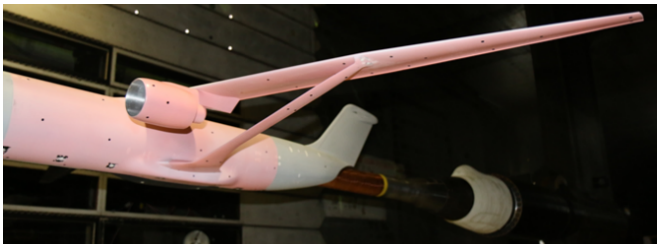

Figure 7.7 – The left-hand side of the model was coated with pressure-sensitive paint (on top of the base layer of primer) .

Upon arrival at Ames, the entire model was first painted with a grey epoxy primer coat. To ensure the longest test window in which the PSP would be effective, the active coat was applied to the left side of the model on top of the primer coat immediately prior to testing. (Figure 7.7) The pressure measurements obtained were compared to discrete surface pressure measurements taken using orifices at constant spanwise locations on the model. Data acquired by the PSP system was mapped onto a digital model of the aircraft geometry and the results are shown in Figure 7.8.

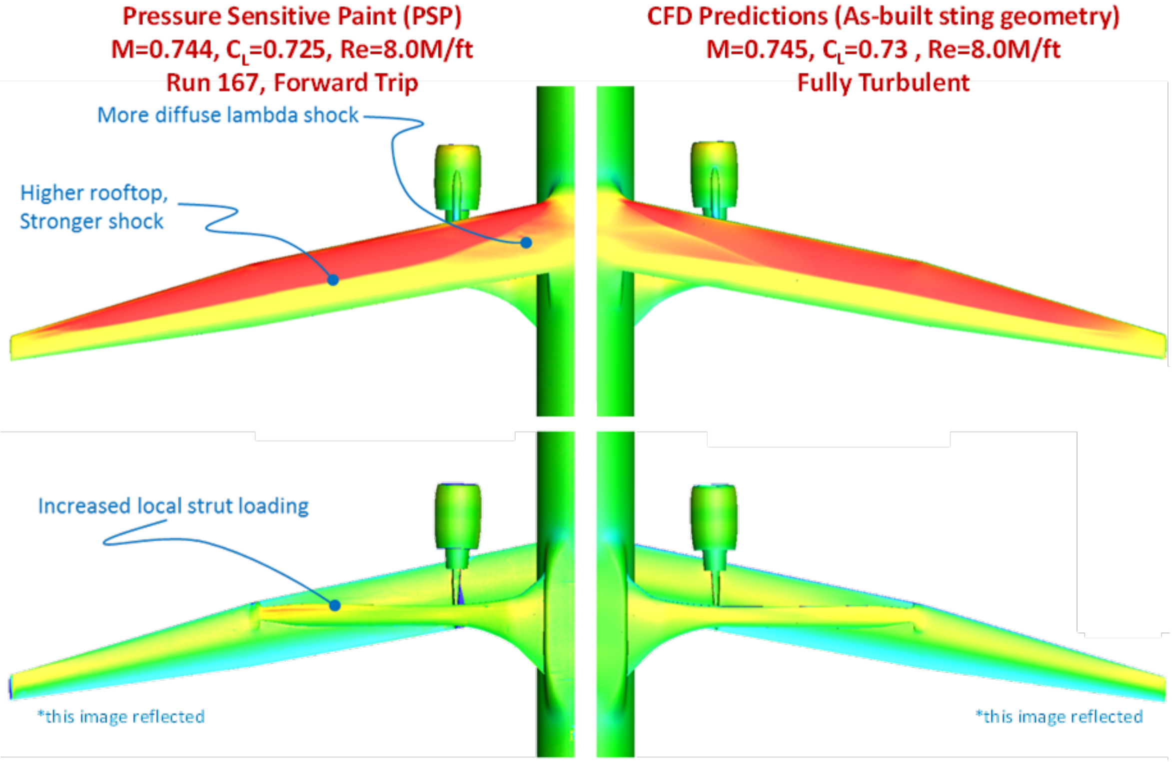

Figure 7.8 – Comparison of Pressure Sensitive Paint (PSP) with CFD Results.

7.4.2 Infrared (IR) Imaging

Figure 7.9 – The right-hand side of the model was coated with black paint to provide additional contrast for IR imaging (on top of the base layer of primer)

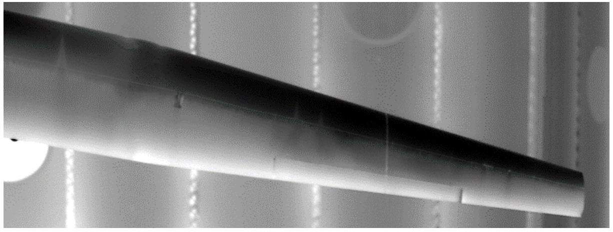

Figure 7.10 – Sample IR image showing aft trip.

The right-hand side of the model was coated with black paint (in addition to the base primer coat) to provide additional contrast for IR shock and boundary layer transition imaging on the wing and strut surfaces (Figure 7.9). A total of four cameras captured different views of the model (including the upper wing, Figure 7.10, lower wing, and lower strut surfaces. These views aided in qualitative determinations of boundary later trip effectiveness, shock location, and in the identification of potential areas of flow separation. Based on the IR imaging, it was determined that the boundary layer trips functioned as planned – ultimately the forward trip locations were selected for the duration of the test.

7.4.3 Tunnel Corrections

The wind tunnel data processed by the Ames 11-Foot TWT facility were based on the facility's standard set of corrections. These corrections included buoyancy, blockage (determined using the in-tunnel pressure measurement-based WICS system), and a model cavity correction. A sample of the data correction build-up for drag coefficient, lift coefficient, and pitching moment are shown in Figure 7.11 - Figure 7.13.

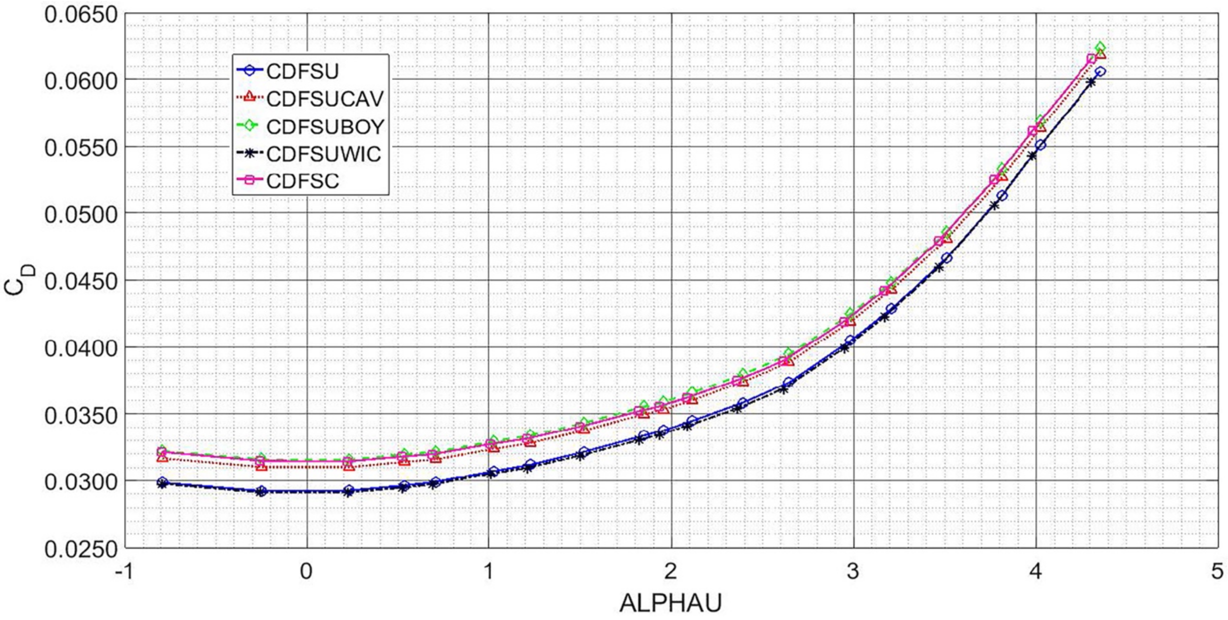

Figure 7.11 – Drag Coefficient Data Corrections for test data (Config 24, Run 381, M = 0.745, Re = 8.0M/ft).

The drag data presented in Figure 7.11 shows the relative size of the data corrections as applied to the drag coefficient for the baseline configuration (Config 24, Run 381). The cavity correction has the largest effect on the raw data, with a delta drag coefficient of ~15-20 cts depending on the vehicle angle of attack. The tunnel blockage and buoyancy corrections' effect on drag was comparatively small, with a net effect of ~1-2cts. The correction to lift coefficient (Figure 7.12) is also relatively small since the high aspect ratio model has a relatively small effect on tunnel blockage and therefore, a small effect on the flow's dynamic pressure local to the model. As described in more detail in Section 7.5.2, a significant change in pitching moment of the model (Figure 7.13) results from effects associated with the model installation on the sting. Corrections to the remaining force and moment coefficients were negligible. Figure 7.14 shows the magnitude of the of the cavity correction as a function of lift coefficient for configuration 24 for the wind tunnel and computational data. There is excellent correlation between these corrections.

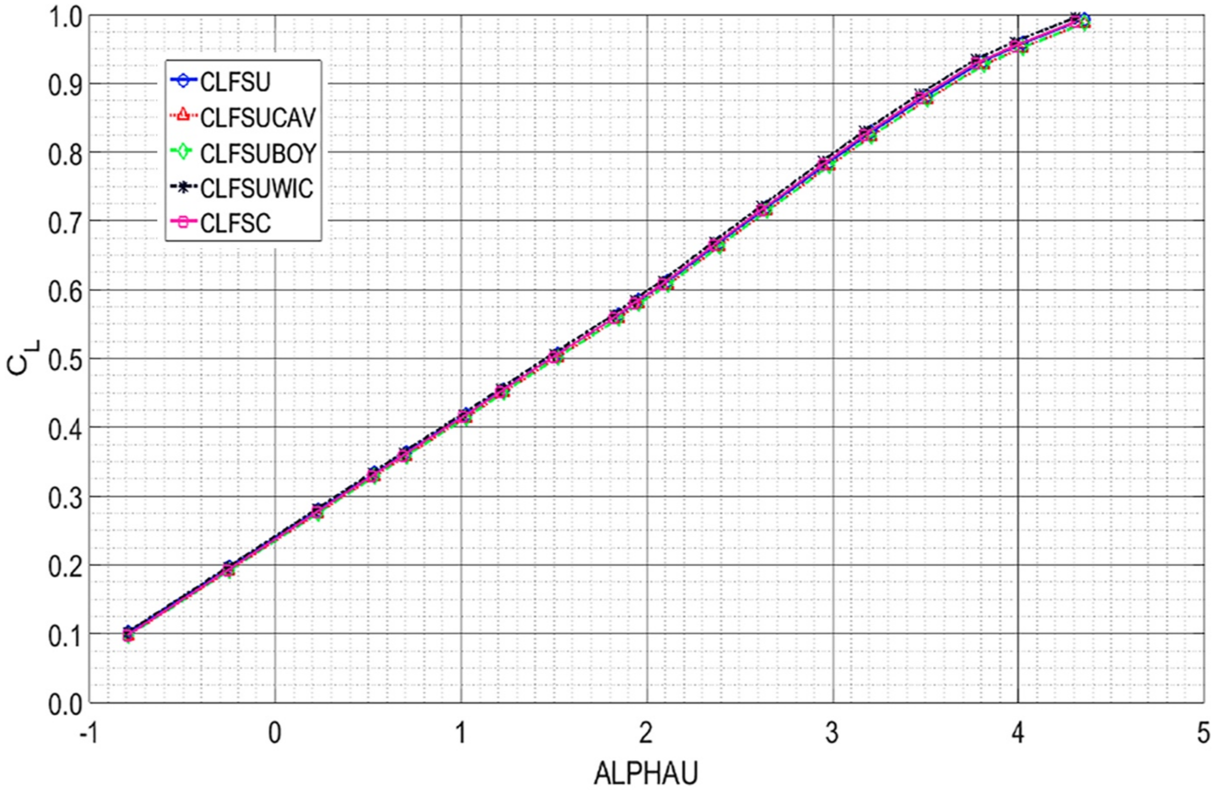

Figure 7.12 – Lift Coefficient Data corrections for test Data (Config 24, Run 381, M = 0.745, Re = 8.0M/ft) .

The data presented in Figure 7.14 shows that the computed magnitude of the fuselage cavity correction was shown to be in good agreement with the magnitude of the cavity correction measured during wind tunnel testing. This suggests that the cavity's effects were accurately captured in the CFD model's drag bookkeeping.

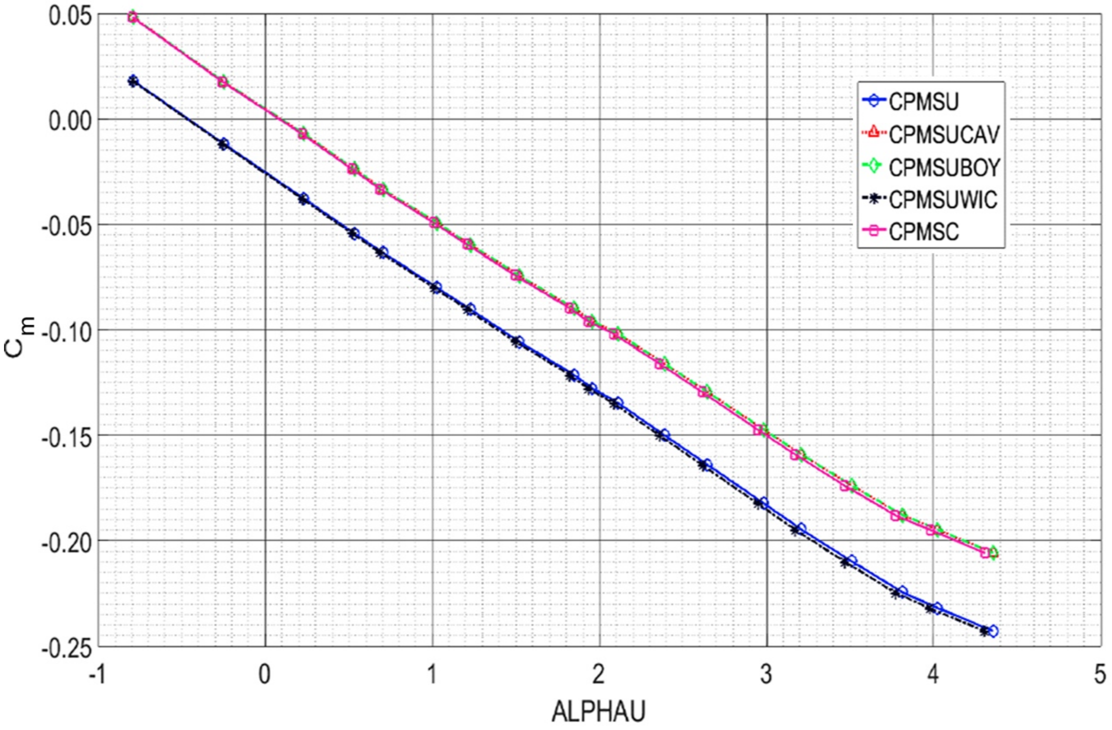

Figure 7.13 – Pitching Moment Data Corrections for test data (Config 24, Run 381, M = 0.745, Re = 8.0M/ft).

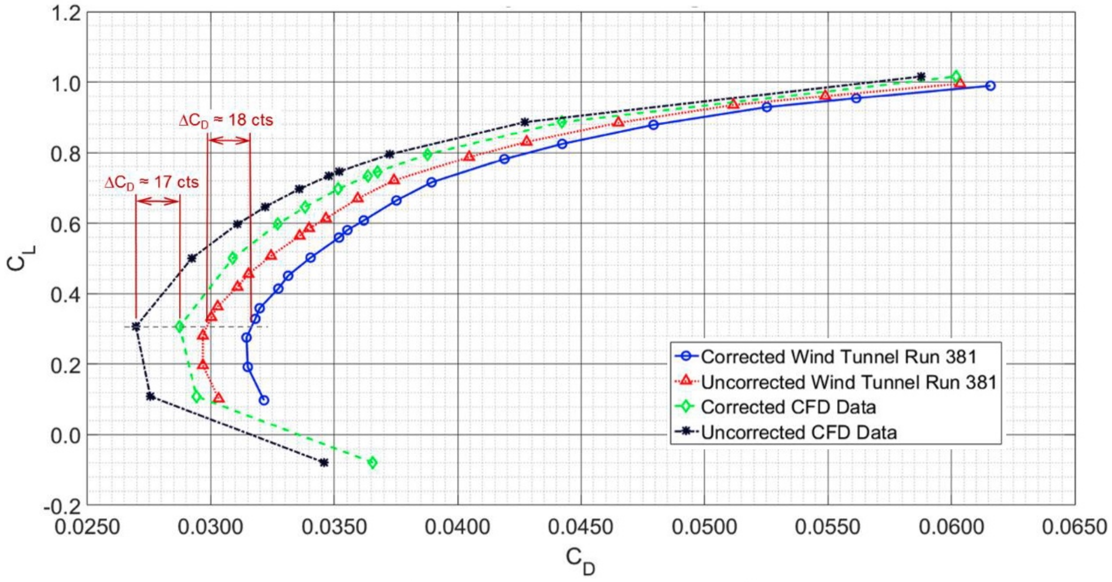

Figure 7.14 – Cavity Correction Magnitude (As-built geometry, including aft fuselage fairing. Config. 24, Run 381, M = 0.745, Re = 8.0M/ft).

7.4.4 Model Roughness Effects

The surface paint and primer coatings applied to the model were selected prior to testing to enable the collection of IR and PSP data. However, during the test, it was determined that the black IR paint coat, which covered the wing and strut (including the leading edges), had a substantially higher roughness level than anticipated. The IR coat was measured to have a surface roughness ranging from 120-140µin, depending on location. Comparatively, the grey epoxy coat had a roughness of 60µin prior to PSP application. The epoxy coat verses IR paint roughness difference led to a significant asymmetry in the model yaw and rolling moment coefficients. To reduce the effects of the roughness, the IR side of the model was sanded. Post-sanding values for roughness of the black paint reduced it to between 100-110µin (depending on the location). This level of roughness was similar to the estimated 100µin for PSP. Following the removal of the IR and PSP paints and additional sanding of the model, the leading-edge surface roughness was reduced to ~50µin on both the left and right wings. While this level of roughness was higher than was desired, it became the best achievable condition short of stripping the primer, which could not be realistically accomplished given the test window.

Based on the concerns noted during the wind tunnel test and the associated challenges in determining absolute levels of aircraft performance for a given level of roughness, empirical data from Schlichting (Figure 7.15) can be used for first-order quantification of allowable levels of model roughness (note: the y-axis is 1000 times the admissible roughness height, i.e., mm rather than µin). This target level can then be compared to values measured on the TTBW wind tunnel model. According to Schlichting, for the range of chord Reynolds numbers tested (~1.6-3.3M) and given a mean aerodynamic chord of 4.96" (126mm) the range of maximum roughness values varies from ~0.003-0.008mm (118-315 µin). These numbers are however for a flat plate at zero incidence and should not be considered as the absolute level for allowable model roughness. The values, do however highlight the severity of discrepancy from the original state of the painted model (roughness of approximately 140µin) as well as to the final surface finish of the model (roughness of ~50µin). Without more detailed analysis, it is not possible to truly quantify what level would be acceptable, it does suggest that the model performance may still be strongly affected by its current state, and may hinder absolute comparisons of performance level relative to computational methods and predictions.

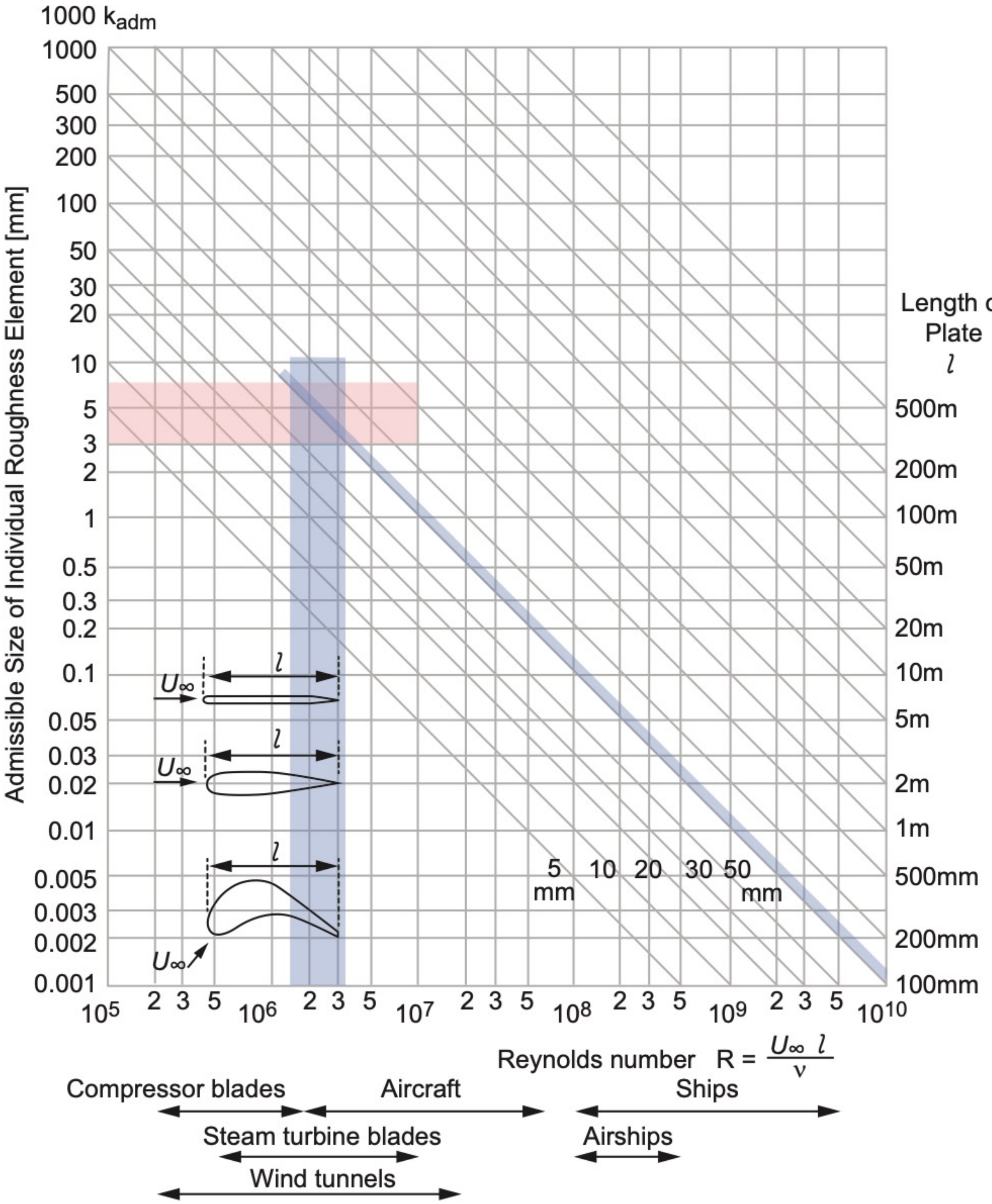

Figure 7.15 – Admissible roughness for aircraft wings (14).

The force and moment data in Figure 7.16 - Figure 7.18 show the effect on aircraft performance due to changes in surface roughness for the wing, strut, engine/pylon, and vertical-on configuration over a range of Reynolds numbers. The results indicate effects consistent with a forward displacement of the wing shock for surfaces with higher roughness. This roughness promotes a more rapid growth of the boundary layer, which effectively increases the local airfoil thickness. As a result, the flow accelerates more quickly, reaching a critical condition at a more forward location on the wing. In the lift coefficient, this manifests as a decrease in lift at a given angle of attack as airfoil loading is reduced. The forward shock movement also drives pitching moment more nose-up as the airfoil becomes more forward loaded. Since some configurations tested were not symmetric in roughness between the left and right sides of the model, a strong rolling moment is also present. Drag coefficient decreases proportionally as roughness decreases due to reductions in skin friction.

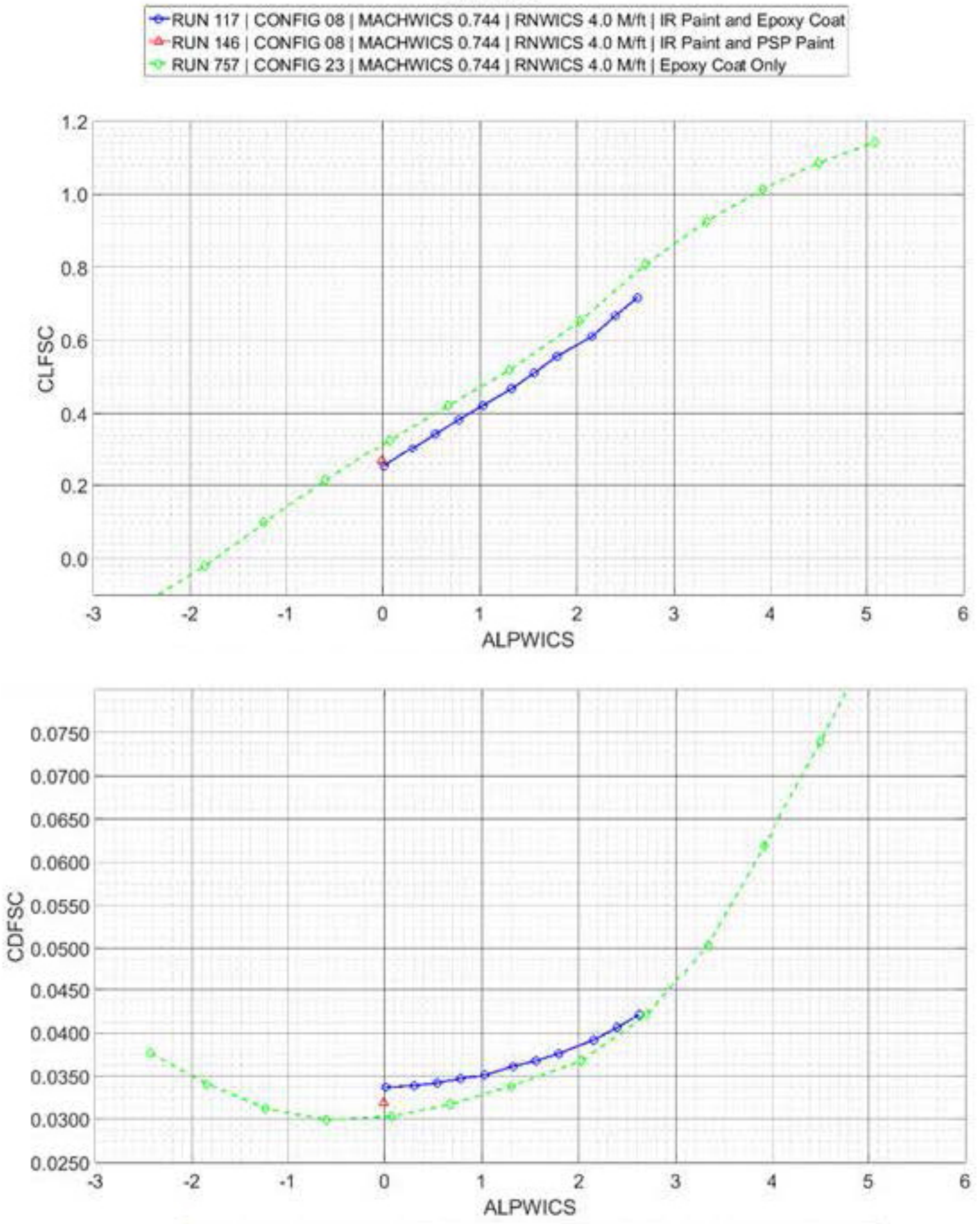

Figure 7.16 – Force and Moment Coefficients comparing the effects of model roughness (Re = 4.0M/ft).

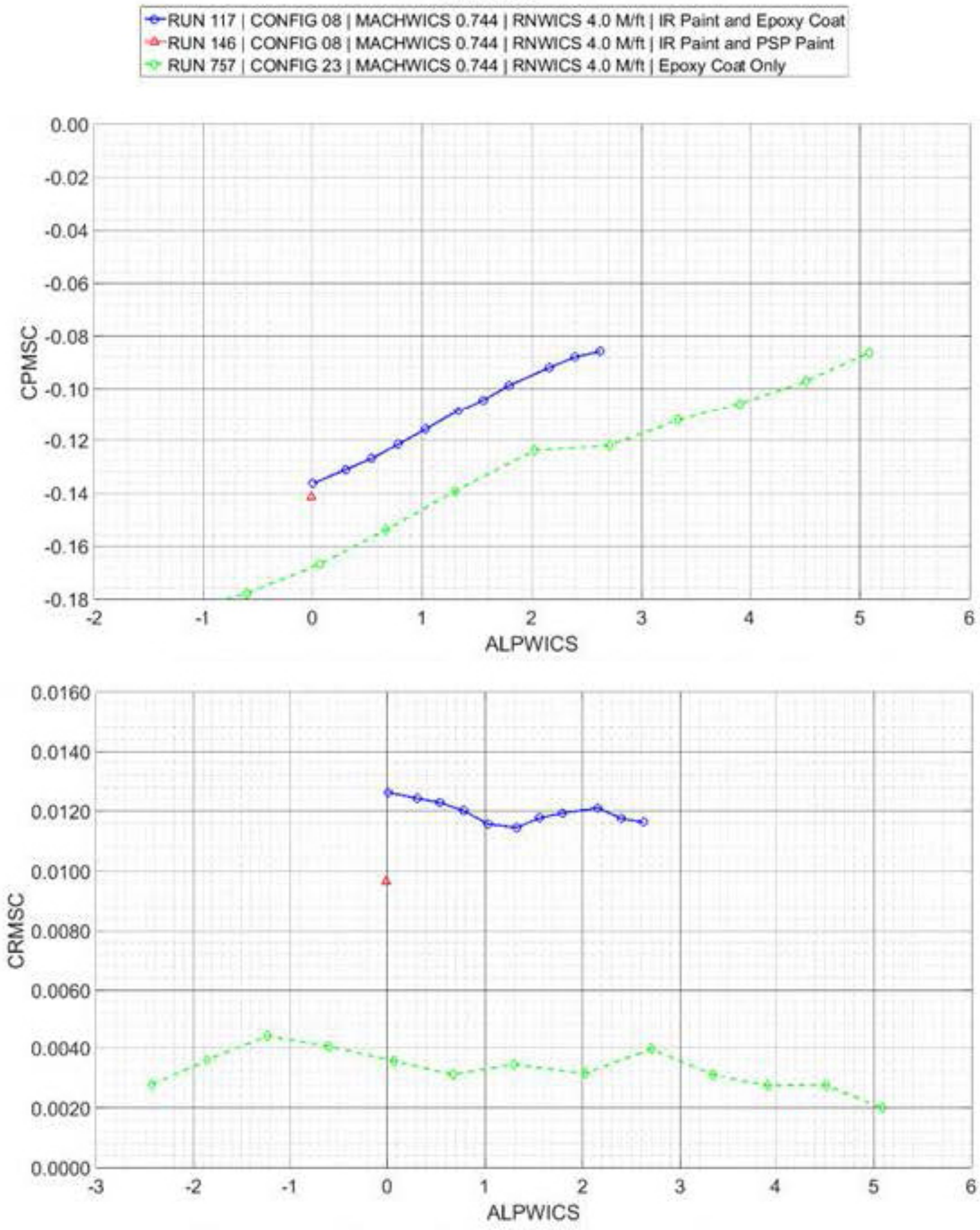

Figure 7.16 – Continued.

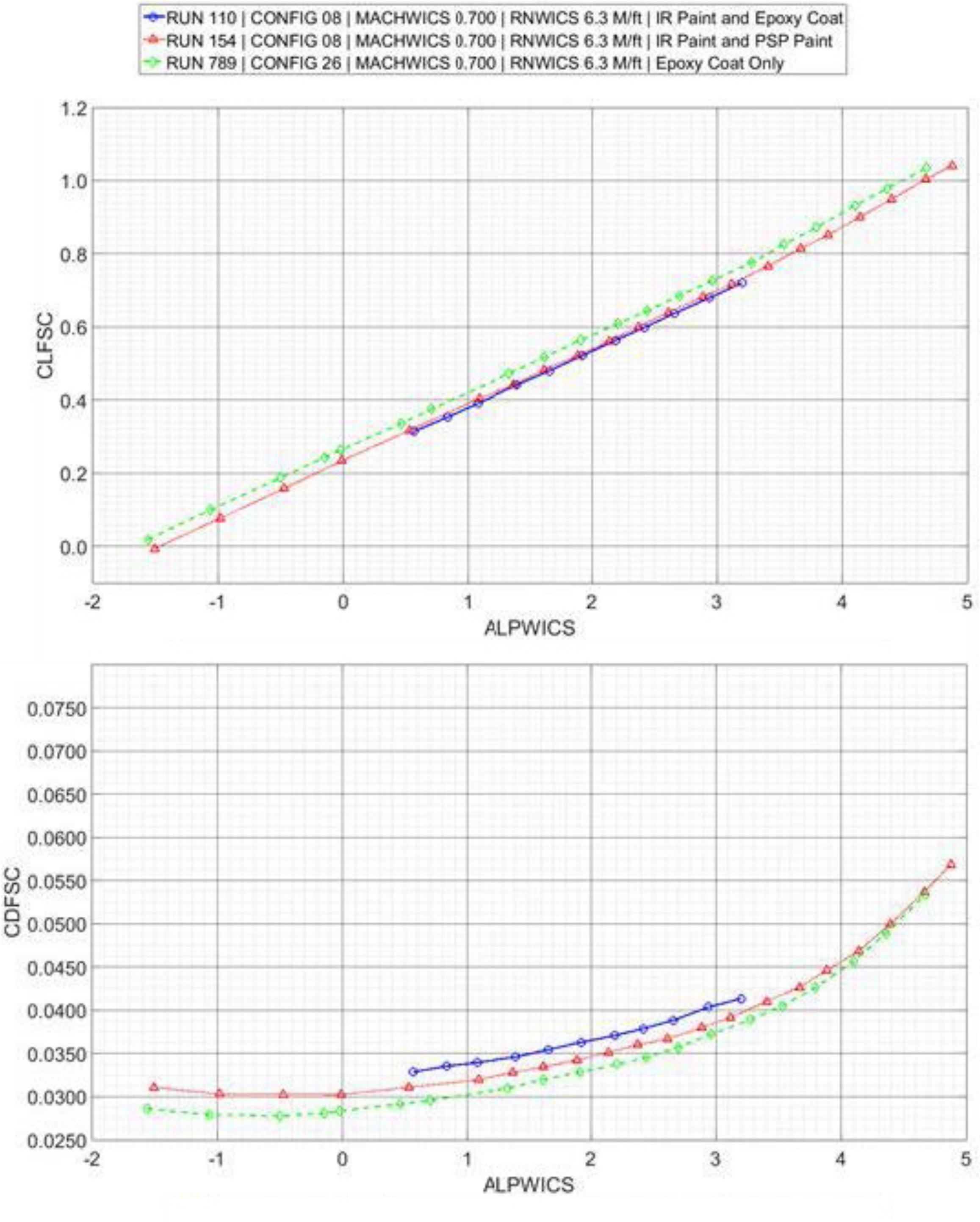

Figure 7.17 – Force and Moment Coefficients comparing the effects of model roughness (Re = 6.3M/ft).

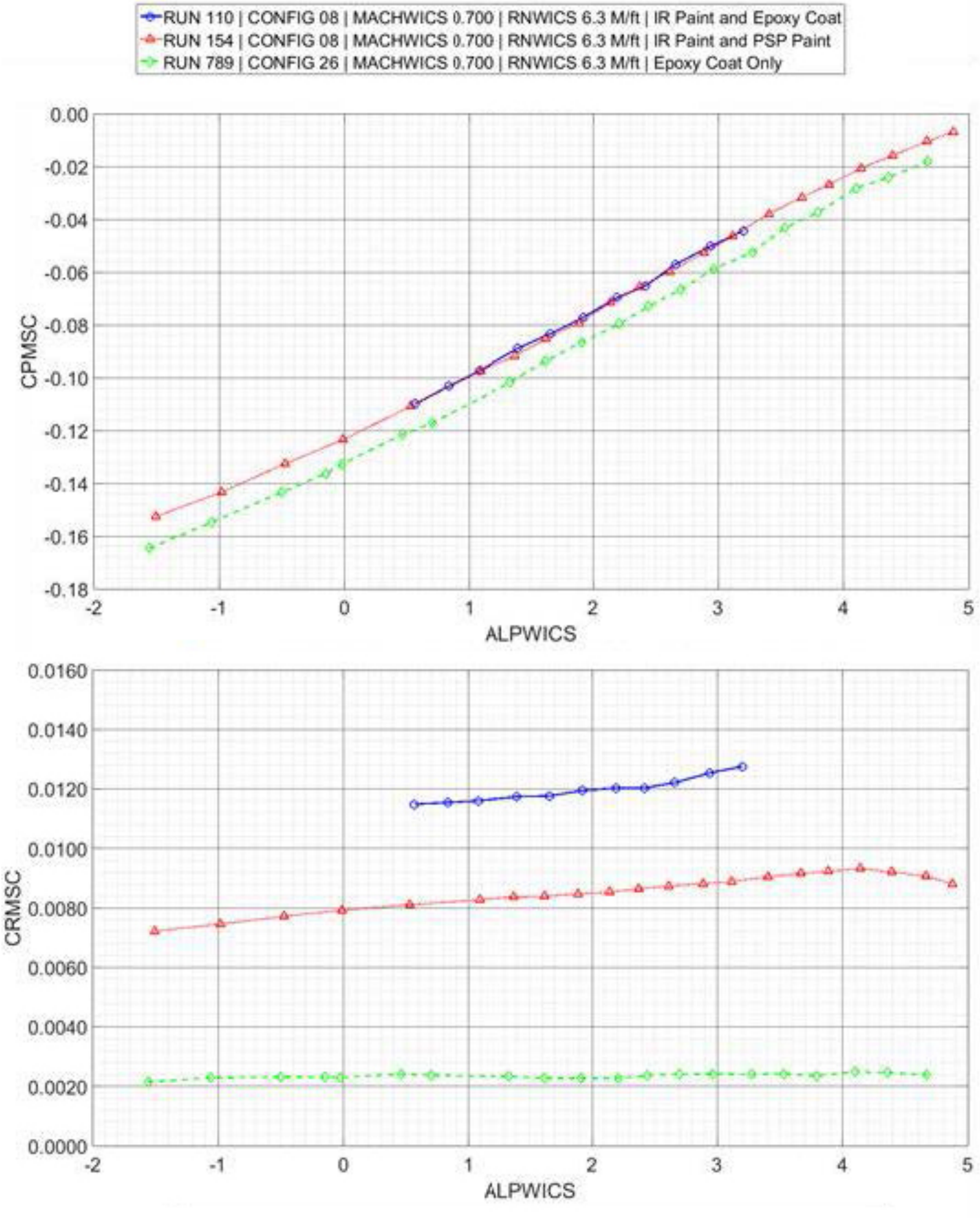

Figure 7.17 – Continued.

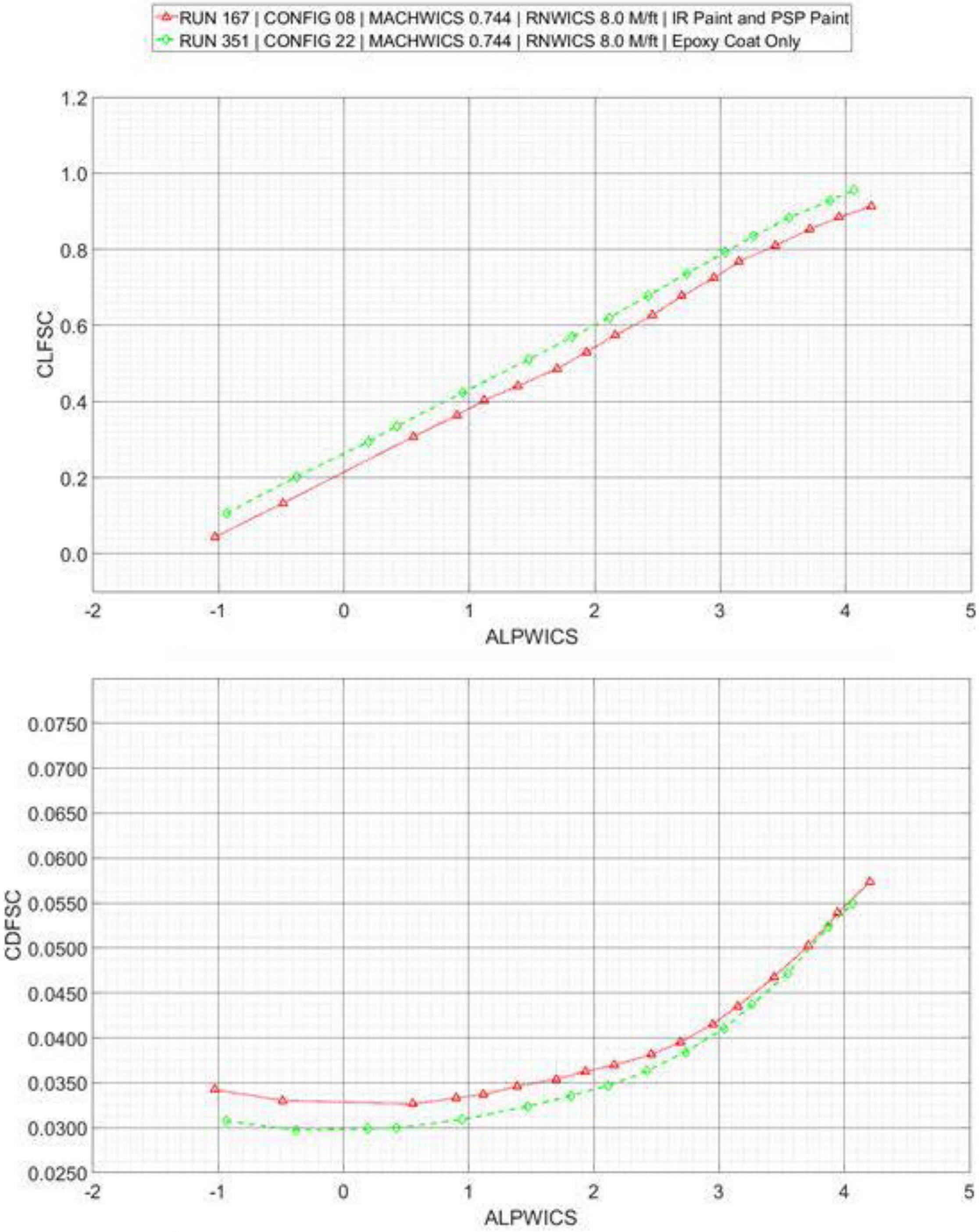

Figure 7.18 – Force and Moment Coefficients comparing the effects of model roughness (Re = 8.0M/ft).

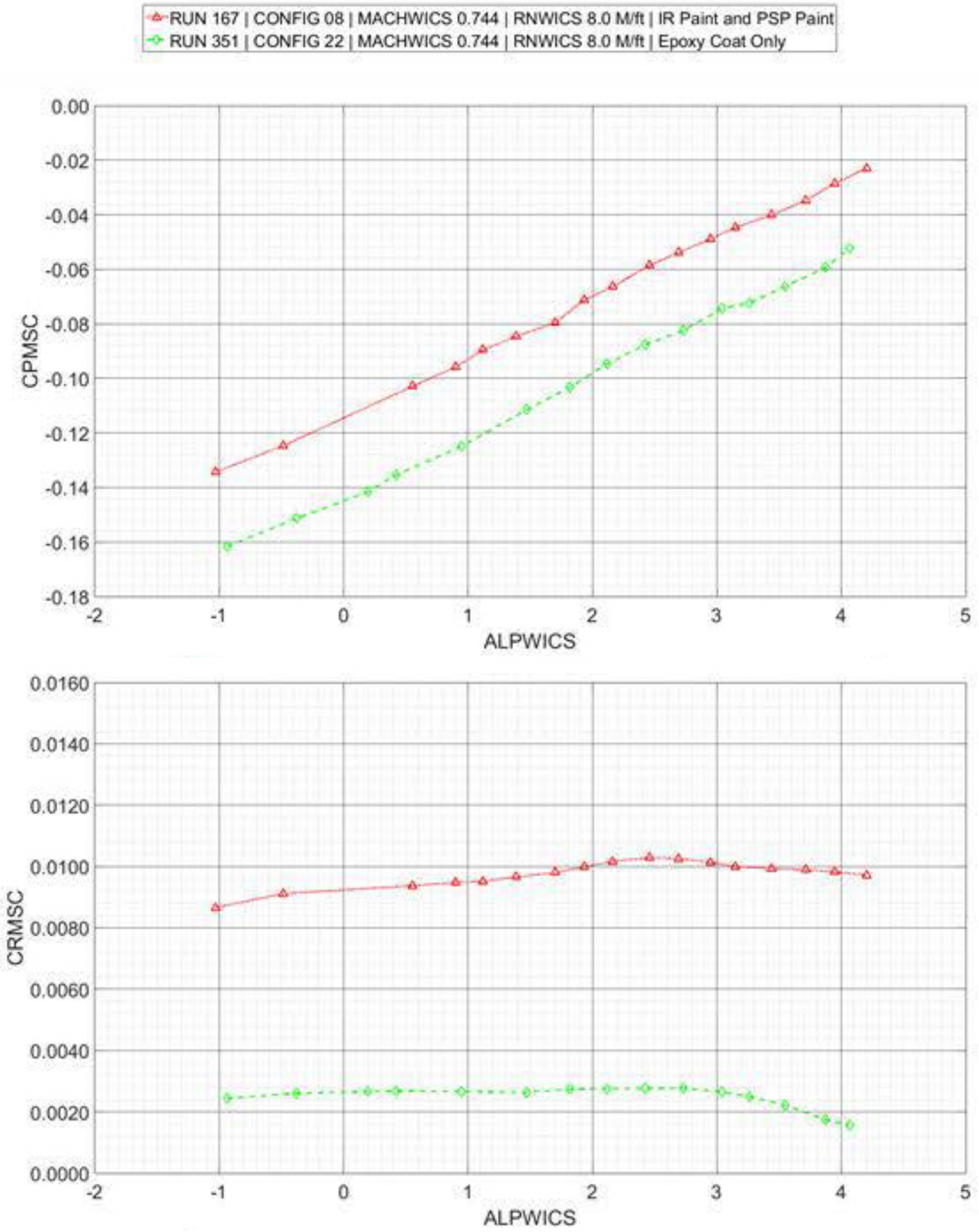

Figure 7.18 – Continued.

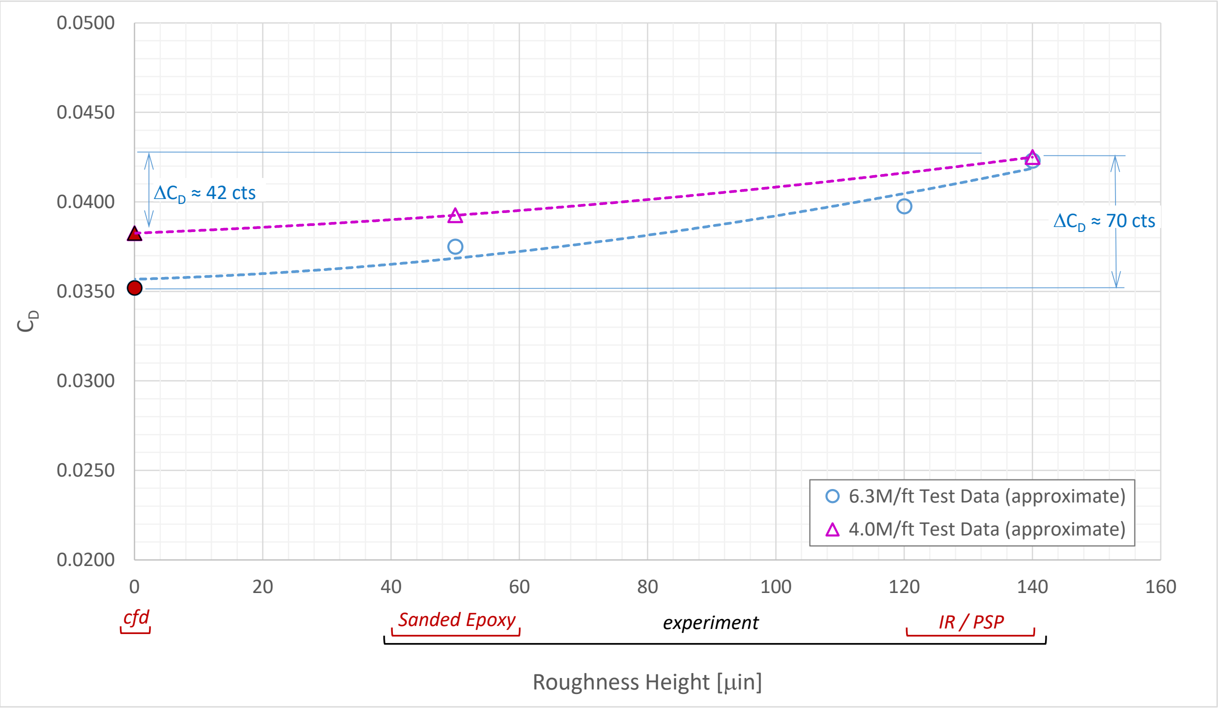

Figure 7.19 – Effects of Roughness on model drag for constant unit Reynolds Number (approximation).

The data from Figure 7.16 - Figure 7.18 were combined with CFD predictions of the as-built model geometry operating at wind tunnel conditions to create an approximate quantification of the effects of roughness on the model. The relationship presented in Figure 7.19 is based on a quick linear interpolation of the results for each run, which for each series is at the same Mach, C_L, and unit Reynolds number. Absolute values of drag obtained from CFD should not be considered 'gospel truth' as variations in the turbulence model or spatial discretization method can have a significant impact on these results. In addition, the roughness values for each run are approximate as it is not possible to accurately quantify the average roughness of the entire model – different areas on the model have different roughness levels. However, when combined with CFD-based 'zero-roughness' results, these results show a strong correlation to roughness height, with drag decreasing with each subsequent reduction in model roughness. This correlation continues to hold as the data exhibits the expected increase in sensitivity to roughness when operating at higher unit Reynolds numbers as evidenced by a larger change in drag from the highest to lowest roughness level for the 6.3M/ft runs.

Additional evidence for roughness effects is presented in Figure 7.20, which shows the pressure coefficient measurements obtained by PSP and pressure taps as compared to CFD projections. In this figure, the surface pressure measurements from the (right-hand side) wing coated in infrared high-contrast paint (IR taps) are compared to surface pressures from the model (left-hand side), which is coated in pressure sensitive paint (PSP taps). These plots show that measured shock location is well forward of CFD predictions, and pressure rooftop values higher than predicted. These effects are consistent with increased model roughness.

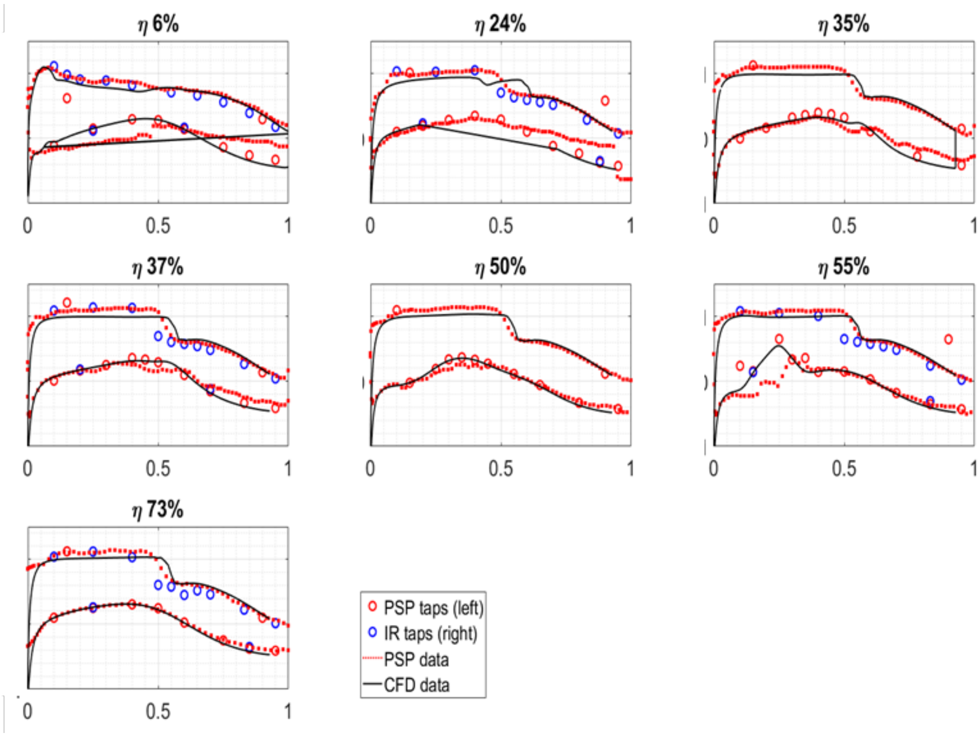

Figure 7.20 – Comparison of pressure data on the wing (x-axis is chord, y axis is pressure coefficient).

7.4.5 Model Deformation Measurement (MDM) System Results

The deformation of the model from a static state was determined using a photographic-based system. This system tracks the movement of targets applied to the wind tunnel model and determines the relative model twist at discrete span stations where targets are applied (Figure 7.21). Data for the twist could be acquired simply from a single image with reduced accuracy, or from a 10-image average with a significant amount of manual labor.

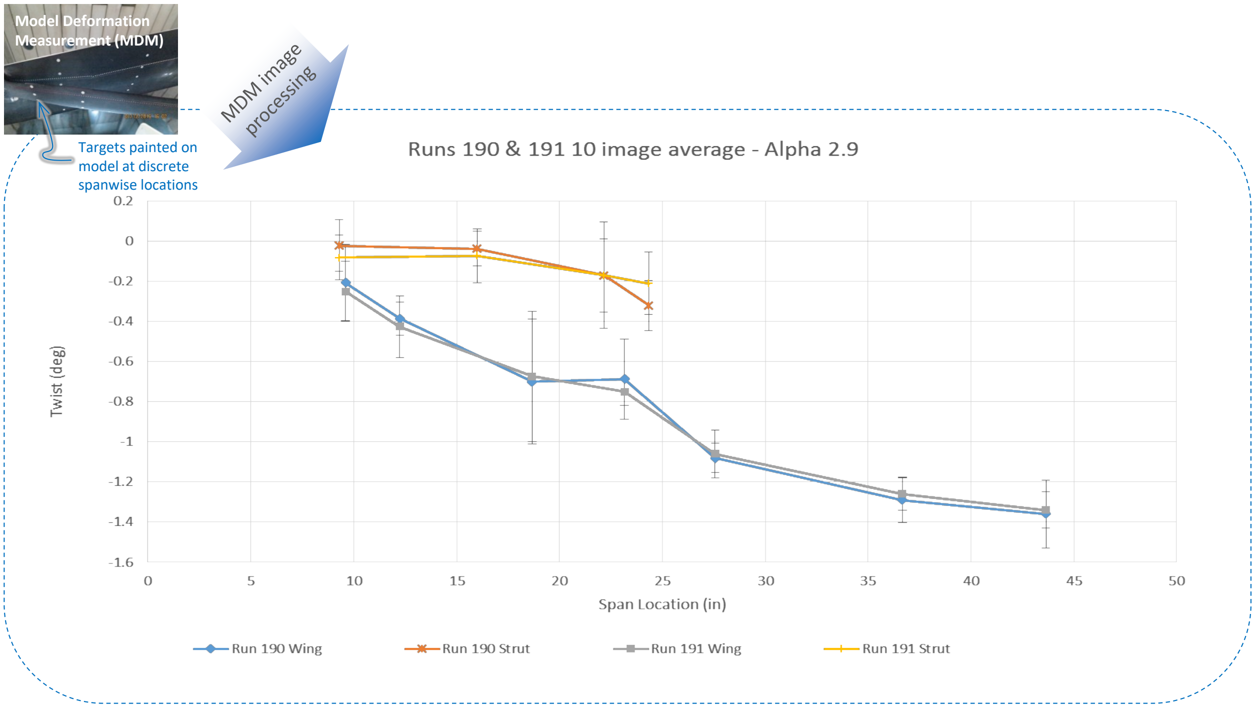

Figure 7.21 – Model Deformation Measurement (MDM) System.

The data shown in Figure 7.22 shows the progression of data quality output by the MDM system starting with the original data provided by NASA. The MDM data went through a reprocessing step in which errors in marker positions were rectified, improving the data quality. The final set of data shows that producing a 10-image average produces the smoothest twist distribution and also provides a confidence interval on the measurement based on statistical analysis. While the potential error bandwidth is still large relative to the measurements, repeat runs of the same geometry measure very similar twist changes. The MDM collected data were combined with the 'as-built' model measurements provided by TriModels to produce an 'as-tested' geometry.

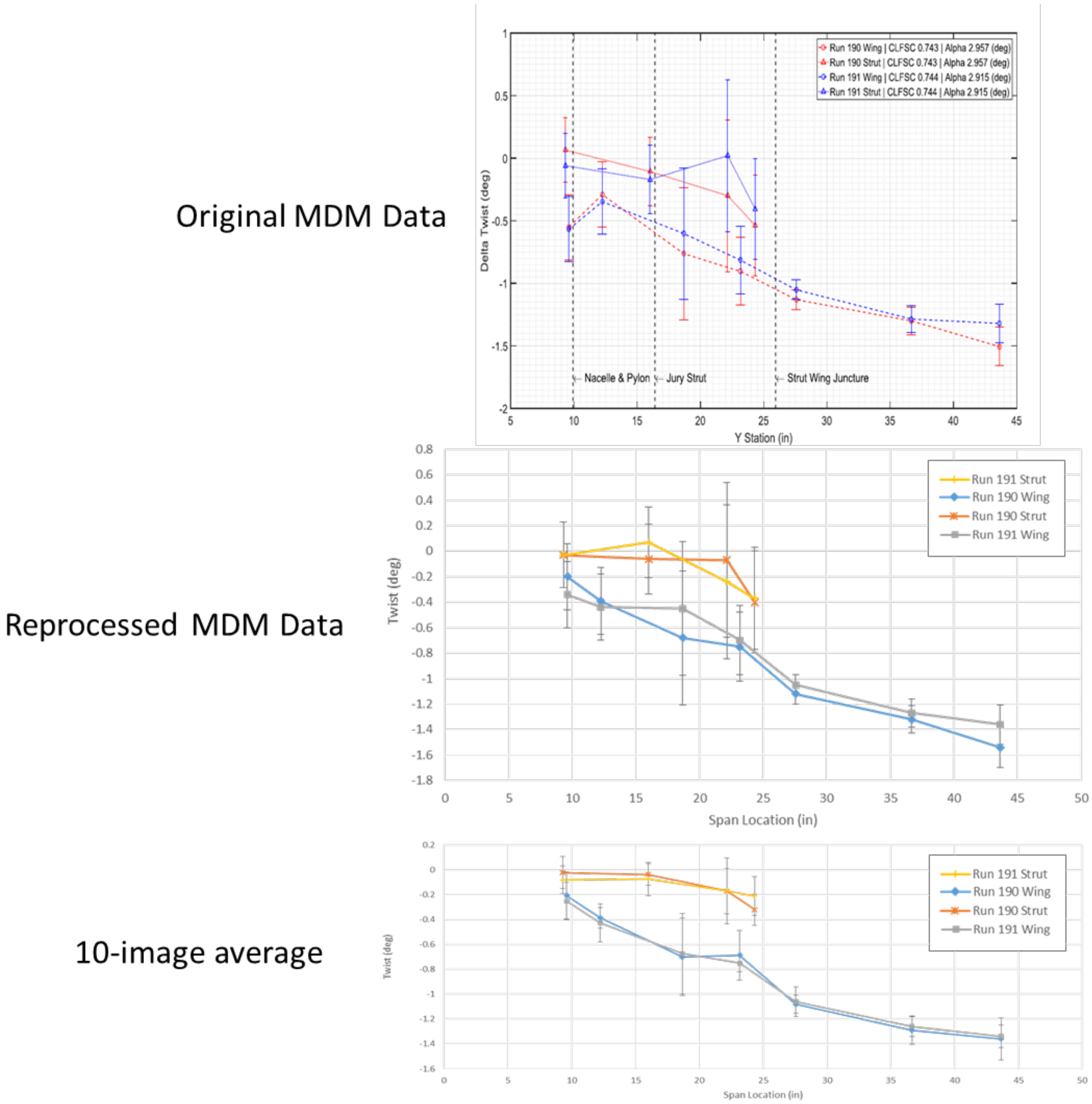

Figure 7.22 – Data acquired by NASA Model Deformation Measurement (MDM) System.

7.4.6 Boundary Layer Trip Effects

The model was tested with a series of boundary layer trip locations with the goal of achieving similar drag divergence Mach number and compressibility drag as the flight condition. The locations tested included: no trip, forward trip, and aft trip locations. As shown in Figure 7.23 there are significant laminar runs when the wing is untripped, due to the low leading-edge wing sweep, laminar-friendly pressure distributions, and small model scale. The forward trip is effective in moving the transition location fully forward across a wide range of conditions. The aft trip shows varied results based on the condition being tested – in some conditions the trips are useful, but in the majority of cases transition occurred prior to the trip location. It was decided that the unpredictable extent of laminar flow from the aft trip would decrease the repeatability of the data over a range of conditions and duration of the test. Therefore, the forward trip location was selected for the remainder of the test.

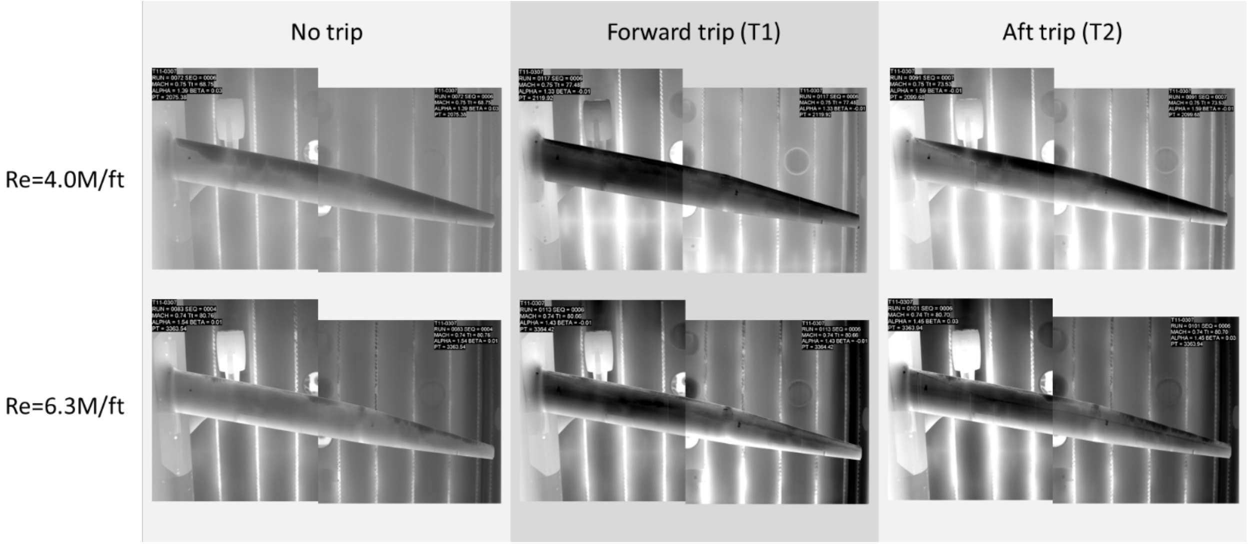

Figure 7.23 – Infrared (IR) Images of Boundary Layer Trip Effects.

The effect of the trips on the vehicle lift and drag performance are presented in Figure 7.24. As expected, the ‘No trip’ configuration had the lowest drag as it allowed for the longest laminar run. Conversely, the forward trip had the highest drag.

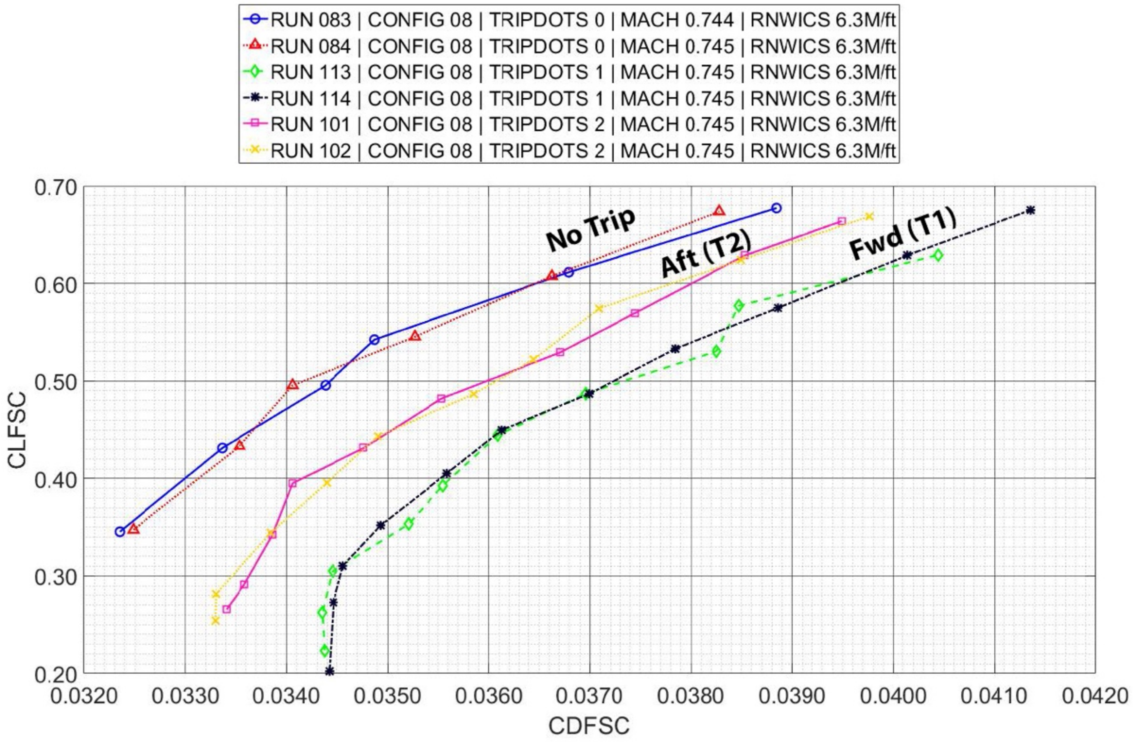

Figure 7.24 – Effects of Boundary Layer Trip Location.

7.5 Post-Test CFD Investigations

During the test, several high-priority items were identified for more detailed investigations following the completion of the test entry. Because of the model's high-aspect ratio and increased potential for aeroelastic effects under load, measurements from the NASA MDM system were used to help determine the shape of the model while performance data were being acquired. In addition, cavity pressure variations caused by model fuselage-sting interaction were experienced in the tunnel, which led to an increased interest and higher fidelity modeling at the aft end of the model. These items were examined in detail using computational methods.

7.5.1 Model Twist Correction

The deflected wind-on geometry of the model while it was being tested (i.e. the aerodynamically loaded shape) was engineered by a process designed to produce the desired twist at the design Mach and lift coefficient. This process adjusted the designed '1g' loft based on results of aeroelastic analysis to produce a target jig geometry for the model vendor to manufacture. Under load, this geometry would ideally exactly represent the target 1g geometry. To aid in the determination of the 'as tested' geometry, a Model Deformation Measurement (MDM) system was used to measure the wing deflection during testing. Additionally, a detailed scan of the as-installed model was taken by NASA personnel using a FARO laser-scanning system. The accuracy of this process was quantified by determining the final geometry tested in the tunnel. Adjustments to the CFD models were made to account for the 'actual' model twist.

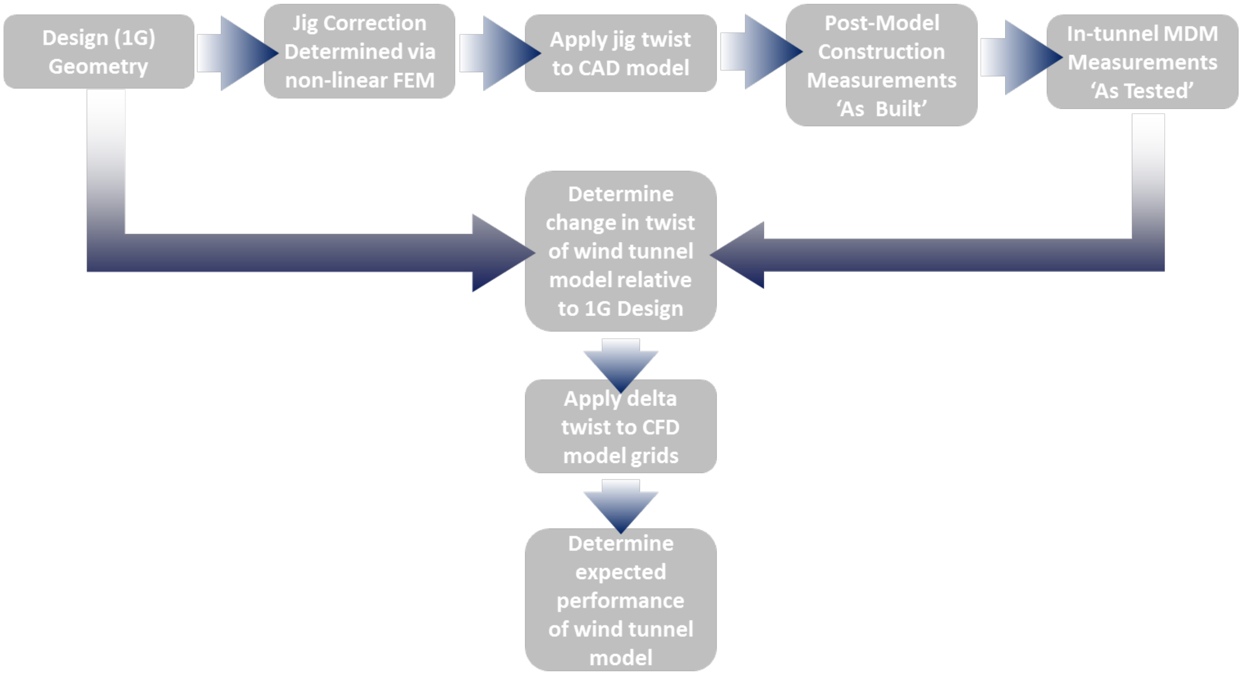

Figure 7.25 – Model Deformation Process.

Since the vertical shearing of the wing sections due to wing bending produces a secondary effect on wing performance, this element was neglected. This was particularly true for the wind tunnel model, which had a higher stiffness than a representative flight article.

7.5.1.1 1g to Jig Geometry

Since the high aspect ratio wing was more prone to aeroelastic effects than typical configurations, a detailed nonlinear finite element model (FEM) of the wind tunnel geometry was constructed by Boeing. The results of this analysis (shown in Figure 7.26), provided a model twist modification that would be applied to the design geometry to produce the targeted 'Jig' geometry. The FEM analysis showed that as the wing was loaded (as lift coefficient was increased) the wing load-relieved, washing out the twist of the wing at the tip. The application of the predicted twist change to the design geometry was executed in CATIA utilizing its shape deformation capability. The resulting Jig geometry was provided to the model vendor for model fabrication.

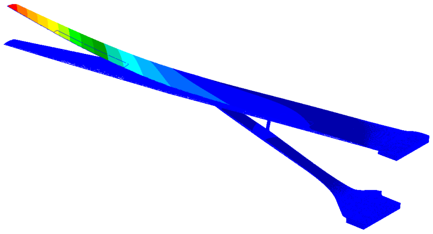

Figure 7.26 – Nonlinear FEM was used to determine the 1G-to-jig Twist Conversion.

7.5.1.2 As-built Measurements

Measurements were taken of the wind tunnel model following manufacture by the model vendor TriModels Inc. (TMI). The measurements were taken using a FARO system with a touch ball. The measurements quantified the contour of the model, and determined the rigging and relative twist of the model wing and strut as installed. The data suggests that the right-hand airfoils are slightly thinner than the left hand airfoils. This will cause a small degree of negative rolling moment for the model. When examining the final twist distributions of the wing and strut (Figure 7.27), a small discrepancy in left-right wing twist is evident, which would create a tendency to have a small positive rolling moment.

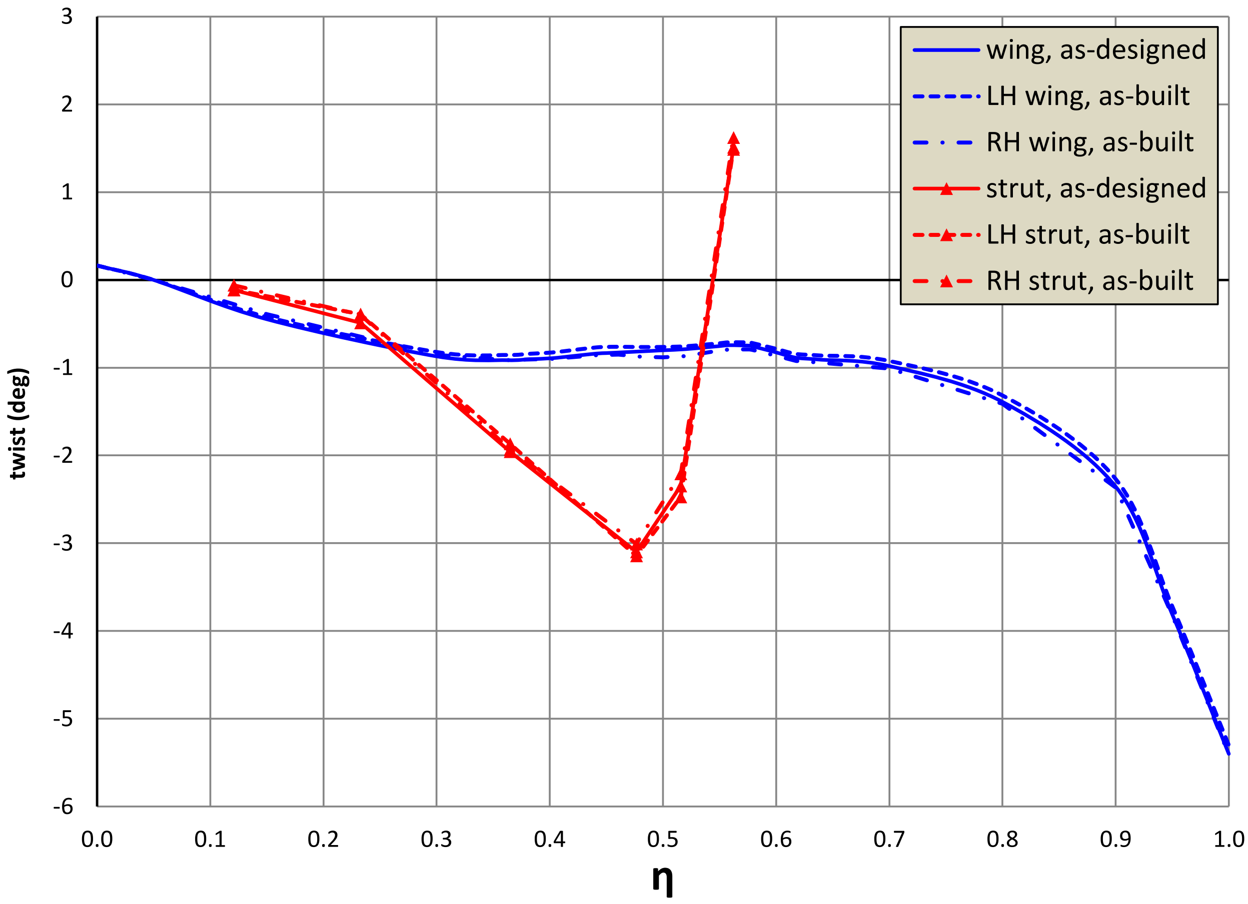

Figure 7.27 – Post-shim wing and strut twist measurements from TriModels as compared to desired loft show good agreement.

Examination of the post-manufacture wing twist led to a minor shimming of the left hand wing. This was required since the heat treat of the left wing resulted in a small amount of warpage. The final wing and strut twist comparison (Figure 7.27) shows that the left- and right-hand wings had minor deviations in twist relative to the desired geometry. The effect of this twist difference was predicted to be small, and well within the reasonable expectations for the manufacture of such a thin high-aspect-ratio wing and strut. These 'as-built' results were then combined with aeroelastic measurements taken in the tunnel during testing to produce the 'as-tested' geometry, which was Boeing's best possible estimate of model geometry during the test.

7.5.1.3 Twist Predictions for 'as-tested' Geometry

By combining the target jig twist (determined via FEM), model measurements taken by TMI, and MDM measurements taken during testing by NASA personnel, a final 'as tested' geometry could be determined. The absolute values of the twist distributions obtained via the sequence defined in Section 7.5.1 were then compared with the original design (1g) geometry twist to determine a net twist change.

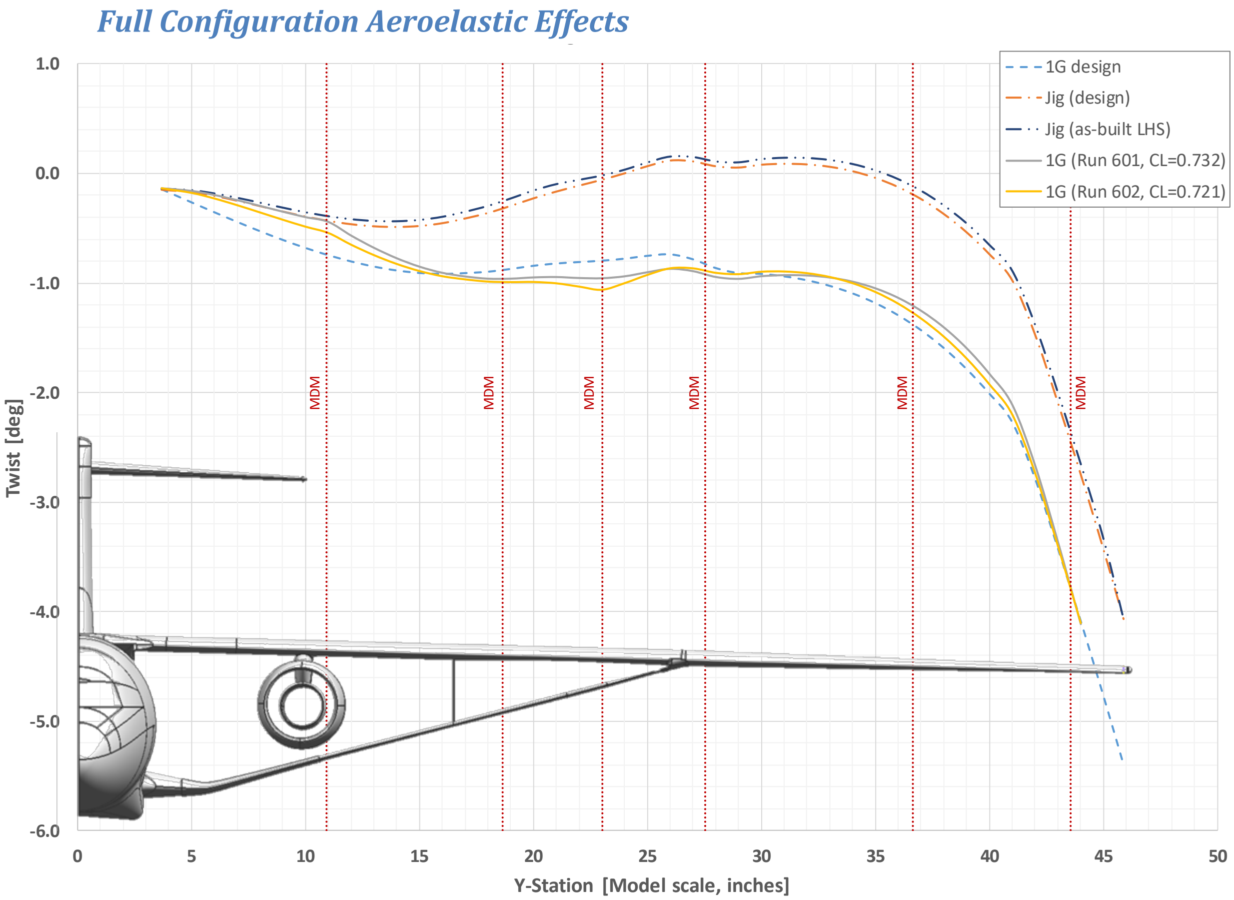

Figure 7.28 – Wing Twist Distribution from MDM measurements in tunnel within 0.3deg of target 1G distribution.

The results of the process to determine the final model twist in the tunnel for Run 601 and 602 (Re=8M/ft, C_L≈0.73) are shown in Figure 7.28 and Figure 7.29. The twist distributions obtained via this method from the repeat runs resulted in consistent twist distributions as determined by the MDM data. The wing twist is within 0.3 deg of the target twist, whereas the strut twist seems to deviate more midspan as compared to the design. It should be noted that the resulting twists should be considered as a ‘best guess’ for the model geometry as data were being collected in the tunnel. Despite the number of measurements taken, there are significant portions of the wing and strut span where MDM data were not taken. It is recommended that future testing consider a greater number of spanwise locations at which to collect data so a more comprehensive twist distribution can be obtained but at fewer overall conditions.

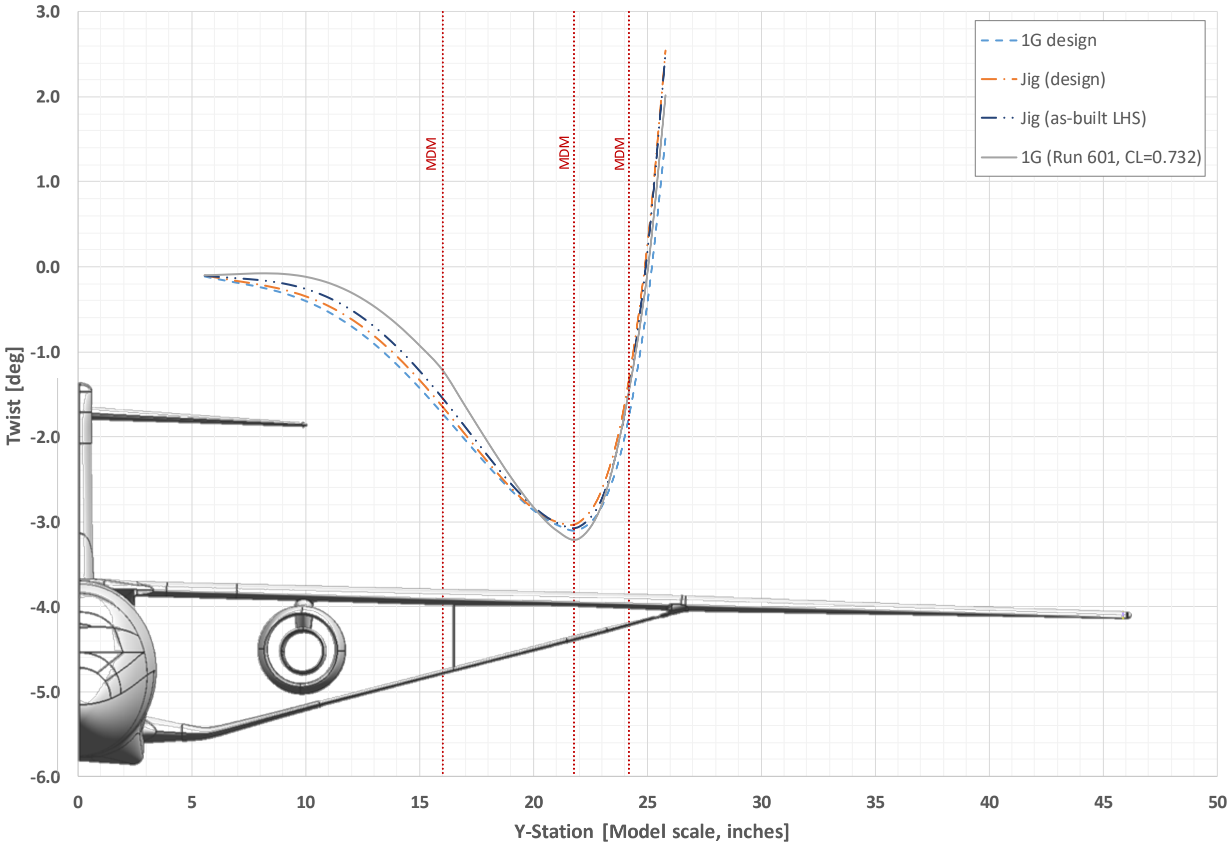

Figure 7.29 – Strut twist distribution from MDM measurements has a 0.5° offset midstrut.

Once the delta twist distributions were determined, they were applied to alter the original CFD surface grids so that predictions of the 'as-tested' geometry could be made. The resultant CFD data were compared to data measured in the tunnel to validate the computational methods. In order to simplify the grid alterations necessary to implement the measured twist values, the wing had two small spanwise regions in which the twist was held constant – the engine and engine pylon, and the wing-strut attachment. In these regions, implementing variations in twist would alter the integration between these surfaces, forcing the creation of a unique geometry specific to the model twist distribution. For this reason, these regions went through a solid body rotation to preserve the surface intersection geometry. The delta distributions for the wing (Figure 7.30) therefore show how the target twist distribution was altered to obtain the final CFD geometry. The applied twist change for the strut (Figure 7.31) was comparatively unconstrained, with the exception that the outboard end of the strut had to connect to the rotated wing geometry. For both the wing and strut, the MDM measurements showed nonmonotonic twist changes as compared to the static position measured in the tunnel.

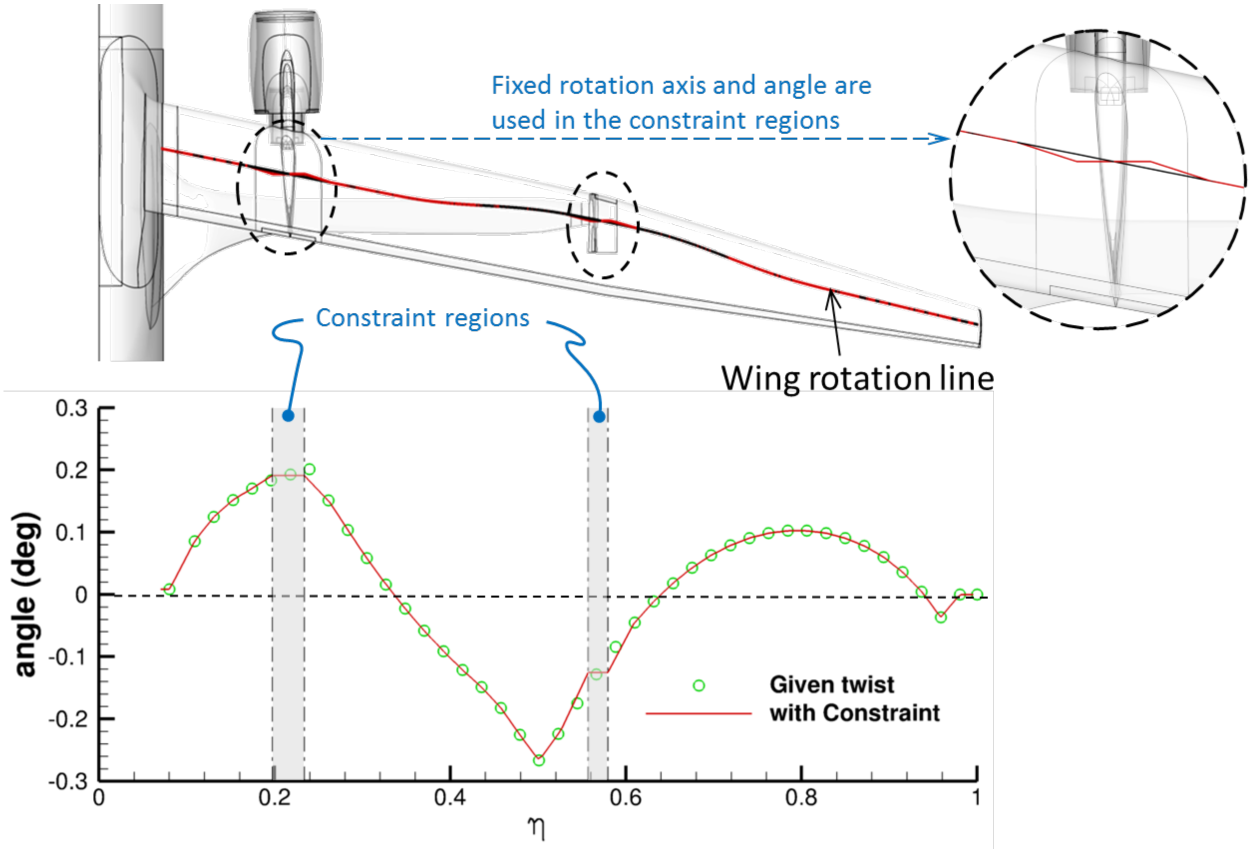

Figure 7.30 – Twist correction applied to the 1g (design) wing CFD Grid.

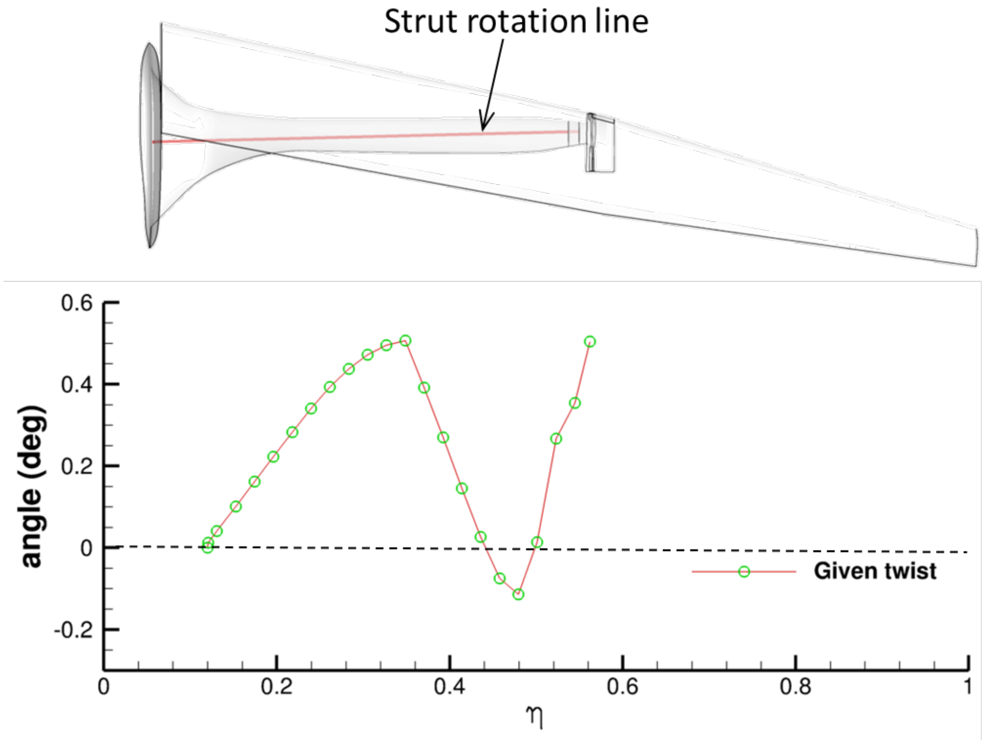

Figure 7.31 – Twist correction applied to the 1g (design) strut CFD Grid.

The CFD results from OVERFLOW for the 'as-tested' geometry were then compared to the geometry from the pretest predictions.

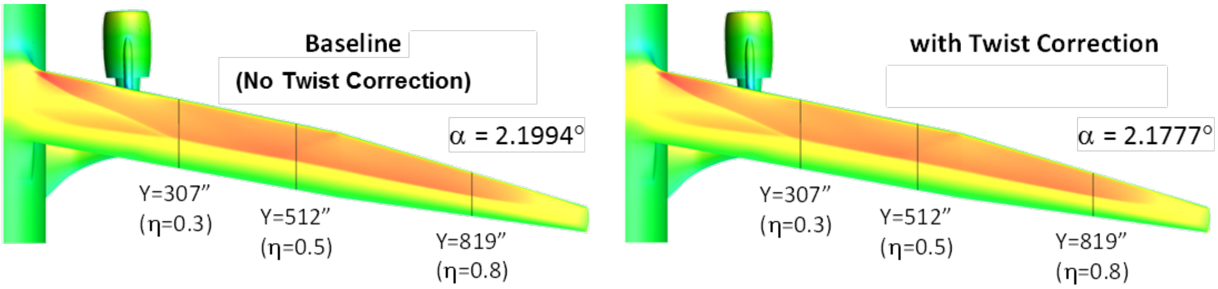

Figure 7.32 – Wing C_p Distribution showing the effect of the MDM twist measurements.

The comparison of surface pressure coefficient (C_p) between these results (Figure 7.32) shows that the as-tested geometry of the wing accurately represented the target wing geometry at the cruise design point. There is very little difference in the wing pressure distributions from the target performance when comparing constant C_L-conditions. The pressure distributions on the strut (Figure 7.33) show a larger deviation from the target pressures due to the increased incidence midstrut. Fortunately, the incidence increase wasn't sufficient to result in a shock on the strut upper surface at this condition. However, the increase in the leading-edge pressure peak suggests a higher loading than the baseline geometry that may grow (relative to the baseline) with increasing angle of attack. As angle of attack increases, this may result in the formation of a shock not present in the baseline. In addition, the changes may increase the severity of the shock that is forming in the most outboard end of the strut. Despite the pressure differences on the strut, at a C_L=0.73 the difference in drag between the two geometries is less than 0.1 counts of drag, well within the expected accuracy of the CFD predictions. It is likely that the small decrease in vehicle angle of attack offsets any additional drag on the strut due to its increased incidence.

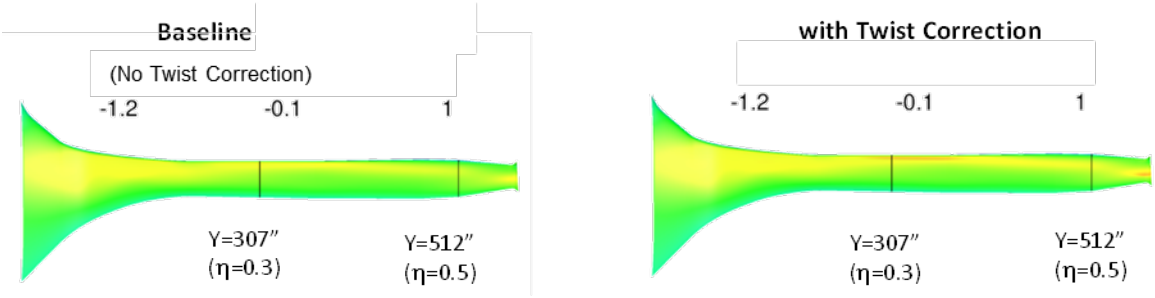

Figure 7.33 – Strut C_p Distribution showing the effect of MDM twist measurements.

Wing-Only Aeroelastic Effect

Following the analysis of the wing-strut configuration, a configuration was analyzed that did not have the strut installed. It was believed that the strut-off geometry would exhibit significantly higher deflections, and would result in a significant increase in model aeroelastic effects relative to the strut-on cases. The measurements obtained during Run 213 of the wing-only configuration show that the aeroelastic deflection angles (shown in Figure 7.34) were larger than for the wing-strut case, but were still relatively small with a maximum twist change under load of 0.4° at the tip. Despite this increase in twist, the net result of final twist on the model still did not differ greatly from the design 1G geometry. Figure 7.35 shows the difference in the desired (1g design) twist distribution and the measured (1g Run 213) twist distributions. Unfortunately, the model could not be tested to higher dynamic pressures due to the expected model loads on the very high aspect ratio wing. Because of these high loads, the wing was designed to be very stiff under load. As such, it did not exhibit the degree of aeroelasticity that would be expected on a flight-scale vehicle.

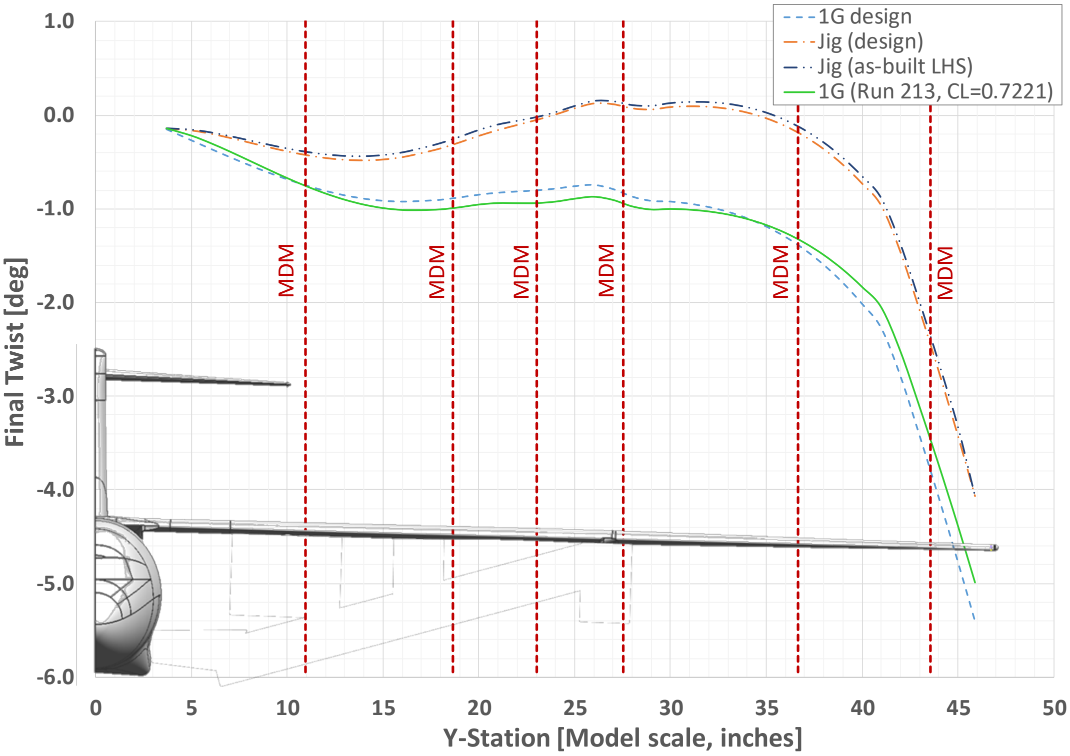

Figure 7.34 – Wing-Only Configuration twist distribution as compared to 1g target.

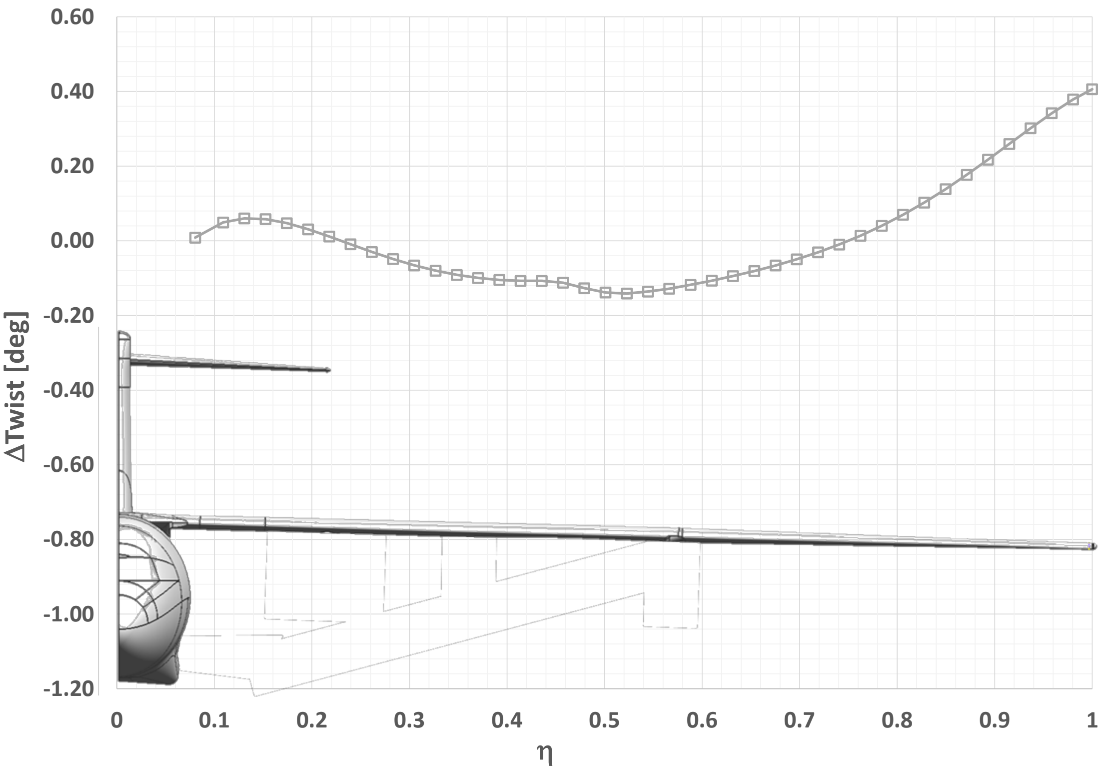

Figure 7.35 – Delta twist distribution (1g vs. measured in tunnel) for wing-only configuration (Run 213, C_L = 0.7221).

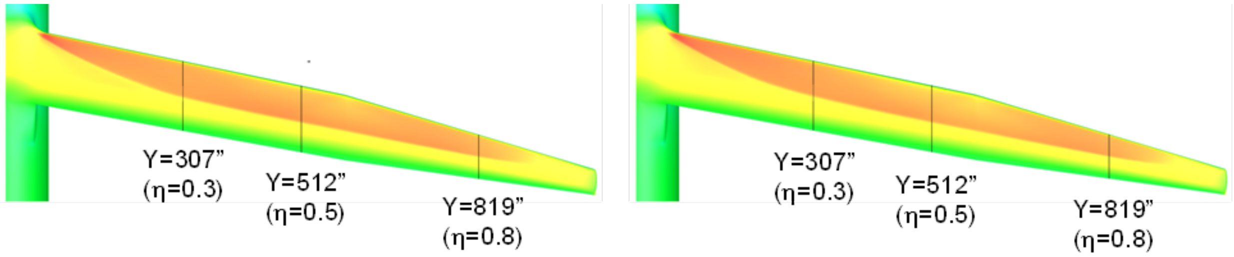

Figure 7.36 – Results from CFD Analysis of Re-twisted 'wing-only' case shows very little effect.

The results of the CFD with the retwisted wing-alone geometry had a similar result to that obtained for the retwisted wing-strut – the performance was almost indistinguishable from the 1G design performance. The final drag delta between the 1G and retwist geometry was a 0.77 count change in drag. This level of drag cannot be resolved in the wind tunnel. Therefore, the wind tunnel results with the strut off are not significantly altered by aeroelastic effects. The effects of the change are highlighted in Figure 7.36, which shows only a very small change in the wing pressure distributions due to the aeroelastics – there is only a small increase in the airfoil rooftop pressures, and no significant change in shock strength or location.

7.5.2 Sting Effects

During the wind tunnel test entry, early data runs showed bimodal behavior indicating the flowfield was bouncing between different states of equilibrium. Test engineers began to focus on model-sting interface as a source for this unsteadyness, particularly in regards to the flow within the model cavity. Unsteady pressures within the cavity led to large variations in model forces for both corrected and uncorrected variables (Figure 7.37). It was conjectured that the model cavity, sting clearance, and noncircular penetration of the sting into the fuselage resulted in a bimodal yaw instability on the aft fuselage as flow moved across the strut's circular cross-section. This flow across the strut had a tendency to snap between two different states in yaw. To potentially rectify this problem, a modification for the aft fuselage was designed. The modification was comprised of a 3D-printed aerodynamic fairing that was affixed to the aft fuselage of the model while it was in the tunnel. Once added, this fairing was successful in eliminating the yaw instability and cavity pressure fluctuations, and dramatically improved the quality of data being collected. However, Boeing committed to reexamine the pretest computational predictions to determine why this behavior was not predicted prior to the test.

The following sections recap the pretest CFD predictions, and examine the sting-model interface in greater detail, including characterizing the effects of the aft fuselage modification that resolved the flow instability. The purpose of the analysis was primarily to develop a 'lessons learned' approach to prevent similar issues from reappearing in subsequent wind tunnel testing.

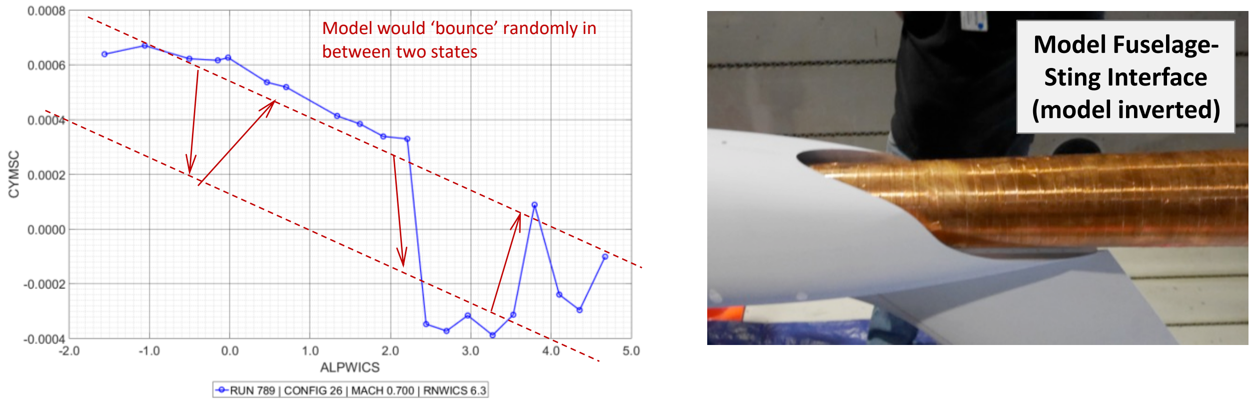

Figure 7.37 – Model experienced a bimodal instability in yaw.

7.5.2.1 Pretest Predictions (Summary)

Prior to wind tunnel testing, CFD predictions using OVERFLOW examined the effects of the strut on the model forces and moments. The configuration modeled (shown in Figure 7.38) was based on engineering drawings of the sting obtained from NASA Ames. As shown, the CFD predictions were based on a half-span model with the model symmetry plane modeled as an inviscid wall. The sting-fuselage interface was represented by a simple sting-fuselage intersection, in which the sting surfaces were not counted in the model force integration (Figure 7.39). This geometry did not represent the as-built model geometry as it did not model the sting-fuselage clearance or the cavity inside the model. Since the purpose of this modeling was to determine effects on model force and moment coefficients because of the presence of the sting (i.e., volumetric effects) and revised fuselage surface area (surface removed where sting penetrated the fuselage), this was a reasonable set of assumptions. However, because of these modeling choices, it was not possible to detect the yaw unsteadiness that was experienced in the tunnel since by definition there was no flow across the symmetry plane of the aircraft.

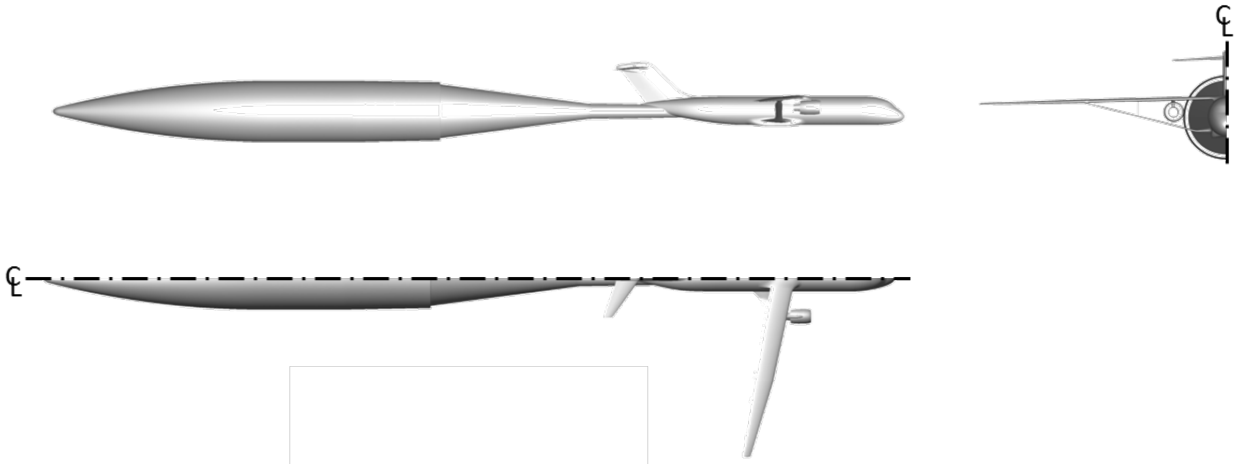

Figure 7.38 – Model Installation on Sting (Pretest configuration).

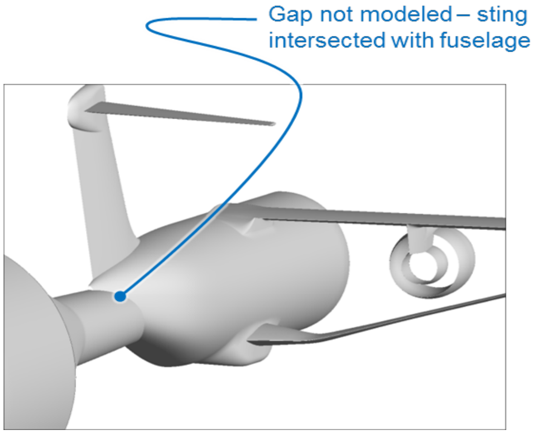

Figure 7.39 – Pretest Modeling of sting did not include gap and cavity between fuselage and sting.

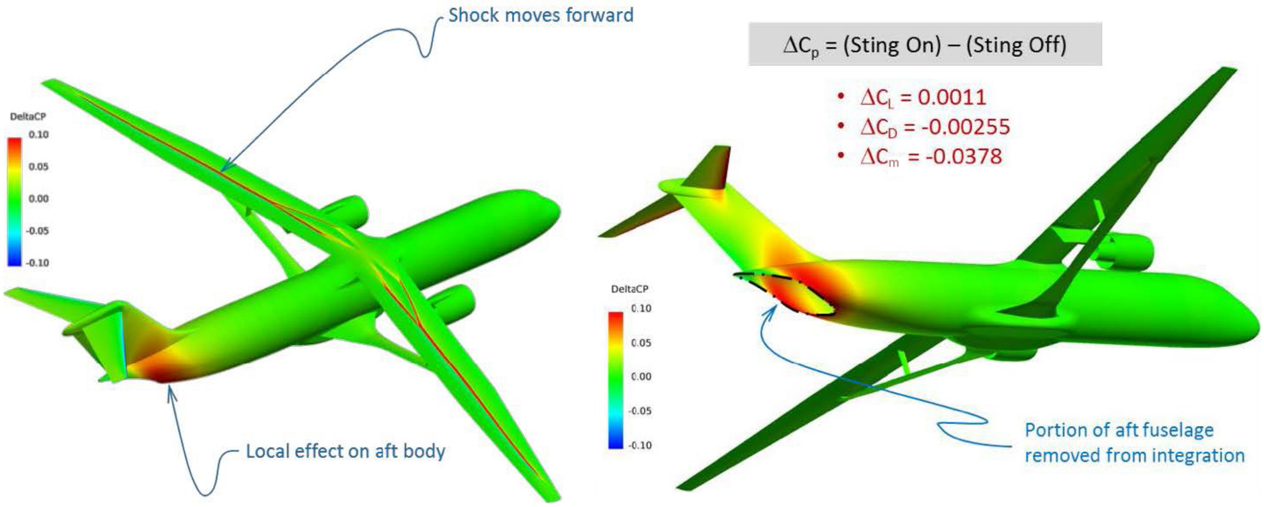

Figure 7.40 – Pretest CFD predictions show forward movement of shock, decrease in drag of 25.5 cts: Re_{mac} = 3.3M (Re = 8.0M/ft), Mach = 0.745, and α = 2.193°.

The pretest CFD showed that the sting integration had a substantial effect on the vehicle. The most significant of these effects was a substantial increase in drag and a significant increase in horizontal stabilizer effectiveness. The change in drag was driven primarily by the removal of some area in the aft fuselage force accounting where the sting intersected the fuselage. The second large effect was a small change in the wing upper surface shock location, which also changed the drag of the configuration. These factors (combined with a small change in vehicle lift) led to a net decrease in drag of 25.5 counts as compared to the no-sting geometry.

The changes in horizontal tail effectiveness was driven primarily by a flow angle change on the aft fuselage induced by the presence of the sting. This induced effect increased the local incidence of the horizontal stabilizer as depicted in Figure 7.41. The net effect of the incidence change was an increase in tail lift coefficient by 0.0075 (at the cruise design point). The increase in tail lift coefficient resulted in an increase in nose-down pitching moment as compared to the baseline (no sting) configuration.

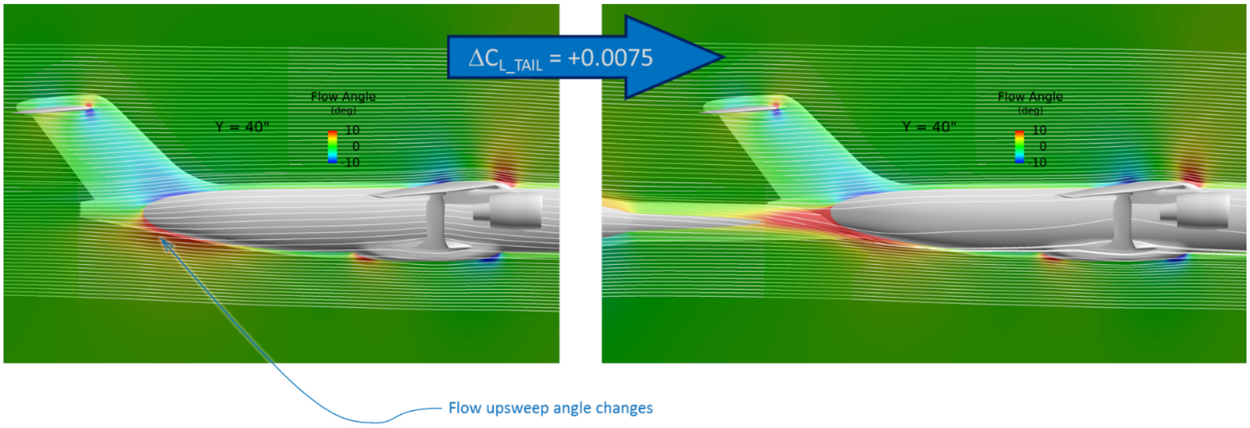

Flow upsweep angle changes

Figure 7.41 – Sting increases incidence on the tail.

Examining the force and moment coefficient effects of the sting influence around the design point (Figure 7.42) shows that the wing experiences a small decrease in lift coefficient (at a given angle of attack). When combining the wing lift change with changes to the horizontal tail's effectiveness, the net effect on aircraft lift is a small increase in vehicle-level lift.

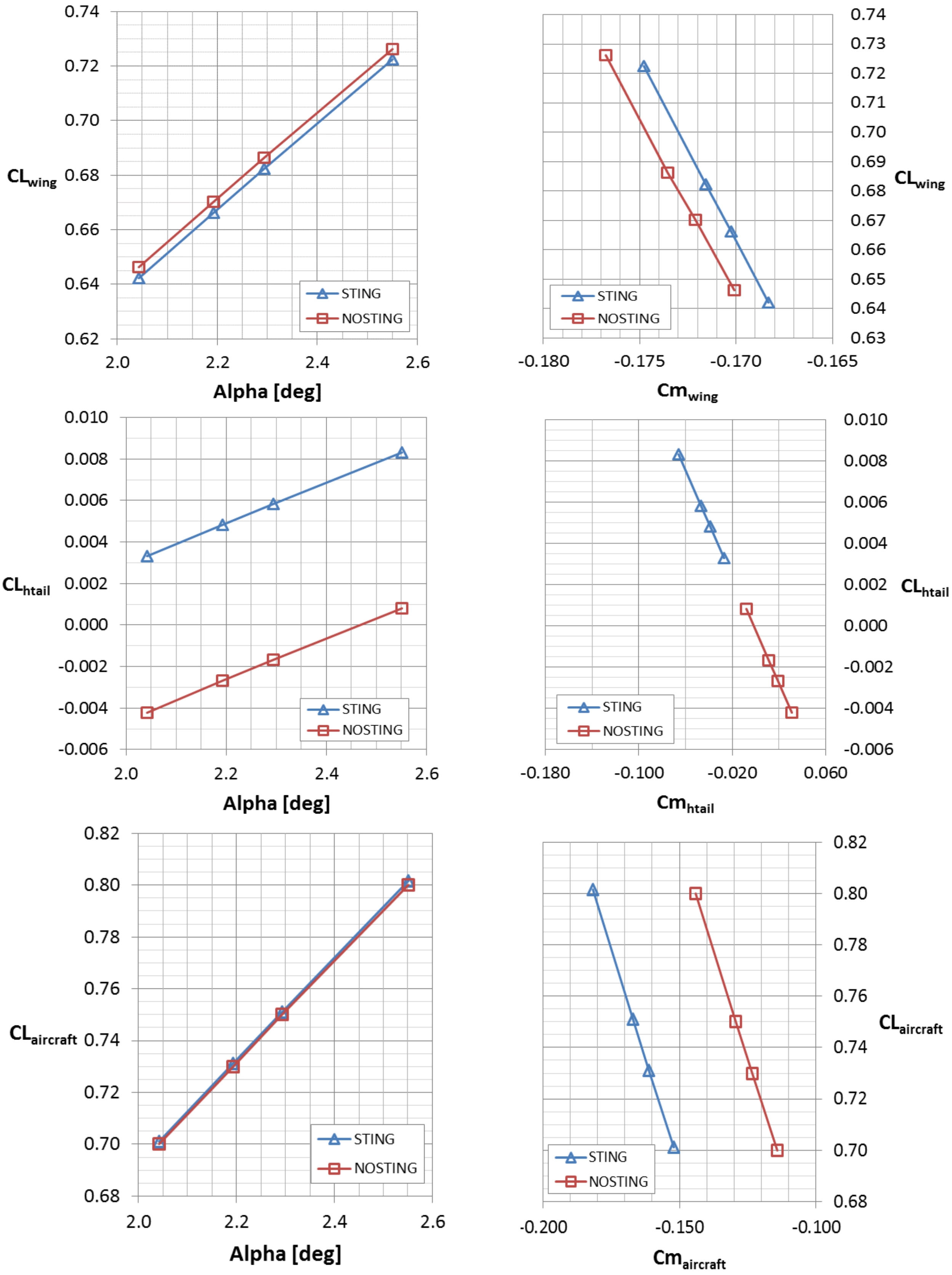

Figure 7.42 – Sting effects on aircraft force and moment coefficients (Pretest CFD).

7.5.2.2 Effects of as-built sting interface

Flow unsteadiness measured in the tunnel via the model cavity pressures led to the closer examination of the as-built sting installation. The pretest CFD model of the geometry was modeled as a half-span model, in which the sting-fuselage geometry was modeled as a simple intersection of the sting and fuselage surfaces. To better represent the geometry for post-test analysis, a more accurate representation of the gap around the sting and a significant portion of the model cavity was modeled (Figure 7.43). The cavity itself was opened up to a forward station of FS = 47.06”, or ~3.2 opening diameter-to-length ratio as determined by the mid-streamwise point of the fuselage opening. (It is possible that the volume of the cavity may have a direct effect on the frequency of the unsteadiness within the cavity. However, this effect was not studied in detail in this contract.)

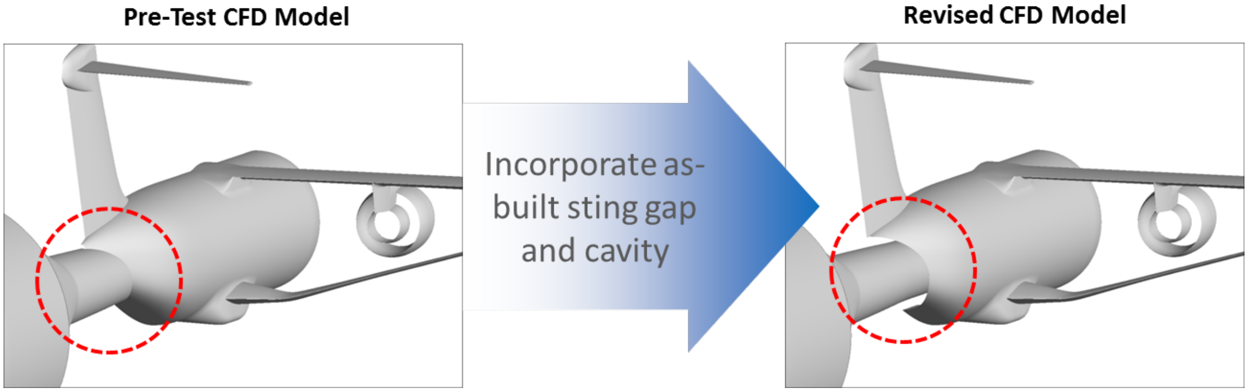

Pre-Test CFD Model

Revised CFD Model

Figure 7.43 – Pretest CFD model did not accurately represent sting-fuselage interface.

To complete the CFD analysis of the as-built geometry, the overset grids used in the OVERFLOW analysis had to be modified. The geometry for the revised CFD analysis (Figure 7.44) came directly from the TriModels wind tunnel model geometry CAD file to ensure accuracy. Grids were otherwise maintained to preserve as much consistency with previous CFD predictions as possible. It should be noted that the sting cavity opening does not look circular in depicted orientations. This is due to the fuselage upsweep and sting cavity surfaces creating an unusual intersection, which is amplified by the chosen viewing angle.

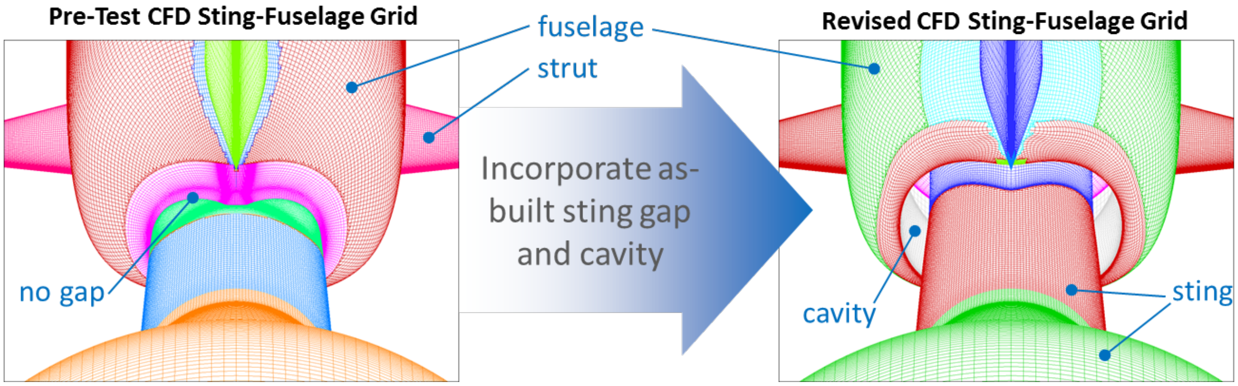
Pre-Test CFD Sting-Fuselage Grid

Revised CFD Sting-Fuselage Grid

Figure 7.44 – CFD grid modified to model as-built sting-fuselage geometry including cavity (view looking fwd from aft of fuselage).

The results of the CFD analysis show a significantly different flow field on the sting when including the as-built details of the sting-fuselage interface (shown in Figure 7.45). Since the pretest CFD did not model the cavity, the flow inside the model is not represented. What is of particular interest, however, is how the flow field on the sting changes when the fuselage is trimmed away from the sting to provide clearance – the flow off the fuselage keel line increases in incidence, directing the flow up across the sting’s circular cross section rather than flowing parallel to it. Since this increase in upsweep across the sting and the flow interaction with the cavity could not be predicted without modeling the cavity, it is not surprising that the pretest analysis could not capture the unsteadiness effects.

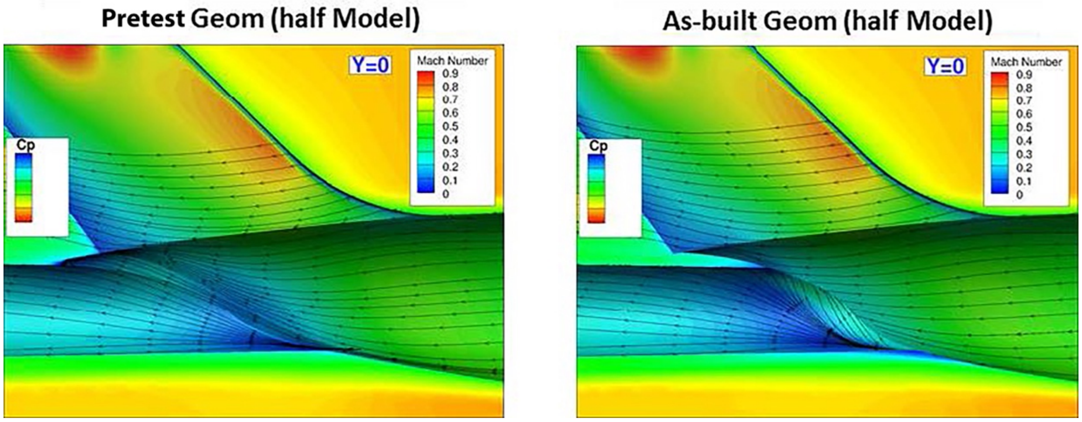
Pretest Geom (half Model)

As-built Geom (half Model)

Figure 7.45 – The aft body flow is significantly altered when incorporating the as-built geometry.

As described previously, the force and moment effects from the pretest CFD configuration were able to account for the volumetric effects of the sting presence. However, the differences in the flow field resulting from the as-built sting-fuselage geometry were greater than expected. Once the geometry was more completely modeled, it was possible to determine revisions to those predictions that would more completely account for differences in performance measured in the tunnel vs. CFD predictions in free air.

For the pretest CFD configuration operating at the design condition (M=0.745, C_L=0.73) and at wind tunnel Reynolds number of 8M/ft, there was a 26 ct offset in drag coefficient (Figure 7.46). Incorporating an accurate representation of the model sting clearance and the associated internal cavity (shown previously in Figure 7.43) offset the drag coefficient by ~4 cts from the pretest predictions. Removing the internal cavity surfaces from the force integration (analogous to the cavity correction in the data reduction equations) offset the drag by an additional 12 cts. The net effect of the increased fidelity in modeling increased the configuration's overall drag from pretest levels by a total of 16cts. This reduced the total offset from the pretest predicted 1G (design) drag coefficient from 26 cts down to 10 cts. Similar corrections can be shown for lift and pitching moments for both the whole aircraft as well as the components identified in pretest analysis (wing, horizontal stabilizer). The results (summarized in Figure 7.47) show that as compared to the pretest predictions (labeled 'sting'), the as-built geometry resulted in no change in tail lift coefficient as compared to pretest estimates. Net vehicle pitching moment did however increase significantly (nose-down) due to the additional removal of fuselage area (to provide clearance for the sting).

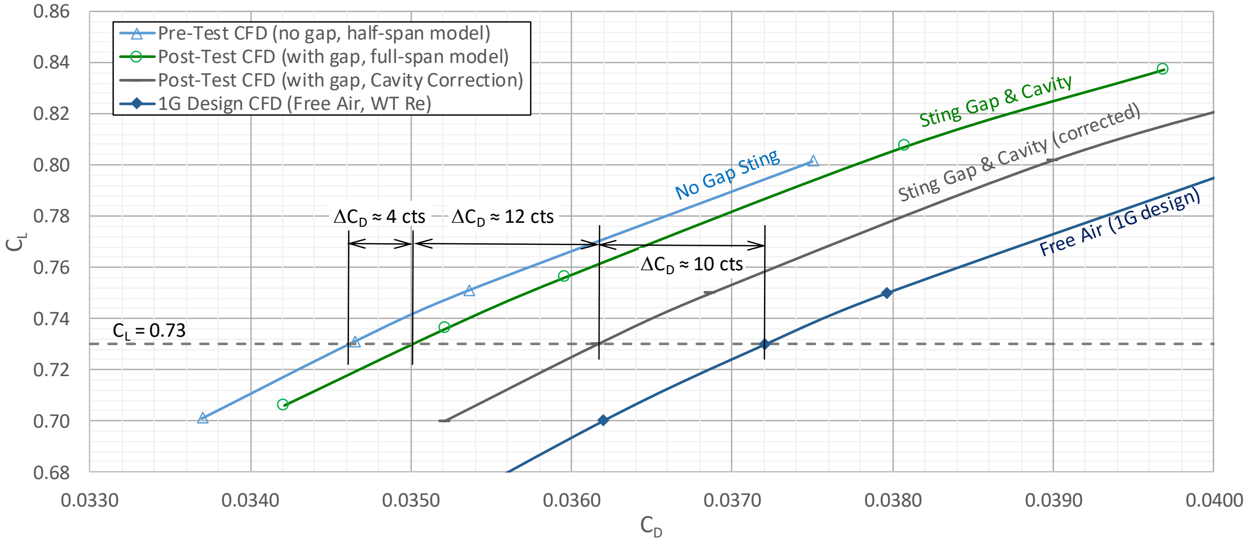

Figure 7.46 – CFD Predictions for Installed Model (all curves for Re = 8M/ft).

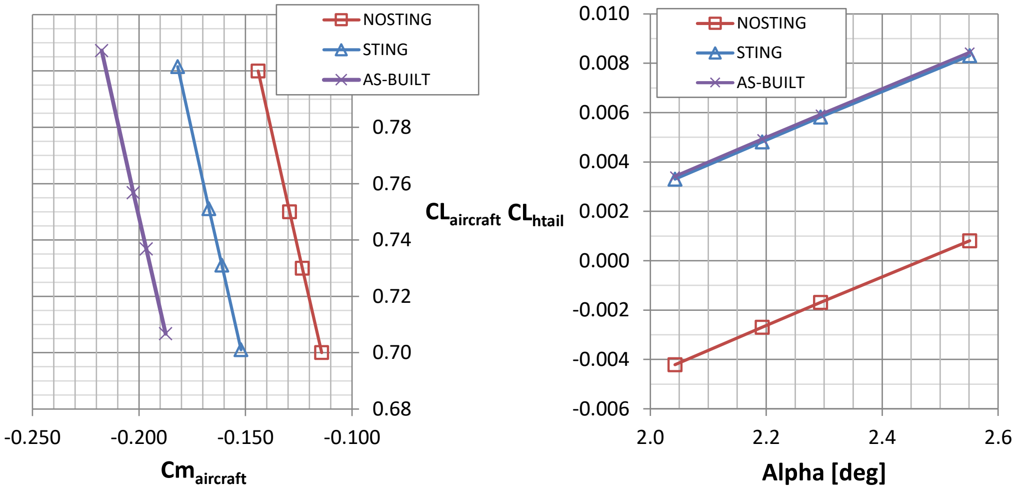

Figure 7.47 – Force and Moment Effects for the As-Built Geometry.

These effects are further demonstrated by the comparison of off-body flow angles plotted for the pre- and post-test geometries, as shown in Figure 7.48. The net effects of the revisions to the fuselage geometry (including the inclusion of the cavity) shows an almost imperceptible effect on flow angularity at the aft end of the fuselage.

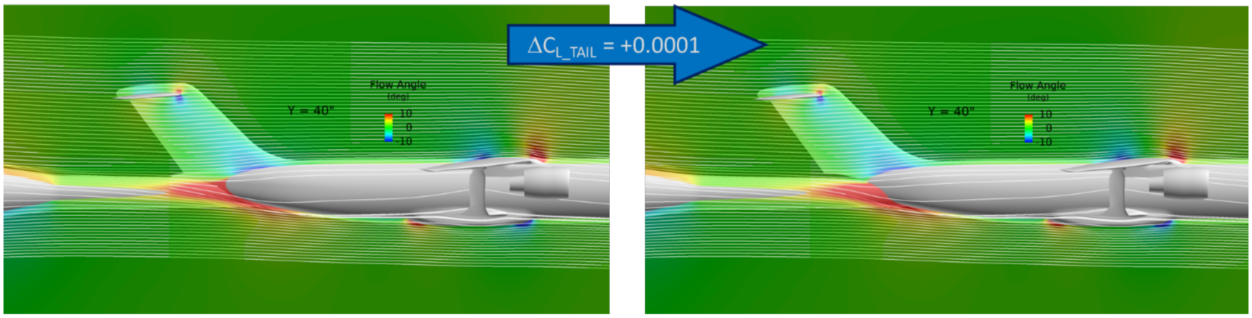

Figure 7.48 – Incorporation of the 'as-built' sting-fuselage interface (no aft fairing installed) had virtually no effect on tail effectiveness relative to the pretest CFD estimate.

Detailed revisions to the fuselage aft sting and fuselage geometry improved the accuracy of CFD predictions and provided updated offsets between the in-tunnel and ‘free air’ state (no sting). The computations also provided significant insight into the flow physics that may have been responsible for unsteadiness on the aft fuselage. Based on this evidence, Boeing took the additional step of running unsteady computations to confirm the suspected flow mechanisms, with the end goal of providing guidelines for future model construction.

7.5.2.3 Unsteady Computations of Sting-Fuselage Flowfield using URANS

The detailed representation of the model (including sting gap and cavity) was analyzed in OVERFLOW using Unsteady Reynolds Averaged Navier-Stokes (URANS) analysis to further investigate the source of the model unsteadiness around the aft fuselage. Results from this analysis confirmed the flow unsteadiness mechanism that was predicted in the tunnel – flow interactions between the fuselage cavity and sting lead to unsteadiness on the aft body. This unsteadiness causes pressure fluctuations within the model cavity, and results in significant variations in model drag and side force coefficients as shown in Figure 7.49.

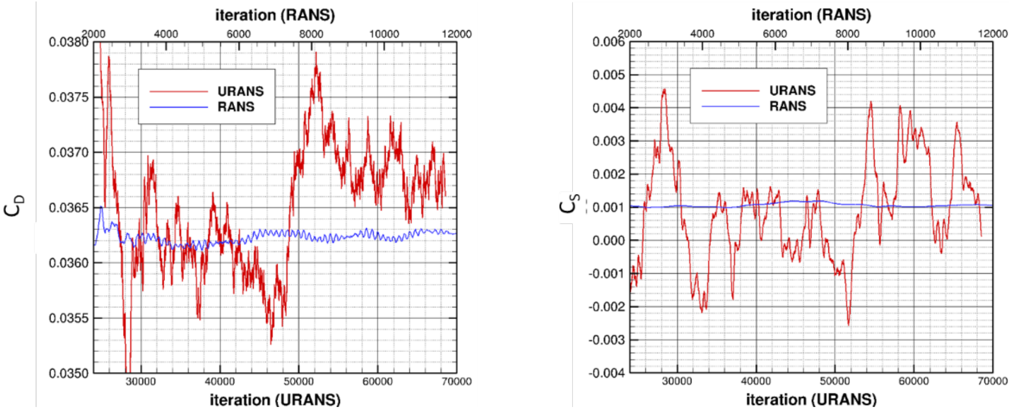

Figure 7.49 – Drag and Side Force Coefficient for RANS and URANS Analysis of As-built Configuration (prefuselage modification)

The flow fluctuations on the aft body are shown in the following series of images (Figure 7.50), each of which depicts a different snapshot in time from the URANS solution. These images show a rolling pressure fluctuation on both the sting and on the sides of the fuselage, as well as on the trailing edge of the vertical tail.

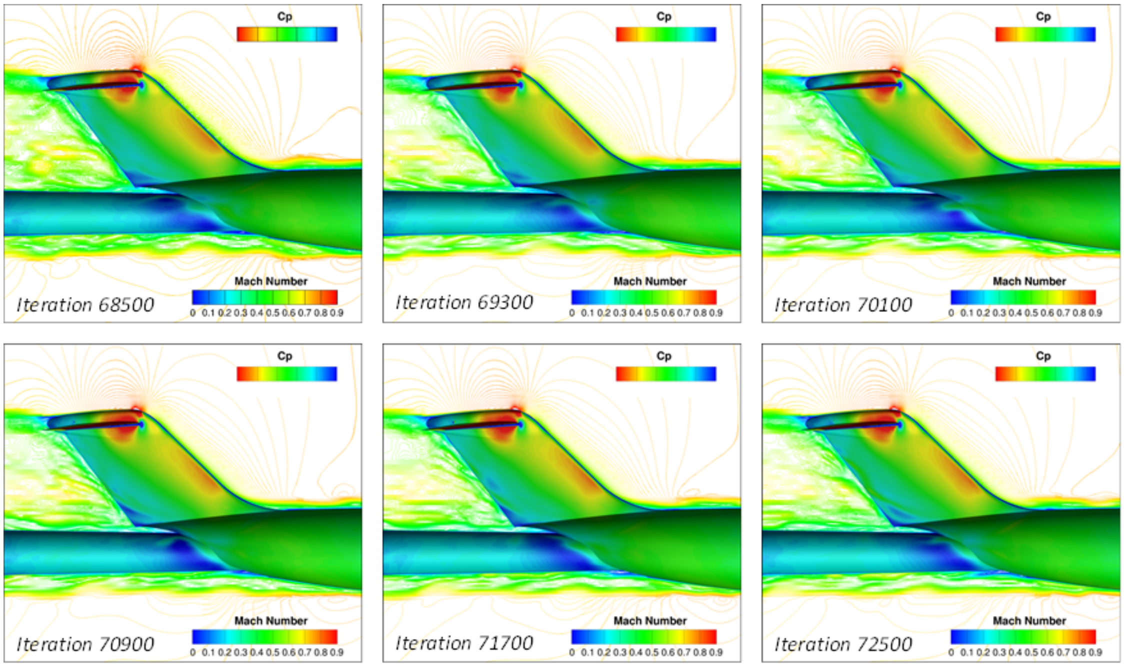

Figure 7.50 – Snapshots in time from URANS analysis of the as-built geometry shows significant unsteadiness.

7.5.2.4 Aft-Fairing Installation

An unsteadiness in the model cavity pressure and bimodal instability in yaw measured in the tunnel led the Boeing team to consider the flow on the aft fuselage and sting. It was believed that the large clearance left to prevent fouling on the sting during testing combined with a non-circular fuselage cross-section (a feature common to high-wing aircraft) resulted in an unusual aft fuselage trim geometry for the wind tunnel model. Of particular concern was the creation of two swept edges on the lower fuselage near the keel line. These edges (shown in Figure 7.51) formed a ‘V’ shape, which was believed to be creating vortical flow structures that were interacting with the model sting to create flow unsteadiness.

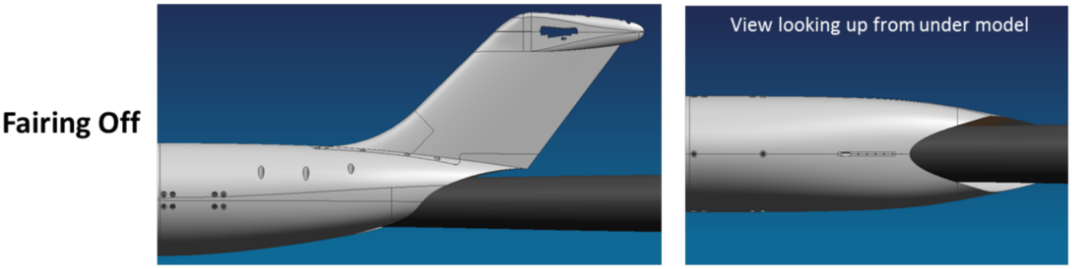

Figure 7.51 – Unmodified Aft Fuselage Geometry.

The general flow structure of the ‘as-built’ fuselage geometry showed that flow was moving off the aircraft keel line and up across the sting. As shown in Figure 7.52, the flow within the cavity did not stagnate. This was in direct contrast to a desired state in which the flow in the cavity is stagnant and the forces being applied to the internal surfaces of the model also remain constant. However, as discussed in Section 7.5.2.3, the process was demonstrated to be unsteady.

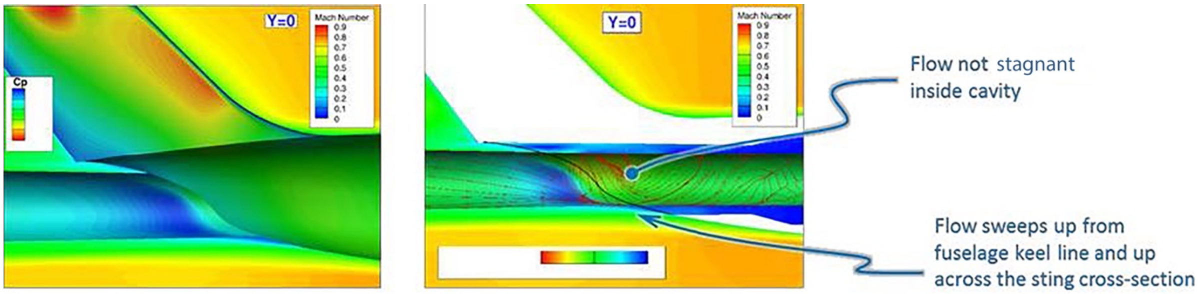

Figure 7.52 – Flow from unaltered aft fuselage has a strong flow across the sting.

To combat this unsteadiness, a fairing was developed to modify the shape of the fuselage at the aft keel line. The fairing shape (shown in red in Figure 7.53) covered the V-shape of the aft fuselage and created a more planar aft fuselage trim, blending into the existing loft. The fairing also flared to be parallel to the sting surface at the keel line to discourage flow from moving across the sting’s circular cross-section. The resulting aft fuselage fairing design was manufactured on-site at NASA using 3D printing technology, and adhered to the model using adhesive and speed tape.

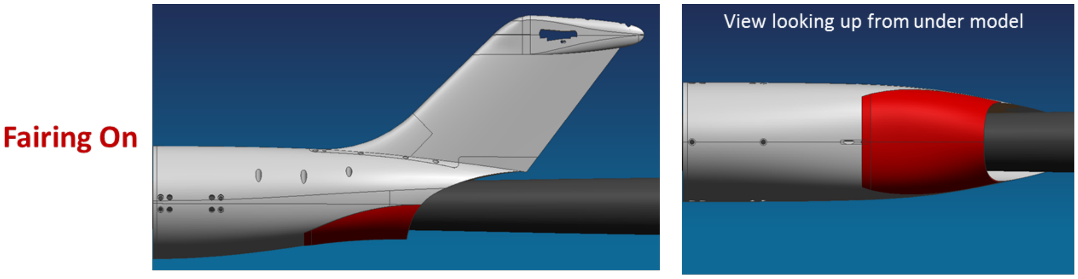

Figure 7.53 – Aft fuselage with fairing (red) installed.

When this fairing was installed on the wind tunnel model, it was immediately shown to have eliminated the aft body flow unsteadiness, and stabilized the cavity pressure. As a result, the data collected became considerably smoother. The success of the fairing was also validated post-test through detailed CFD analysis. The outer mold line from the fairing was added to the as-built model geometry and analyzed in OVERFLOW. The results of this analysis (shown in Figure 7.54) demonstrated that the flow off the keel line was successfully modified to travel parallel to the sting, and flow across the sting was significantly reduced. In addition, the flow within the cavity stabilized making for a more consistent cavity correction. At present, this geometry has not been analyzed using URANS methods.

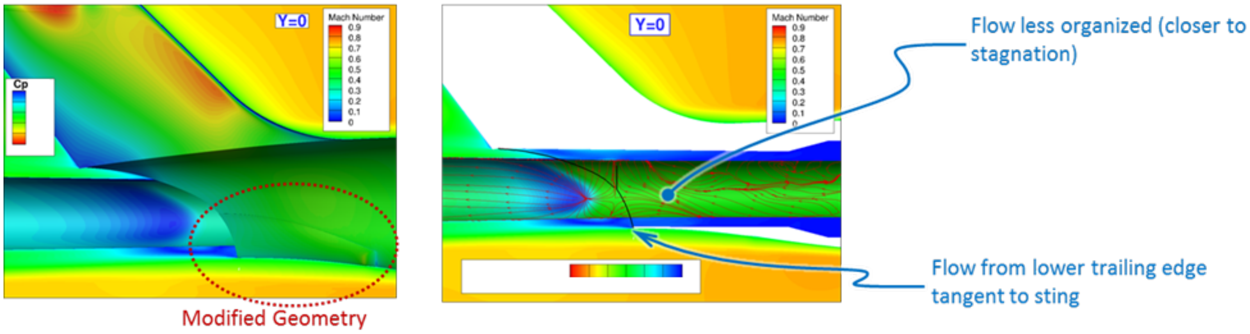

Figure 7.54 – The Aft Fuselage fairing reduces model sting interaction by directing the flow parallel to the sting

Variation in the drag coefficient for the aft-fairing installed (Figure 7.55) geometry was negligible. Even though the aft fairing adds drag to the configuration, it also increases the lift on the body. When accounting for the additional lift in the corrected force coefficients, there is no net change in vehicle drag at the design condition. The effects on the tail and aircraft force and moment coefficients are shown in Figure 7.56. These plots show that the aft-fairing-installed configuration has almost identical performance, with the exception of the aircraft pitching moment. Due to the creation of lift by the fairing on the aft end of the body (far from the center of gravity), there is a net change in pitching moment that returns it to the same levels predicted by pretest CFD analysis.

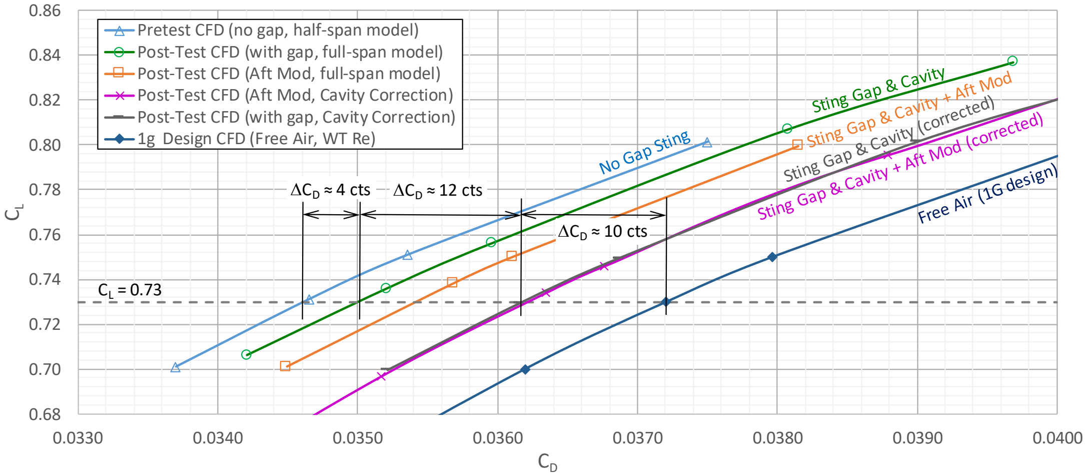

Figure 7.55 – Effect of the aft fairing on vehicle drag coefficient (Re = 8M/ft).

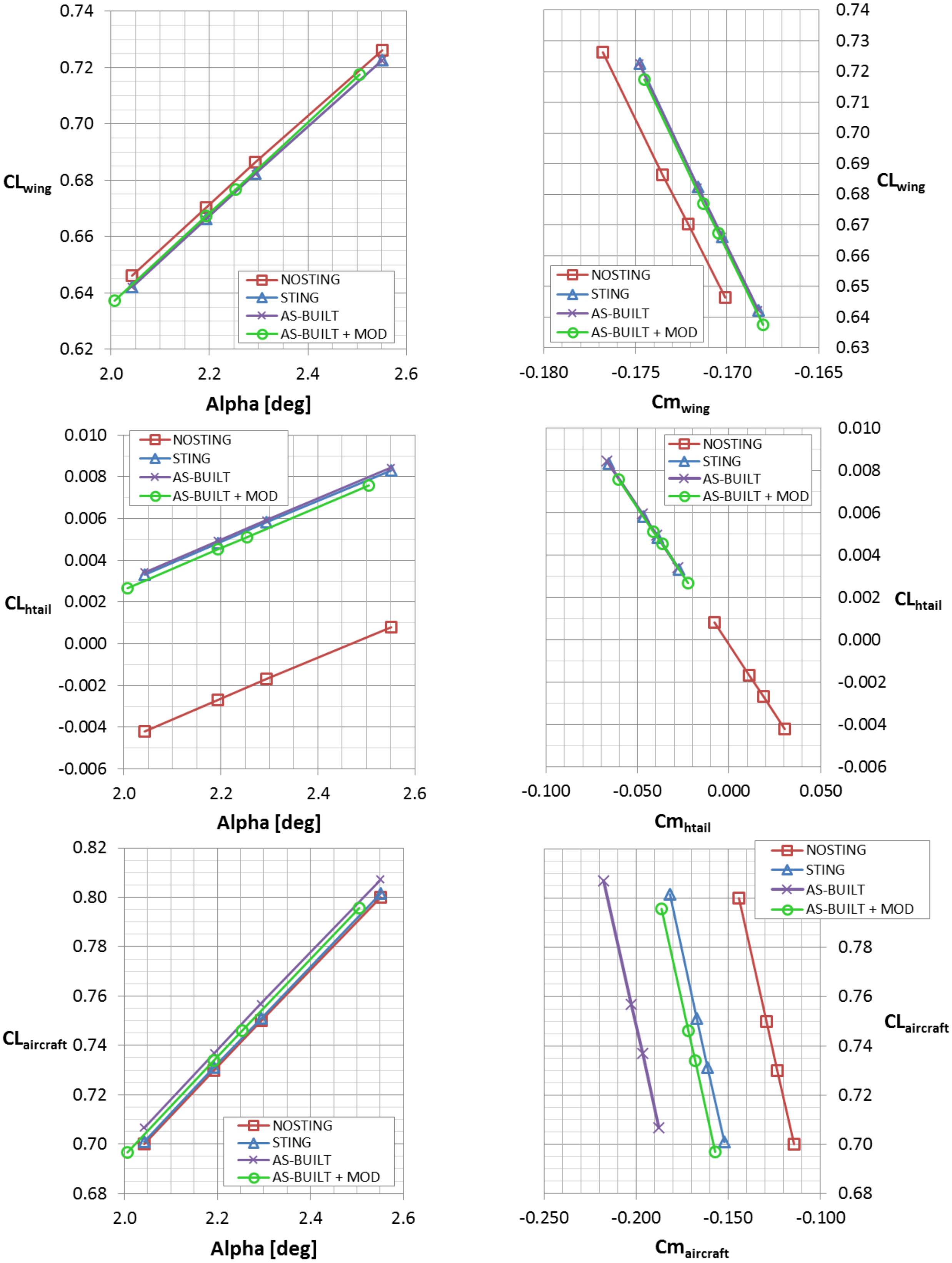

Figure 7.56 – Force and Moment Corrections for As-Built Model Geometry (including aft fuselage fairing).

7.6 Performance Predictions

The results of the test were compared to CFD estimates based on the 'as-built' geometry, including sting gap, cavity, and aft fairing. Unless otherwise specified wing twist based on measurements taken using the tunnel's MDM system are not included as their effects are only truly applicable for the condition for which they were collected. When comparing test and CFD data, it is typically only appropriate to compare deltas or increments in performance between configurations as absolute values of drag can be highly dependent on the turbulence model and spatial discretization method selected.

7.6.1 Reynolds Number Effects

The test results shown in Figure 7.57 show test data collected for the baseline configuration (wing, baseline strut, nacelle and pylon, and empennage) at two different Reynolds numbers. These data are compared to Reynolds effects predictions from CFD. The results show that the test data exhibits less separation due to Reynolds number than predicted by the CFD methods. This result is consistent with roughness effects – nominally the lower Reynolds number case should have higher drag due to its comparatively thicker boundary layer. However, since the higher Reynolds number flows are more sensitive to surface roughness, the expected increment is significantly decreased. This trend will perpetuate through all collected data, with lower surface roughness configurations exhibiting less of an effect.

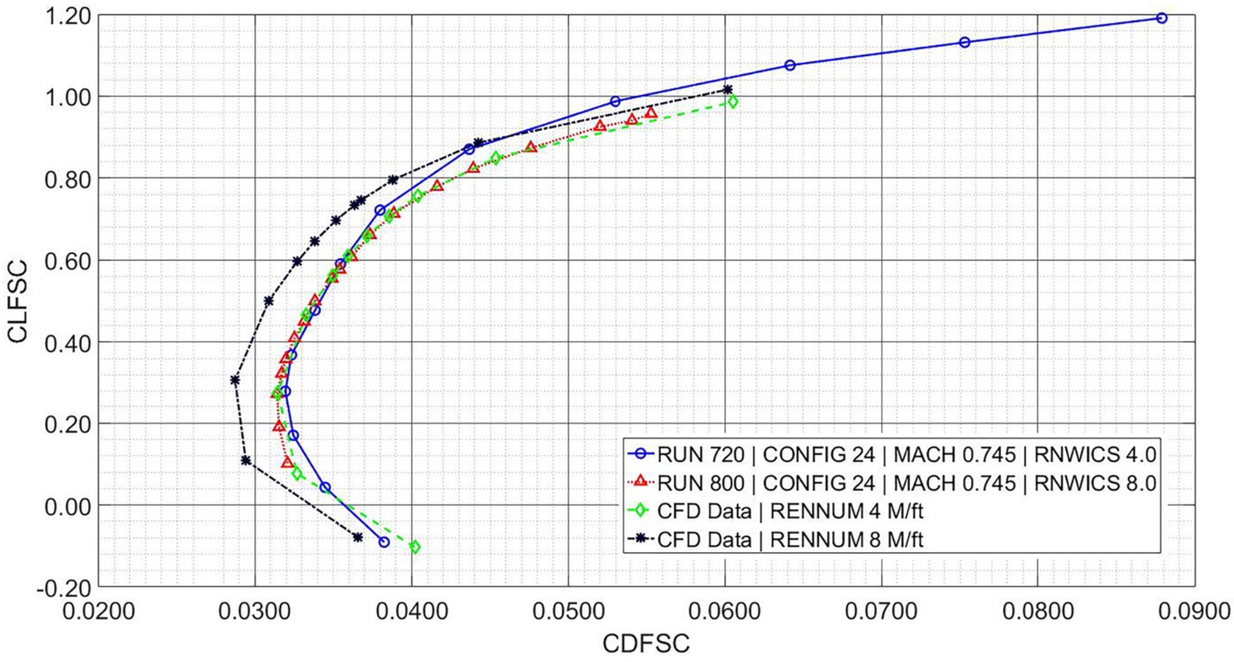

Figure 7.57 – Reynolds number effects.

7.6.2 Baseline and Alternate Strut Performance

Comparisons of the baseline strut performance were made at Re=4.0M/ft since the model was structurally limited in testing due to high wing loads when the strut was not installed. The comparison of test data to CFD projections of the as-built geometry (Figure 7.58) shows that the strut-on drag was higher than anticipated. While CFD projections showed a drag increment of 33 cts at the design condition, drag increments strut-on to strut-off from the wind tunnel data show an increment of ~46 cts. It is believed (based on analysis detailed earlier in this report) that roughness was a strong contributor to this offset. Since the strut's drag increment is of particular interest to the program, it is suggested that the data be recollected with a smooth model.

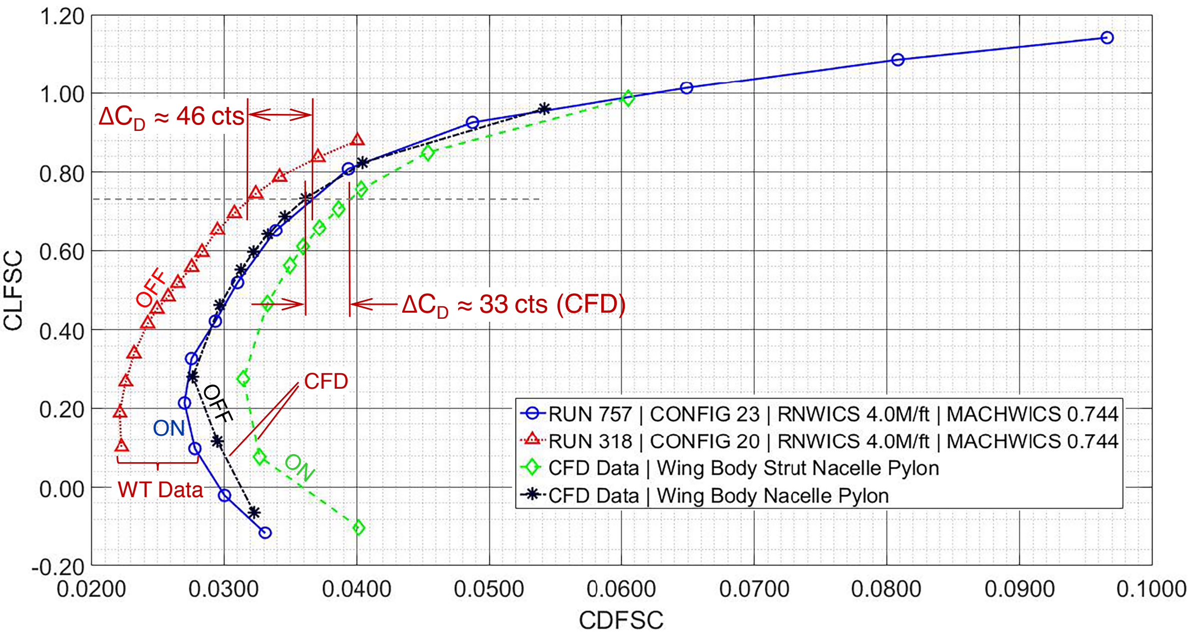

Figure 7.58 – Strut Increments of Drag Coefficient (Nacelle increment removed from Re = 8.0M/ft).

When comparing the performance of the baseline strut to the alternate strut configuration at the design Mach of 0.745 (Figure 7.59), there is little to no discernable difference in the performance except at low lift coefficients where the alternate strut outperforms the baseline strut by roughly 5 counts in drag. When the Mach number is increased for a constant Reynolds number (Figure 7.60), this benefit is magnified. This is an expected outcome since the alternate strut was designed to provide relief to the strut-wing juncture when operating at higher Mach numbers. These results confirm that as the Mach number of the vehicle is increased, the more desirable it is to decouple the wing and strut from each other. It is possible that the alternate strut type of arrangement may be preferable. This will need to be studied at a vehicle level to determine the optimum configuration.

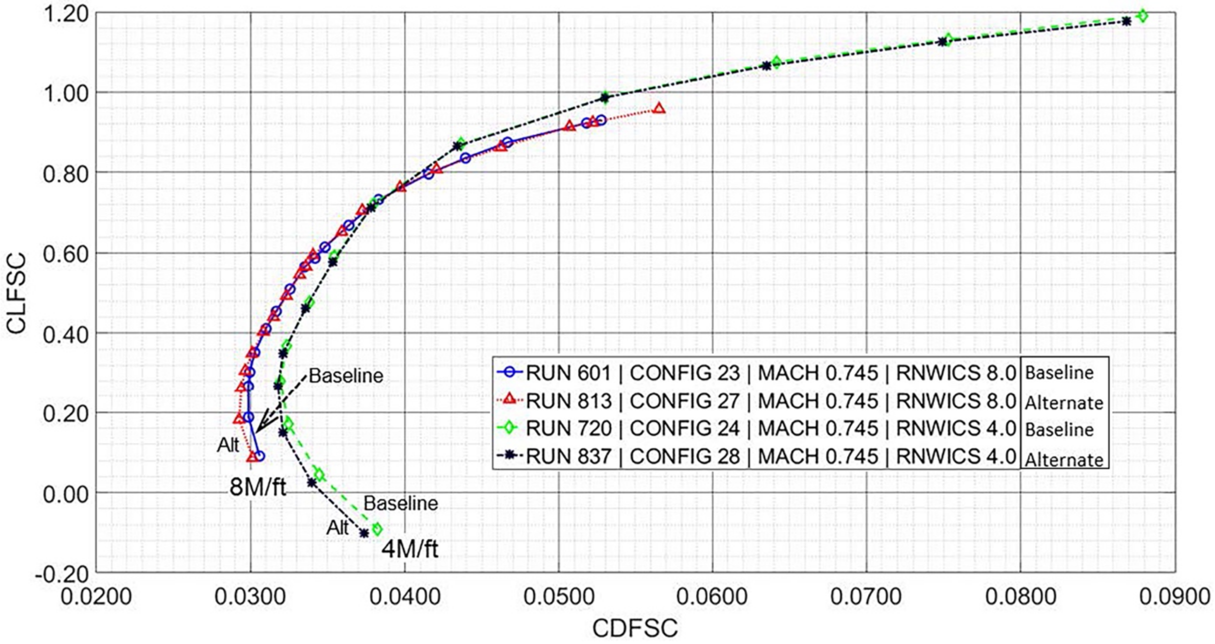

Figure 7.59 – Test data comparing baseline and alternate strut performance shows that at the design Mach the alternate strut outperforms the baseline strut at low lift coefficients.

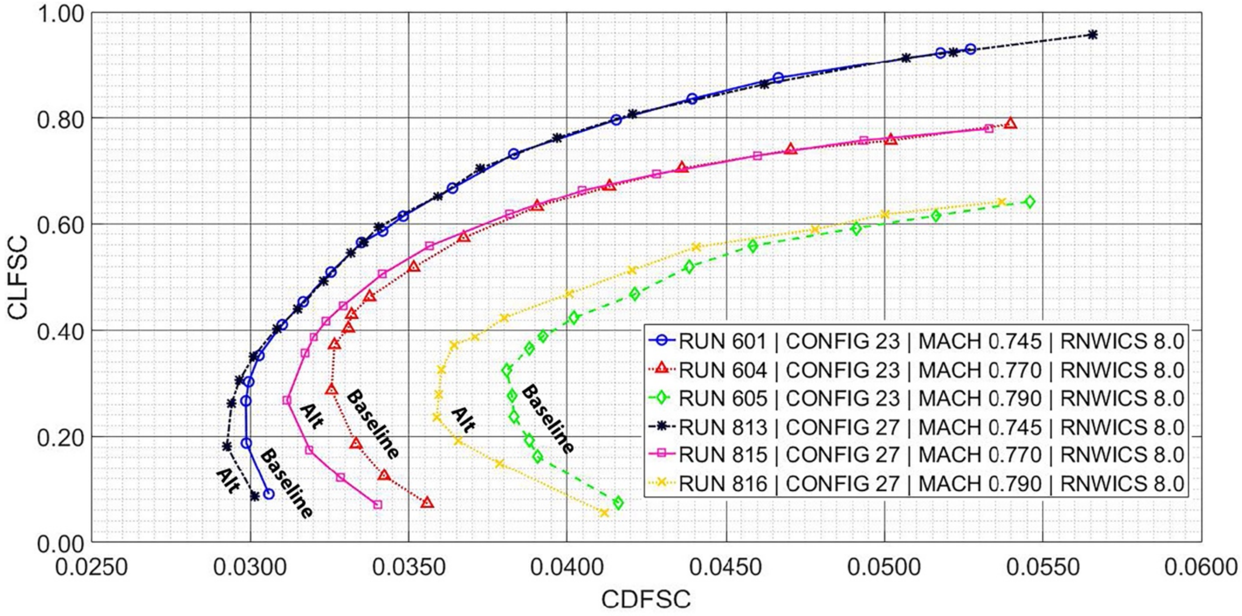

Figure 7.60 – Alternate Strut Performance -- Effect of Mach number.

7.6.3 Additional Component Increments

Comparisons of test data and CFD data can help to validate the design codes and methods used to build up the configuration performance predictions. Drag data from each component tested in the build-down was collected for comparison to pretest predictions.

The increment collected for the nacelle and pylon (Figure 7.61) show a close correlation to CFD predictions. At the design condition there is only 1 ct of drag difference between the test and

CFD data. This increment is well within the wind tunnel test data repeatability. Even though roughness has an effect on this installation, the majority of the surface area of the nacelle was unpainted. In addition, the nacelle does not have as strong a dependency on roughness since there are no strong shocks on the nacelle or pylon. As such, a good correlation between CFD and test data was expected.

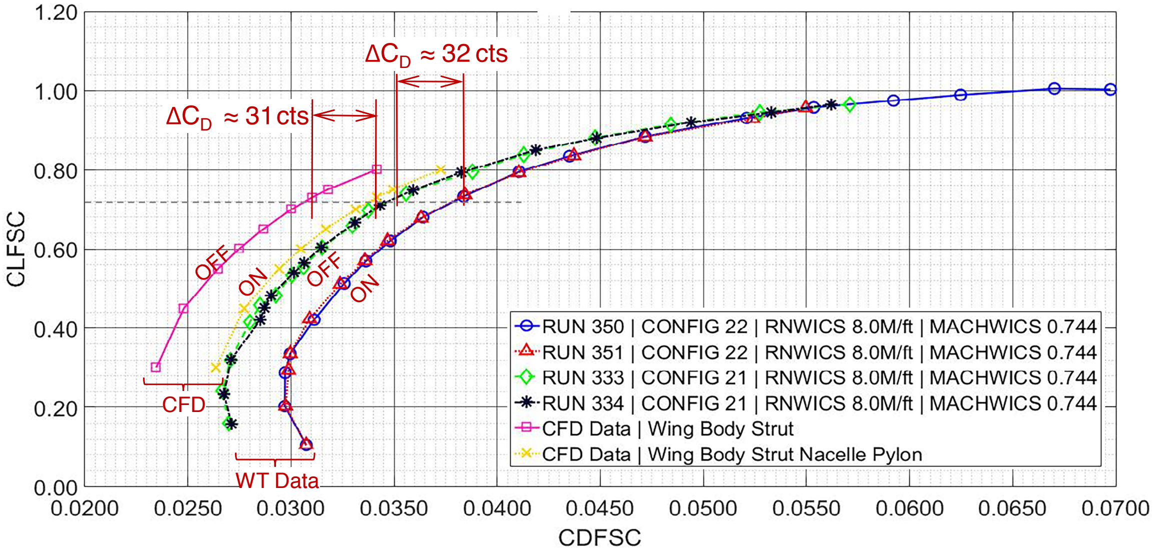

Figure 7.61 – Nacelle and Pylon Drag Coefficient Increments.

The empennage data comparison between CFD and test data was not collected on the same configuration. All CFD runs were either tail on or tail off, whereas test data were typically collected with the vertical stabilizer on, but the horizontal stabilizer off. Therefore, to make a comparison between test and CFD, the increments shown are corrected to account for the presence of the horizontal stabilizer. However, this does not account for any interference effects on the vehicle that result from the installation of the horizontal tail. The drag increment for the empennage from CFD predictions with the sting installed shows a 25.2 ct increase when operating at Mach=0.745, C_L=0.73, and Re=8M/ft. When linearly combining the horizontal and vertical stabilizer increments from test data, a net difference of 25 cts is obtained.

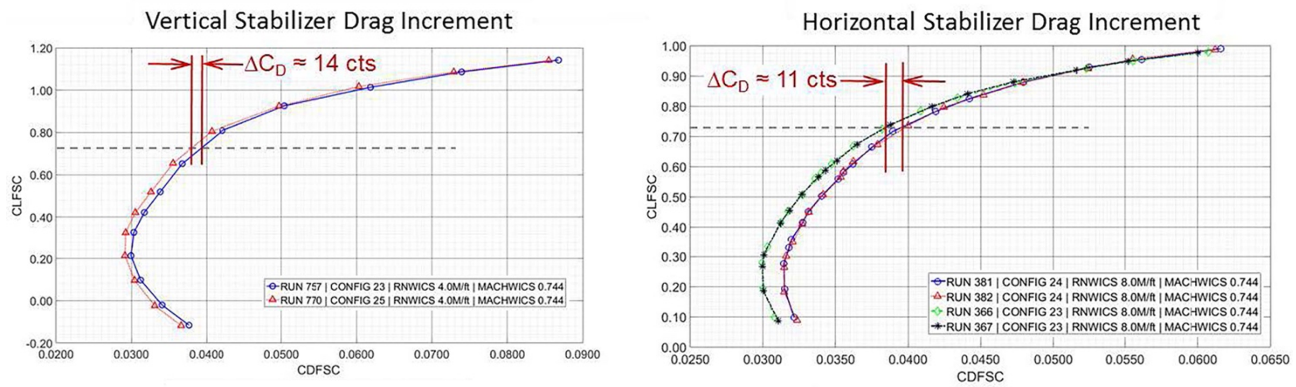

Figure 7.62 – Empennage Increment of Drag Coefficient.

The remaining increments in the build-up were relatively insensitive to changes in vehicle angle of attack (Figure 7.63), and were all collected to provide validation to build-up methods which analyze this contribution to vehicle drag at M=0.5 and a lift coefficient of C_L=0.

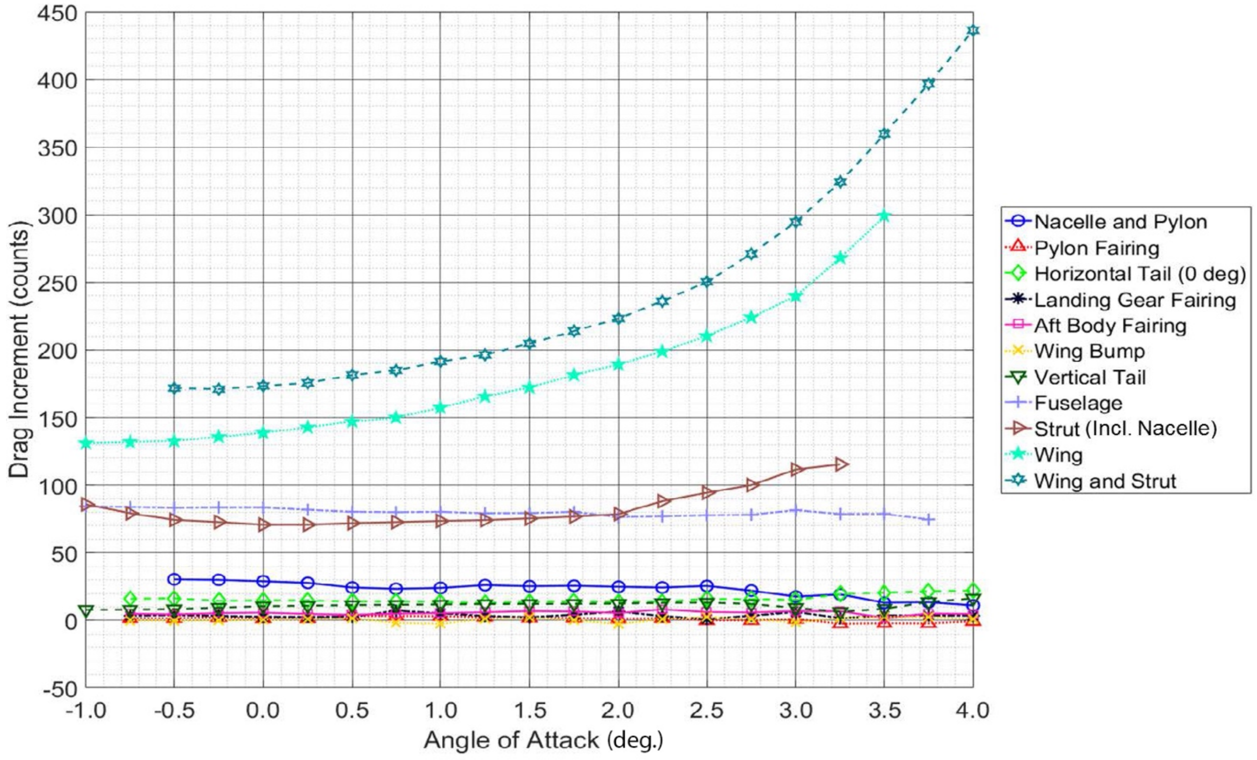

Figure 7.63 – Component Drag Coefficient Increments from Wind Tunnel Test at Mach = 0.745.

7.6.4 Drag Divergence and Long Range Cruise

The drag divergence Mach number of the complete configuration (including wing, strut, nacelle, empennage, aft fuselage fairing) was compared to CFD results of the most accurate representation of the wind tunnel model (including sting, sting gap, cavity, aeroelastic twist). These results (Figure 7.64) show that the predicted drag divergence Mach number of the tested configuration is slightly below the CFD estimates. While the drag levels at low Mach number match well between the test and CFD results, the most noticeable difference is the presence of a significant amount of compressibility drag creep through the lower range of the M_{DD} curve. This creep in compressibility has a high likelihood of correlation to increased model roughness – as the dynamic pressure increased and the Reynolds number grew the model would have increased sensitivity to roughness. As a result, the predicted difference in drag divergence Mach was a $\Delta M=0.0066$.

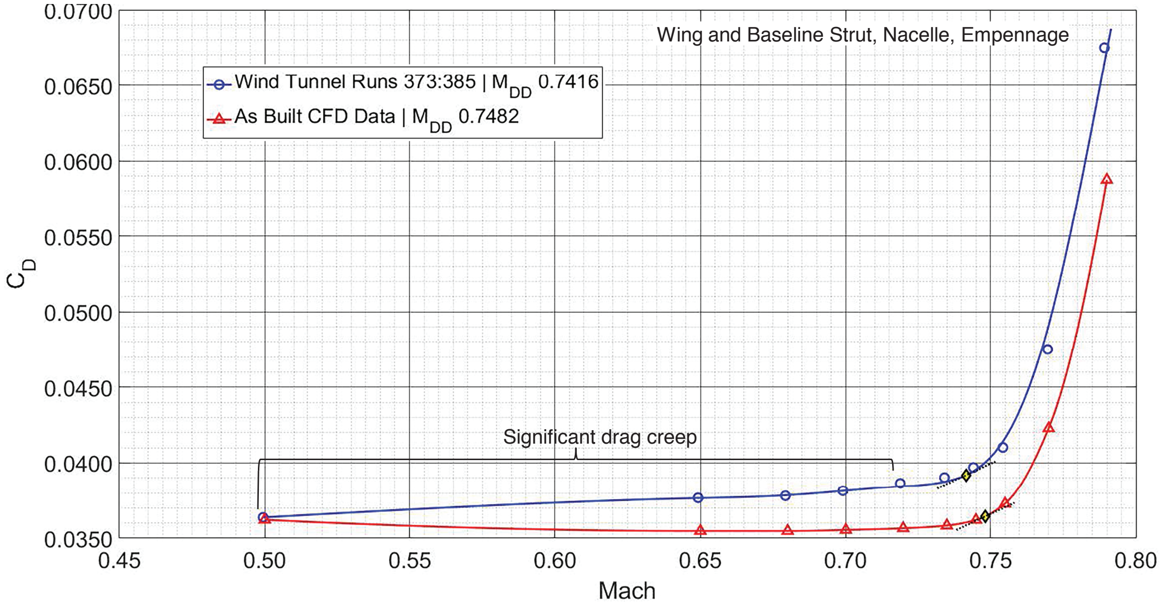

Figure 7.64 – Drag Rise Curves for CFD and Wind Tunnel Test.

7.6.5 Final CFD Predictions vs. Test Data

Based on the updated computational models following the test, a revised comparison of the CFD vehicle predictions was made for comparison to the test data. This computational model considered all revised elements of the geometry considered post-test. This includes: sting, sting gap, sting cavity, aft fairing, and MDM-based aeroelastic twist from the design point. To improve on this comparison, there are several elements that are critical for improving both the CFD predictions and the test data.

- Recollect the test data for a smooth model to eliminate the effects of model roughness.
- Further updates to the computational model – run with model trip locations rather than fully turbulent, and compute a revised aeroelastic twist for each point on the polar to ensure the most accurate simulation of the model geometry.

Even though there is still room for the data to collapse further, the revision of the computational models post-test moved that difference in the correct direction, reducing the delta drag between test and CFD by roughly 16 cts as shown in Figure 7.65. This leaves 32 cts of drag discrepancy relative to CFD predictions that remains unresolved with indications pointing to surface roughness as the primary contributor. A repeat test with a refinished model is recommended to resolve the data disagreement.

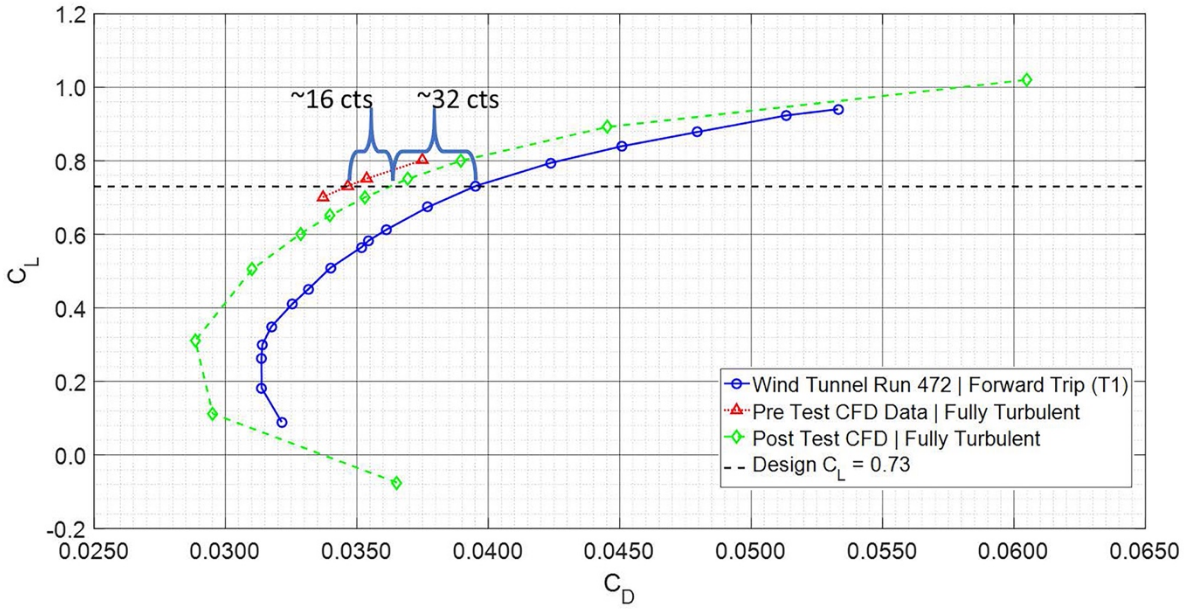

Figure 7.65 – Performance Comparison of Full Configuration – 'Final' CFD Model (including as-built fuselage, aft fuselage fairing, and C_L = 0.73 aeroelastic twist) vs. Test Data (Run 472).

7.7 Stability and Control

A first level estimate of the stability and control characteristics were generated during the vehicle design phase of the contract. During the wind tunnel test, stability and control was assessed with sideslip runs and roll control surface deflections (inboard aileron, outboard aileron, and spoiler). These surface deflections were measured in isolation and their combined effect is not considered. All stability and control runs were conducted using full built up configurations without the horizontal tail (unless specified). In addition, these data were collected at 4 Million Reynolds number per foot for reduced model loads as test conditions included Mach numbers up to dive speed and high angles of attack.

7.7.1 Aileron Effectiveness

The inboard aileron effectiveness was measured and compared to pretest calculation, a prediction at cruise angle of attack and Mach 0.75. Tunnel conditions reported are the closest data representative of these conditions. A blue bracket labeled “Pretest Prediction” is shown in the following figures and indicates the expected control authority. The “Pretest Prediction” is offset to correlate with the nonzero rolling moment resulting from a small model asymmetry. The data presented in both Figure 7.66 and Figure 7.67 show the aileron control authority predictions are nearly identical to the tunnel data.

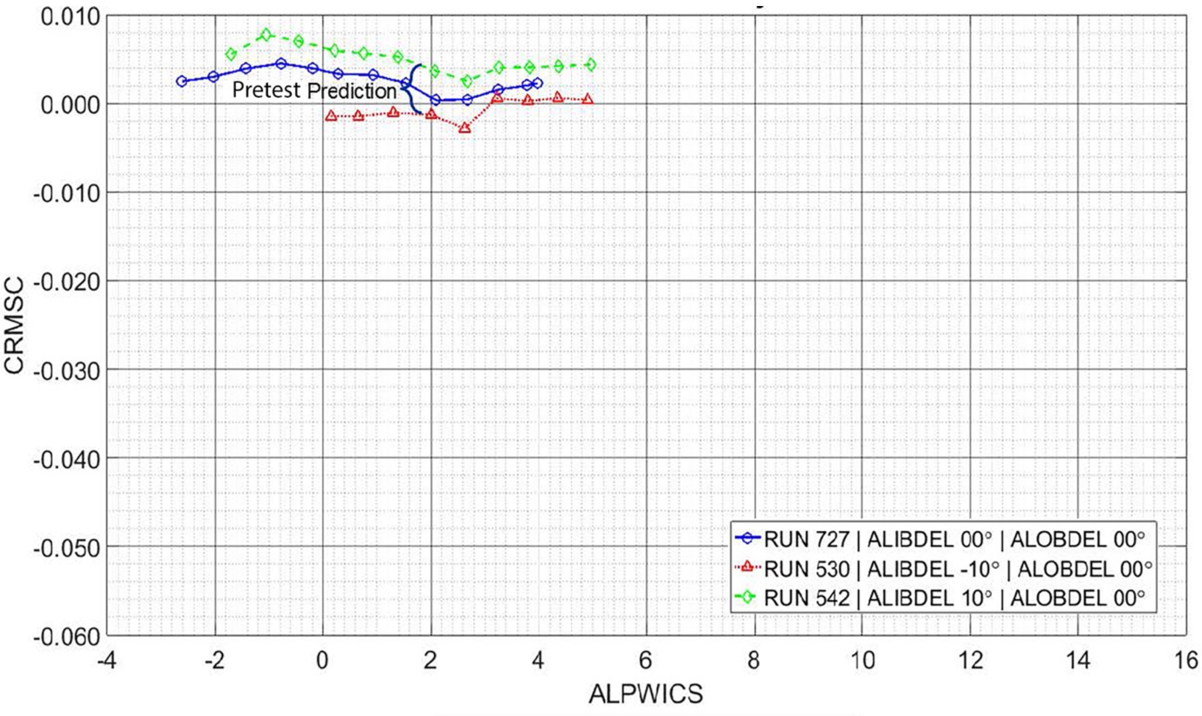

Figure 7.66 – Inboard Aileron Deflections Mach = 0.77, unit Reynolds Number = 4.0 M/ft.

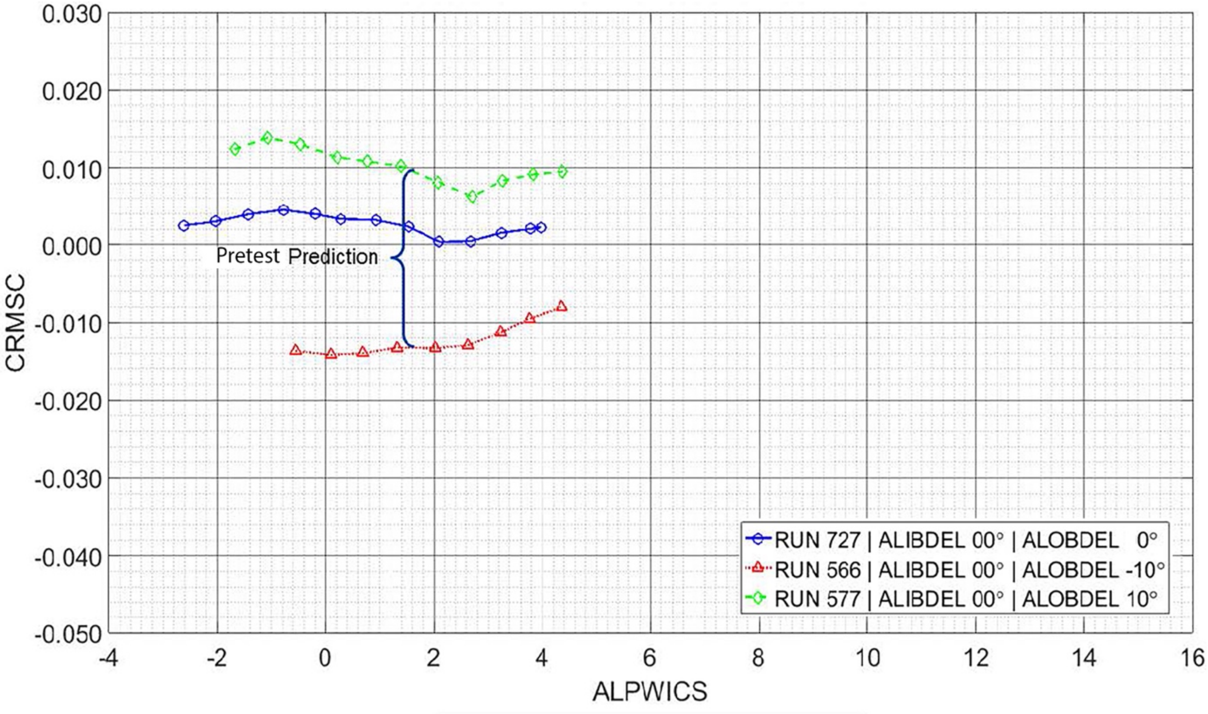

Figure 7.67 – Outboard Aileron Deflections, Mach = 0.77, unit Reynolds Number = 4.0 M/ft.

7.7.2 Spoiler Effectiveness

Spoiler effectiveness was also measured in the tunnel. Like aileron control authority, it is compared with pretest predictions by a blue bracket. In Figure 7.68, the spoiler effectiveness at -10 degrees is more effective than predicted and shows approximately two thirds of a full -60 degree deflection. Testing was conducted at dive speed for the TTBW and spoiler effectiveness at this condition is shown in Figure 7.69. At this condition, the data shows signs of slight reversal at low spoiler deflection. This is not completely unexpected as other configurations have shown a similar trend. However, if additional testing is performed, an attempt to expand the load limits of the model should be investigated and full deflections should be considered for testing.

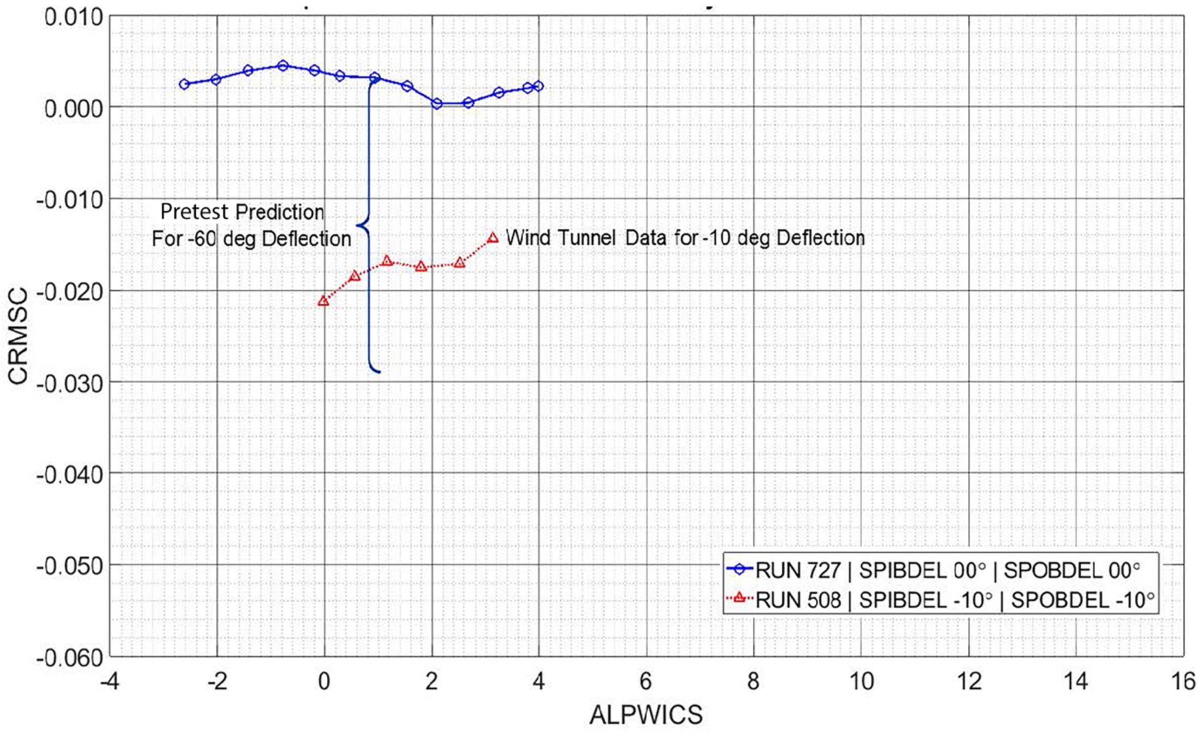

Figure 7.68 – Spoiler Deflections Mach = 0.77, unit Reynolds Number = 4.0 M/ft.

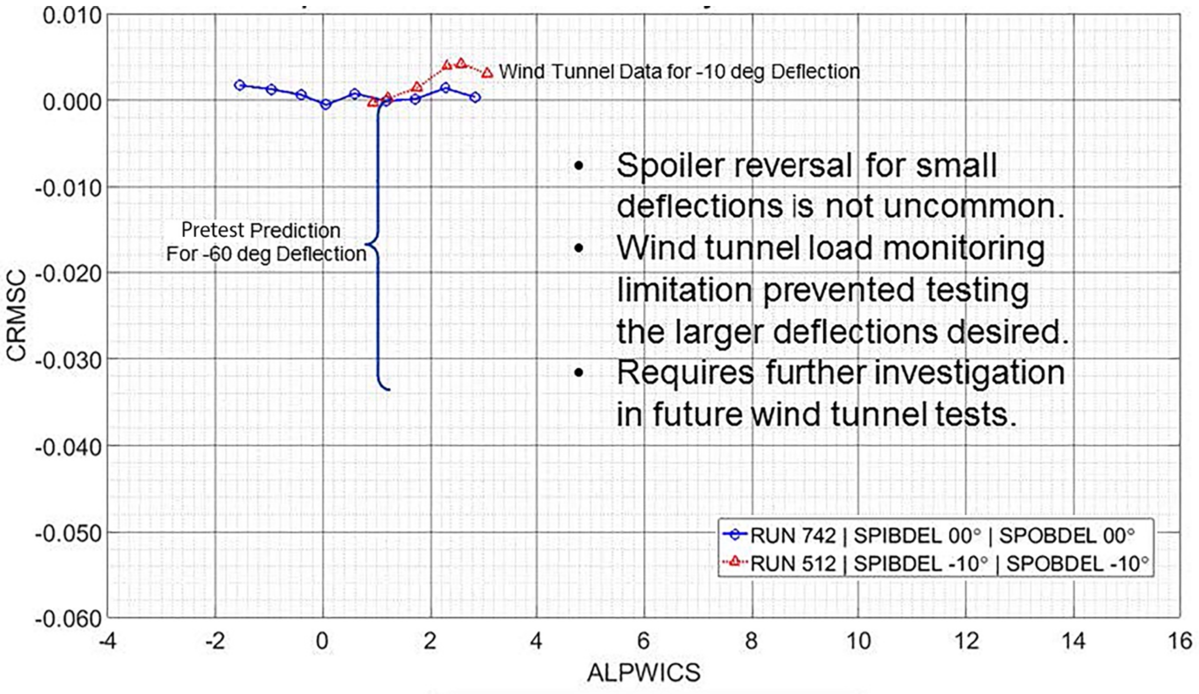

- Spoiler reversal for small deflections is not uncommon.
- Wind tunnel load monitoring limitation prevented testing the larger deflections desired.
- Requires further investigation in future wind tunnel tests.

Figure 7.69 – Spoiler Deflections Mach = 0.87, unit Reynolds Number = 4.0 M/ft.

7.7.3 Horizontal Tail Effectiveness

The effectiveness of the horizontal tail was also predicted. The data are shown for the low speed Mach 0.2 test case run at 2.8 Million per Foot unit Reynolds number in Figure 7.70. This condition is representative for takeoff and landing conditions. Full effectiveness was not run conceptually, however, the -1.07 degree tail incidence increment to trim agrees favorably with the full -6 degree increment. Also, the pitching moment tail off is very close to the pretest prediction. This is not surprising because the configuration is very conventional in the pitch plane.

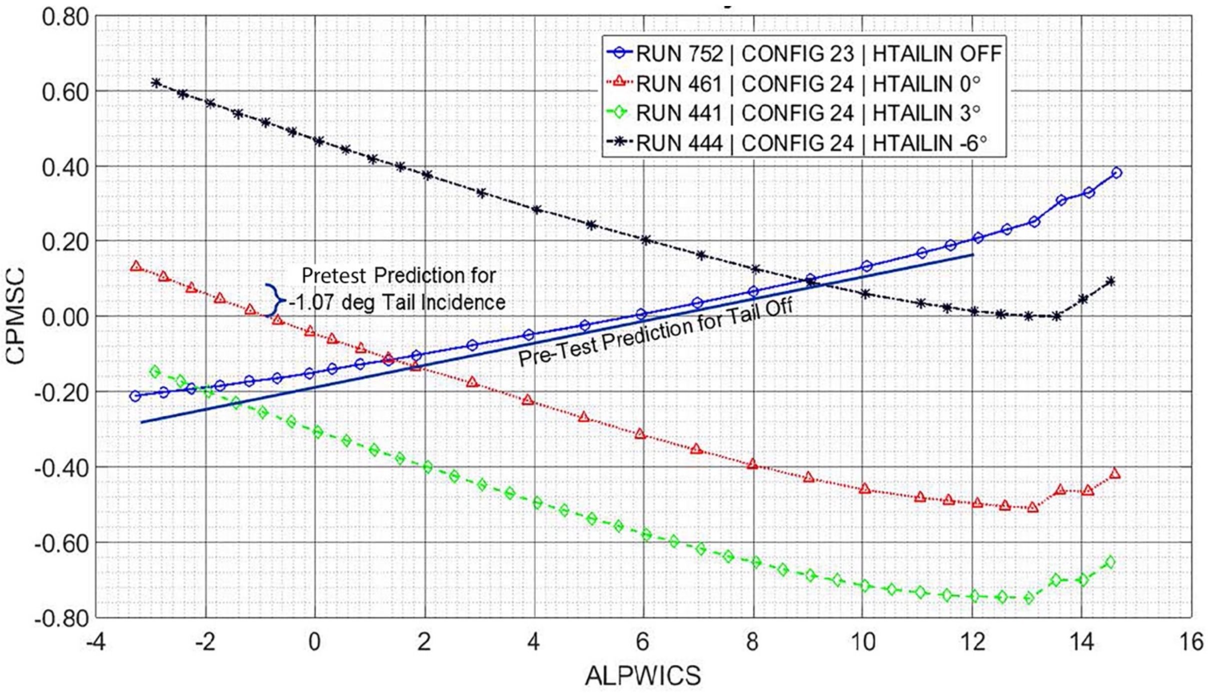

Figure 7.70 – Horizontal Tail Effectiveness, Mach = 0.2, unit Reynolds Number = 2.8 M/ft.

7.7.4 Lateral Directional

Lateral directional stability is also assessed for the configuration. The test data were collected at and compared at takeoff and approach conditions. The test data shows (Figure 7.71) that for 13 degree beta, the yawing moment tail off is approximately half the prediction. This would indicate the tail off configuration is significantly more stable than the predictions. The tail on data shows a stable configuration as expected. No pretest prediction for tail effectiveness was made.

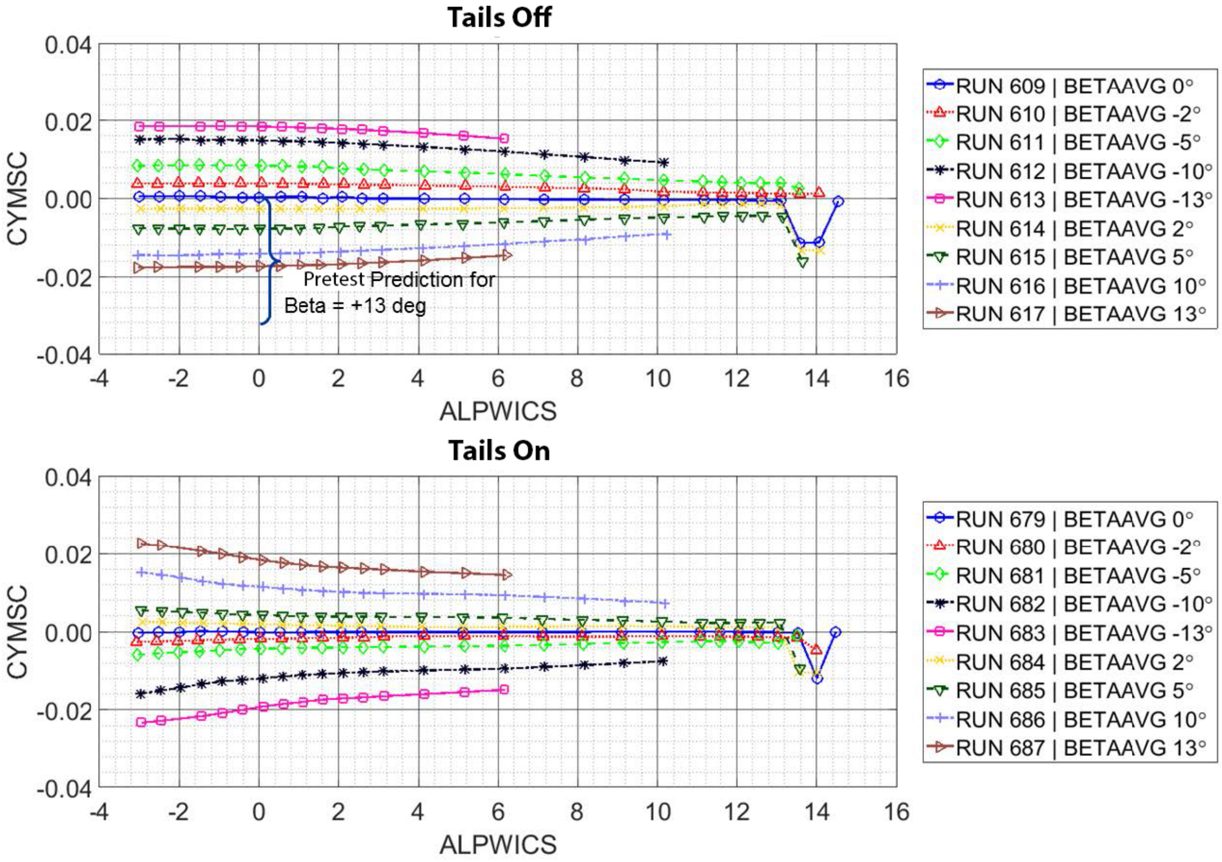

Figure 7.71 – Lateral Directional Data: Mach = 0.20 and unit Reynolds number = 2.8M/ft.

7.8 Test Conclusions

In many aspects, the wind tunnel test program was a success. Pretest drag divergence was predicted to be Mach 0.748 at wind tunnel Reynolds Number while the test results indicate drag divergence at Mach 0.742. The global pressure architecture captured with pressure sensitive paint showed generally good agreement with the computational flowfield with differences primarily indicating stronger shock strength in the tunnel and a wing root lambda shock system that is slightly more diffuse. In addition, the aeroelastic predictions for model deformation show excellent agreement with the data acquired from the tunnel's MDM system. The aeroelastic deformation error between the design 1g and actual 1g shape accounted for a tenth of a count drag offset, a value substantially less than the balance accuracy, between design and test. The MDM data were essential to verifying the in tunnel shape, which helped the team isolate the differences between the pretest predictions and the tunnel data.

Post-test, significant work was completed to increase understanding of the sting and cavity effects for the model. Boeing completed a detailed CFD analysis of the as-built model geometry. The results of this study substantially decreased the offset between the predicted and measured data. Additionally, the source of unsteadiness was verified post-test with URANS analysis, which strongly indicates flow features that would influence the model pitch and drag data. This unsteady CFD verifies the aft body fix as necessary for increased data accuracy and was a significant development during the test.

The wind tunnel data for the baseline strut and alternate struts clearly show the alternate is superior at high Mach numbers and lower lift coefficients. This is the region where the alternate strut was designed to be superior so these results are not unexpected. However, the data corroborates the design intent.

Stability and roll control assessments were made and compared to pretest prediction. Aileron increments, both inboard and outboard compare favorably to the pretest predictions. The horizontal tail trim increments also agree with pretest prediction – this is expected due to the similarity of the empennage configuration as compared to conventional T-tail configurations. Lateral directional data shows that the tail off configuration is approximately twice as stable as the pretest prediction. Overall predictions for spoiler effectiveness agree well with pretest predictions. However, at small deflections and high Mach number the spoiler shows a reversal in effectiveness. This is not an uncommon behavior and can be observed in empirical data – however, additional study should be performed to verify that this trend does correct at higher deflections.

Although many areas of study show good correlation between test and prediction, the largest discrepancies are in the areas of drag performance and component increments. Significant post-test work has been performed to determine the source of these discrepancies and the results show a strong likelihood that model surface roughness is a primary culprit. The test team developed a low risk high efficiency approach to gathering test data, which involved a build-down approach (starting with the full configuration and removing components to determine increments) with PSP and IR paint applied prior to test entry. This approach allowed for full configuration testing prior to high-risk strut off runs and also avoided paint application during tunnel occupancy. The side effect was increased model roughness and roughness asymmetry for initial test runs. The final data regression suggests strongly that surface roughness is the primary reason that the wind tunnel data does not precisely match CFD performance predictions. It is recommended the model be stripped of paint, polished, and retested.

7.9 Recommendations for future testing

The test team has completed a first test entry for the extremely high aspect ratio TTBW configuration in the Ames 11-Foot TWT. The test provided valuable insight to the design of the TTBW but has also provided additional insight for future testing.

7.9.1 Model Deformation Measurement System

The model deformation system proved to be invaluable for post-test data reduction. The system allowed for definitive verification that the 1g twist was attained to a tolerance well within balance accuracy. Based on the experience gained in this first TTBW test entry, several recommendations have been generated. The MDM system was most useful when multi-image results were utilized. These multi-image results provided shapes that closely matched expected deformations. At the time of testing, these multi-image results were fairly manual and required significant work to generate. The single image results were somewhat unreliable and provided uncertainty bands outside acceptable levels. Additionally, the test collected a wide array of test conditions with MDM collection at nearly all conditions in the test envelope. The amount of data collected is significant and is more than can be digested in a reasonable length of time. It is suggested for future testing that only 10-image MDM measurements be performed on a limited set of runs. Also, doubling the number of spanwise stations would provide better resolution on the twist data.

To summarize, future MDM testing will be improved by:

- Using only multi-image average results
- Limit the number of data acquisitions to reduce tunnel occupancy
- Increase the number of spanwise locations to provide better resolution of model twist
- Improve repeatability of target applications to the model
- Increase camera resolution or increase the number of cameras to reduce uncertainty

7.9.2 Infrared Imagery

Infrared imagery is a valuable resource for model testing. However, the IR paint should be omitted from this process OR a smoother formulation should be utilized. The paint improves visibility of the flow features, but also increases the model surface roughness to levels incompatible with testing at these Reynolds numbers. It is suggested that all future testing utilize IR imagery for transition, shock location, and vortex detection on a clean polished model. Having these images real time in the customer area (as provided at Ames) is ideal and image collection should be automatic for all test conditions run. An improvement might be to have a real time panning camera controlled from the customer area.

7.9.3 Pressure Sensitive Paint

Pressure sensitive paint is a valuable resource for this type of model. Due to the limited numbers of pressure taps that could be integrated due to structural concerns, PSP was the only means available to gather sufficient surface pressures for flow field diagnostics. Testing with PSP, however, does come with some challenges. The process used for this test requires an epoxy base layer be used for PSP application. This base layer is then painted with PSP. The surface roughness of these paint layers adversely affects the boundary layer thickness, which drives shocks forward and increases their intensity. Several recommendations are suggested for future testing utilizing PSP:

- Collect performance data prior to painting the model
- Sand the base layer to a very smooth finish prior to PSP application
- Maintain a clean leading edge at least to the trip dots
- Work PSP formulation to reduce surface roughness
- Determine feasibility for PSP camera in fuselage to obtain wing-strut junction pressures

7.9.4 Model Design Changes

Overall the wind tunnel model performed well especially in light of the fact that the test matrix was expanded during testing to include significant strut off testing to Mach numbers significantly higher than planned. Some small model modifications could enhance future tests. The aft fuselage geometry, driven by the configuration integration constraints, is flatter at the keel than heritage experience. This caused an hourglass shaped cutout that, in combination with a larger than needed sting interference clearance, drove unexpected cavity pressure unsteadiness. To mitigate this, it is suggested that the aft fuselage be modified to turn the flow streamwise prior to the sting opening. The sting clearance envelope should also be reduced to a minimum clearance level. Additionally, precoordination work with the model vendor on expected rigging tolerances and areas of importance will ease the model buyoff process. Additionally, nacelle pressures should be included in future testing to provide insight to inlet mass flow rate.

7.9.5 Computational modeling

The geometry used for pretest predictions should be as representative as possible of the as-built geometry. This suggests including the stagnant regions of flow in the cavity, which can be a significant contribution to the sting corrections. To improve pretest predictions, the inclusion of the tunnel test section and model support structure should be considered. Also, as previously stated, MDM data are extremely helpful when attempting to isolate increments and fully understand the actual deformed shape for the model.

8.0 Future Technical Milestones

Significant accomplishments in the area of high-speed design, structural layout, and low-speed design have been made during this phase of program execution. There are several areas for additional risk mitigation which are discussed within this section.

8.1 High-Speed Design

The high-speed design of the TTBW should be updated to a cruise Mach number of M=0.8 so current levels of commercial transport productivity can be maintained. The developed design should be validated in a high-speed wind tunnel test at the NASA Ames 11-Foot TWT. The primary objective of the high-speed design effort will be to investigate the performance potential of a M=0.80 design, quantify the wing-strut interference levels, and to update aircraft sizing and performance prediction tools.

Primary areas of risk that should be included with further study are the examination of:

- Buffet boundary: Work done in Phase III indicate that local shaping to reduce shock strength in the wing-strut channel created a risk of experiencing buffet during operations at very low lift coefficients. This was the result of local downloading of the strut local to the strut-wing intersection, which results in significant flow acceleration on the underside of the strut when at large negative angles of attack. An investigation of potential solutions and mitigation strategies including (but not limited to): local area ruling, alternative wing-strut attachment arrangements, and aerodynamic devices such as flaps should be performed.
- Strut aerodynamic-structural coupling and optimization: Load requirements in the strut have a very strong influence on the aerodynamic shaping of the strut. The M=0.8 configuration will have increased sensitivity to weight-drag trades due to the nonlinear effects of increasing shock strength at higher cruise Mach numbers. The aerostructural trades should be investigated by determining design trade factors and exercising multi-disciplinary studies.

8.2 Low-Speed Design

The high-lift system requires further development and testing in order to validate the low-speed performance of the TTBW configuration. This should include the continued refinement and optimization of the current baseline leading-edge Krueger and trailing-edge single-segment flap as well as the development of an alternate high-lift system design. Both high-lift systems should be tested to validate their performance levels as well as to quantify parametric studies on the leading-edge device spanwise cutouts due to the wing strut location, outboard wing fold location, and the nacelle/pylon installation. The test results for both high-lift system concepts should then be used to support the MDO studies leading to the final design of the high-lift system.

The risk areas for the high-lift development of the TTBW configuration include validation of the low-speed performance levels as well as the assessment of the effect of the leading-edge device spanwise cutouts due to the wing strut attachment, nacelle/pylon installation, and the wing fold location. The performance of the leading-edge device will be significantly impacted by those regions. The refinement of the leading-edge device to mitigate the impact of those regions could affect the high-speed wing and strut design.

8.3 Additional Risk Mitigation Tasks

This work includes investigation in the three primary areas for TTBW: buffet margin (at high and low lift coefficients), bird strike / damage tolerant design, and a configuration MDO which will facilitate mission, Mach number, and planform optimization for a TTBW and cantilever configurations with consistent configuration rules and levels of analysis.

SUGAR Phase III design activities identified buffet boundary as a risk to the TTBW technology. Shock induced separation on the wing upper surface, strut lower surface, and strut-wing intersection all have potential to generate buffet. Existing methods are developed for cantilever configurations and their applicability to externally braced configurations is unknown. Arguments can be made for increased buffet susceptibility in TTBW due to its very stiff inboard wing or the ability for small strut vibrations to generate large wing response. Planning for understanding TTBW buffet boundary through test is critical as development continues.

An additional risk mitigation activity will be focused on current assumptions about the susceptibility of the truss system to bird strike. Our concepts currently call for a titanium leading-edge element to deflect the substantial bird energy away from the strut. This plan is conceptual only and requires structural analysis to verify the approach is sound. Additionally, the jury strut and all strut attachments are bird strike critical and armoring / deflection tactics will require careful thought in this phase.

Finally, the comparison of the TTBW system to a cantilever baseline is required so as to verify the performance advantage offered by our concepts have been maintained and or is of sufficient value to justify a flight test program. The timing of this task will require careful thinking. Detailed planning of these activities has not yet been performed.

9.0 Summary

In Phase I of the SUGAR project, a truss-braced wing configuration was identified as having the potential to enable dramatic reductions in fuel consumption and emissions on a domestic passenger transport mission. The two primary areas of risk identified were aeroelastics and aerodynamic interference at transonic Mach numbers. During Phase II, the first of these risk areas was addressed through the development of a detailed analytical model and an aeroelastic wind tunnel test in the NASA Transonic Dynamics Tunnel. Both flutter speed and mechanism were found to be analytically predictable, and the weight penalties associated with flutter margin were found to be lower than anticipated. Further work remains in introducing unsteady aerodynamic effects to better capture the aeroelastic boundary shapes with the theoretical model, but the results indicate that aeroelastic phenomena should not pose a major barrier to the development of transonic truss-braced wing aircraft. Additional uncertainty remains, however, in the proper method for testing and certifying transport configurations with nonlinear aeroelastic boundaries.

In Phase III, the second primary risk area identified in Phase I was addressed through a detailed high-speed aerodynamic design and analysis. Several methods of aerodynamic shape optimization were utilized to refine the configuration and reduce adverse aerodynamic coupling effects between the primary components. Overall airplane drag was reduced significantly and strut drag was more than halved relative to the initial baseline design. After a comprehensive analysis using Navier-Stokes CFD methods, it was found that drag resulting from aerodynamic interference between the wing and strut can be reduced to approximately 1% of airplane drag (approximately 10 percent of strut drag) at cruise. These analytical predictions will be validated experimentally within the remaining Phase III effort.

Full operability range was established at cruise Mach number with no predicted adverse aerodynamic characteristics, however, maximum Mach conditions may present some concern due to the lack of validated analytical methods for predicting buffet in configurations of this type. Existing buffet predication methods were developed using cantilever wing flight and wind tunnel test data. Uncertainty in buffet margin and analysis methods represents an additional area of risk for transonic truss-braced wings which bears further investigation.

The integrated performance results indicate continued progress toward the NASA N+3 goals, and after addressing two of the most significant technical risk areas, the transonic truss-braced wing configuration still appears to hold promise for enabling reductions in fuel consumption on domestic passenger transport missions with potential additional benefit to larger configurations, which remain unstudied. The overall configuration, though cycled through many disciplines such as weights, structure, aeroelastics, and stability and control, should not be considered fully closed. The configuration is currently sized with body fuel (a nonstandard practice) and has significant wing scaling applied for optimum vehicle performance. This phase, as well as the previous Phase II effort, focuses primarily on gathering data for further design space optimization. Now that these data have been obtained, significant work should be completed to converge the vehicle planform with the mission constraints including fuel volume while optimizing vehicle aspect ratio. This work should be mirrored on a conventional configuration so as to be able to draw an even comparison between TTBW and cantilever configurations.

The configuration developed under this contract was tested in the Ames 11-Foot TWT. Drag rise data collected compares well with CFD prediction indicating that interference effects are minimal and that the truss system is not changing the overall cruise speed of the configuration. The stability and control data indicates the configuration compares well with pretest predictions in all areas except spoiler effectiveness at dive Mach number. Here spoilers indicate reversal at low deflections, a phenomenon the test team has experienced in prior configurations that should clear at higher deflections. Test data could not be generated to verify this due to model load limitations. The drag buildup data shows mixed results with some increments matching and some that do not. The root cause for this has been determined to be an unacceptably high level of surface roughness that is unable to be closed via post-test analysis. This also caused the overall drag levels of the wind tunnel test data to be offset from the test predictions by 30 counts at the design lift coefficient and Mach number. It is recommended the model be stripped of paint, polished, and a second tunnel entry be made.

The test team employed many methods of data collection including PSP, IR, and MDM data. These test techniques were important due to the limited surface pressure data available from the physical pressure taps. In the future, surface roughness caused by using these techniques should be carefully considered during the test planning phase. Recommendations for testing using these techniques have been developed.

9.1 Technical Results

A detailed aerodynamic design was carried out to refine the truss-braced wing configuration developed during Phase II of the SUGAR project. During Phase II, the cruise drag coefficient was estimated to be 298.1 counts using an empirically-based advanced design build-up. After detailed aerodynamic design using modern computational fluid dynamics, the cruise drag coefficient was reduced to 296.1 cts. Some differences exist between the Phase II and III on a component-by-component basis, and the close agreement in total cruise drag is partially the result of cancelling deltas. Had the drag discrepancies been additive rather than cancelling, however, the Phase II estimate would have been within 5% of total airplane drag and well within expectations for conceptual design of an unconventional configuration. These aerodynamic estimates were solidified using high-fidelity tools in Phase III, significantly reducing uncertainty in predicted aircraft performance.

During Phase II, it was assumed that an interference-free design could be obtained in which aerodynamic coupling effects between the wing and the strut result in no additional cruise drag. Though interference effects were significantly reduced from the 765-095-RD starting point during the Phase III design study, about 3 counts of interference drag remain. This is equivalent to about 1% of total airplane drag and is not believed to pose a significant barrier to further development of the truss-braced wing, particularly since this drag increase was more than offset by drag reductions elsewhere. Additionally, it is estimated that the truss system drag may be further reduced by at least one count (and possibly more) with continued work. This reduction would come from all forms of drag, not just interference.

An alternate strut configuration was investigated, in which the outboard end of the strut ties into a vertical pylon connecting it to the wing and providing some additional offset. At Mach 0.745, drag and weight penalties associated with the pylon were found to outweigh aerodynamic benefits from reduced wing-strut coupling. It is anticipated, however, that such alternate configurations may be a key enabler for truss-braced wing designs with cruise Mach numbers of 0.8 or higher and may mitigate the possible buffet issue at maximum operating Mach. Configurations such as these require aeroelastic study to verify their viability at a vehicle level.

The Phase II performance estimate represented a 54% reduction in fuel consumption compared to the equivalently sized SUGAR Free baseline cantilever wing aircraft (which represents a 2008 fleet technology level). The predicted fuel consumption reduction at the end of Phase III is 57% despite an increase in cruise Mach number. This represents continued progress toward the NASA N+3 goal of 60%.

9.2 Conclusions

- The SUGAR High transonic truss-braced wing design has made continued progress toward NASA N+3 emissions and fuel consumption goals achieving 57% reduction over the baseline.
- Uncertainty in performance estimates has been greatly reduced through detailed aerodynamic design of the fuselage, wing, strut, jury, nacelle, gear sponson, tails and fairings using computational fluid dynamics.
- Wing to strut junction stiffness is a critical factor for mitigating aeroelastic effects (flutter). Additionally, the higher fidelity FEM with detailed strut modeling showed that nonlinear effects may increase flutter speed which is opposite the findings from Phase II.
- Strut drag was found to be significant, accounting for about 10% of airplane drag. Only about 1% of airplane drag can be attributed to interference effects. This is likely to change as cruise Mach number is increased.
- FAR operability requirements were satisfied at the cruise Mach number.

- Uncertainty remains regarding buffet margin at the maximum operating Mach number. Additional technologies such as flow control, smart materials or simple hinged flaps may mitigate these higher Mach concerns and were not investigated in this study.
- Please refer to Section 7.8 for a detailed discussion of wind tunnel test conclusions

9.3 Recommendations

- Conduct high-fidelity aerodynamic design (similar to the work contained in this document) for a Mach 0.8 transonic truss-braced wing to enable increased fleet productivity. (Section 8.1)
- Undertake a dedicated buffet analysis and test effort to increase understanding and collect data for transonic buffet in truss-braced wing configurations. This study could be performed with either the Mach 0.745 or the Mach 0.8 configuration discussed in the previous recommendation. (Section 8.0 and 8.3)
- Perform equivalent conceptual-level design, sizing and optimization studies of cantilever and truss-braced wing aircraft of the same technology level to allow a fair and transparent comparison of the two configurations with all newly available data. This study should include planform trades to optimize the overall integrated performance of each airplane at a fallout aspect ratio while enforcing wing volume allocations for landing gear (low wing) and mission fuel. (Section 8.3)
- Stiffness requirements for the strut-wing connection should be investigated. The structural changes performed to close the higher fidelity FEM are likely lower efficiency than unexplored alternatives.
- Conduct initial planning for a possible transonic truss-braced wing demonstrator aircraft.
- Please refer to Section 7.9 for a detailed list of recommendations for future testing.

References

1. **Bradley, M. and Droney, C.** *Subsonic Ultra Green Aircraft Research: Phase I Final Report.* s.l. : NASA, 2011. CR-2011-216847.

2. **Bradley, M., Droney, C. and Allen, T.** *Subsonic Ultra Green Aircraft Research Phase II: Volume I - Truss Braced Wing Design Exploration.* s.l. : NASA, 2014. CR-2015-218704/VOLI.

3. **Bradley, K. and Droney, C.** *Subsonic Ultra Green Aircaft Research Phase II: Volume II - Hybrid Electric Design Exploration.* s.l. : NASA, 2014. CR-2015-218704/VOLII.

4. **Allen, T., Bradley, M. and Droney, C.** *Subsonic Ultra Green Aircraft Research Phase II: Volume III - Truss Braced Wing Aeroelastic Test Report.* s.l. : NASA, 2014. CR-2015-218704/VOLIII.

5. **Drela, M.** *A User's Guide to MSES 3.05.* Cambridge, MA : MIT Department of Aeronautics and Astronautics, 2007.

6. **Drela, M.** Athena Vortex Lattice (AVL) Method. [Online] MIT. http://web.mit.edu/drela/Public/web/avl/.

7. **Jameson, A. and Caughey, D.** *A Numerical Calculation of the Transonic Flow Past a Swept Wing.* s.l. : NASA, 1977. CR-153297.

8. **Henne, P. and Hicks, R.** *Wing Analysis Using a Transonic Potential Flow Computational Method.* s.l. : NASA, 1978. TM 78464.

9. **NASA.** Cart3D. [Online] http://people.nas.nasa.gov/~aftosmis/cart3d/.

10. **Campbell, R.** *Efficient Viscous Design of Realistic Aircraft Configurations.* s.l. : AIAA Journal, 1998. Paper 98-2539.

11. **Nichols, R. and Buning, P.** *User's Manual for OVERFLOW Version 2.1t.* 2008.

12. **Suhs, N., Rogers, S. and Dietz, W.** *PEGASUS 5: An Automated Pre-processor for Overset-Grid CFD.* s.l. : AIAA Journal, 2002. 2002-3186.

13. **NASA.** HYPGEN. [Online] http://people.nas.nasa.gov/~wchan/cgt/doc/hypgen.html.

14. **Schlichting, Herrmann.** *Boundary-Layer Theory.* s.l. : Springer, 2000. 978-3540662709.

Appendix A – Wind Tunnel Data

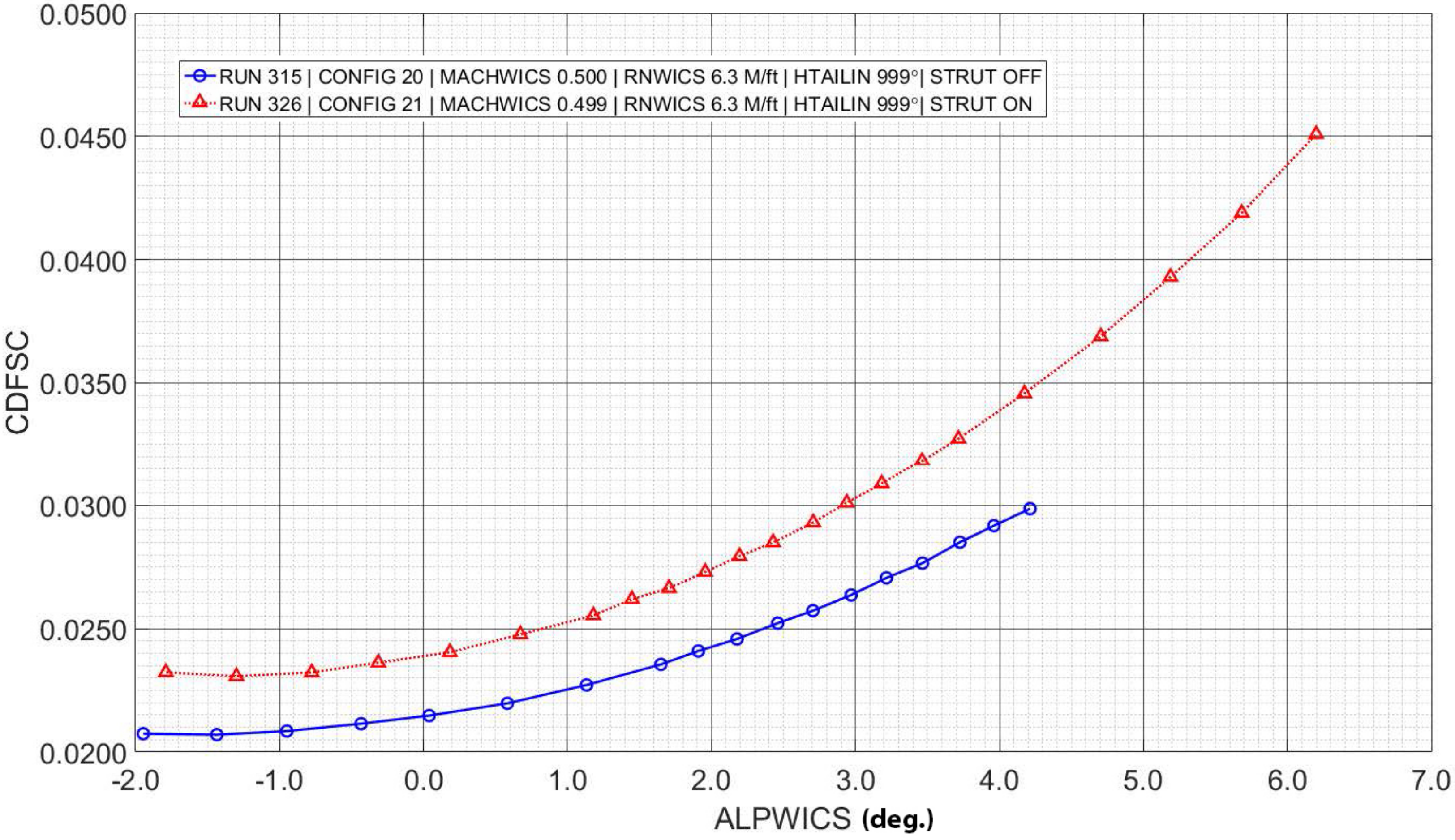

Figure A.1 – Strut effects on the drag characteristics: Mach = 0.50 and unit Reynolds number = 6.3M/ft.

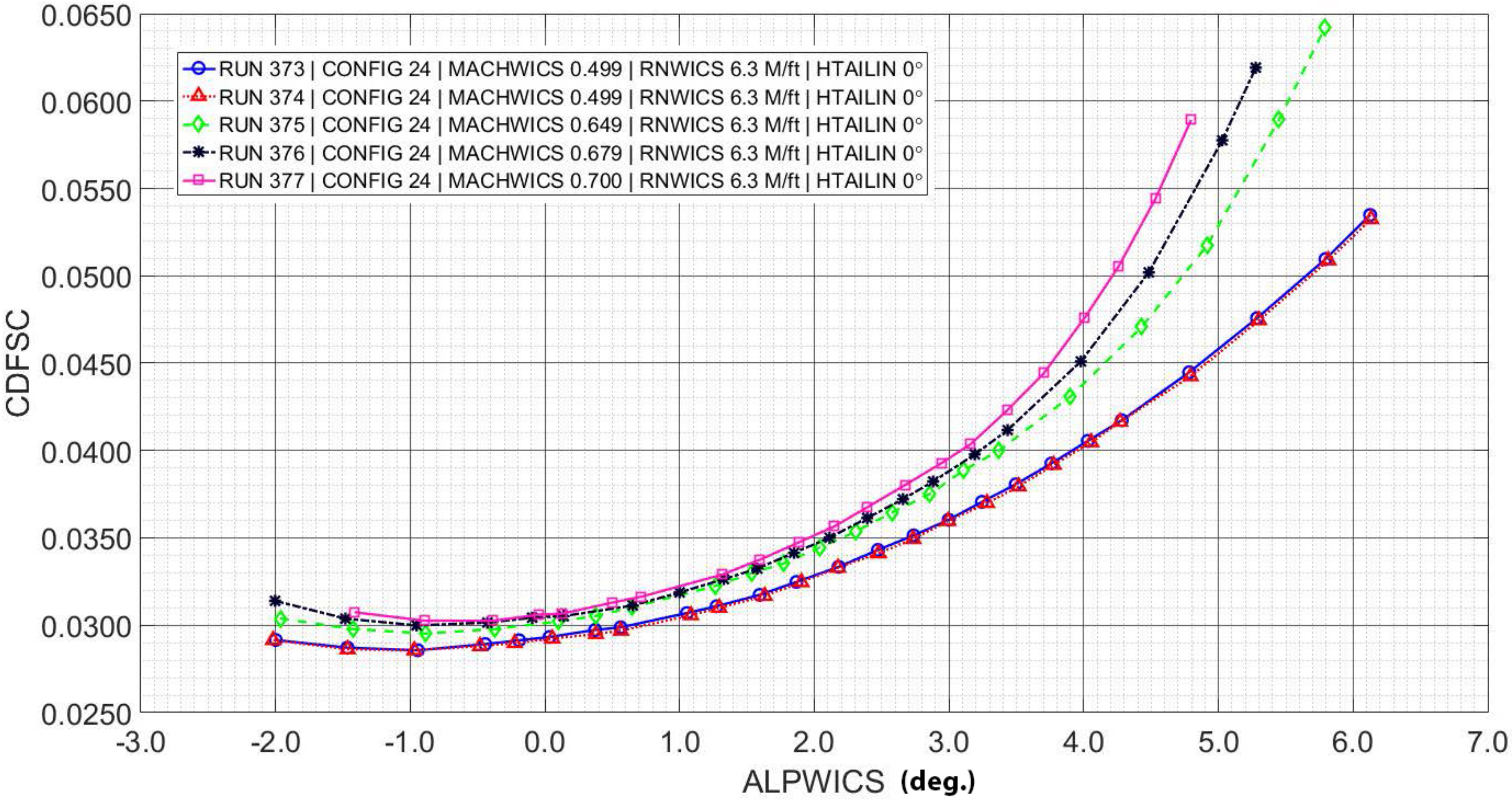

Figure A.2 – Effect of Mach number on the drag characteristics: unit Reynolds number = 6.3M/ft.

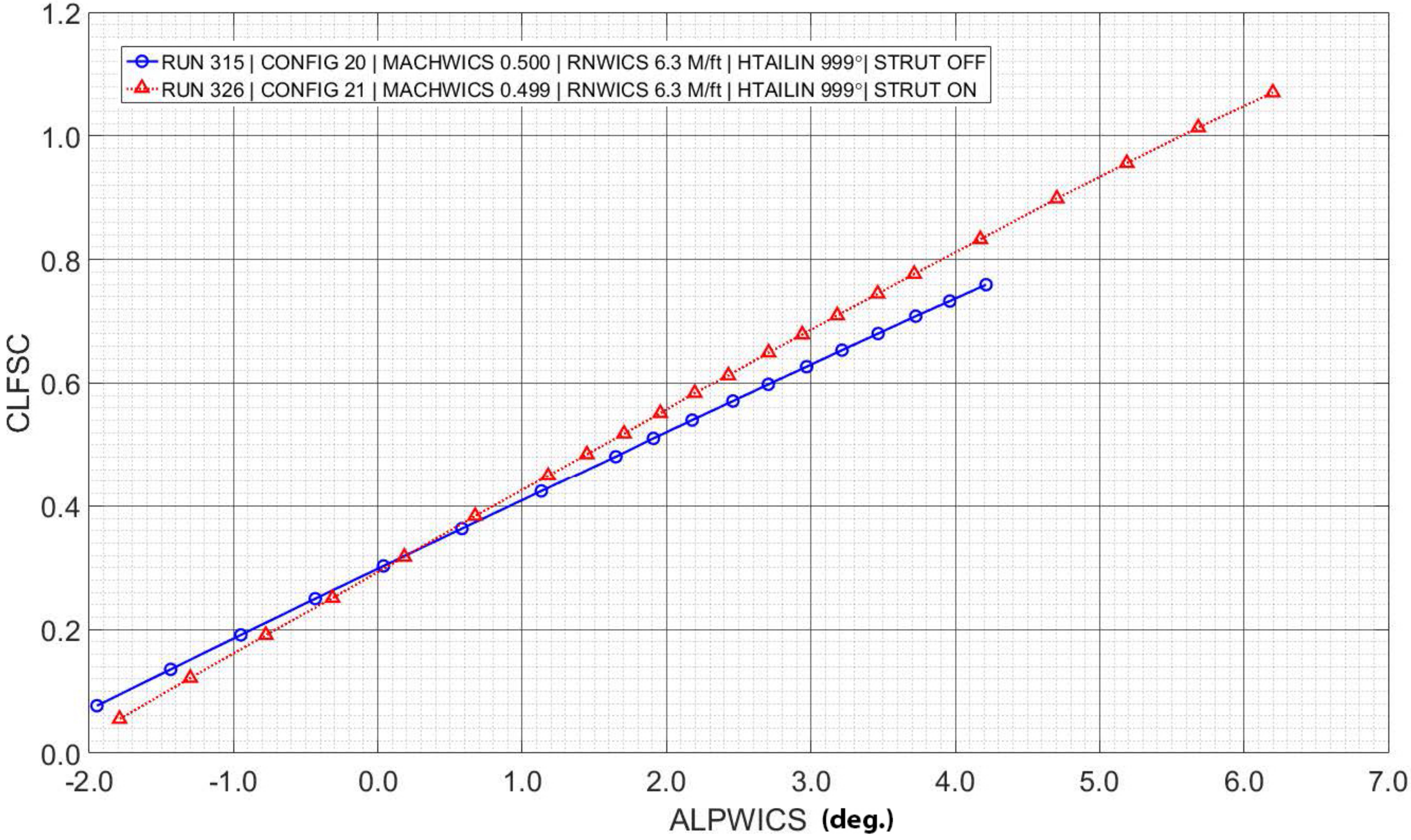

Figure A.3 – Strut effects on the lift characteristics: Mach = 0.50 and unit Reynolds number = 6.3M/ft.

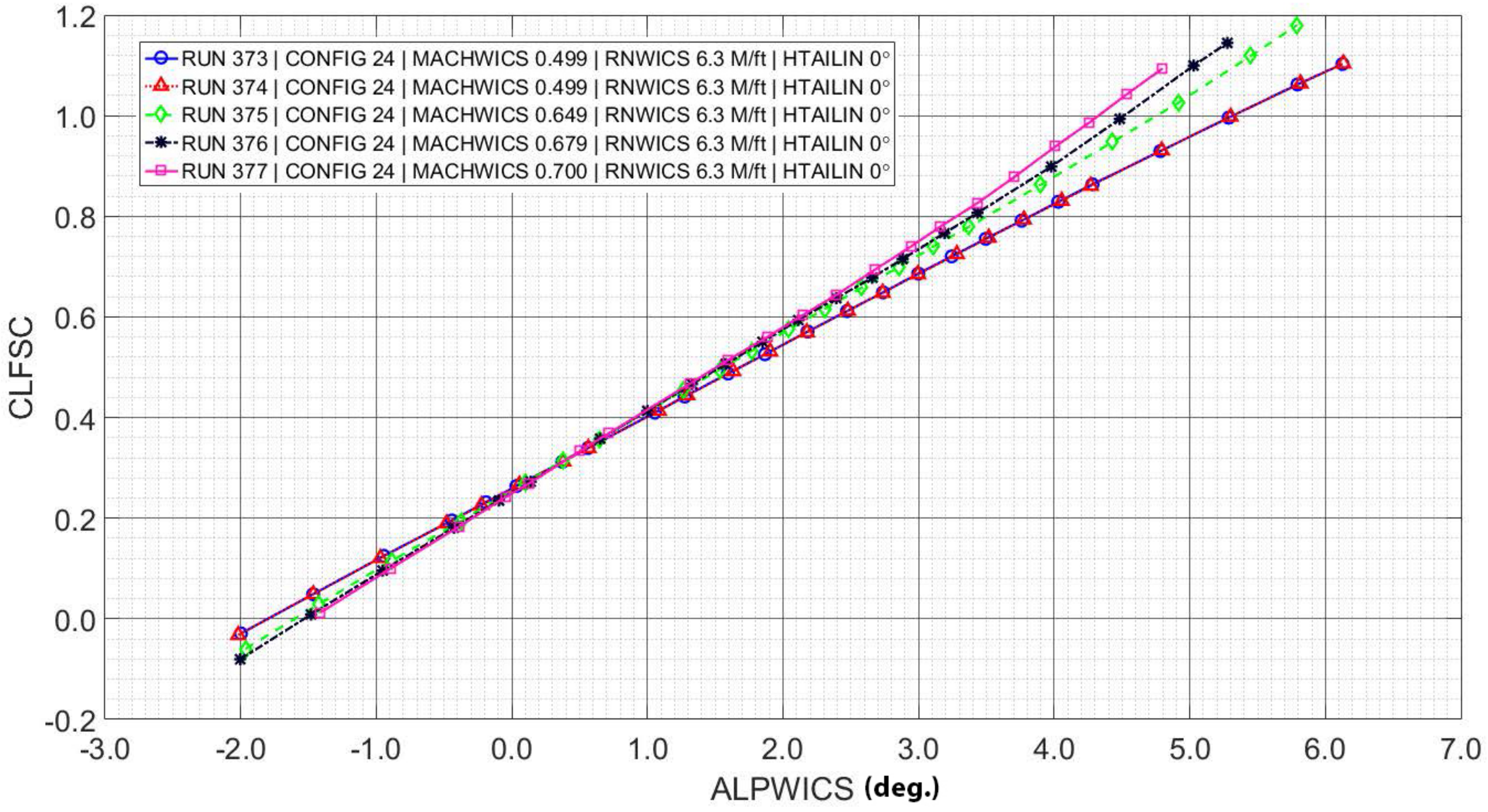

Figure A.4 – Effect of Mach number on the lift characteristics: unit Reynolds number = 6.3M/ft.

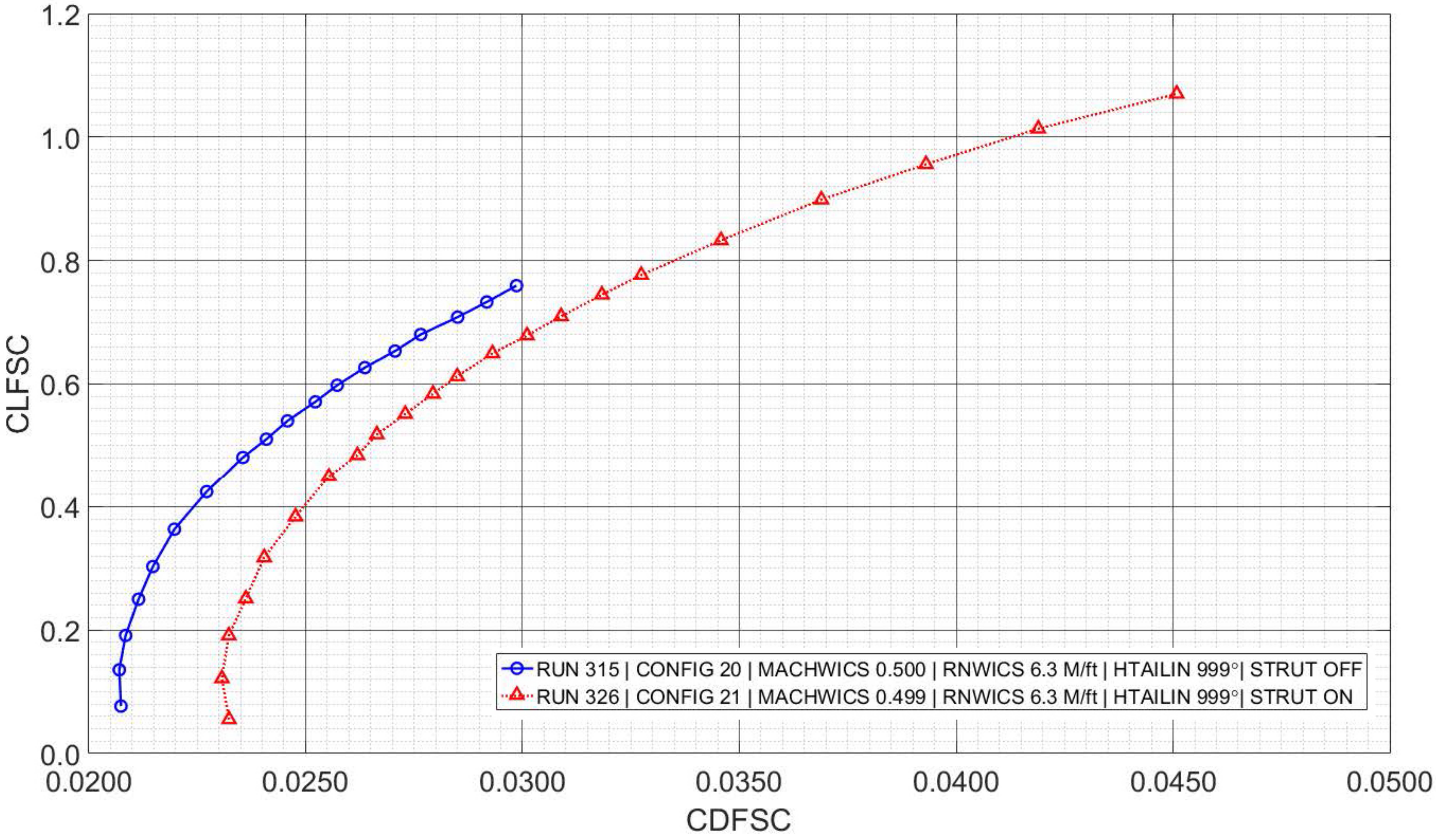

Figure A.5 – Strut effects on the drag polar: Mach = 0.50 and unit Reynolds number = 6.3M/ft.

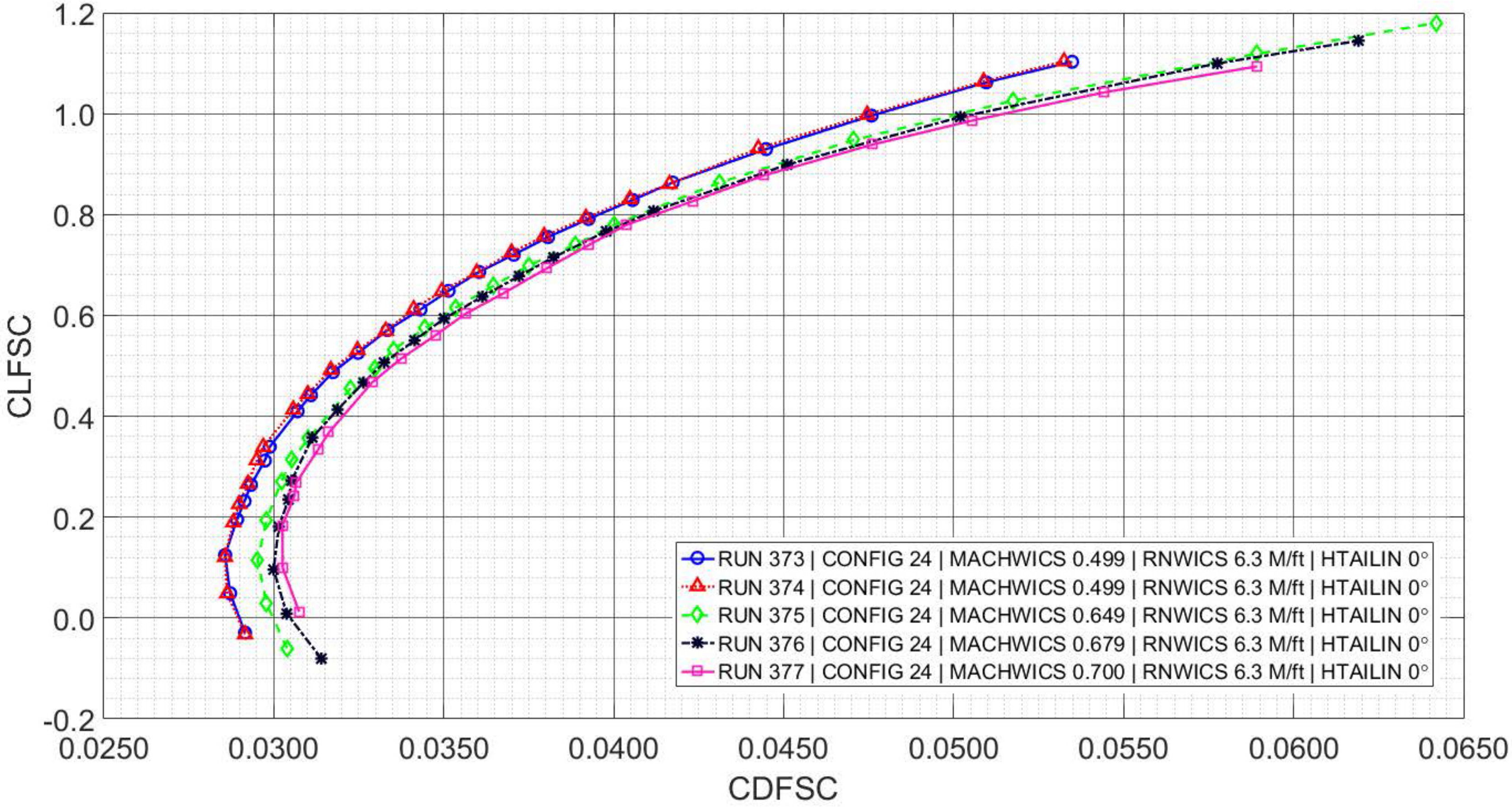

Figure A.6 – Effect of Mach number on the drag polar: unit Reynolds number = 6.3M/ft.

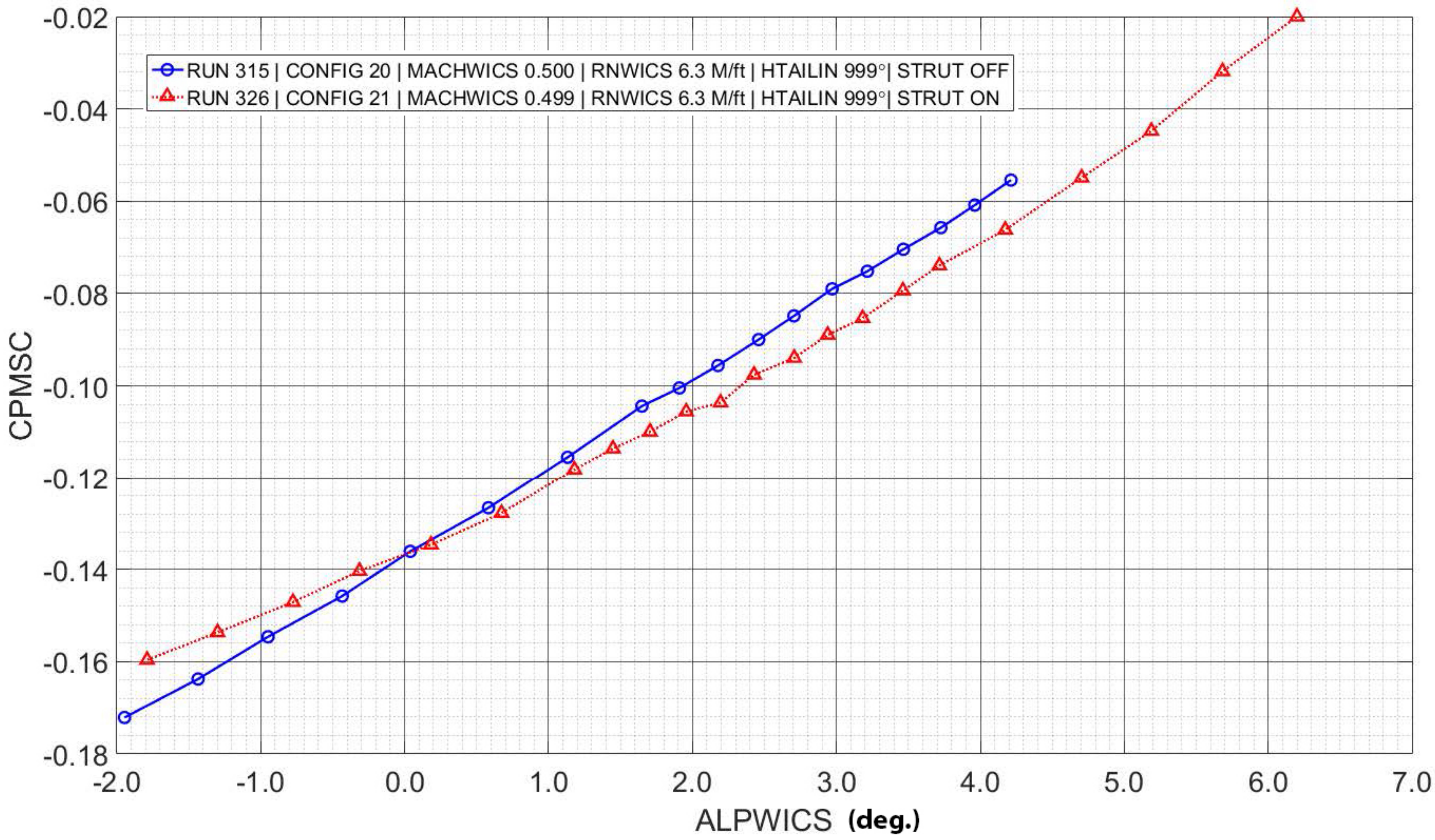

Figure A.7 – Strut effects on the pitching moment characteristics: Mach = 0.50 and unit Reynolds number = 6.3M/ft.

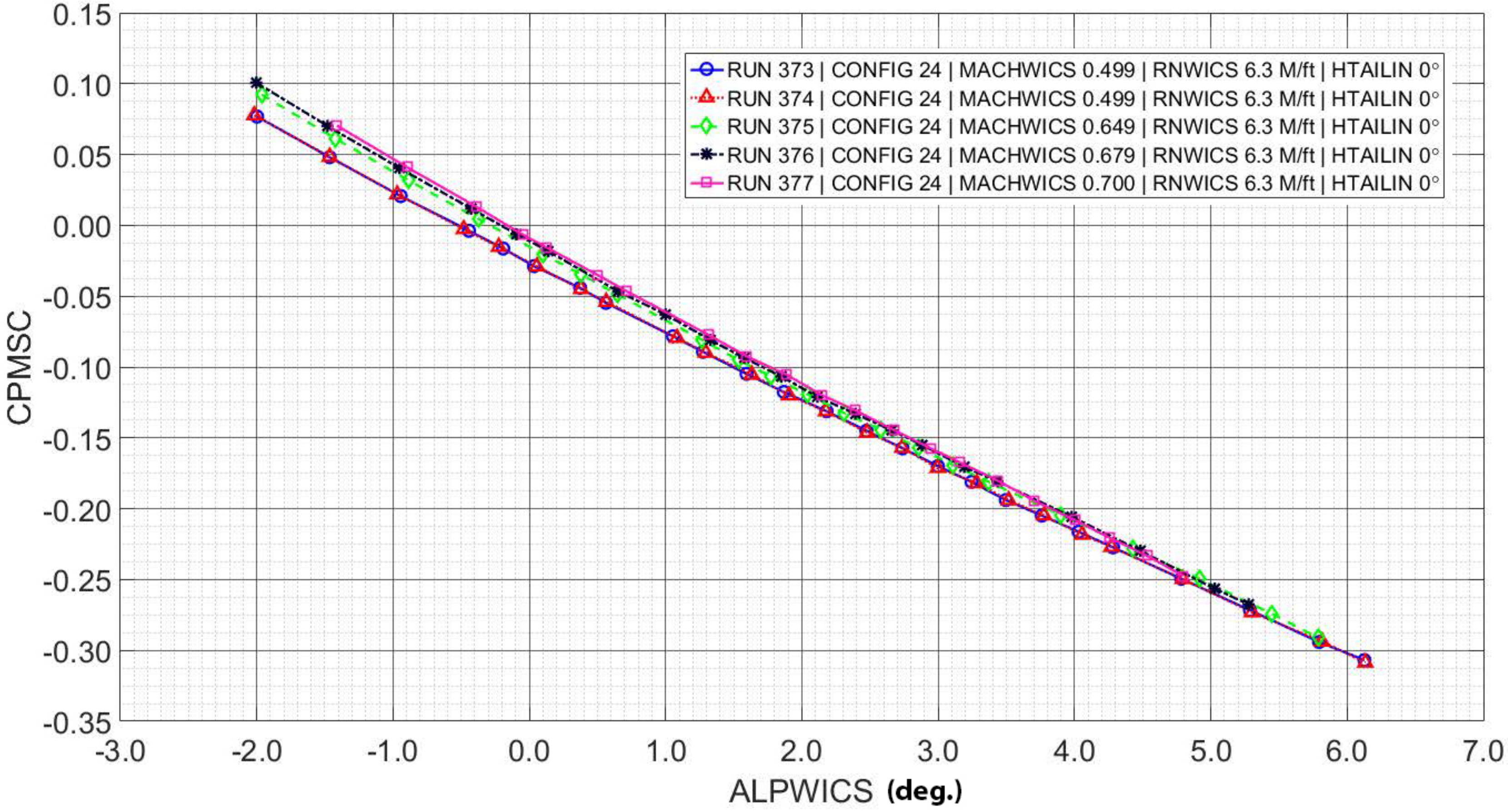

Figure A.8 – Effect of Mach number on the pitching moment characteristics: unit Reynolds number = 6.3M/ft.

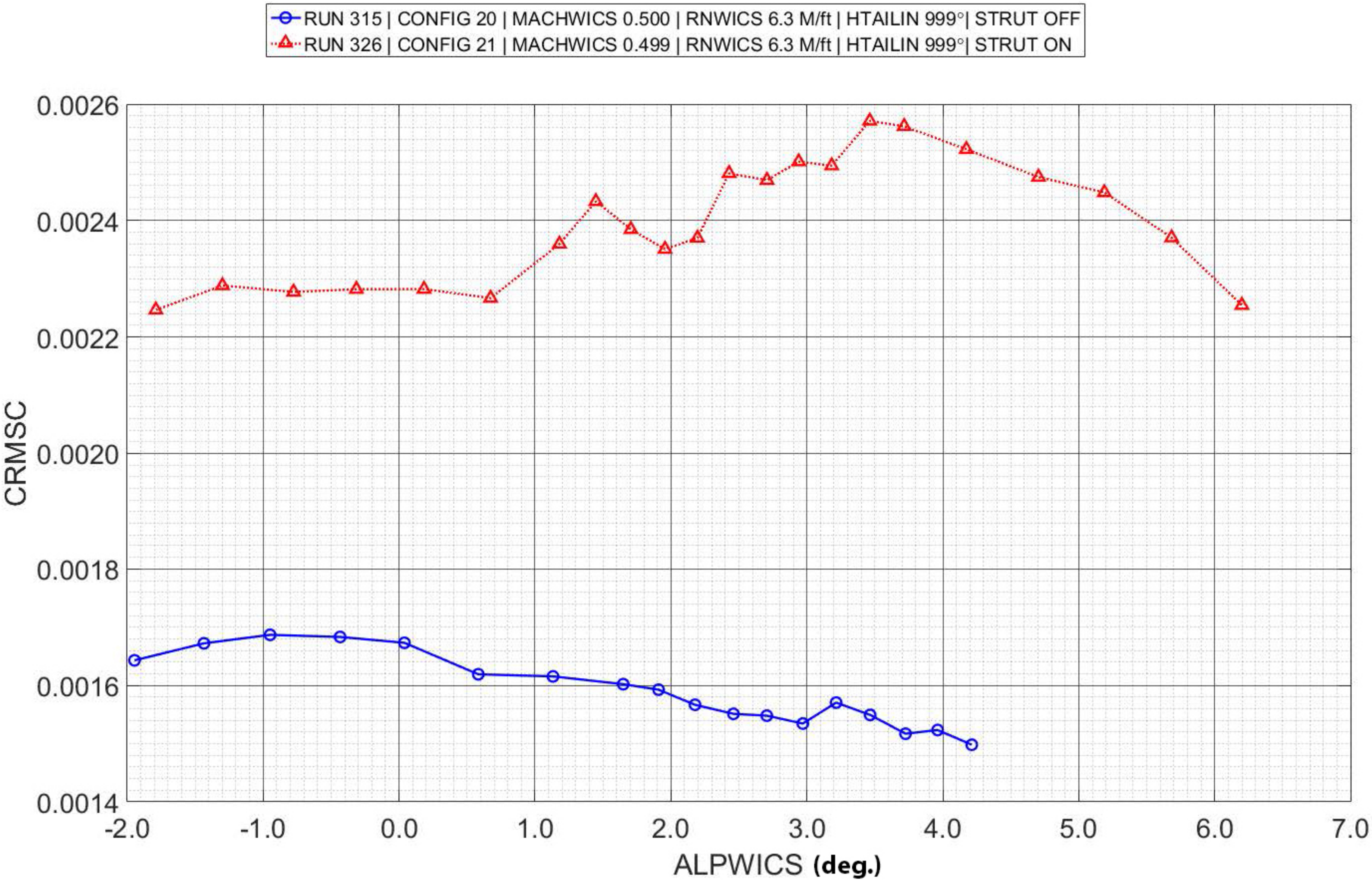

Figure A.9 – Strut effects on the rolling moment characteristics: Mach = 0.50 and unit Reynolds number = 6.3M/ft.

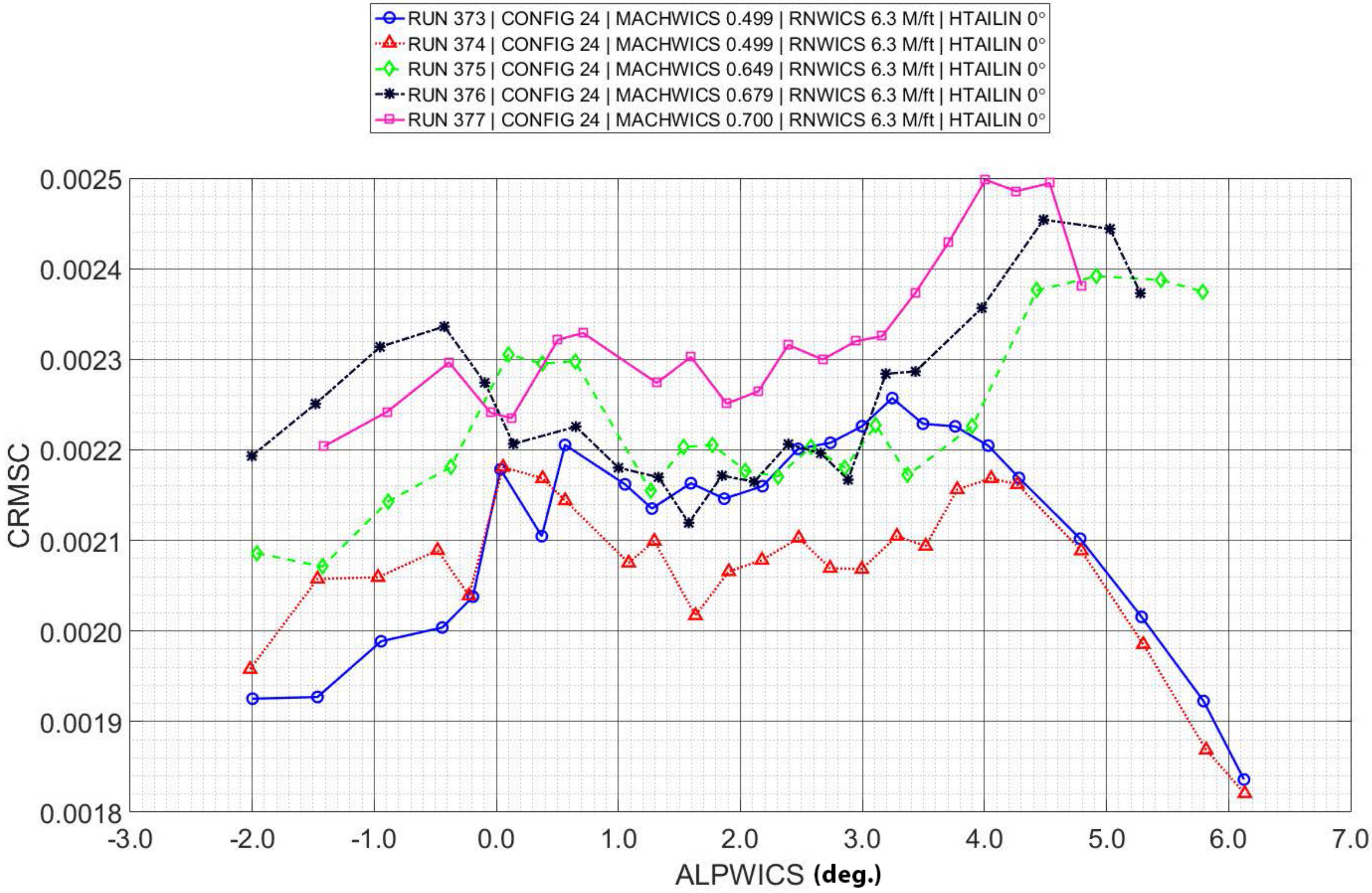

Figure A.10 – Effect of Mach number on the rolling moment characteristics: unit Reynolds number = 6.3M/ft.

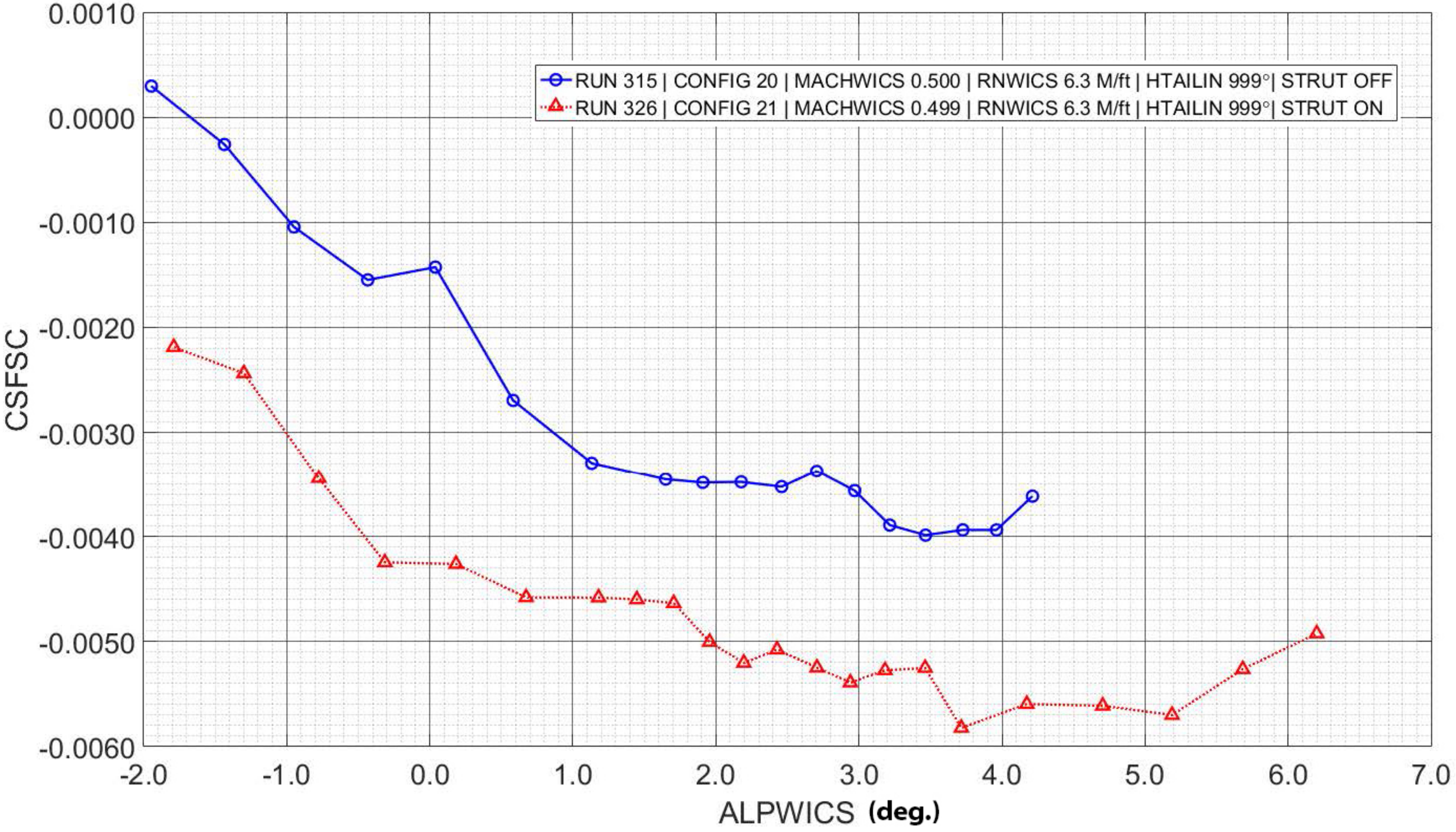

Figure A.11 – Strut effects on the side force characteristics: Mach = 0.50 and unit Reynolds number = 6.3M/ft.

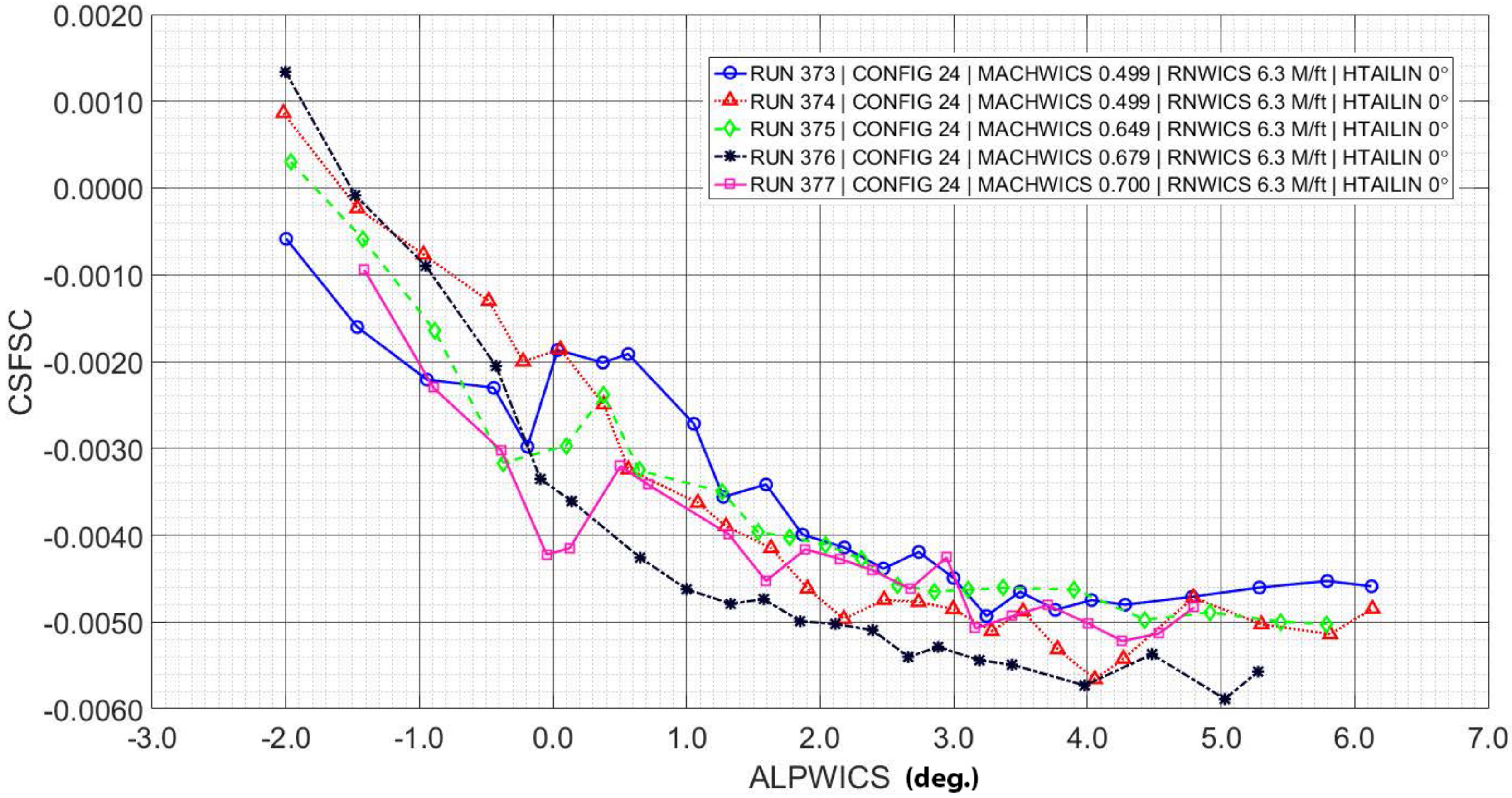

Figure A.12 – Effect of Mach number on the side force characteristics: unit Reynolds number = 6.3M/ft.

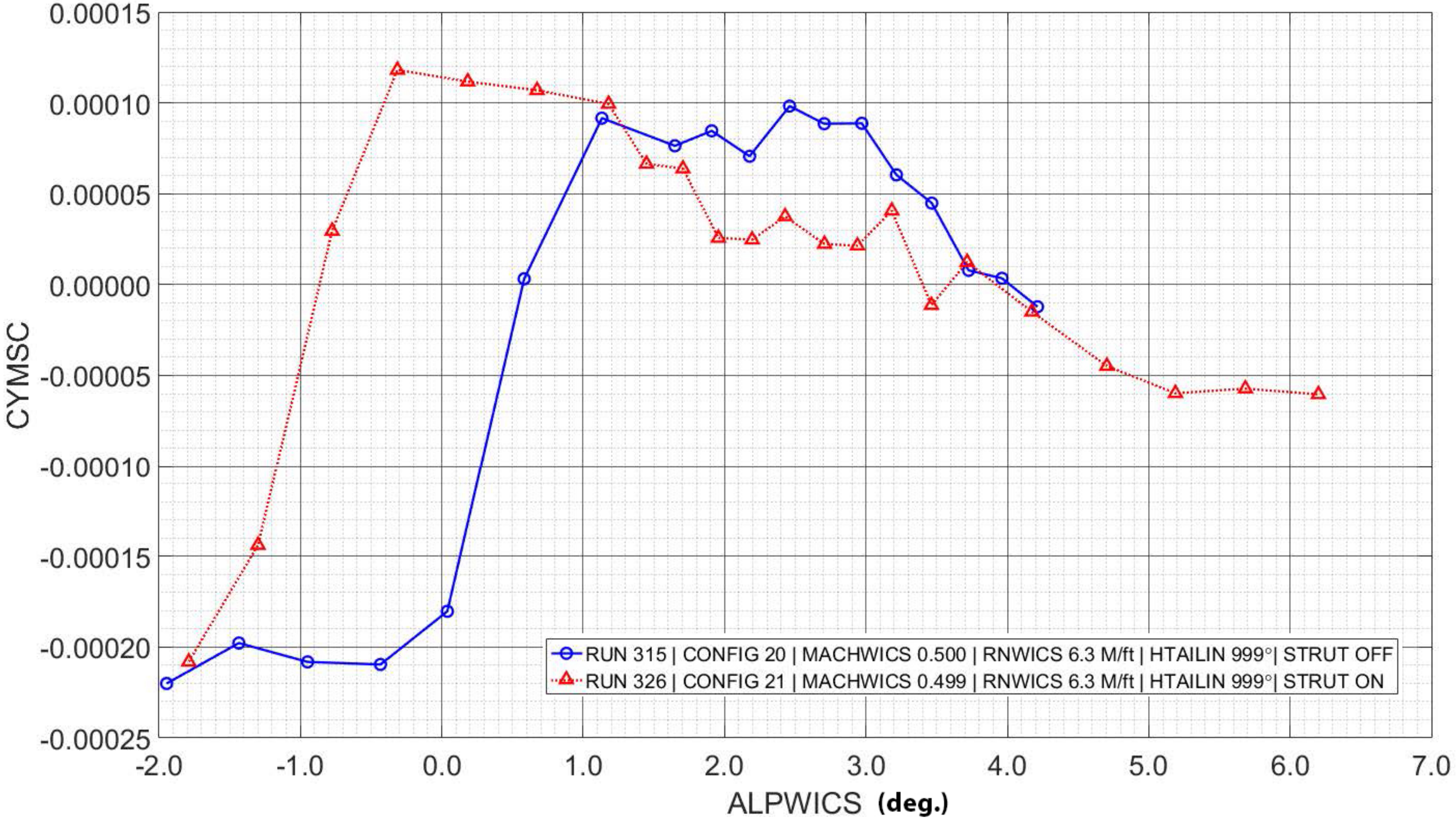

Figure A.13 – Strut effects on the yawing moment characteristics: Mach = 0.50 and unit Reynolds number = 6.3M/ft.

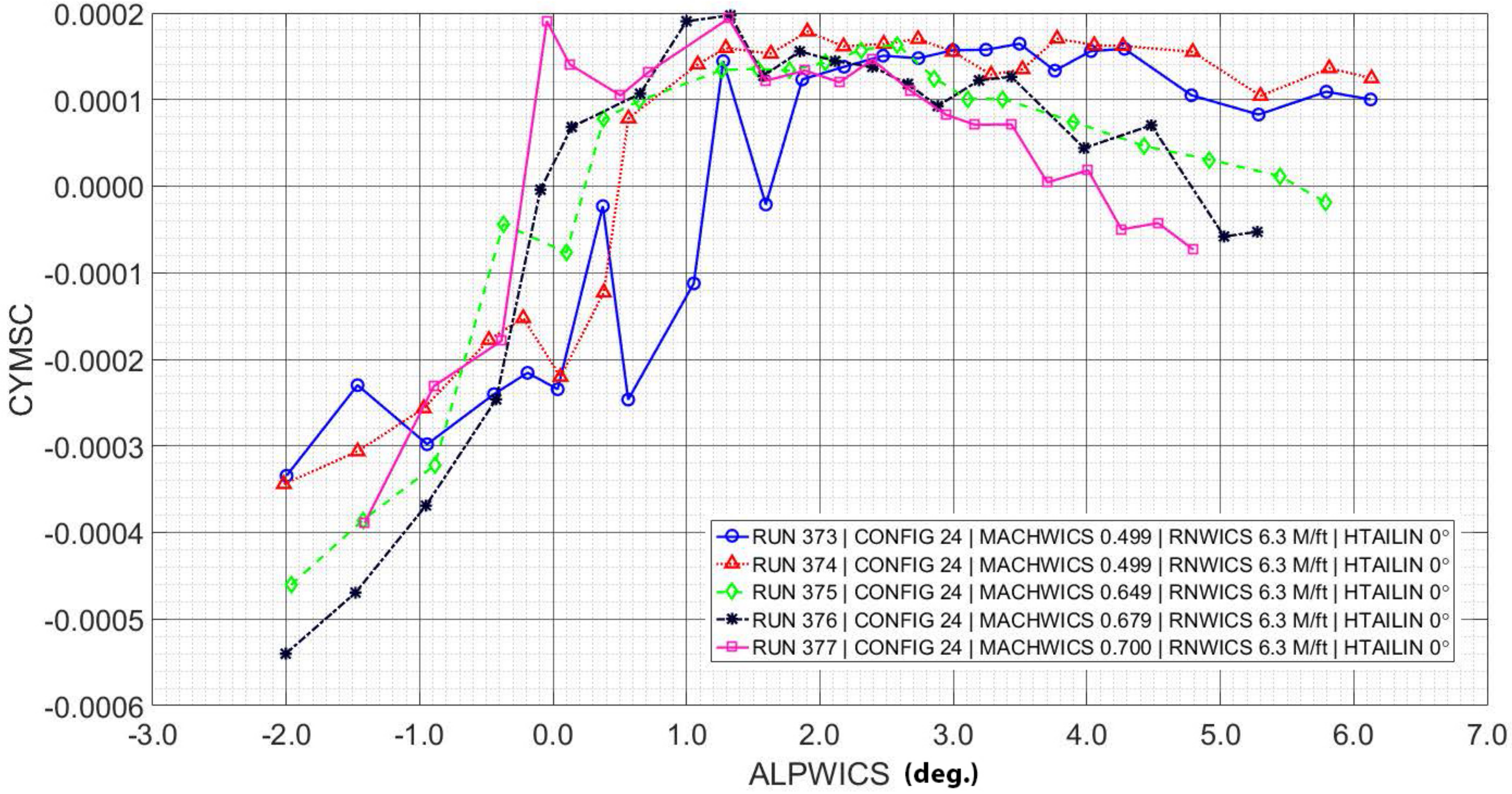

Figure A.14 – Effect of Mach number on the yawing moment characteristics: unit Reynolds number = 6.3M/ft.

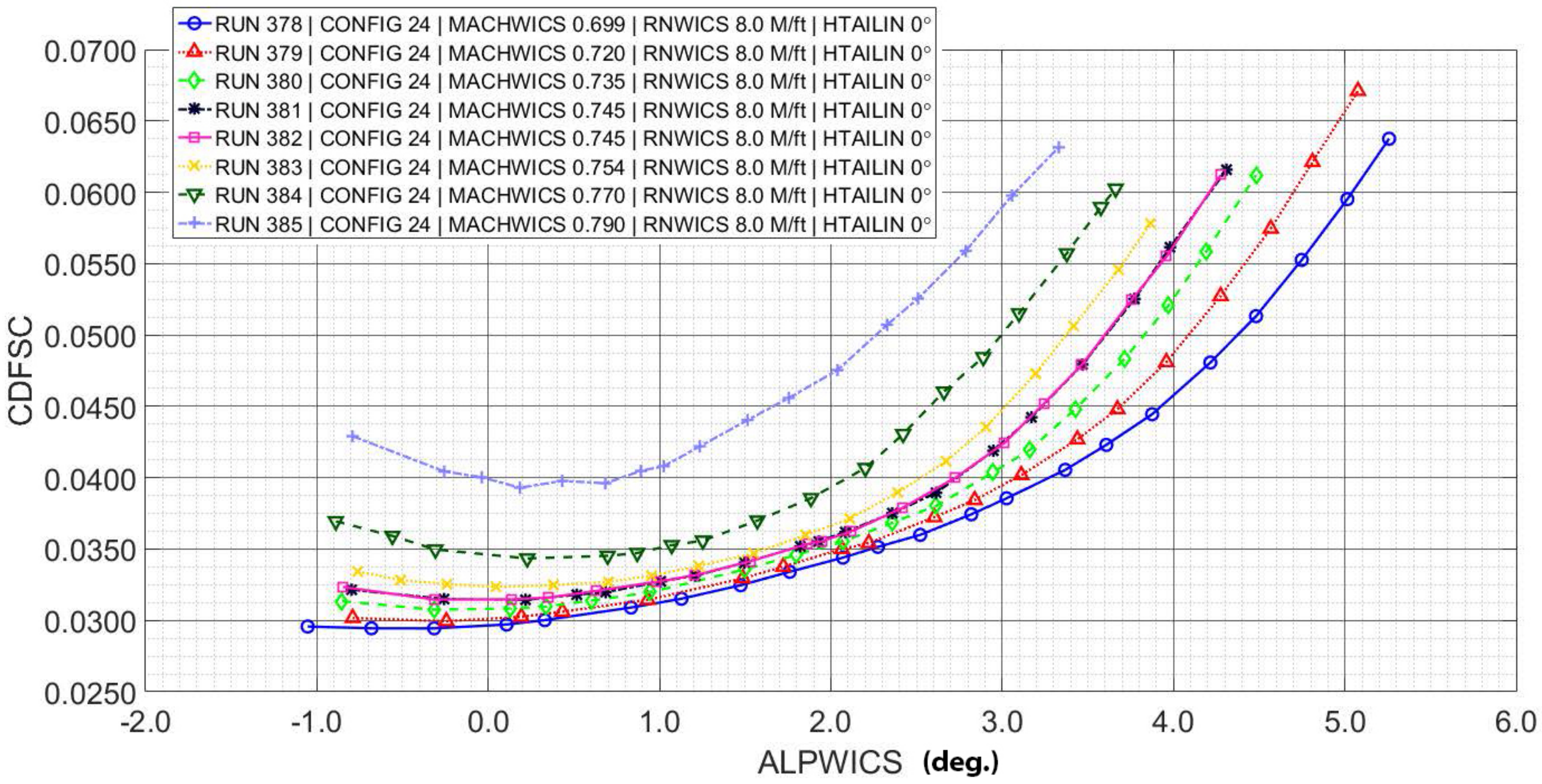

Figure A.15 – Effect of Mach number on the drag characteristics: unit Reynolds number = 8.0M/ft.

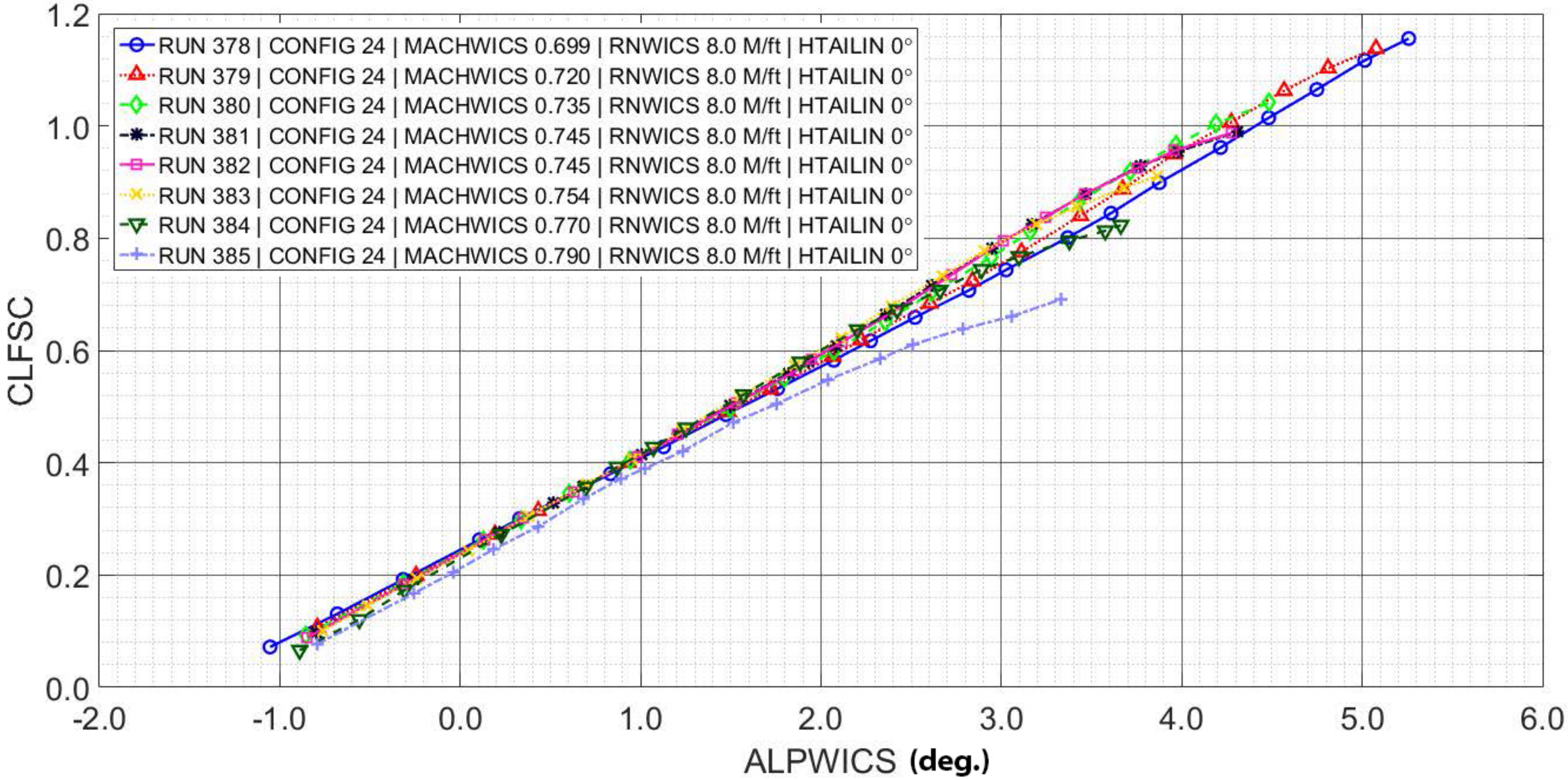

Figure A.16 – Effect of Mach number on the lift characteristics: unit Reynolds number = 8.0M/ft.

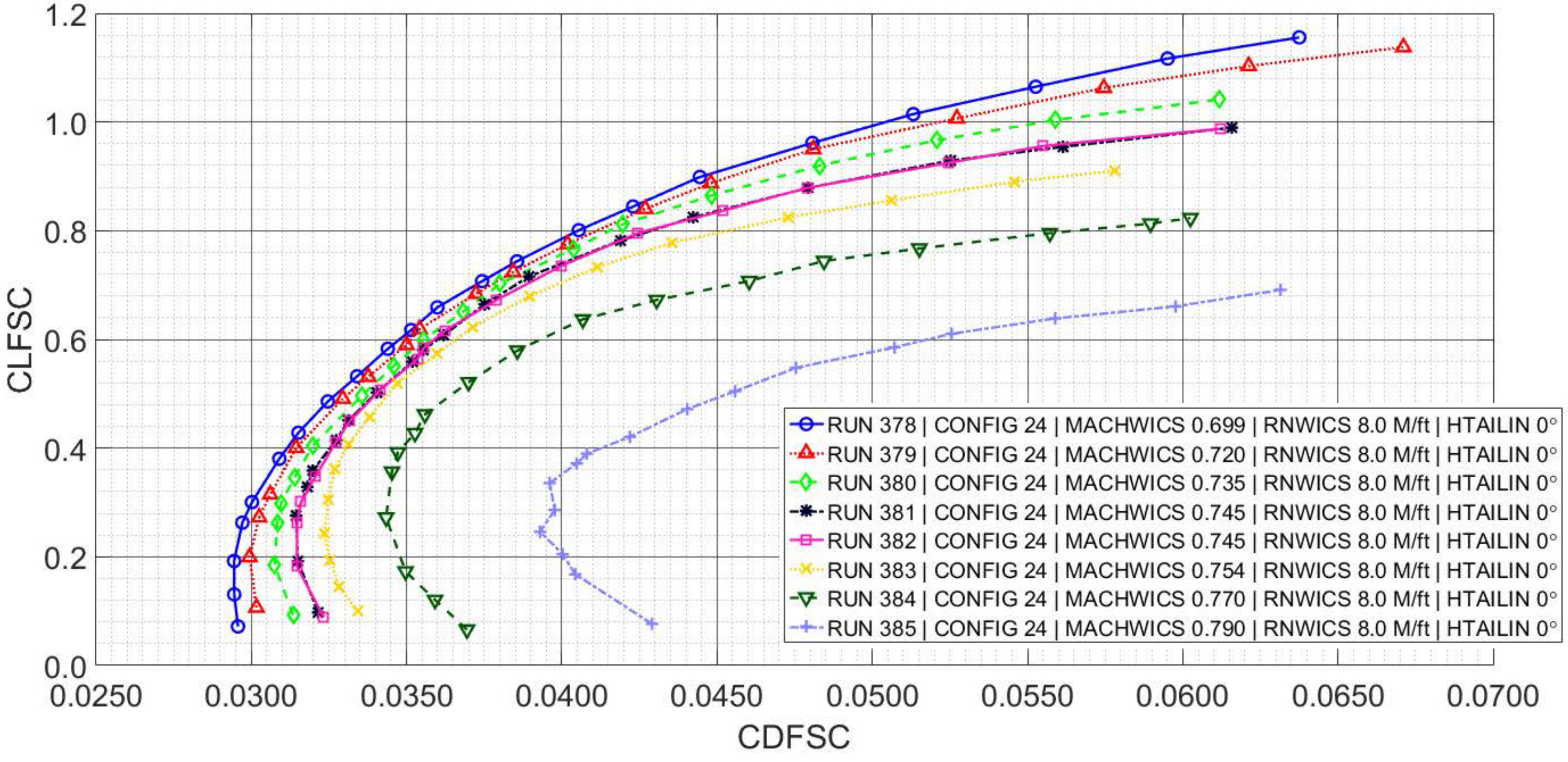

Figure A.17 – Effect of Mach number on the drag polar: unit Reynolds number = 8.0M/ft.

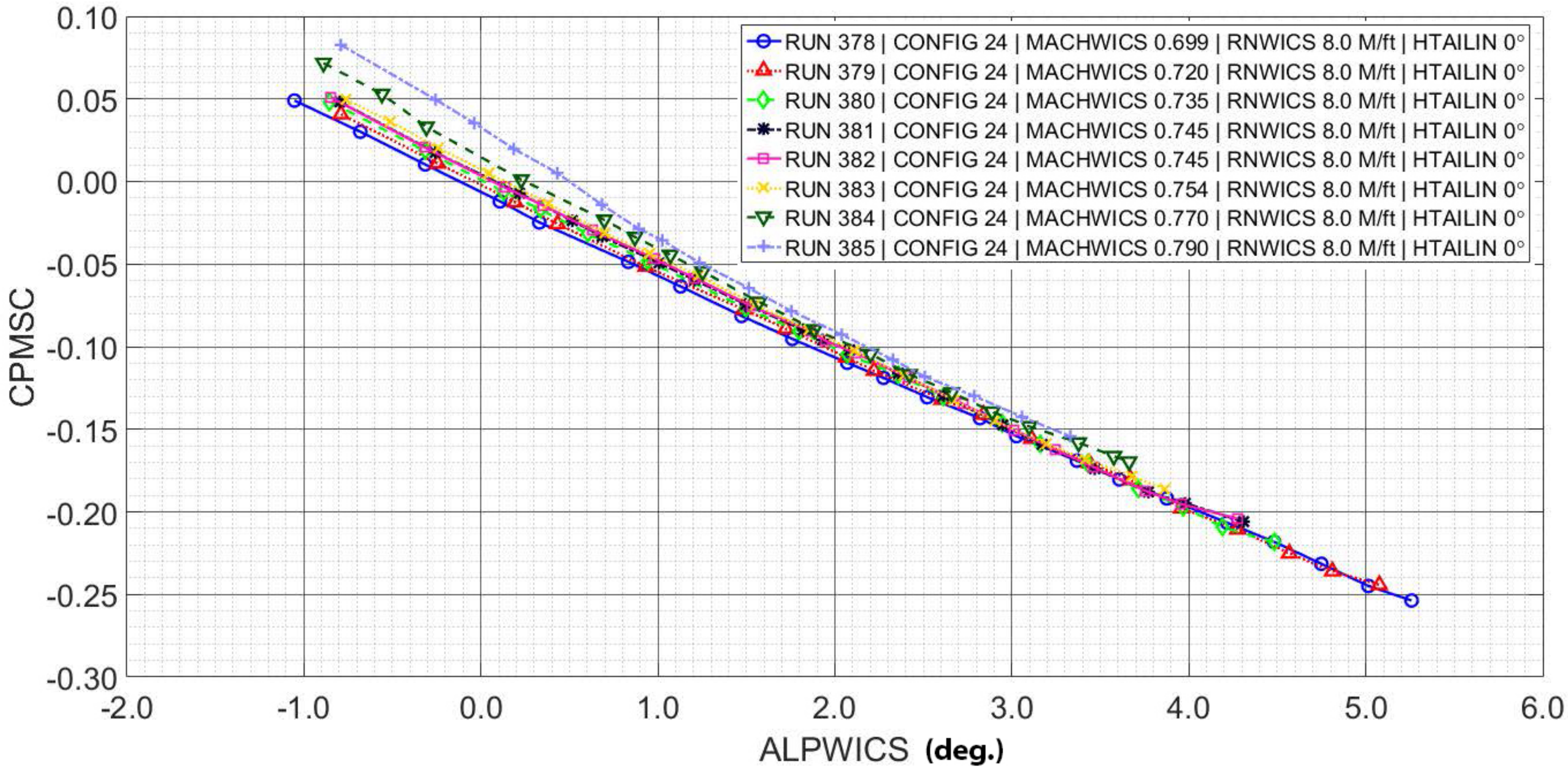

Figure A.18 – Effect of Mach number on the pitching moment characteristics: unit Reynolds number = 8.0M/ft.

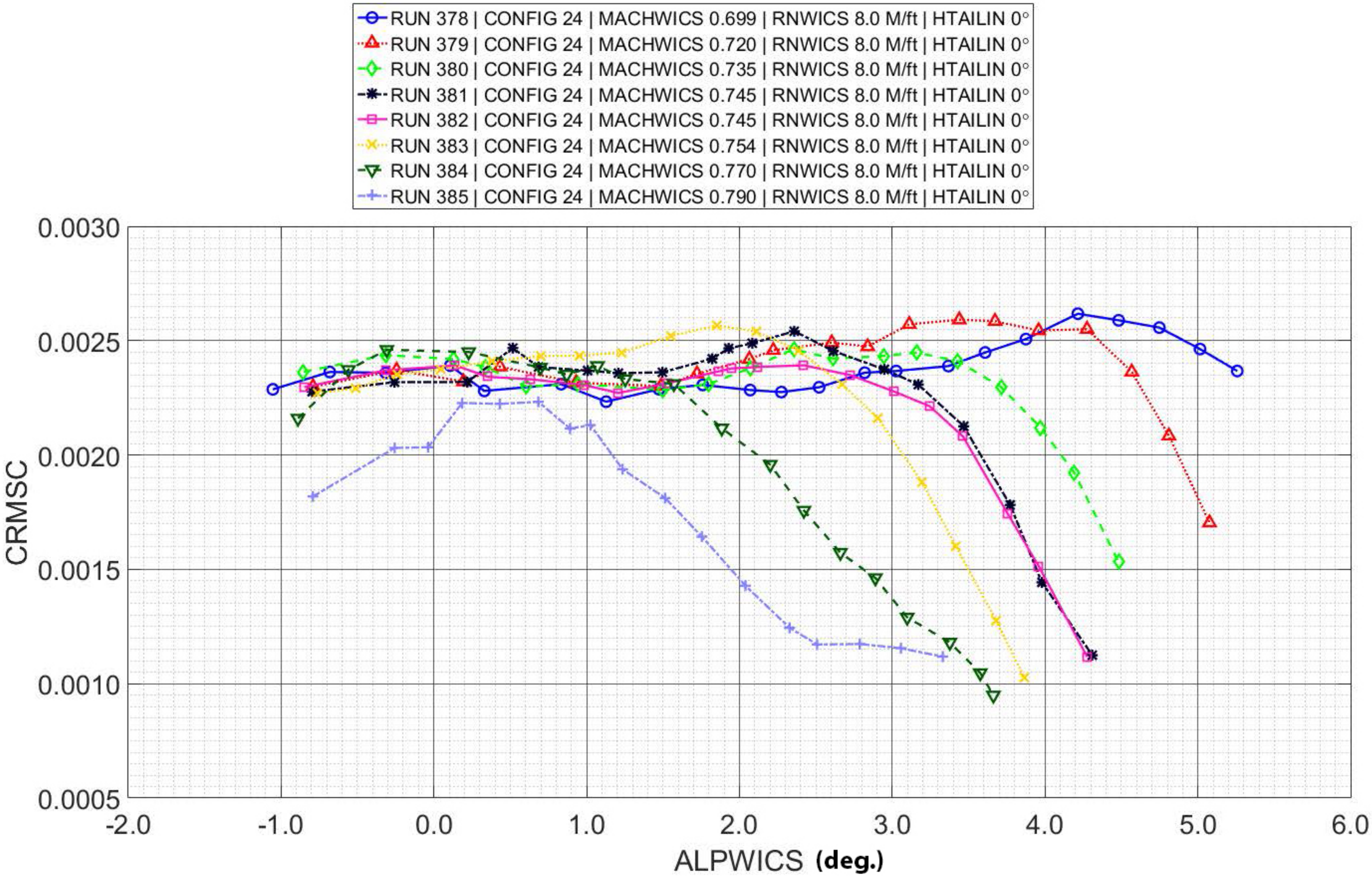

Figure A.19 – Effect of Mach number on the rolling moment characteristics: unit Reynolds number = 8.0M/ft.

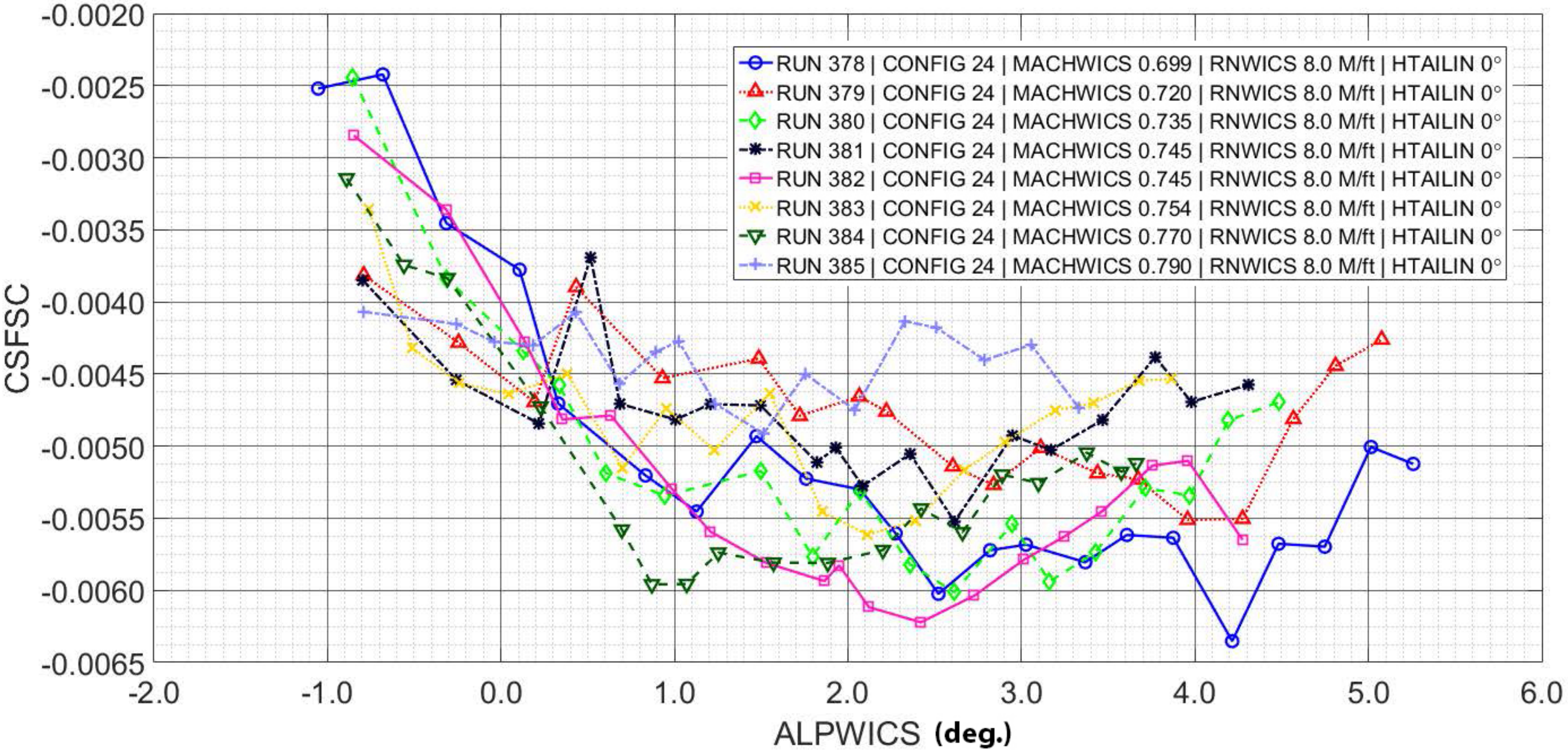

Figure A.20 – Effect of Mach number on the side force characteristics: unit Reynolds number = 8.0M/ft.

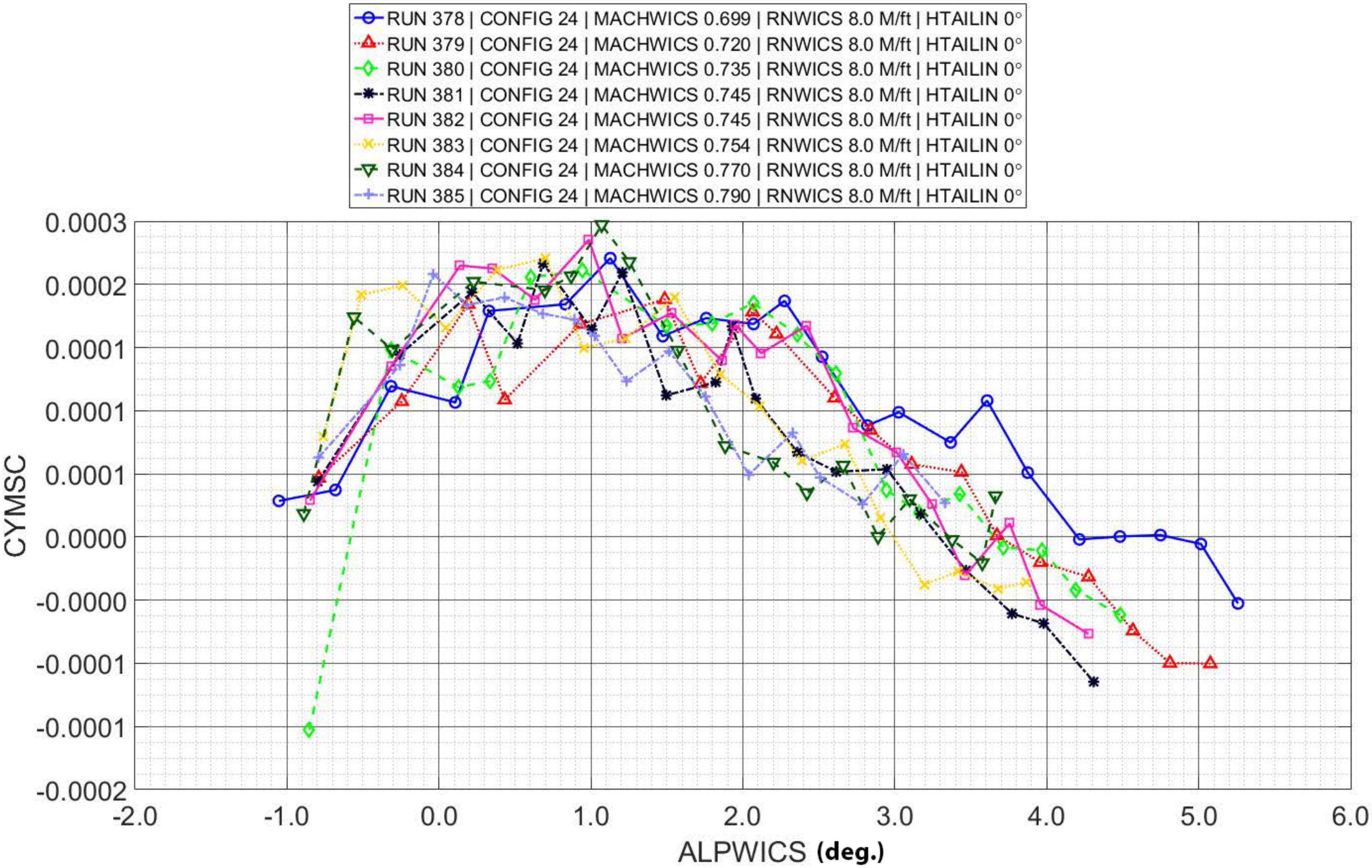

Figure A.21 – Effect of Mach number on the yawing moment characteristics: unit Reynolds number = 8.0M/ft.

REPORT DOCUMENTATION PAGE	*Form Approved* *OMB No. 0704-0188*

1. REPORT DATE *(DD-MM-YYYY)* 01-09-2020	**2. REPORT TYPE** Contractor Report	**3. DATES COVERED** *(From - To)* JULY 2014 - OCTOBER 2016

4. TITLE AND SUBTITLE Subsonic Ultra Green Aircraft Research: Phase III – Mach 0.75 Transonic Truss-Braced Wing Design	**5a. CONTRACT NUMBER** NNL10AA05B
	5b. GRANT NUMBER
	5c. PROGRAM ELEMENT NUMBER
6. AUTHOR(S) Droney, Christopher K.; Sclafani, Anthony J.; Harison, Neal A.; Grasch, Adam D.; Beyar, Michael D.;	**5d. PROJECT NUMBER**
	5e. TASK NUMBER NNL14AB51T
	5f. WORK UNIT NUMBER 081876.02.07.02.01.02
7. PERFORMING ORGANIZATION NAME(S) AND ADDRESS(ES) NASA Langley Research Center Hampton, Virginia 23681-2199	**8. PERFORMING ORGANIZATION REPORT NUMBER**
9. SPONSORING/MONITORING AGENCY NAME(S) AND ADDRESS(ES) National Aeronautics and Space Administration Washington, DC 20546-0001	**10. SPONSOR/MONITOR'S ACRONYM(S)** NASA
	11. SPONSOR/MONITOR'S REPORT NUMBER(S) NASA-CR-20205005698

12. DISTRIBUTION/AVAILABILITY STATEMENT
Unclassified---
Subject Category: Aerodynamics
Availability: NASA STI Program (757) 864-9658

13. SUPPLEMENTARY NOTES

Langley Technical Monitor: Gregory M. Gatlin

14. ABSTRACT

This design report summarizes the Transonic Truss-Braced Wing (TTBW) work accomplished by the Boeing Subsonic Ultra-Green Aircraft Research (SUGAR) team during the time period of July 2014 through October 2016 under SUGAR Phase III.

15. SUBJECT TERMS

Truss-Braced Wing; Transonic; Commercial transport

16. SECURITY CLASSIFICATION OF:			**17. LIMITATION OF ABSTRACT**	**18. NUMBER OF PAGES**	**19a. NAME OF RESPONSIBLE PERSON**
a. REPORT	**b. ABSTRACT**	**c. THIS PAGE**			STI Help Desk(email help@sti.nasa.gov)
					19b. TELEPHONE NUMBER *(Include area code)*
U	U	U	UU	261	(757) 864-9658